PEELING OF PLATES ADHESIVELY BONDED TO REINFORCED CONCRETE BEAMS

by

M.S. Mohamed Ali Sahib
B.E.(Hons)(Civil Engg.,)(Madurai, India)
M.E.(Structural Engg.,)(Anna University, Madras, India)

A thesis presented for the degree of

Doctor of Philosophy (Ph.D)

DEPARTMENT OF CIVIL AND ENVIRONMENTAL ENGINEERING,
THE UNIVERSITY OF ADELAIDE, ADELAIDE.

July 2000

ABSTRACT

The technique of adhesively bonding steel or fibre reinforced plastic (FRP) plates to the surfaces of reinforced concrete (RC) structural elements is being adopted worldwide to strengthen or repair RC buildings and bridges as it is inexpensive and unobtrusive. It can be used for both strengthening and stiffening and also for reducing crack sizes. However, the prevention of premature debonding or peeling of external plates bonded to RC beams and slabs is the most significant design aspect. Hence, the theme of the present research is to thoroughly study the peeling mechanism in plated beams.

Fifty eight beam tests were carried out on simply supported RC beams bonded with steel or FRP plates to investigate the different debonding modes such as: shear peeling, flexural peeling, the interaction between shear and flexure peeling: and axial peeling. The major contribution of this thesis is towards the shear peeling mechanism and the development of comprehensive analytical procedures to quantify the shear peeling strength of steel plated beams. Design rules are developed for shear peeling, axial peeling and the interaction between shear and flexural peeling in steel plated beams. These design rules can be used with existing procedures for flexural peeling to produce a comprehensive design package for adhesively bonded steel plating that can now be used in practice. The other noteworthy feature is in confirming the resemblance between steel and FRP plating peeling mechanisms and the derivation of a few tentative peeling design rules for FRP plated beams.

Statement of Originality

This work contains no material which has been accepted for the award of any other degree or diploma in any university or other tertiary institution and, to the best of my knowledge and belief, the thesis contains no material previously published or written by another person, except where due reference is made in the text of the thesis.

I give consent to this copy of my thesis, when deposited in the University Library, being available for loan and photocopying.

Signature:.

20/7/2000

PUBLICATIONS

The following papers were written based on the work presented in this thesis.

Journal papers

1. Oehlers, D.J., Mohamed Ali,M.S.. and Weimin-Lou. (1998). "Upgrading continuous reinforced concrete beams by gluing steel plates to their tension faces." *Journal of Structural Engineering (ASCE)*, 24(3),224-232

2. Oehlers, D.J., Mohamed Ali, M.S. (1998) "Debonding of steel plates glued to RC flexural members." *Progress in Structural Engineering and Materials*, Vol. 1, No 2, Jan, 185-192

3. Mohamed Ali,M.S., Oehlers,D.J., Bradford,M.A. (2000). "Shear peeling of steel plates adhesively bonded to the sides of reinforced concrete beams." *Structures and Buildings, Proc.Instn. Civil Engrs.(U.K.),* Accepted for publication.

4. Mohamed Ali,M.S., Oehlers,D.J., and Park,S.M. "Comparison between FRP and Steel Plating of Reinforced Concrete Beams." Submitted for publication to *Composites-Part A* in April 2000.

5. Mohamed Ali,M.S., Oehlers,D.J., Bradford,M.A. "Shear peeling of steel plates bonded to the tension faces of RC beams." Submitted for publication to *Journal of Structural Engineering (ASCE)* in July 2000.

6. Mohamed Ali M.S., Oehlers D.J. and Bradford M.A.. "Peeling of plates bonded to the compression faces of RC beams." Submitted for publication to *ACI.* in July 2000.

7. Oehlers D.J., Wright H. and Mohamed Ali M.S. "Composite vertical shear capacity of composite profiled slabs." Submitted for publication to *Structures and Buildings, Proc.Instn. Civil Engrs.(U.K.)* in July 2000.

8. Mohamed Ali M.S., Oehlers D.J. and Bradford M.A.. "Interaction of Side plated beams and Compression Face Plated Beams. Under preparation for submission to *Magazine of Concrete Research.*

Discussion on Journal papers

1. Oehlers, D.J. and Ali, M. (1998). Discussion to "Prediction of the maximum plate end stresses of FRP strengthened beams", Magazine of Concrete Research, Dec. 1996, pp343-351. Published Magazine of Concrete Research, 50, No.1 Mar. 91-92.

Conference papers

1. Mohamed Ali,M.S, Oehlers,D.J. "Enhancing the shear capacity of reinforced concrete beams by bonding steel plates to their sides" 15th ACMSM '97, Melbourne, 1997.

2. Mohamed Ali, M.S., Oehlers, D.J. and Bradford, M. "Design rules for gluing steel plates to the tension faces of reinforced concrete beams and slabs." EASEC - 6, The Sixth East Asia-Pacific Conference on Structural Engineering and Construction, Taipei, Taiwan, R.O.C. Jan. 1998.

3. Mohamed Ali, M.S. and Oehlers, D.J. "Failure mechanism of reinforced concrete beams strengthened by gluing steel plates to the surfaces". International conference on the mechanics of structures, materials and systems." University of Wollongong, February 1999.

4. Mohamed Ali M.S., Oehlers, D.J. and Park S.M. Comparison between FRP and Steel Plating of Reinforced Concrete Beams. ACUN-2: Composites in the Transportation Industry. February 2000, University of New South Wales.

ACKNOWLEDGEMENTS

In the Name of Allah, the Beneficent, the Merciful. May His Peace and Blessings be upon the Holy Prophet Muhammad and his beloved companions.

At the outset, I would like to express my sincere gratitude and indebtedness to Dr.D.J.Oehlers for his enlightening and inspiring guidance, motivating and encouraging supervision and the optimism he reposed in my endeavour. I deem it a great honour to have worked with such an internationally recognised expert on composite structures for the past four years.

I am grateful to Prof.Mark Bradford, University of New Southwales for the useful interaction during the course of this work and his kindness in permitting the usage of funds from an Australian Research Council grant that was jointly managed by Prof. Bradford and Dr.Oehlers. Many thanks are due to Dr. William Kaggwa, Senior Lecturer in Civil Engineering at Adelaide University for his clarifications and explanation on the theory of plasticity concepts that formed the basis of the mathematical models developed in this thesis.

This research project involved enormous amount of testing on plated concrete beams and Mr.David Hale, Laboratory Technician played a crucial role in it. I am sincerely grateful for his efforts, excellent workmanship and timely co-operation.

I am thankful to the academics, staff and fellow post-graduates for their kindness, advice and assistance. My special thanks are due to Dr.Carr, Dr. Rudi, Dr.Ninh, Bernie, Diane and Marfique Ahmed.

I was sponsored by a Scholarship provided by AUSAID and a study leave by my employer Director, Central Road Research Institute (CRRI), New Delhi. I am thankful to Prof.D.V.Singh, the former Director of CRRI for granting a long study leave of four years. I also thank the officials of Australian High Commission at New Delhi for their help in realising such a wonderful ADCOS Scholarship. I am thankful to all my colleagues at Bridges Division of CRRI, particularly to Sh..M.V.B.Rao, Dr.Laxmi Kantha Rao and Sh.S.K.Sharma for their help. My special thanks are due to Thiru.Rangarajan and Dr.Sunil Bose for their kindness and encouragement.

I deeply appreciate the love and affection I received from my mother, wife, children, maternal uncle, brothers and sisters. It is their prayers and well wishes that kept me going. I thank and remember with humility and emotion my father who lives in my heart.

Finally, I dedicate this thesis to Hazrat Fatima and her two beloved sons Imam Hasan and Imam Husain as a mark of respect and love.

PEELING OF PLATES ADHESIVELY BONDED TO REINFORCED CONCRETE BEAMS

TABLE OF CONTENTS

Peeling of plates adhesively bonded to reinforced concrete beams

M.S. Mohamed Ali Sahib

Errata:

page 31 line 13: 'formation' should read 'formation of'.
page 60 lines 14 and 15: 'Ehasni' should read 'Ehsani'.
page 65 line 10: 'Meir' should read 'Meier'.
page 107 line 3: 'Rostacy' should read 'Rostasy'.
page 111 lines 7 and 8: 'Coulomb' should read 'Coloumb'.
page 112 line 22: 'Coulomb' should read 'Coloumb'.
page 113 line 10: 'Coulomb' should read 'Coloumb'.
page 115 line 14: 'Coulomb' should read 'Coloumb'.
page 122 line 6: '19977' should read '1997'.
page 468 line 12: 'they' should read 'it'.
page 579 line 11: 'Ahamed' should read 'Ahmed'.

NOTATIONS

a	shear span; distance between centre of support plate and edge of load plate
a_0	distance between the tip of diagonal crack and the edge of the support plate in beams subject to uniformly distributed load
A	transformed area of plate
A_{frp}	total area of FRP plates
A_{isp}	transformed area of side plates crossing the inclined plane of the crack
A_p	area of plates
A_s	area of longitudinal reinforcement
A_{sc}	area of compression reinforcement
A_{sof}	effective area of soffit plates in angle plated beams
A_{sp}	area of side plates
$A_{sp.eff}$	effective area of side plates allowing for partial anchorage
A_{st}	area of tension reinforcement
A_{sv}	area of the shear stirrup
A_{tfp}	area of tension face plate
$A_{tfp.eff}$	effective area of tension face plate
b	width of beam; the dimension of the body perpendicular to the n,t plane
B	bond force
b_{cfp}	width of compression face plate
b_p	width of plate
b_{sof}	width of soffit plate of an individual angle
b_{tfp}	width of tension face plate
b_w	width of beam web
c	cohesion
C	an empirical constant; net compressive force
C_1, C_2	constants of integration
c_{all}	allowable coefficient of shear cohesion for the epoxy concrete-steel surface
c_{eff}	effective cohesion
cfp	compression face plate
d_0	distance of the extreme compression fibre of the concrete to the centroid of the outermost layer of tensile reinforcement
d_{bot}	distance between the bottom of the side plate and bottom of the concrete beam
d_{sc}	distance between centroid of compression reinforcement and the concrete beam top
d_{se}	distance between centroid of prestressing tendon and the concrete beam top
d_{st}	distance between centroid of tension reinforcement and the concrete beam top
d_{sp}	depth of an individual side plate
d_{top}	distance between beam top and plate top
E_c	Young's modulus of concrete
E_{frp}	elastic modulus of FRP plate

E_p	Young's modulus of plate
$E_{p,long}$	Young's modulus of FRP plate along the longitudinal axis
E_s	Young's modulus of steel
$(EI)_{cp}$	flexural rigidity of cracked plated section
f	plastic potential function
f_1, f_2, f_3	parameters used in computing the effective factor γ_0
f_4	function dependent on prestressing level in computing $\gamma_{0.se}$
f_b	Brazilian tensile strength of concrete
f_c	cylindrical compressive strength of concrete
f_c^*	effective compressive strength of concrete
F_c	total compressive force in the plated concrete beam
F_{cc}	total compressive force in the concrete section
F_{cp}	total compressive force in both the side plates
f_{ctm}	concrete surface tensile strength
f_{cu}	cube strength of concrete
F_{ic}, F_{jc}	force in ith and jth slices of the concrete section
F_{ip}, F_{jp}	force in ith and jth slices of the side plates
FRP	fibre reinforced plastic
F_{sc}	force in compression steel
F_{se}	prestressing force
F_{st}	force in tension steel
$f_{sy,f}$	yield strength of shear stirrup
f_t	tensile strength of concrete
F_t	total tensile force in the plated concrete beam
f_{tbm}	beam tensile strength of concrete
F_{tc}	total tensile force in the concrete section
f_{tef}	effective tensile strength of concrete
F_{tp}	total tensile force in both the side plates
f_y	yield strength of reinforcement
f_{yp}	yield strength of plate material
f_{ysc}	yield strength of the compression steel
f_{yst}	yield strength of the tension steel
f_u	ultimate strength of reinforcement
f_{up}	ultimate strength of plate material
G_a	shear modulus of adhesive
G_{int}	overall interfacial shear modulus
h	depth of beam
h_j	depth of jackets
h_s	depth of FRP strips
h_{cmp}	depth to neutral axis of composite plated section
h_p	depth to plate; effective depth of plate
$h_{p,bnd}$	height of the angle bonded to the side
h_w	depth of wings
i	individual test result
I_{cmp}	second moment of area about neutral axis of fully composite section transformed to steel

I_p	second moment of area of plate about its centroid
k	an experimental constant; $\frac{1+\sin\phi}{1-\sin\phi}$ in theory of plasticty
K	constant equal to $2\,k_1k_2s$
k_1, k_2	coefficients that define the shape of bond stress distribution
k_b	factor accounting for the relative widths of plate and beam
k_{cfp}	coefficient of peeling moment of compression face plated beam
k_{tfp}	coefficient of peeling moment of tension face plated beam
K	a constant equal to $2k_1k_2s$
K_n	normal stiffness/ unit length of adhesive layer
K_s	hear stiffness/unit length of adhesive layer
L	span of beam
la_{sp}	lever arm of the force component exerted by side plate from load plate edge
L_b	bond length of plate
$L_{b,e}$	active bond length
$L_{b.sof}$	bond length of a soffit plate in angle plated beam
$L_{b.sp}$	bond length of a side plate in angle plated beam
$L_{d.crit}$	location of critical diagonal crack from support
L_{end}	distance from plate-end to support
L_i	measured initial transfer length in a composite joint
L_{in}	bond length of the side plate from the tension face plate end to the inner edge of the side plate
L_{isp}	length of side plate crossing the inclined crack plane
L_o	length of support plate
L_{sp}	length of external side plate
L_{min}	minimum bond length
L_{out}	bond length of the side plate measured from the end of tension face plate to the outer edge of the side
l_p	lever arm of the shear force component in side plates from the edge of load plate
L_t	length of the transverse stress distribution
m	modular ratio (E_p/E_c); mean test result
M	applied moment ; ultimate moment capacity of the beam
mc	number of slices in the concrete beam below the neutral axis
M_{end}	applied moment at plate-end
mp	number of slices in the side plate below the neutral axis
M_{pure}	moment to cause peeling in region of pure moment; flexural peeling strength
$M_{pure.a}$	flexural peeling capacity of angle plated beams
$\left(M_{pure,a}\right)_{side}^{mean}$	mean flexural peeling resistance assuming the angle is bonded only to the side
$\left(M_{pure,a}\right)_{soff}^{mean}$	mean flexural peeling resistance assuming the angle is bonded only to the soffit
$M_{pure.cfp}$	flexural peeling capacity of compression face plated beams

$M_{pure.frp}$	flexural peeling capacity of FRP plated beams
$M_{pure.sp}$	flexural peeling capacity of t side plated beams
$M_{pure.steel.eqv.}$	theoretical mean flexural peeling strength of the beam plated with a steel plate having the same thickness as that of the FRP plate
$M_{pure.tfp}$	flexural peeling capacity of the tension face plated beams
$M_{pure.test}$	experimental flexural peeling strength
$M_{pure.theory}$	theoretical flexural peeling strength
$M_{tfp\text{-}end}$	bending moment at the tension face plate end
nc	number of slices in the concrete beam above the neutral axis
np	number of slices in the side plate above the neutral axis
ns	number of slices in the concrete beam
p	uniformly distributed load intensity per unit area over the entire span of the beam
P	applied load
P_b	bond strength of a plated beam
$P_{b.max}$	maximum bond strength of a plated beam
$P_{b.sof}$	bond strength of soffit plates in angle plated beams
$P_{b.sp}$	bond strength of side plates in angle plated beams
$(P_b)_y$	yield strength of the plates
P_c	axial load in concrete prism
p_{cr}	intensity of the uniformly distributed load needed to cause shear crack in a beam
P_{cr}	applied concentrated load needed to cause shear crack in a fixed or continuous beam
P_s	axial load in steel plate
p_u	intensity of the uniformly distributed load needed to cause shear failure in a beam
R	$\varepsilon_{frp.e}/\varepsilon_{frp.u}$; ratio of effective strain ($\varepsilon_{frp.e}$) to the ultimate strain of FRP plates ($\varepsilon_{frp.u}$)
RC	reinforced concrete
s	spacing of the shear stirrup
S	non-dimensionalised stress
$s(h)$	factor for the reduction in tensile strength due to size effect
sf_t	mean stress in the tensile region of transverse stress distribution
sp	side plate
s_s	spacing of FRP strips
T	net tensile force
t_a	adhesive thickness
t_{cfp}	thickness of compression face plate
t_p	plate thickness
tfp	tension face plate
t_{sof}	thickness of soffit plate of an individual angle
t_s	thickness of FRP strips; thickness of a single slice
t_{sp}	thickness of an individual side plate
t_{tfp}	thickness of tension face plate

u_n, u_t	displacements along the n and t axes
V	applied vertical shear force
V_{cr}	shear load required to cause a shear crack at a given location in reinforced concrete beam
$V_{cr.angle}$	shear load required to cause a shear crack at a given location in a beam bonded with steel angles to both sides and soffits
$V_{cr.se}$	shear load required to cause a shear crack at a given location in a prestressed concrete beam
$V_{cr.sp}$	shear load required to cause a shear crack at a given location in a side plated beam
$V_{cr.tfp}$	shear load required to cause a shear crack at a given location in a tension face plated beam
$V_{cr.udl}$	shear load required to cause a shear crack at a given location in reinforced concrete beam subject to uniformly distributed load
V_{cr}^{I}	shear load needed to cause a critical diagonal crack at a distance from the support (Stage I crack) in a compression face plated beam
V_{cr}^{II}	shear load required to cause a debonding crack from the tip of the stage I crack that propagates along the bottom edge of the plate to the load point (Stage II crack) in a compression face plated beam
V_{cr}^{III}	shear load at the formation of Stage III crack in a compression face plated beam
V_{end}	applied shear at plate-end
V_{frp}	theoretical shear capacity of the external FRP plates
V_{max}	maximum shear load sustained by the shear span
V_{pure}	shear load to cause peeling in region of predominant shear; shear peeling strength
$V_{pure.angle}$	shear peeling strength of angle plated beam
$V_{pure.cfp}$	shear peeling strength of compression face plated beam; V_{cr}^{III}
$(V_{pure})_{exp}$	experimental shear peeling strength
$(V_{pure})_{th}$	theoretical shear peeling strength
$V_{pure.sp}$	shear peeling strength of side plated beam
$V_{pure.tfp}$	shear peeling strength of tension face plated beam
$V_{pure.nsp}$	pure shear peeling capacity of tension face plated beam with no side plates
$V_{pure.wsp}$	pure shear peeling capacity of tension face plated beam bonded with with additional sides
$V_{tfp\text{-}end}$	shear force at the tension face plate end
V_u	ultimate shear strength of the reinforced concrete beam; shear load needed to cause shear failure along an existing crack
$V_{u.angle}$	shear load required to cause shear failure in a beam bonded with angles to both sides and soffits
$V_{u.tfp}$	shear load required to cause shear failure in a tension face plated beam
V_{uc}	shear strength of reinforced concrete beam without stirrups
$V_{uc.expt}$	shear strength of the beam without stirrups as determined from experiment
V_{us}	shear strength of internal shear stirrups
$V_{u.se}$	shear load required to cause shear failure in a prestressed concrete beam

$V_{u,sp}$	shear load required to cause shear failure in a side plated beam
$V_{u,udl}$	shear load required to cause shear failure in reinforced concrete beam subject to uniformly distributed load
W_E	external work done
W_I	internal work done when sliding takes place along the crack
W_l	work done per unit length
x	horizontal projection of diagonal crack
x_{crit}	horizontal projection of critical diagonal crack
y	distance from the neutral axis to the centroid of the plate
y_{ic} ,y_{jc}	depth of *i*th and *j*th concrete slices from the top of the cross section
y_n	depth of neutral axis from the topmost compressive fibre of the concrete beam
z	ratio of applied load to the maximum load ($P_{b,max}$)
z_o	ratio of load at first cracking in concrete to the maximum load ($P_{b,max}$)
α_v	inclination of the shear stirrup
β	orientation of the fibres in FRP plate to the longitudinal axis of the beam
Δ_{max}	maximum recorded beam deflection
ε_o	ratio of load at first cracking in concrete to the maximum load ($P_{b,max}$)
ε_1	major principal strain
ε_3	minor principal strain
ε_{crack}	concrete cracking strain
$\varepsilon_{frp,e}$	strain in FRP at the instance of peeling ;effective FRP strain
$\varepsilon_{frp,u}$	ultimate strain of FRP plates
ε_{ic}, ε_{jc}	strain at the middle of *i*th and *j*th slices in the concrete cross section
ε_{ip}, ε_{jp}	strain at the middle of *i*th and *j*th slices in the side plates.
ε_n^p	longitudinal plastic strain
ε_n,ε_t	axial strains along the *n* and *t* axes
ε_{nor}	normalised strain
$\varepsilon_{p,max}$	maximum strain in the plate at the instance of peeling (positive is tension and negative is compression)
ε_{sc}, ε_{st}	strain at the centroid of the compression and tension reinforcement
ε_{sh}	strain hardening strain of steel
ε_t	tensile strain in concrete corresponding to the tensile strength f_t
ε_u	ultimate FRP plate strain
ε_{ult}	external plate strain at peeling
ε_y	yield strain of steel
φ	angle of friction
γ	neutral axis depth factor
γ_{nt}	shear strain in *nt* plane
γ_0	effectiveness factor
$\gamma_{0,angle}$	effectiveness factor for angle plated beam
$\gamma_{0,udl}$	effectiveness factor of RC beam subject to uniformly distributed load
$\gamma_{0,se}$	effectiveness factor of prestressed concrete beam
$\gamma_{0,sp}$	effectiveness factor for side plated beam
$\gamma_{0,tfp}$	effectiveness factor for tension face plated beam

γ_1 and γ_2	factors that define the shape of the loading and unloading portions of the concrete stress-strain curve
γ_{eff}	resulting effective factor
γ^p	plastic shear strain
γ_s	sliding reduction factor
χ	curvature
λ	an experimental constant that depends on load type;1.6 for point load and 1.2 for uniformly distributed load
μ	coefficient of friction
ρ_{frp}	ratio of the cross section area of FRP plate to the beam cross section area
$\rho_{frp}E_{frp}$	axial rigidity of the FRP sheet
ρ	longitudinal reinforcement ratio
ρ_{angle}	angle plate reinforcement ratio
ρ_{cfp}	compression face plate reinforcement ratio
ρ_0	reduction factor applied to the separation failure
ρ_{sof}	soffit plate reinforcement ratio of the angle plated beam
ρ_{sp}	side plate reinforcement ratio
ρ_{tfp}	tension face plate reinforcement ratio
σ	applied normal stress; specified compressive stress in concrete
σ_1	major principal stress
σ_2	intermediate principal stress
σ_3	minor principal stress
σ_{frp}	stress in the FRP plate at failure
σ_{ic}, σ_{jc}	stress in *i*th and *j*th slices of the concrete section
σ_{ip}, σ_{jp}	stress in *i*th and *j*th slices of the side plate
σ_{pk}	peak normal tensile stress
$(\sigma_{pk})_z$	normal stress the plate end
σ_{sc}, σ_{st}	stress at the centroid of the compression and tension reinforcement
σ_{se}	average prestressing stress
σ_u	compressive strength of concrete in 28 days
τ	shear stress due to longitudinal shear flow/ shear stress
τ_b	bond stress
τ_{ave}	average shear stress at peeling
τ^*_c	shear strength of concrete
τ_{mean}	mean shear stress
τ_{pk}	peak shear stress
$(\tau_{pk})_z$	shear stress at the plate end and
τ_{sta}	standard shear stress
τ_{ult}	interface shear strength
Δ_{max}	maximum recorded deflection
ΔV_{cr}	resistance to the formation of diagonal crack by a pair of side plates
$\Delta V_{cr.sp}$	resistance to the formation of diagonal crack by the area of side plates crossing the crack plane

$\Delta V_{cr.sof}$	resistance to the formation of diagonal crack by the inclined area of the soffit plates crossing the crack plane
ΔV_{pure}	$V_{pure.wsp} - V_{pure.nsp}$; increase in the pure shear peeling capacity due to additional side plate
ΔV_{sp}	resistance to the formation of diagonal crack by a pair of side plates in a tension face plated beam bonded with additional side plates

PART-I: INTRODUCTION

CHAPTER-1: INTRODUCTION

CONTENTS

1.1 Background

Reinforced concrete structures such as buildings and bridges require strengthening and stiffening for various reasons. This may be due to increased live loads, damages due to natural calamities like earthquakes, controlling excessive deflection and crack widths or deterioration due to corrosion. Further due to cost benefit advantage considerations, extensive rehabilitation works are preferred rather than to demolish a structure which has outlasted its original intended purpose (Raithby 1980 and Warner 1981). Some of the techniques commonly adopted for strengthening and stiffening reinforced concrete structural elements include: provision of additional reinforcement with a cast-in-place or gunited cover of concrete; the technique of external prestressing; provision of additional beams; impregnating the concrete with a polymer such as epoxy resin under high pressure; and bolting shear stirrups externally on reinforced concrete beams weak in shear (Warner 1981). Another way of strengthening and stiffening is to bond steel plates to the surfaces of the reinforced concrete beams and slabs. This technique is becoming increasingly popular for enhancing the strength and stiffness, as it is inexpensive, easy to apply, it causes the minimal disruption to moving traffic and negligible loss in headroom. However, a considerable amount of surface preparation is required to achieve a high quality bond between the steel and the concrete.

Adhesively bonding a plate to a reinforced concrete (RC) beam produces a plated beam with full interaction. Therefore, the plated beam can be analysed using all the conventional methods that are applicable to reinforced concrete structures. However, adhesively bonded plates are highly prone to premature debonding or peeling. Peeling

can severely restrict the application of plating particularly in beams. The most common forms of peeling that were identified from tests on simply supported beams glued with tension face plates, can be categorised as shear peeling, flexural peeling and the interaction between flexural and shear peeling. The failure mode depends on the location where the plate ends are terminated as shown in Figs.1.1a, 1.1b and 1.1c (Oehlers 2000).

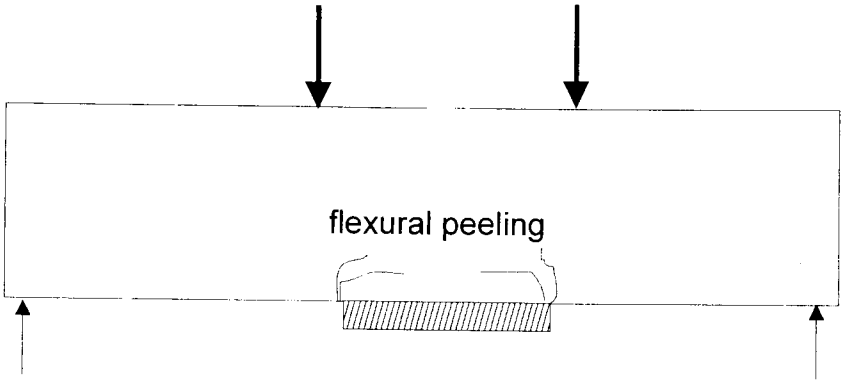

(a) Plate end in predominantly flexure region

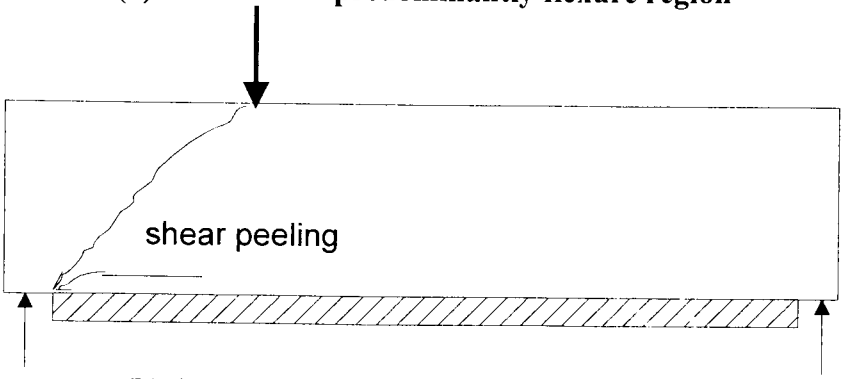

(b) Plate end in predominantly shear region

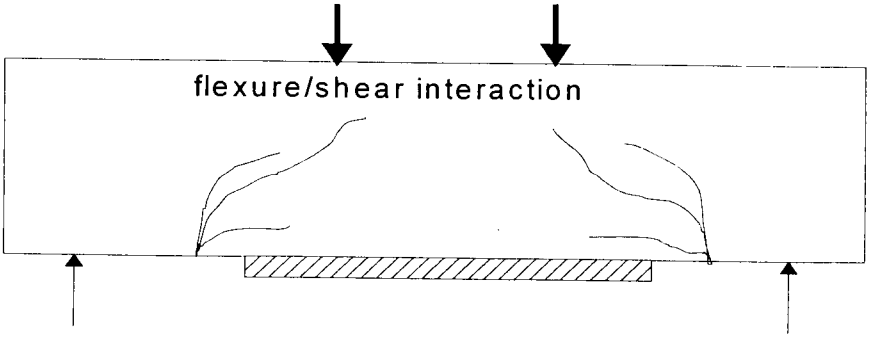

(c) Plate end subjected to flexure and shear

Fig.1.1. Peeling modes in a plated simply supported beam

Another form of peeling that occurs within the plate ends is axial peeling, as shown in Fig.1.2. Unlike shear or flexural peeling that generally occur in the vicinity of plate ends, axial peeling occurs when a flexural or shear crack crosses the plane of the plate. If no instantaneous debonding occurs as in the shear peeling at the plate ends, in theory the plates will be subjected to infinite strains. The large amount of strains in the plate has to be accommodated at the point where the crack crosses the plate by inducing debonding cracks that propagate away from the flexural cracks (Oehlers 2000).

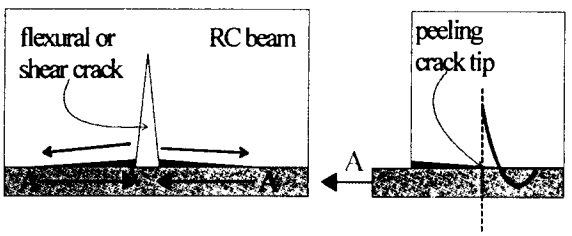

Fig.1.2. Axial peeling

1.2 Scopes and objectives

The main objective of the present study is to thoroughly investigate reinforced concrete beams adhesively bonded with plates of different configurations. Keeping this in mind, the literature was thoroughly studied and the areas that need further investigation were identified for the four major modes of debonding, i.e. flexural peeling, shear peeling, the interaction between flexural and shear peeling, and axial peeling. Then, tests were carried out to identify the parameters that influence a particular form of peeling for the configurations of the external plates used. These test results and those identified in the literature review were then used to develop mathematical models, analytical procedures and useful guidelines. It may be noted that in this study, only simply supported beams were tested and in most of the cases, steel plates were used. However, fibre reinforced plastic (FRP) plated beams were also used in order to compare their behaviour with that

of steel plated beams for flexural peeling and shear peeling. It is stressed here that the focus of this study is on debonding of the plated beams and not on the conventional full composite behaviour of the plated beams. This thesis is organised in seven parts and the contents of each part are explained subsequently.

1.2.1 Part-1: Introduction

Chapter-1 briefly introduces the topic and describes the scope and objectives of this research.

1.2.2 Part-2: Literature review

The literature review part is divided into four chapters. Chapter-2 critically reviews the work on the steel plated beams. Firstly, the different plate configurations and their evolution are described. Secondly, the experimental work on each configuration of the plated beams is categorised according to the region where the plate end is terminated. Finally, the mathematical models pertaining to each configuration of the plated beams are discussed.

In Chapter-3, the literature pertaining to the reinforced concrete beams bonded with fibre reinforced plastic (FRP) plates is reviewed. The relative advantages and disadvantages between steel plating and FRP plating are discussed first. Then, the experimental works and the mathematical models dealing with FRP plated beams are described in a similar manner to those of steel plated beams.

In Chapter-4, the experimental studies on axial peeling for both steel plated and FRP plated beams that were conducted by many researchers are presented and the available theoretical formulations are also described.

As shear-friction theory helps to understand the shear peeling phenomenon better, in Chapter-5 a review is undertaken on the analytical methods that incorporate this theory to work out the shear strength of the concrete beams. In this chapter, the basic shear-friction concepts and theory of plasticity as applied to plain concrete is discussed first and how these concepts are applied to develop a model for a simply supported, non-shear reinforced concrete beam loaded with a single concentrated load is explained. The modifications needed for uniformly distributed load and the extension of the model to fixed and continuous beams and prestressed concrete beams are also described.

1.2.3 Part-3: Shear peeling

Part-3 on shear peeling is subdivided into six chapters. The first five of these chapters deal with the experimental investigation of shear peeling of beams bonded with various plate configurations. The last chapter of Part-3 deals with the development of comprehensive mathematical models for shear peeling.

Chapter-6 deals with the tests conducted on shear peeling in reinforced concrete beams glued with steel plates to the sides. The objective of this study is to understand the parameters that influence the shear peeling in side plated beams. The main parameters varied were the position of the side plates and the presence of shear stirrups. The behaviour of side plated beams is also compared with that of a corresponding unplated beam and a tension face plated beam.

Chapter-7 describes a series of tests conducted to compare qualitatively the shear peeling mechanism in reinforced concrete beams adhesively bonded with FRP plates to their sides with that of conventional steel plated beams. The major parameter varied was the elastic modulus of the external plates used. In this chapter, the specimens, the test set-

up and the material properties are described first. Then, the observations from each test are described individually. Finally, the implications of the test results are discussed.

Continuing with the investigation of shear peeling in plated beams, the next series of tests were carried out to study the shear peeling mechanism in reinforced concrete beams bonded with steel angles to the sides and soffits. The test results, the shear peeling mechanism observed in angle plated beams and the major implications of the investigations are discussed in Chapter-8.

In practice, plates may have to be bonded to the compression face of the reinforced concrete beams as in the case of a continuous beam where a need may arise to extend the tension face plate-ends in to the hogging moment region, in order to prevent peeling of the tension face plates. In this case, the debonding models for tension face plated beams are not directly applicable to the compression face plated beams. Furthermore, plates may have to be bonded to the compression face in addition to the tension face, to improve the ductility of the over-reinforced tension face plated beams. Hence, the present study in Chapter-9 was undertaken to investigate shear peeling in compression face plated beams so as to develop debonding models. In Chapter-9, the test results from the study conducted on the pure shear peeling aspects are presented first. Then, the shear peeling behaviour of compression face plated beams is compared with that of the tension face plated beams and the salient conclusions are presented.

One way of improving the shear peeling strength of tension face plated beams is to bond additional plates to their sides in the region above the plate ends. This delays the formation and propagation of the critical shear crack at the plate end. In Chapter-10, the experimental study conducted on such beams is summarised first. Then, the

improvement in the shear peeling strength from these test results is also presented and the inferences from the test results are described.

Chapter-11 deals with the development and validation of mathematical models for shear peeling in reinforced concrete beams bonded with the different configurations of plates that were studied in Chapters-6 to 10. From these studies, the significance of the formation of the critical shear crack, its impact on debonding and the efficiency of the internal shear reinforcement in preventing shear peeling are evaluated. As only a few empirical guidelines are available for shear peeling in plated beams in the documented literature, there is a need to develop analytical procedures for a variety of plate configurations. Keeping this in mind, analytical procedures are developed by using the shear friction and crack sliding failure concepts as explained in Chapter-5. In Chapter-11, a procedure developed to compute the bond strength of the steel plated beams is described first. The subsequent sections describe the models for side plated beams, tension face plated beams, angle plated beams, compression face plated beams and tension face plated beams bonded with additional side plates. All the models are validated against the test results from the present study and also the test results from other studies. Finally, the applicability of the procedure developed for steel plated beams is verified for FRP plates bonded to the sides of the beams.

1.2.4 Part-4: Flexural peeling

Chapter-12 deals with the pure flexural peeling aspect of compression face plated beams. The tests conducted on large beams to compare the flexural peeling behaviour of compression face plated beams with that of the tension face plated beams is first discussed. Then, the tests conducted at the University of Adelaide on microbeams as a

pilot study to undertake the large beam tests are presented. Finally, the test results are used to develop a procedure to quantify the flexural peeling strength of compression face plated beams on the same line as those developed by Oehlers and Moran (1990) for tension face plated beams.

The objective of the study described in Chapter-13 is to compare the flexural peeling behaviour of RC beams bonded with FRP plates to that of conventional steel plated RC beams. The study is used to check the applicability of the mathematical models developed for steel tension face and side plated beams to FRP plated beams. The major parameter varied was the stiffness of the plate, by using different thicknesses of plate that ranged from 5 mm-32 mm and five different plate materials in which the elastic moduli ranged from 8,800-200,000 MPa. Chapter-13 is divided into three major parts. Firstly, tests conducted on tension face plated beams are discussed. Secondly, tests conducted on side plated beams are described. Finally, the test results are compared and calibrated to incorporate FRP plate into an analytical procedure.

1.2.5 Part-5: Shear/flexure interaction

Chapter-14 deals with a series of tests conducted to study the peeling behaviour of compression face plated beams when the plate ends are terminated in regions where both shear forces and bending moments are present. The study was further divided into two groups. In the first group of beams, the plate ends are subjected to the least bending moment than in the other regions of the plate. In the second group of beams, the plate ends are at a higher moment than in the other locations of the plates. The only parameter varied was the point of termination of the plate end from the support so as to place the

plate ends in regions with varying ratios of moment to shear force. Finally, interaction equations are prescribed for the compression face plated beams.

In Chapter-15, the interaction between the shear and flexural peeling of side plated beams is investigated using the available test results. A refined model for shear/flexure interaction for side plated beams is suggested.

1.2.6 Part-6: Axial peeling

Chapter-16 deals with the axial peeling of steel side plated beams that occur within the plate ends. The phenomenon is first observed through studies and then the test results are analysed for various modes of debonding. Finally, useful guidelines are presented to determine the capacity of side plated beams susceptible to axial peeling.

In Chapter-17, the peeling within plate ends of fully anchored side plated beams and tension face plated beams is investigated. The debonding phenomenon is evaluated for differing shear span to depth ratios. The test results are analysed using the methods discussed in Chapters-11 and 16.

1.2.7 Part-7: Conclusion

Chapter-18 summarises the significant conclusions derived from this study.

References

Oehlers,D.J. (2000) Development of design rules for retrofitting by adhesive bonding or bolting either FRP or steel plates to RC beams in bridges and buildings. Proceedings of the ACUN-2, International Composites Conference, Sydney. 14-18 February, 2000. Vol.1, pp.110-119.

Raithby,K.D.(1980). External strengthening of concrete bridges with bonded steel plates. TRRL Supplementary Report 415, Transport and Road Research Laboratory, Crowthorne, UK. 1980.

Warner,R.F. (1981). Strengthening, stiffening and repair of concrete, Proceedings of IABSE, May 1891, S17/89.

PART-II: LITERATURE REVIEW

CHAPTER-2: REVIEW ON REINFORCED CONCRETE FLEXURAL MEMBERS BONDED WITH STEEL PLATES TO THEIR SURFACES

CONTENTS

2.1 Introduction

The technique of adhesively bonding steel or fibre reinforced plastic (FRP) plates to the surfaces of reinforced concrete (RC) structural elements is being adopted worldwide to strengthen or repair RC buildings and bridges as it is inexpensive and unobtrusive. This technique is becoming increasingly popular for enhancing the strength and stiffness as it is inexpensive, easy to apply, it causes minimal disruption to moving traffic and negligible loss in headroom. However, a considerable amount of surface preparation is required to achieve a high quality bond between the steel and the concrete.

The main objective of this chapter is to summarise and critically review the work on the premature peeling of steel plates adhesively bonded to the reinforced concrete beams and slabs. As a first step, the constructional aspects of plate bonding and the different configurations of external plates are briefly discussed. The major part of this review describes the gains in strength and stiffness that have been achieved by plating, the different forms of debonding that have been encountered experimentally, the parameters that affect these debonding mechanisms, and the mathematical models that have been developed in an attempt to prevent premature debonding. Most of the tests are described very briefly in this chapter. However, some tests are described in detail as these test data will be used later to validate the mathematical models developed in this research project. Finally, the aspects of steel plating that need further research are identified and discussed.

2.2 Plate bonding

2.2.1 Constructional aspects

2.2.1.1 Epoxy resins

Epoxy resins possess excellent adhesion and performance in dry, damp and wet conditions. They can be used to bond all constructional materials and they are the most suitable structural adhesives to bond concrete and steel surfaces. Moreover, they are highly resistant to the attack of acids, oils, alkalis and solvents (Raina 1988, Rao, Ali and Kurmi 1992). Epoxy resin systems consists of a resin and a hardener responsible for curing and hardening. At normal ambient temperature, the mixed resin and hardener react chemically to transform from a liquid state to solidify in a matter of minutes without thermal shrinkage.

2.2.1.2 Surface preparation and bonding procedure

Proper surface preparation of both the concrete and steel plate is a prerequisite for the successful plate bonding. The concrete surface should be grit blasted or abraded with a grinder to remove laitance and expose the aggregates. The surface should then be brushed mechanically to remove all loose particles. The remaining dust and debris should be removed by blowing air (Adams and Wake 1984, Raithby 1980).

The external plates need thorough sand blasting to remove completely rust or loose particles. The steel surface should also be free from grease, oil or moisture. Grease should be removed by applying non-inflammable solvents such as trichloro-ethylene and carbon tetra chloride. Traces of solvents or moisture should be removed by blowing hot air over the surface.

The adhesives should be mixed strictly to the specifications recommended by the resin manufacturer and there should not be any air bubble or voids entrapped in the adhesive when cured. The adhesive is applied to the steel plate and then the plate

is pressed onto the concrete all over, and surplus adhesive is squeezed out at the edges.

2.2.2. Plate Configurations

2.2.2.1 Tension face plated beams

The different configurations of plating studied in the literature are shown in Fig.2.1. The most common form of plating is to bond steel plates to the tension faces of beams as shown in Fig. 2.1a as the plate is at its furthest extremity from the compression region and, hence, the composite flexural action is at its maximum (Mcdonald 1982 and Swamy, Jones and Bloxham 1987).

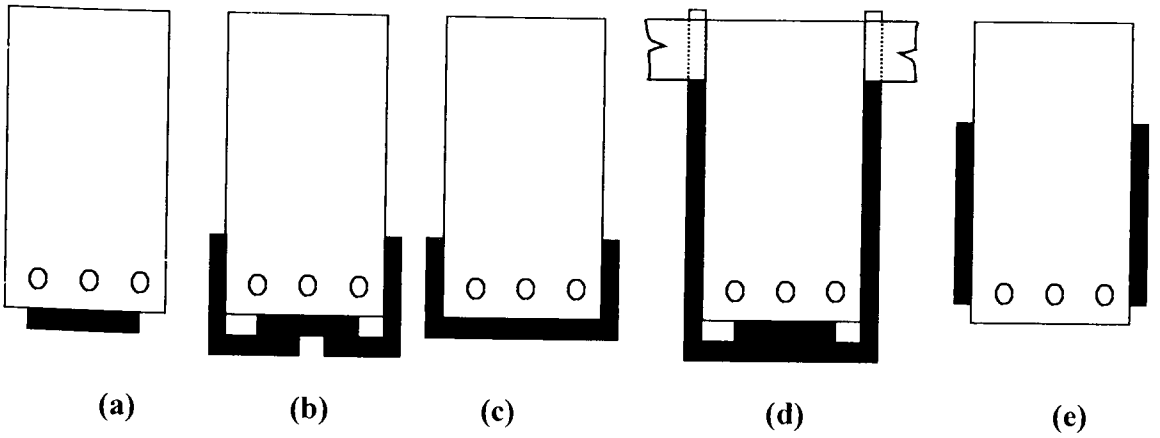

Fig. 2.1. Types of plating

2.2.2.2 Evolution of other forms of plating

The tension face plates have a tendency to peel away from the reinforced concrete beam, as shown in Figs. 2.2, 2.3, and 2.4. The peeling mode shown in Fig.2.2 depends on the curvature of the beam at the plate end and is referred as flexural peeling (Oehlers and Moran 1990). The peeling mechanism shown in Fig.2.3 is induced by vertical shear forces and is caused by the formation of diagonal shear cracks; this mechanism will be referred to as shear peeling (Oehlers 1992). A combined form of shear and flexural peeling modes occurs as shown in Fig. 2.4 when the plate end is subjected to both flexure and shear (Oehlers 1992).

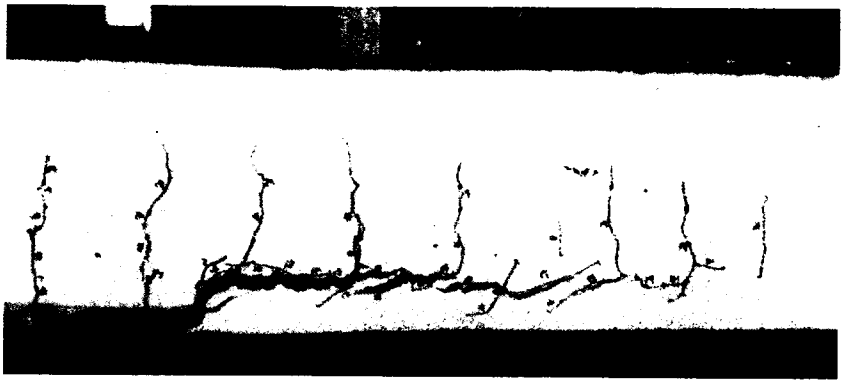

Fig.2.2. Plate-end in predominantly flexure region

Fig.2.3. Plate-end in predominantly shear region

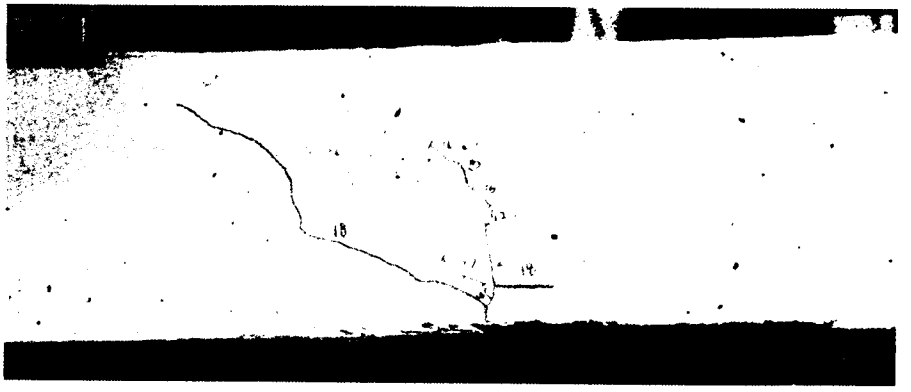

Fig.2.4. Plate-end subjected to flexure and shear

As slabs normally do not require stirrups to resist the applied vertical shear forces, the effect of shear peeling is negligible. That is why the technique of tension face plating works well for reinforced concrete slabs. On the other hand, reinforced concrete beams generally require stirrups and the vertical shear forces are relatively large, so that tension face plates frequently fail prematurely by shear peeling. This may make plating impractical for beams (Oehlers 1992).

As described previously, tension face plates have a tendency to debond prematurely and this can be prevented by anchoring the tension face plate with angles (Jones, Swamy and Charif 1988) as shown in Fig. 2.1b. Alternatively, channel sections can be used (Sharif , Al-Sulaimani, Basunbul , Baluch and Husain 1995) as in Fig. 2.1c as they are less prone to debonding. External stirrups and tension face plates can be combined as in Fig. 2.1d where the external stirrups both increase the shear capacity and inhibit debonding of the tension face plate (Orr and Lynch 1993), or straps can be used by themselves as in Fig.2.1e to improve the shear performance (Sharif , Al-Sulaimani, Basunbul , Baluch and Husain 1995). Premature debonding can also be prevented by adding side plates, as the side plates can substantially increase the shear peeling resistance (Weimin-Lou 1993). These side plates are always placed adjacent to the tension face plate end as their main function is to increase the shear peeling resistance.

In addition to the problem of shear peeling, the tension face plates may reduce the ductility of the beam or make it over-reinforced as it acts as additional tension reinforcement and this may further limit the application of this technique. Therefore, the alternative is to bond deep side plates, that is plates which are almost as deep as the reinforced concrete beam or the web of the beam. This automatically enhances the shear peeling strength and even increases the ductility of the beam (Ahmed 1996, Smith and Bradford 1995). Moreover, side plates can be used along with tension face plates to significantly increase the range of structures to which plating can be applied.

2.3 Experimental work on tension face plated beams

Most if not all of the experimental research on composite plated beams has dealt with both simply supported beams, as shown in Fig.2.5, and with beams in which the plates are bonded to the tension face. This research has been categorised below in terms of

the region of the tension face in which the plate-ends have been terminated, as shown in Fig.2.5.

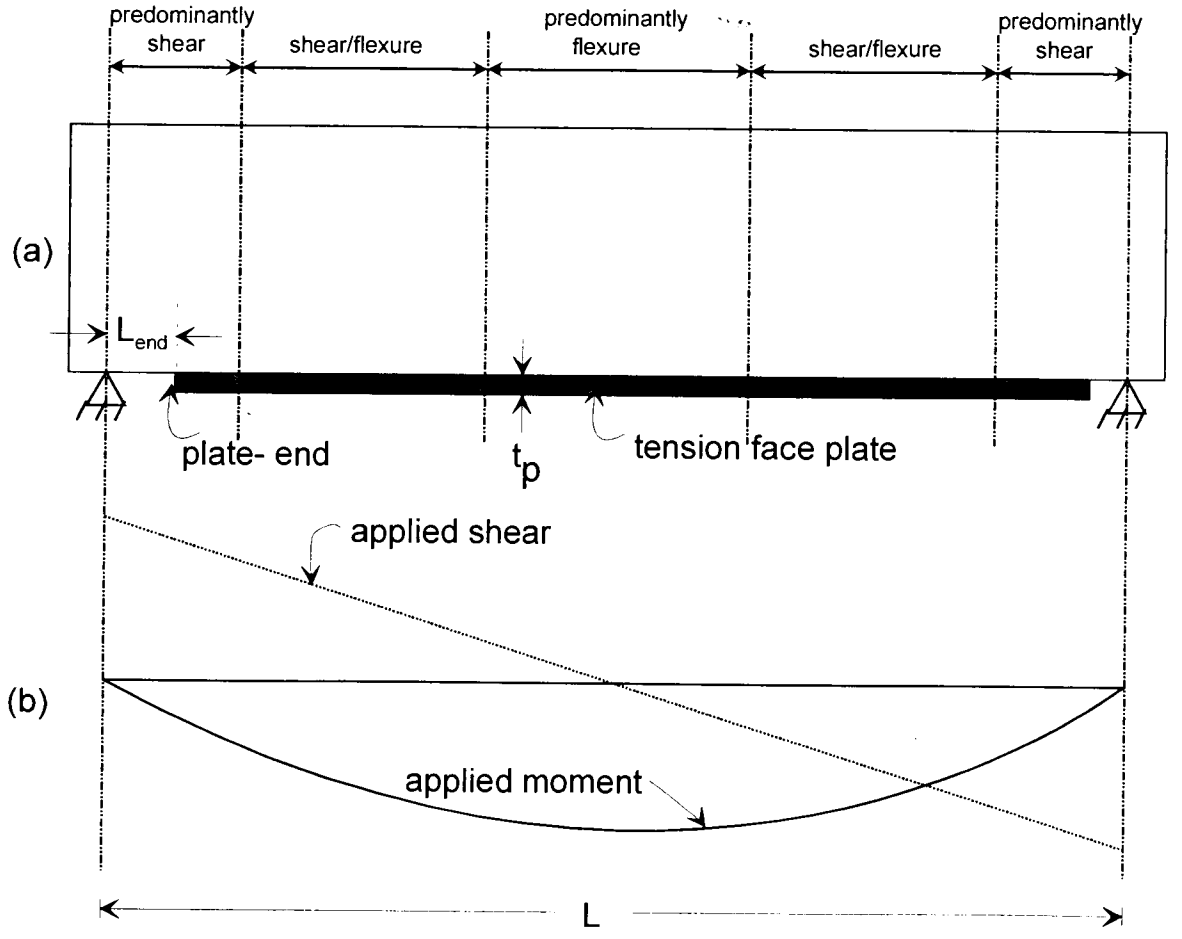

Fig.2.5. Region of termination of plate-end

The range of variables used in the tests on tension face plated beams is given in Table-2.1. In Table-2.1, b and h are the breadth and depth of the beams, L is the effective span of the beam, L_{end} is the distance between the plate end and the centre of the support, f_{cu} is the cube compressive strength of concrete, t_a is the thickness of adhesive and b_p and t_p are the width and thickness of plate respectively. It can be deduced from Table-2.1 that a wide range of plate thickness (1.5-15 mm), thickness of adhesive layer (1.5-8mm) and concrete grade (28 –118 MPa) were used in the studies. However, most of the tests were carried out on short span beams (1.2-2.5 m) with the exception of 3.5 m long beams tested by Mcdonald (1982). Another outstanding

feature of the studies was that the plate ends were terminated mostly in the predominantly shear region with the exception of the studies conducted by Oehlers and Moran (1990) and Oehlers (1992) wherein the position of the plate ends was a significant variable. The subsequent sections deal with the experimental as well as analytical studies according to the region where the plate ends were terminated.

Table-2.1: Variables in tension face plated beam tests

Reference	No. tests	b (mm)	h (mm)	L (m)	L_{end} (mm)	t_a (mm)	t_p (mm)	f_{cu} (MPa)	b_p (mm)
Mcdonald 1982	17	150	250	3.5*	-	-	1.1-4.8	-	57-150
Swamy et.al 1987	24	155	255	2.3	50	1.5-6	1.5-6	63-73	125
Jones et.al 1988	7	155	255	2.3	50	1.5	3-6	52-56	125
Swamy et.al 1989	9	155	255	2.3	50	1.5-3	1.5	52-55	125
Oehlers&Moran 1990	57	120-125	150-240	1.65-2.5	∞**	-	2-15	28-48	25-125
Oehlers 1992	26	130	175	-	50-1300	-	5	47-57	130
Orr & Lynch 1993	5	100	232	-	-	1.5	3-5	30	-
Hussain 1995	8	150	150	1.2	50	1.5	1-3	31***	100
Sharif et.al 1995	10	150	150	1.2	-	1.5	1.5	40	150
Swamy et.al 1995	21	155	255	2.3	-	2-8	1.5	110-118	125

* Length of beam ** Constant moment region *** Cylinder strength

2.3.1 Plate ends in predominantly shear region

2.3.1.1 Debonding modes

When the plate ends are placed in predominantly shear region (refer Figs.2.5a and 2.5b), failure due to plate separation occurs as shown in Fig.2.3. This mode of debonding caused by the shear cracks is referred to as shear/bond failure (Jones, Swamy and Charif 1988 and Swamy, Jones and Bloxham 1987) or shear peeling (Oehlers 1989). Failure does not occur at the plate/adhesive or adhesive/concrete interfaces but fracture invariably takes place in the concrete cover (Swamy, Jones and Bloxham 1987 and Oehlers 1992). This debonding mechanism is initiated by a shear crack that induces a horizontal crack at the level of the tension reinforcement which propagates rapidly towards the load point and eventually causes separation of the plate (Swamy, Jones and Bloxham 1987 and Oehlers 1992), as shown in Fig.2.6.

Debonding always occurs in beams with stirrups before the shear strength of the beams is reached (Oehlers 1992 and Husain, Sharif, Basunbul, Baluch and Al-Sulaimani 1995).

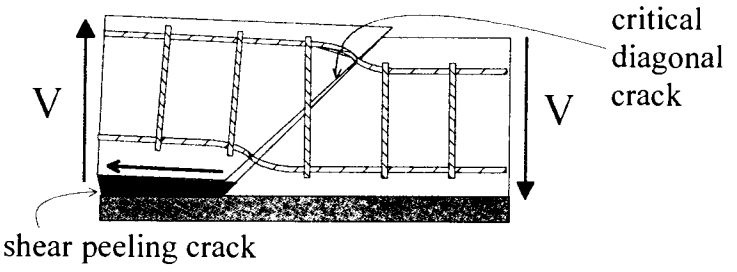

Fig.2.6. Shear peeling mechanism

As shown in Fig.2.6 (Oehlers 2000), the sliding or rotation of the critical diagonal crack causes the debonding crack to start at the base of the diagonal crack and propagate in the direction shown by the arrow. Tests on steel plated beams by Oehlers (1992) have conclusively shown that the presence of stirrups does not affect the shear load to cause debonding. This is because the stirrups that cross the diagonal crack, as in Fig.2.6, have to be stretched before they can contribute to the shear strength of the beam, but as steel plates are fairly rigid they debond as soon as the sliding action occurs. Hence, shear peeling is unlikely to be a major concern when plating slabs where the shear strength is governed by the shear strength of the beam without stirrups V_{uc}. However, shear peeling may severely restrict the plating of beams where the shear load is greater than V_{uc} and where stirrups are supplied to resist the additional shear load V_{us} above V_{uc}.

2.3.1.2 Debonding stress resultant

Experimentally determined (Jones, Swamy and Charif 1988) bond shear stresses at the tension face plate/adhesive interface are zero at the plate-end, as would be expected, reach a peak value at about $10t_p$ from the plate-end and then reduce to the linear elastic theoretical values at about $70t_p$. The maximum bond stresses at the

interface are about $\sqrt{2}f_t$, where f_t is the Brazilian or splitting tensile strength of the concrete, and bear no consistent relationship to the linear elastic theoretical values (Jones, Swamy and Charif 1988).

2.3.1.3 Adhesive

To gain the maximum increase in stiffness and crack control, a stiff adhesive should be used to bond the plate fully to the concrete (Mcdonald 1982). Adhesive thicknesses of 1.5 to 6 mm have no significant or visible effect on the ultimate load capacity (Swamy, Jones and Bloxham 1987), nor would it appear, from the tests results, on the shear/bond failure load. Debonding may occur at the adhesive/concrete or adhesive/plate interface due to bad workmanship, improper preparation of steel and concrete surfaces and usage of an epoxy resin beyond its pot life (Oehlers 1989). As the adhesive strength and its bond strength are normally much larger than the tensile strength of concrete, it is quite unlikely that an adhesive-bond failure will take place if specified procedures are followed.

2.3.1.4 Stress concentrations at plate-end

Using two layers of plates and staggering the positions of the plate-ends(Swamy, Jones and Bloxham 1987 and Jones, Swamy and Charif 1988) did not prevent shear/bond failure, nor did tapering the plates at the plate-ends (Jones, Swamy and Charif 1988).

2.3.1.5 Plate size

It is suggested that, until more results are available, the width to thickness ratio of the plate $b_p/t_p > 50$ or 60 to prevent shear/bond failure (Mcdonald 1982 and Swamy, Jones and Bloxham 1987).

2.3.1.6 Mechanical anchorage of plate-ends

The use of anchor bolts at the plate end region has a limited but useful effect on the performance of the plated system. Bolting the plate-ends only increases the shear/bond failure load by 10% and 8% (Jones, Swamy and Charif 1988). The reason for this is that the bolts are acting in shear and the shear deformation before debonding is very small. However, if debonding does occur, for whatever reason, the bolts are useful in preventing total plate separation. They enhance the load capacity slightly and also prevent the plates from falling off. For this reason, the bolts used in the bonding operation are usually left in place. L-shaped anchor plates, as in Fig.2.1b, prevented the tension face plates from debonding and allowed the theoretical ultimate loads to be reached which were 36% greater than that of the unplated beam (Jones, Swamy and Charif 1988). External stirrups, such as in Fig.2.1d, can be used to inhibit shear peeling especially if the straps are inclined (Orr and Lynch 1993). Side straps and channel sections, as in Figs.2.1c and 2.1e, increased the shear strength of beams without stirrups (Sharif, Al-Sulaimani, Basunbul, Baluch and Husain 1995).

2.3.1.7 Pre-cracking and pre-cambering

Beams have been pre-cracked by applying 70% of the flexural capacity then unloaded prior to plating (i.e. unpropped construction), and beams have been pre-cambered by applying 70% of the flexural capacity and plated whilst still loaded (i.e. propped construction) (Swamy, Jones and Charif 1989). These beams had 1.5 mm plates, shear/bond failure did not occur in either the propped or unpropped beams, and the strengths were increased by 10% to 15% (Swamy, Jones and Charif 1989). Beams have also been loaded up to 85% of their flexural capacity prior to plating and have been found to perform satisfactorily with suitably dimensioned plates (Husain, Sharif, Basunbul, Baluch and Al-Sulaimani 1995).

2.3.1.8 Ultimate strength

Increases in the flexural strength of up to 40% (Mcdonald 1982) and 16% (Swamy, Jones and Bloxham 1987) have been achieved by plating. Inclined external stirrups, as in Fig. 2.1d, increased the flexural capacity by 66% (Orr and Lynch 1993).

2.3.1.9 Flexural stiffness

Increases in the flexural rigidities of up to 85% at the initial cracking stage (Swamy, Jones and Bloxham 1987), up to 190 % (Mcdonald 1982) and 140% (Swamy, Jones and Bloxham 1987) at serviceability loads, and up to 300% (Swamy, Jones and Bloxham 1987) near failure have been achieved. Plating has increased the serviceability stiffness of precracked beams by 250% (Macdonald 1982).

2.3.1.10 Concrete cracks

The greatest effect of the glued plate is on the steel bar strain which is reflected, in turn, on the maximum crack width (Swamy, Jones and Bloxham 1987 and Swamy, Jones and Charif 1989). Plating can increase the load to cause the first visible crack by 80 %.

2.3.1.11 Durability

Tests on beams (Swamy, Hobbs and Roberts 1995) that were subjected to 11-12 years of exposure in industrially polluted areas were found to be very satisfactory. Many of the beams retained their structural integrity and ductility, and all of the beams failed at loads of 1% to 29% higher than those of the short term control plated beams. In another study conducted at Transport and Road Research Laboratory, U.K. (Calder 1987), the steel plated beams were exposed to three different environmental conditions, namely, a rural site with relatively high rainfall, an industrial site characterised by high levels of atmospheric sulphates and a marine site situated near a harbour exposed to high levels of atmospheric chlorides. After ten years of exposure, it was found that corrosion had spread from the edge of the plate by ingress of

moisture at the interface between the resin and steel. Even though corrosion had weakened the steel to resin interface relative to the concrete, the effect on overall structural performance was small. The failure loads of naturally exposed beam specimens were only slightly less than that of specimens stored in controlled laboratory environments. Further, corrosion can be reduced significantly by coating the steel plates with an epoxy primed paint prior to assembly of specimens.

2.3.2 Plate ends in predominantly flexure region

Whereas the most of the studies on tension face plated beams concentrated on the plate ends in a predominantly shear region, the only study reported on the plate ends placed in a predominantly flexure region were conducted by Oehlers and Moran (1990). The results are summarised in this section.

2.3.2.1 Debonding modes

The flexural peeling mechanism is a simple one and can be explained through Fig. 2.7. When a moment, i.e. curvature is applied to a plated beam, then the plate tries to remain straight. This induces cracks at the plate end that propagate inwards. Thus, an axial force and moment have to be applied at the plate ends as shown in Fig. 2.7 so that the deformation of the plate would be the same as if it had been attached to the beam. Eventually, debonding is caused by the transfer of these axial and flexural stress resultants from the RC beam to the external plate (Oehlers 2000). Moreover, flexural peeling causes the flexural strength of the plated beam to reduce to that of the reinforced concrete beam so that further increases in applied loads will then lead to flexural failure of the beam.

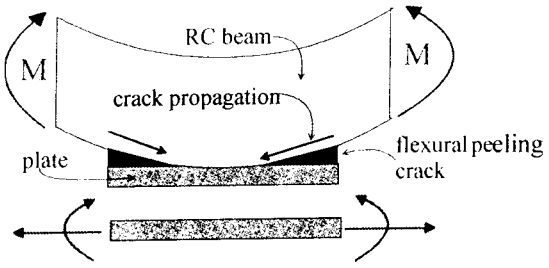

Fig.2.7 Flexural peeling failure mechanism

In the event of flexural peeling, the plate separation starts at the plate end as a horizontal crack at the level of the tension reinforcement (Oehlers and Moran 1990). Further increases in the applied load, increase the curvature and extend the peeling crack away from the end of the plate and form flexural cracks ahead of the peeling cracks, as shown in Fig. 2.2. A further increase in the applied load then causes a very rapid propagation of the crack system which continues to extend until the plate is ineffective. The initial horizontal peeling crack occurs at about half the load at which rapid debonding due to flexural peeling occurs. Hence, crack propagation in flexural peeling gives ample warning of imminent failure as compared to shear peeling where there is very little warning.

2.3.2.2 Debonding stress resultant

Flexural peeling occurred at strains ranging from 130 to 1,110 microstrains and, hence, cannot be prevented by imposing limitations on the strains in the plate (Oehlers and Moran 1990).

2.3.2.3 Pre-cracking and pre-cambering

Beams have been pre-cracked and pre-cambered prior to plating using loads of 60% of the flexural capacity of the unplated beam to represent propped and unpropped construction (Oehlers and Moran 1990). Flexural peeling was found to depend on the moment applied after plating (Oehlers and Moran 1990), that is the curvature induced in the plate.

2.3.2.4 Concrete cover

Cover to the tension reinforcing bars was varied from 10 mm to 50 mm and was found not to affect flexural peeling(Oehlers and Moran 1990).

2.3.2.5 Width of plate

The width of the plate was varied from 20% to 100% of the width of the beam (Oehlers and Moran 1990). It was found that narrow plates were less susceptible to flexural peeling than wide plates of the same plate thickness (Oehlers and Moran 1990).

2.3.3 Plate ends in shear/flexure region

In a series of tests on tension face plated beams, Oehlers (1992) changed the distance L_{end} from the support reaction to the end of the plate end and the length of shear span a to vary the moment to shear force ratio at the end of the plate. The second major parameter varied was the amount of internal shear reinforcement. A typical example of the crack formation just prior to debonding of a plate end that is terminated in a region of shear and flexure is shown in Fig.2.4. In this case, a flexural crack first occurred in the vicinity of the plate end and this was followed by an inclined shear crack. A further increase in the applied load induced the rapid formation of a horizontal peeling crack similar to that shown in Figs.2.2 and 2.3. The resistance to flexural peeling was found to reduce with the presence of vertical shear forces and vice versa.

2.3.4 Plate ends in zero flexure and zero shear region

Under this study by Weimin-Luo (1993), peeling of reinforced concrete beams bonded with full length tension face plates, as shown in Fig.2.8, was investigated. The full length plate enables the plate end to be in a region where shear force and moments are absent. Three beams were bonded with 3 mm, 5 mm, and 10 mm thick tension face plates to the full length of the beam. The fourth beam was not plated and

used as control specimen. Only three shear stirrups were provided in order to hold the reinforcement cage and also to eliminate the contribution to the shear strength of the reinforcement concrete beam by the stirrups.

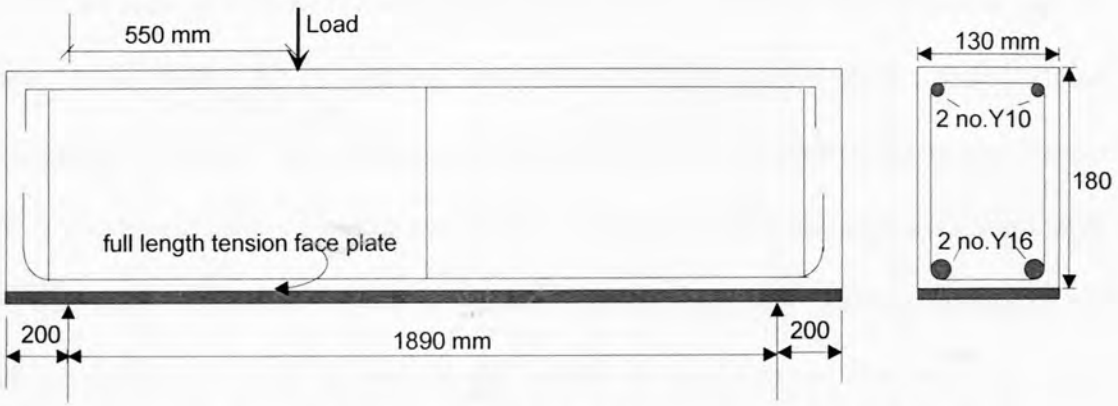

Fig.2.8. Typical detail of a plated beam tested by Weimin-Lou

The tests revealed that all the plated beams failed by the formation of extensive diagonal shear cracks. The debonding is due to the horizontal debonding crack that originated from the diagonal crack closest to the support; the debonding crack then extended backwards to the support and then to the end of the beam as shown in Fig.2.9. The test results revealed that the shear load to cause complete peeling of the plates beam were about 88%, 160% and 215% more than the shear strength V_{uc} of the unplated beam for the beams bonded with 3 mm, 5 mm and 10mm plates respectively.

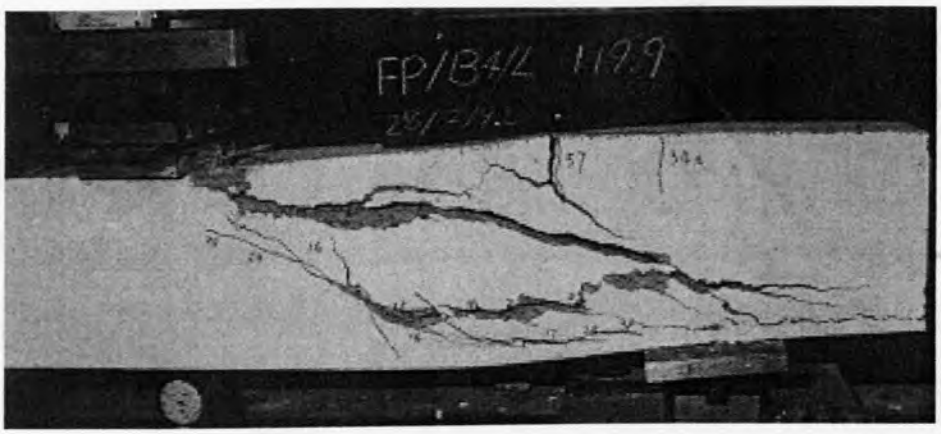

Fig.2.9. Failure mode of plated beams

2.4 Experimental work on side plated beams

As discussed in Section 2.2.2.2, bonding plates to the sides of RC beams can overcome the problems posed by tension face plated beams such as inadequate shear peeling strength and ductility. The present literature survey reveals that the only comprehensive study on the different peeling mechanisms on side plated beams was carried out at the University of Adelaide. In this section, the important outcomes from these investigations are categorised as in the case of tension face plated beams in the preceding section. It may be noted that most of the test results are presented in detail, as these will be used later to validate the mathematical models developed in this thesis.

2.4.1 Plate ends in predominantly shear region

Apart from the studies conducted by Oehlers, Nguyen and Bradford (2000a), another study on this aspect was reported by Sharif, Al-Sulaimani, Basunbul, Baluch and Husain (1995). Tests were conducted on short beams of span 1200 mm to evaluate the shear peeling behaviour with different arrangement of plates such as side plates covering the whole shear span termed as wings (Fig.2.10a), strips of plates bonded at regular intervals (Fig.2.10b), U-shaped strips bonded at regular intervals (Fig.2.10c) and channel sections bonded over the entire shear span termed as jackets (Fig.2.10d). In these tests, the beams bonded with U-strips, strips and wings failed suddenly by the formation of diagonal shear cracks that lead to the tearing and splitting of the concrete cover. On the other hand, the jacket plated beams did not peel off due to shear and there was improvement in ductility and they developed flexural type failure. Whilst the shear peeling strengths of the beams with the strips and U-strips were about 20% higher than the shear strength of RC beam (V_{uc}), it was about 35% more for the beams with full side plates, i.e. wings. Moreover, the shear load at failure of the jacketed beam was about 66% greater than V_{uc}. All these figures should be interpreted with

caution as the basic RC beam contained minimal internal shear stirrups that did not contribute towards the shear strength of the beam and the short span beam had a shallow cross section (150 mm x 150 mm).

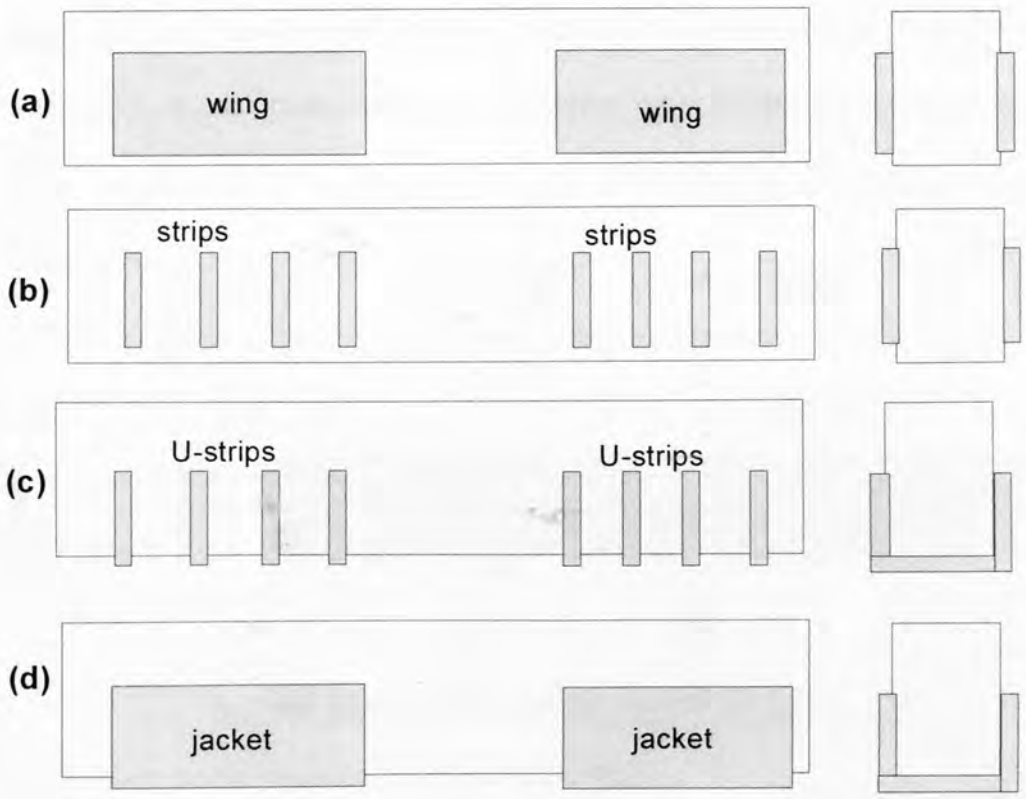

Fig.2.10 Different plate configurations tested by Sharif et.al

2.4.1.1 Specimens tested by Nguyen and Oehlers

Oehlers, Nguyen and Bradford (2000a) conducted a limited study on the shear peeling of the side plated beams using long span (5000 mm) beams that reflects the real life situation. Figure 2.11 shows the typical detail of a beam tested by them. While tests 2n1 and 2n2 were performed on a beam glued with a side plate of 65 mm depth and 5 mm thick, the corresponding values for 2n3 and 2n4 were 65 mm and 8 mm respectively. Whereas shear spans 2n1 and 2n3 had no shear stirrups, the spans 2n2 and 2n4 were provided with shear stirrups. Another test 2a conducted on a shear span without internal shear stirrups and without external plates was used to quantify the shear strength of the concrete beam V_{uc}. The side plates were terminated over the

supports so that the plate end was subjected to pure shear. The concrete properties consisted of a compressive cylinder strength of f_c= 58 MPa, Young's modulus E_c = 37 GPa, and Brazilian tensile strength f_b = 4.64 MPa. All the plated beams failed by shear peeling due to the formation of critical diagonal shear cracks and the failure occurred rapidly with virtually no warning, as occurred with tension face plated beams.

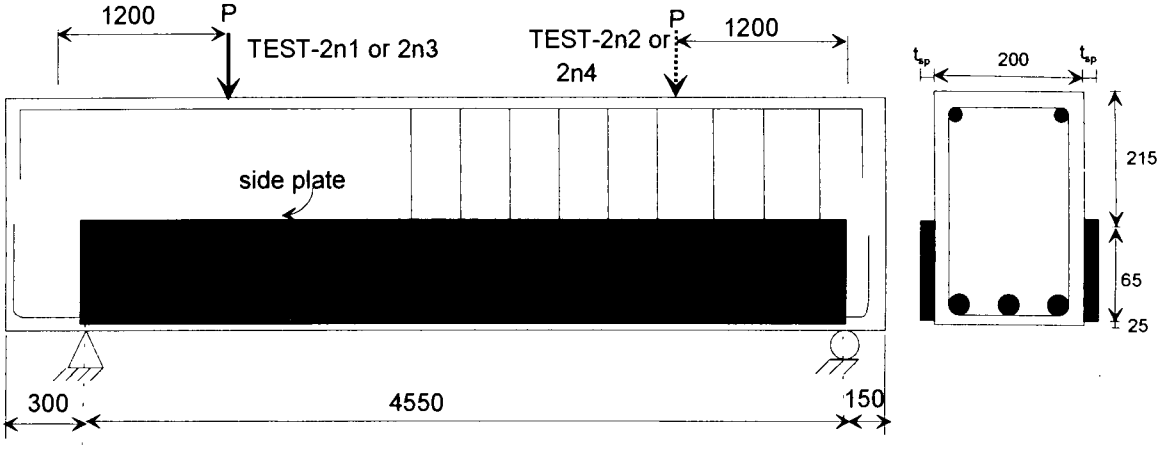

Fig.2.11. Details of 2n1, 2n2, 2n3 and 2n4

2.4.1.2 Test results

Table-2.2 compares the analytical and test results obtained for all the specimens tested. Column(2) gives the shear load at the instance of either the failure of the beam in the case of the unplated beam or the shear peeling of the external plate. Column(3) gives the theoretical shear strength of the beam as per AS-3600 (1994); the value of V_{uc} in Column(3) is the experimental failure load of the beam 2a and the shear strength of shear stirrups (V_{us}) was calculated using AS-3600 (1994) formula. It is worth noting that the shear peeling strength of the spans without stirrups is only 20% higher than V_{uc} and the stirrups had only marginally improved the shear peeling strength by an additional 25%. Therefore, the shear peeling strength can be said to be independent of the strength of the stirrups as the stirrups, in theory, would have increased the shear strength of the beam by 185%. It is also worth noting that the

shear stresses due to longitudinal shear flow at debonding τ derived from well known $VAy/I_p b_p$ formula varies between 1-1.9 MPa for the four tested span and these are much less than the tensile strength of the concrete (f_b = 4.64 MPa). Therefore, shear flow due to interfacial shear stresses was not the cause of debonding.. Here, V is the maximum shear force due to ultimate beam loading, A is the transformed area of the plate, y is the distance from the neutral axis to the centroid of the plate and b_p is the width of the plate.

Table-2.2: Experimental and analytical results-Side plated beams

Specimen (1)	V_{pure} 'kN' (2)	$V_u = V_{uc,expt} + V_{us}$ 'kN' (3)	V_{pure}/V_{uc} (4)
2a	85.1 (V_{uc})	85.1	-
2n1	103.0	85.1	1.21
2n2	125.9	242.1	1.48
2n3	108.6	85.1	1.28
2n4	126.5	242.1	1.49

2.4.2 Plate ends predominantly under flexure

2.4.2.1 Debonding modes

The only study on this aspect was conducted by Oehlers, Nguyen and Bradford (2000b). Six 5 m long beams were tested with plates in constant moment regions as shown in Fig.2.12. The plate thickness was varied from 6 to 12 mm and the plate depth from 60 to 240 mm. All the beams failed by flexural peeling in a similar fashion to the tension face plated beams. Failure mechanisms were the same both for the shallow and deep plated beams. The debonding was initiated by the formation a flexural crack at the plate end at a very low load, it stabilised until there was very rapid crack propagation at the maximum peeling moment. This rate of debonding is extremely important in plated beam construction because it means that initial peeling is not a prelude to unstable crack propagation or ultimate peeling. This is in contrast

with shear peeling where once the critical diagonal crack is formed, the debonding is sudden and imminent.

Fig.2.12. A typical flexural peeling of a side plated beam (Nguyen and Oehlers)

2.4.2.2 Debonding stress resultants

Flexural peeling occurred at maximum strains recorded in the centre of the side plates that ranged from 790 (compressive) to 1,110 (tensile) microstrains. Hence, flexural peeling cannot be prevented by imposing limitations on the strains in the plate.

2.4.2.3 Depth and thickness of the plates

For the same thickness of the plate, the ultimate flexural peeling moment increases with the depth of the plate initially and then levels off when the plate depth is about 60% of the beam depth. Moreover, for the same plate depth, the ultimate flexural peeling moment decreased as the plate thickness was increased from 6 to 12 mm.

2.4.3 Plate ends in shear/flexure region

The interaction between shear peeling and flexural peeling in side plated beams was determined experimentally by Nguyen and Oehlers (1997a). The test beam and test rig were similar to that shown in Fig.2.10 except the effective span was 4700 mm and the shear span was increased from 1200 mm to 1400 mm; the plate depth and thickness were kept constant at 65 mm and 8 mm respectively. The plate end was terminated between the support and the applied load P at a distance L_{end} from the support as shown in Table-2.3. The concrete material properties were f_c= 52.4 MPa,

f_b = 4.49 MPa and E_c = 40.4 GPa. A typical peeling pattern observed due to shear/flexure interaction is shown in Fig.2.13.

Fig.2.13. A typical shear/flexural peeling interaction in side plated beam

Table- 2.3: Shear/Flexure peeling tests of side plated beams

Tests (1)	L_{end} (mm) (2)	V_{end} (kN) (3)	M_{end} (kNm) (4)	ε_{peel} (10^{-6}) (5)	τ (N/mm^2) (6)
3c1N	300	103.1	30.9	1241	1.52
3c1S	300	103.1	30.9	1243	1.52
3c2N	300	104.5	31.3	1245	1.54
3c2S	300	104.5	31.3	1272	1.54
3d1N	910	74.7	68.0	725	1.10
3d1S	910	72.6	66.1	773	1.07
3d2N	910	87.5	79.6	836	1.29
3d2S	910	76.9	70.0	710	1.14
3e1N	2740	40.3	110.3	890	0.6
3e1S	2740	36.2	99.3	980	0.53
3e2N	2395	42.1	100.9	979	0.62
3e2S	2395	28.6	68.6	770	0.42
3f1N	1200	65.2	78.3	831	0.96
3f1S	1200	52.0	62.4	709	0.77
3f2N	1200	55.7	66.9	718	0.82
3f2S	1200	55.7	66.9	812	0.82

The shear load at the plate end at debonding V_{end} and the moment at the plate end at debonding M_{end} are indicated in columns 3 and 4 in Table-2.3. The maximum shear stress due to longitudinal shear flow τ computed from $VAy/I_p b_p$ formula is also indicated. Here, V is the maximum shear force due to ultimate beam loading, A is the transformed area of the plate, y is the distance from the neutral axis to the centroid of the plate and b_p is the width of the plate. The strain in the plate at debonding ε_{peel} is

also indicated. As the debonding occurred over a range of τ (0.82-1.54 MPa) and ε_u (709-1272 microstrain), these parameters cannot be used to predict debonding due to shear/flexure interaction.

2.5 Enhancing the shear peeling strength of the tension face plated beams using side plates

The shear peeling of tension face plated beams is always caused by the formation of diagonal shear cracks in the vicinity of the plate end and the presence of internal shear stirrups hardly makes any difference, as discussed in Section 2.3.1.1. In this regard, there were a few attempts such as the studies conducted by Jones, Swamy and Charif (1988) to improve the shear peeling strength of the tension face plated beams by adhesively bonding additional 'anchor plates'. These tests were limited in nature; in fact only two tests were carried out. However, they established the effectiveness of the additional anchor plates in the form of glued angles as they facilitated the full composite action of the tension face plated beams. Therefore, Weimin-Luo (1993) conducted an extensive investigation on the improvement in shear peeling strength of the tension face plated beams by bonding additional plates to their sides in the region above the plate ends. Here, the test results and their implications are fully described as the data from this study is used to develop empirical guidelines as well as in validating the mathematical models in Chapter-11.

2.5.1 Test specimens

The aim of these tests was to determine directly through experimental testing the increase in the pure shear peeling capacity ΔV_{pure} that the side plates provided, i.e. $\Delta V_{pure} = V_{pure.wsp} - V_{pure.nsp}$, where $V_{pure.nsp}$ is the pure shear peeling capacity with no side plates and $V_{pure.wsp}$ is the pure shear peeling capacity with side plates. The pure shear peeling capacity of beams with no side plates $V_{pure.nsp}$ was determined from tests

of beams with only tension face plates and it was the shear load at which the tension face plates debonded. Similarly, the pure shear peeling capacity of beams with side plates $V_{pure\cdot wsp}$ was the shear load at which the tension face plates debonded. Both shear spans of nine plated reinforced concrete beams were tested giving seven results for $V_{pure\cdot nsp}$ and eleven results for $V_{pure\cdot wsp}$.

The beams are shown in Figs.2.14-2.16 and had the following common properties: 2290 mm long, 130 mm wide and 180 mm deep; were only provided with three stirrups, to hold the longitudinal reinforcement in position, which were placed well away from the plate ends so that they did not affect the results; the tension face plates were 5 mm thick and as wide as the beam, that is 130 mm; and the side plates were as deep as the beams, that is 180 mm.

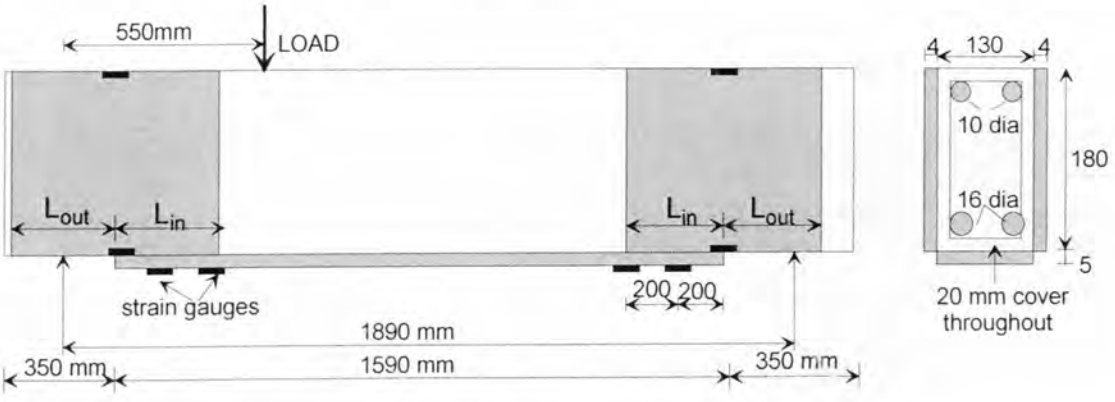

Fig.2.14 Details of a beam tested in Series 1

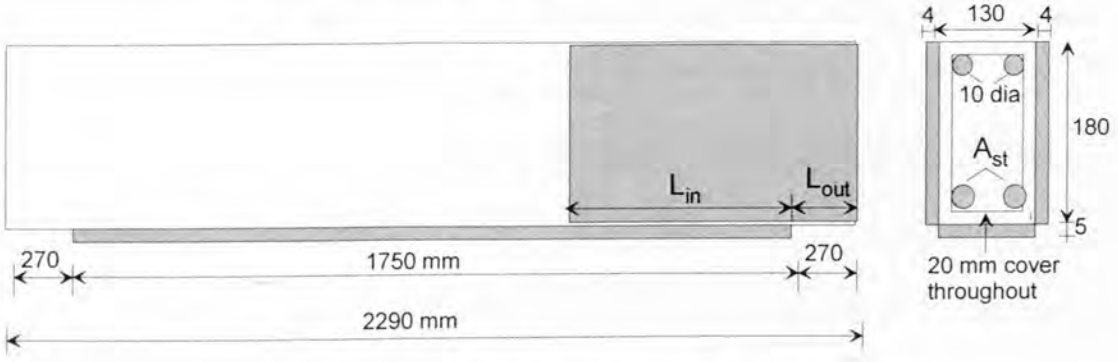

Fig.2.15 Details of a beam tested in Series 2

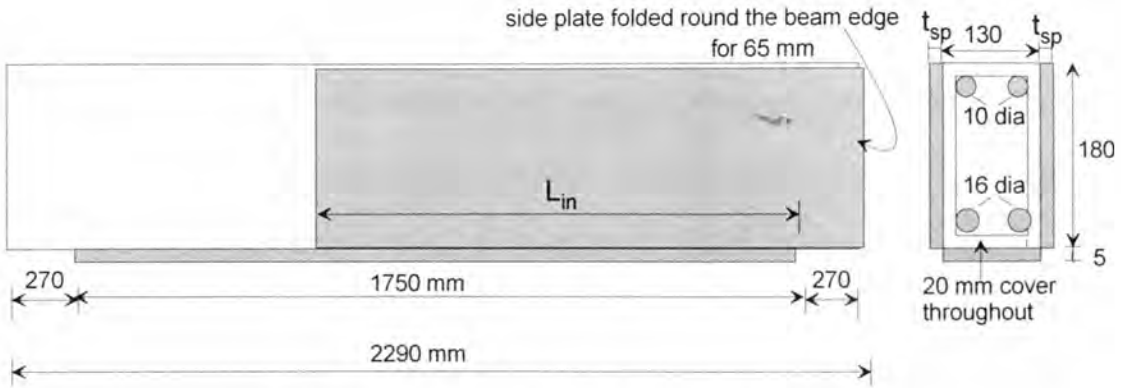

Fig.2.16 Details of a beam tested in Series 3

All the beams were tested as simply supported with a span of 1890 mm and a shear span of 550 mm as shown in Fig.2.14. Strain gauges were placed on the side plates and tension face plates to determine the onset of debonding. The details of the beams tested and the test results are summarised in Table-2.4. Each shear span of the beams were tested and these are listed in Column 1 in Table-2.4; where, for example, S2B5L refers to Series 2, Beam 5 and the Left shear span of that beam. The tests were arranged in three series and the geometric variations within and between series are given in Columns 2-4, where L_{out} = bond length of the side plate measured from the end of the tension face plate to the outer edge of the side plate as shown in Fig.2.14; L_{in} = bond length of the side plate from the tension face plate end to the inner edge of the side plate; t_{sp} = thickness of side plate; and A_{st} = area of the tension reinforcing bars. The predominant variable in Series 1 was the bond length, that in Series 2 was the area of the tensile reinforcing bars A_{st}, and that in Series 3 was the thickness of the side plates t_{sp}. In Series 3, the plate was folded around the end of the beam as shown in Fig.2.16 so that L_{out} in Column 3 in Table-2.4 included the length of the fold. The side plate thicknesses t_{sp} varied from 1 mm to 4 mm, the area of tension reinforcement A_{st} from 157 mm^2 to 628 mm^2, and the minimum bond length L_{min}, that is the lesser of L_{in} and L_{out}, varied from zero to 345 mm.

TABLE-2.4-BEAM TESTS

	GEOMETRIC PROPERTIES				TEST RESULTS		
Shear span	L_{in} mm	L_{out} mm	t_{sp} mm	A_{st} mm^2	V_{pure} kN	ΔV_{pure} kN	first plate
(1)	(2)	(3)	(4)	(5)	(6)	(7)	(8)
Series-1: Varying lengths of side plates							
S1B1L	0	0	4.0	402	33.4	0	tfp
S1B2L	0	0	4.0	402	26.4	0	tfp
S1B3L	45	45	4.0	402	30.8	0.9	sp
S1B2R	90	90	4.0	402	37.0	7.1	sp
S1B4R	135	135	4.0	402	35.0	5.1	both
S1B1R	180	180	4.0	402	43.2	13.3	both
S1B3R	270	270	4.0	402	50.0	20.1	tfp
S1B4L	345	345	4.0	402	60.6	30.7	tfp
Series-2: Varying tension reinforcing bars							
S2B5L	0	0	0	157	33.0	0	tfp
S2B5R	270	420	4.0	157	62.8	29.8	tfp
S2B6L	0	0	0	628	31.5	0	tfp
S2B6R	270	420	4.0	628	69.8	38.3	tfp
Series:3-Varying thickness of side plates							
S3B7L	0	0	0	402	27.9	0	tfp
S3B7R	335	915	1.0	402	54.6	26.7	tfp
S3B8L	0	0	0	402	33.1	0	tfp
S3B8R	335	915	2.0	402	64.7	33.4	tfp
S3B9L	0	0	0	402	33.0	0	tfp
S3B9R	335	915	3.0	402	72.6	39.6	tfp

2.5.2 Material Properties

The concrete was tested at the time of the beam tests and had a cylinder compressive strength f_c = 35.1 N/mm^2, a Brazilian tensile strength f_b = 3.60 N/mm^2 and a Young's modulus of E_c = 34.2 kN/mm^2. The steel plates of thickness 1, 2, 3, 4 and 5 mm had a yield strength of 317, 310, 320, 243 and 317 N/mm^2 and a Young's moduli of 200, 215, 203 and 210 kN/mm^2 respectively. A two part epoxy with a tensile strength and steel-concrete bond strength much greater than that of the concrete was used, as this ensured that the failure plane always occurred within the concrete.

2.5.3 Test results

The first plate to debond is listed in Column 8 of Table-2.4. In most cases the tension face plate (tfp) debonded completely before the side plate (sp) showed signs of

debonding, and in some cases it was difficult to determine which plate debonded first and this has been referred to as (both) in Table-2.4. The shear loads in these beams when the strains in the tension face plates sudden reduced due to debonding are listed as V_{pure} in Column 6 in Table-2.4. The increase in the pure shear peeling capacity ΔV_{pure} is given in Column 7. In deriving ΔV_{pure} for Series 1, the shear peeling strength with no side plates $V_{pure\text{-}nsp}$ was taken as the average of V_{pure} for tests S1B1L and S1B2L. However in Series 2 and 3, each beam had a shear span without a side plate and this was taken as $V_{pure\text{-}nsp}$ for the shear span with the side plate.

The results for Series 1 are shown in Fig.2.17a where the minimum bond length L_{min} is plotted non-dimensionally in terms of the depth of the side plate d_{sp} which was constant at 180 mm. It can be seen that the increase in the shear peeling strength due to plating is a function of the minimum bond length. The results from Series 3 are shown in Fig.2.17b where it can be seen that the shear peeling strength depends on the plate thickness.

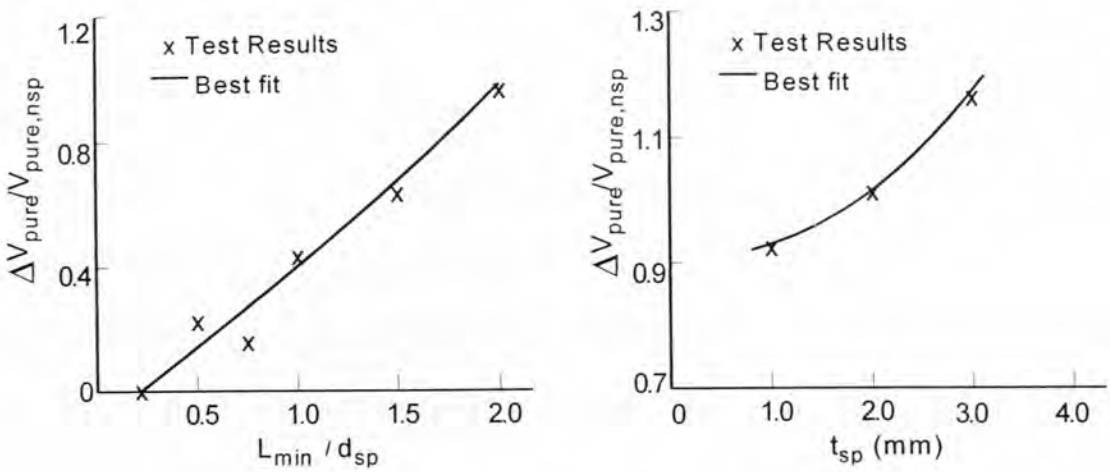

(a) Series 1 **(b)Series-3**

Fig.2.17 Test Results

2.6 Experiments on beams bonded with angles

In yet another unique study, Nguyen and Oehlers (1997b) evaluated the performance of bonded angles in which the plate ends were subjected to bending moments only and a failure mechanism similar to side plate was observed, as shown in Fig.2.18.

Fig.2.18. A typical flexural peeling of angle plated beam (Nguyen and Oehlers)

2.7 Debonding models for tension face plated beams

In the tests described above, debonding of the plates always started from the plate-ends where stress concentrations are induced by the discontinuity at the plate-end. Experimental research (Swamy, Jones and Bloxham 1987), theoretical analyses (Roberts 1989) and computer simulations (Oehlers and Moran 1990) suggest that the distributions of stresses at the plate-end have the form shown in Fig. 2.19. These stress distributions are fundamental to the following mathematical models. In Fig. 2.19, the interface shear stress indicated by the solid line is zero at the plate end and shoots up to a maximum value τ_{pk} at a short distance approximately equalling the plate thickness and thereafter decays to a standard magnitude τ_{sta} given by $VAy/I_p b_p$ formula. Associated with these shear stresses due to the longitudinal shear flow forces are the normal peeling stresses indicated by dotted lines in Fig.2.19. The

maximum normal stress σ_{pk} occurs right at the plate end and it reduces rapidly to zero at a short distance from the plate end.

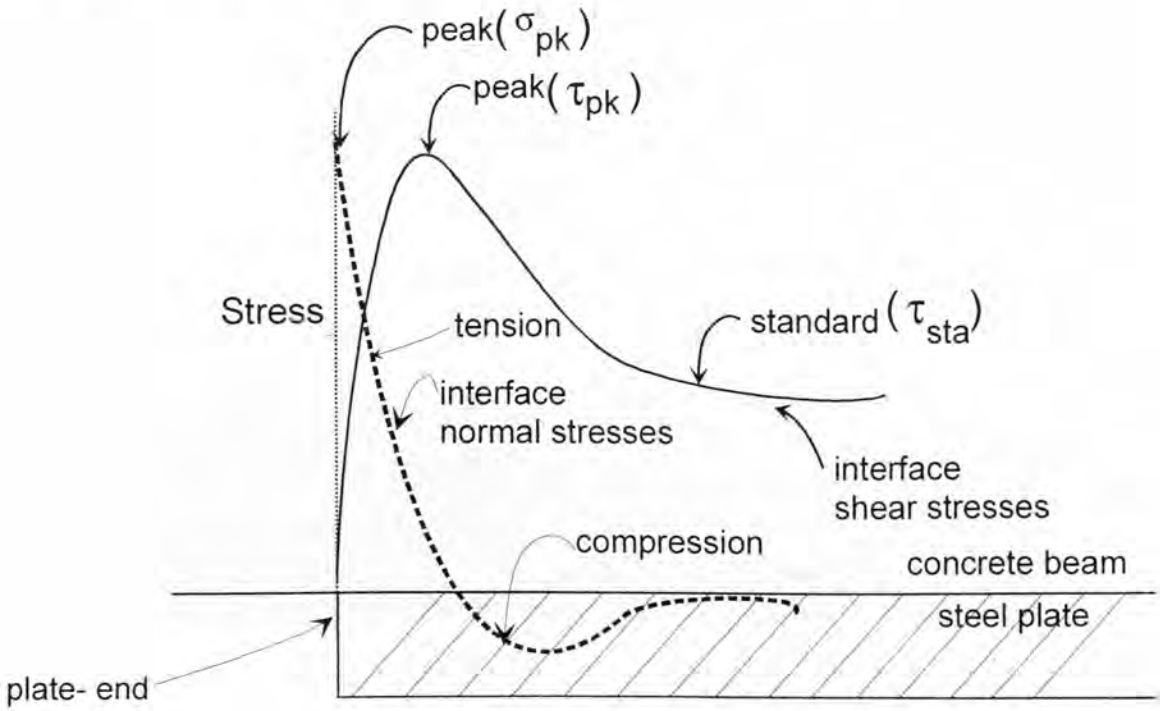

Fig.2.19. Interface stresses

2.7.1 Swamy, Jones and Charif's model

This model was developed to ensure that the shear stresses at the plate/beam interface, shown in Fig.2.19, do not cause debonding through cracking of the concrete (Jones, Swamy and Charif 1988 and Swamy, Jones and Charif 1989).

The 'standard' shear stress τ_{sta} in Fig.2.19, which occurs away from the plate-end, can be determined from conventional elastic theory using the well known $VAy/I_p b_p$ equation. Experimental research (Jones, Swamy and Charif 1988) has shown that the 'peak' shear stress τ_{pk}, caused by the discontinuity of the plate, is approximately twice the 'standard' shear stress and, furthermore, that the concrete can resist a shear stress of $\sqrt{2} f_b$. Hence, shear flow debonding can be prevented by ensuring that

$$\tau_{xia} \leq \frac{f_b}{\sqrt{2}} \tag{2.1}$$

2.7.2 Roberts and Haji-Kazemi's model

An elegant partial interaction theoretical model has been developed to determine the distribution of both the normal and shear stresses at the concrete/adhesive interface and in particular the peak of these stresses σ_{pk} and τ_{pk} shown in Fig.2.19 (Roberts and Haji-Kazemi 1989 and Roberts 1989). This model is based on the linear and non-linear analysis of partially composite steel and concrete beams proposed by Newmark (1951). It is assumed in the analysis that the positions of peak normal stress and peak shear stress coincide at the plate end. The model allows for the effect of both the applied shear V_{end} and the applied moment M_{end} at the plate-end, and is given by

$$\tau_{pk} = \left(V_{end} + \left(\frac{K_s}{E_p b_p t_p} \right)^{\frac{1}{2}} M_{end} \right) \frac{t_p}{I_{cmp}} \left(h_p - h_{cmp} \right) \tag{2.2}$$

$$\sigma_{pk} = \tau_{pk} t_p \left(\frac{K_n}{4 E_p I_p} \right)^{\frac{1}{4}} \tag{2.3}$$

where K_s = shear stiffness/unit length of adhesive layer, E_p = Young's modulus of the plate, I_{cmp} = second moment of area about the neutral axis of the fully composite section transformed to steel, h_p = depth from top fibre to plate, h_{cmp} = depth from top fibre to the neutral axis of composite plated section, K_n = normal stiffness/unit length of adhesive layer, and I_p = second moment of area of plate about its own centroid. The above equations show the shear and normal stress concentrations in the adhesive layers at the plate ends depend significantly on the shear and normal stiffness of the adhesive, the thickness and point of termination of the steel plate. This leads to the conclusion that the peeling stresses can be reduced by using a more flexible adhesive,

reducing the thickness of steel plate, and for a simply supported beam, by terminating the plate as close to the support as possible.

The mathematical model has been validated from tests in which the plate end was terminated in a region of predominantly shear (Swamy, Jones and Bloxham 1987) and should, therefore, be only applied in this region. It is worth noting that the model is sensitive to the adhesive properties because it is considering the stresses at the adhesive/concrete interface. In practice, debonding occurs at the level of the tension reinforcement, as shown in Fig.2.2, so that the adhesive properties may not be that important and the adhesive bond failure also occurs only due to bad workmanship. Furthermore, the theory does not model major zones of failure or mechanisms of failure and the effect of cracking on peeling is also neglected.

2.7.3 Oehlers and Moran's model for tension face plated beams

This model uses a semi-empirical approach to quantify debonding of the plate-end when terminated in any region of the beam (Oehlers and Moran 1990, Oehlers 1992 and Oehlers 1995). The form of debonding considered is shown in Figs.2.2 to 2.4, where a horizontal crack forms at the level of the tension reinforcement causing a plate/adhesive/concrete sandwich element to peel away from the reinforced concrete beam.

2.7.3.1 Shear peeling

When the plate is terminated in a region in which shear predominates, tests have shown that debonding is initiated by the formation of diagonal shear cracks and, hence, it is assumed that the shear load to cause peeling $V_{pure.tfp}$ is given by the shear strength of the unplated RC beam without stirrups V_{uc}.

$$V_{pure.tfp} = V_{uc} \tag{2.4}$$

It may be noted that the above equation gives a lower bound for shear peeling strength and more refined models are needed to exactly quantify $V_{pure.tfp}$.

2.7.3.2 Flexural peeling

For plates terminated in constant moment regions, the normal stresses shown in Fig.2.19 were found to depend on the curvature induced in the plated section. It was assumed in this analysis that the peak shear stress τ_{pk} and the peak normal stress σ_{pk} are not coincident but are displaced as shown in Fig.2.19. The model was calibrated empirically to give the following moment $M_{pure.tfp}$ to cause flexural peeling when the plate is terminated in a region of pure flexure.

$$M_{pure.tfp}(mean) = \frac{(EI)_{cp} f_b}{0.474 E_p t_p} \tag{2.5}$$

where $(EI)_{cp}$ = flexural rigidity of the cracked plated section and E_p = Young's modulus of the plate material. This equation is based on a mathematical model that was calibrated against test results from fifty seven simply supported reinforced concrete beams under two point loading, covering a range of geometrics and materials. It may be noted that the factor 0.474 in the above equation is an empirical constant and it represents the mean value of the data obtained from a wide spectrum of experimental results. The constant 0.474 is replaced by 0.901 in Eqn.2.5 to get the 5% characteristic value in design, implying a wide scatter in data. The scatter can be attributed to the flexural peeling mechanism in real beams by flexural cracks that causes large local variations in the axial strain in concrete, the curvature along the beam and the flexural rigidity. The scatter can be reduced by more refined models that incorporates the local variations in flexural rigidities, aggregate interlock across the peeling cracks, and the tension stiffening effect, as peeling cracks initiate from flexural cracks and occurs along the level of bottom reinforcement.

2.7.3.3 Flexure/shear interaction

When the plate is terminated in a region of shear V_{end} and flexure M_{end} then the combination of these stress resultants to cause debonding is given by the following failure envelope which was determined empirically. The magnitudes of $M_{pure,tfp}$ and $V_{pure,tfp}$ used in calibrating the following equations were the actual test values and therefore they have a small scatter. However, in practice, one may have to use Eqns.2.4 and 2.5 for estimating $M_{pure,tfp}$ and $V_{pure,tfp}$ that have inherent deviations and hence Eqn.2.6 should be used with caution.

$$\frac{M_{end}}{M_{pure,tfp}(mean)} + \frac{V_{end}}{V_{pure,tfp}} = 1.17 \tag{2.6}$$

where $M_{end} \leq M_{pure,tfp}$ *and* $V_{end} \leq V_{pure,tfp}$.

2.8 Debonding models for side plates

2.8.1 Oehlers Nguyen and Bradford's model for side plated beams

2.8.1.1 Pure flexural peeling

Oehlers, Nguyen, and Bradford (2000b) developed procedures to analyse the debonding in side plates in a similar fashion to the tension face plated beams by Oehlers and Moran (1990). The following equations were derived to estimate the pure flexural peeling strength of side plated beams ($M_{pure,sp}$)

$$M_{pure,sp}(mean) = \frac{f_b(EI)_{cp}}{E_p(0.0185h_{p,cmp} + 0.185t_{sp})} \; and \tag{2.7a}$$

$$M_{pure,sp}(characteristic) = \frac{0.805f_b(EI)_{cp}}{E_p(0.0185h_{p,cmp} + 0.185t_{sp})} \tag{2.7b}$$

where $(EI)_{cp}$ is the flexural rigidity of the cracked plated section that is based on linear elastic analysis in which the tensile strength of the concrete is ignored; $h_{p,cmp}$ is the distance between the centroid of the composite plated beam and the centroid of plate and t_{sp} is the thickness of one side plate. Unlike the prediction equation for the

tension face plated beams, the prediction equation for the mean ultimate peeling strength of side plated beams had a small scatter with a low standard deviation of 0.0059 even though a wide range of plate thicknesses, from 6 mm to 12 mm, and a wide range of plate depths, from 60 to 240 mm, had been used to calibrate the prediction equation. Another noteworthy feature is that the prediction equation has been validated over a very wide range of plate strains (790 (compressive) to 1110 (tensile) microstrains) at debonding.

2.8.1.2 Interaction between flexural and shear peeling

When the side plate end is terminated in a region of both shear V_{end} and flexure M_{end}, then the combination of these stress resultants to cause peeling is given by the failure envelop shown in Fig.2.20. The equation derived by Oehlers, Nguyen, and Bradford (2000b) is

$$\left[\frac{M_{end}}{M_{pure,sp}(mean)}\right]+\left[\frac{V_{end}}{V_{pure,sp}}\right]\leq 1.28 \qquad (2.8)$$

which has a standard deviation of 0.147. It may be noted that in the above equation, the magnitude of $V_{pure,sp}$ was determined from the test 2n4 (Refer Section 2.4.1.1).

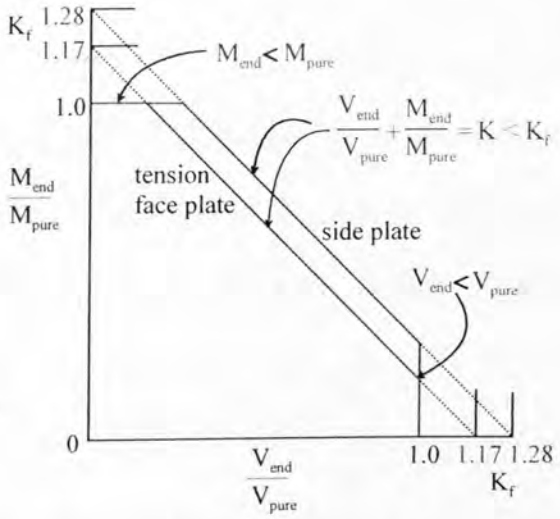

Fig.2.20 Envelopes for shear/flexural peeling interaction

Figure 2.20 also shows the failure envelop for the tension face plated beams and it shows that the side plated beams have a slightly weaker interaction.

2.9 Debonding model for angle plated beams

2.9.1 Nguyen , Oehlers and Bradford's model for flexural peeling

Nguyen, Oehlers and Bradford (1998) developed a complex mathematical model for debonding of angle section glued to the edges of RC beams, due to flexural forces. The procedure involved in calculating the pure flexural peeling capacity of the angle plated beams $M_{pure,a}$ is as follows.

(1) Compute the mean flexural peeling resistance assuming the angle is bonded only to the side $\left(M_{pure,a}\right)_{side}^{mean}$ as

$$\left(M_{pure,a}\right)_{side}^{mean} = \frac{0.88 f_b h_{p,bnd}^3 (EI)_{cp}}{E_p\left(2.220 I_p + 0.0185 h_{p,cmp} h_{p,bnd}^3\right)} \tag{2.9}$$

where $h_{p,bnd}$ is the height of the angle bonded to the side.

(2) Compute the flexural peeling resistance assuming the angle is bonded only to the soffit $\left(M_{pure,a}\right)_{soff}^{mean}$ as

$$\left(M_{pure,a}\right)_{soff}^{mean} = \frac{f_b (EI)_{cp}}{E_p (0.485 t_{p,soff} - 0.0012 h_{p,cmp})} \tag{2.10}$$

where $t_{p,soff}$ is the thickness of the angle plate bonded to the soffit.

(3) The largest of the peeling resistance from these two equations is suggested to be used as a lower bound to the pure flexural peeling resistance of angles that are bonded to both sides and the soffit. A comparison of these equations with test results showed that the side bonding strength generally governs the design and the soffit bonding strength would only govern the design when the height of the angle web is very small.

2.10 Miscellaneous models for debonding

2.10.1 Ziraba, Baluch, Basunbul, Sharif, Azad and Al-Sulaimani's model

The fundamental parameters that control the debonding stresses along the adhesive layer that were developed by Roberts(1989) and which are given in Eqns.2.2 and 2.3 were calibrated by Ziraba, Baluch, Basunbul, Sharif, Azad and Al-Sulaimani(1994) using a non-linear finite element parametric study to give the following shear stress at the plate end $(\tau_{pk})_z$ and normal stress the plate end $(\sigma_{pk})_z$

$$(\tau_{pk})_z = 35 f_t \left(\frac{\tau_{pk}}{f_c} \right)^{\frac{5}{4}} \tag{2.11}$$

$$(\sigma_{pk})_z = 1.10 \sigma_{pk} \tag{2.12}$$

where τ_{pk} and σ_{pk} are given by Eqns.2.2 and 2.3, f_t = tensile strength of the concrete and f_c = compressive strength of the concrete. The interface stresses are assumed to be acceptable when

$$(\tau_{pk})_z + (\sigma_{pk})_z \tan 28^0 \leq c_{all} \tag{2.13}$$

where c_{all} = the allowable coefficient of shear cohesion for the epoxy concrete-steel surface.

The model requires the plate to be terminated within three times the depth of the beam from the support of a simply supported beam, that is in a region in which the shear predominates. As with Roberts' model, this model is sensitive to the adhesive properties even though debonding occurs at the level of the tension reinforcement.

2.10.2 Zhang, Raoof and Wood's model

Unlike the debonding models described above which considered debonding that started at the plate-end, this model developed by Zhang, Raoof and Wood(1995) looks at debonding that initiates between the plate-ends.

A unique debonding mechanism is postulated in which the force generated in the tension face plate at the position of maximum moment is transferred to the concrete beam by a herringbone formation of cracks or 'teeth' in the concrete cover between the plate and the tension reinforcing bars. Further experimental validation of this mechanism is required because in the tests by Oehlers (Oehlers and Moran 1990, and Oehlers 1992) that were used to validate the model, debonding always started from the plate-end, and the formation of the herringbone cracks postulated in this model did not occur in these tests.

2.11 Discussion and Recommendations

It needs to be remembered that most if not all of the steel plated beam research is based on tests on simply supported beams that rarely occur in practice. Therefore, the results from these tests and the debonding models that have either been developed from them or have been calibrated by them, have to be applied with caution to continuous beams.

Consider, for example, the continuous reinforced concrete beam in Fig.2.21a with the applied stress resultants in Fig.2.21b. The experimental research and the debonding models described previously dealt with simply supported beams and, hence, only apply directly to the sagging or positive region A-A of the continuous beam, where the stress resultants have the same shape as those in a simply supported beam as shown in Fig.2.5b. Furthermore, the plates in the tests were bonded to the tension face and, hence, these results are only directly applicable plate-ends bonded to the tensile face D-D of the continuous beam in Fig.2.21a; they are not directly applicable to terminating plate-ends, such as C, in the compression face region E-D. Further, compression face plates may also be needed to enhance the ductility of the reinforced concrete beam as the additional tension plate reinforcement makes the

beam over-reinforced. However, the debonding behaviour of compression face plated beams is not documented and hence, further research is needed to categorise and quantify the peeling forces in compression face plated beams. Tests have shown that bonding steel plates to the tension face of simply supported beams can substantially increase the stiffness and strength but that the technique is prone to debonding that emanates from the plate end. However, further research is necessary to identify and quantify all of the debonding modes.

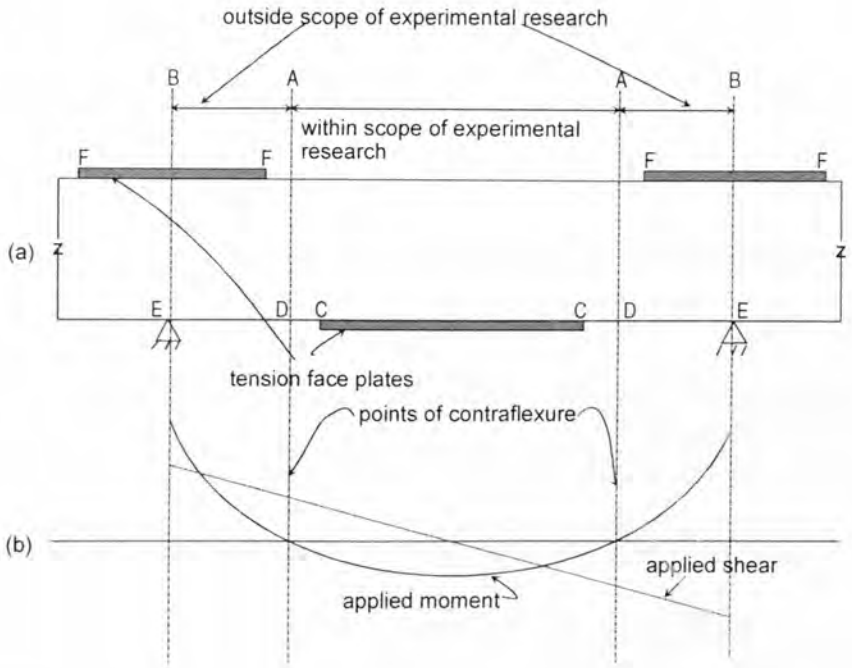

Fig.2.21. Plating continuous beams

It can be said that the studies on flexural peeling of plated beams with different configurations such as tension face plates, side plates and angles plates are exhaustive. Suitable mathematical models are also readily available to quantify the flexural peeling strength of the beams. The only area that needs further research is the flexural peeling of the compression face plated beams.

In so far as the shear peeling is concerned, almost three-fourths of the test data on plated beams pertains to the shear peeling of tension face plated beams. Limited data is also available on the shear peeling of side plated beams. Some studies were also performed on tension face plated beams bonded with limited length side plates or angles to enhance the shear peeling strength. Moreover, only some empirical guidelines are available to prevent the shear bond or shear peeling failure. Hence, further research is necessary for side plated beams, angle plated beams and compression face plated beams and tension face plated beams bonded with additional side plates. This will help to identify the parameters that influences the formation of the critical diagonal crack that leads to this catastrophic failure and hence to facilitate the development of a reliable mathematical model.

Most of the research has concentrated on debonding of the plate-ends such as at C in Fig.2.21(a). Theoretically, debonding can also occur between the plate-ends such as due to the shear stresses given by $VAy/I_p b_p$. However, as the stress resultants in the simply supported beams that were tested and in the sagging region of the continuous beams are similar, that is the positions of maximum shear and maximum moment do not coincide, the tests can be assumed to indirectly cover debonding between the plate-ends.

Plating the tension face of the hogging or negative region A-B in Fig.2.21(a) poses difficulties because the stress resultants within this region, as shown in Fig. 2.21(b), do not have the same shape as the stress resultants in the simply supported beam tests, as in the hogging region the positions of maximum shear and maximum moment now coincide. The research on plate-end debonding that can be applied to the sagging region can also be applied to plate-ends in the hogging region, such as at F. However, debonding between the plate-ends F is now not covered indirectly by the

tests as the positions of the peak moment and shear now coincide. At present, there is only a limited test data on the peeling that occurs within the plate ends such as the work done by Weimin-Lou(1993). Further studies are necessary on this aspect.

2.12 Concluding remarks

In this chapter, the various debonding modes in reinforced concrete beams externally bonded with steel plates of different configurations were categorised based on the available test data. The different mathematical models that deal with these peeling mechanisms were also discussed and their applicability was discussed. Based on this literature study, the aspects that need further investigations were recommended.

References

Adams,R.D. and Wake, C.W.(1984). Structural adhesive joints in Engineering. Elsevier Applied Science Publishers, London. 1984.

Ahmed, M. (1996) Strengthening of reinforced concrete beams by bolting side plates to their sides. University of Adelaide. M.Eng.Sc thesis, University of Adelaide, October,1996.

AS3600 (1994). Australian Standard- Concrete Structures, Standards Australia, 1994.

Baluch MH, Ziraba YN, Azad AK, Sharif AM, Al-Sulaimani GJ and Basunbul IA.(1995). Shear strength of plated RC beams. Magazine of Concrete Research, 47, No.173, Dec. 1995, 369-374.

Calder, A.J.J.(1987). Exposure tests on externally reinforced concrete beams - Performance after 10 years. TRRL RR 129 Transport and Road Research Laboratory, Department of Environment, Crowthorne(U.K.), 1987.

Hussain,M., Sharif,A., Basunbul,I.A., Baluch,M.H. and Al-Sulaimani,G.J.(1995). Flexural behaviour of precracked reinforced concrete beams strengthened externally by steel plates. ACI Structural Journal 1995, V.92, No.1, Jan.-Feb., 14-22.

Jones,R., Swamy,R.N., Bloxham,J. and Bouderbalah,A.(1980). Composite behaviour of concrete beams with epoxy bonded external reinforcement. The International Journal of Cement Composites, Vol.2, No.2, May 1980, pp.91-107.

Jones,.R, Swamy,R.N. and Charif,A.(1988). Plate separation and anchorage of reinforced concrete beams strengthened by epoxy-bonded steel plates. The Structural Engineer 1988: Vol.66/No.5/March: 85-94.

Mcdonald,M.D.(1982) The flexural performance of 3.5 m concrete beams with various bonded external reinforcements. Transport and Road Research Laboratory, TRRL Supplementary Report 728, 1982, Crowthorne, UK.

Newmark, N.M.(1951) Tests and analysis of composite beams with incomplete interaction. Proc.Soc.Experimental Stress Analysis, 1951, (9)1, pp.75-92.

Nguyen,N.T. and Oehlers , D.J. (1997a). Experimental Investigation of Side-Plated Beams Subjected to Both Flexural Peeling and Shear Peeling. Research Report No.R142, Dept.of Civil and Env.Engg., University of Adelaide, Adelaide. April 1997. p45.

Nguyen,N.T. and Oehlers , D.J. (1997b). Experimental Investigation of pure Flexural and pure shear Peeling of angle plates glued the sides and tension faces of RC-beams. Research Report No.R151, Dept.of Civil and Env.Engg., University of Adelaide, Adelaide. April 1997. p44.

Nguyen,N.T., Oehlers, D.J., and Bradford, M.A.(1998). Models for the flexural peeling of angle plates adhesively bonded to R-C beams. Advances in Structural Engineering, Vol.1,No.4,1998. pp.287-300.

Oehlers, D.J. (1989). Discussion on Roberts, T.M., and Haji-Kazemi.,(1989). Proc.Instn.Civ.Engrs., Part 2, Vol.87, Dec.1989, pp.651-663.

Oehlers,D.J.(1992) Reinforced concrete beams with plates glued to their soffits. Journal of Structural Engineering (ASCE), 1992, Vol.118, No. 8, Aug.: 2023-2039.

Oehlers,D.J.(1995). Rules for bonding steel plates to existing reinforced concrete slabs. Australian Civil Engineering Transactions, Vol.CE37, No.1, Feb. 1995, 15-20.

Oehlers,D.J. (2000) Development of design rules for retrofitting by adhesive bonding or bolting either FRP or steel plates to RC beams in bridges and buildings. Proceedings of the ACUN-2, International Composites Conference, Sydney. 14-18 February, 2000. Vol.1, pp.110-119.

Oehlers,D.J.and Moran,J.P.(1990). Premature failure of externally plated reinforced concrete beams. Journal of Structural Engineering (ASCE), 1990, Vol.116, No. 4, April: 978-995

Oehlers, D.J., Nguyen,N.T., and Bradford, M.A.(2000a). Retrofitting by adhesive bonding steel plates to the sides of RC beam. Part 1: Debonding of plates due to shear and design rules. To appear in Structural Engineering and Mechanics: An international Journal.

Oehlers, D.J., Nguyen,N.T., and Bradford, M.A.(2000b). Retrofitting by adhesive bonding steel plates to the sides of RC beam. Part 1: Debonding of plates due to flexure. To appear in Structural Engineering and mechanics: An international Journal.

Orr,D.M.F. and Lynch,C.(1993). Design of externally bonded flexural and shear reinforcement for strengthening reinforced concrete T-beams. *Proceedings of the 13th* Australasian Conference on the Mechanics of Structures and Materials, Univ. of Wollongong, July 1993, Wollongong, Australia: 651-656.

Raina,V.K.(1988). Concrete Bridge Practice. Tata McGraw-Hill Publishing Co. New Delhi. 1988.

Raithby,K.D.(1980). External strengthening of concrete bridges with bonded steel plates. TRRL Supplementary Report 415, Transport and Road Research Laboratory, Crowthorne, UK. 1980.

Rao, M.V.B., Ali,M.S.M., and Kurmi,D.P.K.(1992). Strengthening of RCC bridges by externally bonded plates. Indian Highways, April 1992.

Roberts,T.M.(1989). Approximate analysis of the shear and normal stress concentrations in the adhesive layer of plated RC beams. The Structural Engineer, Vol. 67, No.12, 20, June 1989, 229-233.

Roberts,T.M. and Haji-Kazemi,H.(1989). Theoretical study of the behaviour of reinforced concrete beams strengthened by externally bonded steel plates. Proc. Instn Civ. Engrs, Part 2, 1989, 87, Mar., 39-55.

Sharif,A, Al-Sulaimani,G.J., Basunbul,A., Baluch,M.H. and Husain,M.(1995). Strengthening of shear-damaged RC beams by external bonding of steel plates. Magazine of Concrete Research, 47, No.173, Dec. 1995, 329-334.

Smith, S.T., and Bradford, M.A.(1995). Ductility of reinforced concrete beams with side and soffit plates. Proceedings of the 14th Australian conference on the mechanics

of structures and materials, University of Tasmania, Hobart, Australia, December, 1995.

Swamy,R.N., Jones,R. and Bloxham,J.W.(1987) Structural behaviour of reinforced concrete beams strengthened by epoxy-bonded steel plates. The Structural Engineer 1987: Vol.65A/No.2/Feb: 59-68.

Swamy,R.N., Jones,R., and Charif,A.(1989). The effect of external plate reinforcement on the strengthening of structurally damaged RC beams. The Structural Engineer 1989: Vol.67/No.3/Feb.: 45-56.

Swamy,R.N., Hobbs,B., Roberts,M.(1995). Structural Behaviour of externally bonded, steel plated RC beams after long-term exposure. The Structural Engineer, Vol.73, No.16, Aug. 1995, 255-261.

Weimin-Luo (1993). Strengthening of post-tensioned and reinforced concrete beams strengthened by steel plates. M.Engg., thesis, University of Adelaide, Adelaide, Australia.

Zhang,S., Raoof,M.and Wood,L.A.(1995). Prediction of peeling failure of reinforced concrete beams with externally bonded steel plates. Proc. Instn Civ Engrs Structs & Bldgs, 1995, 110, Aug., 257-268.

Ziraba Y.N., Baluch M.H., Basunbul I.A., Sharif A.M., Azad A.K., Al-Sulaimani G.J. (1994). Guidelines toward the design of reinforced concrete beams with external plates. ACI Structural Journal, V.91, No.6, Nov.-Dec. 1994. 639-646.

CHAPTER-3: REVIEW ON STRENGTHENING OF REINFORCED CONCRETE BEAMS WITH EPOXY-BONDED FIBRE REINFORCED PLASTIC (FRP) PLATES

CONTENTS

3.1 Introduction

Bonding steel plates to the surfaces of reinforced concrete structural elements has been adopted widely as a convenient and effective method to strengthen existing buildings and bridges for several decades. However, it suffers from some disadvantages like deterioration of the bond at the steel-concrete interface due to the corrosion of steel, difficulty in manipulating the plates at the construction site due to heaviness and the need to form proper joints due to the limited delivery length of steel plates (6-8 m). Therefore recently, steel plates are increasingly being replaced by fibre reinforced plastic (FRP) plates.

FRP sheets are normally made of continuous carbon, aramid, or glass fibres that have a diameter in the range of 5-25 μm in one (unidirectional) or two perpendicular direction (pseudo-isotropic or bi-directional) and they are bonded together with a matrix such as epoxy or polyester resins. The resulting FRP material possesses superior structural tailorability, excellent corrosion resistance and high resistance to environmental degradation. The density of FRP is only 20% of the density of steel but it possesses high tensile strength of the order 1000-3000 MPa. The stiffness also has a wide range as the Young's modulus in the direction of fibre orientation is of the order of 50, 120 and 150-300 GPa for unidirectional FRPs with glass, aramid and carbon fibres respectively. Unlike mild steel, FRP materials are brittle but they are linearly elastic up to failure strains of about 10000-20000 microstrain for carbon fibre and 25000-30000 microstrain for other fibres. (Triantafillou and Plevris(1992), Meier(1995), Triantafillou(1998a), Hollaway and Leeming(1999)). Although FRP materials are many times more expensive than mild steel, they are often cost-effective as FRP plates have a high strength-to-weight ratio

and the costs involved such as in transportation, labour and handling are less. In this regard, Meier (1995) suggests that FRP plates have an edge in applications such as bridges, multi-storey parking spaces, railway stations and specialised industrial structures where corrosion, length of strengthening component (>8m) and handling on construction site plays a dominant role.

3.2 Failure modes in FRP plated RC beams

There are several modes of failure that are reported in the literature and they can be classified into two major categories. In the first category, the failure modes in plated beams are similar to the classical failure of reinforced concrete beams such as steel yielding followed by FRP plate fracture, steel yielding followed by concrete compressive crushing or concrete compressive crushing only. The second major category of failure is the premature peeling of the FRP plates as in the case of steel plated beams (Refer Chapter-2). The major difference in the documented literature between steel plated beams and FRP plated beams is that there is hardly any study reported on flexural peeling and the interaction between shear and flexural peeling mechanisms in FRP plated beams. However, there exists quite a good amount of information on peeling caused by diagonal shear cracks and axial peeling in FRP plated beams. Another mode of debonding is caused by uneven bonding layers that can induce peeling forces. In the case of steel plates, a minimum thickness of 3 mm is needed to avoid deformations due to sand blasting for preparing the surface. No such restriction is there for FRP plates and very thin or flexible plates can be used for strengthening. In this case, the thin FRP plate tries to align itself under tensile forces leading to local peeling (Arockiasamy 2000).

3.2.1 Debonding failure modes

For the convenience of discussion, the research on debonding FRP plated beams can be divided into three major groups. Firstly, many experiments are reported in the literature on simply supported beams that were bonded with FRP plates to their tension faces in which the plates were terminated very close to the supports. As the plate ends are subject to high shear forces and negligible moments, they are vulnerable to premature failure due to the formation of shear cracks. Debonding can occur well before the shear strength of even the unplated beam could be realised as the shear stirrups are mobilised only after the formation of shear cracks. In the second group, studies were conducted to enhance the shear strength of the plated beams by bonding FRP plates or strips to the webs. Several analytical methods were also proposed to quantify the shear strength or the shear peeling strength of these beams. Parallel to these two major efforts, a third component was concentrated entirely to understand the debonding behaviour between concrete elements and external plates that are subject to axial loads i.e. axial peeling. In this Chapter, the debonding aspects related to tension face plated beams as well as side plated beams are dealt with. The studies on axial peeling of FRP plates as well as steel plates are described in the next Chapter.

There is an enormous amount of documented literature on the implications of bonding FRP plates to reinforced concrete beams. Unlike steel plated beams, the studies of FRP plated beams involves a wide range of parameters such as fibre orientaion, FRP plate strength and stiffness, shape of the plates and prestressing the plates before bonding them to concrete. Therefore, it poses problems in summarising the research on FRP plated beams and drawing straightforward conclusions from those studies. The need for further understanding of the failure processes and their governing parameters have been stressed by many investigators as mentioned by

Buyukozturk and Hearing (1998). Therefore, only a few significant studies on FRP plated beams are highlighted in this review.

3.3 Experimental investigations on tension face plated beams

3.3.1 Tests by Ritchie, Thomas, Lu and Connelly

Ritchie, Thomas, Lu and Connelly(1991) tested sixteen reinforced concrete beams of size 150 mm x 300 mm bonded with various types of FRP plates such as glass, carbon-glass, carbon, aramid and their elastic moduli varied between 10,000 MPa and 115,000 MPa. The FRP plates were pseudoisotropic excepting for the unidirectional aramid FRP and the thickness of the plates ranged between 1.3 mm and 10 mm. The lengths of the plates were also varied between 1.8 m to 2.4 m. Two unplated beams and two mild steel plated beams were used for reference. The beams were simply supported over a span of 2.4 m and tested under four point loading.

The failure of the beams with partial length tension face plates did not occur in the maximum moment region. Rather, they failed by debonding at the plate ends along the concrete cover in spite of the provision of adequate shear stirrups to prevent shear failure in concrete. In order to shift the location and the mode of failure of the plated beams, the authors tried various modifications. In the first scheme, the tension face plated beams were bonded with additional unequal leg fibre glass angles such as those used by Jones, Swamy and Charif (1988) in steel plated beam tests (Refer section 2.3.1.6). Although the additional angle plates increased the failure loads substantially, the failure modes i.e. peeling of tension face plates could not be avoided. In the second scheme, full height side plates were bonded at the tension face plate ends as in the case of steel plated beams tested by Weimin-Luo (1993) (Refer Section 2.5.1 and Fig.2.14). The side plates were then connected to the tension face plates using bonded fibre glass angles. In this case, the failure load was enhanced and

the failure mode of one of the beams could be altered from shear peeling at the end to the failure by yielding of the steel bars followed by the fracture of the external plate in the constant moment region. In the third scheme, the tension face plates were replaced with a pair of angles bonded to the sides and soffits of the beam. Having the angles extended above the internal steel reinforcement would be beneficial as the shear peeling in tension face plated beam occurred along the concrete cover. However, the shear peeling of the angles occurred as the angles did not extend high above the steel. Finally, the plates were extended right up to the supports and this method was successful in both increasing the failure load and the failure mode was shifted from the plate peeling at plate end to the plate fracture at the maximum moment region. Increases in stiffness under working load ranged from 17% to 99% and increases in ultimate strength from 40% to 97% were achieved for the beams bonded with FRP plates.

3.3.2 Tests by Saadatmanesh and Ehasni

In another study, Saadatmanesh and Ehasni(1991a) tested five rectangular and one T-beam that were bonded with 6 mm thick glass FRP plate that had an ultimate strength of 400 MPa, and an elastic modulus of 37,230 MPa. The failure strain of the GFRP plate was 10,774 microstrain compared to the steel bar yield strain of 2,280 microstrain. The beams were tested under four point loading with a shear span to depth ratio of 5 which is generally not critical for shear failure. The beam with inadequate shear stirrups failed by compression concrete crushing and the recorded strain in the external plate was about 4,000 microstrain. All other beams failed due to premature debonding of the bonded plates along the concrete covers due to shear, even when a moderate amount of prestress was induced in the FRP plates. The recorded strains in the FRP plates varied between 4,000 to 8,000 microstrain. This

compares with the failure strain of GFRP plate which was 10,774 microstrain and the steel bar yield strain of 2280 microstrain. None of the plated beams reached their theoretical full flexural capacity. However, all of them showed an enhanced ultimate load capacity which was accompanied with loss of ductility.

3.3.3 Tests by Sharif, Al-Sulaimani, Basunbul, Baluch and Ghaleb

The tests conducted by Sharif, Al-Sulaimani, Basunbul, Baluch and Ghaleb (1994) at King Fahd University also throws light on the merits and demerits of bonding GFRP plates to strengthen RC beams. The beams were pre-cracked before testing and they were load tested at a shear span to depth ratio of 3.5. The GFRP plates had a width to thickness ratio of 33 to 100 and the ultimate failure stain was 11000 microstrain compared to the yielding strain of the steel tension bars of about 1700 micro-strain. When the plates were bonded to the tension face alone, flexural failure occurred due to the fracture of the plate for the thinner plates. In the case of the beams with thicker plate, premature failure by plate debonding and plate separation occurred with clear reductions in ductility despite the presence of closely spaced shear stirrups. In this study, two anchorage schemes at the plate ends were tried. Firstly, the tension face plate ends were anchored by additional bolts. In this case, the peeling occurred due to diagonal shear cracks in the vicinity of the plate end and the peeling strength improved marginally by 10%. Secondly, the whole shear span was bonded with full depth side plates along with the anchor bolts at the tension face plate ends to arrest the premature failure. The results in this case was mixed. While in one beam flexural failure occurred by crushing of concrete with a 20% improvement in ultimate strength, the side plates prematurely debonded in the second beam. This clearly shows that even to post moderate increases in ultimate load capacity, the regions susceptible to high shear stresses have to be heavily protected against shear peeling failure.

3.3.4 Tests by Triantafillou and Plevris

In this study, Triantafillou and Plevris(1992) first categorised different types of failure modes in FRP plated beams as: steel bars yielding followed by FRP plate rupture, steel bar yielding followed by concrete crushing; concrete crushing before steel yielding; and debonding of FRP plates. Steel bars yielding followed by FRP plate rupture can occur if the steel and FRP area fraction (ρ_{frp}, ratio of the cross section area of FRP plate to the beam cross section area) are quite small. If for the same beam cross section, FRP area fraction is high, then the beam can fail due to concrete crushing while the steel section may have yielded or not depending on steel area fraction. Finally, debonding can occur by shear cracks in the concrete, debonding along concrete cover due to shear flow forces and failure along the adhesive layer. This study also prescribes equations for each mode of failure. For the first three failure modes, prediction equations were derived by modifying conventional RC beam equations. On the other hand, the predictive equations for debonding that describe the interface crack propagation were based on complex fracture mechanics approaches that still need experimental inputs for parameters such as critical strain energy release rate. The equation suggested for the peeling induced by shear crack also needs experimental calibration as the authors postulate that shear peeling occurs when the ratio of the horizontal to vertical concrete opening reaches a critical value. This critical crack opening ratio is considered to vary with the combined shear stiffness of the steel reinforcement and the FRP sheet. Another mode of peeling mentioned was the concrete shear delamination which involves shear failure of concrete layer between the FRP plate and the steel reinforcement due to high shear stresses due to longitudinal shear flow at the plate end region. This mode of peeling can be prevented by limiting the maximum interface shear stress that depends on the strength of the

concrete. The limiting value suggested was 8 MPa for normal strength concrete. This can be compared with the limiting value of $\sqrt{2}f_t$ suggested for steel plated beams by Swamy et.al (Refer section2.7.1)

Under this investigation, eight RC beams of size 76 mm x 127 mm and 1350 mm long that contained shear stirrups were tested. The beams were bonded with a unidirectional CFRP plates of elastic modulus 186 GPa, ultimate tensile strength 1450 MPa with a failure strain of 7800 microstrain. The beams were simply supported over a span of 1220 mm and they were tested under four point loading with a shear span to depth ratio of 3.5. The main variable in the study was the five different CFRP ratios (ρ_{frp}), namely 0.09%, 0.13%, 0.43%, 0.59% and 1.26%. Whereas the unplated beam failed in a typical under reinforced concrete beam failure mode, the plated beams with a very low FRP plate ratios of 0.09% and 0.13% failed by steel yielding followed by FRP rupture. On the other hand, beams with higher FRP plate ratio failed due to debonding. The increase in ultimate load over that of the unplated beam varied progressively from 50% to 300% accompanied with proportional loss of ductility.

3.3.5 Tests by Swamy and Co-workers

In a study conducted by Spadea, Bencardino and Swamy (1998), three beams with carbon FRP plates bonded to the tension face were tested under four point bending over a span of 4.8 m. It is worth noting that two of these beams were provided with external anchorages at the plate ends in the form of side plates such as shown in Fig.2.14. Furthermore, plates were bonded to the sides of the compression region of the beams; these were termed as confinement plates and they were used to improve the ductilty of the plated beams. It may be noted that the tension face plate was a 1.2 mm thick CFRP sheet while the external anchorages and confinement plates were

made of mild steel. Whereas the failure of the beam bonded with only tension face plate occurred in a brittle manner accompanied with explosive debonding of the CFRP sheet, the beams with additional anchorages maintained the composite action up to almost its ultimate load. The tension face plated beams with such anchorages carried about 70% higher load than the unplated beam, developed concrete compressive strains of 4500 microstrain, enabled the utilisation of the strain capacity of the bonded CFRP plate and the structural ductility was vastly improved.

In a related study, Swamy and his co-workers at the University of Sheffield (Mukhopadhyaya, Swamy, and Lynsdale 1998; Swamy, Mukhopadhyaya, and Lynsdale 1999) compared the performance of the beams bonded with glass FRP plates to the tension faces with that of the steel plated beams. The elastic modulus of the GFRP plates was only one-eighth that of the steel plates. The effect of various parameters on the external plating such as the amount of internal stirrups, lateral confinement of concrete in compression zone, and the amount of flexural reinforcement were critically assessed. These tests revealed that premature peeling in beams bonded with low modulus tension face plates can be prevented by using properly designed plate end anchors such as U-shaped strips and lateral confinement plates. The study indicated that the shear strength of RC beams without internal shear reinforcement can be enhanced by the above mentioned plating schemes. However, the researchers could not quantify the shear contribution of the various bonded plate components. This was attributed to the different behaviour of plates and stirrups under shear and the need for further research on this topic was stressed.

3.3.6 Closure

The above mentioned studies clearly bring out how varied were the different strengthening schemes and the various FRP plate materials used. It also highlighted

the failure modes in tension face plated beams and some of the methods used to mitigate the premature debonding. FRP plates bonded to the tension face of RC beams have a tendency to fail in the vicinity of the plate ends when subjected to high shear forces and low moments, and when the plates are thick. Otherwise for very thin plates, failure occurs by plate rupture that is preceded by steel bar yielding. Another major conclusion is that shear stirrups are ineffective in preventing when debonding occurs by the formation of diagonal shear cracks. Bonding additional side plates or angles in the vicinity of the plate end region in most cases could postpone the premature debonding. These findings were confirmed in many more studies that were conducted in Europe and in North America such as reported by Meir and Kaiser (1991), Quantrill, Hollaway and Thorne (1996), Varastehpour and Hamelin (1997), He, Pilakoutas and Waldron (1997), Buyukozturk and Hearing (1998), and Bencardino, Spaeda and Swamy(1997).

3.4 Studies on RC beams bonded with FRP plates to the sides

3.4.1 Introduction

Failure through shear peeling in simply supported reinforced concrete beams with FRP plates that are bonded to the tension faces and terminated closer to the supports occurs in the same fashion as in steel plated beams. That is to say, in the case of concrete beams with nominal shear stirrups peeling occurs due to the extension of shear cracks from the end of the plate to the load point. When the beams are provided with shear stirrups, the debonding occurs due to the formation of debonding cracks along the concrete cover (Buyukozturk and Hearing 1998). As shear peeling of tension face plated beams occurs at relatively low load levels, the increase in the flexural strength of such beams is heavily inhibited. Therefore, a number of studies

have been reported in the literature on the techniques to improve the shear peeling strength.

3.4.1.1 Strengthening schemes

Several strengthening schemes were studied. Beams were bonded only with FRP strips at regular intervals (Fig.3.1a) or strips in combination with tension face plate (Fig.3.1b) (Sharif et.al 1994). FRP wings were used alone or in combination with tension face plate (Fig.3.1c and 3.1d) (Al-Sulaimani, Sharif, Basunbul, Baluch and Ghaleb 1994). Bonding full length plates to the sides of the beams, as shown in Fig.3.1e is widely reported (Mitsui, Murakami, Takeda and Sakai 1998). Performance of U shaped FRP jackets (Fig.3.1f) was also investigated. In one study, a single piece GFRP I-jacket was used, as shown in Fig.3.1g (Sharif, et.al 1994).

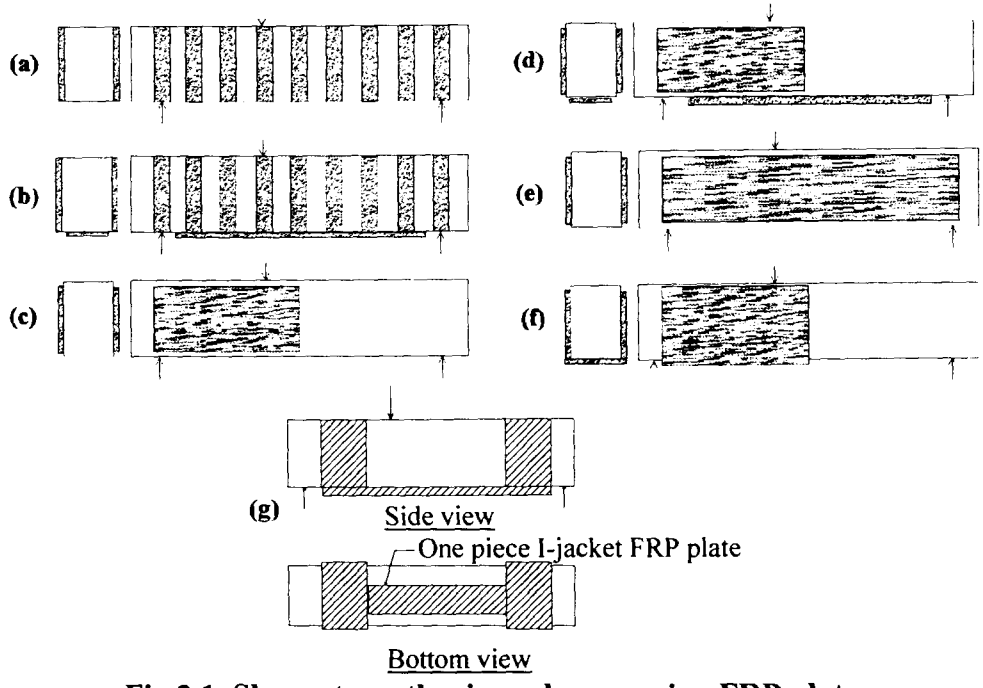

Fig.3.1. Shear strengthening schemes using FRP plates

Although most studies were conducted on rectangular RC beams, some investigators used RC T-beams that were wrapped totally with FRP fabrics or only to the webs and bottom flanges as shown in Fig.3.2a (Chajes, Januszka, Mertz, Thomson and Finch 1996) or to their sides as shown in Fig.3.2b. In some cases mechanical

anchors were also used additionally (Fig.3.2c). Another variable involved in several studies was the direction of fibre orientation in FRP material. As FRP is an anisotropic material characterised by high strength along the direction of fibre orientation, the fibres were oriented in the directions best suited for resisting the shear cracks (90° or 45°) as shown in Figs.3.3a and 3.3b (Khalifa, Gold, Nanni and Aziz 1998). Alternatively, pseudo-isotropic FRP plates such as shown in Figs.3.3c and 3.3d were used. They were fabricated by orienting the fibres in two perpendicular directions.

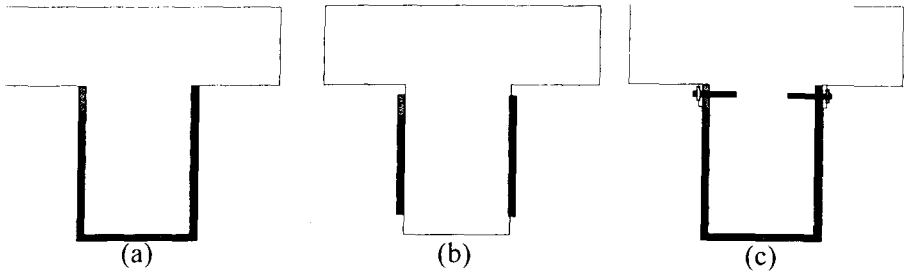

Fig.3.2. Shear strengthening schemes for T-beams

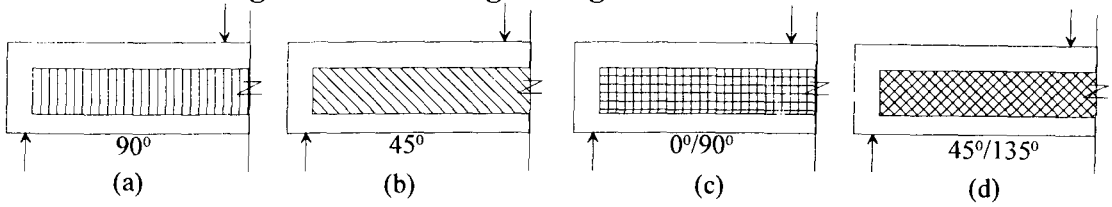

Fig.3.3. Fibre orientations

3.4.2 Overview of experimental investigations

3.4.2.1 Tests by Al-Sulaimani, Sharif, Basunbul, Baluch and Ghaleb

Al-Sulaimani, Sharif, Basunbul, Baluch and Ghaleb (1994) conducted studies on rectangular reinforced concrete beams, 150 mm x 150 mm in cross section and 1200 mm in span, that were damaged to the level of the appearance of first diagonal cracks. These beams were then repaired by GFRP plate bonding. The beams tested in this series may not represent a real life situation as they were of short span (1200 mm) and the internal shear stirrups were ineffective in resisting shear as the stirrup spacing (200 mm) was greater than the depth of the beam (150 mm). The GFRP plates were 3 mm

thick and had an ultimate strength of 200 MPa in the direction of fibre. The study shows that beams strengthened by a series of strips bonded to their webs as shown in Fig.3.1a or side plates that covered the entire shear span, either alone (Fig.3.1e) or in combination with tension face plates (Fig.3.1d) were only marginally effective in increasing the shear strength by 25-30%. Moreover, the strips and the wings debonded due to the formation of critical diagonal shear cracks. These beams failed before achieving their full theoretical flexural capacity. However, beams bonded with anchored U-jackets (Fig.3.1f) over the entire shear span with or without a bonded tension face plate could achieve the flexural strength with adequate ductility and the shear strength of the beam was enhanced by about 65%. This is due to the prevention of premature failure, as the jackets were well anchored at the bottom of the beam and the continuity rendered by the geometry of the jacket could minimize the effect of peeling stress concentrations at the jacket ends.

3.4.2.2 Tests by Chajes, Januszka, Mertz, Thomson and Finch

Chajes, Januszka, Mertz, Thomson and Finch (1996) tested micro-T beams that were wrapped with three different composite fabrics (aramid, E-glass and graphite composite fabrics) to their webs and the bottom flanges as shown in Fig.3.2a. This permitted them to study the effects of various FRP stiffnesses and strengths on the increase in the shear strength. The beams were not provided with internal shear stirrups and the thickness of the wrapping used were thin, i.e. varied between 0.5-1 mm. The beams were tested in flexure and the performance of eight beams with external shear reinforcements was compared with that of four control beams with no external reinforcement. All beams experienced a brittle-mode of shear failure due to the formation of diagonal shear cracks.

For beams bonded with E-glass and graphite fabrics, the fabric immediately failed by being torn along a line corresponding to the diagonal shear crack. For the beams wrapped with aramid fabrics, the shear failure was indicated by rapid unloading and the toughness of the fabric enabled it to resist tearing. The strain measurements indicated that the external fabrics had not reached their full tensile capacity. The average increase in the ultimate load capacity over the unplated beam for the beams wrapped with aramid, E-glass and graphite fabrics with 0/90 degree fibre orientation was 85 % and that for the case of graphite fabric with 45/135 degree fibre orientation was 125%. Even though these tests are done on micro-beams and hence have a limited use, they do show the significance of the diagonal shear cracks and the fibre orientation in shear peeling.

3.4.2.3 Tests by Triantafillou

In yet another study, Triantafillou (1998b) conducted tests on eleven non-shear stirrupped, rectangular, reinforced concrete beams, of which nine were strengthened in shear with epoxy-bonded uni-directional carbon FRP fabrics attached on both sides to the full depth, as shown in Fig.3.1e and two were used as control specimens. The micro-beams were 70x110 mm in cross-section and they were simply supported over a span of 800 mm. They were tested under four-point loading and the shear span was 320 mm. The constant bending moment region was 160 mm long and it was not plated. The CFRP fabrics used had an elastic modulus of 235 GPa and a tensile strength of 3300 MPa. The FRP fabrics were quite thin and three different thicknesses 0.12 mm, 0.18 mm and 0.24 mm were used. All the plated beams failed by the formation of diagonal shear cracks in the constant shear span followed by CFRP debonding. Failure occurred at loads significantly higher than the unplated control beams and the increase in strength varied between 65% to 95%.

3.4.3 Closure

The previous discussion shows that various FRP plating schemes such as side plates, strips and wings are prone to debonding due to the formation of diagonal shear cracks. The U-shaped wings are able to resist the shear peeling well as they are better gripped to the beam due to the continuity of geometry. Most of the studies were carried out on small scale RC beams and in most cases, either internal shear stirrups were absent or they were ineffective in resisting the shear loads. Had adequate amounts of stirrups been provided, the debonding of external plates could have probably preceded the overall shear failure of the RC beam as in the case of steel plated beams (Chapter-2). Hence, any reported improvement in shear strength of RC beams due to FRP plating should be interpreted carefully.

3.5 Analytical approaches for FRP plated beams

3.5.1 Model for classical failure modes

The failure modes in tension face plated or side plated beams that are similar to the classical failure of reinforced concrete beams are not reviewed in this Chapter as the main thrust of the present study is the debonding of plated beams. Moreover, the flexural and shear capacities of the plated beams in such a case can be derived in the same manner as for a reinforced concrete beam by assuming perfectly linear-elastic behaviour of FRP materials till failure, a perfect bond between the concrete and plate, and no-slip between the interfaces. Such models were presented by Saadatmanesh and Ehsani(1991b), Triantafillou and Plevris(1992), and Meier(1995).

Neubauer and Rostasy (1997) suggested that in order to prevent the separation of the FRP plate from the concrete at flexural cracks and to avoid yielding of the steel reinforcement under service loads, the ultimate plate strain for bending design should not exceed (a) five times the yield strain of the internal steel reinforcement and (b)

half the ultimate strain of the FRP material. However these guidelines should be used with caution as the peeling of steel plates as discussed in Chapter-2 and some of the tests on FRP plated beams described in this chapter clearly show that certain debonding modes cannot be prevented by controlling the strains in the external plates.

3.5.2 Models for failure by debonding in tension face plated beams

The most critical failure mechanism in tension face plated beams is the debonding of FRP plate ends due to high shear forces. To analyse this mechanism, Malek, Saadatmanesh and Ehsani(1998) suggested analytical solutions for normal stresses and shear stresses at the plate ends. Their modeling is similar to the one proposed by Robert's model for steel plated beams (Section 2.7.2). The main assumptions made by Malek, Saadatmanesh and Ehsani(1998) were: the linear elastic and isotropic behaviour of the FRP, epoxy resin, concrete, and steel reinforcement; and complete composite action between plate end and concrete. The mathematical model was validated from a single test in which the plate-end was terminated in a region of predominantly shear and should, therefore, be only applied in this region. Malek, Saadatmanesh and Ehsani(1998) also tried to include the effect of flexural cracks on the shear stresses but the equations essentially give the stresses in the adhesive layer. It is worth noting that the model is sensitive to the adhesive properties because it is considering the stresses at the adhesive /concrete interface. In practice, debonding occurs at the level of the tension reinforcement so that the adhesive properties may not be that important.

3.5.3 Quantification of shear strength of the FRP plated beams

From the previous discussions in Sections 3.3 and 3.4, it can be inferred that the studies on shear strengthening of reinforced concrete beams using FRP materials is

quite limited. However, most of the studies are concerned with beams of relatively small sizes and in some cases the beams had no shear stirrups. Therefore, the test results may not fully reflect the ground realities. Moreover, a variety of FRP materials and configurations have been used and in most cases the thickness of the plates was very small. The matter is further complicated by the different orientation of fibres that were used for the same material in different studies. All these factors contributed to the development of different models for quantifying the contribution from the external plates and the available literature does not provide a universal approach.

3.5.4 Methods based on effective strain in FRP plate

3.5.4.1 Idealising FRP plates as shear stirrups

In most of the models, the external FRP reinforcement is idealised similar to internal shear stirrups, perfect bond is assumed between the FRP plate and concrete until failure, and the stress-strain relationship of FRP material is linear until failure. The well known equation for the shear strength of a reinforced concrete beam (Warner, Rangan and Hall 1989) is given by

$$V_u = V_{uc} + V_{us} \tag{3.1}$$

where V_{uc} is the shear resisted by the concrete and V_{us} is the part of the shear resisted by the stirrups and is given by Warner et.al (1989) as

$$V_{us} = \frac{A_{sv}}{s} f_{sy.f} d_0 (\cos\alpha_v + \sin\alpha_v) \tag{3.2}$$

Here, A_{sv}, s, $f_{sy.f}$ *and* α_v are the area, spacing, yield strength and inclination of the stirrup respectively and d_0 is the distance of the extreme compression fibre of the concrete to the centroid of the outermost layer of tensile reinforcement. Most researchers postulated that the contribution of shear strength by the FRP plates (V_{frp}) should be added to the two other components V_{uc} and V_{us} in Eqn.3.1 to get the shear

strength of the FRP plated RC beams. Most of the researchers developed the equation for V_{frp} in the same form as Eqn.3.2 for V_{us}. For example, for continuous external FRP side plates (Fig.3.1e) such as those used by Mitsui et.al (1998) or for FRP wrapping (Fig.3.2a) such as those used by Chajes et.al (1996), the equation for the theoretical shear capacity of the external plates (V_{frp}) can be written as

$$V_{frp} = A_{frp}\sigma_{frp}d_0(\sin\beta + \cos\beta) \tag{3.3}$$

where A_{frp} is the total area of the plates, σ_{frp} is the stress in the plate at failure and β is the orientation of the fibre to the longitudinal axis of the beam.

Unlike internal shear stirrups where failure normally occurs by stirrup yielding, the FRP plate material fails by debonding well before reaching its ultimate strength. As the FRP material is brittle and linear elastic till failure, the stress and strain at failure in case of FRP plate material are unknown. In order to overcome this problem, there are various schools of thought exist among the investigators. The first category of researchers prescribed a definite magnitude of strain in the FRP plate at failure that was determined from the tests conducted by them. A second group of researchers suggested equations to calculate the strain magnitude at failure which were calibrated against a pool of test data. A third group of researchers prescribed a limiting bond stress between concrete and FRP plate in order to derive predictive equations for V_{frp}.

3.5.4.2 Equations based on definite magnitudes of plate strains at failure

In the first category, Chajes et.al (1996) suggested an average value of strain in FRP plate at failure to be 0.005 and they suggest the following equations for V_{frp}.

$$V_{frp} = A_{frp}(0.005E_{frp})d_0, \quad \textit{if fibre orientation } \beta = 0/90^0 \tag{3.4a}$$

$$V_{frp} = A_{frp}(0.005E_{frp})d_0\sqrt{2}, \quad \textit{if } \beta = 45/135^0 \tag{3.4b}$$

The equations were found to be in good agreement with the test results obtained by them. However, it may be noted that the size of the beam and the thickness of the FRP plate used were comparatively very small and the beams contained no shear stirrups. Hence, this calibration does not reflect the real life situation for shear strengthening. Others who suggested similar models are Ohuchi et.al (1994) who performed tests on reinforced concrete beams that were strengthened for shear with wrapped-around carbon fabrics. The shear capacity of the CFRP was modelled as analogous to steel stirrups and the limiting strain is assumed to be either the ultimate tensile strain of CFRP or two-third of it depending on its thickness. Mavlar, Warren, Inaba (1995) suggested the limiting strain to be that of the ultimate tensile strain of FRP.

3.5.4.3 Equations to predict plate strain at failure

In the second category, Triantafillou (1998) analysed about 42 test results from various studies in which the FRP plates were bonded either to the sides to the full depth of the web as in Fig.3.1e or wrapped around as in Fig.3.2a. The strain in the FRP at the instance of debonding was termed as effective FRP strain ($\varepsilon_{frp,e}$) and it was observed to be a function of the axial rigidity of the FRP sheet ($\rho_{frp}E_{frp}$) where ρ_{frp} is the FRP area fraction. The parameter ρ_{frp} is defined as the ratio of the FRP plate area to the beam cross sectional area; for a beam bonded with full depth side plates, ρ_{frp} equals $2t_{sp}/b_w$, where t_{sp} is the thickness of the side plates b_w is the width of the beam web and E_{frp} is the elastic modulus of FRP plate. From the experimental data, the magnitudes of V_{frp}, d_0, β and A_{frp} are known and therefore, the stress in FRP plate at failure σ_{frp} and hence the effective strain $\varepsilon_{frp,e}$ can be determined from Eqn.3.3. Thus,

the following relationship was established by Triantafillou between effective strain $\varepsilon_{frp,e}$ and axial rigidity of FRP plates $\rho_{frp}E_{frp}$.

$$\varepsilon_{frp,e} = 0.0119 - 0.0205(\rho_{frp}E_{frp}) + 0.0104(\rho_{frp}E_{frp})^2 \quad \text{for } 0 \le \rho_{frp}E_{frp} \le 1\,\text{GPa} \qquad (3.5a)$$

$$\varepsilon_{frp,e} = 0.00245 - 0.00065(\rho_{frp}E_{frp}) \quad \text{for } \rho_{frp}E_{frp} > 1\,\text{GPa} \qquad (3.5b)$$

It was noted by the author that some of the experimental data used by him pertained to relatively small-sized concrete beams and they may not represent practical sizes of beams used in buildings and bridges. However, the author feels that the equations for $\varepsilon_{frp,e}$ would be conservative for large sized practical beams. Nonetheless, RC beams in practice normally contain a good amount of shear stirrups and hence debonding may occur well before the shear capacity V_u of the unplated beam is reached. Other limitations are the data base contained only three different types of the FRP fibre orientation of 45, 56 and 90 degrees and about 85% of the data pertained to CFRP plates that had an elastic modulus of 230 GPa. The rest of the data pertains to a low elastic moduli value in the range of 10-20 GPa and hence, there is a big gap in the material properties.

Khalifa, Gold, Nanni and Aziz(1998) took a further lead from Triantafillou's work and they included newly available results to the pool of test data used by Triantafillou . It was found that the axial rigidity $\rho_{frp}E_{frp}$ did not exceed 1.1 GPa in all the data. They suggested a modification to eliminate the effects of various types of FRP sheets. A relationship was established between the ratio of effective strain ($\varepsilon_{frp,e}$) to the ultimate strain of FRP plates ($\varepsilon_{frp,u}$), $R=\varepsilon_{frp,e}/\varepsilon_{frp,u}$ and the axial rigidity ($\rho_{frp}E_{frp}$). The equation for R is

$$R = 0.778 - 1.2188(\rho_{frp}E_{frp}) + 0.5622(\rho_{frp}E_{frp})^2 \le 0.50 \text{ for } \rho_{frp}E_{frp} \le 1.1\text{GPa} \qquad (3.6)$$

The upper limit on R of 0.50 is to limit the effective strain of FRP to half of its ultimate strain in order to maintain the shear integrity of the concrete as at higher strain levels, the wider shear cracks will cause the aggregate interlock to be lost. However, a close inspection of the plot of the results for Eqn.3.6 shows a wide scatter for $\rho_{frp}E_{frp,e} < 0.5$ and therefore, this equation should be applied with caution. In general, the methods based on effective strain is based on a data base wherein most of the results relate to the CFRP material of elastic modulus 230 GPa and limited fibre orientations. Furthermore, the bond between the concrete and the FRP depends largely on the concrete tensile strength and the bonded area.

3.5.5 Method based on limiting interface shear stresses

The debonding of beams bonded with side plates (Fig.3.1e) or strips (Fig.3.1a) occurs due to the formation of diagonal shear cracks that exhausts the interfacial bond stress; the stirrups are ineffective in this case as they are activated only after the formation of the shear cracks. Hence, FRP plates or strips that are not wrapped around the beam section entirely debond before the fracture of FRP occurs. To cater for this, Al-Sulaimani et.al (1994) prescribed the limiting interface shear stress at failure based on limited test data.

Al-Sulaimani et.al (1994) suggest the following formula to calculate the shear contribution by a series of FRP strips of thickness t_s and depth h_s bonded to both sides of the beam at a spacing of s_s. The magnitude of V_{frp} is calculated assuming that peeling of the strips will occur when the maximum shear stress τ_{pk} at the bottom of the strips reaches the interface shear strength τ_{ult} and in this model τ_{ult} is assumed as 3.5 MPa. The shear stress distribution is assumed to have an average value at peeling (τ_{ave}) of 1.2 MPa as estimated from beam tests. The equation to compute V_{frp} is

$$V_{frp}(strip) = \frac{2\tau_{b,ave}\left(\frac{t_s h_s}{2}\right)d_0}{s_s} \text{ where } \tau_{ave} = 1.2 \text{ MPa} \quad (3.7)$$

Similarly, for beams bonded with wings of depth h_w (Fig.3.1c), the average shear stress at peeling as estimated from the tests was 0.8 MPa and the equation to compute V_{frp} is

$$V_{frp}(wing) = 2\tau_{ave}\left(\frac{d_0 h_w}{2}\right) \text{where } \tau_{ave} = 0.8 \text{ MPa} \quad (3.8)$$

In the case of the beams bonded with U-shaped jackets of depth h_j (Fig.3.5f), V_{frp} is calculated assuming that no peeling of the jacket occurs, as observed experimentally. As the sides of the jackets are well anchored to the soffit of the beam due to geometric continuity, the ill effects of stress concentrations are prevented. Hence, Al-Sulaimani et.al (1994) assumed a uniform shear stress distribution across the depth of the sides of the jackets with a maximum value at failure (τ_{pk}) of 3.5 MPa. The following equation is used to compute V_{frp} for the jacket.

$$V_{frp}(jacket) = 2\tau_{pk}\left(\frac{d_0 h_j}{2}\right) \text{where } \tau_{pk} = 3.5 \text{MPa} \quad (3.9)$$

One of the difficulties with the application of Eqns.3.7-3.9 is that the magnitudes suggested for peak shear stress at failure τ_{pk} of 3.5 MPa were estimated from double-lap tests for a particular strength of concrete (f_c=37 MPa) and the 3 mm thick Glass FRP plate with an ultimate strength of 200 MPa. Therefore, τ_{pk} has to be evaluated experimentally for different kinds of concrete/FRP plate interfaces.

In an approach similar to Al-Sulaimani et.al (1994), Khalifa et.al(1998) modified the equation suggested by Maeda et.al (1997) using the work done by

Horiguchi and Saeki (1997) to compute the average bond strength between CFRP plate and the concrete (τ_{ave}).

$$\tau_{ave} = k(f_c / 42)^{2/3} E_{frp} t_p \qquad (3.10)$$

where k is the experimental constant and equals to 110.2 x 10^{-6} mm^{-1}. The advantage of the above equation is that it can be used for any grade of concrete and any thickness of plate. However, this equation is again valid only for CFRP continuous sheets or strips.

3.6 Concluding Remarks

From this literature study, it is realised that FRP materials are being widely researched as possible steel replacement materials for applications in strengthening of concrete structures. Whereas most of the experimental studies investigated the suitability of carbon FRP plates that had an elastic modulus (150-230 GPa) close to that of steel plates, other FRP materials such as glass and aramid were also tried. The following major conclusions can be drawn from the available reports:

1. In the case of tension face plated beams, most of the studies were performed on simply supported beams in which the plates were curtailed adjacent to the supports. Therefore, shear peeling of the plated beams was the major failure mode and there is a need to develop a suitable mathematical model to quantify the shear peeling strength.
2. The second major development in the FRP plated beams was to investigate shear strengthening schemes such as bonding plates to the sides or using a series of FRP strips. Most of the researchers visualised the FRP side plates or strips as conventional steel stirrups. The equations prescribed to compute the shear contribution were empirical and most of the vital parameters such as the variations

in concrete strength and the failure by debonding were not properly accounted for. Therefore, there is a need for an approach that will consider all the vital parameters such as the stiffness of the plates, strength of the concrete and the role of the shear stirrups in the peeling mechanism.

References

Al-Sulaimani,G.J., Sharif,A., Basunbul,I.A., Baluch,M.H., and Ghaleb,B.N. (1994) Shear repair for reinforced concrete by fibre glass plate bonding. ACI Structural Journal, V.91. July-August 1994, 458-464.

Arockiasamy, M (2000). Recent developments in retrofitting and strengthening of structures using continuous fibres-A review. Proceedings of ACUN-2, International Composites Conference, Sydney, 14-18 February,2000. Vol.1, pp39-43.

Bencardino,F., Spaeda,G. and Swamy,R.N.(1997). Design to repair/ Up-grade R.C. structures: the key to a successful utilisation of CFRP laminates. Structural Faults and Repair-97, Edinburgh, July . pp.183-190.

Buyukozturk,O., and Hearing,B. (1998) Failure behaviour of precracked concrete beams retrofitted with FRP. Journal of composites for construction, Vol.2., No.3, August 1998. pp.138-144.

Chajes,M.F., Januszka,T.F., Mertz,D.R., Thomson,Jr.T.A., and Finch,Jr.,W.W. (1996) Shear strengthening of reinforced concrete beams using externally applied composite fabrics. ACI Structural Journal, V.92, May-June 1995, 295-303.

He,J.H., Pilakoutas,K. and Waldron,P (1997). CFRP plate strengthening of RC beams Structural Faults and Repair-97, Edinburgh, July . pp.119-127.

Hollaway,L.C., and Leeming,M.B. (1999) Strengthening of Reinforced concrete structures using externally-bonded FRP composites in Civil and Structural Engineering. Woodhead Publishing Limited, Cambridge, England..pp11-45.

Khalifa,A., Gold,W.J., Nanni,A., and Aziz,A.M.I.(1998). Contribution of externally bonded FRP to shear capacity of RC flexural members. Journal of composites for construction (ASCE), Vol.2, No.4, Nov.1998. pp.195-202.

Maeda,T., Asano,Y., Sato,Y., Ueda,T., and Kakuta,Y.(1997) A study on bond mechanism of carbon fiber sheet. Non-Metallic (FRP) Reinforcement of Concrete Structures Proceedings of the Third International Symposium Vol.1, Oct.,1997, pp279-286.

Malek,A.M., Saadatmanesh,H. and Ehsani,M.R.(1998) Prediction of failure load of R/C beams strengthened with FRP plate due to stress concentration at the plate end. ACI Structural Journal, V.95, March-April 1998, 142-152.

Malek,A.M., and Saadatmanesh,H.(1998). Ultimate shear capacity of reinforced concrete beams strengthened with web-bonded fiber-reinforced plastic plates. ACI Structural Journal, V.95, July-August 1998, 391-399.

Malvar,L.J., Warren,G.E., and Inaba, C.(1995). Rehabilitation of navy pier beams with CFRP. Non-metallic (FRP) reinforcement for concrete structures. E&FN Spo, London, 1995. pp.534-540.

Meier,U. (1995). Strengthening of structures using carbon fibre/epoxy composites. Construction and Building Materials, Vol.9, No.6, 1995. pp.341-351.

Meir and Kaiser(1991). Strengthening of structures with CFRP laminates in Advanced composite materials in civil engineering structures(ASCE)

Mitsui,Y., Murakami,K., Takeda,K., and Sakai,H.(1998). A study on shear reinforcement of reinforced concrete beams externally bonded with carbon fiber sheets. Composite Interfaces, Vo.5, No.4,1998. PP 285-295.

Mukhopadhyaya,Swamy,and Lynsdale (1998). Optimising structural response of beams strengthened with GFRP plates, ASCE Journal for Composites for Construction, Vol.2, No.2, May 1998. Pp87-95.

Neubauer,U., and Rostasy,F.S.(1997). Design aspects of concrete structures strengthened with externally bonded CFRP-plates. Structural Faults and Repair-97, Edinburgh, July . pp.109-118.

Ohuchi,H., Ohno,S., Katsumata,H., Kobatake,Y., Meta,T., Yamagata,K., Inokuma,Y., and Ogata,N. (1994). Seismic strengthening design technique for existing bridge columns with CFRP. Seismic design and retrofitting of reinforced concrete bridges, edited by R.Park,1994. pp 495-514.

Quantrill,R.J., Hollaway,L.C., and Thorne,A.M. (1996). Part 1. Experimental and analytical investigation of FRP strengthened beam response. Magazine of Concrete Research, Vol.48, No.177. pp331-342

Ritchie,P.A., Thomas,D.A., Lu,L., and Connelly,G.M.(1991). External reinforcement of concrete beams using fiber reinforced plastics. ACI Structural Journal, V.88, July-August 1991, 491-500.

Saadatmanesh,H. and Ehsani,M.R.(1991a). RC beams strengthened with GFRP plates I: experimental study. Journal of Structural Engineering (ASCE), Vol.117, No.11, 1991. pp.3417-3433.

Saadatmanesh,H. and Ehsani,M.R.(1991b). RC beams strengthened with GFRP plates II: analytical and parametric study. Journal of Structural Engineering (ASCE), Vol.117, No.11, 1991. pp.3434-3455.

Sharif,A., Al-Sulaimani,G.J., Basunbul,I.A., Baluch,M.H., and Ghaleb,B.N. (1994) Strengthening of initially loaded reinforced concrete beams using FRP plates. ACI Structural Journal, V.91, March-April 1994, 160-168.

Spadea,G., Bencardino,F. and Swamy,R.N.(1998). Structural behaviour of composite RC beams with externally bonded CFRP. Journal of Composites for Construction (ASCE), Vol.2, No.3, August 1998. pp 132-137.

Swamy, Mukhopadhyaya, and Lynsdale (1999). Strengthening for shear of RC beams by external plate bonding. The Structural Engineer, 15th June, 1999.pp19-30.

Triantafillou,C.T.(1998a). Strengthening of structures with advanced FRPs. Progress in Structural Engineering and Materials. Vol.1(2),1998. pp.126-134.

Triantafillou,C.T.(1998b). Shear strengthening of reinforced concrete beams using epoxy-bonded FRP composites. ACI Structural Journal, V.95, March-April 1998, 107-115.

Triantafillou,T.C. and Plevris, N.(1992). Strengthening of RC beams with epoxy-bonded fibre-composite materials. Materials and Structures, Vol.25,1992. pp201-211.

Varastehpour,H. and Hamelin,P.(1997). Strengthening of concrete beams using fiber-reinforced plastics. Materials and Structures, Vol.30, April 1997, pp 160-166.

Warner,R.F., Rangan,B.V., and Hall,A.S.(1989) Reinforced Concrete-3rd Edition. Longman Cheshire Pty.Ltd., Melbourne. pp118-139.

CHAPTER-4: REVIEW ON AXIAL PEELING AND LOCAL BOND STRESSES IN BEAMS BONDED WITH FRP OR STEEL PLATES

CONTENTS

4.1 Introduction

Axial peeling occurs when a flexural or shear crack crosses the plane of the plate resulting in a debonding crack along the edges of the plate, as shown in Fig.4.1. If instantaneous debonding did not occur where the crack intersects the plate, as in the case of shear peeling due to diagonal shear cracks, then the plates would be subjected to an infinite strain that cannot happen in practice. As these 'infinite' strains have to be accommodated at the point of intersection of the crack and the plate, debonding cracks are induced and they propagate away from the flexural crack as shown in Fig.4.1 (Oehlers 2000). The axial load A in the plate is now resisted by the uncracked concrete at the end of the peeling crack as well as by aggregate interlock or friction across the interface. Therefore, it is essential to study the behaviour of the composite interface under an axial load in order to quantify the axial force that can be sustained. Keeping this in view, the experimental studies on axial peeling of both steel plated and FRP plated beams conducted by many researchers are presented and also the available theoretical formulations are also described.

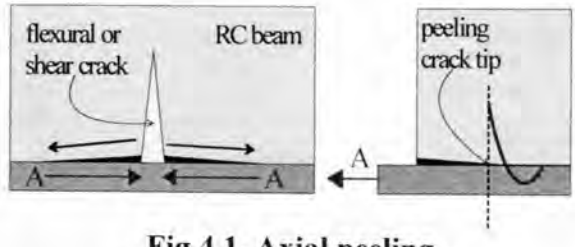

Fig.4.1. Axial peeling

4.2 Ranisch and Rostasy's model for steel plated beams

4.2.1 Tests

Ranisch and Rostasy (1986) conducted tests on double-lap steel-to-concrete bond specimens and developed expressions for the critical bond length $L_{b,crit}$. Here, the critical bond length is defined as that bond length of the external plate, beyond which

there is no further increase in the axial load carrying capacity of the plate/concrete interface. A typical test results for a 50 mm wide and 5 mm thick steel plate is shown in Fig.4.2. In this test, the bond length L_b for the plate is 360 mm and the adhesive layer is 1mm thick and it has a shear modulus G_a of 770MPa. The bond stress distribution along the anchorage length has a peak in the proximity of the loaded end of the plate and the position changes with the applied load due to the onset of concrete cracking. However, the peak bond stresses does not increase beyond a certain applied load which in this case is 20 kN. Even if the bond strength is locally exceeded, the concrete will still be able to carry load by a combination of shear and friction, i.e. aggregate interlocking across the debonding crack.

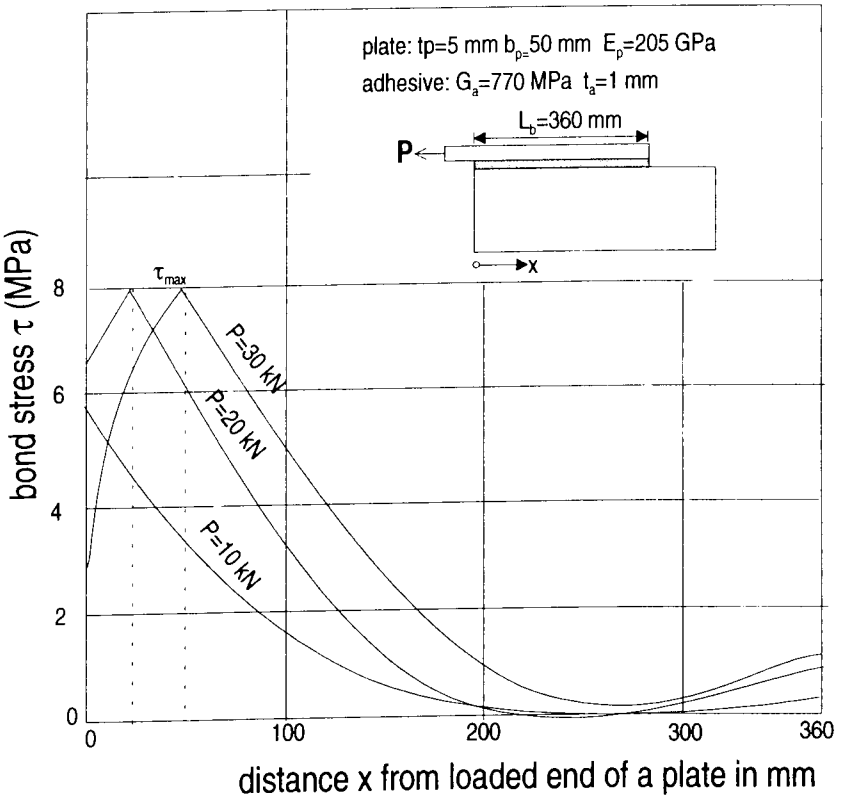

Fig.4.2. Typical test results by Ranisch and Rostasy

4.2.2 Bond stress distribution

From these tests, a bond distribution was assumed as shown in Fig.4.3. It consists of a linear branch ascending to the peak bond stress τ_{pk} and from thereon a descending

linear branch representing the elastic-plastic behaviour of the bond. The peak bond stress can be set equal to the shear strength of the concrete (τ^*_c), even though it was not explicitly stated by the authors. They suggest a magnitude of 8 MPa for a mean concrete cube compressive strength of 30 MPa.

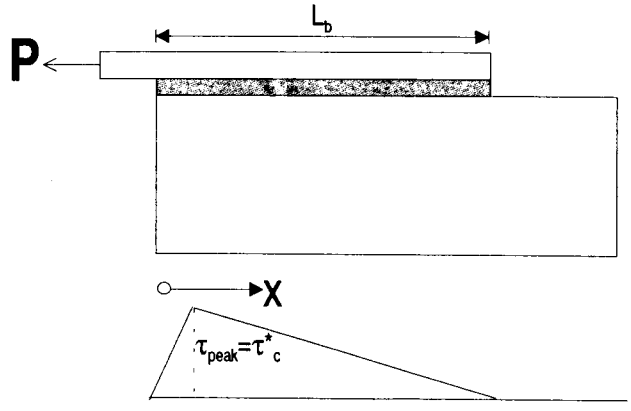

Fig.4.3. Idealised bond stress distribution by Ranisch and Rostasy

Bond failure will occur if

$$\int_0^{L_b} \tau(x) b_p dx \le P_{b,\max} \text{ and } \tau(x=0)=0. \tag{4.1a}$$

$$\text{with } P_{b,\max} = f_{yp} b_p t_p \,/\, \text{factor of safety} \tag{4.1b}$$

The formula for computing the critical bond length $L_{b,crit}$ to transfer a load of $P_{b,max}$ is given as

$$L_{b,crit} = C \frac{P_{b,\max}^{\ 2}}{E_p . b_p^{\ 2} . t_p . \tau_{pk}} \tag{4.2}$$

Equation 4.1b suggests that the maximum bond strength $P_{b,max}$ is controlled by the yield strength of the steel plate and it can also be deduced from Eqn.4.2 that for a given thickness of steel plate t_p, $L_{b,crit}$ is independent of the width of the plate. In Eqns. 4.1b and 4.2, C=18500 when the factor of safety is 1.45, f_{yp} is the yield strength of the steel plate, b_p and t_p are the width and thickness of the external plate.

4.3 Tests by Swamy, Jones and Charif on steel plated beams

4.3.1 Specimens

Swamy, Jones and Charif (1986) conducted pull out tests by gluing two steel plates 60 mm wide and 3 mm thick to the opposite sides of a concrete prism 60 mm wide, 60 mm deep and 150 mm long, as shown in Fig.4.4. The main parameters varied in this study were glue thickness, 0.5 to 3.0 mm, and concrete cube strength, 25 to 75 MPa. Six specimens were tested for each category. The specimens were instrumented with strain gauges along the joints from which the local axial forces and shear stress distribution could be computed.

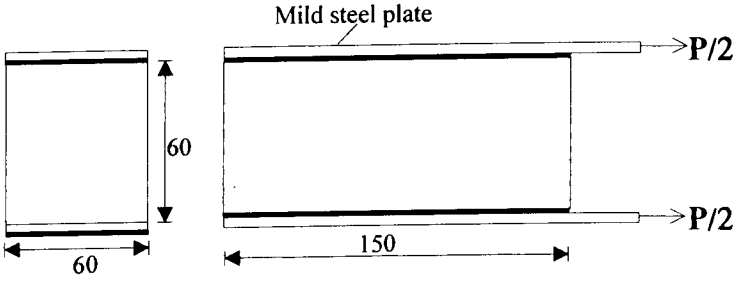

Fig.4.4. Pull out test specimen by Swamy, Jones and Charif

4.3.2 Test results

The test results are summarised in Table-4.1. The tests have shown that the local axial forces in the plate (shown as A in Fig.4.1) at the various strain gauge locations were proportional to the applied load as would be expected. However, they changed rapidly due to micro-cracking at the interfaces. Both the axial force and shear stress distributions along the joint were found to follow exponential trends similar to that shown in Fig.4.2 and at about 60% of the ultimate load, the joint started failing due to concrete cracking at the most stressed end. However, the remaining part of the joint continued to exhibit the trend of exponential variation. Near the ultimate load, a 10 to 20 mm portion of the most stressed end failed completely as the concrete cracking caused the plate separation.

Table-4.1 shows that both the mean and the maximum shear stress increased with the increase in concrete strength; the mean stress from 2.17 to 3.33 MPa and the maximum stress from 6 to 8 MPa. It may be noted that the ultimate shear stresses were higher than the tensile splitting strength of the concrete (3.1 to 4 MPa). This indicates that even if the tensile strength of the concrete is locally exceeded, the concrete is still able to carry load by a combination of shear and friction, i.e. aggregate interlocking. Furthermore, the bond strength is approximately twice the Brazilian tensile strength of the concrete as observed by Ranisch and Rostasy (1986) also.

Table-4.1: Test results by Swamy, Jones and Charif

Effect of concrete strength (glue thickness = 1 mm)			Effect of glue thickness (Concrete grade = 45 MPa)		
f_{cu} (MPa)	τ_{mean} (MPa)	τ_{pk} (MPa)	adhesive thickness (mm)	τ_{mean} (MPa)	τ_{pk} (MPa)
25.1	2.17	6.0	0.5	2.42	6.9
44.9	2.52	6.8	1.0	2.52	6.8
60.2	2.77	7.4	1.6	2.38	6.7
71.3	3.33	8.3	3.0	2.83	6.9

f_{cu}= cube strength of concrete, τ_{mean} = mean shear stress = ultimate load/bond area and τ_{pk} = maximum shear stress obtained from recorded distribution.

The test results also showed that variation in the thickness of adhesive had negligible effect on the shear stresses. The mean shear stress varied from 2.4 to 2.8 MPa and the maximum shear stress varied from 6.7 to 6.9 MPa, for a wide range of adhesive thickness (0.5 mm to 3 mm). Another noteworthy feature of these test series is that all the pull out specimens failed through the concrete as the epoxy resin has higher bond strength than concrete.

4.4 Tests by Taljsten on steel and FRP plated beams

4.4.1 Specimens

Taljsten (1997) conducted extensive tests to evaluate the bond between an external plate and the concrete when a crack in the concrete propagates along the bond line

parallel with a steel plate or CFRP plate. These tests were also used to determine the anchor lengths that provide a more effective force transfer between the adherents, i.e. the concrete beam and the external plate. The tests were conducted on concrete prisms, which were either bonded with mild steel or CFRP plates as shown in Fig.4.5 to determine the anchor length that will ensure an effective force transfer between the adherents. A pure tensile force was applied by a hydraulic jack and transferred to the plate through a moment-free link.

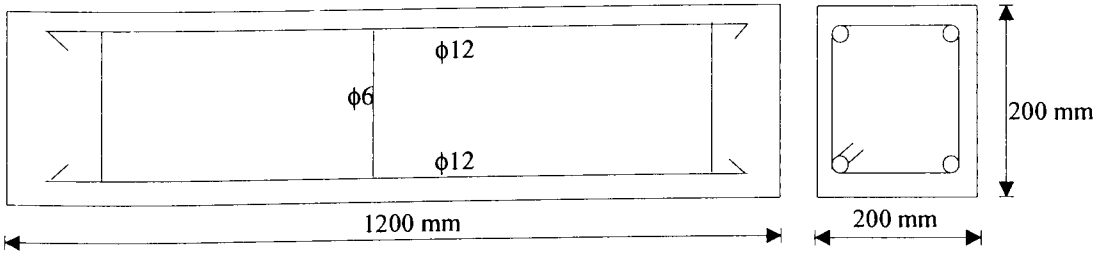

(a) Dimensions of the concrete prism

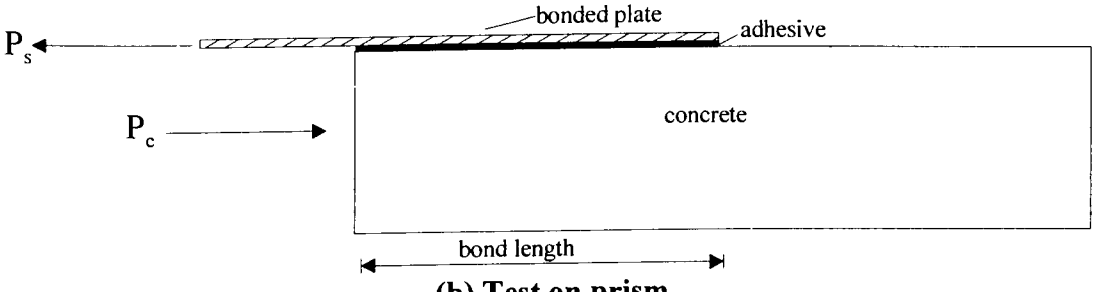

(b) Test on prism

Fig.4.5. Schematic detail of test done by Taljsten

4.4.2 Test results

The tests were conducted in two series. Mild steel plates were used in series S and CFRP plates were used in series-C.

4.4.2.1 Steel plated beams

Series-S : In series -S, the thickness of the steel plate was kept constant at 2.9 mm but the width and bond length of the plates were varied. Test results and material properties for this series are summarised in Table-4.2.

Table-4.2: Series-S

Steel plate : thickness = 2.9 mm, Young's modulus = 205 GPa,
Concrete : Young's modulus = 35 GPa

Specimen	Bond length (mm)	Plate width (mm)	f_t (MPa)	f_{yp} (MPa)	f_{up} (MPa)	$P_{b,max}$ (kN)
1	100	40	4.2	330.2	399	21.1
2	200	40	3.9	330.2	399	39.5
3	400	40	4.3	330.2	399	41.1
4	50	60	4.2	339.1	403	12.7
5	100	60	4.1	330.2	399	20
6	150	60	4.3	339.1	403	46.3
7	200	60	4.1	330.2	399	48.8
8	400	60	4.3	339.1	403	58.4
9	400	60	4.1	330.2	399	53
10	100	80	4.4	339.1	403	39.6
11	150	80	3.9	339.1	403	50.9
12	200	80	4.3	339.1	403	67.3
13	300	80	4.1	339.1	403	68
14	500	80	4.4	330.2	399	67.3
15	600	80	4.1	339.1	403	71.4
16	800	80	4.1	339.1	403	61.6

f_t = direct tensile strength of the concrete f_{yp},f_{up} = yield and ultimate strengths of the steel plate, and $P_{b,max}$ = the maximum measured tensile force in the specimen.

All the specimens failed by cracking and splitting in the concrete; in some cases steel plates yielded before failure. The test results showed the existence of a critical anchor length that is needed to carry the maximum load. Plates of longer anchor lengths did not improve the load carrying capacity any further. It was also found that in most of the tests, the average value of the critical steel plate strain at which the fracture of concrete occurred varied between 850 to 1000 microstrain. This implies that the concrete fractured before the steel plates yielded.

4.4.2.2 Carbon FRP plated beams

Series-C: In series-C, both the width and the thickness of the plate were kept constant at 50 mm and 1.2 mm respectively but the length of the plates was varied. Test results

and material properties for this series are summarised in Table-4.3. All the specimens failed by cracking and splitting in the concrete; as the CFRP material had a tensile strength of approximately 2500 MPa, no fracture of the plate occurred. The tests have shown that only about one-fifth of the theoretical tensile strength of the FRP material can be utilised as fracture develops in the concrete beyond this stress level. As these tests were limited in number, neither a critical bond length nor a critical strain at which the fracture in the concrete is initiated could be identified for series-C.

Table-4.3: Series-C

CFRP plate: thickness = 1.2 mm, Young's modulus = 170 GPa
Concrete: Young's modulus = 35 GPa

Specimen	Bond length (mm)	Plate width (mm)	f_t (MPa)	f_{up} (MPa)	$P_{b,max}$ (kN)
1	100	50	3.9	2496.8	17.3
2	200	50	4.1	2496.8	27.5
3	300	50	4.3	2496.8	35.1
4	400	50	4.3	2496.8	26.9

4.5 Analytical models by Taljsten

Taljsten (1997) did not present any mathematical model for determining the maximum axial strength based on debonding at the concrete-adhesive-plate interface. He compared the test results with linear elastic theory for lap joints that predicts the interfacial stresses in the joint only for moderate levels of load. Consider the geometrical relationship depicted in Fig.4.6, in which u and v are the displacements in the plate and the concrete respectively; the origin x is fixed at the least stressed end of the plate. For a unit width of the plate, the governing equation for the shear stress $\tau(x)$ is given by

$$\frac{d^2\tau(x)}{dx^2} - \omega^2\tau(x) = 0, \tag{4.3a}$$

$$\text{where } \omega^2 = \frac{G_a}{t_a}\left[\frac{1}{E_p t_p} + \frac{1}{E_c h}\right] \tag{4.3b}$$

Table-4.2: Series-S

Steel plate : thickness = 2.9 mm, Young's modulus = 205 GPa,
Concrete : Young's modulus = 35 GPa

Specimen	Bond length (mm)	Plate width (mm)	f_t (MPa)	f_{yp} (MPa)	f_{up} (MPa)	$P_{b,max}$ (kN)
1	100	40	4.2	330.2	399	21.1
2	200	40	3.9	330.2	399	39.5
3	400	40	4.3	330.2	399	41.1
4	50	60	4.2	339.1	403	12.7
5	100	60	4.1	330.2	399	20
6	150	60	4.3	339.1	403	46.3
7	200	60	4.1	330.2	399	48.8
8	400	60	4.3	339.1	403	58.4
9	400	60	4.1	330.2	399	53
10	100	80	4.4	339.1	403	39.6
11	150	80	3.9	339.1	403	50.9
12	200	80	4.3	339.1	403	67.3
13	300	80	4.1	339.1	403	68
14	500	80	4.4	330.2	399	67.3
15	600	80	4.1	339.1	403	71.4
16	800	80	4.1	339.1	403	61.6

f_t = direct tensile strength of the concrete f_{yp},f_{up} = yield and ultimate strengths of the steel plate, and $P_{b,max}$ = the maximum measured tensile force in the specimen.

All the specimens failed by cracking and splitting in the concrete; in some cases steel plates yielded before failure. The test results showed the existence of a critical anchor length that is needed to carry the maximum load. Plates of longer anchor lengths did not improve the load carrying capacity any further. It was also found that in most of the tests, the average value of the critical steel plate strain at which the fracture of concrete occurred varied between 850 to 1000 microstrain. This implies that the concrete fractured before the steel plates yielded.

4.4.2.2 Carbon FRP plated beams

Series-C: In series-C, both the width and the thickness of the plate were kept constant at 50 mm and 1.2 mm respectively but the length of the plates was varied. Test results

and material properties for this series are summarised in Table-4.3. All the specimens failed by cracking and splitting in the concrete; as the CFRP material had a tensile strength of approximately 2500 MPa, no fracture of the plate occurred. The tests have shown that only about one-fifth of the theoretical tensile strength of the FRP material can be utilised as fracture develops in the concrete beyond this stress level. As these tests were limited in number, neither a critical bond length nor a critical strain at which the fracture in the concrete is initiated could be identified for series-C.

Table-4.3: Series-C

CFRP plate: thickness = 1.2 mm, Young's modulus = 170 GPa
Concrete: Young's modulus = 35 GPa

Specimen	Bond length (mm)	Plate width (mm)	f_t (MPa)	f_{up} (MPa)	$P_{b,max}$ (kN)
1	100	50	3.9	2496.8	17.3
2	200	50	4.1	2496.8	27.5
3	300	50	4.3	2496.8	35.1
4	400	50	4.3	2496.8	26.9

4.5 Analytical models by Taljsten

Taljsten (1997) did not present any mathematical model for determining the maximum axial strength based on debonding at the concrete-adhesive-plate interface. He compared the test results with linear elastic theory for lap joints that predicts the interfacial stresses in the joint only for moderate levels of load. Consider the geometrical relationship depicted in Fig.4.6, in which u and v are the displacements in the plate and the concrete respectively; the origin x is fixed at the least stressed end of the plate. For a unit width of the plate, the governing equation for the shear stress $\tau(x)$ is given by

$$\frac{d^2\tau(x)}{dx^2} - \omega^2\tau(x) = 0, \tag{4.3a}$$

$$\text{where } \omega^2 = \frac{G_a}{t_a}\left[\frac{1}{E_p t_p} + \frac{1}{E_c h}\right] \tag{4.3b}$$

and the solution of Eqn.4.3a is given as

$$\tau(x) = C_1 e^{\omega x} + C_2 e^{-\omega x} \tag{4.4}$$

$$\frac{d\tau(x)}{dx} = \omega C_1 e^{\omega x} - \omega C_2 e^{-\omega x} \tag{4.5}$$

In Eqns.4.4 and 4.5, C_1 and C_2 are constants of integration. When applying the boundary conditions $P_s(x)=0$ at $x=0$ and $P_s(x)=P_s(L_b)$ when $x=L_b$, we get the shear stress in the adhesive layer as

$$\tau(x) = \omega P_s(L_b) \frac{\cosh(\omega x)}{\sinh(\omega L_b)} \tag{4.6}$$

where is L_b the bond length of the plate.

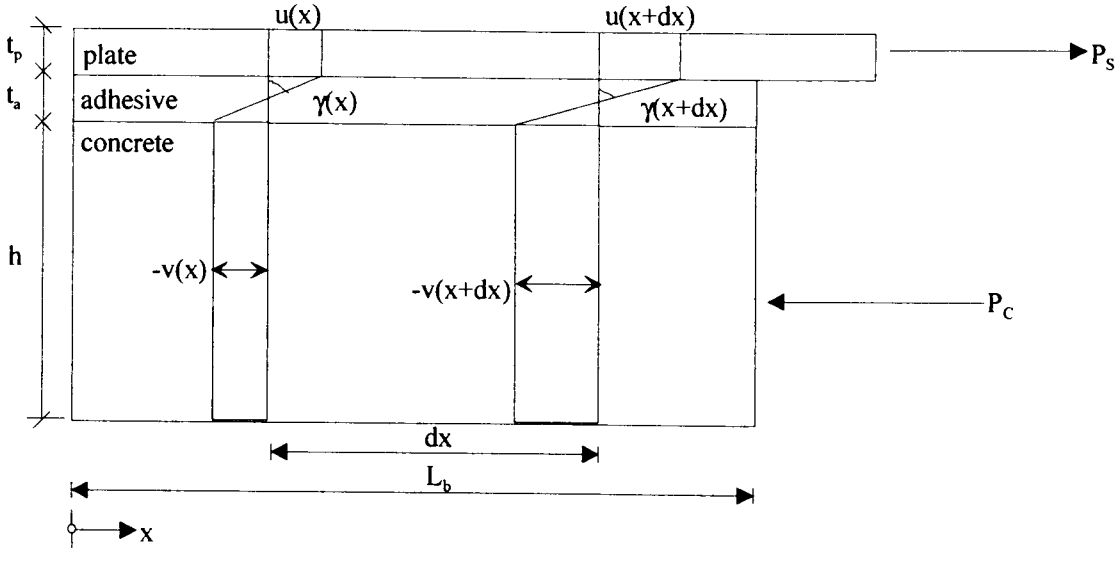

Fig.4.6. Plate-concrete joint loaded in pure shear

A comparison of the analytical results with that of the test results by Taljsten showed that the linear elastic theory could be used for moderate levels of load to predict the shear stress distribution. At higher stress levels, the theoretical stress distribution deviates from the experimentally determined one. This is due to the starting of concrete fracture and the corresponding decrease in bond length, which is not accounted for in this model. Furthermore, one of the critical parameters in the

above model is ϖ as defined in Eqn.4.3b and its value heavily depends on the factor G_a/t_a. However, the tests conducted by Taljsten (1997) clearly showed that failure did not occur along the adhesive layer and the tests by Swamy et.al (1986) on steel plated beams (Section 4.3) clearly showed that the thickness of adhesive t_a did not affect the magnitudes of both mean and peak shear stresses. Moreover, this model predicts that the peak shear stress occurs at the end of the plate while the tests indicate that the largest shear stress occurs at a distance from the plate end. Hence, the applicability of this model is very limited.

To overcome the limitations posed by the linear elastic models, Taljsten in a related work (1996) used a fracture mechanics approach for crack propagation in the concrete along the bond line. In this work, a non-linear fracture mechanics approach was used to derive the basic equations. A fictitious crack model for shear is introduced to compute the elastic energy created by the shear stress over a unit length and it is used to create a new crack in the bond zone. This step in conjunction with a known shear slip curve for the adhesive was used to predict the joint behaviour. The difficulty with this approach is that it does not propose design rules that can be easily applied, as defining and measuring experimentally the fracture energy for shear failure (mode II failure) poses practical difficulties. Another problem with this approach is the assumption that all the materials are isotropic which is not the case with most of the composite plates.

4.6 Tests by Horiguchi and Saeki on FRP plated beams

Horiguchi and Saeki(1997) conducted a limited number of tests to study the bond between concrete and high modulus carbon fibre reinforced plastic plates (CFRP). The bond was evaluated by three different test methods, namely a shear-type bond

test, bending-type bond test, and direct tensile test for bonding as shown in Fig.4.7. The only parameter varied in these tests was the compressive strength of the concrete.

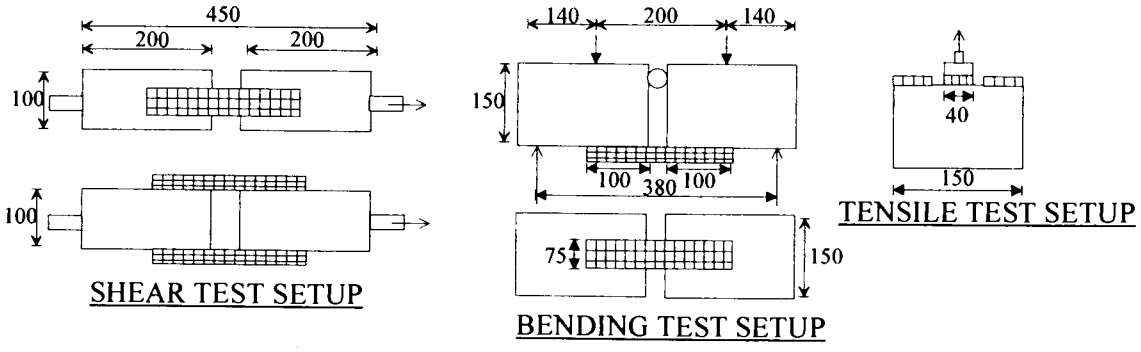

Fig.4.7. Bond test arrangement (Horiguchi and Saeki)

Four different types of failure modes were observed in this study. Failure occurred through the fracture of the concrete matrix in case of low strength concrete with f_c= 10.5 MPa. Delamination of the FRP plate occurred when the compressive strength of the concrete was high or when the shear-type test was conducted. However, fracture of the CFRP sheet was observed in the bending test for concrete with f_c= 46.1 MPa. Aggregate/ mortar matrix interfacial fracture caused the concrete fracture in the case of the tensile tests with high strength concrete. These tests have shown a high correlation between the bond strength and the compressive strength of the concrete as given by the following equations. The bond strength, i.e. the peak shear stress at peeling τ_{pk}, decreases with decrease in the compressive strength of the concrete, as shown by the following empirical equations.

$$\tau_{pk}(shear) = 0.09 f_c^{(2/3)} \tag{4.7}$$

$$\tau_{pk}(bending) = 0.22 f_c^{(2/3)} \tag{4.8}$$

$$\tau_{pk}(tensile) = 0.36 f_c^{(2/3)} \tag{4.9}$$

4.7 Tests by Chajes et.al

Chajes, Finch, Januszka and Thomson.(1996) conducted single lap shear tests (Fig.4.8) to study the effect of adhesive type, surface preparation of the concrete and the concrete compressive strength upon the bond strength of concrete-composite joints.

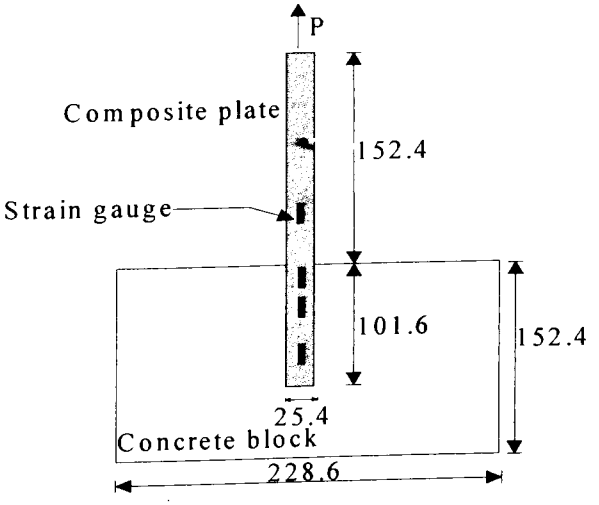

Fig.4.8. Single-lap shear test specimen by Chajes et.al

In all the tests, an FRP sheet consisting of graphite fibres in a toughened epoxy resin was used. The thickness of the plate was about 1 mm with a width of 25.4 mm. The material properties of the plate were: (a) along the fibre direction: elastic modulus E=108.5 GPa, ultimate strain ε_{ult} = 15000 microstrain, tensile strength = 1655 MPa and Poisson's ratio =0.268; (b) the corresponding values in the direction perpendicular to the fibre orientation were E=11.6 GPa, ε_{ult} = 3397 microstrain, tensile strength = 39.1 MPa and Poisson's ratio =0.025.

It was found that failures occurred as a result of concrete shearing beneath the bond surface in case of the three adhesives with Young's moduli of 1584 MPa, 2207 MPa and 5173 MPa. For the adhesive with the lowest Young's modulus ie 220 MPa, the failure occurred through the adhesive layer. The mechanically abraded concrete surface resulted in the highest average stress at failure. The limited number of tests

conducted with three different concrete strengths showed a trend of increased bond strength with increased concrete compressive strength and the shear stress at failure of the concrete was about $0.92(f_c)^{1/2}$, where f_c is probably the cylinder strength, although not explicitly stated in the paper. The authors stated that as a limited test data was used to derive this relationship, additional testing is needed before a more final relation can be drawn.

The best parameters from these preliminary tests were used to design further tests to study the effect of bond length of the composite plate on the bond strength. The bond lengths used were 50 mm, 100 mm, 150 mm and 200 mm and the concrete grade was 36.4 MPa. The critical bond length $L_{b,crit}$ for this test series was about 95 mm and the maximum strain recorded in the composite sheet at the instance of the failure was 4250 microstrain ie only about 25% of the ultimate strain. The following relationship was suggested by the authors for calculating the maximum bond force ($P_{b,max}$) for the epoxy/graphite FRP sheet and concrete interface tested in this study.

$$P_{b,max}=4.94\, b_p L_b \quad \text{if } L_b \le L_{b,crit} \tag{4.10}$$

$$P_{b,max}=4.94\, b_p L_{b,crit} \quad \text{if } L_b > L_{b,crit} \tag{4.11}$$

Here, b_p = width of the plate, L_b = actual bond length and $L_{b,crit}$ = critical bond length. For this study $L_{b,crit}$ was 95 mm.

4.8 Tests by Maeda, Asano, Sato, Ueda and Kakuta

4.8.1 Specimens

Maeda, Asano, Sato, Ueda and Kakuta (1997) investigated the bond between two different types of carbon FRP sheets by using the test arrangement as shown in Fig.4.9. The first CFRP sheet used has a thickness of 0.110 mm, while the tensile strength and Young's modulus in the direction of the fibre were 3500 MPa and 230

GPa respectively. The corresponding values for the second sheets were 0.165 mm, 3000 MPa and 380 GPa. The width of the sheets was kept constant at 50 mm and the concrete prism was 100 mm wide and 100 mm deep. Both sides of the prisms were bonded with FRP sheets.

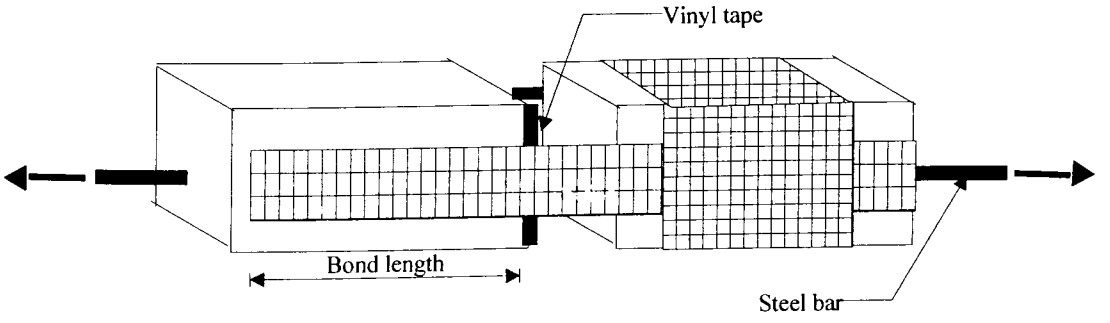

Fig.4.9. Test specimen used by Maeda et.al

4.8.2 Test results and design guidelines

The test results are summarised in Table-4.4.

Table-4.4: Test results by Maeda et.al

Specimen	Bond length (mm)	Plate thickness (mm)	E_p (GPa)	f_c (MPa)	Ult. load (kN)	Failure mode	Mean bond strength (MPa)
1	75	0.110	230	40.8	11.8	CFRP delamination	1.67
2	150	0.110	230	40.8	18.4	CFRP delamination	1.23
3	300	0.110	230	43.3	23.9	CFRP delamination	0.80
4	75	0.165	380	42.4	20.0	concrete fracture	2.60
5	150	0.165	380	42.4	14.6	CFRP breakage	0.97
6	65	0.220	230	42.7	19.1	concrete fracture	2.94
7	150	0.220	230	42.7	32.5	CFRP delamination	2.17
8	700	0.110	230	42.7	20.0	CFRP delamination	0.31

These tests showed that when the bond length was more than 100 mm, the tensile load carried by the CFRP sheets did not depend upon the bond length. This is

explained by the fact that the load is sustained by the bond in the vicinity of the most stressed end of the plate, in the early stages of the loading. When delamination is initiated in this vicinity due to the fracture of concrete, the active debonding area is shifted to the adjacent area and this process is repeated till the plate is completely debonded. Hence, the active bonding area alone resist the bond stresses and Maeda et.al(1997) termed the length of this area as the active bond length ($L_{b,e}$).

The following equation was derived by Maeda, Asano, Sato, Ueda and Kakuta (1997) for the active bond length $L_{b,e}$ by calibrating all the test results.

$$L_{b,e}=exp(6.134-0.584ln(t_pE_{p,long})) \quad (4.12)$$

The above equation shows that as the axial stiffness of the plate is increased, the active bond length decreases. Hence, the bond stress(τ_b) increases with increasing stiffness and it is defined by

$$\tau_b=kE_pt_p \quad (4.13)$$

where k is the experimental constant equal to 110.2 x 10^{-6} mm^{-1}. Therefore, the ultimate bond strength ($P_{b,max}$) of the CFRP sheet is computed by multiplying the bond stress by the active bond area.

$$P_{b,max}=L_{b,e}b_p\tau_b \quad (4.14)$$

It may be noted that the experimental constant and also the critical bond length (in this case 100 mm) were obtained for a narrow band of plate thickness (0.11-0.22 mm) and a single grade concrete (approximately 40 MPa). Hence, these equations should be applied cautiously.

4.9 Tests by Izumo, Saeki, Asamizu and Shimura

4.9.1 Specimens

Izumo, Saeki, Asamizu and Shimura(1997) reported bond tests on aramid and carbon FRP sheets by using the arrangement shown in Fig.4.10. The properties of the FRP sheets are shown in Table-4.5. They termed these FRP sheets as 'biaxial' because they were pseudo-isotropic. The parameters varied in the study were the compressive strength of concrete (12.5, 25 and 45 MPa) and the bond length of the FRP sheets (50, 100, 150 and 200 mm). A tensile load was applied to the FRP sheets by pulling the steel bar embedded at the centre of the prism.

Table-4.5: Tests results by Izumo, Saeki, Asamizu and Shimura

Type	Thickness (mm)	Ultimate tensile strength(MPa)	Elastic modulus(GPa)	Ultimate elongation(%)
Aramid	0.144	2493	85.9	3.1
Carbon	0.112	3879	242.0	2.1

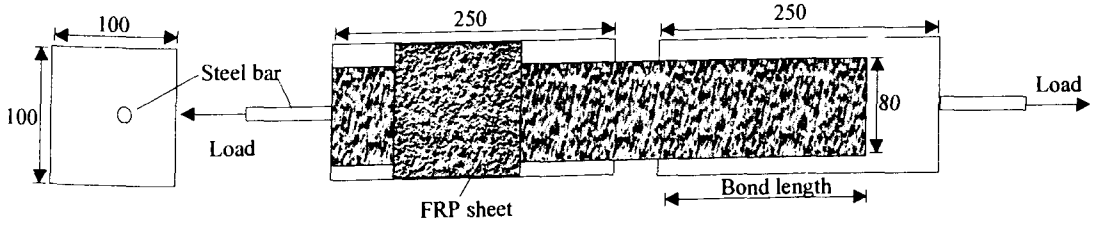

Fig.4.10. Test specimen used by Izumo et.al

4.9.2 Test results and empirical relationships

In all these tests, the failure occurred by the peeling of the sheets from the concrete surface and the critical bond length was 100 mm beyond which no increase in bond strength was observed. Based on the test results, Izumo et.al (1997) suggested the following two equations for aramid and carbon FRP sheets for estimating the maximum bond strength $P_{b,max}$.

$$P_{b,max}\ (aramid\ sheet)=(3.4f_c^{2/3}+69.0)L_b.b_p.t_p/10^6\ ,\ L_b\leq 100\ mm; \qquad (4.15)$$

$$P_{b,max}\ (carbon\ \ sheet)=(3.8f_c^{2/3}+15.2)L_b.b_p.t_p/10^6\ ,\ L_b\leq 100\ mm \qquad (4.16)$$

In Eqns.4.15 and 4.16, the value of L_b should be set as 100 mm, when L_b>100 mm. It is worth noting that the above equations show that the bond strength is directly proportional to $f_c^{2/3}$ in line with the studies done by Horiguchi and Saeki (Eqns.4.7-4.9). Moreover, the above equations were calibrated against test results from the present study as well as those from some other studies and the correlation was found to be good.

4.10 Tests by Mukhopadhyaya, Swamy and Lynsdale

4.10.1 Specimens

Mukhopadhyaya, Swamy and Lynsdale (1998) performed elaborate tests to evaluate the durability of adhesive bonded concrete-GFRP joints when exposed to aggressive exposure conditions. However, the discussion herein is limited to the control specimens that were not exposed to severe environment. The concrete prisms were 100 mm x 100 mm in cross section and 300 mm long as shown in Fig.4.11 and the GFRP plates bonded to the both faces of the prisms were 90 mm wide, 3.5 mm thick and 470 mm long. A constant bond length of 200 mm was used for all the specimens. The only parameter varied was the compressive strength of concrete and they were 41.0 and 50.3 MPa at the instance of testing the plated prisms. The material properties of the GFRP plate both along longitudinal and transverse axes are shown in Table-4.6.

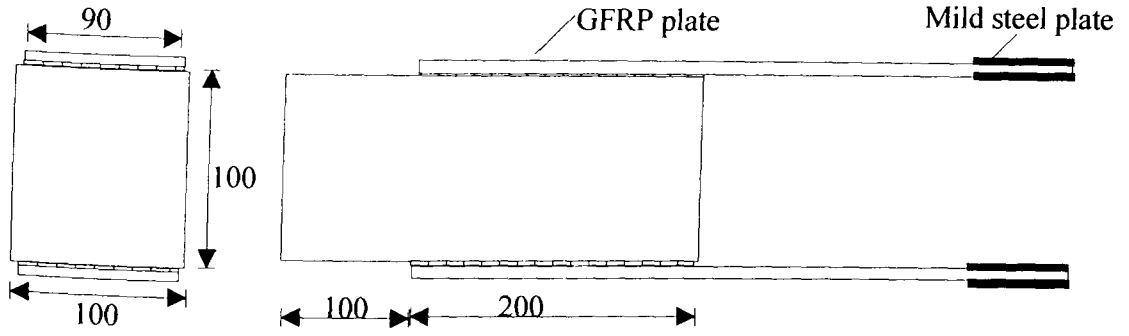

Fig.4.11. Test specimen used by Mukhopadhyaya et.al

Table-4.6: Tests by Mukhopadhyaya et.al

Direction	Thickness (mm)	Ultimate tensile strength(MPa)	Elastic modulus(GPa)	Ultimate elongation(%)
Longitudinal	3.5	328	22.9	1.43
Transverse	3.5	70	5.2	1.35

4.10.2 Test results

These tests have shown that the shear stress distribution along the GFRP/concrete interface is fairly linear and increases under load at a uniform rate till the concrete starts cracking at the plate end. At higher applied loads, the stress distribution becomes much more non-uniform and non-linear, with local debonding at the free edge. Hence, the location of the local peak shear stress moves away from the free edge with increased applied loads due to the local loss of bond between the plate and the concrete. The failure of the specimens finally occurred by 'concrete shearing' and this shows the adhesive used was capable of providing stronger adhesion bond than the shear strength of the concrete. The test results are summarised in Table-4.7.

Table-4.7 :Tests by Mukhopadhyaya et.al

Concrete grade	f_c=41 MPa			f_c=50.3 MPa		
Specimen	1	2	3	1	2	3
Failure load (kN)	45.1	43.6	43.8	41.8	59.4	50.2
Shear stress at failure(MPa)						
(a) Average	1.25	1.21	1.22	1.16	1.65	1.39
(b) Local peak	5.16	3.13	5.01	4.71	4.43	2.77

4.11 Investigation by Neubauer and Rostasy

Neubauer and Rostasy (1997) performed bond tests on 51 concrete blocks that were bonded with CFRP plates that had a longitudinal elastic modulus varying between 150-230 GPa, tensile strength 2000-3000 MPa and ultimate elongation 3-5%. The major parameters varied in this test were the bond length, plate width, plate thickness and concrete cube strength. Unfortunately, the authors did not report these details and the individual test results were also not presented.

There was a remarkable difference in the failure pattern between the prisms with different concrete strengths. For the lower grade concrete like 25 MPa, 85% of the plate failures occurred due to the concrete tensile failure that penetrated about 1-7 mm in the concrete sub-base. On the other hand, for the higher grade concrete such as 55 MPa, the failure was initiated by concrete fracture in the first 20-50% of the bond length and subsequent debonding occurred due to the interlaminar plate failure. The following equations were suggested to compute the maximum bond force and the critical bond length. These equations were derived by calibrating the test results against a fracture mechanics approach.

$$L_{b,crit} = \sqrt{\frac{E_p t_p}{4 f_{ctm}}} \tag{4.17}$$

$$P_{b,\max} = 0.5 k_b b_p \sqrt{(E_p t_p f_{ctm})}, \; if \; L_b \geq L_{b,crit}$$

$$where \; k_b = 1.06 \sqrt{\frac{2 - \frac{b_p}{b}}{1 + \frac{b_p}{400}}} \geq 1 \tag{4.18}$$

$$otherwise \; P_b = P_{b,\max} \frac{L_b}{L_{b,crit}} \left(2 - \frac{L_b}{L_{b,crit}} \right) \tag{4.19}$$

Here, f_{ctm} is the concrete surface tensile strength, b_p is the plate width and b is the width of the beam soffit or the spacing of the plates in slabs. The factor k_b in the above equation accounts for the influence of the plate width relative to the width of the concrete member. The authors suggested that the concrete surface tensile strength f_{ctm} should be limited to a maximum value of 3 MPa. Moreover, the factor k_b Eqn.4.18 will not be applicable to a CFRP plate with a different matrix material, fibre type, different process of manufacturing and a different grade of concrete that were used in the tests as these factor could possibly affect the interfacial bond strength.

4.12 Tests by Bizindavyi and Neale

4.12.1 Specimens

Bizindavyi and Neale (1999) performed tests on concrete blocks of dimensions 150x150x400 mm that were bonded either with glass or carbon FRP plates (Fig.4.12). The concrete compressive strength was 42.5 MPa, flexural tensile strength was 3.5 MPa and the Young's Modulus was 33.5 GPa. The GFRP laminates had a mean strength of 472 MPa, longitudinal Young's modulus of 29.2 GPa and the epoxy resin used had a shear modulus (G_a) of 1.18 GPa and Poisson's ratio of 0.4. The carbon FRP laminate had a mean strength of 1014 MPa and longitudinal Young's modulus of 75.7GPa. The epoxy resin used to bond the CFRP plate was not tested but the authors assume the magnitude of Poisson's ratio to be 0.38.

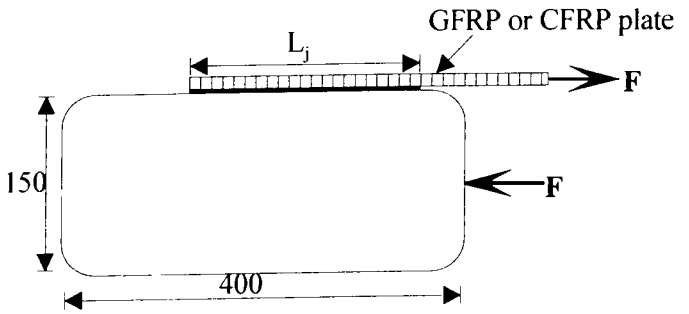

Fig.4.12. Test specimen used by Bizindavyi and Neale

The tests were conducted in two phases. In the preliminary phase, the effects of various parameters such as the type of material (GFRP and CFRP), the thickness of the laminates (1,2 and 3 plies) and the bonded width (25.4 mm and 50.8 mm) on the development length were evaluated. These tests showed that the width of the plate had little influence on the strain distribution along the joint and hence, the second stage of the tests was limited to plates with 1 and 2 plies of 25.4 mm width.

4.12.2 Test results

In the second stage of the testing, the major parameters varied were the thickness of the plates and the bond length of the plates. These details along with the observed failure modes are shown in Tables-4.8 and 4.9.

Table-4.8: Failure modes

Number of plies	Thickness (mm)	Bonded lengths (mm)	Failure mode
Glass FRP plates			
1	1.00	135,145,150,155	Concrete shearing
1	1.00	160,180,240,280	FRP plate rupture
2	2.00	120,210,220	Concrete shearing
2	2.00	240 (3 specimens)	Concrete shearing or FRP plate rupture
2	2.00	260,280,305,320	FRP plate rupture
Carbon FRP plates			
1	0.33	50	Concrete shearing
1	0.33	80,135,145,160	FRP plate rupture
2	0.66	100,120,160	Concrete shearing
2	0.66	220	Concrete shearing and FRP plate rupture
2	0.66	240,260,320	FRP plate rupture

Table-4.9: Initial crack loads and final failure loads

Plate type	t_p (mm)	z_0	$P_{b,max}$ (kN)	L_i (mm)
GFRP	1.00	0.625	11.41	75
	2.00	0.580	21.4	100
CFRP	0.33	0.625	8.5	55
	0.66	0.670	15.1	70

z_o=ratio of load at first cracking in concrete to the maximum load ($P_{b,max}$) and L_i=measured initial transfer length

It may be noted that the authors did not provide individual failure load for plates with different bond lengths. Only, the load at which the crack was initiated at the most highly stressed region and the corresponding initial transfer length for a particular thickness of the plates are reported. The initial transfer length L_o was defined as the distance from the loaded end of the joint to the point where the plate strain profiles reach zero strain. In the case of GFRP bonded joints, cracking at the most highly stressed end began at 55% to 63% of the ultimate tensile capacity of the GFRP laminates, while for the CFRP bonded joints cracks began between 62% and 68% of the ultimate tensile capacity of the CFRP laminates. The authors did not prescribe any critical bond length beyond which there was no further increase in the ultimate failure load, even though the bond lengths were progressively varied over a wide range. However, Table-4.8 shows that the failure mode changes from concrete shearing beneath the glue line to the FRP laminate rupture after development of its full tensile capacity at a particular bond length for each category.

4.12.3 Analytical modelling

Like Taljsten (1997), Bizindavyi and Neal(1999) also used the conventional linear elastic theory to analyse the test results and it may be recalled that this theory is applicable only in the elastic range (Section 4.5). However, the authors have effected a simple modification for the factor ϖ in Eqn.4.3b. The shear modulus of the adhesive (G_a) in Eqn.4.3bwas replaced by an overall interfacial modulus G_{int}. This is due the transfer of shear force from the laminate to the concrete across a zone of about a 2 to 3 mm thick layer of concrete just beneath the bond line at the failure. The magnitude of G_{int} was determined as the slope of the shear stress/shear strain curves of the experimental data and it was then plotted as a function of the relative load level (z=applied load/maximum load), and fitted to a function of the form

$$G_{int} = a.(z)^3 + b.(z)^2 + c.z + d \quad (4.20)$$

where a, b, c and d are constants.

The analytical model predicts fairly well the maximum strains and the transfer lengths for service loads for 1-ply bonded joints. However, for stiffer plates, it tends to overestimate the response. This is due to the debonding of the plate that was not accounted for in the linear elastic theory and which becomes more predominant with an increase in the plate stiffness.

4.13 Discussion on various test results and analytical models

4.13.1 Test results

The preceding sections show that there is no dearth of experimental data on the behaviour of steel plated and FRP plated concrete beams under an axial load. In most of the studies, the test procedure involves different type of concrete prisms or blocks, different dimensions for the external plates, and different type of application of loads. Hence, there is an overwhelming need for formulating a standard test to evaluate the bond strength of concrete/plate interfaces. Furthermore, most of the studies are limited in nature as they involved a few parameters that affect the axial peeling. Still, one can arrive at the following common conclusions.

1. Axial peeling is initiated by the cracking of concrete below the adhesive layer at the plate end in the early stages of loading and the active debonding area is shifted to the adjacent area. This mechanism is repeated till the plate is completely debonded and no further load could be transferred across the composite interface.
2. In the case of the steel plated beams, the fracture in the concrete commences at a plate strain corresponding to approximately 50 to 60 % of the yielding strain of the steel plate. The peak shear stress at failure (full debonding along the concrete

layer 2 to 3 mm beneath the adhesive layer) could be twice the tensile strength of the concrete and the steel plate may also yield, if sufficient bond length is available. In most cases of FRP plated beams, the debonding occurred along the concrete beneath the bond surface as FRP plates possess very high tensile strengths (1000-2500 MPa) when compared to that of steel plates (250-350 MPa). However, in test specimens with higher grade concrete, the failure occurred due to aggregate/mortar matrix debonding and the resulting local stress concentration induced the plate rupture.

3. The bond strength increases linearly with the increased bond length up to a certain bond length beyond which no further increase in bond strength could be observed and this bond length is known as critical bond length. Further, it is difficult to prescribe a common value of the critical bond length as in most of the studies the parameters such as concrete strength, thickness and elastic modulus of the plate were varied. For example, in the case of 3 mm thick steel plated beams (E_p=200 GPa), the critical bond length $L_{b.crit}$ was found to be 200 mm (Taljsten 1997); the corresponding value for a 1mm thick graphite FRP plated beams (E_p=108.5 GPa) was 95 mm (Chajes et.al 1996). Izumo et.al (1997) estimated the magnitude of $L_{b.crit}$ to be 100 mm for both 0.144mm thick aramid plated beams (E_p=85.9 GPa) and 0.112 mm thick CFRP plated beams (E_p=242 GPa).

4. When all other parameters were fixed, the bond strength was found to depend on the compressive strength of concrete. While most of the researchers postulated that the peak shear strength at debonding is directly proportional to $f_c^{2/3}$, in one study it was found to depend on $f_c^{1/2}$ (Chajes et.al 1996). It is worth noting that both $f_c^{2/3}$and $f_c^{1/2}$ indirectly represents the magnitude of the tensile strength of the

concrete. In one study by Ranisch and Rostacy (1986), this critical term was considered to be the surface tensile strength of the concrete f_{ctm}.

5. In none of the studies, the debonding occurred through the adhesive layer. In fact, in one study by Swamy et.al (1986), the variation in the adhesive thickness (0.5-3 mm) was shown to have negligible effect on both mean and peak shear stresses at failure.

4.13.2 Analytical models

The most outstanding aspect of the research on axial peeling is that while there is abundant test data on both steel and FRP plated beams, there is no one universal formula either to estimate the bond strength or to determine the bond length needed to sustain certain bond force. Most of the researchers prescribe some form of equation to compute the maximum axial strength sustained and in some cases, to determine the critical bond length. However, these equations are not universal as they involve some sort of experimental constants. That is, they were derived for the particular type of the plate and the concrete grade used in the study and they were calibrated against the same data.

Some researchers such as Taljsten (1997) and Bizindavyi and Neale(1999) attempted to formulate analytical techniques that are based on linear elastic approach and that depend heavily on the adhesive properties. These equations are helpful to study the behaviour up to the first fracture in concrete and they go astray once the concrete is cracked. There was even an attempt by Taljsten (1996) to use fracture mechanism approach but it is not a general design approach, as experimental input is still needed in the form of defining and measuring experimentally the fracture energy for shear failure. Therefore, there is a need to formulate an analytical approach that will incorporate the different types of plates with differing orientation and the concrete

grade. The inadequacy of the existing models is demonstrated in the next section by comparing the test results for steel plated beams with that of the design guidelines prescribed by Ranisch and Rostacy (Section 4.2).

4.13.3 Comparison between theoretical and test results for steel plated beams

We find there are three different studies conducted on the axial peeling aspects of steel plated beams by Ranisch and Rostasy (Section 4.2), Swamy, Jones and Charif (Section 4.3) and Taljsten (Section 4.4). In this section, the empirical relationship developed by Ranisch and Rostasy (Eqns. 4.1 a, 4.1b and 4.2) is compared with the test results from Swamy et.al (Section 4.3) and Taljsten (Section 4.4.2.1).

Equations 4.1 a, 4.1b and 4.2 can be rewritten to compute the bond strength of a steel plated beam of width b_p and thickness t_p with a bond length of L_b as

$$P_b = \sqrt{\frac{L_b E_p b_p^2 t_p \tau_{pk}}{18500}} \leq \left(f_{yp} b_p t_p / 1.45\right) \tag{4.21}$$

In the above equation, the peak bond stress τ_{pk} is given as 8 MPa for a concrete strength of 30 MPa and for other grades of concrete, no relationship or magnitudes were prescribed. Therefore, we make use of the facts that $\tau_{pk} \alpha f_c^{2/3}$ (Refer Section 4.13.1) and τ_{pk}=8 MPa when f_c=30 MPa to deduce the relationship τ_{pk} =0.8 $f_c^{2/3}$. Figure 4.13 compares the test results from Taljsten (Section 4.4.2.1) and Swamy et.al (Section 4.3.2) with that obtained from Eqn.4.21. It can be seen from Fig.4.13 that Eqn.4.21 consistently underestimates the bond strength for both set of test results and the ratio between the actual bond strength to the computed bond strength is 0.47 with a standard deviation of 0.126 for all the results.

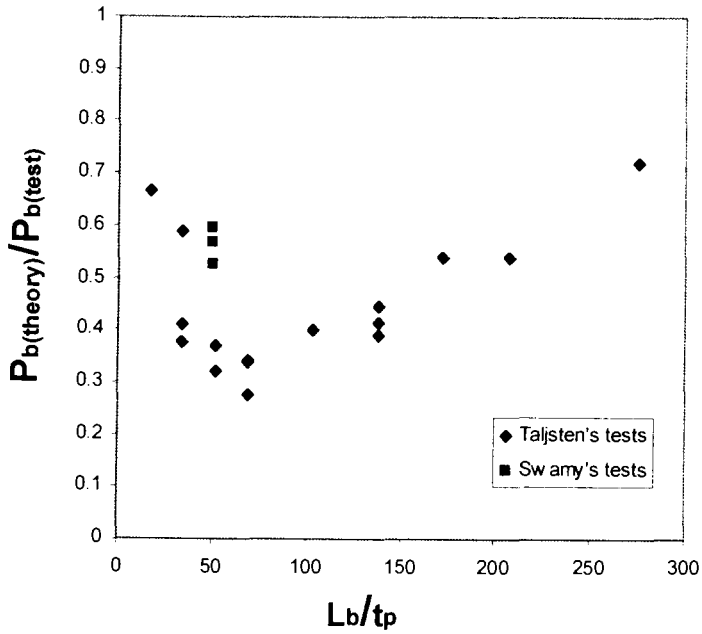

Fig.4.13. Comparison between theoretical and test bond strengths

4.14 Concluding Remarks

From this literature study, it is realised that axial peeling of FRP or steel plated beams is another major phenomenon that was widely investigated experimentally. Most of the studies came out with some general guidelines such as the critical bond length for a particular type of FRP plates and empirical equations for determining the maximum axial force, i.e. bond strength that can be sustained across an interface. Some linear elastic models also exist that can give some indications about the initiation of the debonding but not the total debonding phenomenon. Therefore, there is a need to develop a general approach for calculating the bond strength that will consider any type of FRP material and concrete strength.

References

Bizindavyi,L., and Neale,K.W.(1999) Transfer lengths and Bond Strengths for Composites Bonded to Concrete. ASCE Journal of Composites for Construction. Nov'99 pp153-160.

Chajes,M.F., Finch,Jr.,W.W., Januszka,T.F., and Thomson,Jr.T.A.(1996) Bond and force transfer of composite material plates bonded to concrete ACI Structural Journal, V.93,March-April 1996, 208-217.

Horiguchi,T and Saeki,N (1997) Effect of test methods and quality of concrete on bond strength of FRP sheet. Non-Metallic (FRP) Reinforcement of Concrete

Structures Proceedings of the Third International Symposium Vol.1, Oct.,1997, pp265-270.

Izumo,K., Saeki,N., Asamizu,T., and Shimura,K(1997) Strengthening Reinforced Concrete Beams by Using Prestressed Fiber Sheets. Non-Metallic (FRP) Reinforcement of Concrete Structures Proceedings of the Third International Symposium Vol.1, Oct.,1997, pp379-386.

Maeda,T., Asano,Y., Sato,Y., Ueda,T., and Kakuta,Y.(1997) A study on bond mechanism of carbon fiber sheet. Non-Metallic (FRP) Reinforcement of Concrete Structures Proceedings of the Third International Symposium Vol.1, Oct.,1997, pp279-286.

Mukhopadhyaya, Swamy and Lynsdale(1998) Influence of aggressive exposure conditions on the behaviour of adhesive bonded concrete-GFRP joints. Construction and building Materials, Vol.12(1998), pp.427-446.

Neubauer,U., and Rostasy,F.S.(1997). Design aspects of concrete structures strengthened with externally bonded CFRP-plates. Structural Faults and Repair-97, Edinburgh, July . pp.109-118.

Oehlers,D.J. (2000) Development of design rules for retrofitting by adhesive bonding or bolting either FRP or steel plates to RC beams in bridges and buildings. Proceedings of the ACUN-2, International Composites Conference, 14-18 February 2000, Sydney (Australia). pp.110-119.

Ranisch, E.-H. and Rostasy,F.S.(1986) Bonded steel plates for the reduction of fatigue stresses of coupled tendons in multispan bridge. Proceedings of International symposium on Adhesion between polymers and concrete (RILEM, Paris), September 16-19,1986. pp561-570.

Sharif,A., Al-Sulaimani,G.J., Basunbul,I.A., Baluch,M.H., and Ghaleb,B.N. (1994) Strengthening of initially loaded reinforced concrete beams using FRP plates. ACI Structural Journal, V.91, March-April 1994, 160-168.

Swamy,R.N., Jones,R. and Charif,A.(1986) Shear adhesion properties of epoxy resin adhesives. Proceedings of International symposium on Adhesion between polymers and concrete (RILEM, Paris), September 16-19,1986. pp741-755.

Taljsten,B.(1996). Strengthening of concrete prisms using the plate-bonding technique. International Journal of Fracture Vol.82 pp.253-266.

Taljsten,B.(1997). Defining anchor lengths of steel and CFRP plates bonded to concrete. International journal of Adhesion and Adhesives, Vol.17,No.4.319-327.

CHAPTER-5 REVIEW ON THEORY OF PLASTICITY CONCEPTS FOR SHEAR STRENGTH OF REINFORCED CONCRETE BEAMS

CONTENTS

5.1 Introduction

It has been shown in the preceding Chapters 2 and 3 that shear peeling of plated beams is caused by the formation of a critical crack that induces a plane of discontinuity across the plate-concrete interface and failure occurs by sliding along this plane. As shear-friction theory helps to understand such failures better, in this chapter a review is undertaken of such concepts as well as the analytical methods that incorporate these concepts to work out the shear strength of concrete beams. This information will eventually be used in Chapter-11 to develop mathematical models for shear peeling in reinforced concrete beams that are bonded with plates of any configuration. It may be noted that most of the work discussed in this chapter was carried out at the Technical University of Denmark as described in the following sources: Nielsen (1998), Zhang (1994 and 1997) and Hoang (1997).

In this chapter, the basic shear-friction concepts based on the theory of plasticity for plain concrete is discussed first. It is then shown how these concepts were used by Zhang (1994 and 1997) to develop a model for a simply supported, non-shear reinforced concrete beam loaded with a single concentrated load. Afterwards, the modifications needed for uniformly distributed loads are described. The last part of this chapter deals with the extension of Zhang's Model to fixed and continuous beams by Hoang (1997). Finally, the special case of a prestressed concrete beam is also described.

5.2 Shear-friction concepts

5.2.1 Modified Coloumb's criterion for uncracked concrete

According to Columb's frictional hypothesis, the failure of a material often occurs along certain sliding planes or yield planes. As shown in Fig.5.1, the sliding failure along a surface will take place when the shear stress τ exceeds the sliding resistance

which depends on the cohesion c, the coefficient of friction μ and the applied normal stress σ.

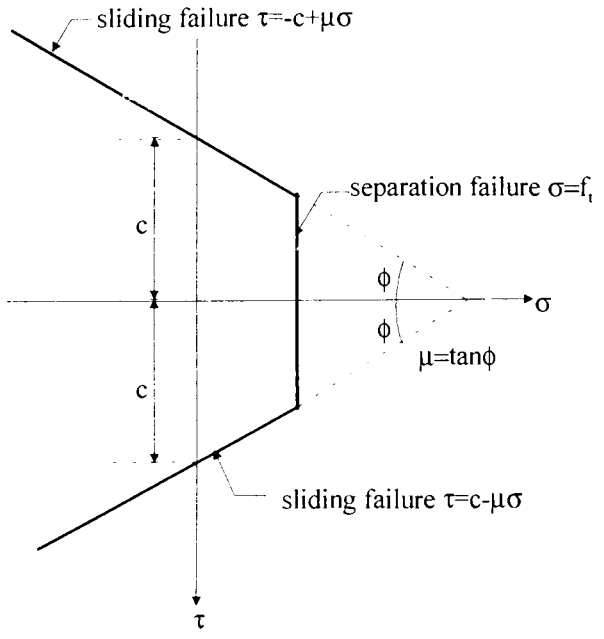

Fig.5.1. Coulomb's modified failure criterion (Zhang 1994)

The failure criterion is stated as

$$|\tau| = c - \mu\sigma, \text{ where} \tag{5.1a}$$

$$\mu = \tan\phi, \tag{5.1b}$$

and where ϕ = angle of friction and σ is positive for tensile stress.

However, concrete could fail additionally also by separation across the surface if the normal stress exceeds the tensile strength of the concrete f_t, ie

$$\sigma = f_t \tag{5.1c}$$

Therefore, concrete is classified as a modified Coloumb material as it can fail by separation or sliding along the yield lines. This failure envelop is illustrated in Fig.5.1. Alternatively, equations 5.1a and 5.1b for sliding failure can be expressed in terms of the principal stresses σ_1 and σ_3, as shown in the Mohr's circle in Fig.5.2.

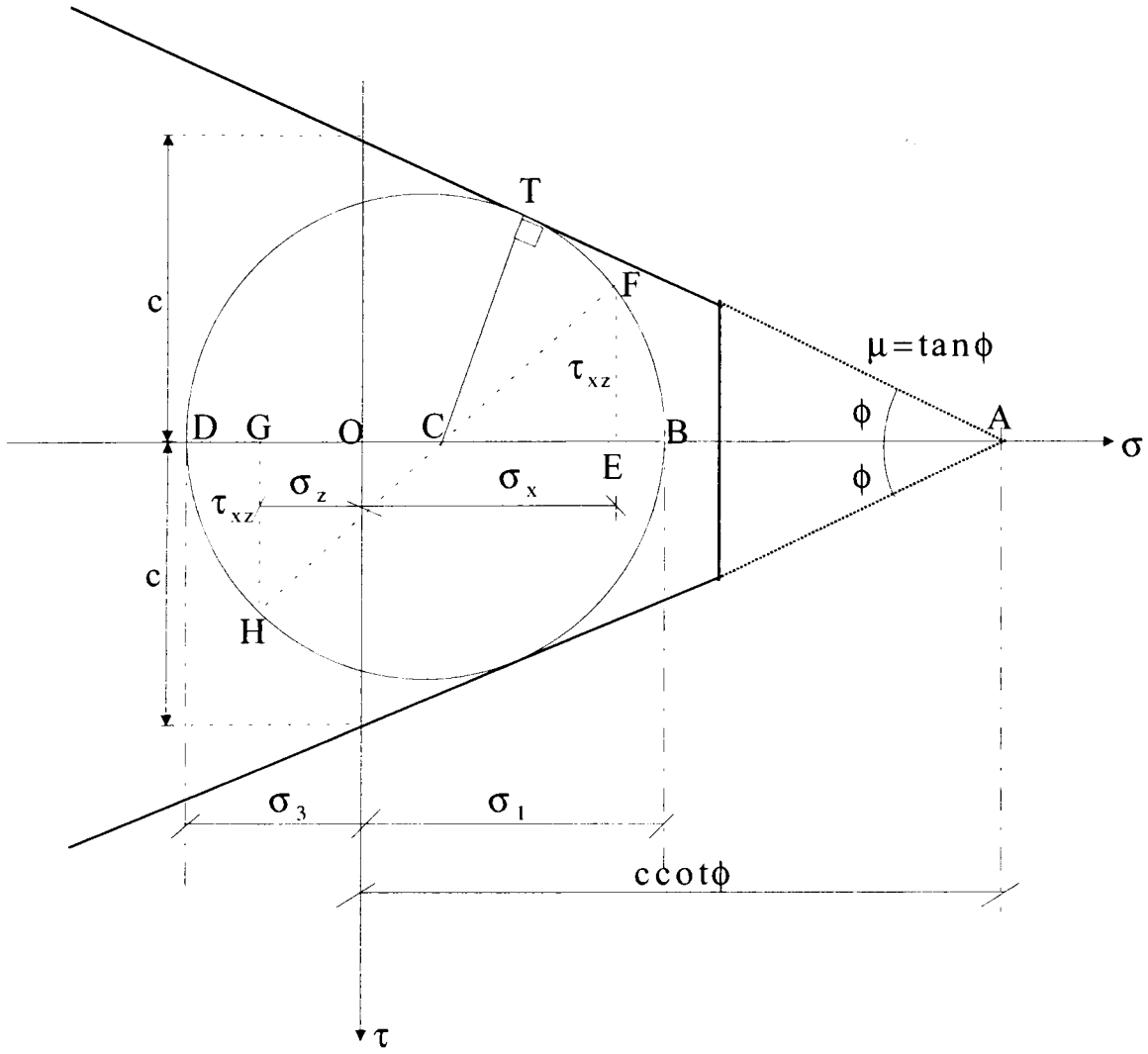

Fig.5.2. Mohr's circle for sliding failure

In Fig.5.2, C is the centre of Mohr's circle. Therefore,

$$TC = BC = CD = \frac{1}{2}BD = \frac{1}{2}(\sigma_1 - \sigma_3) \tag{5.2a}$$

and

$$\begin{aligned} AC &= OA - OC = OA - (OB - BC) = c\cot\phi - (\sigma_1 - \frac{1}{2}(\sigma_1 - \sigma_3)) \\ &= c\cot\phi - \frac{1}{2}(\sigma_1 + \sigma_3) \end{aligned} \tag{5.2b}$$

From the right angled triangle ATC, TC=ACsinϕ and therefore

$$\frac{1}{2}(\sigma_1 - \sigma_3) = (c\cot\phi - \frac{1}{2}(\sigma_1 + \sigma_3))\sin\phi .$$

Which upon simplifying,

$$\frac{1}{2}(\sigma_1-\sigma_3)=c\cos\phi-\frac{1}{2}(\sigma_1+\sigma_3)\sin\phi \tag{5.3}$$

Substituting $\mu=\tan\phi$ (Eqn.5.1b) in Eqn.5.3 and simplifying, we have

$$k\sigma_1-\sigma_3=2c\sqrt{k},$$
$$\text{where } k=\left(\frac{\cos\phi}{1-\sin\phi}\right)^2=\frac{1+\sin\phi}{1-\sin\phi}=\left(\mu+\sqrt{1+\mu^2}\right)^2 \tag{5.4}$$

The compressive strength of the concrete f_c is determined from the uniaxial test in which the stress field at failure is defined by $\sigma_1=\sigma_2=0$ *and* $\sigma_3=-f_c$. and the compression failure always involves sliding failure. Therefore, we can deduce from Eqns.5.3 and 5.4 that

$$-\sigma_3=f_c=2c\sqrt{k} \tag{5.5}$$

Upon trigonometrically manipulating k and rearranging, we get the equation for cohesion c as

$$c=\frac{1}{2}f_c\frac{\cos\phi}{1+\sin\phi} \tag{5.6}$$

5.2.2 Modified Coloumb's criterion for cracked concrete

It may be noted that the failure envelop shown in Fig.5.1 pertains to uncracked concrete subjected to homogeneous stress fields. However, for complicated states of stress or structural configurations, the sliding resistance should be reduced by multiplying the cohesion c with an effectiveness factor γ_0, as depicted in Fig.5.3. Figure 5.3 also shows a similar reduction factor ρ_0 applied to the separation failure. These effectiveness factors are applied to account for the micro-cracks in concrete due to shrinkage of the cement paste or induced by the applied loads. This is an approximate way to compensate for the softening effects due to the falling branch of the stress-strain relationship for compression as well as tension.

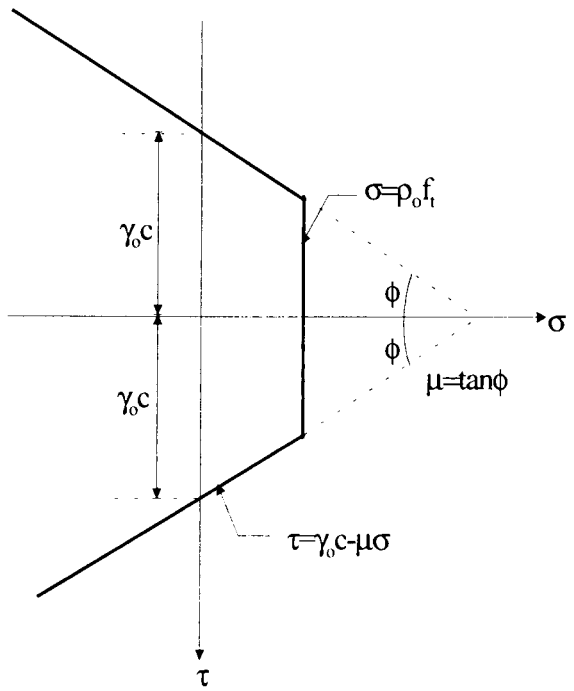

Fig.5.3. Failure envelop accounting for strain softening effect (Zhang 1994)

Zhang (1994) has established through a micro-mechanical model that the cohesion along a macro-crack is approximately half that for the uncracked concrete. This reduction in cohesion is accounted by a sliding reduction factor γ_s and the suggested value is

$$\gamma_s = 0.5 \tag{5.7}$$

However, the angle of friction ϕ remains unchanged. As softening will also be present along a macro-crack during sliding, the easier way to include this is to assume the resulting effective factor γ_{eff} as a product of γ_s and γ_0., i.e.

$$\gamma_{eff} = \gamma_s \gamma_o \tag{5.8}$$

The final failure envelop is shown in Fig.5.4, where $c_{eff}=\gamma_s\gamma_0 c$ and where c is defined in Eqn.5.6. Therefore, the effective cohesion c_{eff} can be written as

$$c_{eff} = \frac{1}{2}\gamma_s \gamma_0 f_c \frac{\cos\phi}{1+\sin\phi} \tag{5.9}$$

Furthermore, once a major or macro-crack develops, the resistance is due to sliding and no tensile stresses are transferred across the crack i.e. $\rho_0 f_t=0$.

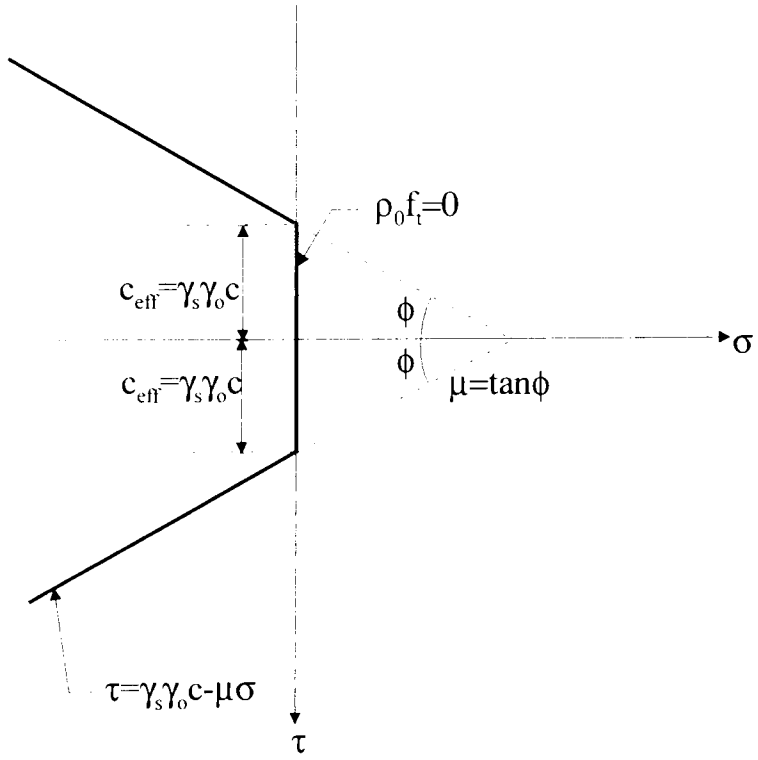

Fig.5.4. Failure envelop for a sliding macro-crack including strain softening effect (Zhang 1994)

In Eqn.5.9, the factor $\gamma_s\gamma_0 f_c$ is termed the effective compressive strength of the concrete f_c^* and the relationship between the principal stresses σ_1 and σ_3 at the instance of sliding can be modified by using Eqns.5.4 and 5.5 as

$$k\sigma_1-\sigma_3=f_c^*, where\ f_c^*=\gamma_s\gamma_0 f_c \tag{5.10}$$

5.2.3 Dissipation of energy along a line of discontinuity or a sliding macro-crack

Two important assumptions are made in the case of reinforced concrete beams for simplifying a three dimensional complex problem into a two dimensional one. First a state of plane stress is assumed as the width of the beam is normally small compared

with the depth and the span of the beam. The second assumption is that the tensile strength of concrete f_t is neglected when the failure occurs by sliding.

5.2.3.1 Relationship between maximum and minimum principal strains

In a perfect linearly elastic body, the strains are recoverable upon removing the applied loads and the stress-strain relationship is defined by Hooke's law. On the contrary, in a perfect plastic body, the work done during an increment of plastic deformation is dissipated. Hence, plastic strains are not recovered on unloading. At the ultimate state, the plastic strains at failure can increase or decrease indefinitely and therefore, a plastic flow occurs (Atkinson 1993 and Scott 1980). Furthermore, it is impossible to determine the magnitudes of plastic strains at failure and hence in the theory of plasticity, the relative rates of different strains are studied. The laws governing the strain rates at failure or plastic flow are termed as flow rules similar to Hooke's law for elastic conditions. For our case of a Mohr-Coulomb material such as concrete and soil, Von Mises (Refer to Scott 1980 and Chen 1975) suggested that the flow rule can be stated in terms of a plastic potential function (f), which can be defined by the equation

$$\frac{\dot{\gamma}^p}{\dot{\varepsilon}_n^p} = \frac{\delta f / \delta \tau}{\delta f / \delta \sigma_n} \tag{5.11}$$

In the above equation, ε= longitudinal strain with a subscript to denote the direction, here n stands for normal strain, γ=shear strain and the superscript p denotes plastic strain.

Von Mises also suggested that it may be often useful to assume the potential function to be identical with the failure criterion such as defined by Eqn.5.1a for a Coulomb material. For a Coulomb material, the plastic potential function (f) is stated as

$$f = \tau - c + \sigma_n \tan\phi \leq 0$$

(5.12)

and the associated flow rule derived from Eqns.5.11 and 5.12 is

$$\frac{\dot{\gamma}^p}{\dot{\varepsilon}_n^p} = \frac{1}{\tan\phi} \tag{5.13}$$

Likewise the function f can also be formed from Eqn.5.12 as

$$f = \sigma_1(1+\sin\phi) - \sigma_3(1-\sin\phi) + 2c\cos\phi \tag{5.14}$$

and the associated flow rule is

$$\frac{\dot{\varepsilon}_3^p}{\dot{\varepsilon}_1^p} = \frac{\delta f / \delta\sigma_3}{\delta f / \delta\sigma_1} \text{ where } \varepsilon_1 \text{ and } \varepsilon_3 \text{ are major and minor principal strains.} \tag{5.15}$$

Simplifying Eqns.5.14 and 5.15, we get

$$\frac{\dot{\varepsilon}_1^p}{\dot{\varepsilon}_3^p} = -\frac{1+\sin\phi}{1-\sin\phi} \tag{5.16}$$

For a reinforced concrete beam to fail by sliding, a macro-crack must develop beforehand and hence, the plastic strain is far greater than the elastic strain before yielding. Furthermore, we cannot define absolute magnitudes of plastic strains and in the theory of plasticity only the changes in strains are defined. Hence, Eqn.5.16 can be written for convenience of discussion by dropping the superscript p for plastic state and the dot for change in strains as

$$\frac{\varepsilon_1}{\varepsilon_3} = -\frac{1+\sin\phi}{1-\sin\phi} = -k \tag{5.17}$$

5.2.3.2 Computation of energy dissipated along a crack plane

Now we need to calculate the energy dissipated along a crack plane. As we know a macro-crack at failure or after yielding in terms of theory of plasticity causes a plane of displacement discontinuity as shown in Fig.5.5. A plane homogenous strain is

assumed in the volume bound by the two parallel planes which are δ apart and the parts I and II move as rigid bodies in a *n*, *t* plane as shown in Fig.5.5 (Nielsen, 1998).

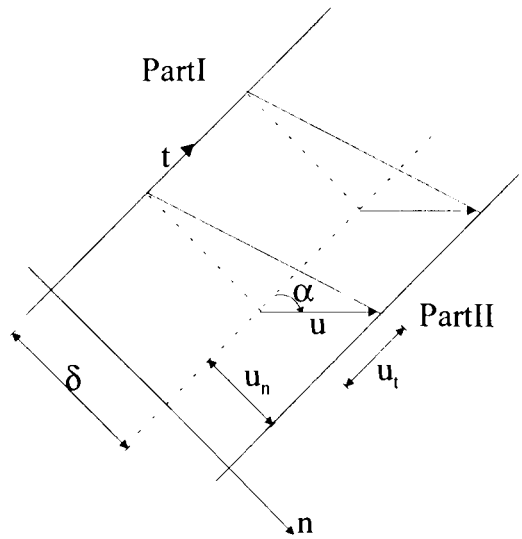

Fig.5.5. Yield line defined by a narrow strip (Nielsen 1998)

Part I is assumed to be stationary and Part II is assumed to displace by an amount u that has offsets u_n and u_t along the n and t axes respectively; the displacement vector u forms an angle α with the t-axis as shown in Fig.5.5. Therefore, the axial strains ε_n and ε_t and the shear strain γ_{nt} can be written as

$$\varepsilon_n = \frac{u_n}{\delta} = \frac{u\sin\alpha}{\delta}, \tag{5.18a}$$

$$\varepsilon_t = 0$$
(due to rigid body displacement) (5.18b)

and the rotation

$$\gamma_{nt} = \frac{u_t}{\delta} = \frac{u\cos\alpha}{\delta}. \tag{5.18c}$$

Therefore, the minimum and maximum principal strains from a standard Mohr-strain circle can be written as

$$\varepsilon_1 = \frac{\varepsilon_n + \varepsilon_t}{2} + \sqrt{\left(\frac{\varepsilon_n - \varepsilon_t}{2}\right)^2 + \left(\frac{\gamma_{nt}}{2}\right)^2} = \frac{1}{2}\frac{u\sin\alpha}{\delta} + \frac{1}{2}\sqrt{\frac{u^2\sin^2\alpha}{\delta^2} + \frac{u^2\cos^2\alpha}{\delta^2}} \quad (5.19a)$$

$$= \frac{1}{2}\frac{u}{\delta}(\sin\alpha + 1)$$

$$\varepsilon_3 = \frac{\varepsilon_n + \varepsilon_t}{2} - \sqrt{\left(\frac{\varepsilon_n - \varepsilon_t}{2}\right)^2 + \left(\frac{\gamma_{nt}}{2}\right)^2} = \frac{1}{2}\frac{u}{\delta}(\sin\alpha - 1) \quad (5.19b)$$

Therefore, the principal strain corresponding to σ_1 is

$$\varepsilon_1 = \frac{1}{2}\frac{u}{\delta}(\sin\alpha + 1) \quad (5.20)$$

and that corresponding to σ_3 is

$$\varepsilon_3 = \frac{1}{2}\frac{u}{\delta}(\sin\alpha - 1) \quad (5.21)$$

Substituting ε_1 and ε_3 from Eqns.5.20 and 5.21 into Eqn.5.17, we get

$$k = \frac{\sin\alpha + 1}{1 - \sin\alpha} \quad (5.22)$$

Now, the dissipation or work done per unit length W_t measured in the direction of the t-axis in Fig.5.5 is given by

$$W_t = (\sigma_1\varepsilon_1 + \sigma_3\varepsilon_3)b\delta = \varepsilon_3(\sigma_1\frac{\varepsilon_1}{\varepsilon_3} + \sigma_3)b\delta$$

As

$$\frac{\varepsilon_1}{\varepsilon_3} = -k,$$

then $$W_t = \varepsilon_3(-k\sigma_1 + \sigma_3)b\delta \quad (5.23)$$

where b is the dimension of the body perpendicular to the n,t plane. Substituting the values of ε_3 from Eqn.5.21 into Eqn.5.23 and as $k\sigma_1$-σ_3=f_c^* from Eqn.5.10, we get

$$W_f = \frac{1}{2} f_c^* ub(1-\sin\alpha) \qquad (5.24)$$

5.3 Zhang's crack sliding model for non-shear reinforced simply supported concrete beams

By applying the fundamental concepts described above, an ingenious crack sliding model has been developed at the Technical University of Denmark by Zhang (1994, 19977), for predicting the position and strength of the critical diagonal crack that causes shear failure in simply supported, non-shear reinforced concrete beams. The technique is illustrated in Fig.5.6.

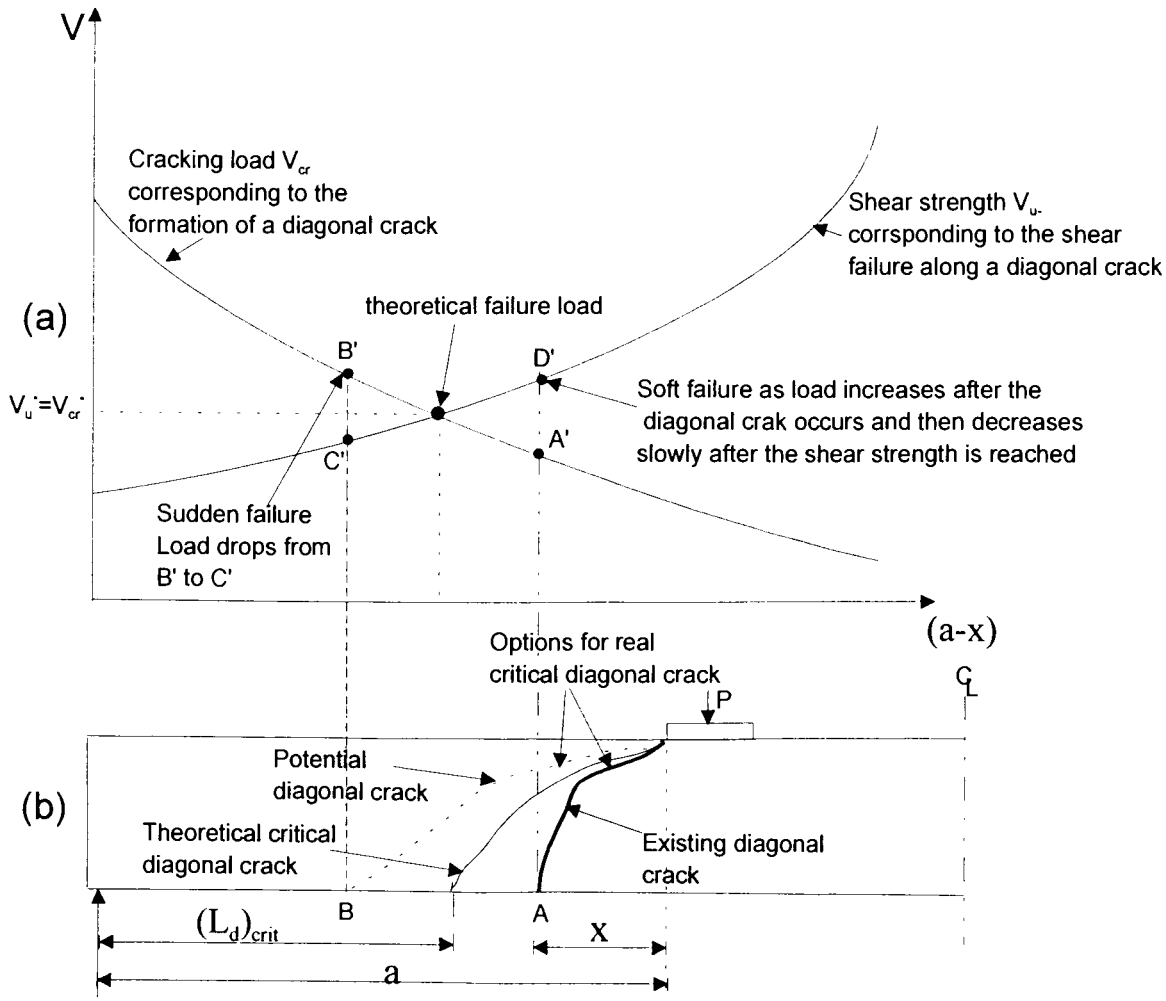

Fig.5.6. Zhang's model to determine shear strength of non-shear reinforced concrete beam (Zhang 1997)

In Fig.5.6a, *a* is the length of shear span as measured from the support to the edge of the load plate, *x* is the horizontal projection of any crack and (*a*-*x*) represents

the position of the root of a crack from the support. In this technique, for every possible location of a diagonal crack such as those shown in Fig.5.6b, it is necessary to determine both the applied shear force required to form the diagonal crack V_{cr} and the applied shear force to fail the cracked section V_u as shown in Fig.5.6a.

As observed in tests on simply supported RC beams without internal shear stirrups subject to a concentrated load such as shown in Fig.5.6b, the first cracks are normally formed in the region of maximum moment and they are vertical, i.e. flexural cracks. Then, as the applied loads are increased, flexural shear cracks and then diagonal shear cracks appear in the shear span. These cracks are formed closer and closer to the support and on prolonged application of load they will approximately intersect the top face of the loading point. This sequence is reflected by the curve for the load to cause shear crack (V_{cr}) that shows the farther the position of the crack, the more shear load is needed to cause a crack at that position. However, the mere formation of a shear crack at a given location does not automatically mean the shear failure along that crack plane and the shear strength V_u at that position has to be exceeded. Then and only then will shear failure due to sliding occur due to the formation of a diagonal shear crack. Normally, this failure crack is the last shear crack to occur in the shear span and it is termed as the critical diagonal shear crack (Zhang 1997; Hoang and Nielsen 1998). These two shear parameters (V_u and V_{cr}) are plotted and where they intercept gives both the position of the root of the critical diagonal crack from the support $(L_d)_{crit}$ and the shear strength of the beam.

5.3.1 Expression for ultimate shear load for a beam subject to concentrated load

A typical beam with a critical diagonal crack is shown in Fig.5.7. For simplicity, the diagonal crack is assumed as a straight line ending at the edge of the load platen and let its horizontal projection be x. Further, it is assumed that the beam is over-

reinforced in the longitudinal direction such that shear failure precedes the flexural failure and hence, the relative displacement u along the critical diagonal crack is vertically directed as shown in Fig.5.7.

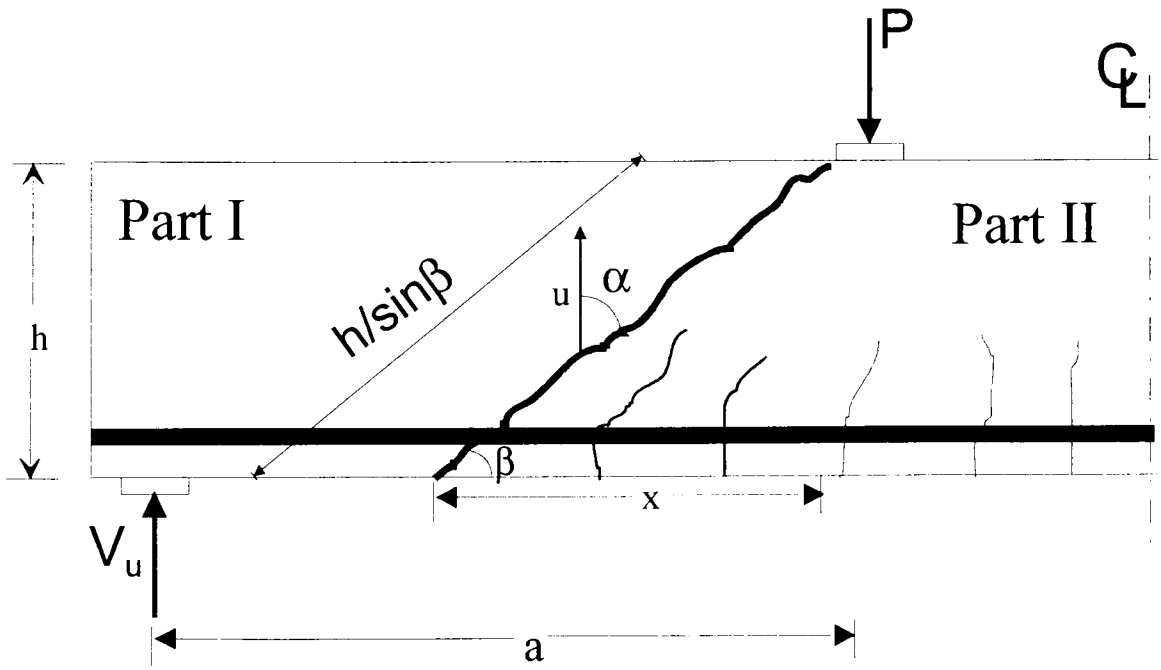

Fig.5.7. Sliding along simplified critical diagonal crack (Zhang 1994)

As part I is moved vertically up by an amount u, the internal work done (W_I) when sliding takes place along the crack can be found out using energy dissipation principles as explained in section 5.2. The parameter W_1 is obtained by multiplying the work done per unit length (W_I),as given in Eqn.5.24 and the length of the crack ($h/\sin\beta$). Here β is the inclination of the crack with reference to the longitudinal axis of the beam as shown in Fig.5.7.

$$W_1 = W_I\left(\frac{h}{\sin\beta}\right) = \frac{1}{2}\gamma_s\gamma_0 f_c b(1-\sin\alpha)\left(\frac{h}{\sin\beta}\right)u \qquad (5.25)$$

From Fig.5.7, $\sin\alpha = \frac{x}{\sqrt{x^2+h^2}}$ and $\sin\beta = \frac{h}{\sqrt{x^2+h^2}}$

Hence, $W_1 = \frac{1}{2}\gamma_s\gamma_0 f_c bh\left(\sqrt{1+\left(\frac{x}{h}\right)^2}-\frac{x}{h}\right)u$ (5.26)

Where γ_0 = effectiveness factor for uncracked concrete which is given by Zhang (1997) as

$$\gamma_0 = \lambda.f_1(f_c).f_2(h).f_3(\rho) \tag{5.27a}$$

where

$$f_1(f_c) = \frac{3.5}{\sqrt{f_c}} \qquad 5 < f_c < 60\ MPa\ (f_c\ in\ MPa), \tag{5.27b}$$

$$f_2(h) = 0.27\left(1+\frac{1}{\sqrt{h}}\right) \qquad 0.08 < h < 0.7m\ (h\ in\ m) \tag{5.27c}$$

$$f_3(\rho) = 0.15\rho + 0.58 \qquad where\ \rho = \frac{A_s}{bh} * 100\ and\ \rho < 4.5 \tag{5.27d}$$

Here, λ is an experimental constant that depends on load type and it equals 1.6 for point load and 1.2 for uniformly distributed load, γ_s is the sliding reduction factor due to cracking as given in Eqn.5.7, A_s is the area of the longitudinal reinforcement, b is the width of the beam, h is the depth of the beam and f_c is the cylindrical compressive strength of concrete. By equating the external work done (W_E) by the reaction V_u with the internal work done (W_I), the shear capacity is given by the following equation.

$W_E = V_u u = W_1$

$$V_u = \frac{1}{2}\gamma_s\gamma_0 f_c bh\left(\sqrt{1+\left(\frac{x}{h}\right)^2}-\frac{x}{h}\right) \tag{5.28}$$

5.3.2 Expression for diagonal cracking load

A certain shear force V_{cr} is needed in order to form a diagonal crack with a specific horizontal projection x and it is termed the diagonal cracking load. The diagonal crack is assumed to end at the edge of the loading plate by neglecting the depth of the

compression zone. This force V_{cr} can be estimated by assuming that the distribution of the normal stress along the developing crack will be constant and is equal to the effective plastic tensile strength f_{tef}, as shown in Fig.5.8a. The stress distribution for the curved crack is idealised by Zhang(1997) as a straight crack with the same horizontal crack projection x (Fig.5.8b) as apparently both the distributions have identical stress resultants.

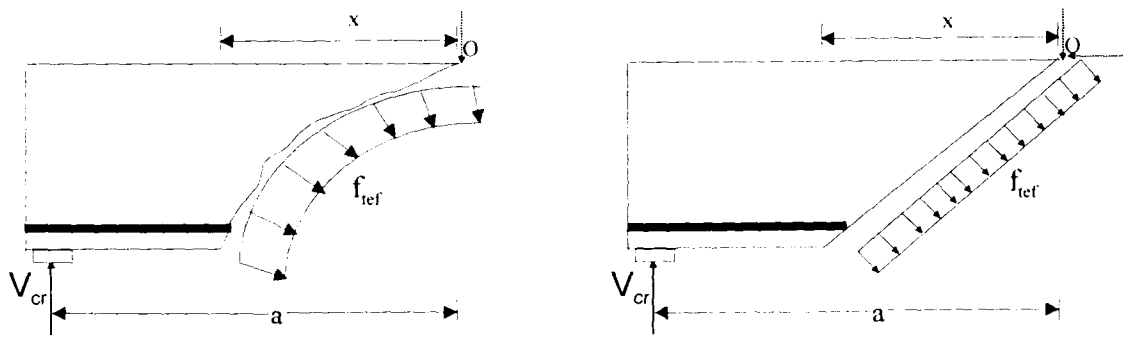

(a) **(b)**

Fig.5.8. Equivalent plastic stress distribution along the crack (Zhang 1994)

By considering the moment equilibrium around the upper tip of the straight crack in Fig.5.8b, the shear load to cause the crack V_{cr} is given by

$$V_{cr} = \frac{1}{2} f_{tef} \frac{b}{a}(x^2 + h^2) \tag{5.29}$$

The effective plastic strength of the concrete is given as

$$f_{tef} = 0.156.f_c^{2/3}.s(h) \tag{5.30}$$

where $s(h)$ accounts for the reduction in tensile strength due to size effect and it is given as

$$s(h) = \left(\frac{h}{100}\right)^{-0.3} \quad (h \text{ is the depth of beam in mm}) \tag{5.31}$$

5.3.3 Determination of the theoretical shear strength and the location of critical diagonal crack

The curves for shear failure load V_u (Eqn.5.28) and the shear cracking load V_{cr} (Eqn.5.29) can be generated as shown Fig.5.6a using an electronic spread sheet. Both

the shear strength of the beam and the location of the critical diagonal shear crack can be read off at the point of intersection of the two curves, i.e.where $V_u = V_{cr}$. However, in reality, the potential critical diagonal shear crack can occur on either side of the potential diagonal shear crack, as in the region AB in Fig.5.6b. For example, if the shear failure occurs by the formation of a diagonal shear crack at the point A that is further away from the support, then a higher shear load is needed to cause failure at point A rather than the shear load to cause a crack. In this case, a soft failure occurs as the the load increases to point D' in Fig.5.6a after the shear crack occurs and then it decreases slowly after the shear failure load at point A' is achieved. On the other hand, if the failure were to occur by the formation of a crack at point B, which is closer to the support, then a sudden failure occurs. This is due to the increased shear load required to cause a crack (point B' in Fig.5.6a) rather than the shear load to cause the shear failure (point C' in Fig.5.6a). In either case, Zhang's theory gives a lower bound for the shear strength of the concrete beam as the shear loads corresponding to points B' and D' are greater than that at the point of intersection in Fig.5.6a.

5.4 Modifications suggested when the beam is subjected to uniformly distributed load

Consider the RC beam shown in Fig.5.9 that is subjected to a uniformly distributed load of intensity p per unit area over the entire span.

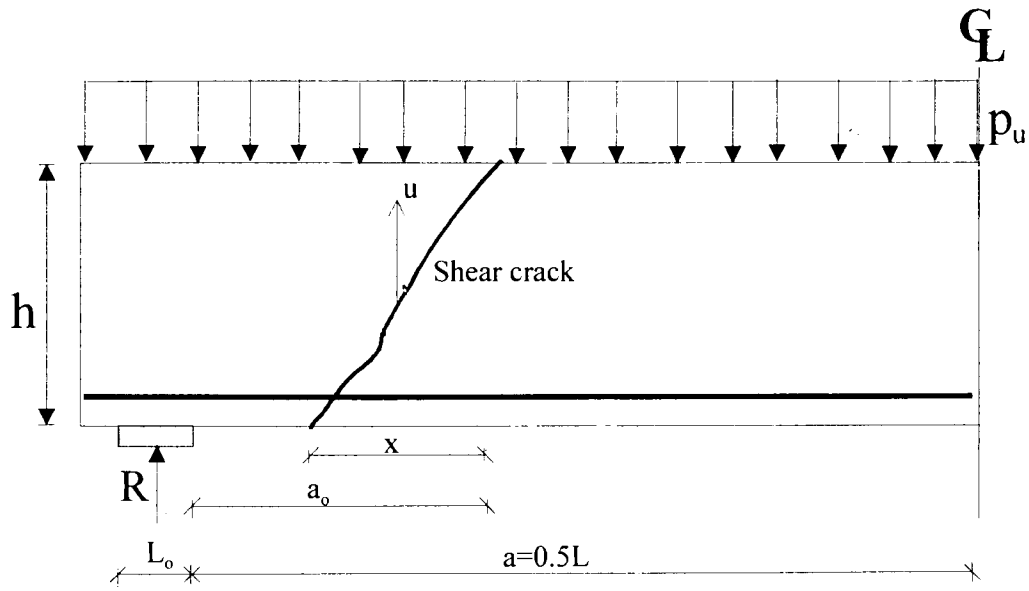

Fig.5.9. Beam subjected to uniformly distributed load (Zhang 1994)

The major parameter that is unknown is the top position of the crack unlike the beam subjected to the concentrated load where the given shear crack always extends to the edge of the load plate. To overcome this difficulty, Zhang(1994) suggests that the crack can be assumed to stop at distance a_0 from the edge of the support plate as shown in Fig.5.9 and it is given as

$$a_o = \frac{a^2 - h^2}{2a} \tag{5.32}$$

Here, the shear span a is assumed to be half of the clear span (L). i.e.

$$a = \frac{1}{2}L. \tag{5.33}$$

Therefore,

$$a_o = \frac{L^2 - 4h^2}{4L} \tag{5.34}$$

5.4.1 Expression for shear load to cause failure ($V_{u,udl}$)

The expression for internal work done W_I (Eqn.5.25) remains the same as in the case of concentrated load but for the modification of the effectiveness factor γ_o in Eqn.5.27a by setting the magnitude of the constant λ to be 1.2.

Internal work done

$$W_I = \frac{1}{2}\gamma_s \gamma_{0,udl} f_c \left(\sqrt{1+\left(\frac{x}{h}\right)^2} - \frac{x}{h} \right) bhu \tag{5.35}$$

$$\gamma_{0,udl} = 1.2.f_1(f_c).f_2(h).f_3(\rho) \text{ and } \gamma_s = 0.5 \tag{5.36}$$

External work done

Refer to Fig.5.10

$$W_E = Ru - p_u b(a_o + 0.5L_o)u \quad \text{Since R} = p_u b(0.5L + 0.5L_o)$$
$$\text{then } W_E = p_u b(0.5L - a_o)u \tag{5.37}$$

As $W_I = W_E$, we get the expression for the shear failure load as

$$p_u = \frac{1}{2}\gamma_s \gamma_{0,udl} f_c \frac{\left(\sqrt{1+\left(\frac{x}{h}\right)^2} - \frac{x}{h} \right) h}{(0.5L - a_o)} \tag{5.38a}$$

and

$$V_{u,udl} = \frac{p_u.(L + L_o)b}{2} \tag{5.38b}$$

Therefore,

$$V_{u,udl} = \frac{1}{2}\gamma_s \gamma_{0,udl} f_c \frac{\left(\sqrt{1+\left(\frac{x}{h}\right)^2} - \frac{x}{h} \right)(L + L_o)bh}{(L - 2a_o)} \tag{5.38c}$$

5.4.2 Expression for the diagonal cracking load ($V_{cr,udl}$)

The moment equilibrium about point O (Refer to Fig.5.10) yields

$$V(a_o + \frac{1}{2}L_o) - \frac{1}{2}p_{cr}b(a_o + \frac{L_o}{2})^2 = \frac{1}{2}f_{tef}b(x^2 + h^2) \tag{5.39}$$

where f_{tef} is the effective tensile strength of the concrete and is the same as in the concentrated load case; p_{cr} is the load per unit area needed to cause the diagonal crack.

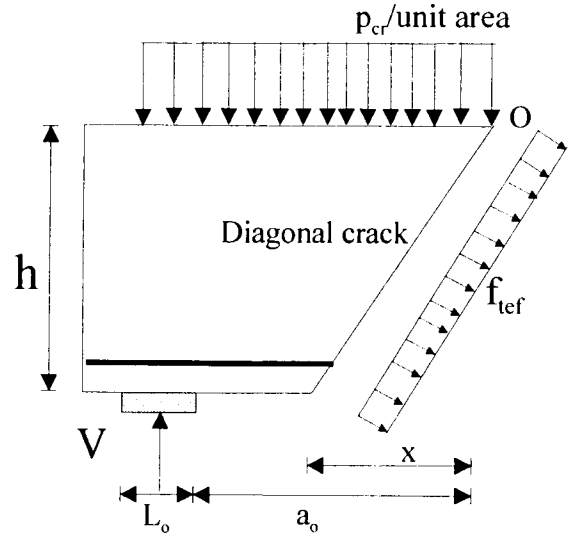

Fig.5.10. Diagonal cracking load (Zhang 1994)

Substituting $V = p_{cr} b(\frac{L}{2} + \frac{L_o}{2})$ and simplifying, we get the expression for p_{cr} as

$$\cdot\ p_{cr} = f_{tef} \frac{(x^2 + h^2)}{(L + L_o)\left(a_o + \frac{L_o}{2}\right) - \left(a_o + \frac{L_o}{2}\right)^2} \tag{5.40}$$

As the diagonal shear cracking load $V_{cr,udl} = p_{cr} b(\frac{L}{2} + \frac{L_o}{2})$,we have

$$V_{cr,udl} = \frac{1}{2} f_{tef} \frac{(x^2 + h^2) b (L + L_o)}{(L + L_o)\left(a_o + \frac{L_o}{2}\right) - \left(a_o + \frac{L_o}{2}\right)^2} \tag{5.41}$$

5.4.3 Estimation of the shear strength

The curves for shear failure load $V_{u.udl}$ (Eqn.5.38c) and the shear cracking load V_{cr} (Eqn.5.41) can be generated as shown in Fig.5.6a using an electronic spread sheet. Both the shear strength of the beam and the location of the critical diagonal shear crack can be read off at the point of intersection of the two curves, i.e. where $V_{u.udl} = V_{cr.udl.}$

5.5 Modification for continuous or fixed beams

5.5.1 Propped cantilever beam or end span of a continuous beam

Hoang(1997) extended the formulation of the simply supported beams to the statically indeterminate beams such as a propped cantilever beam as shown in Fig.5.11a. This beam is also equivalent to the end span of the continuous beam. The assumptions made by Hoang for this case are that the top and bottom reinforcement areas are equal and the shear failure precedes before the reinforcement fails by yielding. The moment envelope is shown in Fig.5.11b and the critical diagonal crack formulation is shown in Fig.5.11c.

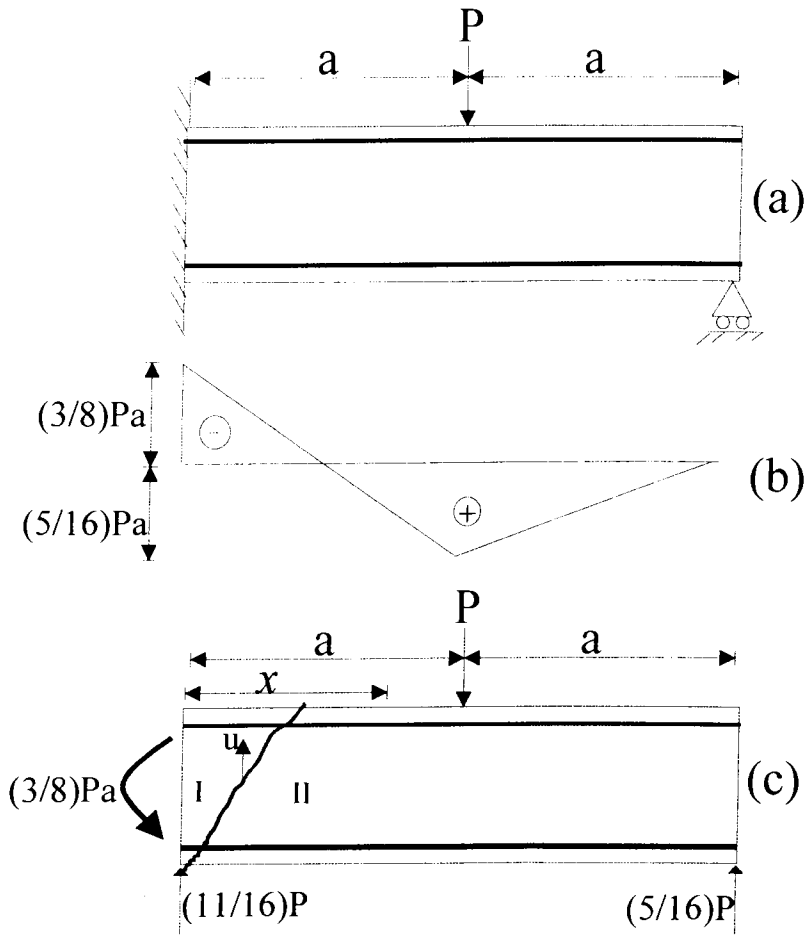

Fig.5.11. Propped cantilever beam (Hoang 1997)

It is worth noting that if there are unequal top and bottom reinforcements, then a moment redistribution analysis is needed to compute the fixed end moments

and reactions. It can be seen that for the negative moment region, the crack can originate at the tension face of the beam anywhere to the left of the applied load P and always terminates at the fixed end or the inner support in case of the continuous beam. The positive moment zone can be treated as a simply supported beam as discussed previously. The shear load to cause crack V_{cr} can be derived by taking moments about the fixed end support in Fig.5.11c,

$$\frac{3}{8}P_{cr}a=\frac{1}{2}f_{tef}b(x^2+h^2) \tag{5.42}$$

$$\text{As } V_{cr}=\frac{11}{16}P_{cr}, \text{ therefore } V_{cr}=\frac{11}{12}f_{tef}\frac{b}{a}(x^2+h^2). \tag{5.43}$$

The equation for calculating V_u remains the same as given by Eqn.5.28. Now, the usual procedure is adopted to calculate the shear strength of the beam.

5.5.2 Beam both ends fixed or inner span of a continuous beam

Figure 5.12 shows a beam fixed in both ends and it is equivalent to the inner span of a continuous beam also. To find the shear strength in the negative moment region, this case is treated the same as before and the only modification needed is to calculate the shear load to cause cracking. Taking moments about the crack tip, in this case the support shown in Fig.5.12c, we get

$$\frac{1}{4}P_{cr}a=\frac{1}{2}f_{tef}b(x^2+h^2) \tag{5.44}$$

$$\text{As } V_{cr}=\frac{1}{2}P_{cr}, \text{ therefore } V_{cr}=f_{tef}\frac{b}{a}(x^2+h^2). \tag{5.45}$$

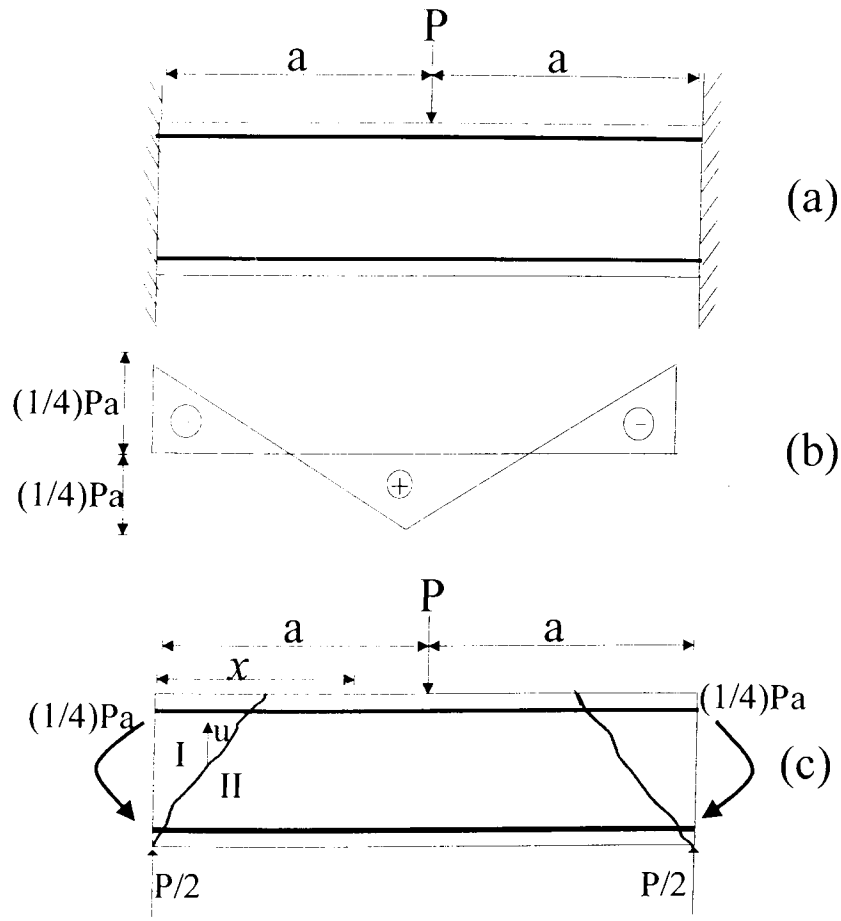

Fig.5.12. Beam fixed at both ends (Hoang 1997)

It may be noted that Eqns.5.42-5.45 have been derived assuming both negative and positive reinforcements areas are the same. However, for different areas of reinforcements, a moment distribution analysis can be carried out assuming plastic conditions and the moments and the reactions at the ends can be found out. Then the equations for V_{cr} and V_u can be modified accordingly.

5.6 Prestressed concrete beams

Consider the prestressed concrete beam that is shown in Fig.5.13. Zhang(1994) suggests two modifications for the prestressed concrete beam. As the prestressing force will affect the stress redistribution and the state of micro-cracks, the value of γ_0 will differ from the conventional reinforced concrete beams. The suggested value for prestressed beam is

$$\gamma_{0,se} = \lambda f_1(f_c) f_2(h) f_3(\rho) f_4\left(\frac{\sigma_{se}}{f_c}\right), \quad \gamma_s = 0.5 \tag{5.46}$$

Here f_1, f_2 *and* f_3 are the same functions as defined in Eqn.5.27b-d and the function f_4 is dependent on prestressing level and is given by Zhang (1994) as

$$f_4\left(\frac{\sigma_{se}}{f_c}\right) = 1 + 2\frac{\sigma_{se}}{f_c} \tag{5.47}$$

In Eqn.5.47, $\sigma_{se}=F_{se}/bh$ is the average prestressing stress and F_{se} is the prestressing force and σ_{se}/f_c is the level of prestressing. Therefore, the shear load to cause failure by sliding $V_{u,se}$ is given as

$$V_{u,se} = \frac{1}{2}\gamma_s \gamma_{0,se} f_c bh\left(\sqrt{1+\left(\frac{x}{h}\right)^2} - \frac{x}{h}\right) \tag{5.48}$$

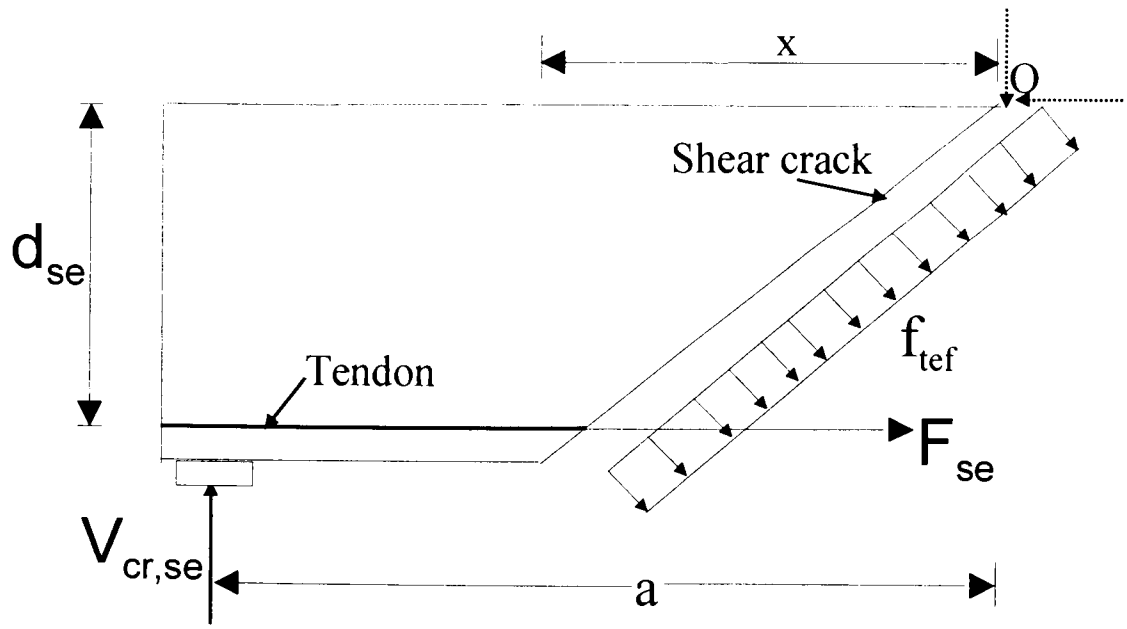

Fig.5.13. Crack formation in prestressed concrete beam (Zhang 1994)

The prestressing force also delays the formation of the diagonal crack and hence, the load to cause crack $V_{cr,se}$ is increased. Referring to Fig.5.13 and taking moment equilibrium about the crack tip, we get

$$V_{cr,se}a - F_{se}d_{se} = \frac{1}{2}f_{tef}b(x^2 + h^2). \tag{5.49}$$

where d_{se} is the distance between centroid of prestressing tendon and the concrete beam top. Rearranging, we get

$$V_{cr,se} = \left[\frac{1}{2} f_{tef} \frac{b}{a}(x^2 + h^2)\right] + \left[\frac{F_{se} d_{se}}{a}\right]. \quad (5.50)$$

Equations 5.48 and 5.50 are used to develop the envelops for $V_{u,se}$ and $V_{cr,se}$ and the point of intersection gives the position of the critical shear crack and shear strength of the prestressed beam.

5.7 Concluding Remarks

In this chapter, the theory to compute the shear strength of the non-shear reinforced concrete beam was discussed. The formulations are based on the theory of plasticity and shear friction concepts. Both the ultimate shear strength and the location of the critical shear crack can be determined. The theory is quite versatile as it can handle both concentrated loading and uniformly distributed loads. It can be extended to any type of support condition and the effect of prestressing force can also be incorporated.

References

Atkinson, J. (1993). The mechanics of soils and foundations. Mc-Graw Hill Book Co., London. p.337.

Chen,W-F.(1975). Limit analysis and soil plasticity. Elsevier scientific publishing company, Amsterdam. pp.68-74.

Hoang,L.C.(1997). Shear strength of non-shear reinforced concrete beams, Part 1- Statically indeterminate beams. Series R,No.16 Technical University of Denmark , Lyngby, Denmark. p.79.

Hoang,L.C. and Nielsen,M.P.(1998). Plasticity approach to shear design. Cement and Concrete Composites, Vol.20(1998). Pp.437-453.

Nielsen,M.P.(1998). Limit analysis and concrete plasticity. CRC Press, Boca Raton, U.S.A. p.908.

Scott,C.R..(1980). An introduction to soil mechanics and foundations. Applied Science Publishers, London. p.406.

Zhang ,J-P .(1994). Strength Of Cracked Concrete Part1 Series-R, Technical University of Denmark , Lyngby, Denmark. p.106

Zhang ,J-P. (1997). Diagonal Cracking And Shear Strength Of Reinforced Concrete Beams. Magazine of Concrete Research. Vol.49,No.178, Mar.1997. pp 55-65.

PART-III: SHEAR PEELING

CHAPTER-6: EXPERIMENTAL INVESTIGATION OF SHEAR PEELING OF STEEL PLATES ADHESIVELY BONDED TO THE SIDES OF RC BEAMS

CONTENTS

6.1 Introduction

This chapter deals with the tests conducted on shear peeling in reinforced concrete beams glued with steel plates to the sides. As discussed in chapter-2, the available information on shear peeling of side plated beams is minimal (Refer section 2.4.1). Hence, the objective of the present tests is to understand the parameters that influence shear peeling in side plated beams. The main parameters varied were the position of the side plates and the presence of shear stirrups. The behaviour of side plated beams is also compared with that of a corresponding unplated beam and that of a tension face plated beam.

In this chapter, the specimens, the test set-up and the material properties are described first. Then, the observations from each test are described individually. Finally, the inferences made from all the test results are discussed. These test results will be used later to validate the mathematical model for shear peeling in side plated beams, as described in Chapter-11. Another objective of these tests is to compare the shear peeling behaviour of steel plated beams with that of FRP plated beams which is described in Chapter-7.

6.2 Specimens

The specimens used for studying the shear peeling of side plated beams consisted of three reinforced concrete beams with steel plates (of dimensions 4700 mm long, 130 mm deep and 10 mm thick) that were bonded to both the sides of the beams such as shown in Figs.6.1b-d. The details of RC beam are given in Fig.6.1a.

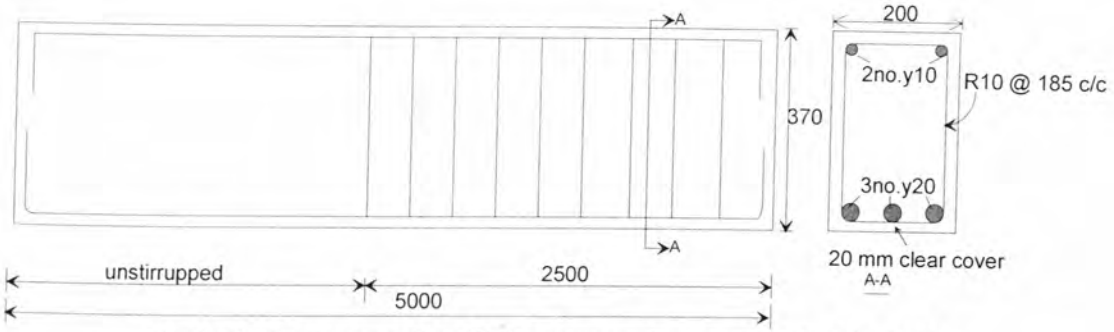

(a). Reinforcement details for beams bonded with side plates

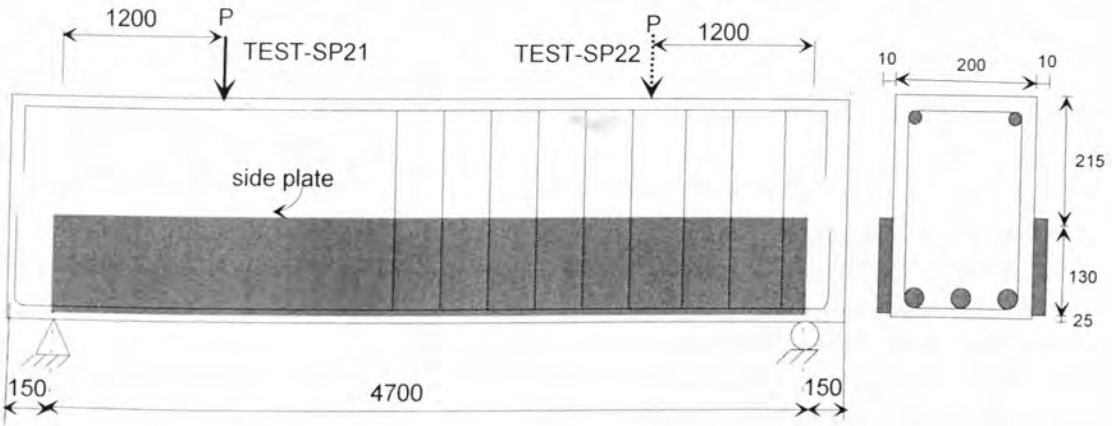

(b) Details of specimen for tests SP21 and SP22

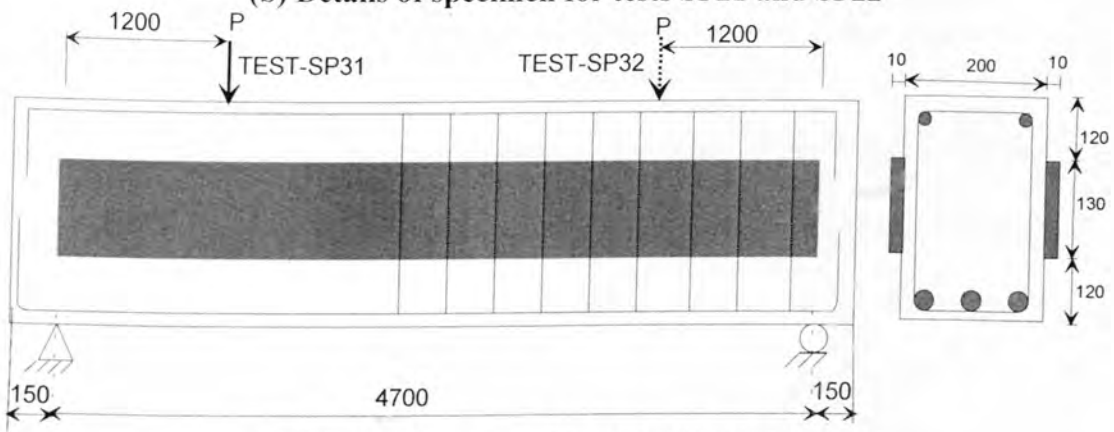

(c) Details of specimen for tests SP31 and SP32

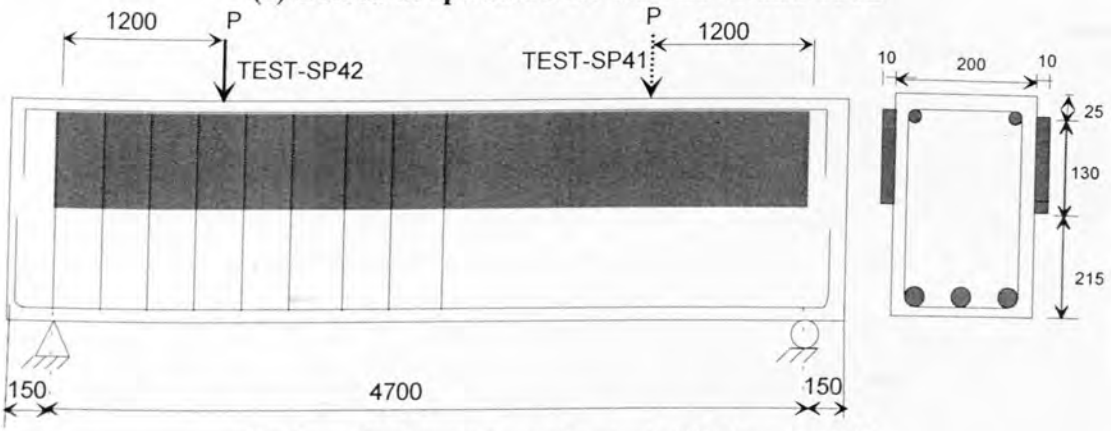

(d) Details of specimen for tests SP41 and SP42

Fig.6.1. Details of side plated beams

The main parameter varied for this study was the position of the side plate along the depth of the beams. The other parameter varied was the presence or otherwise of shear stirrups in a shear span tested; this was facilitated by providing shear stirrups in one half of the beam only such as shown in Figs.6.1b-d. Six tests were performed by testing each shear span individually. The six tests are denoted as SP21, SP 22, SP31, SP32, SP41 and SP42, as shown in Figs.6.1b, 6.1c and 6.1d. A test designated as SPREF was also conducted on a shear span of a beam without any shear stirrups and plates as shown in Fig.6.2 in order to determine the shear strength of the beam without stirrups V_{uc}. Another span of a beam without shear stirrups but bonded this time with a 4200 mm long, 200 mm wide and 10 mm thick tension face plate was tested to determine the pure shear peeling capacity of a tension face plated beam for comparison as shown in Fig.6.3; the test is designated as SP01.

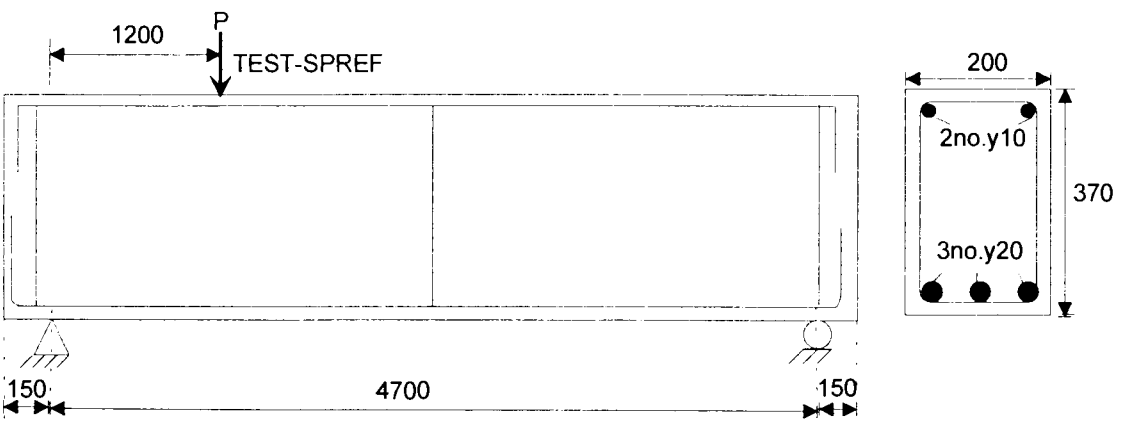

Fig.6.2. Details of specimen for test SPREF (V_{uc})

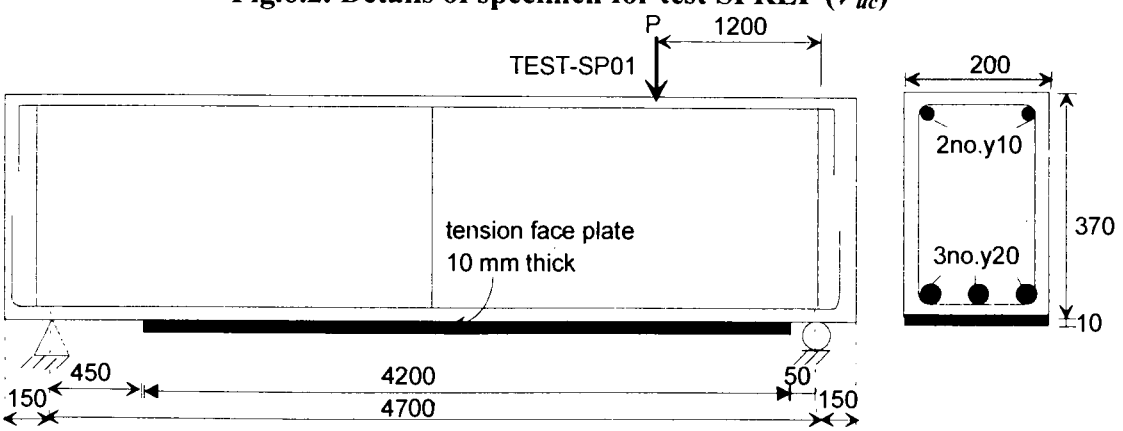

Fig.6.3. Details of specimen for test SP01

For the tests SPREF and SP01 that are shown in Figs.6.2 and 6.3, the beams had just three stirrups to hold the longitudinal bars in position; they were placed at the ends of the beams and at mid span so that they were well away from the failure regions and hence, they did not contribute to either the shear strength or the shear peeling strength. Tests SPREF and SP01 were used as reference beams in the analysis of the side plated beams.

6.3 Test set-up

The beams were simply supported over an effective span of 4700 mm and the load was applied on the top of the beam by a hand operated hydraulic jack through a load cell and a knife edge bearing. The two shear spans of the same side plated beam were tested individually; this was achieved by clamping the longer shear span while testing the shorter shear span to failure as shown in Fig.6.4. From the geometry of the loading arrangement for all the shear spans, the maximum shear load in the shear span tested was 74.5% of the total load applied. The ratio of the distance between the position of the applied load and support (1200 mm) and the depth of the beam (370 mm) was kept greater than 3 to avoid the increase in shear strength due to short span tied arching action.

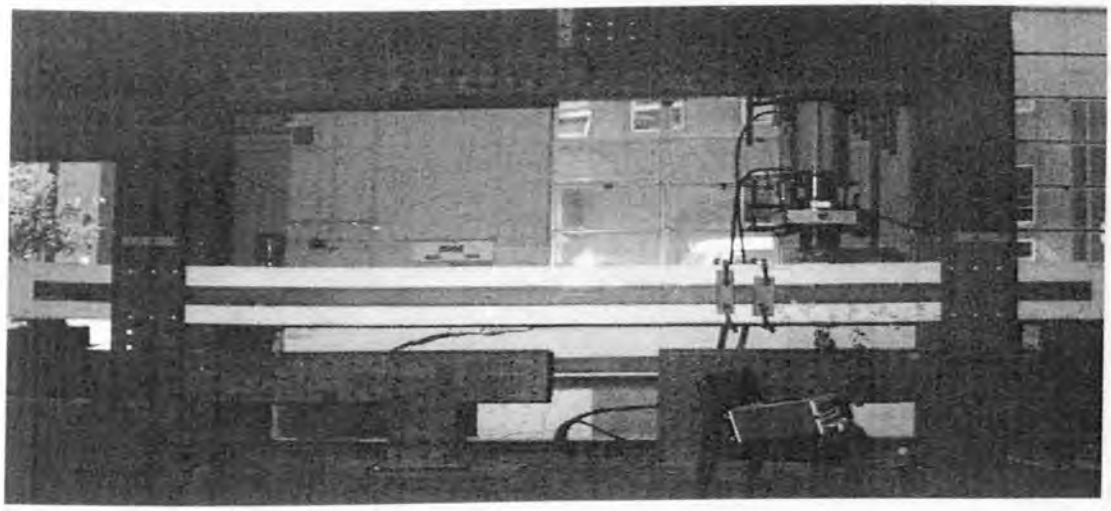

Fig.6.4. Clamping arrangement for testing side plated beams

6.4 Instrumentation

Strain gauges were bonded to both side plates and also to the tension face plates in order to detect the debonding at various sites of the plates. The arrangements of the strain gauges and their numbering are shown in Figs.6.5a, 6.5b, 6.5c and 6.5d for all the four plated beams tested. The beam deflection at the load point were monitored by a dial gauge and also by a transducer.

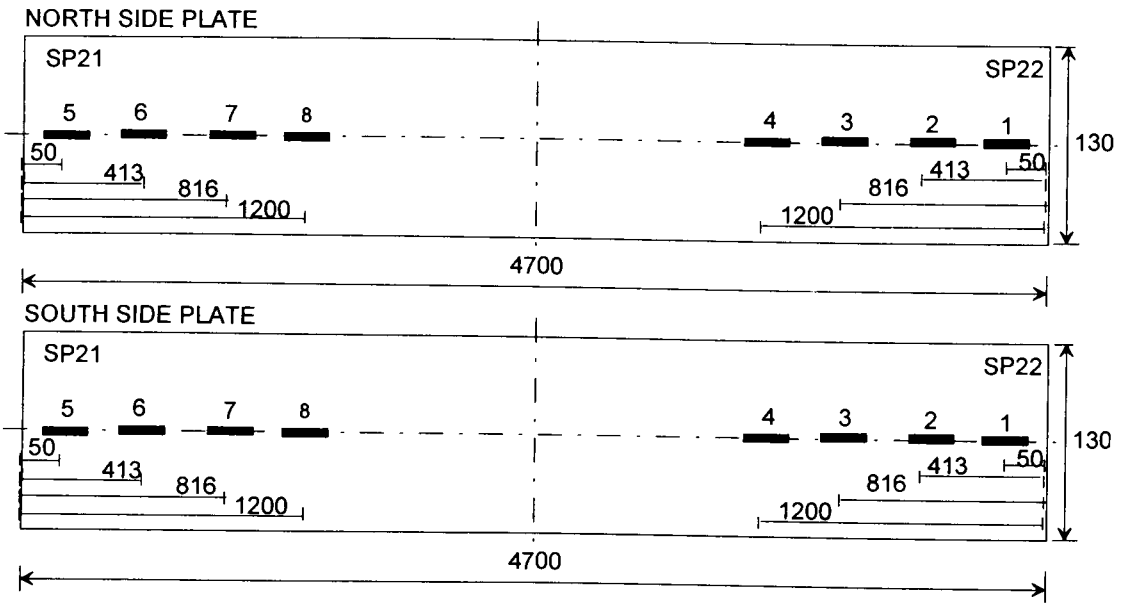

(a)Specimens SP21 and SP22

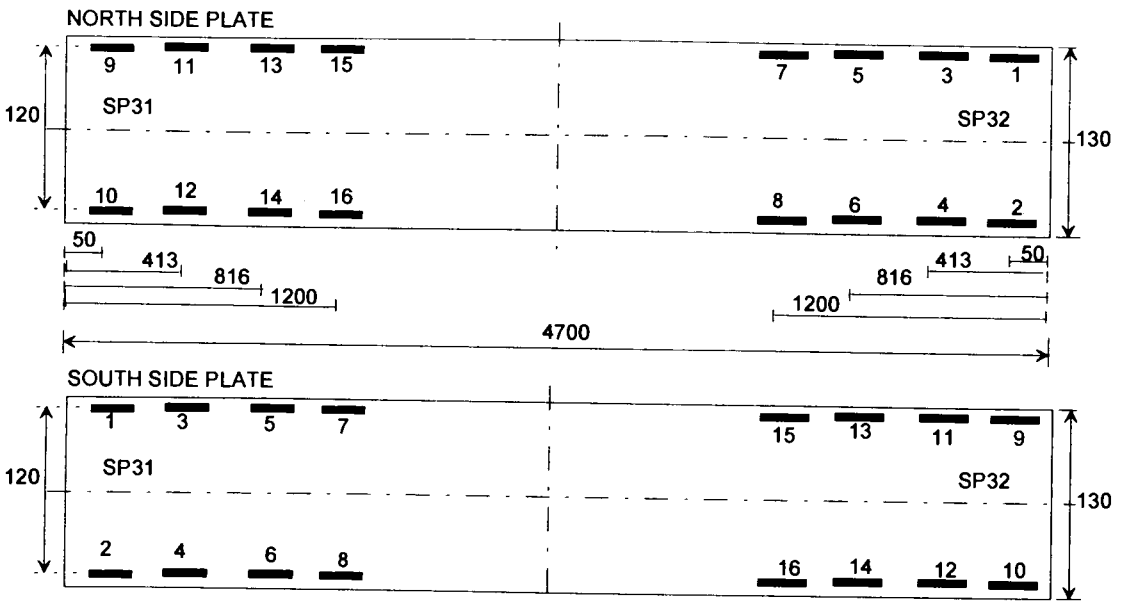

(b) Specimens SP31 and SP32

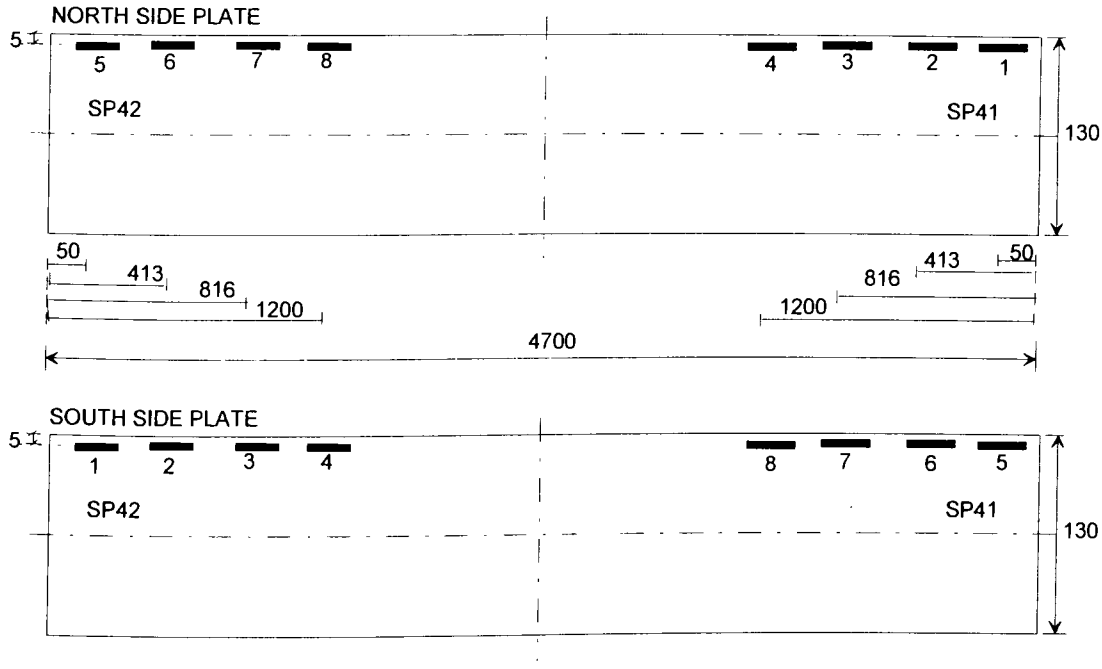

(c) Specimens SP41 and SP 42

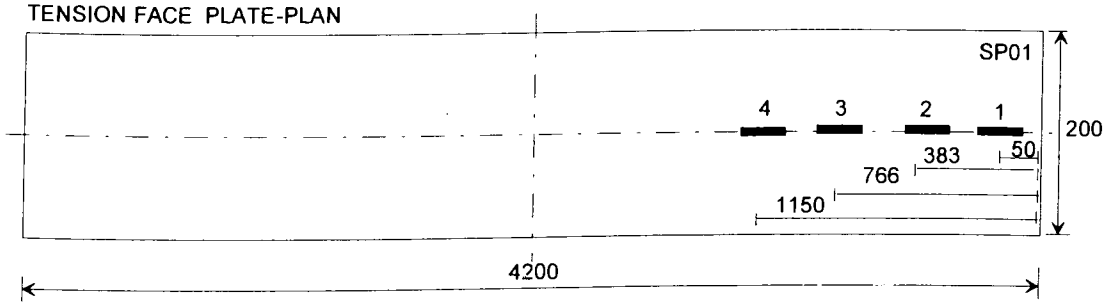

(d) Specimens SP01

Fig.6.5. Strain gauge arrangement

6.5 Material Properties

All the beams were cast in a single pour by using the concrete supplied by a local ready mixed concrete supplier. Material properties of the concrete are shown in Table-6.1. In this table, the individual values for each test are given under the "i" column and their mean value under "m" column. Material properties of the steel plates, reinforcing bars and shear stirrups are shown in Table-6.2. The manufacturer's specifications of the material properties of the epoxy resin used for bonding the steel plates are indicated in Table-6.3.

Table-6.1. Material properties of the concrete

Age	E_c (MPa)		f_b (MPa)		f_{tbm} (MPa)		f_c (MPa)		f_{cu} (MPa)	
(days)	i	m	i	m	i	m	i	m	i	m
84	41572	39922	-	-			49.68	49.3*	48.95	51.2
	36880		-				48.91		52.28	
	41315		-				49.24		52.23	
89	-	-	4.27	4.47			47.36	48.5*		
	-		4.69				49.54			
	-		4.46				48.69			

where E_c= Elastic modulus of the concrete, f_c= Cylinder compressive strength of the concrete, f_{cu}= Cube compressive strength of the concrete, f_b= Brazilian tensile strength of the concrete and f_{tbm} = Beam tensile strength of the concrete.

*As the beams were tested during the period 84-89 days, a mean f_c value of 48.9 MPa is used in the analysis.

Table-6.2. Material properties of the steel

Item	f_y (MPa)				f_u (MPa)			
Sample No.	1	2	3	Mean	1	2	3	Mean
Rebar Y20	436.1	429.7	-	432.9	530.0	522.0	-	526.0
Rebar R6	-	-	-	-	671.2	661.3	658.0	663.5
Steel plates 10mm	332.3	324.6	333.5	330.1	540.6	539.2	542.0	540.6

where f_y = Yield strength of the steel, and f_u = Ultimate strength of the steel.

Table-6. 3. Material properties of the glue Hilti CA 273 after 2 days (as tested by the manufacturer)

Compressive strength (ISO 604)	Tensile strength (ISO 527)	Flexural strength (ISO 178)	Elastic modulus in compression (ASTM D 695)	Tensile bond strength (ISO 527)	Maximum operating temperature
110-120 MPa	30-40 MPa	20-30 MPa	5000-6000 MPa	10-15 MPa	80° C

6.6 Test Results

In the following discussion, the shear force V in the shear span being tested is used for better clarity and the total applied load P is given in the brackets.

6.6.1 Test SPREF

The objective of test SPREF shown in Fig.6.2 was to determine the shear strength of the unplated reinforced concrete beam without any internal shear reinforcement; this serves as a datum for studying the shear peeling strength of plated beams. At a shear load V=30 kN (P=40 kN), the first flexural cracks that were nearly vertical occurred

as can be seen in Fig.6.6. On applying further load, existing cracks were enlarged and new ones appeared in between the existing ones; this phenomenon was observed up to a shear load V=77 kN (P=103kN). When the shear load reached a value of V=85.6 kN (P=115 kN), a critical diagonal shear crack suddenly developed at a distance approximately of 350 mm from the support and extending to the top of the beam near the inner edge of the load paten. The beam failed in shear and the shear load V dropped to 10.7 kN (P=14.4 kN), as shown in Fig.6.7, which shows the variation of deflection recorded with applied shear load.

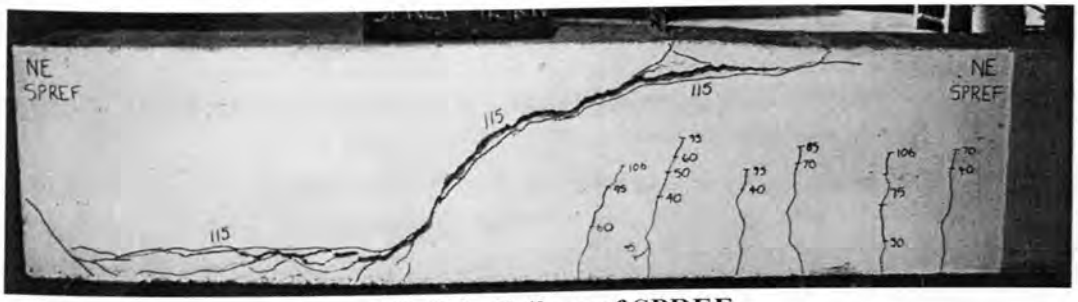

Fig.6.6. Failure of SPREF

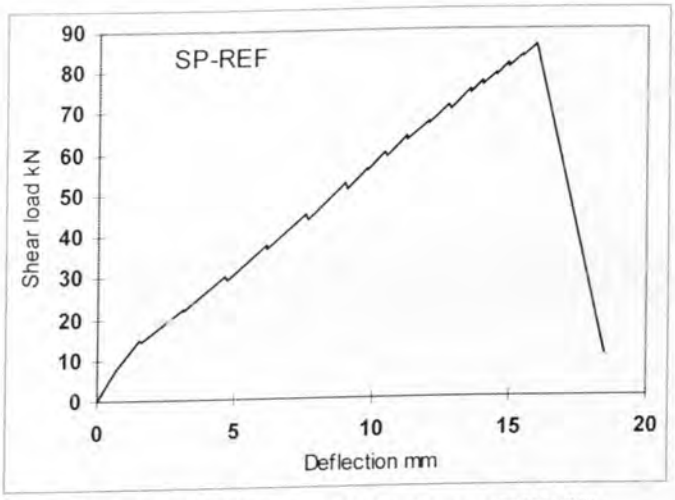

Fig.6.7. Deflection of the beam SPREF

6.6.2 Test SP01

Test SP01 in Fig.6.3 was used to determine the pure shear peeling resistance of the tension face plated beam. The beam was bonded with a tension face plate that had the same thickness as that of the side plates used in this study, i.e.10 mm, and the shear

span tested did not contain any stirrups. The plate was terminated close to the support in order to determine the pure shear peeling resistance, i.e. the shear loat at debonding induced by a critical diagonal crack. The plate end was terminated at a distance 50 mm from the nearest support.

Till V=137 kN (P=182 kN), no cracks were observed. After a small increase in the applied load of 3 kN, corresponding to a shear load V=140 kN (P=185 kN), a critical diagonal shear crack occurred near the plate end. The diagonal crack extended to the beam top near the inner edge of load paten and caused the external plate to peel along the concrete cover as shown in Fig.6.8. Shear failure of the concrete beam occurred simultaneously with shear peeling of the plate; shear failure occurred due to the formation of another diagonal crack from the same root which split the shear span into two as can be seen in Fig.6.8. By comparing the crack patterns in Beam SPREF in Fig.6.6 and Beam SP01in Fig.6.8, it can be seen that the diagonal crack was forced to initiate adjacent to the support in case of SP01. This has caused the shear strength of the span SP01 to increase from 81 kN to 140 kN, i.e. 63% increase in shear strength.

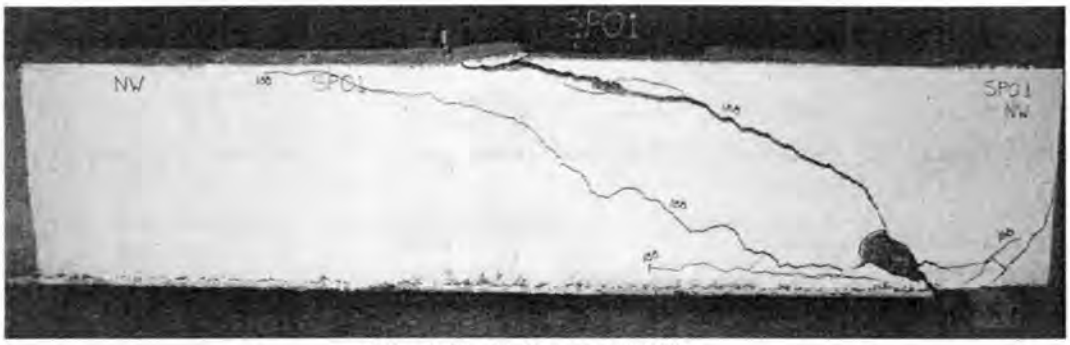

Fig.6.8. Failure of SP01

The variation of longitudinal strains in the tension face plate strain gauge locations in Fig.6.5d with shear load is shown in Fig.6.9.

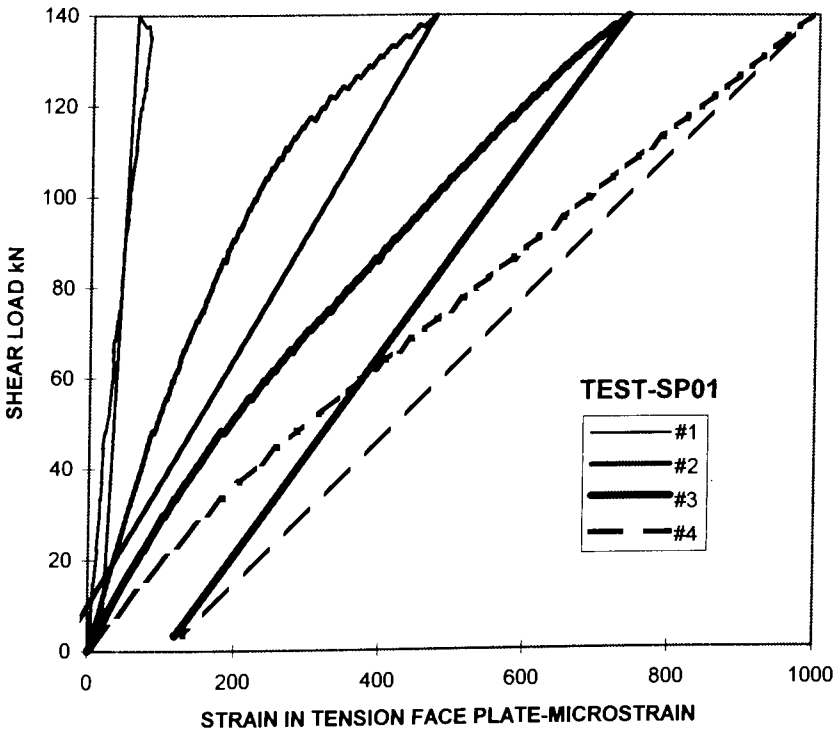

Fig.6.9. Longitudinal strains recorded in the plate (SP01)

The debonding of the plate can be observed clearly from Fig.6.9 by the rapid simultaneous reduction in all the strain gauge locations. Furthermore, the plate did not yield as the maximum recorded strain was about 1000 microstrains. The relationship between the deflection of beam at the load point and shear load is depicted by Fig.6.10, and the shear peeling is marked by the rapid drop in shear load to zero.

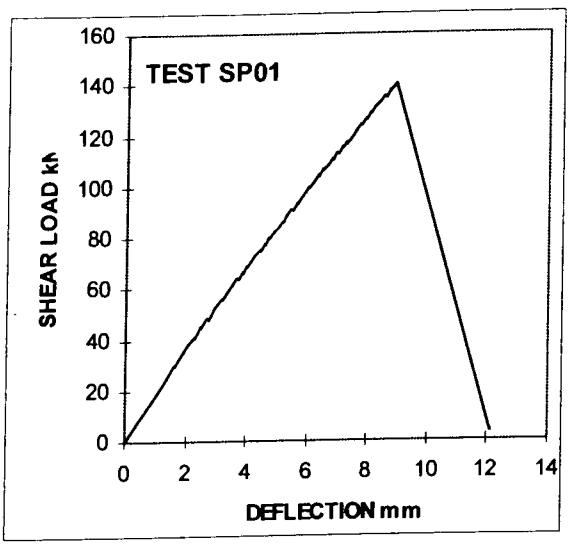

Fig.6.10. Deflection under load point (SP01)

6.6.3 Test SP21

The shear span for test SP21 in Fig.6.1b had no internal shear reinforcement but had side plates of cross section 130 mm deep and 10 mm thick which was terminated exactly over the supports. The plate top was 215 mm from the topmost concrete fibre which caused the side plates to be entirely under tension as confirmed in the test results.

At a shear load of 60 kN (P=80 kN), a vertical crack over the support and along the plate edge appeared as shown in Fig.6.11a; no other crack was visible till the shear load was increased to 155.6 kN (P=209 kN) at which a sudden diagonal shear crack formed that cut across the side plate and extended along the top edge of side plates to the load point, as shown in Fig.6.11b. The shear failure of the beam and shear peeling of both side plates occurred simultaneously. The plates were pushed down to the support and the beam top was fractured into pieces.

(a) Crack at plate end at P= 80 kN

(b)Failure of SP21

Fig.6.11. SP21:Crack pattern

The applied load and, hence the plate strains dropped to zero at shear failure, as can be seen from Figs.6.12a and 6.12b, which show the variation of strain with shear load for both the north and south side plates. The maximum longitudinal strain recorded at the instance of debonding is in the order of 800 to 900 microstrains which is well below the yield strain of the plate. The variation of the deflection beneath the load point with shear load is shown in Fig.6.13.

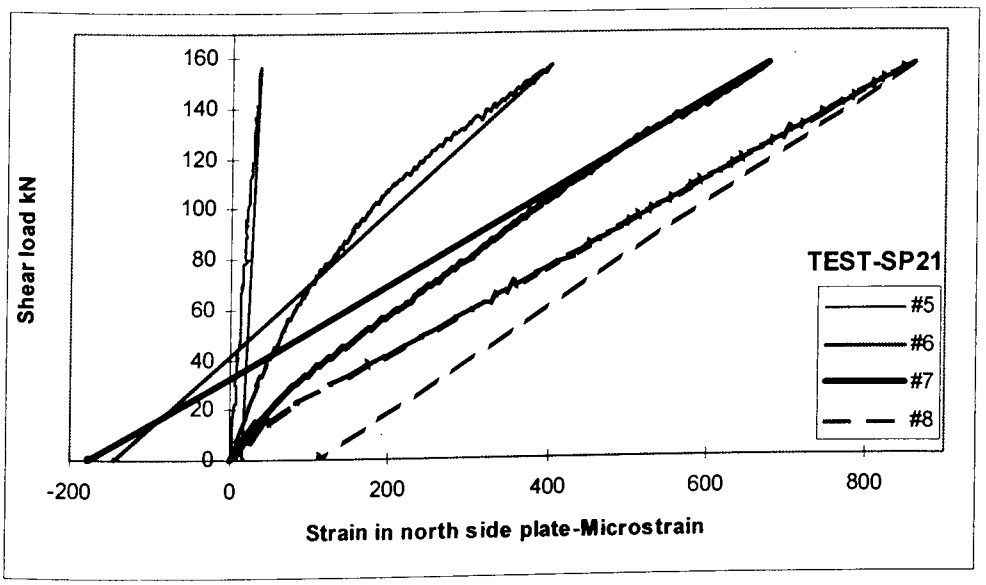

(a)Strains in north side plate

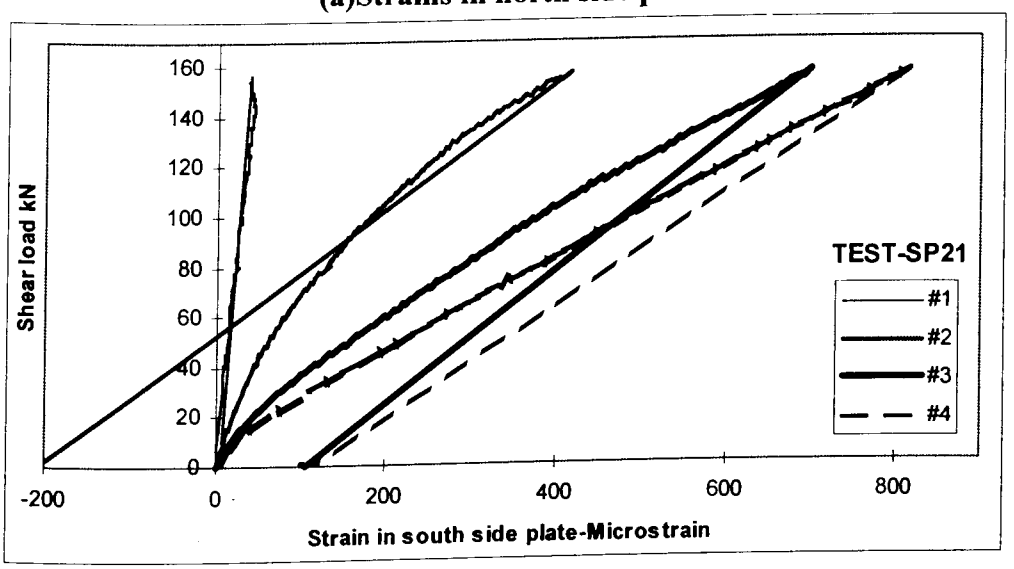

(b) Strains in south side plate

Fig.6.12. Longitudinal strains in the side plates (SP21)

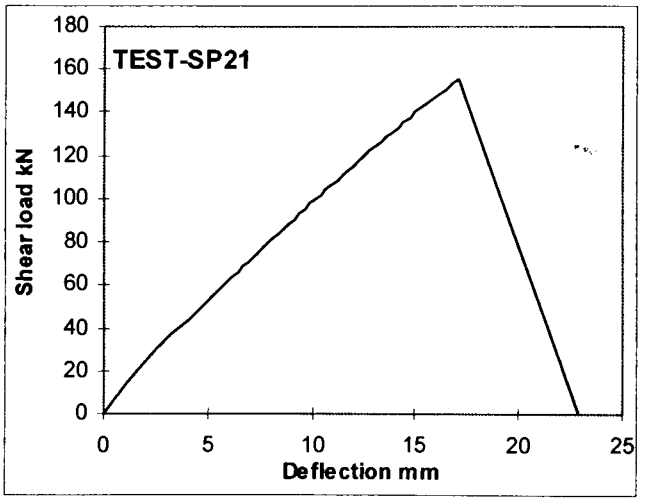

Fig.6.13. Deflection under load point (SP21)

6.6.4 Test SP22

Shear span SP22 in Fig.6.1b was the same as SP21 except for the provision of nominal shear reinforcement (6 mm diameter stirrups at 185 mm spacing). As SP21 was tested to failure prior to testing SP22, the beam was already heavily damaged and, hence, the shear span of the beam was altered to 3.5m; therefore, the shear load in the span SP22 was 67.6% of the applied load.

Cracks were not observed until the applied shear load V was 161.9 kN (P=239 kN), when a long debonding crack formed along the top edge of both side plates. This immediately led to the simultaneous shear peeling of both side plates by the formation of a number of diagonal cracks at regular intervals originating from the horizontal peeling crack as shown in Fig.6.14. Unlike SP21 where the load immediately reduced to zero after failure, in this case the shear load dropped from 161.5 kN to about 100 kN as can be seen from Figs.6.15a and 6.15b which depict the variation of longitudinal strains in the side plates. The maximum strain recorded at the instance of shear peeling was 895 microstrains in the north side plate and 857 microstrains in the south side plate. The shear load-deflection variation is shown in Fig.6.16.

Fig.6.14 SP-22 : Formation of debonding crack and shear peeling

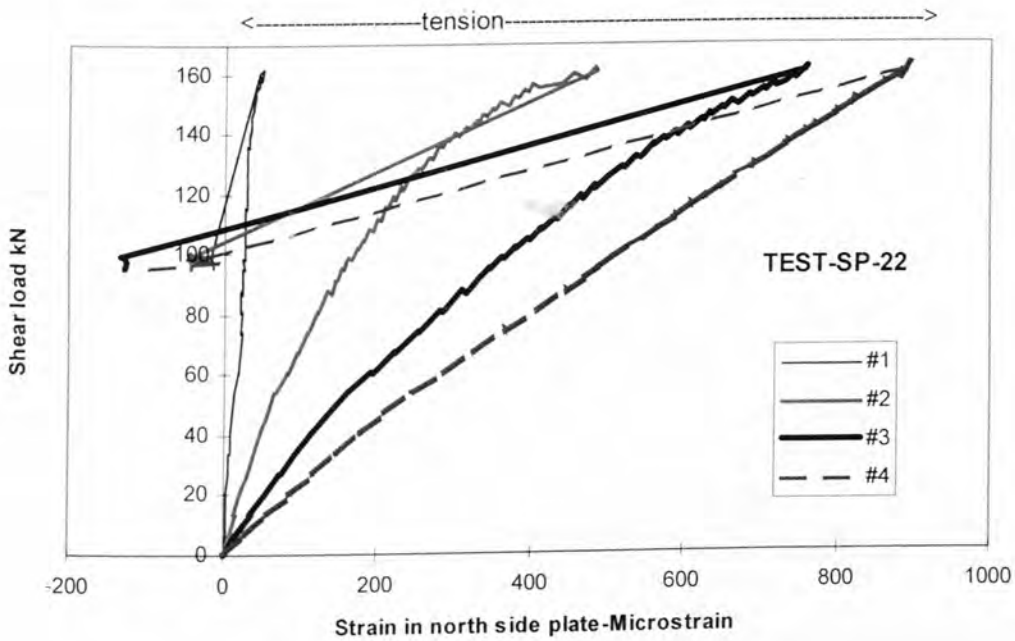

(a) Strains in north side plate

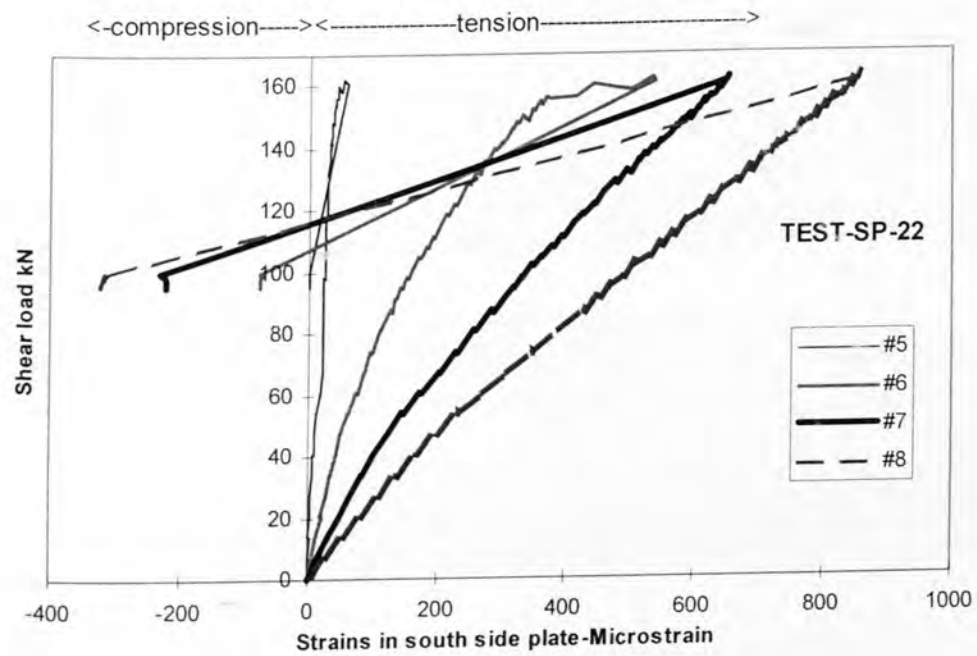

(b) Strains in south side plate

Fig.6.15. Longitudinal strains in the side plates (SP22)

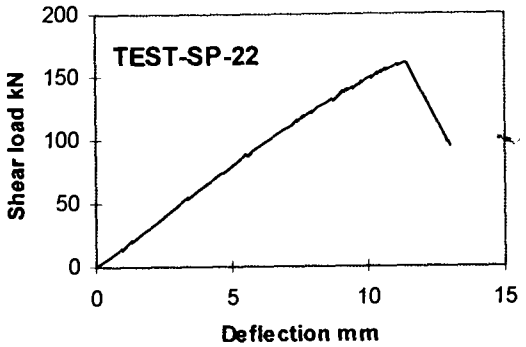

Fig.6.16. Deflection under load point (SP22)

6.6.5 Test SP31

The shear span for test SP31 in Fig.6.1c is same as SP21 in Fig.6.1b but in this case the top edge of the side plate was 120 mm from the topmost fibre of concrete, so that the plate was partially in compression and partially in tension.

The first hairline flexural crack occurred near load point at a shear load of 22.3 kN (P=30 kN); thereafter, several more flexural cracks appeared on either side of the load point and grew in size as can be seen from Fig.6.17a. This process continued and most of the cracks touched the bottom edge of the side plates at an applied load of 80 kN. At a shear load of V=112 kN (P=150 kN), a crack 50 mm high appeared at a distance 350 mm from the support and this was transformed into a diagonal shear crack when shear load was increased to 145 kN (P=195 kN), as shown in Fig.6.17b. Meanwhile, the strain in the south side plate exceeded the yield strain of the plate material (1650 microstrain) when the shear load was 147 kN (P = 198 kN) as shown in Fig.6.18b. A new flexural shear crack then occurred below strain gauges #6 and #14 as shown in Fig.6.17c. The north side plate also recorded a strain greater than the yield strain, when the shear load was 154 kN as shown in Fig.6.18a.

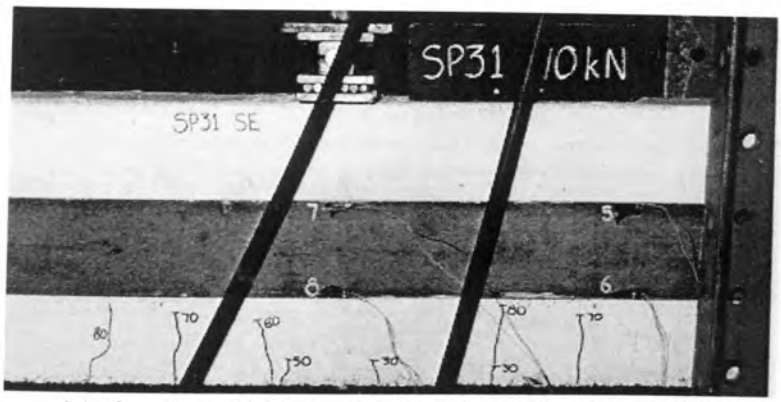

(a) Crack pattern around load point at P=110 kN

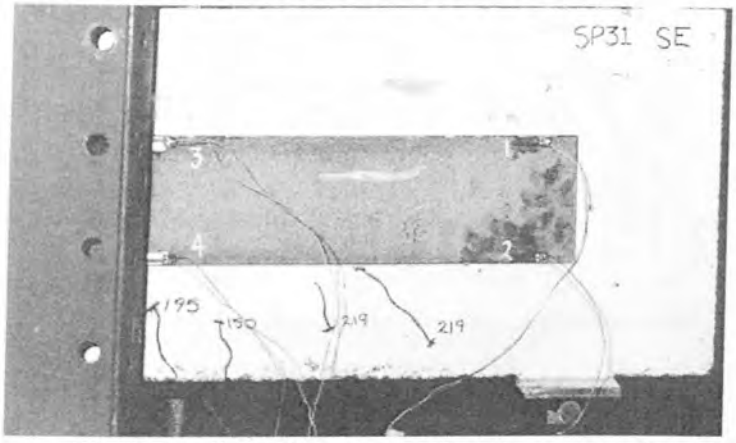

(b) Formation of shear cracks near support

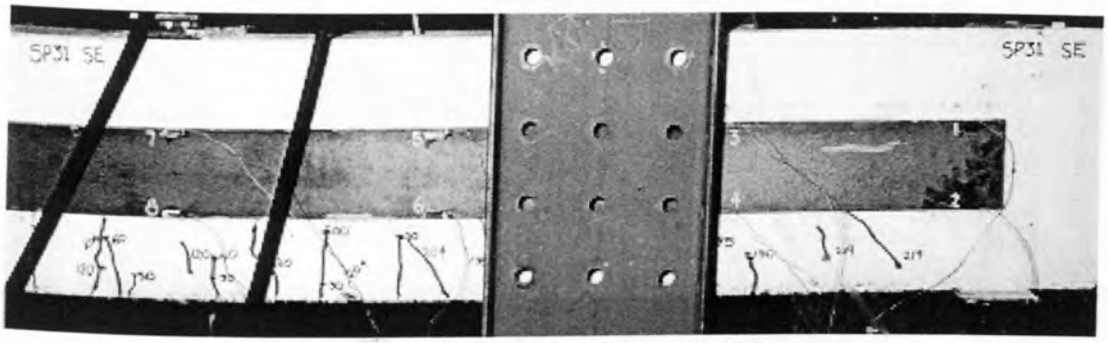

(c) Crack pattern at P=219 kN

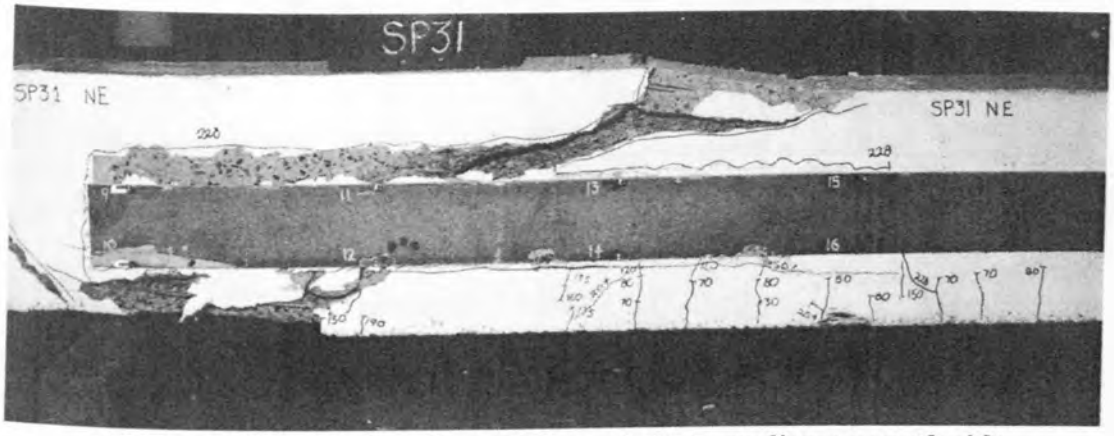

(d) Formation of debonding cracks and shear peeling on north side

Fig.6.17. SP-31 : Crack pattern

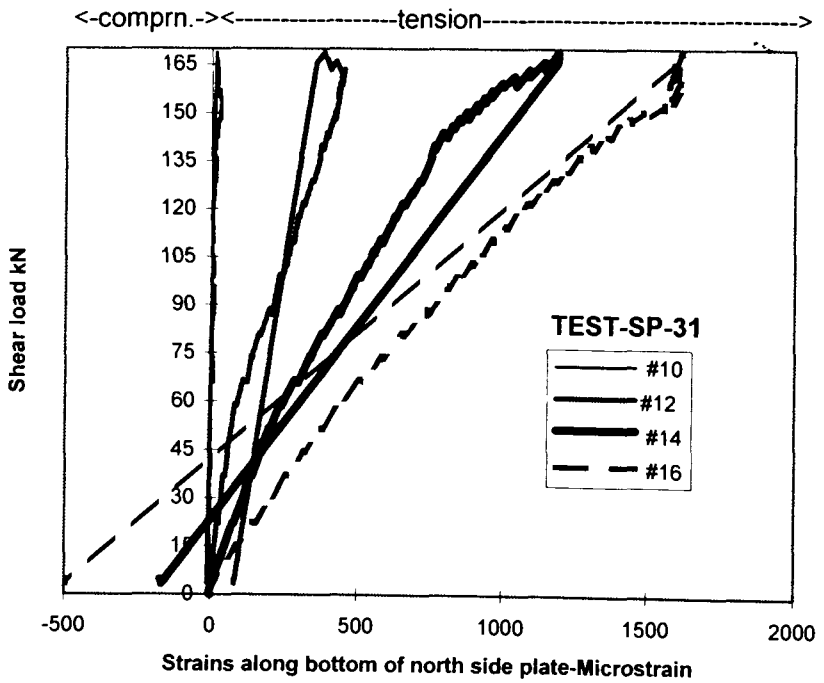

Fig.6.18(a). North side-bottom

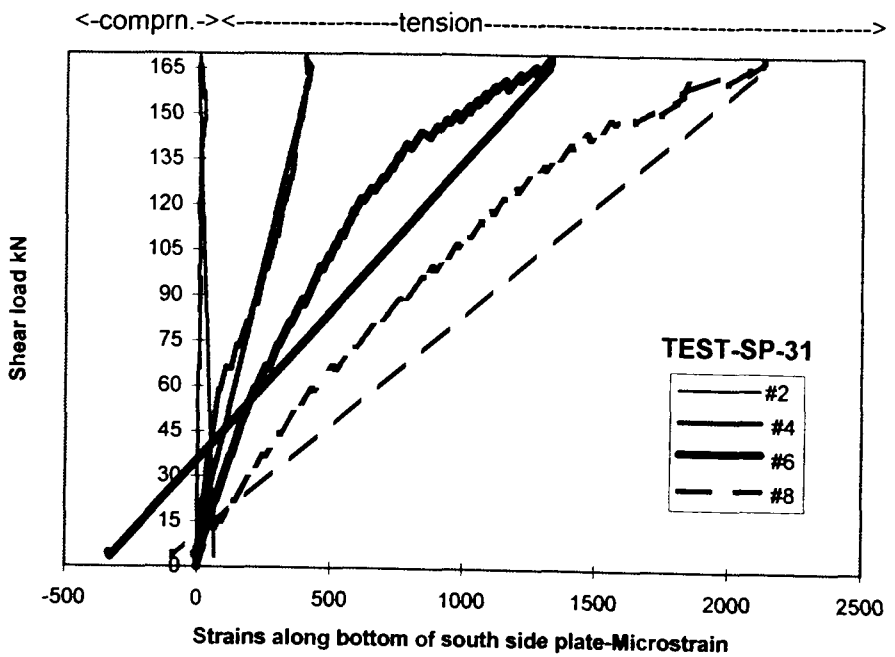

Fig.6.18(b). South side-bottom

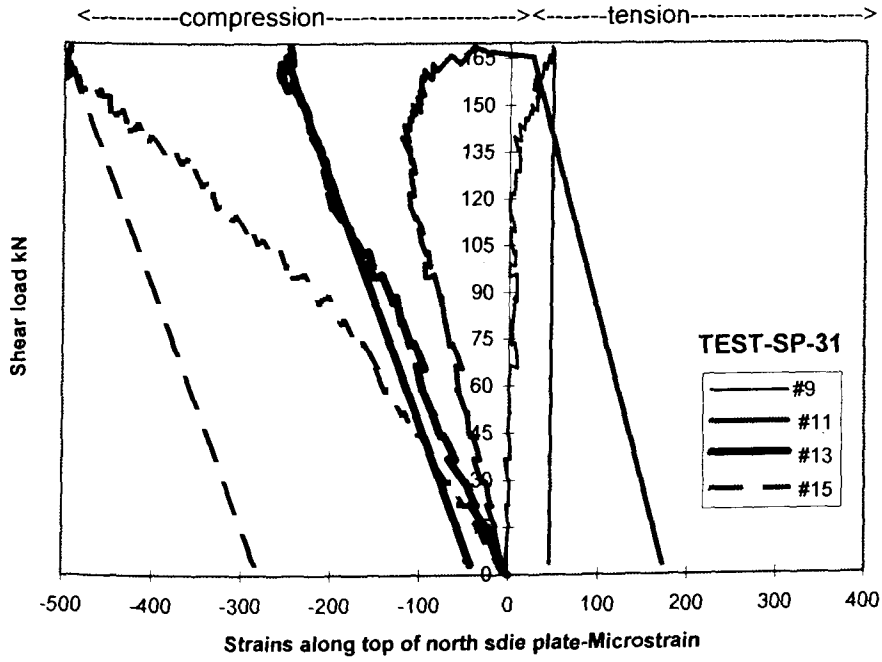

Fig.6.18(c). North side-top

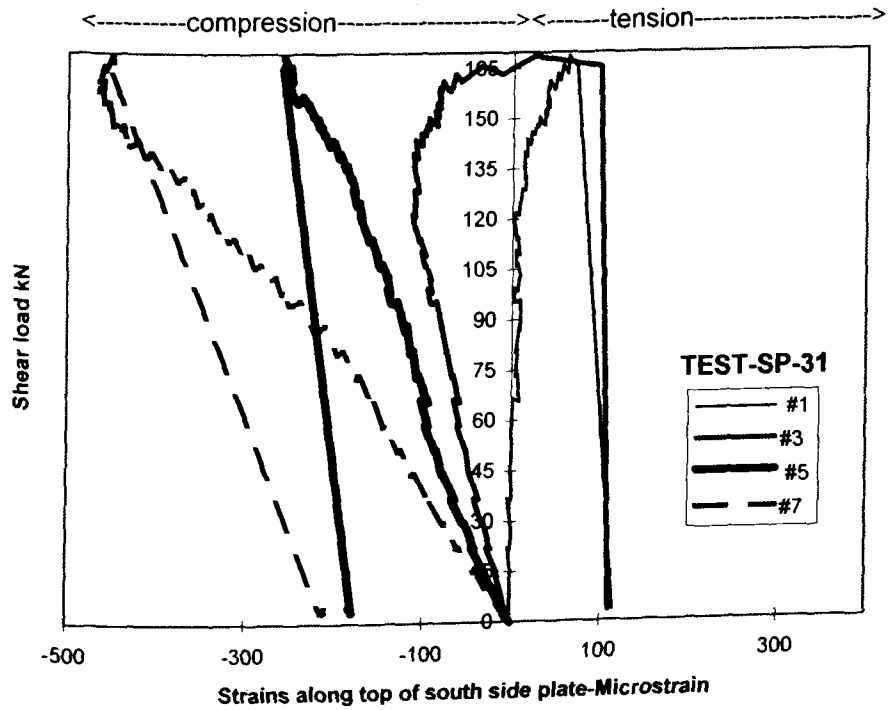

Fig.6.18(d). South side -top

Fig.6.18. Longitudinal strains in the plates-SP31

As the shear load was increased, the critical diagonal crack extended towards the side plate and at V= 168.8 kN (P=226.7 kN) it extended towards the load platen and

caused the shear failure of the concrete beam. The side plates also peeled instantaneously by the formation of long, horizontal peeling cracks, as depicted in Fig.6.17d. Figures 6.18c and 6.18d show the strain variation along the top of the side plates which shows the plate top to be under compression and the maximum recorded strains before peeling are smaller than the yield strain of the steel plate. Figure 6.19 illustrates the variation of deflection with shear load and it also reveals the abrupt nature of failure as the shear load dropped down to zero.

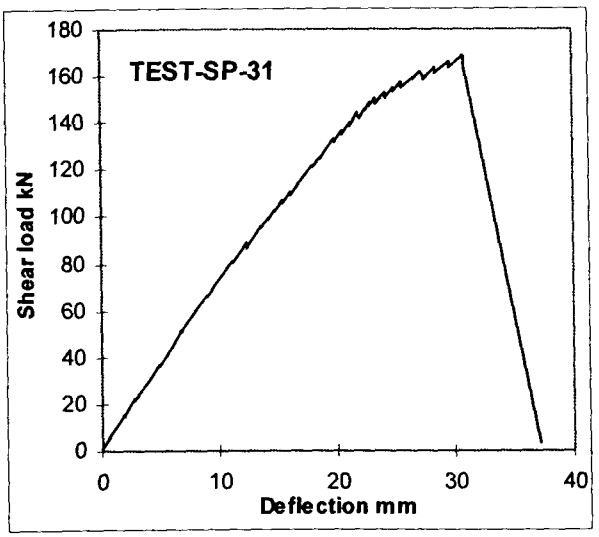

Fig.6.19. Deflection Vs Shear load (SP31)

6.6.6 Test SP32

Shear span SP32 in Fig.6.1c is the same as SP31 except for the inclusion of nominal shear stirrups (6 mm diameter at 185 mm c/c). Several flexural cracks on either side of the load points, where the applied bending moment is at a maximum, started appearing at a shear load V=39 kN (P=70 kN). At a shear load of V=82 kN (P=110 kN), they extended towards the bottom edge of the side plates as shown in Fig.6.20a. Further crack growth could not be observed due to the presence of the side plates; the maximum recorded strains at the bottom which is in tension was just above the yield strain of the steel plate (1650 microstrain) when the shear load was 138 kN (P=185 kN) as shown in Figs.6.21a and 6.21b. Figures 6.21c and 6.21d show the variation of

strains along the top fibres of the steel plate which were under compression with applied shear load.

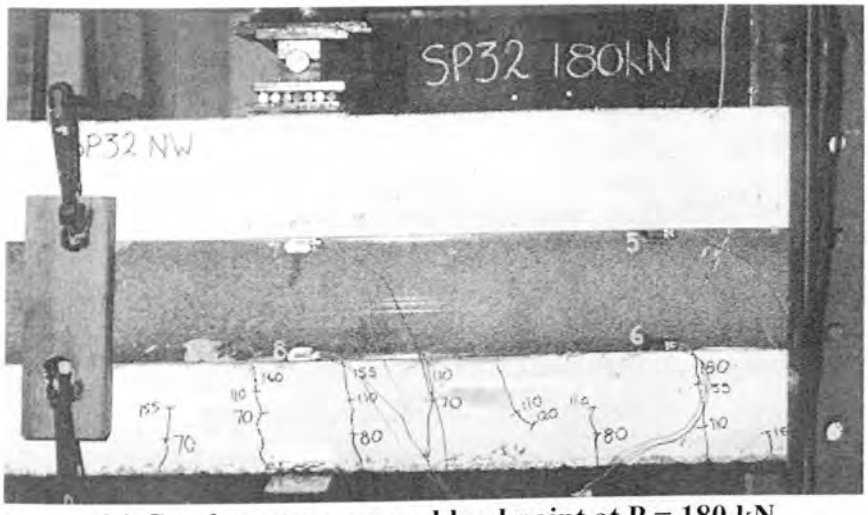

(a) Crack pattern around load point at P = 180 kN

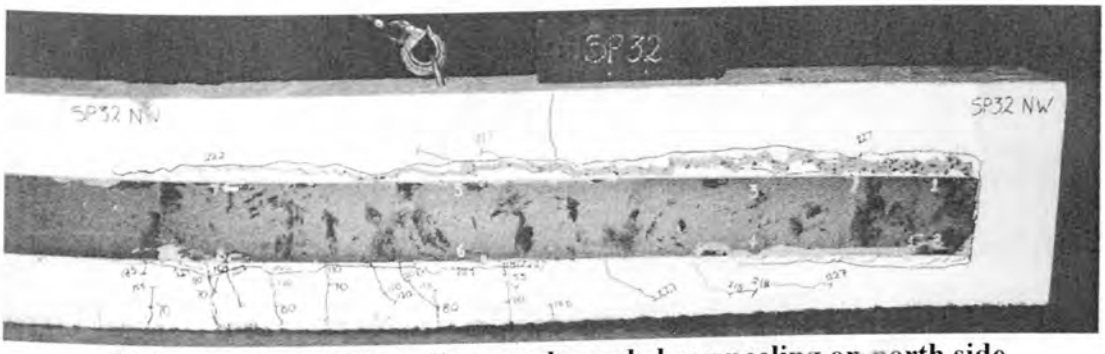

(b) Formation of debonding cracks and shear peeling on north side

Fig.6.20 SP-32 : Crack pattern

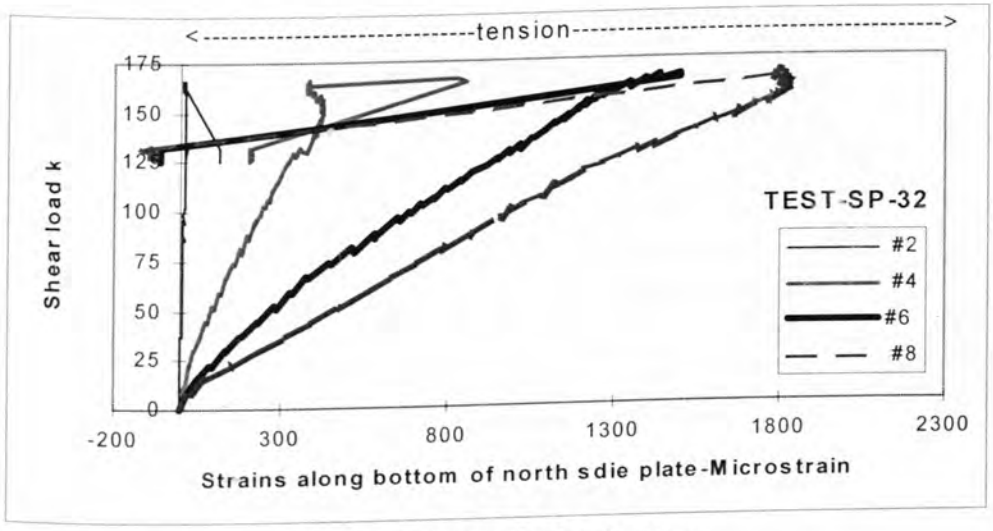

Fig.6.21(a). North side-bottom

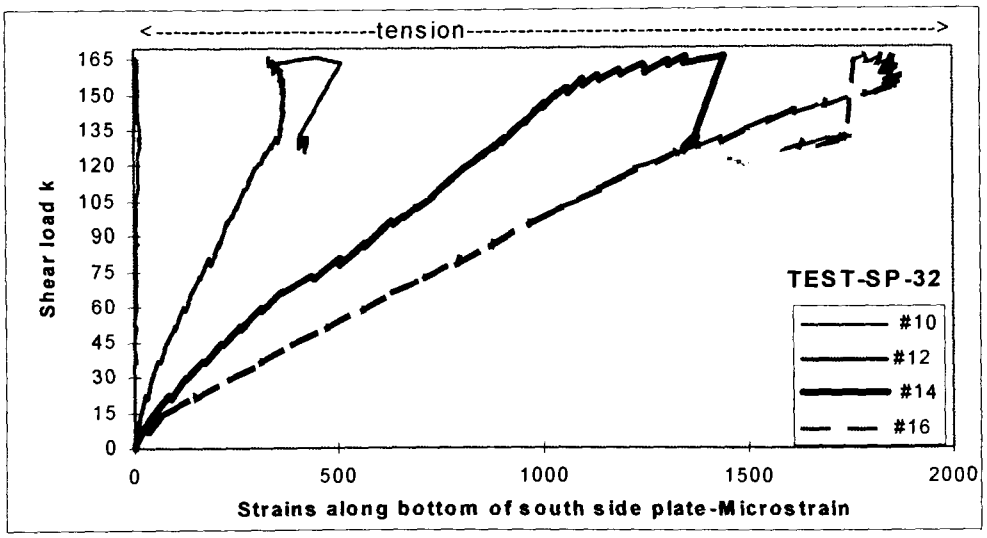

Fig.6.21(b). South side-bottom

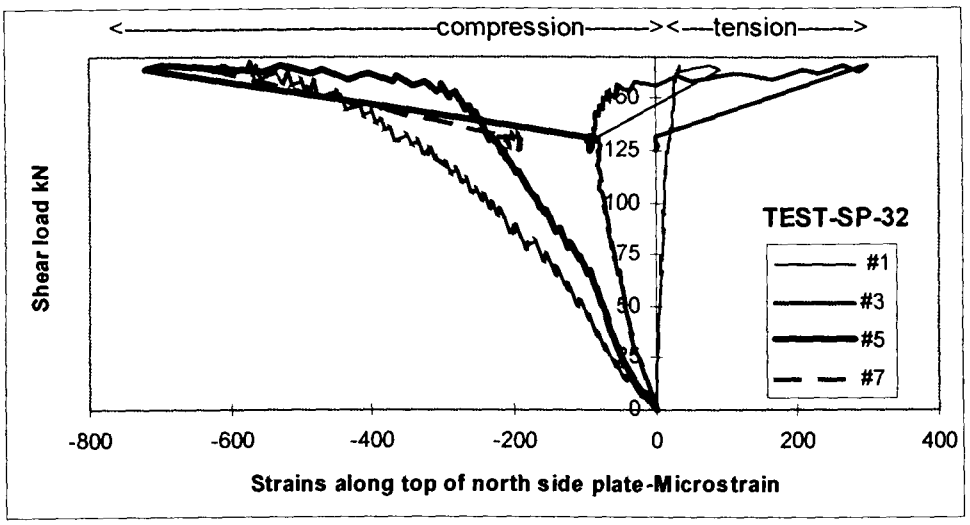

Fig.6.21(c). North side-top

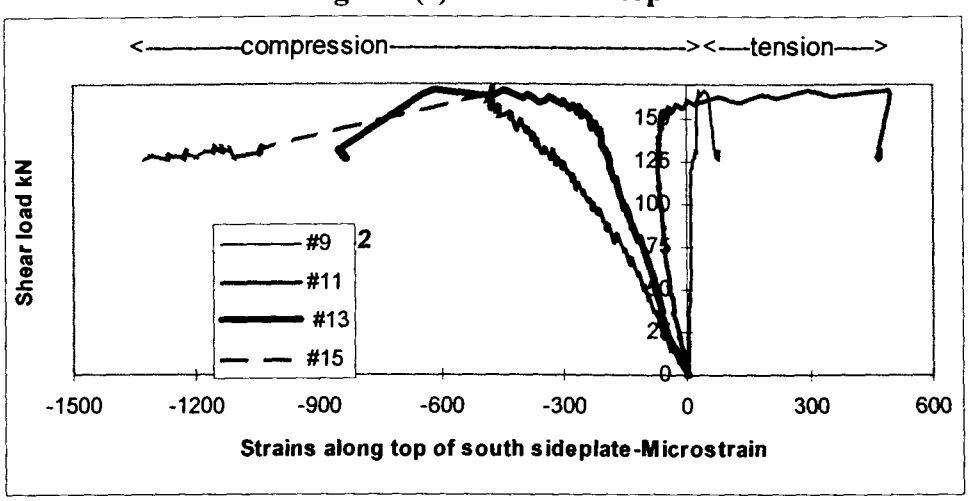

Fig.6.21(d). South side -top

Fig.6.21. Longitudinal strains in the plates-SP32

When the shear load was increased to 160 kN (P=215 kN), an inclined crack appeared below strain gauges #4, as shown in Fig.6.20(b), and #12. This eventually led to the peeling of the side plates when this shear load was 165.9 kN (P=222.8 kN). The peeling occurred by the formation of long horizontal cracks encompassing the plates. A flexural shear crack also formed in between gauges #4 and #6 on the north side in Fig.6.20b and #12 and #14 on the south side. Meanwhile, the two flexural shear cracks on either side of the load point also extended and touched the extreme top fibres of the concrete beam. Therefore, the peeling of side plates in this case was preceded by the complex crack pattern involving flexural shear cracks; strains recorded in the plates were also greater than the yield strain of the plate material. The shear load at failure (166.4 kN) was almost 100% more than the shear capcity of the unplated reinforced concrete beam without stirrups (shear strength as determined from test SPREF (85.6 kN)). Figure 6.22 illustrates the variation of deflection with shear load; it shows the shear load dropped from 166 kN to about 120 kN at peeling of the side plates and it did not reduce rapidly to zero as in SP31.

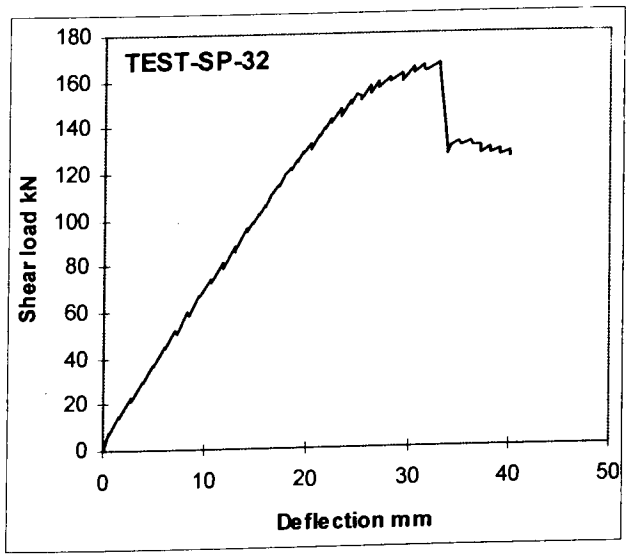

Fig.6.22. Deflection Vs Shear load (SP32)

6.6.7 Test SP41

Shear span SP41 in Fig.6.1d did not have shear stirrups and the top of the side plate was just 25 mm from the extreme top fibre of the concrete so that the plates would be totally under compression.

The first flexural crack appeared beneath the load point when the shear load was 30kN (P=40kN), as shown in Fig.6.23a. Many more flexural cracks appeared when the load was increased and they grew in size and touched the bottom edge of the plate when the shear load was 67 kN (P=90 kN) as can be seen from Fig.6.23b. When the shear load reached a value of 82 kN (P=110 kN), an inclined crack occurred in the middle of the web as shown in Fig.6.23c. It propagated towards the support and stopped at distance of 300 mm from the support when the applied shear load was 93 kN(P=125 kN). This caused the shear load to drop to 89.4 kN (P=120 kN). On reloading the beam, this diagonal shear crack propagated along the bottom edge of the side plate when the shear load was 97 kN (P=130 kN) and the shear load again dropped to 83.4 kN (P=112 kN). On further reloading, the plate peeled off due to the formation of a long horizontal crack along the top edge also; the diagonal shear failure of the shear span also occurred at this stage as the crack cut across the side plates and extended towards the load point as shown in Fig.6.23d. Figures 6.24a and 6.24b show the variation of strains with shear load; the plates did not yield as the maximum recorded strains are in the order of 900 to 1200 microstrains. Figure 6.25 shows the relationship between deflection and shear load and it shows the shear load dropped to 20 kN after peeling.

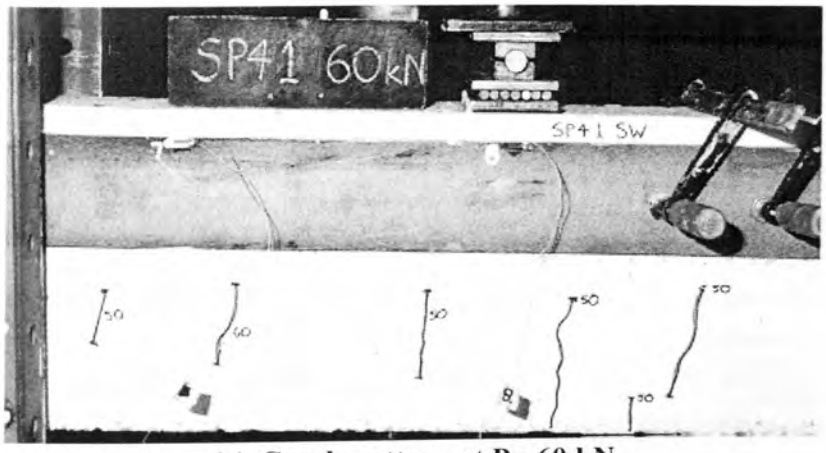

(a) Crack pattern at P= 60 kN

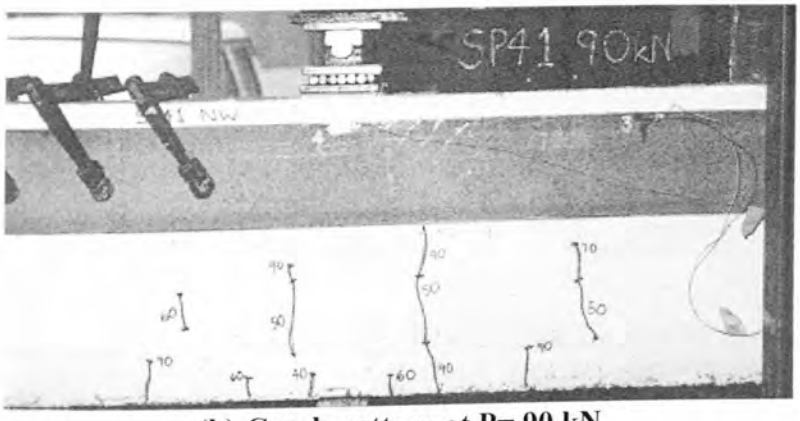

(b) Crack pattern at P= 90 kN

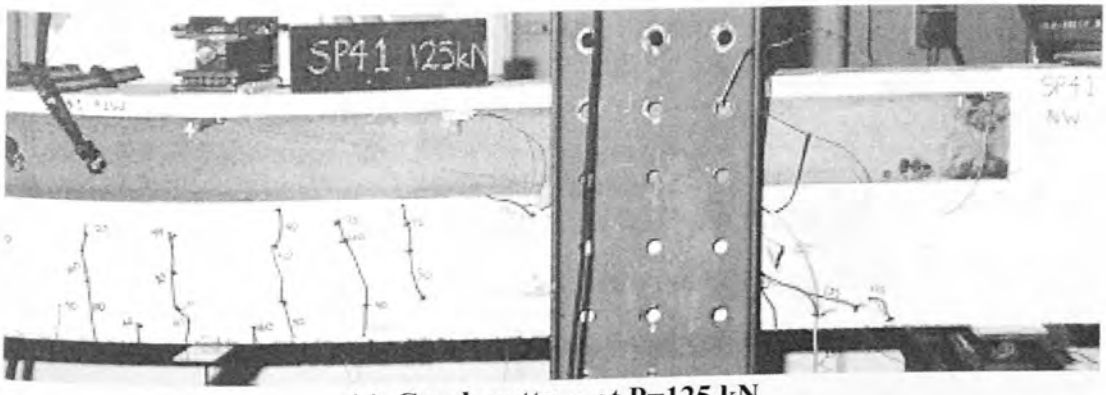

(c) Crack pattern at P=125 kN

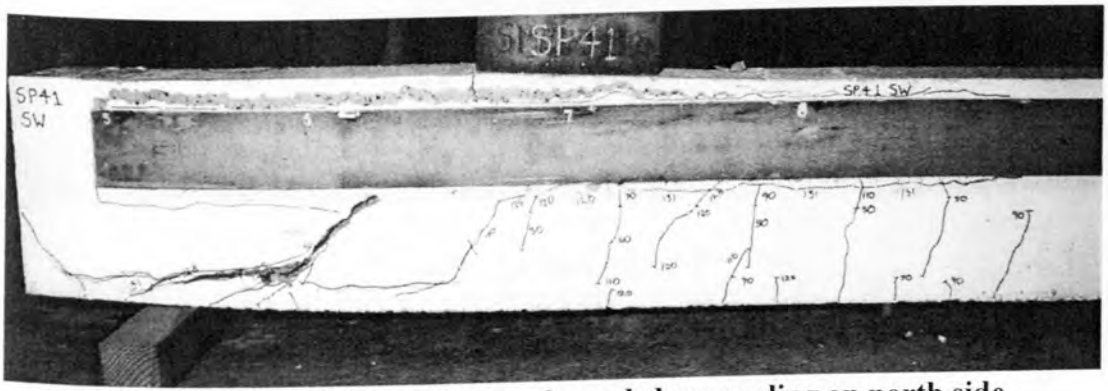

(d) Formation of debonding cracks and shear peeling on north side

Fig.6.23. SP-41 : Crack pattern

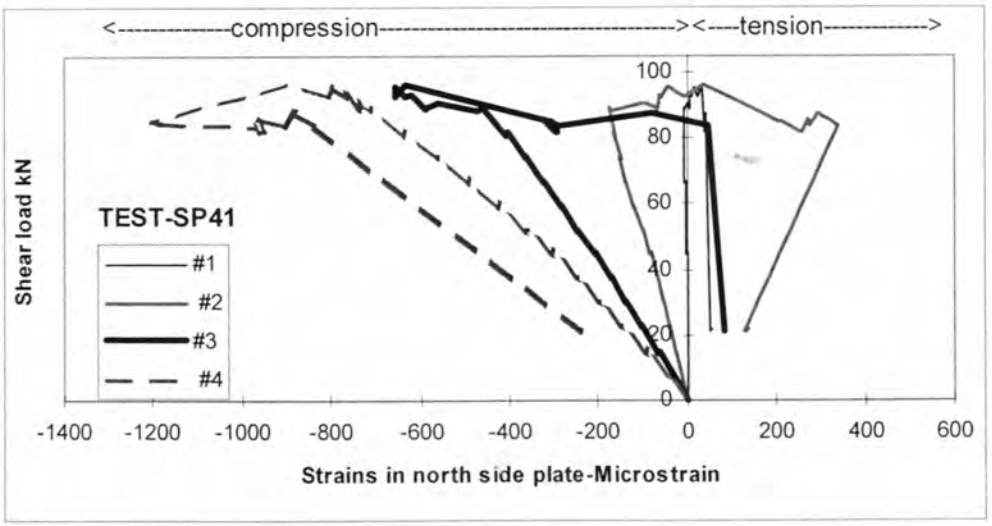

(a) North side plate

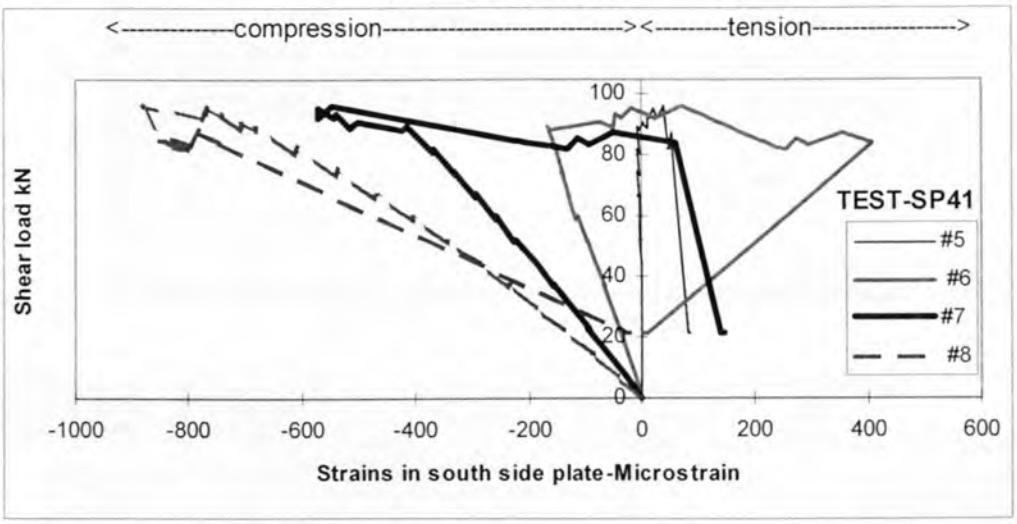

(b) South side plate

Fig.6.24. Longitudinal strains in the plates-SP41

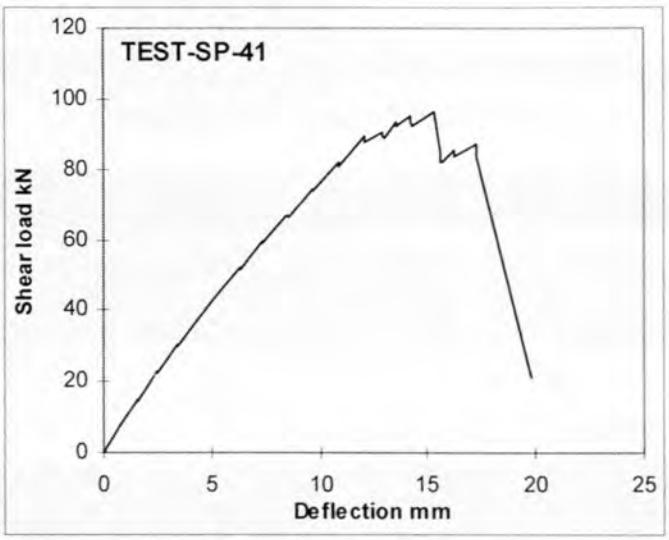

Fig.6.25. Deflection Vs Shear load (SP41)

6.6.8 Test SP42

Shear span SP42 in Fig.6.1d is the same as SP41 but includes nominal shear stirrups. The first flexural crack appeared near the load point when the shear load was 22.5 kN (P=30 kN). More hairline flexural cracks appeared subsequently and when the shear load V was 60 kN (P=90 kN), most of these cracks extended to the bottom edge of the plates and new flexural shear cracks also appeared as shown in Fig.6.26.

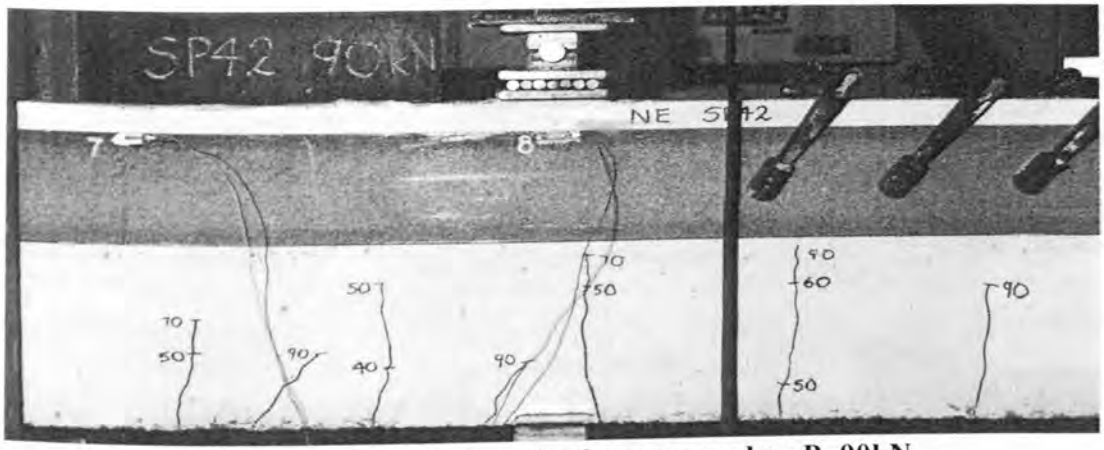

Fig.6.26. Crack pattern in shear span when P=90kN

A typical inclined shear crack at a distance equal to the depth of the beam (370 mm) from the support occurred when the shear load V was 82 kN (P=110 kN), as shwn in Fig.6.27. When the shear load V was increased to 90 kN (P=120 kN), the diagonal crack extended towards the plate bottom and some of the flexural and adjacent flexural shear cracks combined together as shown in Fig.6.28.

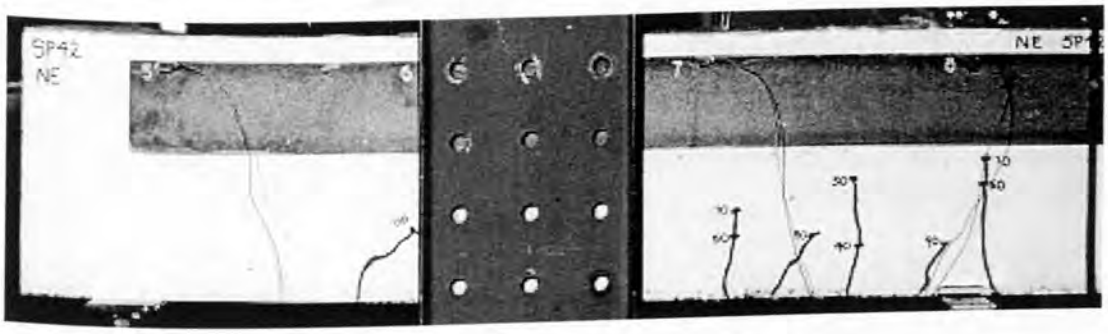

Fig.6.27. Crack pattern when P = 110kN

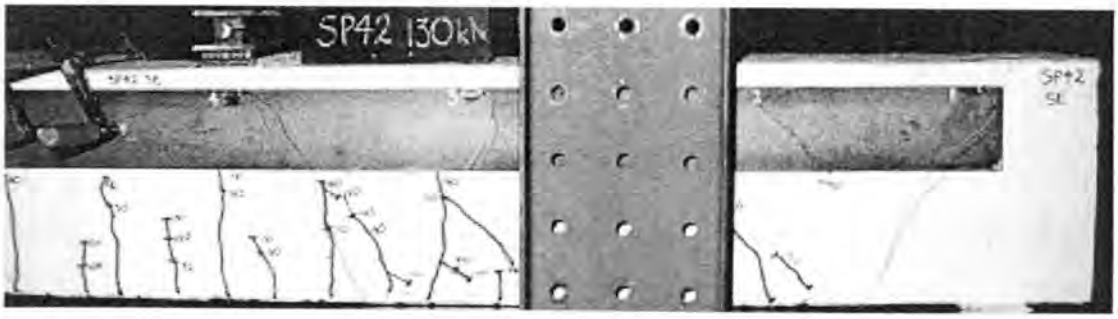

Fig.6.28. Crack pattern when P = 130 kN

When the shear load V was 108 kN (P=145 kN), another shear crack occurred at about 150 mm from the support, as shown in Fig.6.29. On further application of load, the maximum strains recorded in both the side plates were just above the yield strain of the plate material (1650 microstrain) as can be seen in Figs.6.34 and 6.35. When the shear load V was 117 kN (P=157 kN), a horizontal crack was observed below the bottom edge of the north side plate between strain gauges #6 and #7 as shown in Fig.6.28. As a precautionary measure, the load was completely removed when the shear load was 132.5 kN (P=177.9 kN) as span SP41 was yet to be tested and also because the concrete under the load point started crushing, as shown in Fig.6.30. Span SP42 was re-tested after completion of test SP41 but the effective span of the beam was altered to 3.7 m so that the shear load in the span SP42 was 67.6% of the applied load. On reloading, the shear span could sustain a maximum shear load of 134.6kN (P=199.2 kN) and thereafter the load started to fall gradually. The test was terminated when the shear load V was 115 kN (P=170 kN) at which the north side plate peeled completely due to the formation of long horizontal cracks around the plate, as shown in Fig.6.31. As the concrete under load point crushed completely, the north side plate also buckled locally before the occurrence of peeling as shown in Fig.6.32. The south side plate also peeled locally due to concrete crushing and buckling around load point as shown in Fig.6.33.

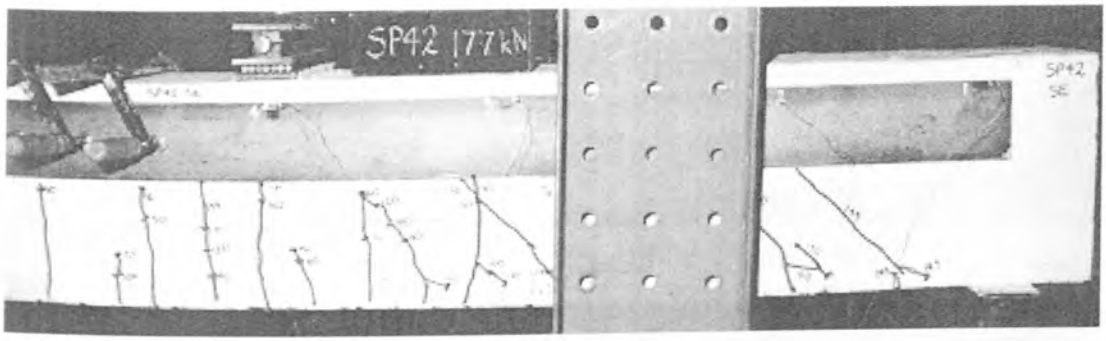

Fig.6.29. Crack pattern when P = 177kN

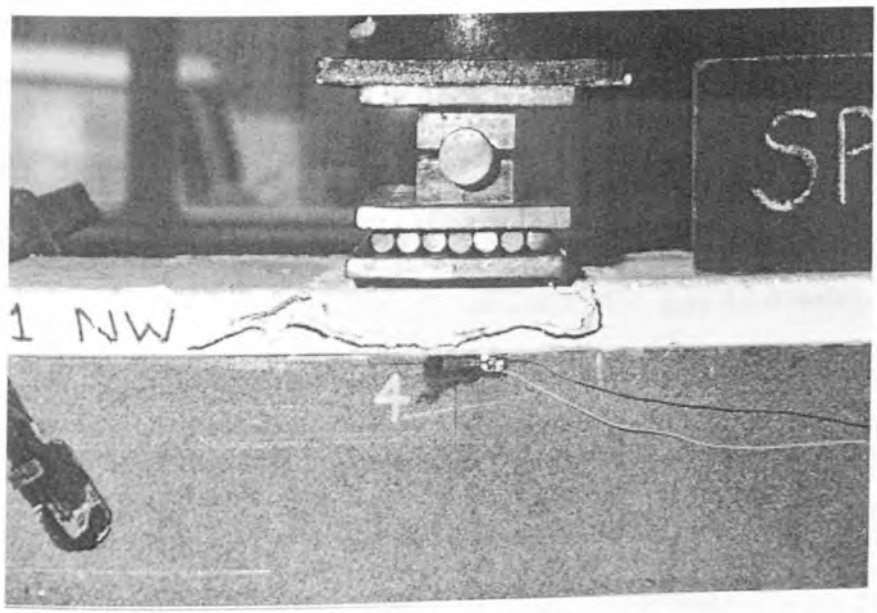

Fig.6.30. Close view of concrete crushing below load plate

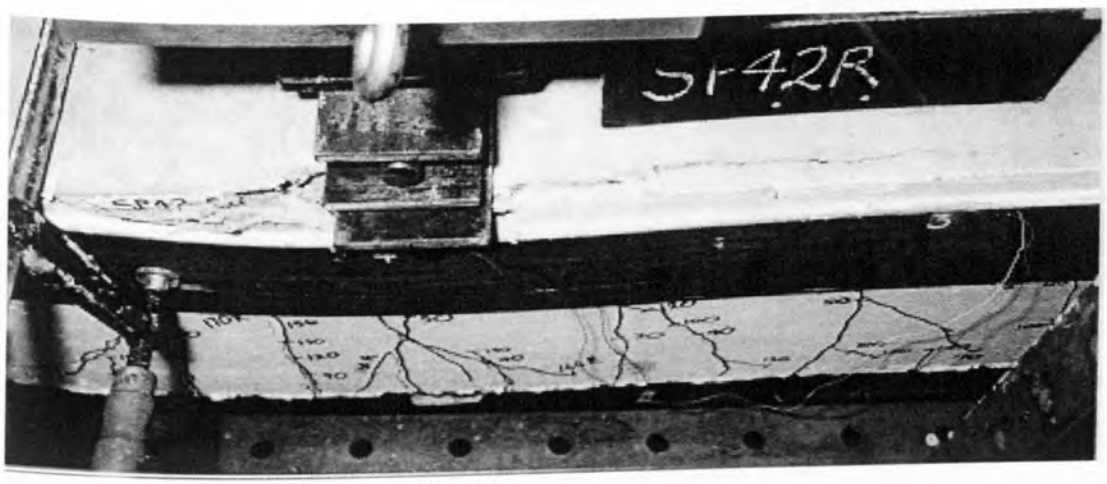

Fig.6.31. Buckling and peeling of northern side plate(SP42)

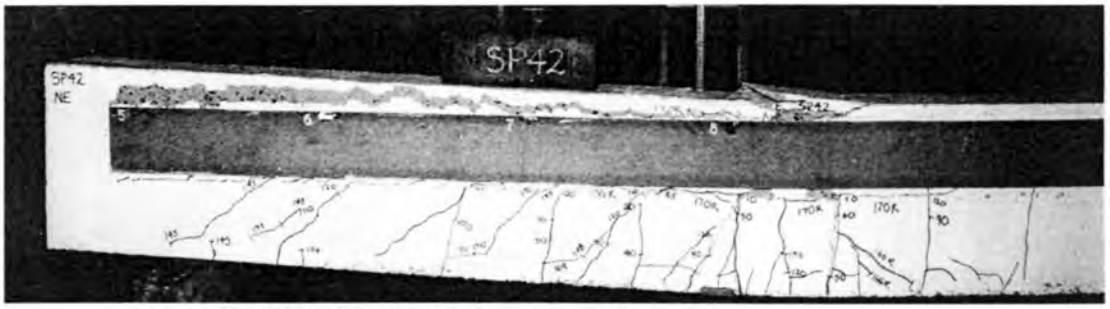

Fig.6.32. Final failure pattern in northern side plate

Fig.6.33. Failure of southern side plate(SP42)

Figures 6.34 and 6.35 illustrate the relationship between the longitudinal strains in the side plates and shear load. It show that the side plates recorded large strains as the maximum strain recorded was about 2700 microstrains in the north side plate and 4000 microstrains in the south side plate. Figure 6.36 shows the variation of deflection and shear load which shows the smooth failure of the span SP42.

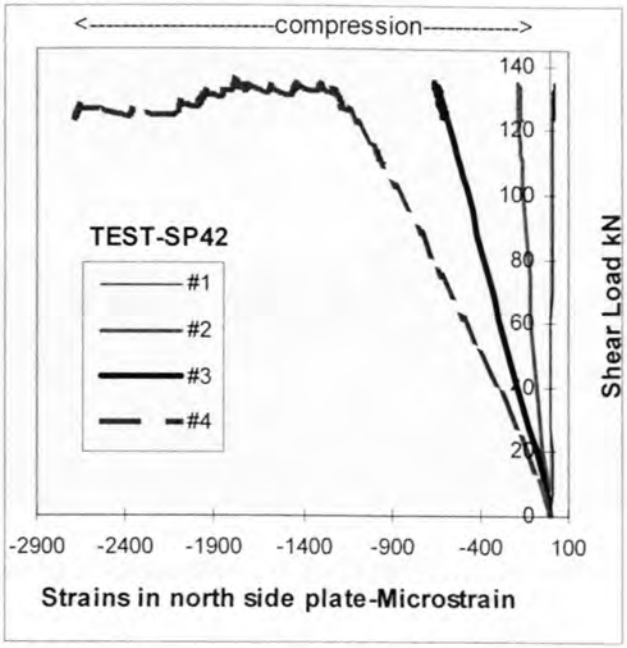

Fig.6.34. Longitudinal strains in North side plates-SP42

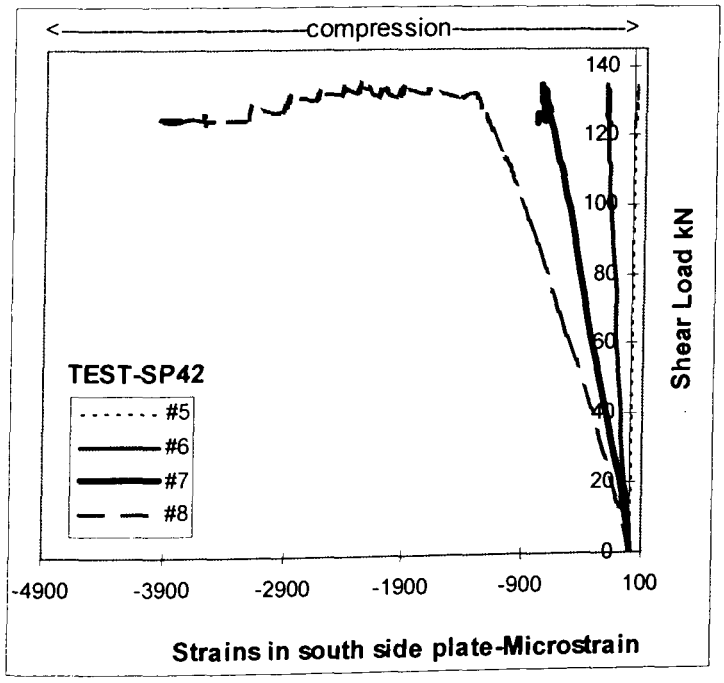

Fig.6.35. Longitudinal strains in South side plates-SP42

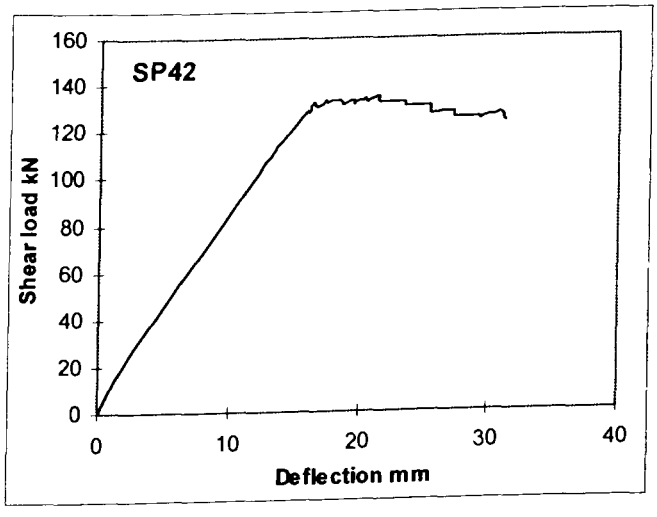

Fig.6.36. Deflection Vs Shear load (SP42)

6.7 Discussion of test results

Table-6.4 summarises the experimental results of all the shear spans tested. The shear strength of the unplated and non-shear reinforced beam (SPREF) was 85.6 kN. This is the shear strength of the beam when the location of the critical diagonal shear crack is not restricted. However, plating the tension face of the non-shear reinforced beam

as in SP01 forced the critical daiagonal crack to occur in the vicinity of the plate end which was 50 mm away from the support. This increased the shear strength to 140 kN, which is 63.5% higher than SPREF. The shear peeling strength of the beams with side plates that were glued in predominantly tensile region (SP21, SP22, SP31, and SP32) ranged from 157 kN to 168.8 kN. This represents an increase in shear strength of 83.4% to 97.2% over SPREF and an increase in shear peeling strength of 12% to 20.5% over the tension face plated beam (SP01).

TABLE-6.4: EXPERIMENTAL RESULTS

Specimen	Nominal Stir-rups	External plate	L_{sp} (mm)	L_{end} (mm)	d_{top} (mm)	V_{max} (kN)	$\varepsilon_{p.max}$	failure mode
SPREF	No	No plates	-	-	-	85.6	-	Shear failure of concrete beam
SP01	No	tension face plate 200x10 mm	4200	50	370	140	990	Simultaneous shear failure of concrete and peeling of plate
SP21	No	side plates 130x10mm	4700	0	215	157	816(N) 859(S)	Simultaneous shear failure of concrete and peeling of side plates
SP22	Yes	side plates 130x10mm	4700	0	215	161.9	895(N) 857(S)	Shear peeling of side plates
SP31	No	side plates 130x10mm	4700	0	120	168.8	2131(N) 1616(S)	Simultaneous shear failure of concrete and peeling of side plates
SP32	Yes	side plates 130x10mm	4700	0	120	165.9	1798(N) 1786(S)	Shear peeling of side plates
SP41	No	side plates 130x10mm	4700	0	25	96.3	-901(N) -881(S)	Simultaneous shear failure of concrete and peeling of side plates
SP42	Yes	side plates 130x10mm	4700	0	25	132.3	- 2071(N) -3251(S)	Crushing of concrete and total peeling of North side plate and local peeling of south side plate

L_{sp} = length of external plate, L_{end}= distance between plate end and nearest support,
d_{top}= distance between plate top and beam top, V_{max}=Maximum shear load sustained by the shear span
$\varepsilon_{p.max}$ = Maximum strain in the side plate at the instance of peeling (microstrains) (positive-tension and negative-compression)

The provision of nominal shear stirrups does not influence the shear peeling strength in the case when the side plates are placed predominantly in the tensile region of the beam. For example, test SP22 (that was provided with a nominal amount of shear stirrups) recorded only a 3% increase in shear peeling strength when compared with SP21 where shear stirrups were not provided and no increase was observed in the case of SP32 over SP31. The position of the plate influences the strains recorded in the side plates at the instance of peeling. While side plates in the shear spans SP31 and SP32 recorded strains above the yield strain of the steel plate, plates in spans SP01, SP21 and SP22 did not yield.

The nominal shear stirrups made a quantitative and qualitative change in the failure mode for the shear spans SP41 and SP42. Shear span SP41 failed by simultaneous shear failure of concrete and shear peeling of side plate at a shear load only slightly higher than the shear strength of SPREF that was not provided with plates. However, shear span SP42 failed smoothly by the crushing of concrete and peeling of plate at a higher shear load of 132.3 kN. The maximum strain recorded in plates in the case of SP42 (3251 microstrain) was higher than the yield strain of the plate material unlike SP41 where the maximum recorded plate strain (901 microstrain) was far less than yield strain.

6.8 Concluding remarks

The following major conclusions can be arrived at from the tests conducted on the shear peeling in beams bonded with steel plates.

1. Specimen SP01, which was identical to the unplated, non-shear reinforced beam (SPREF) except for the presence of a tension face plate, failed and debonded at a shear load of 140 kN. Hence, the presence of the tension face plate has increased the shear strength from 86 kN to 140 kN that is by 63%. Placing the plate on the

sides of the beam in specimen SP21 has further increased the strength to 157 kN which is 83% greater than the unplated beam and 12% greater than the tension face plated beam.

2. By comparing the shear peeling strengths of specimen SP21 with SP22 and SP31 with SP32, it can be seen that the presence of stirrups has virtually no effect on shear peeling when the mean strains in the plate are tensile. However, a comparison of SP41 with SP42 does show that stirrups enhance the shear peeling strength when the strain is compressive.
3. From a comparison of shear peeling strengths of the specimens SP22, SP32 and SP42, it can be seen that the shear peeling resistance depends on the vertical position of the plate.

CHAPTER-7: EXPERIMENTAL INVESTIGATION OF SHEAR PEELING IN RC BEAMS BONDED WITH FRP PLATES TO THE SIDES

CONTENTS

7.1 Introduction

The primary aim of this series of limited number of tests is to compare qualitatively the shear peeling mechanism in reinforced concrete beams glued with FRP plates to their sides with that of conventional steel plated beams. The major parameter varied was the elastic modulus of the external plates used. In this chapter, the specimens, the test set-up and the material properties are described first. Then the observations from each test are described individually. Finally, the implications of the test results are discussed. The analytical results for this test series are presented in Chapter-11.

7.2 Test specimens

A total of five tests were performed in this study. For this purpose, three beams already tested for the flexural peeling of beams bonded with FRP plates to the tension face were reused as the failure plane from the previous study is different from the present study. To avoid the effect of existing shear cracks from the previous study on the shear peeling behaviour of the side plated beams, they were turned upside down and then plated. The details of the basic unplated beam are shown in Fig.7.1.

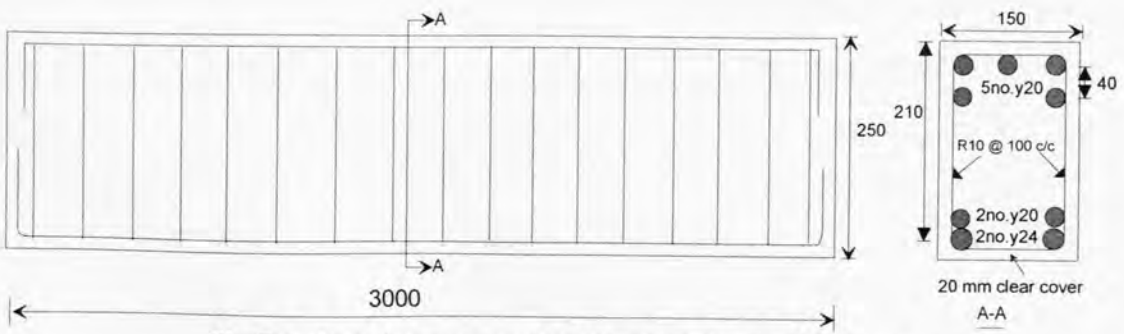

Fig.7.1. Reinforcement details of the basic RC beam

Out of the three beams that were used for this study, one beam was tested without bonding any plates to quantify experimentally the shear strength of the RC beam and this test was denoted as SP-REF as shown in Fig.7.2. The other beams were bonded

with plates to their sides. Whilst one portion of the beam was bonded with FRP plates, the other portion was bonded with a steel plate, as shown in Figs.7.3 and 7.4.

Fig.7.2. Test SP-RF

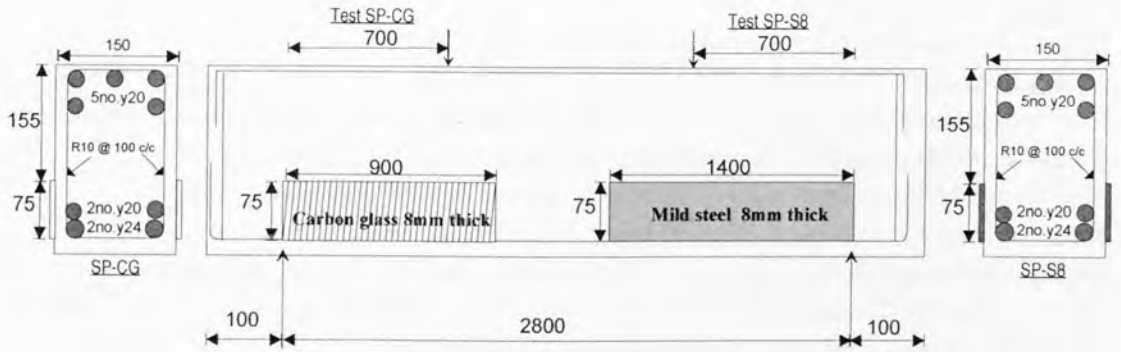

Fig.7.3.Tests SP-CG and SP-S8

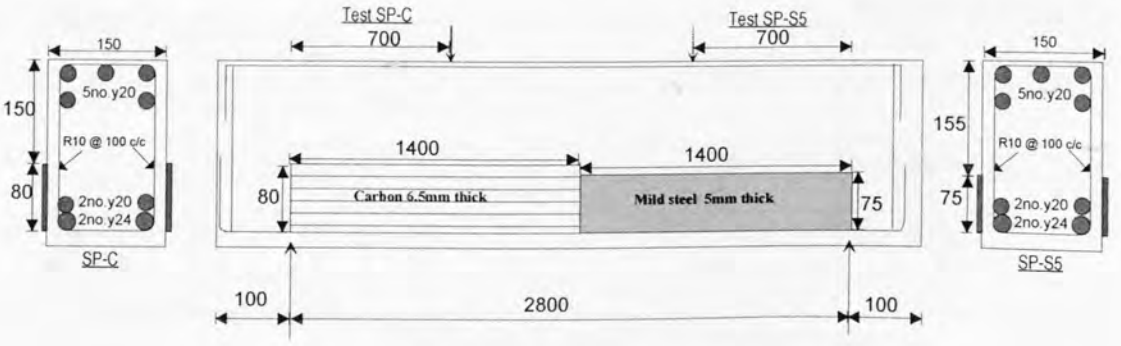

Fig.7.4. Tests SP-C and SP-S5

Two individual shear tests were performed on each of these beams by clamping suitably the longer shear span to preclude any premature debonding of the plates, as

depicted in Fig.7.5. The designation and the geometric properties of all the tested beams are summarised in Table-7.1.

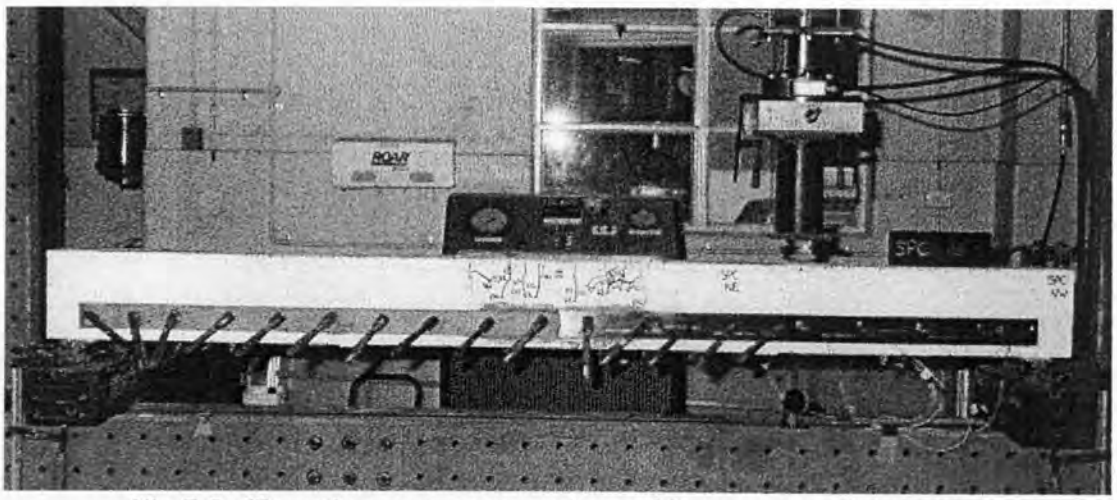

Fig.7.5. Clamping arrangement to avoid premature debonding

Table-7.1: Geometric properties

Common properties

breadth of beam(b)=150 mm, depth of beam = 250 mm,
length of beam= 3000 mm, effective span = 2800 mm ,
length of shear span = 700 mm, and width of load plate and support plate = 75 mm
Tension reinforcement : no. of layers =2 , total area (A_{st})=1533 mm^2
effective depth(d_{st}): first layer = 180 mm, second layer = 210 mm
area: first layer = 905 mm^2, second layer = 628 mm^2
Compression reinforcement: no. of layers =2 , total area (A_{sc})=1570 mm^2
effective depth(d_{sc}): first layer = 40 mm, second layer = 80 mm
area: first layer = 942 mm^2, second layer =628 mm^2
shear reinforcement: area = 157 mm^2, spacing = 100 mm c/c

Specific properties

Sl.No	Designation	Side plates					
		Plate type	L_{sp} (mm)	d_{sp} (mm)	t_{sp} (mm)	d_{top} (mm)	$E_{p,long}$ (MPa)
1	SPREF	unplated	-	-	-	-	-
2	SP-S5	Steel	1400	75	5	155	200,000
3	SP-C	Carbon FRP	1400	80	6.5	150	130,550
4	SP-S8	steel	1400	75	8	155	200,000
5	SP-CG	Carbon & Glass FRP	900	75	8.5	155	8,800

L_{sp} ,d_{sp}, t_{sp} = Length, depth and thickness of side plates,
$E_{p,long}$ = elastic modulus of side plate along its length
d_{top} = distance between the top of the beam and the top fibre of the plate

7.3.Test rig

The beams were simply supported over an effective span of 2800 mm as shown in Fig.7.6 and the load was applied on the top of the beam by a hand operated hydraulic jack through a load cell, load plate 75 mm wide and a pair of knife edge bearings. The geometry of the loading arrangement for all the beams in Fig.7.6 was such that the shear force in the shear span under test was 75% of the applied load, i.e. $V = 0.75P$ and hence, the maximum bending moment that occurs at the load point is $0.525P$ kNm.

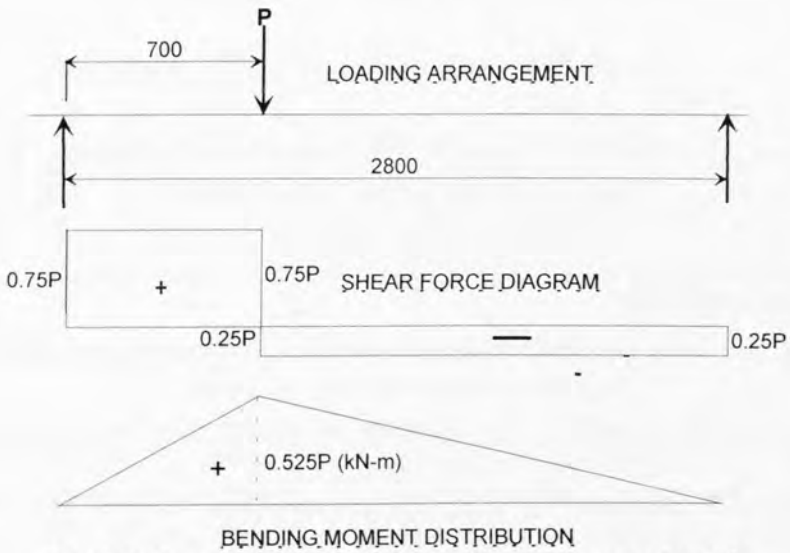

Fig.7.6. Loading arrangement for the beams tested

7.4 Instrumentation

Strain gauges were bonded to the external plates in order to detect the debonding at various sites of the plates. The arrangements of the strain gauges and their numbering are shown in Fig.7.7. The beam deflection at mid-span was monitored by both a dial gauge and also by a transducer.

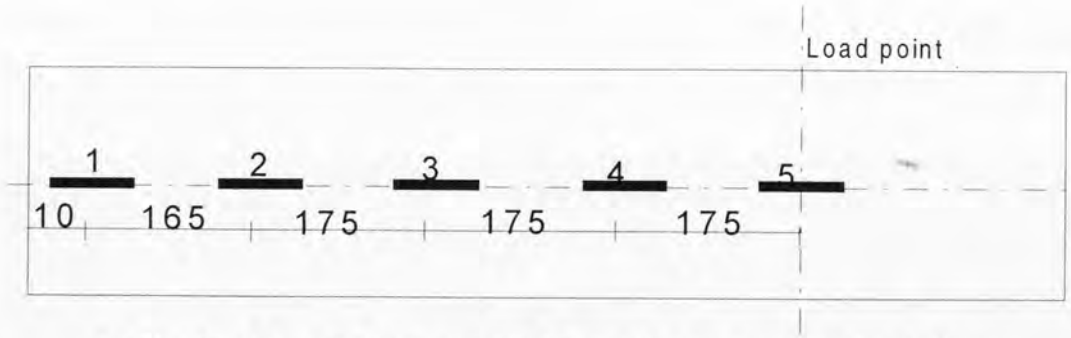

(a) North side of SP-CG and SP-S5, South side of SP-C and SP-S8

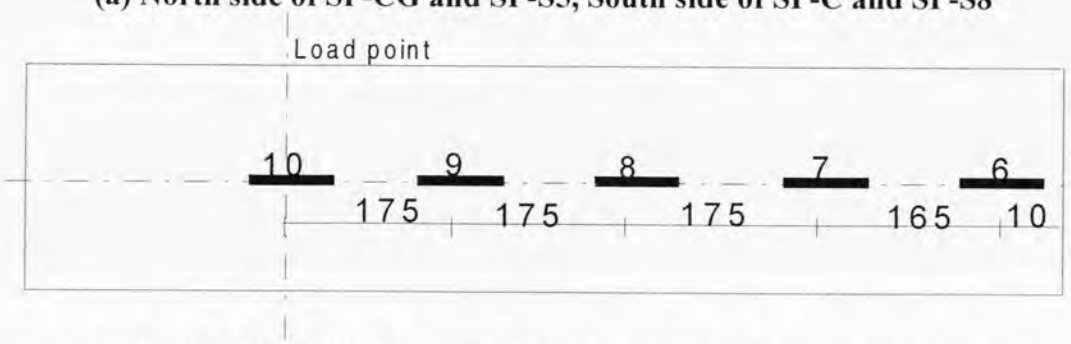

(b) South side of SP-CG and SP-S5, North side of SP-C and SP-S8

Fig.7.7. Strain gauges arrangement

7.5 Test procedure

For each test, the beam was first loaded in steps of 5 kN and the cracks were marked and photographically recorded. The corresponding strains at the various sites of the external plate were measured by strain gauges and were recorded at every load step though a data-logging system. The load step was reduced to 3 kN when there was a fall in strain at any site of the plate. The test was terminated when the plate peeling was total, ie when all of the strain gauges recorded reducing magnitudes of strains; the pure shear peeling strength of the plated beam corresponds to the shear force in the span being tested at this stage.

7.6 Material Properties

All the beams were cast in a single pour using ready mixed concrete supplied by a local manufacturer. Material properties of the concrete are shown in Table-7.2. In this table, the individual values of each test are given under the "i" column and their mean value under "m" column.

Table -7.2: Material properties of the concrete

Age	E_c (MPa)		f_b (MPa)		f_c (MPa)		f_{cu} (MPa)	
(days)	i	m	i	m	i	m	i	m
248	30242	29194	2.25	2.36	21.0	20.9	17.9	18.4
	29542		2.46		21.8		18.5	
	27800		2.37		20.0		18.8	

where E_c = Elastic modulus of the concrete, f_c = Cylinder compressive strength of the concrete, f_{cu} = Cube compressive strength of the concrete and f_b = Brazilian tensile strength of the concrete.

Material properties of the reinforcing bars and shear stirrups are shown in Table-7.3. The manufacturer's specifications of the material properties of the epoxy resinused for bonding the steel plates are indicated in Table-7.4.

Table –7.3. Material properties of the steel

Item	f_y (MPa)				f_u (MPa)			
Sample No.	1	2	3	Mean	1	2	3	Mean
Rebar Y20	455.1	455.1	458.3	456.2	561.8	563.4	566.6	563.9
Rebar Y24	453.1	455.4	454.3	454.3	565.9	563.7	565.9	565.1
Stirrup W10	522.0	522.0	509.3	517.8	541.1	541.1	515.7	532.6

where f_y = Yield strength of the steel and f_u = Ultimate strength of the steel.

Table -7.4: Material properties of the glue Hilti CA 273 after 2 days (as tested by the manufacturer)

Compressive strength (ISO 604)	Tensile strength (ISO 527)	Flexural strength (ISO 178)	Elastic modulus in compression (ASTM D 695)	Tensile bond strength (ISO 527)	Maximum operating temperature
110-120 MPa	30-40 MPa	20-30 MPa	5000-6000 MPa	10-15 MPa	80° C

7.7 Test results

7.7.1 Test SP-REF

Test SP-REF was conducted on the unplated beam that is shown in Fig.2, in order to quantify experimentally the ultimate shear strength of the RC beam ie $V_u=V_{uc}+V_s$. Figures 7.8a, 7.8b and 7.8c show the crack pattern observed at various stages of the test.

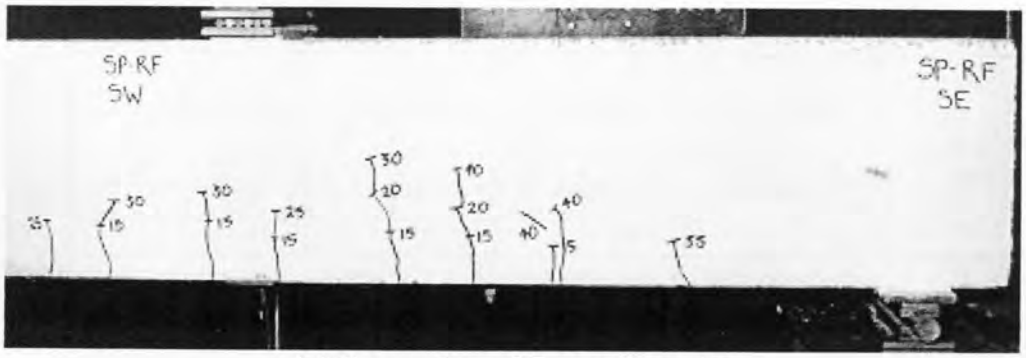

(a) Formation of flexural cracks

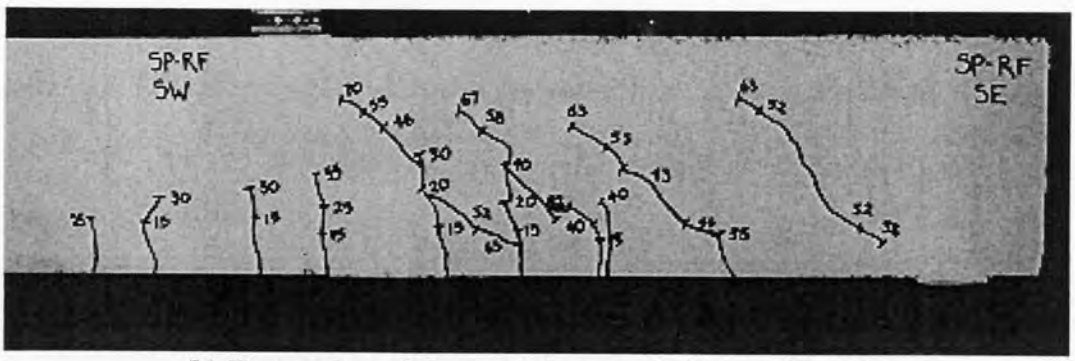

(b) Formation of flexural shear and diagonal cracks

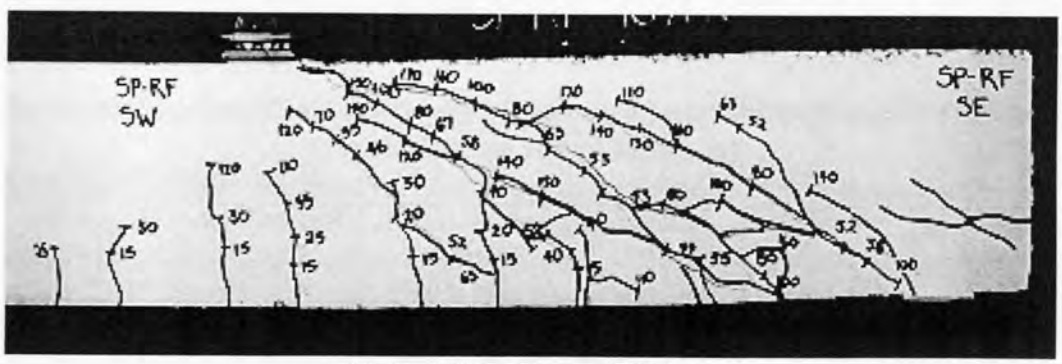

(c) Crack pattern at failure

Fig.7.8. SPREF- Crack patterns

Figure 7.8a shows the formation of several flexural cracks at regular intervals when the shear load in the span (V) was 11.3 kN (applied load P=15 kN). It also shows the occurrence of a flexural shear crack from the root of an existing minor crack. As the shear load was increased to 39 kN (P=52 kN), two web shear cracks formed, one close to the support and another at 100 mm from the first one (Refer Fig.7.8b). Further application of load led to the formation of more inclined cracks from the root of the existing cracks. Most of these cracks propagated upwards to their full extent as the shear load was increased to 75 kN (P=100 kN). Finally, shear failure

of the beam occurred due to the joining of the diagonal cracks, their extension towards the load plate and the crushing of concrete. All this happened when the shear load was 125.3 kN (P=167 kN) and thereafter the applied load suddenly dropped from 167 kN to 104 kN, corresponding to a shear load of 78 kN. At this stage the load test was ended.

From this test, we can conclude that the shear strength of the beam without shear stirrups (V_{uc}) is 39 kN, as this was the shear load at which critical web shear cracks formed closer to the support. They would have propagated all through the load point but for the presence of substantial amount of shear stirrups. The shear strength of the beam with the stirrups is 125.3 kN, as this corresponds to the shear load at which the complete shear failure of the beam occurred.

Figure 7.9 shows the variation of the deflection recorded at the load point with that of the shear load in the shear span. It shows a linear increase in deflection till the shear failure and the drop in shear load from 125.3 kN to 78 kN. The maximum deflection recorded at the end of the test was 21.6 mm.

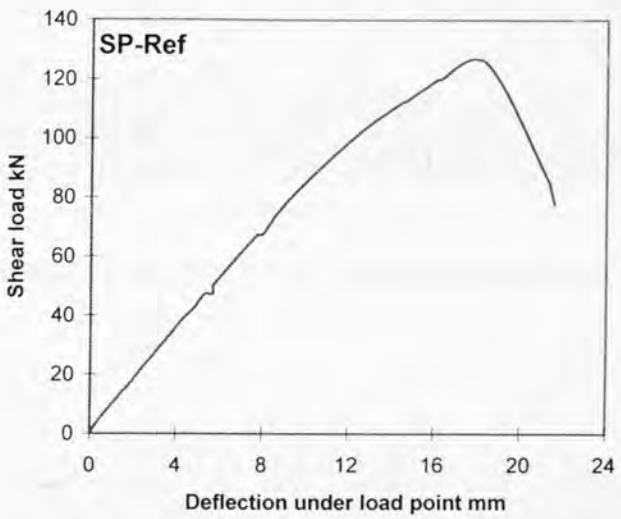

Fig.7.9. SPREF: Shear load Vs deflection

7.7.2 Test SP-S5

The shear span SP-S5 was bonded with a steel plate 1400 mm long, 75 mm deep and 5 mm thick as shown in Fig.7.4. As the debonding of the south side plate preceded that of the north side plate, debonding of each plate is discussed separately.

7.7.2.1 Debonding of south side plate

Figures 7.10a-c depict the crack patterns at the south side plate at various stages of the test.

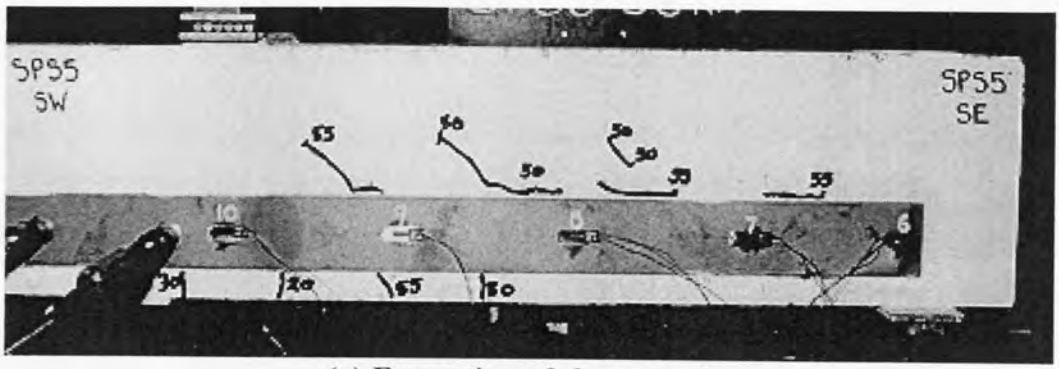

(a) Formation of shear cracks

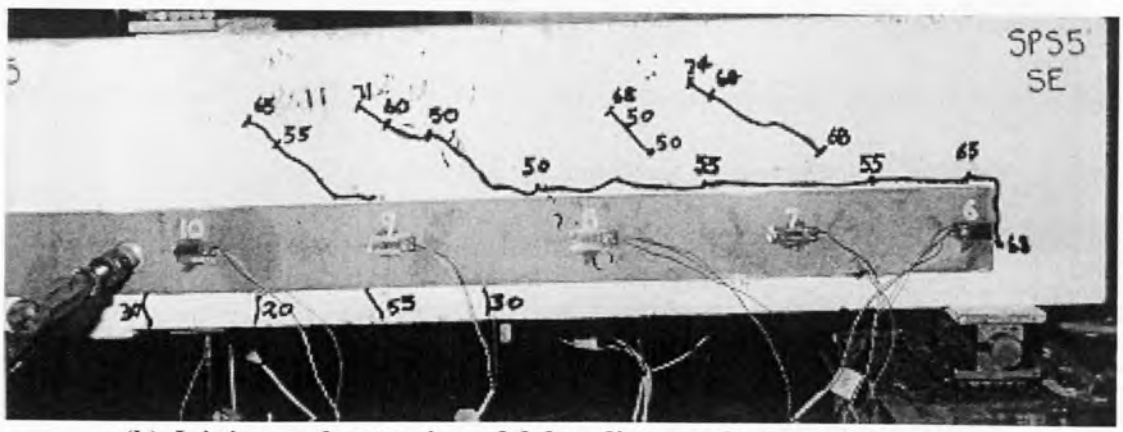

(b) Joining and extension of debonding crack above the support

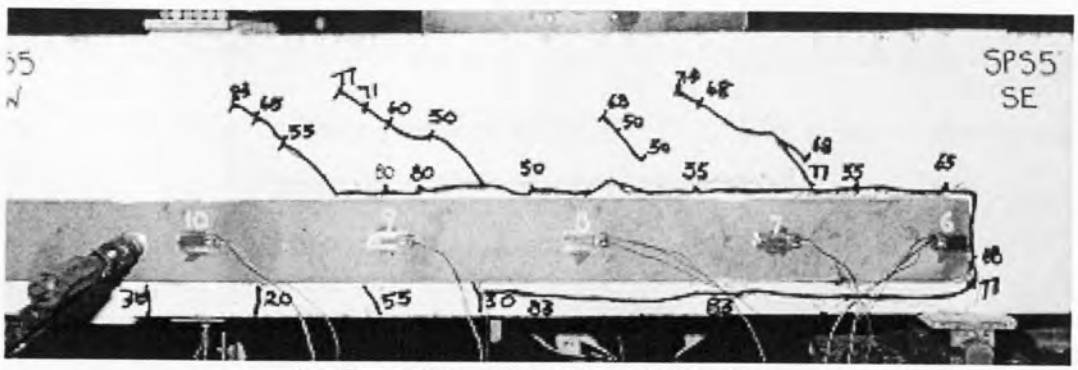

(c) Complete debonding of the plate

Fig.7.10. SP-S5: Crack pattern on the south side

A few flexural cracks could be seen below the plate in the vicinity of the load point, when the shear load in the shear span was 15-22.5 kN (P=20-30 kN), as shown in Fig.7.10a. Three web shear cracks occurred above the side plate when the applied shear load was 37.5-41.3 kN (P=50-55 kN) and the formation of discrete, horizontal debonding cracks at this stage could also be seen in Fig.7.10a. As the shear load was increased to 48.8 kN(P=65 kN), the debonding cracks joined together and they extended to the top corner of the side plate above the support. A small increase in shear load to 51 kN(P=68 kN) caused the debonding crack to propagate along the depth of the side plate above the support as shown in Fig.7.10b. Finally, the complete debonding of the plate occurred as the debonding crack encompassed the perimeter of the plate as shown in Fig.7.10c, when the applied shear load was 62.3 kN (P=83 kN).

7.7.2.2 Debonding of north side plate

A few flexural cracks occurred in the vicinity of the load point, when the shear load in the shear span was 15-30 kN (P=20-40 kN), as shown in Fig.7.11a. Three web shear cracks occurred above the side plate when the applied shear load was 41.3-45 kN (P=55-60 kN). Discrete, horizontal debonding cracks occurred from the root of these diagonal cracks and they propagated backwards along the top side of the plate during the various stages of loading, ie when the applied shear load was in the range 45-60 kN (P=60-80 kN), as shown in Fig.7.11a. As the shear load was increased to 62.3 kN (P=83 kN), the debonding crack above the support propagated along the depth of the side plate as shown in Fig.7.11b. Further application of the load caused the debonding cracks to join together and finally, the complete debonding of the plate occurred as shown in Fig.7.11c, when the applied shear load was 71 kN (P=96 kN).

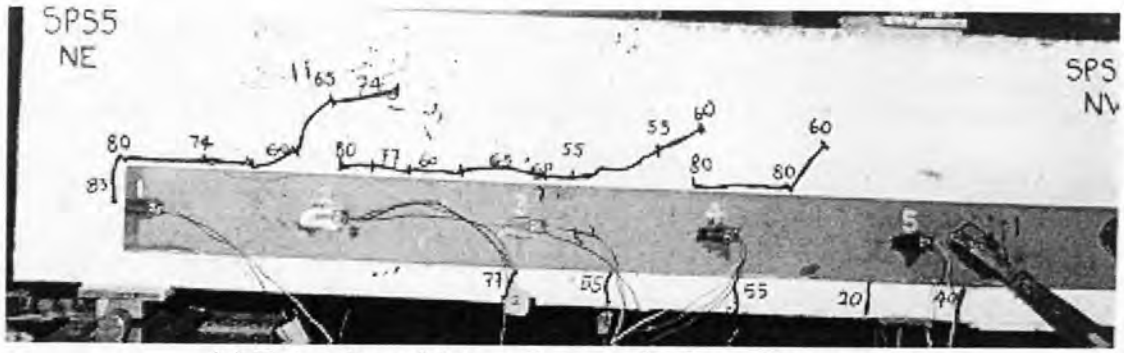

(a) Extension of debonding crack above the support

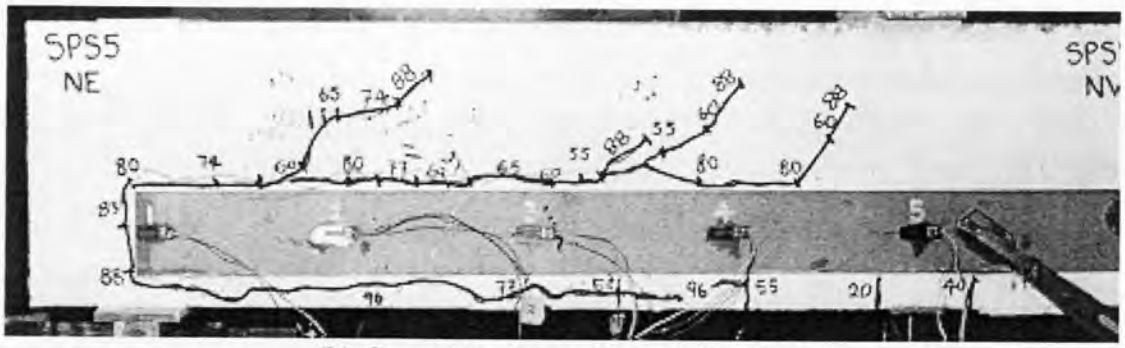

(b) Complete debonding of the plate

Fig.7.11. SP-S5: Crack pattern on the north side

7.7.2.3 Longitudinal strain distribution in the side plates and deflection

Figures 7.12a and 7.12b illustrate the variation of longitudinal strains recorded in all the electrical resistance strain gauge locations (Refer Fig.7.7) with the applied shear load in the shorter shear span. The strain magnitudes are fairly linear until complete debonding of the plate at which all the strain gauge locations recorded abrupt fall in the readings. However, the strain curves do show minor kinks at certain shear load levels indicating local debond either due to the formation of the diagonal cracks or due to the propagation of the debonding crack at these locations. The maximum strain magnitudes were recorded at the gauge locations #5 on the north side plate and #10 on the south side plate that were bonded exactly below the load point just before the complete debonding each plate. These magnitudes were 609 microstrain (north side) and 477 microstrain (south side). It may be noted that the shear load did not fall suddenly after debonding as the unplated RC beam is still capable of sustaining further load as evidenced in the test SP-RF. Figure 7.13 shows the relationship

between the applied shear load and the deflection recorded in the load point. It shows a linear relationship till the debonding and the maximum deflection recorded was 7.83 mm.

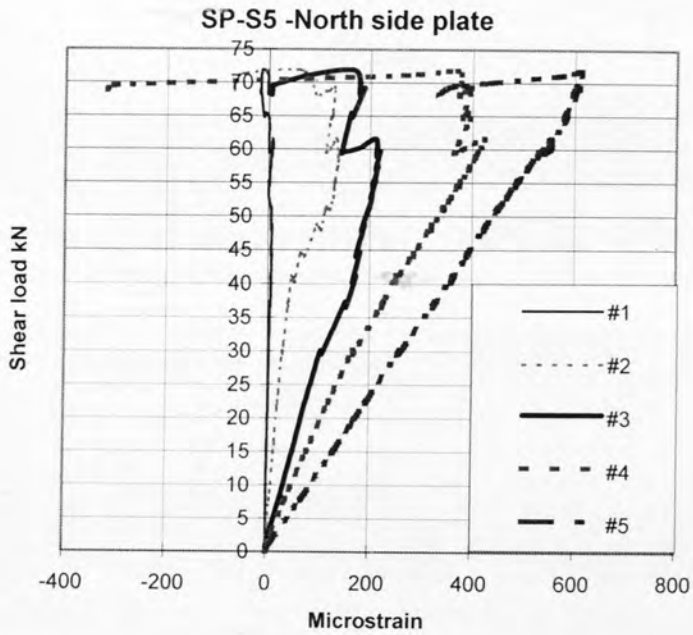

(a)

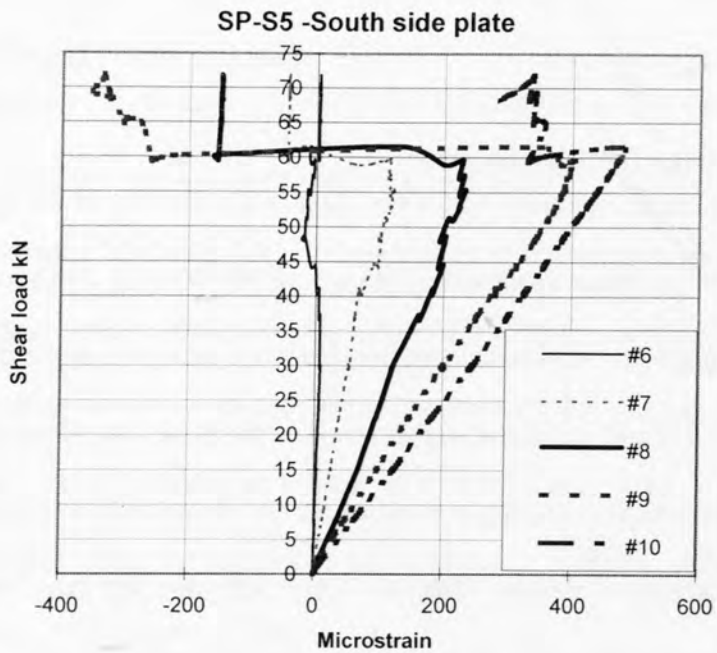

(b)

Fig.7.12 SP-S5 Longitudinal strain distribution in the side plates

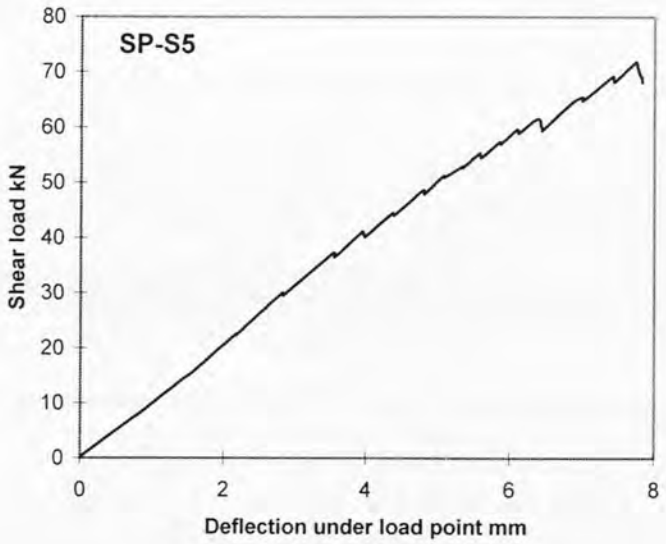

Fig.7.13. SP-S5: Deflection Vs Shear load

7.7.3 Test SP-S8

The shear span SP-S8 was bonded with a steel plate 1400 mm long, 75 mm deep and 8 mm thick as shown in Fig.7.3. As the debonding of the south side plate and the north side plate did not occur simultaneously, debonding of each plate is discussed separately.

7.7.3.1 Debonding of south side plate

Several flexural cracks occurred below the plate in the vicinity of the load point, when the shear load in the shear span was 30-45 kN (P=40-60 kN), as shown in Fig.7.14a. Three web shear cracks occurred above the side plate when the applied shear load was 52.5 kN (P=70 kN) and a crack along the edge of the plate just above the support also occurred simultaneously. A slight increase in the shear load to 54.8 kN(P=73 kN) caused the formation of another diagonal crack and also the extension of the crack parallel to the vertical edge of the plate over the support. Discrete, horizontal debonding cracks at this stage could also be seen in Fig. 7.14a. Finally, the complete debonding of the plate occurred as long debonding cracks that formed both along the

bottom and top edges of the plate as shown in Fig.7.14b, when the applied shear load was 68.3 kN (P=91 kN).

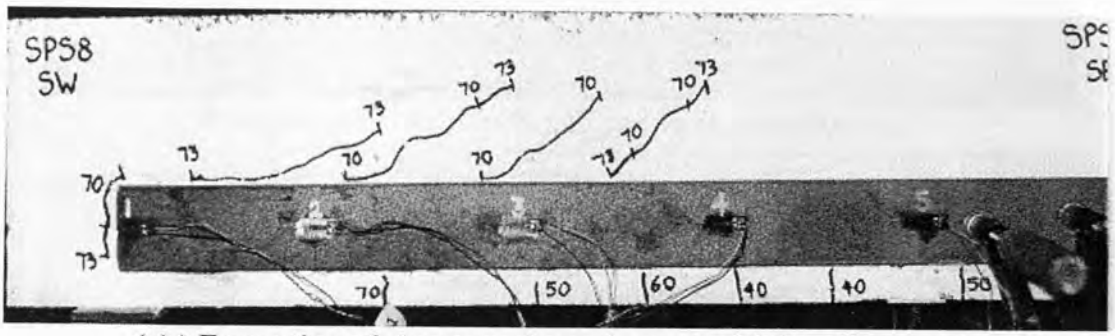

(a)) Formation of shear cracks and on set of debonding cracks

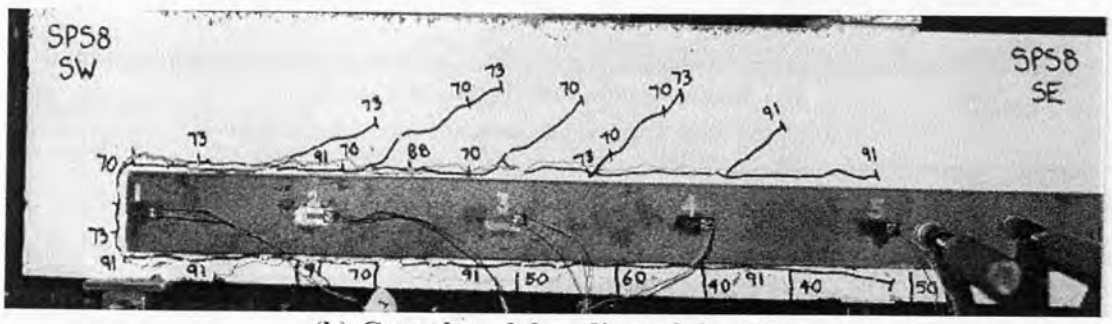

(b) Complete debonding of the plate

Fig.7.14. SP-S8: Crack pattern on the south side

7.7.3.2 Debonding of North side plate

The crack pattern on the north side of the beam was similar to that which occurred in the South side, until the applied shear load was 54.8 kN (P=73 kN). As the shear load was increased to 68.3 kN(P=91 kN), debonding cracks formed from the root of the existing web shear cracks along the top edge of the plate (Refer Fig.7.15a). The complete debonding of the north side plate occurred by the joining together of the local debonding cracks. They were transformed into a long, single debonding crack surrounding the plate from the support to the load point as shown in Fig.7.15b, when the shear load was 77.3 kN(P=103 kN).

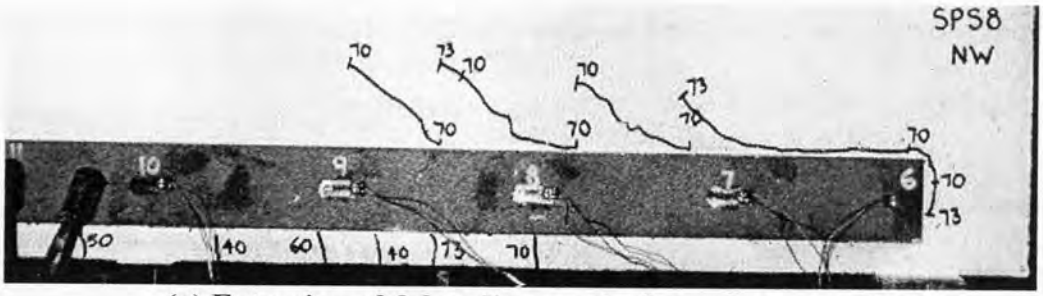

(a) Extension of debonding crack above the support

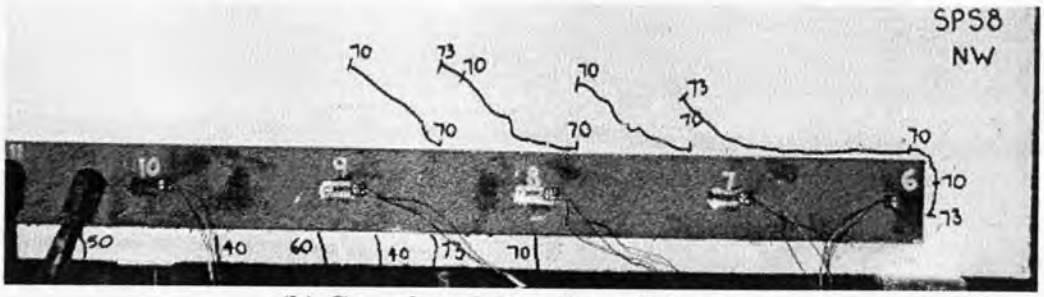

(b) Complete debonding of the plate

Fig.7.15. SP-S8: Crack pattern on the north side

7.7.3.3 Longitudinal strain distribution in the side plates and deflection

Figures 7.16a and 7.16b illustrate the variation of longitudinal strains recorded in all the electrical resistance strain gauge locations (Refer Fig.7.7) with the applied shear load in the shorter shear span. The strain magnitudes are fairly linear until complete debonding of the plate at which all the strain gauge locations recorded abrupt falls in the readings. However, the strain curves do show minor kinks at certain shear load levels indicating local debond either due to the formation of the diagonal cracks or due to the propagation of the debonding crack at these locations. For example, the strain readings show a gradual decline in gauges #2 and #3 on the south side plate in the shear load range 50-55 kN. This is due to the formation of the local debonding cracks in the vicinity of these gauge locations. Even though the north side plate debonded later, the debonding of south side plate at a shear load of 68.3 kN led to a minor drop in shear load magnitude and the strain readings at the all gauge locations on the north side. The maximum strain magnitudes were recorded at the gauge

locations #5 on the north side plate and #10 on the south side plate and these magnitudes were 457 microstrain(north side) and 454 microstrain(south side).

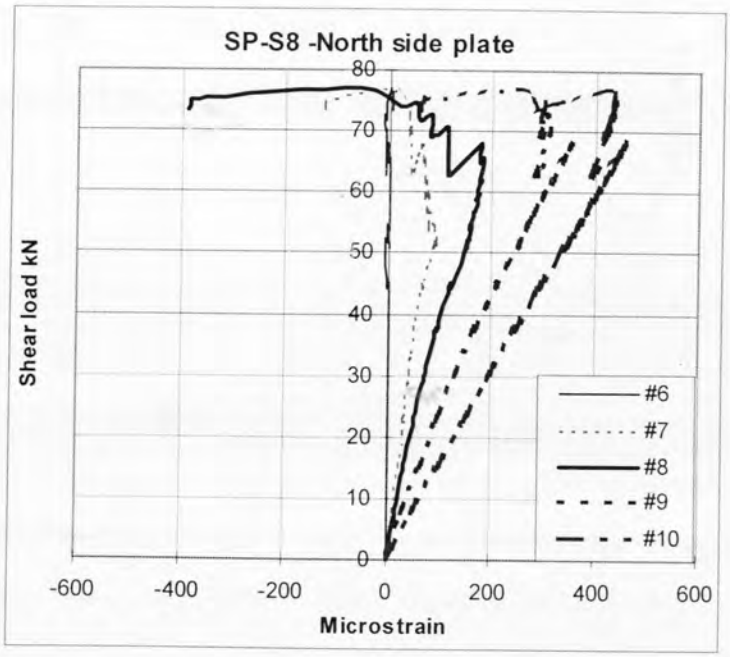

(a)

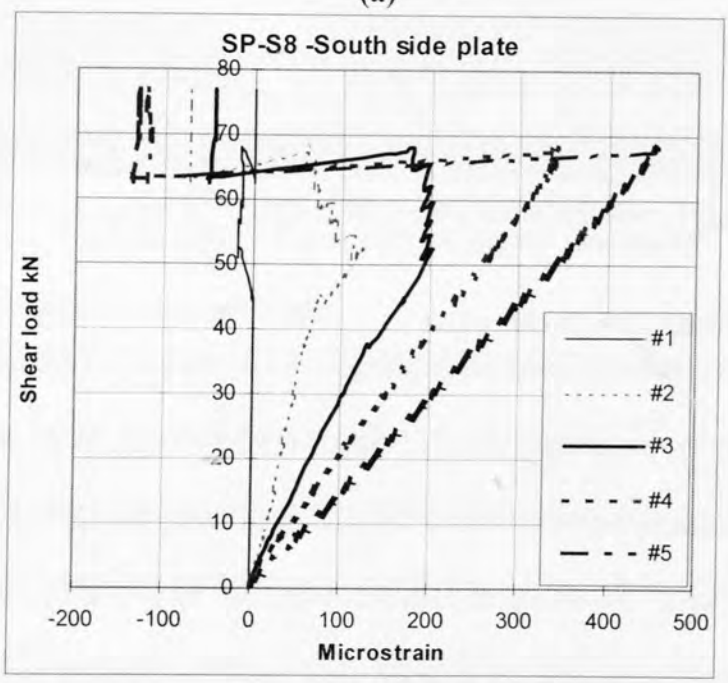

(b)

Fig.7.16. SP-S8: Longitudinal strain distribution in the side plates

Figure 7.17 shows the relationship between the applied shear load and the deflection recorded in the load point. It shows a linear relationship till the termination of the test and the maximum deflection recorded was 7.84 mm.

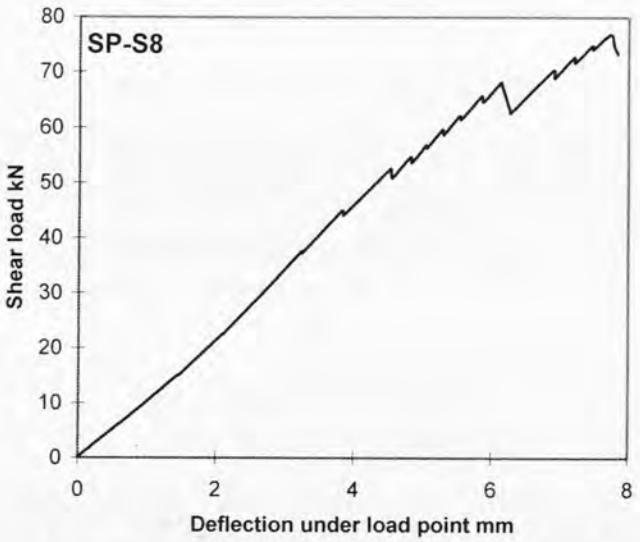

Fig.7.17. SP-S8: Deflection Vs Shear load

7.7.4 Test SP-C

The shear span SP-C was bonded with a carbon FRP plate 1400 mm long, 80 mm deep and 6.5 mm thick as shown in Fig.7.4. The elastic modulus of the FRP plate along the longitudinal axis is approximately two-third that of the steel plate. As the debonding of the south side plate and the north side plate did not occur simultaneously, debonding of each plate is discussed separately.

7.7.4.1 Debonding of south side plate

Several flexural cracks occurred below the plate in the vicinity of the load point, when the shear load in the shear span was 22.5-30 kN (P=30-40 kN), as shown in Fig.7.18a. Two web shear cracks occurred above the side plate when the applied shear load was 41.3 kN (P=55 kN). As the shear load was increased to 47.3 kN (P=65 kN) another shear crack was observed and the existing shear cracks propagated back parallel to the top edge of the plate. At an applied shear load of 53.3 kN (P=71 kN), a crack occurred at the top corner of the plate and it joined with the nearest local debonding crack for the next increment of the shear load ie 55.5 kN (P=74 kN). Other debonding cracks also extended considerably backwards but they were still isolated. The final

debonding of the plate occurred due to the formation of long debonding crack surrounding all the edges of the plate as shown in Fig.7.18b, when the shear load was 71.3 kN (P = 95 kN).

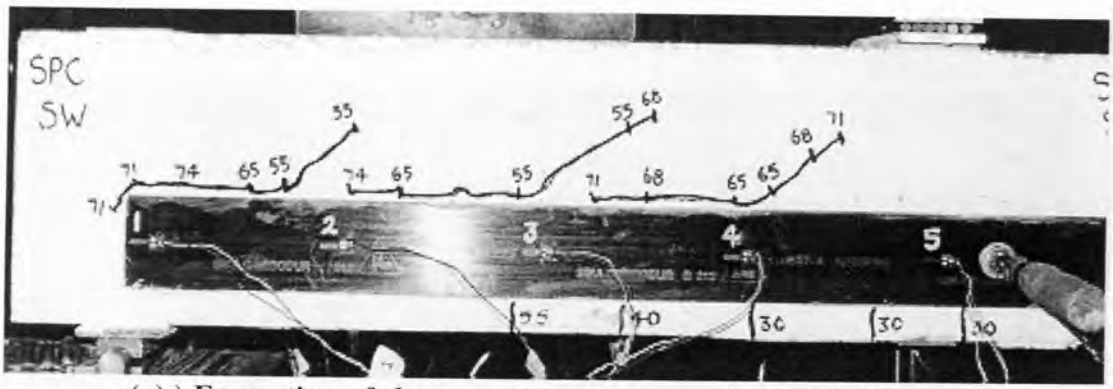

(a)) Formation of shear cracks and on set of debonding cracks

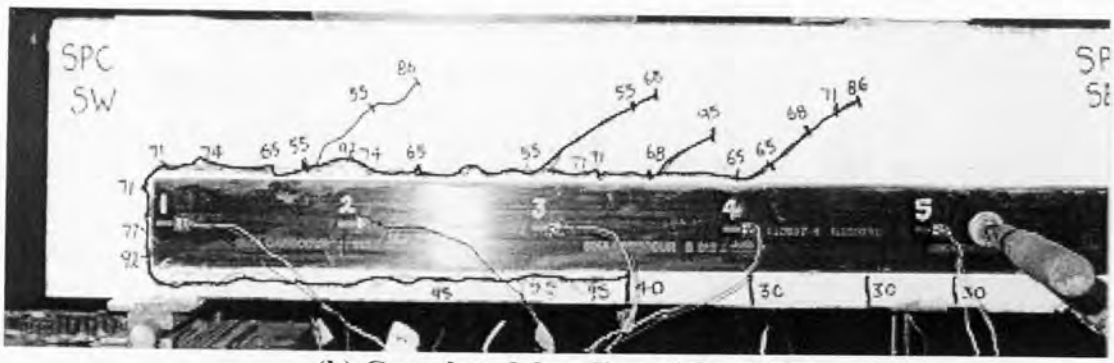

(b) Complete debonding of the plate

Fig.7.18. SP-C: Crack pattern on the south side

7.7.4.2 Debonding of North side plate

A few flexural cracks occurred first in the maximum moment region when the applied shear load was varied between 15 kN and 37.5 kN (P=20-50 kN). When the next increment of the load was applied, corresponding to a shear load of 41.3 kN (P=55 kN), two web shear cracks appeared as shown in Fig.7.19a. The next significant crack to occur was the diagonal crack above the strain gauge #9 that instantaneously propagated backwards along the top edge of the side plate when the shear load was 48.8 8 kN (P=65 kN), as shown in Fig.7.19b. The web shear crack closer to the support also propagated back along the top edge of the side plate and this crack extended to the corner of the side plate when the shear load was 66.8 kN (P=89 kN).

The final debonding of the north side plate occurred as the individual debonding cracks were transformed into one long crack extending along the bottom edge of the plate when the shear load was increased to 90.8 kN (P=121 kN), as shown in Fig.7.19c.

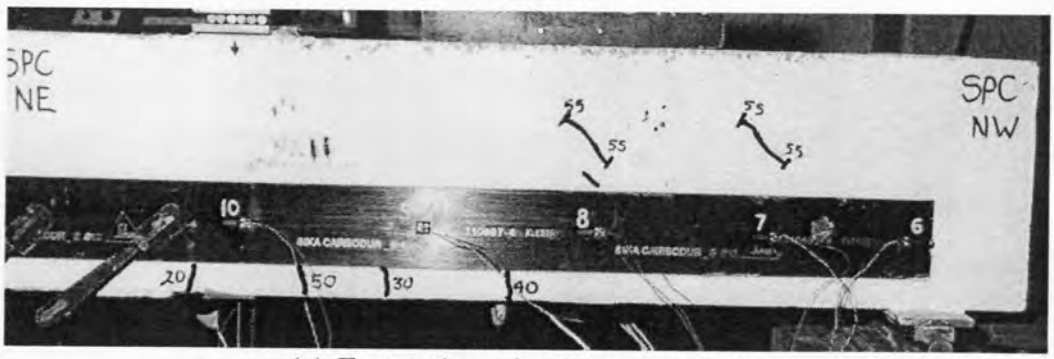

(a) Formation of web shear cracks

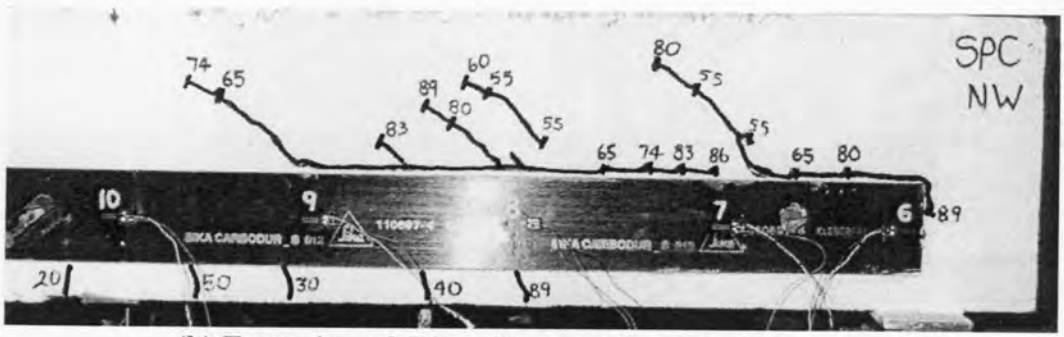

(b) Extension of debonding crack above the support

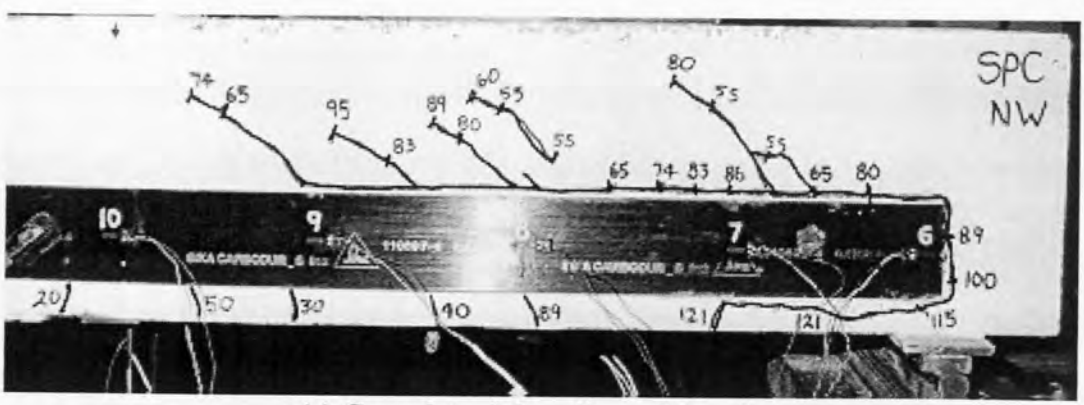

(c) Complete debonding of the plate

Fig.7.19. SP-C: Crack pattern on the north side

7.7.4.3 Longitudinal strain distribution in the side plates and deflection

Figures 7.20a and 7.20b show the variation of longitudinal strains recorded in all the electrical resistance strain gauge locations (Refer Fig.7.7) with the applied shear load in the shorter shear span. The variation of the strains is fairly linear until complete

debonding of the plate at which all the strain gauge locations recorded abrupt fall in the readings.

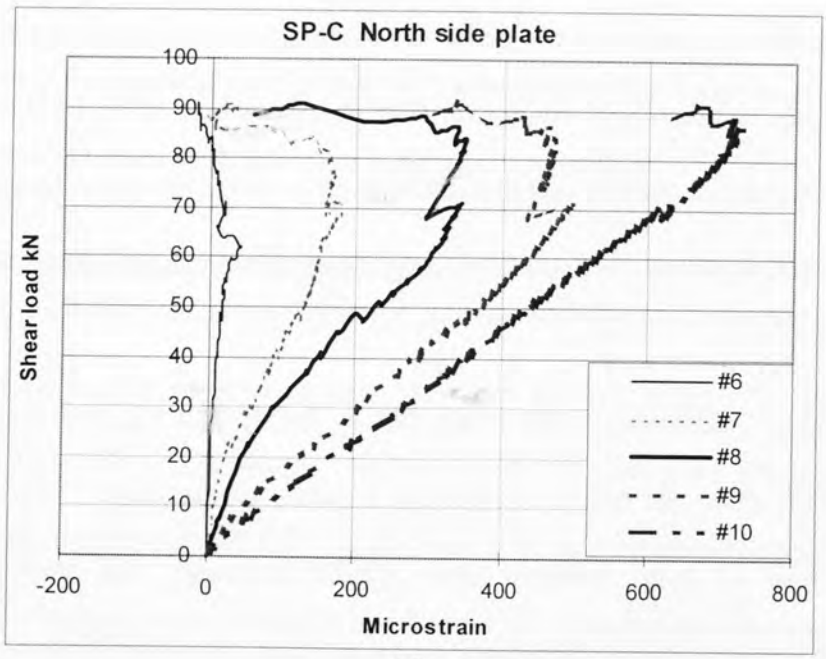

(a)

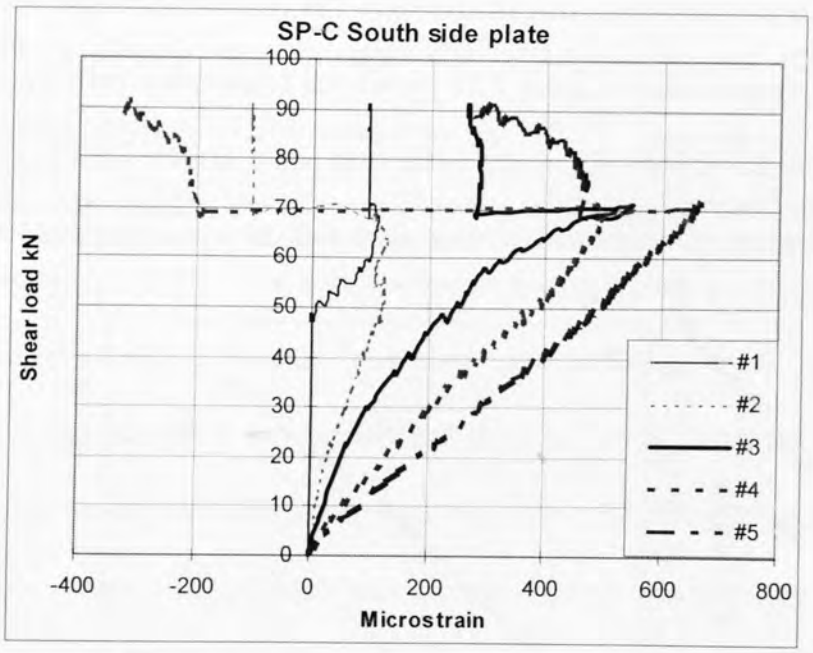

(b)

Fig.7.20. SP-C: Longitudinal strain distribution in the side plates

It can be seen in Figs.7.20a and 7.20b that the strain curves have minor kinks at certain shear load levels indicating the local debond either due to the formation of the diagonal cracks or due to the propagation of the debonding crack at these

locations. For example, the strain readings show a slight change in gauges #1 and #2 on the south side plate when the shear load was 55 kN due to the debonding crack formation at the top corner of the plate. Even though the north side plate debonded totally later, the debonding of south side plate at a shear load of 71.3 kN led to minor drop in shear load magnitude and the strain readings at the all gauge locations on the north side. It also shows the continuous drop in magnitudes in the locations #6, #7, #8 and #9.

Figure 7.20b shows the strain curves for #1 and #2, and for #3 and #4 intersect each other just before complete debonding of the plate. This denotes the complete loss of bond between these gauge locations. The maximum strain magnitudes were recorded at the gauge locations #5 on the north side plate and #10 on the south side plate and these magnitudes were 728 microstrains (north side) and 667 microstrains (south side). Figure 7.21 shows the relationship between the applied shear load and the deflection recorded in the load point. It shows a linear relationship till the termination of the test and the maximum deflection recorded was 10.02 mm.

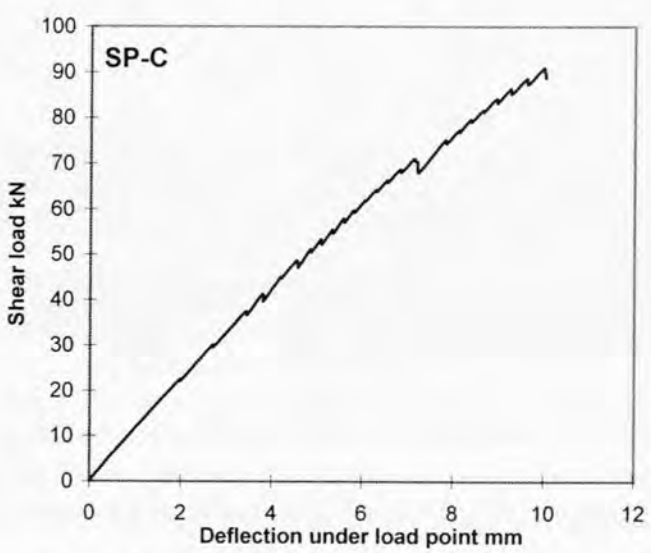

Fig.7.21. SP-C: Deflection Vs Shear load

7.7.5 Test SP-CG

The shear span SP-CG was bonded with a carbon and glass FRP plate 1400 mm long, 75 mm deep and 6.5 mm thick as shown in Fig.7.3. The elastic modulus of the FRP plate along the longitudinal axis is 8800 MPa which is just 4.4% that of the steel plate. As before, the debonding of each plate is discussed separately.

7.7.5.1 Debonding of south side plate

Several flexural cracks occurred below the plate in the vicinity of the load point, when the shear load in the shear span was 18.8-22.5 kN (P=25-30 kN), as shown in Fig.7.22a. Four web shear cracks occurred above the side plate when the applied shear load was 45.0 kN (P=60 kN). As the shear load was increased to 60.0 kN (P=80 kN), local debonding cracks formed from the root of the web shear cracks as shown in Fig.7.22b. All the local debonding cracks were transformed into a single crack and they extended backwards along the edges of the plate to the support, when the shear load was 101.3 kN (P=135 kN). (Refer to Fig.7.22c). The diagonal cracks also propagated rapidly towards the concrete beam top at this stage. When the shear load was increased to 120 kN (P=160 kN), one of the diagonal crack extended to the load point and the concrete below the load plate also started to crush, as shown in Fig.7.22c. It was decided to temporarily halt the load test at this stage as the other shear span that was bonded with 8 mm thick steel plate (SP-S8) was yet to be tested. Therefore, the beam was unloaded and the test SP-CG was repeated again after performing the test SP-S8. The final debonding of the plate occurred by the splitting of the concrete above the support plate as shown in Fig.7.22d, without any further increase in the magnitude of the applied load as recorded in the first test.

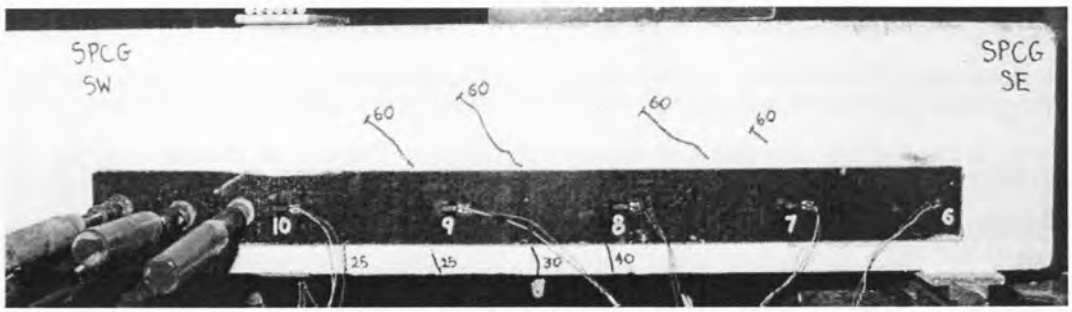

(a) Formation of web shear cracks

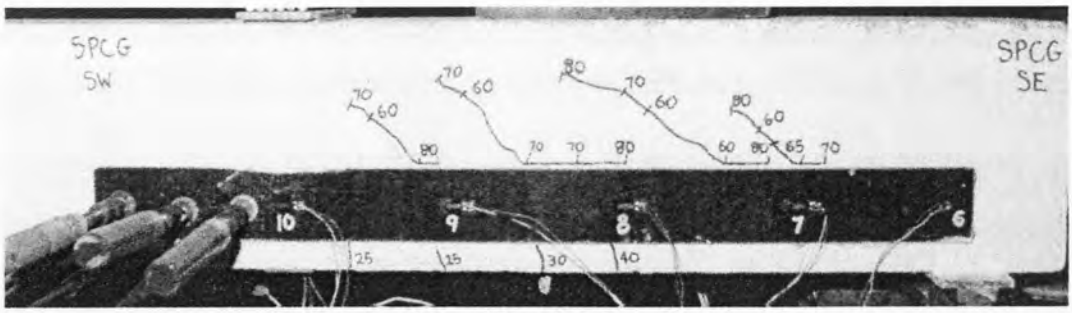

(b) Formation of local debonding cracks

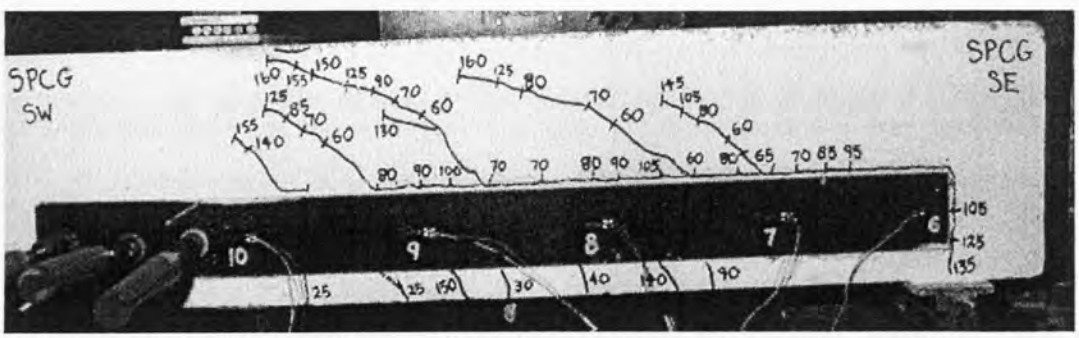

(c) Extension of debonding crack to the support and concrete crushing under load plate

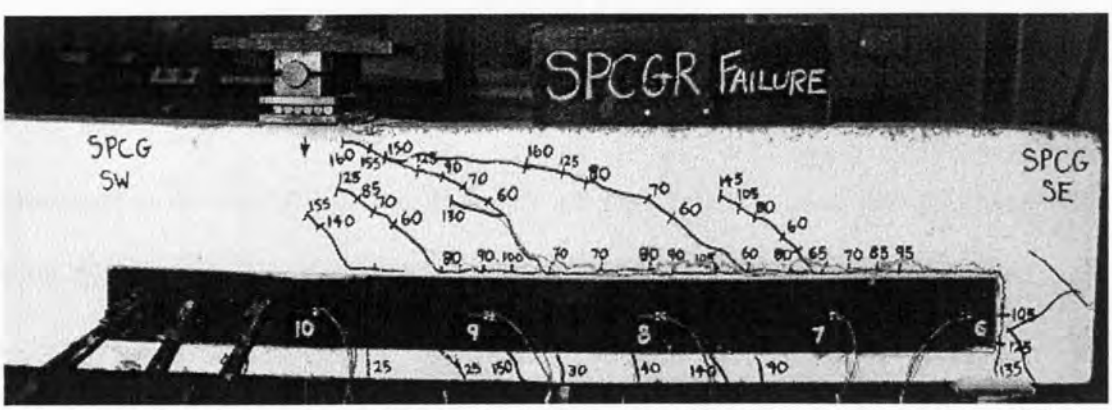

(d) Complete debonding of the plate in the repeat test due to concrete splitting

Fig.7.22. SP-CG: Crack pattern on the south side

7.7.5.2 Debonding of north side plate

Several flexural cracks occurred below the plate in the vicinity of the load point, when the shear load in the shear span was 18.8 kN (P = 25 kN), as shown in Fig.7.23a. Two

web shear cracks occurred above the side plate when the applied shear load was 45.0 kN (P=60 kN) and another at an applied shear load of 48.8 kN (P=65 kN).

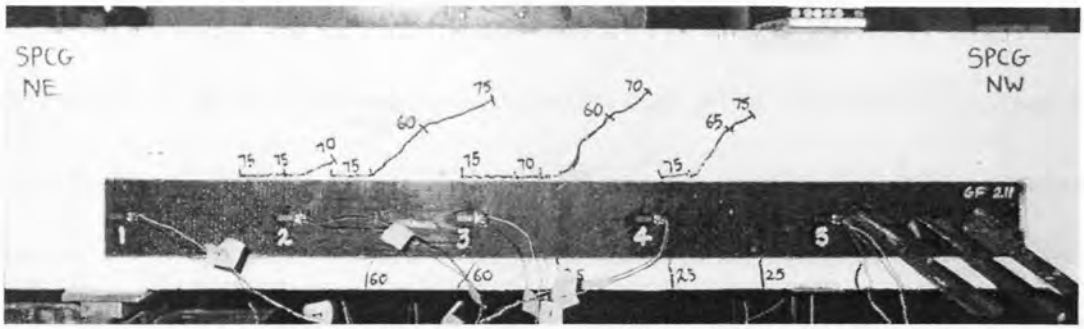

(a) Formation of web shear cracks and local debonding cracks

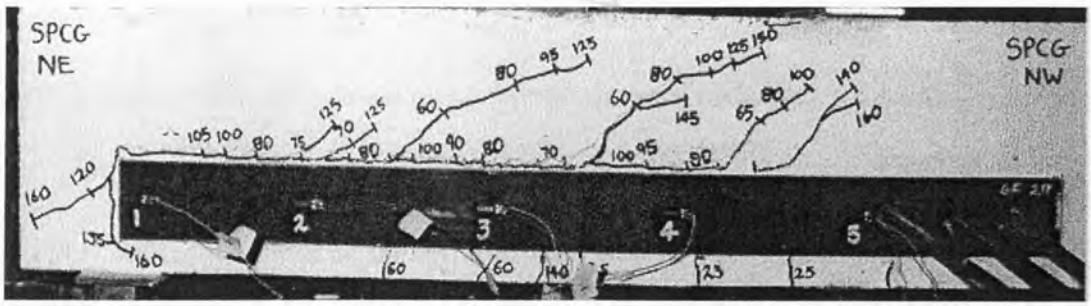

(b) Extension of debonding crack to the support and concrete crushing under load plate

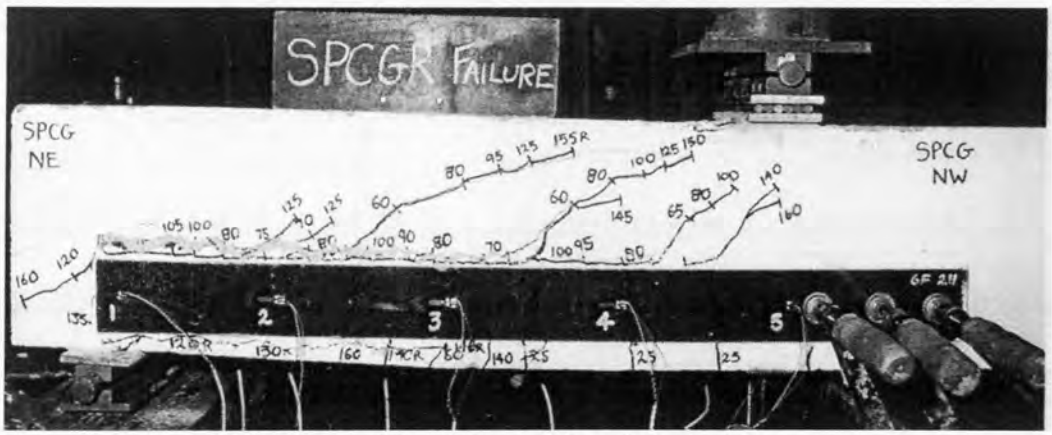

(c) Complete debonding of the plate in the repeat test

Fig.7.23. SP-CG: Crack pattern on the north side

As the shear load was increased to 56.3 kN (P=75 kN), local debonding cracks formed from the root of the web shear cracks as shown in Fig.7.23a. All the local debonding cracks were transformed into a single crack and they extended backwards along the edges of the plate to the top corner of the side plate, when the shear load was 90.0 kN (P=120 kN). This crack further extended down to the bottom corner of the

plate just above the support at an applied shear load of 101.3 kN (P=135 kN) (Refer Fig.7.23b). The diagonal cracks also extended rapidly towards the top of the beam at this stage. When the shear load was increased to 112.5 kN (P=150 kN), one of the diagonal crack extended to the load point and the concrete below the load plate also started to crush as the shear load was increased to 120 kN (P=160 kN), as shown in Fig.7.23b. The final debonding of the plate occurred when the load test was repeated again as stated earlier. The complete debonding of the plate occurred due to the formation of long debonding crack surrounding all the edges of the plate as shown in Fig.7.23c. This occurred when the reapplied shear load was 120 kN (P=160 kN).

7.7.5.3 Longitudinal strain distribution in the side plates and deflection

Figures 7.24a and 7.24b show the variation of longitudinal strains recorded in all the electrical resistance strain gauge locations (Refer Fig.7.7) for the north side plate from the original test and the repeat test with the applied shear load in the shorter shear span. The corresponding strain distributions for the south side plate are shown in Figs.7.25a and 7.25b.

The strain magnitudes increased linearly with the applied shear load but they remained constant or dropped marginally whenever a shear crack or local debonding crack formed in the vicinity of a particular gauge locations. The complete debonding of both side plates can be visualised by the abrupt drop in strain magnitudes in all the gauge locations at a shear load of 120 kN, as can be seen from Figs.7.24b and 7.25b. The maximum strain magnitudes were recorded at the gauge locations #5 on the north side plate and #10 on the south side plate and these magnitudes were 1842 microstrain(north side) and 1527 microstrain(south side).

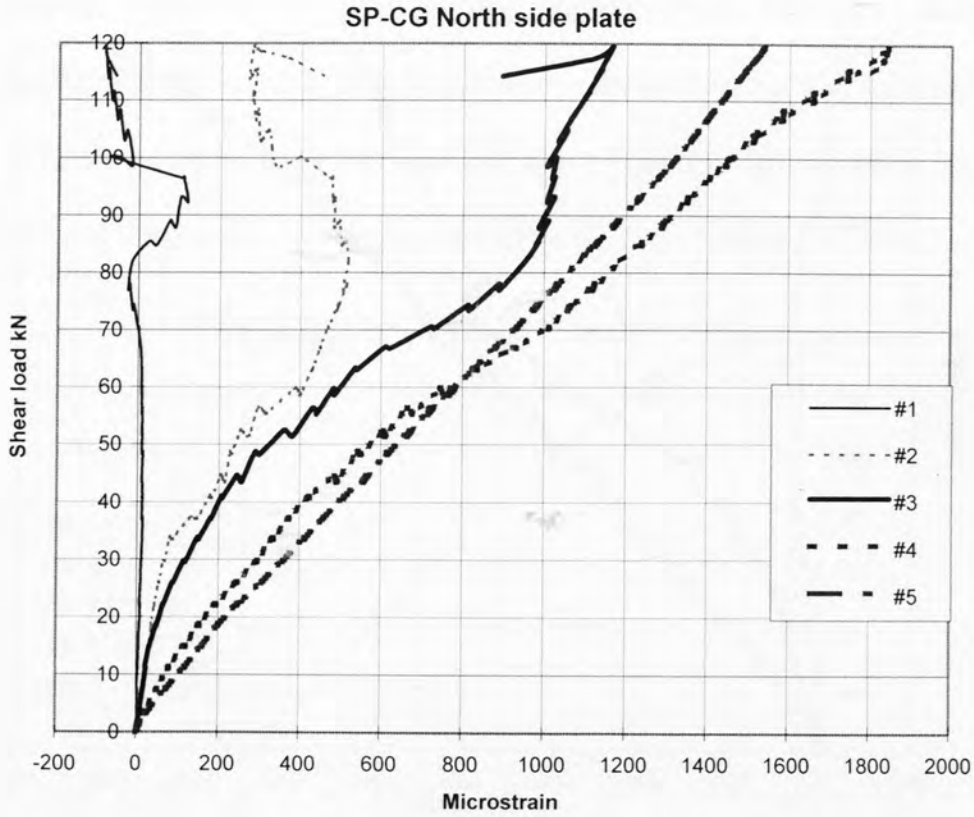

(a) Original test

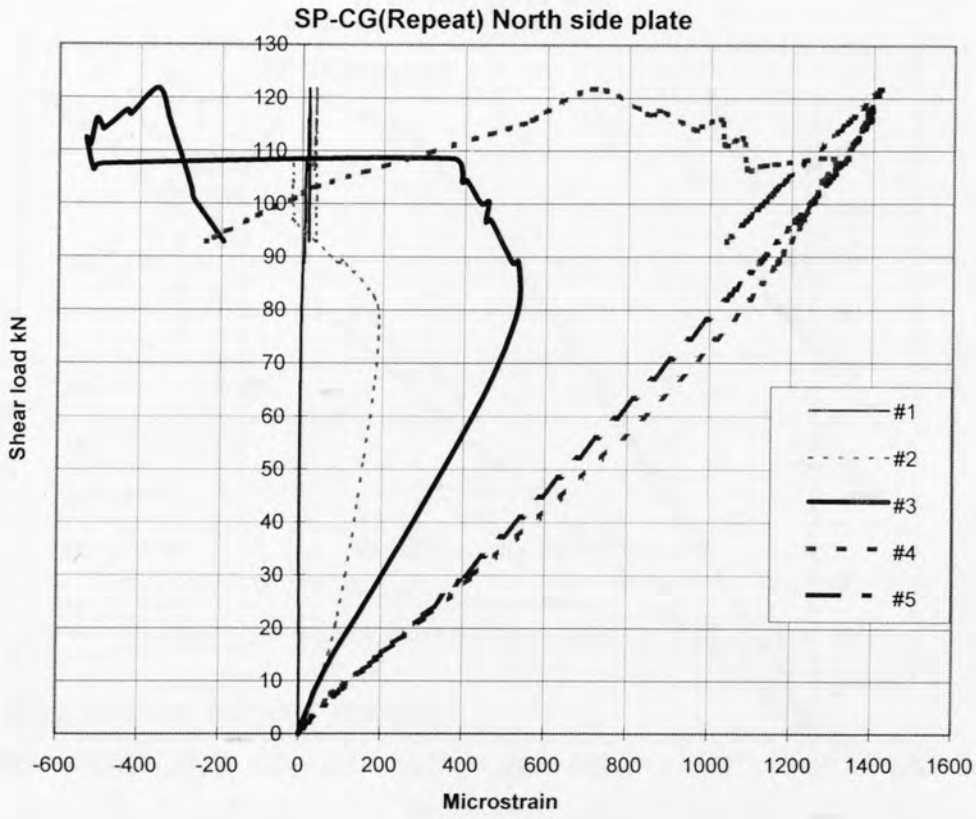

(b) Repeat test

Fig.7.24. Test SP-CG: Longitudinal strain distribution in the north side plate

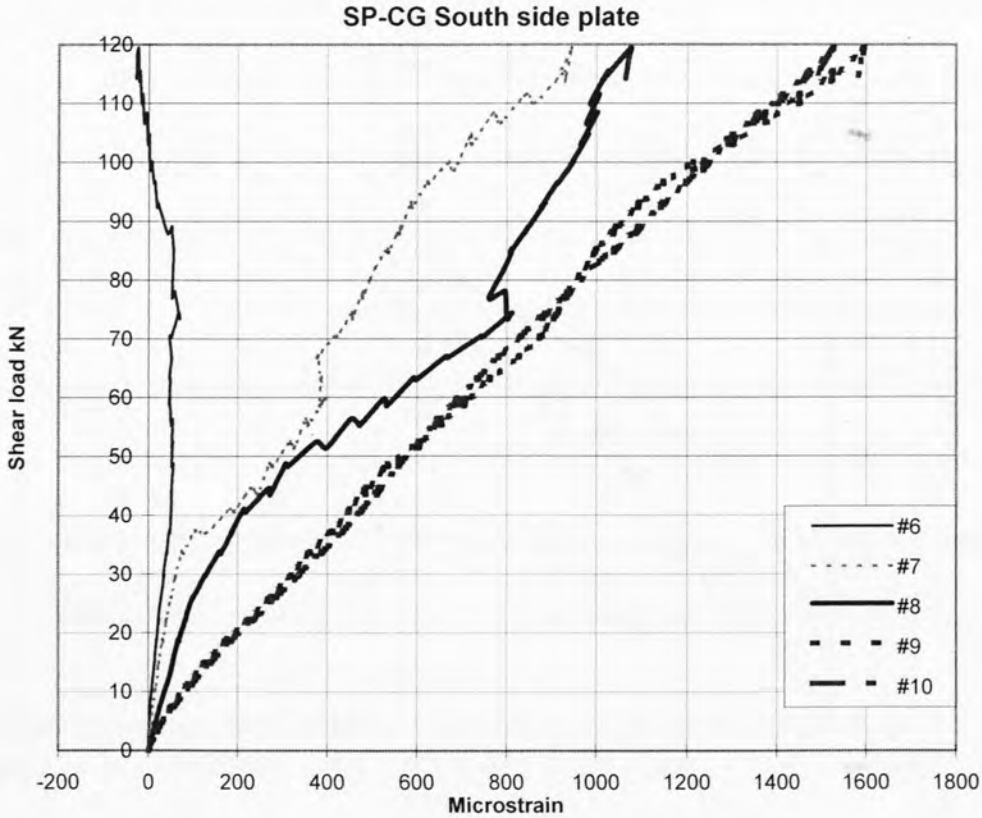

(a) Original test

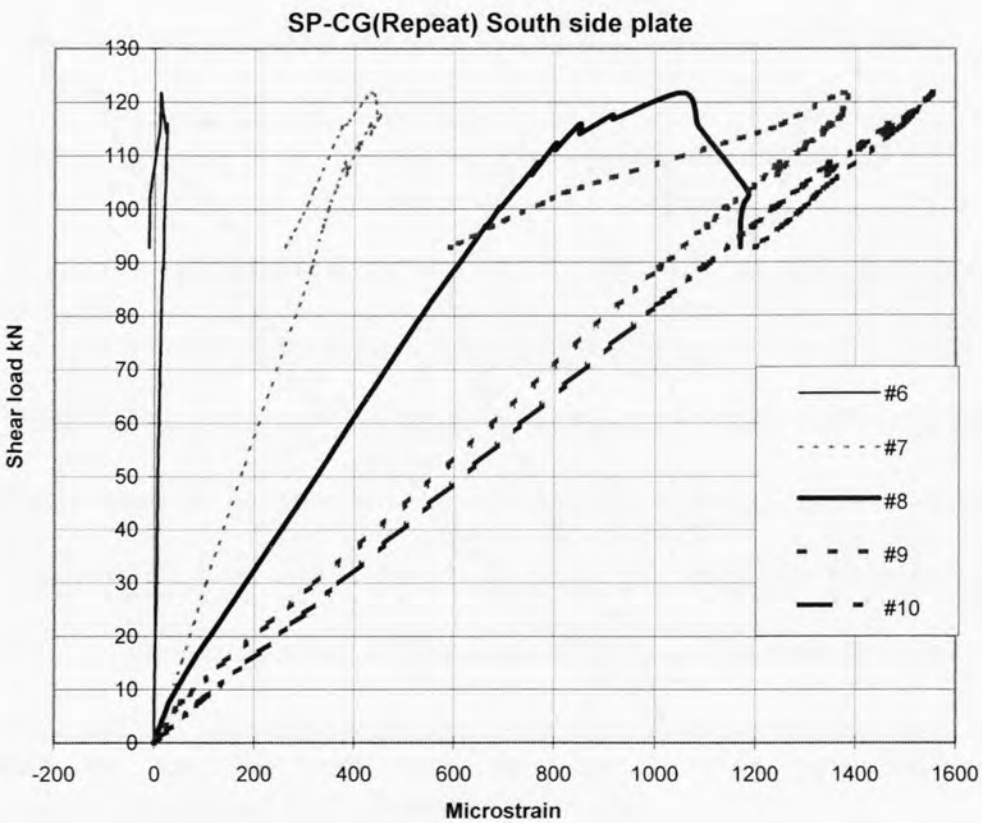

(b) Repeat test

Fig.7.25. Test SP-CG: Longitudinal strain distribution in the south side plate

Figures 7.26a and 7.26b show the relationship between the applied shear load and the deflection recorded in the load point from the original test and the repeat test. Figure 7.26b shows a drop in the shear load from 120 kN to 93 kN due to the shear debonding of the plates and the maximum deflection recorded was 16.57 mm.

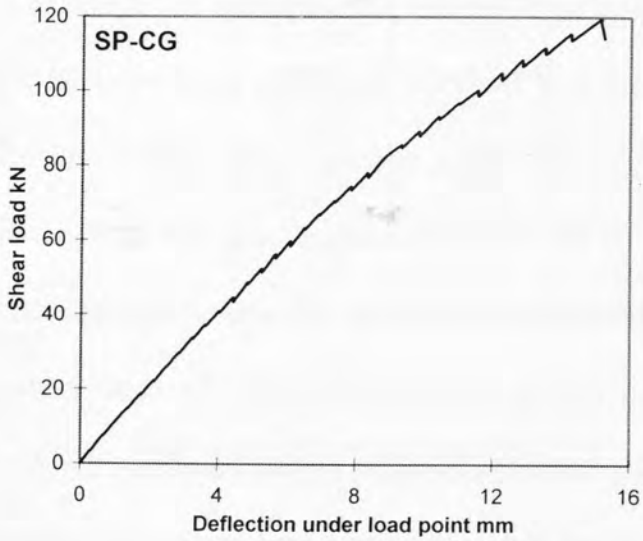

(a) Original test

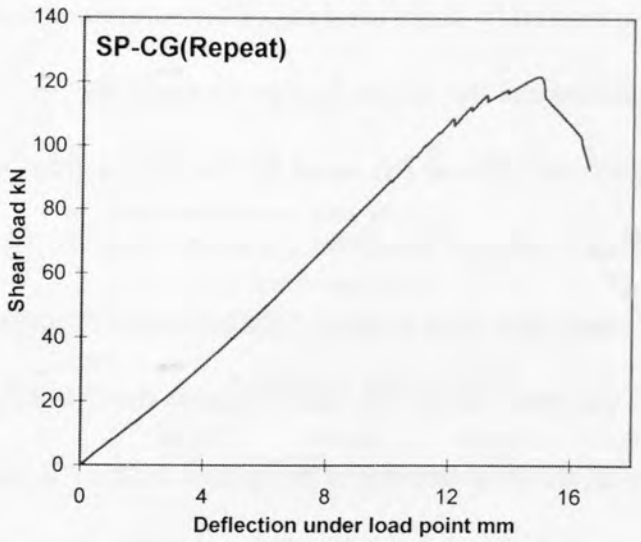

(b) Repeat test

Fig.7.26. Test SP-CG: Shear load Vs Deflection

7.8 Discussion of test results

The tests conducted on the beams bonded with external plates show that the beams bonded with steel plates (SP-S5 and SP-S8) and the carbon FRP plate (SP-C) failed by shear peeling at a shear load substantially lower than the ultimate shear strength of the

RC beam as indicated by test SP-REF. The sequence of events leading to the shear peeling of the all the plated beams can be summarised as follows. First, a few web shear cracks formed above the top edge of the side plates in the shorter shear span. Then, local debonding cracks occurred due to the backward propagation of these web cracks along the top edge of the side plate. Further, increments in the load caused the formation or extension of the local debonding crack over the plate end above the support. Finally, complete shear peeling of the plated beam occurred due to the transformation of all the local debonding cracks into a single crack that suddenly propagate along the bottom edge of the side plates also. In the case of the beam bonded with a very flexible FRP plate (SP-CG), the shear peeling mechanism was similar to the beams bonded with stiffer plates. However, the shear peeling of beam SP-CG occurred almost at the same shear load as the shear strength of the unplated beam and it was also marked by slight crushing of the concrete at the load point.

Table-7.5 summarises the salient feature from all the five tests conducted in this series. The notations (N) and (S) stand for the results from the north side and south side of the beams and (m) stands for the mean value of (N) and (S). Figure 7.27 compares the mean shear load at three different stages of the tests, namely at the first appearance of the shear crack, the occurrence of the debonding crack over the support and the complete shear peeling of the plated beams. It can be seen that the load at which first shear crack occurred for all the plated beams are in a narrow range of 39.4 kN-52.5 kN , when compared with the corresponding value for the unplated beam (39 kN). However, there is a marked difference between the load at the occurrence of debonding crack over the support in the case of steel and CFRP plated beams (54.8-60.1 kN) and in the case of the low modulus GFRP plated beam (101.3 kN).

TABLE-7.5: TEST RESULTS

	SP-RF	SP-S5	SP-S8	SP-C	SP-CG
Plate dimensions(mmxmmxmm)	Nil	1400x75x5 steel	1400x75x8 steel	1400x80x6.5 CFRP	900x75x8.5 GFRP
Area of two side plates(mm^2)	-	750	1200	1040	1275
Elastic modulus of plate (MPa)	-	200,000	200,000	130,550	8,800
V at first shear crack (kN)	39	41.3(N) 37.5(S) 39.4(m)	52.5(N) 52.5(S) 52.5(m)	41.3(N) 41.3(S) 41.3(m)	45.0(N) 45.0(S) 45.0(m)
V at formation of debonding crack over the support (kN)	-	62.3(N) 48.8(S) 55.6(m)	54.8(N) 54.8(S) 54.8(m)	66.8(N) 53.3(S) 60.1(m)	101.3(N) 101.3(S) 101.3(m)
V at shear peeling (kN)	125.3* (V_u)	71.0(N) 62.3(S) 66.7(m)	77.3(N) 68.3(S) 72.8(m)	90.8(N) 71.3(S) 81.1(m)	120.0(N) 120.0(S) 120.0(m)
Maximum plate strain ($x10^{-6}$)	-	609(N) 477(S)	457(N) 454(S)	728(N) 667(S)	1842(N) 1527(S)
Maximum deflection (mm)	21.6	7.83	7.84	10.02	16.57

*Shear strength of beam

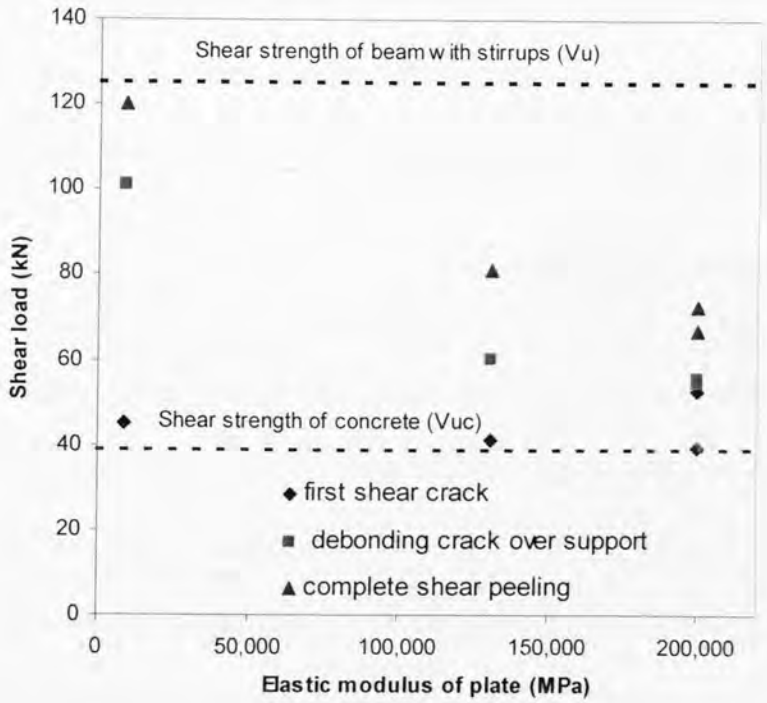

Fig.7.27 Variation of shear peeling strength with elastic modulus of plate

It can be seen that the shear peeling strength of the steel plated beams were only about 80% higher than that of the strength of the unplated RC beam without shear stirrups (V_{uc}), i.e. the shear load at which the first major shear crack was observed in the beam SP-REF. The shear peeling strength carbon FRP plated beam (SP-C) occurred at a higher shear load than that of the steel plated beams. However,

the shear peeling strength is still far less than the ultimate shear strength of the unplated beam (SP-REF). On the other hand, the beam bonded with the more flexible carbon and glass FRP plate debonded almost at the same shear load as that of the unplated beam. This is due to the fact that the shear stirrups were able to carry the shear load effectively after the occurrence of web shear cracks because of the flexibility of the external plate-adhesive-concrete interfaces. On the other hand, the steel plates were stiffer and hence, they debonded before the shear load can be transferred to the shear stirrups. It may also be noted that the maximum strain recorded in the plates at the instance of shear peeling is approximately about one-fourth that of the yielding strain in case of the steel plates and it was about 5% of the ultimate strain in case of the carbon FRP plate. This clearly indicates that shear peeling inhibits mobilising the full strength of the externally bonded plates.

7.9 Concluding remarks

The tests conducted on the reinforced concrete beams bonded with FRP and steel plates to the sides have shown that the shear peeling failure mechanism is qualitatively the same both for steel plates and FRP plated beams. However, the shear peeling strength increases with the decrease in the longitudinal elastic modulus of the plate material for the same area of cross section of side plates. On the one extreme, the plated beam with a very low modulus such as in SP-CG, the shear peeling strength is nearly the same as the ultimate shear strength of the unplated concrete beam with stirrups (SP-REF). On the other extreme, the steel plated beams debonded completely at a shear load that is about half the shear strength of the unplated RC beam (V_u).

CHAPTER-8: EXPERIMENTAL INVESTIGATION OF SHEAR PEELING IN R C BEAMS BONDED WITH STEEL ANGLES

CONTENTS

8.1 Introduction

Continuing with the investigation of shear peeling in plated beams, the next series of tests were carried out to study the shear peeling mechanism in reinforced concrete beams bonded with steel angles to the sides and soffits. The test results, the shear peeling mechanism observed in angle plated beams and the major implications of the investigations are discussed in this chapter. As discussed in section 2.9, there are equations available to determine the pure flexural peeling strength of angle plated beams but not for the shear peeling. Hence, the test results form the present study are used to validate the shear peeling model for angle plated beams in Chapter-11.

8.2 Specimens

The objective of this investigation is to study the shear peeling adjacent to the plate ends in beams glued with steel angles to their sides and tension faces. Two beams were used for this study and the details of the basic beam are shown in Fig.8.1. The beams were glued with angles of different dimensions and area of cross section as shown in Figs.8.2a and 8.2b. The two shear spans of the same beam were tested individually by applying a single point load at a distance 1200 mm form the support. The geometric properties of the beams tested are summarised in Table-8.1. Premature failure in the longer span was prevented by a suitable clamping arrangement.

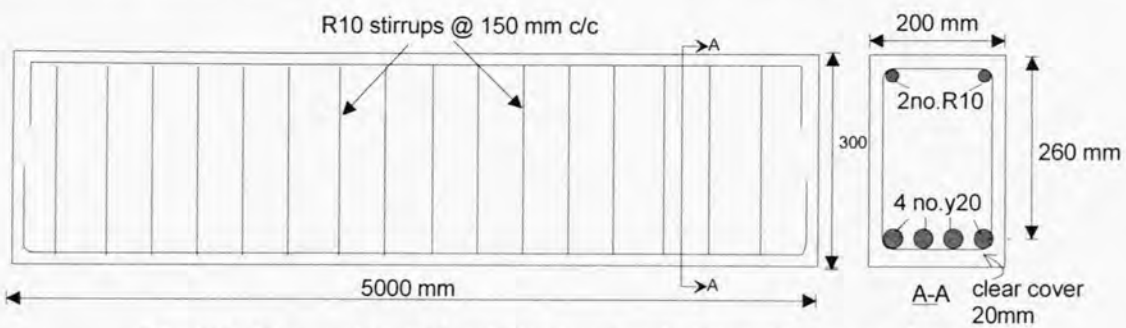

Fig.8.1. General details of the basic reinforced concrete beam

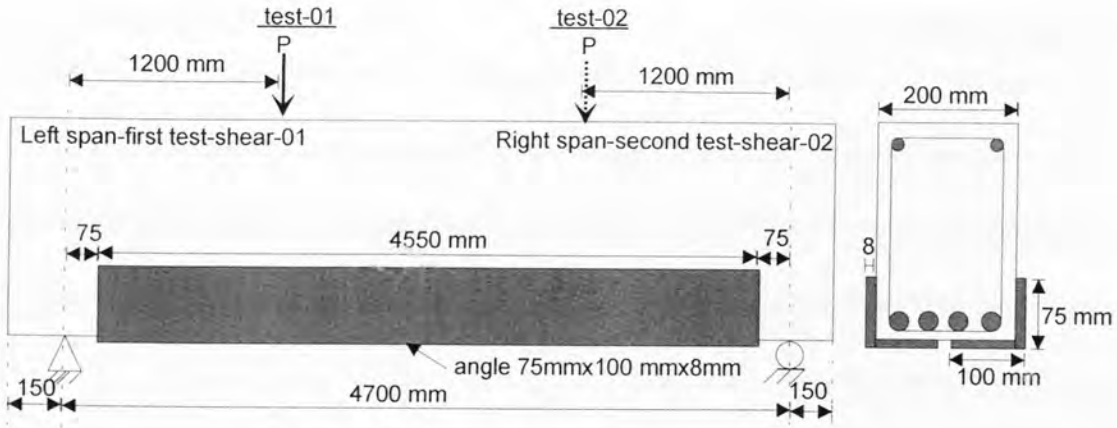

(a) Details of test shear-01 and test shear-02

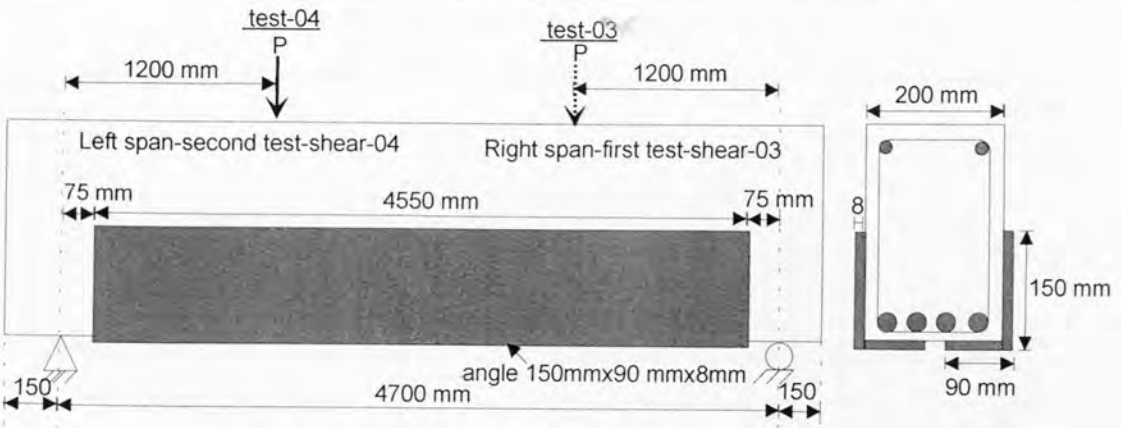

(b) Details of test shear-03 and test shear-04

Fig.8.2. Details of beams tests

TABLE-8.1 : Geometric properties

Common properties

Beam- width = 200 mm and depth = 300 mm

Compression reinforcement- Area A_{sc}=157 mm^2 and effective depth d_{sc} = 35 mm

Tension reinforcement - Area A_{st}=1256mm^2 and effective depth d_{st} = 260 mm

Shear stirrups- Area A_{sv} = 314 mm^2 and spacing s= 150 mm c/c

Total length of the beam = 5000 mm

The beams were simply supported and the effective span = 4700 mm

Shear span/depth of the beam = 4

Shear force in the span tested (V) = 74.5 % of the applied load (P)

Length of the angle = 4550 mm

Distance between the angle end and the nearest support = 75 mm

Specific properties

Test	External angle			
	height (mm)	width (mm)	thickness (mm)	area (mm^2)
Shear-01 and Shear -02	75	100	8	1336
Shear-03 and Shear -04	150	90	8	1856

8.3 Instrumentation

Strain gauges were bonded to the external angles both to their sides and soffits in order to detect the debonding at various sites of the plates. The arrangements of the strain gauges and their numbering are shown in Figs.8.3a and 8.3b for all the four tests conducted. The beam deflections at the load points were monitored by a dial gauge and also by a transducer.

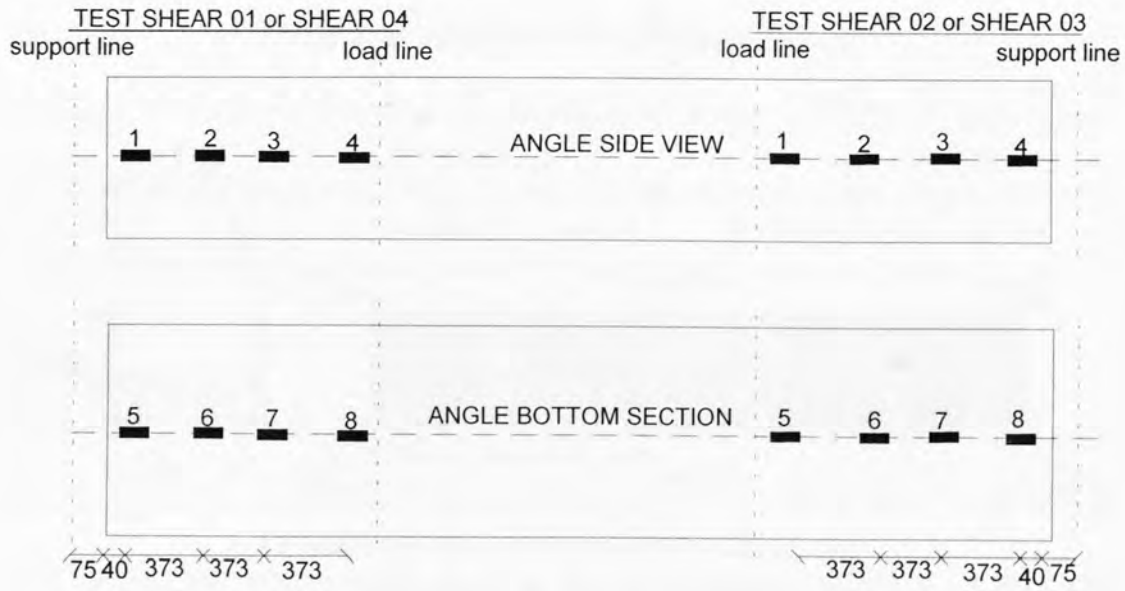

(a) North side angle

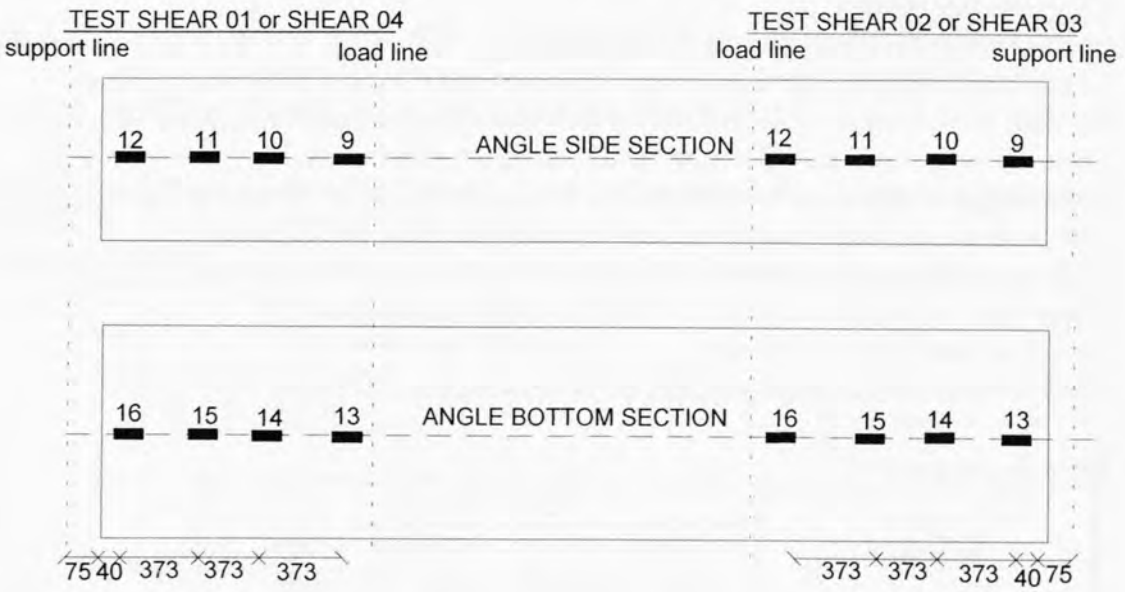

(b) South side angle

Fig.8.3. Strain gauge arrangement for shear-01, 02, 03 & 04

8.4 Material Properties

All the beams were cast in a single pour using ready mixed concrete supplied by a local manufacturer. Material properties of the concrete are shown in Table-8.2. In this table, the individual values of each test are given under the "i" column and their mean value under "m" column. As the beams were tested during a period 258-300 days, the material properties given in Table-8.2 for 302 days were used for analysing the test results.

Table -8.2. Material properties of the concrete

Age	E_c (MPa)		f_b (MPa)		f_c (MPa)		f_{cu} (MPa)		f_{tbm} (MPa)	
(days)	i	m	i	m	i	m	i	m	i	m
126	33786		3.72		46.7		54.9		6.29	
	32870	33329	4.51	4.28	45.4	46.9	55.5	55.7	5.79	6.03
	33240		4.62		48.7		56.6		6.00	
302	38142		4.76		49.7		59.5		5.93	
	36485	36705	4.39	4.41	49.8	50.0	58.3	58.3	5.71	5.63
	35488		4.09		50.4		57.2		5.28	

where E_c = Elastic modulus of the concrete, f_c = Cylinder compressive strength of the concrete, f_{cu}= Cube compressive strength of the concrete, f_b= Brazilian tensile strength of the concrete, f_{tbm} = Beam tensile strength of the concrete, i = individual test results and m = mean value.

Material properties of the steel plates, reinforcing bars and shear stirrups are shown in Table-8.3. The manufacturer's specifications of the material properties of the epoxy resin used for bonding the steel plates are indicated in Table-8.4.

Table -8.3. Material properties of the steel

Item	f_y (MPa)				f_u (MPa)			
Sample No.	1	2	3	Mean	1	2	3	Mean
Rebar Y20	478.7	485.1	478.1	480.6	566.3	567.5	565.3	566.4
Stirrup R10	-	-	-	-	601.0	603.7	606.3	602.4
Angle Plate	359.0	360.8	360.6	360.1	514.3	518.2	522.8	518.4

where f_y = Yield strength of the steel and f_u = Ultimate strength of the steel.

Table-8. 4. Material properties of the glue Hilti CA 273 after 2 days (as tested by the manufacturer)

Compressive strength (ISO 604)	Tensile strength (ISO 527)	Flexural strength (ISO 178)	Elastic modulus in compression (ASTM D 695)	Tensile bond strength (ISO 527)	Maximum operating temperature
110-120 MPa	30-40 MPa	20-30 MPa	5000-6000 MPa	10-15 MPa	80° C

8.5 Test results

8.5.1 Test Shear-01

Test-shear-01 was conducted on the beam glued with 75x100x8 mm angles (Fig.8.2a). The shear force (V) in the span tested was 74.5% of the total applied load (P).

8.5.1.1 Crack pattern and failure mode

The first crack to occur was the diagonal crack at a distance 300 mm from the load point when the applied load was 125 kN (V=93.1 kN). As the load was increased to 144 kN (V=107.3 kN), a diagonal shear crack originated from the support plate adjacent to angle end, as shown in Fig.8.4a and this extended further upwards until the applied was 169 kN (V = 125.9 kN). When the applied load was 184 kN (V= 137 kN), a horizontal debonding crack formed at the angle end from the critical diagonal crack. This crack eventually led to the complete shear peeling of the angle as shown in Fig.8.4b. The debonding crack propagated all along the top edge of the angle and was accompanied by a number of inclined cracks at regular intervals at P=185.4 kN (V= 138.2 kN). The beam was not able to sustain further load and the load dropped to 111.3 kN (V=82.9 kN) suddenly, at which the test was terminated. Figure 8.4c shows the separation of an angle along with cover concrete from the reinforcement cage due to shear peeling.

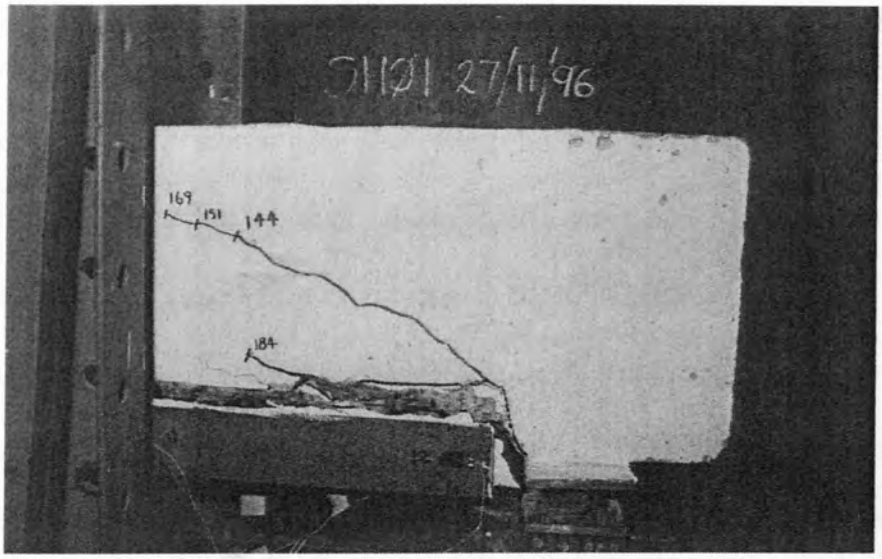

(a) Close view of the diagonal and debonding cracks at the angle end

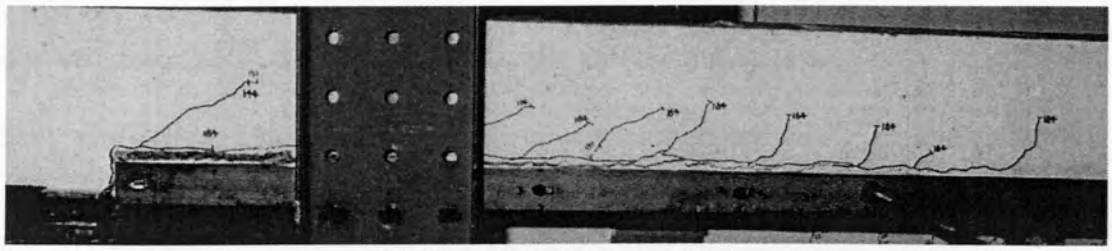

(b) Complete shear peeling

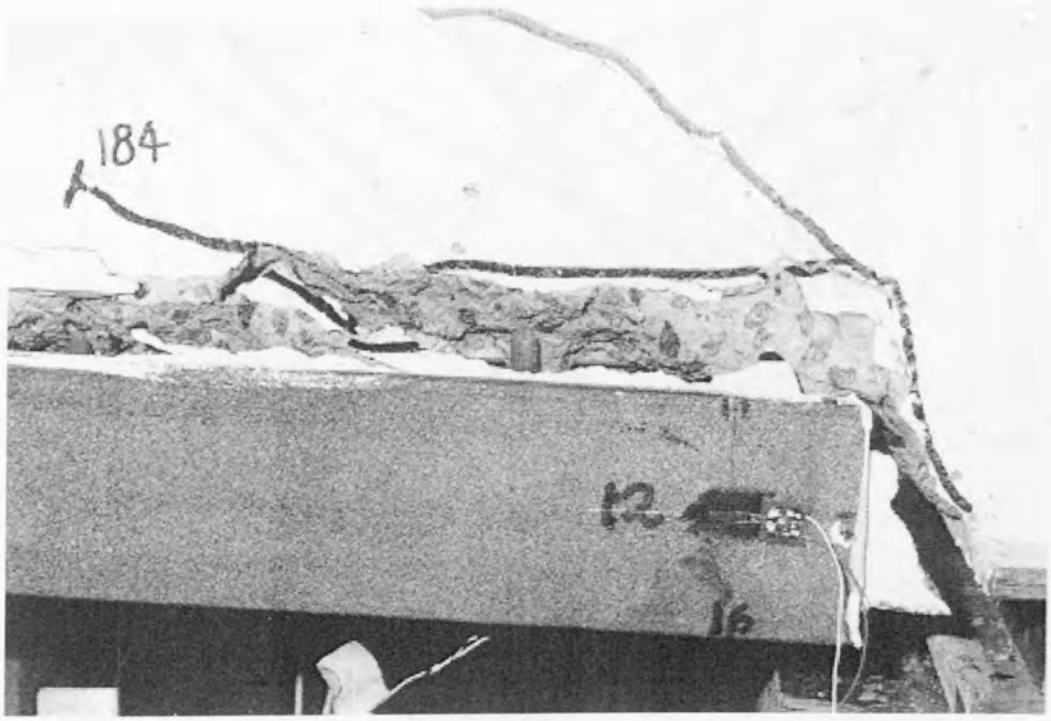

(c) Separation of concrete cover and angle from reinforcement cage

Fig.8.4. Test-Shear-01 : Crack patterns

8.5.1.2 Longitudinal strains in the sides and bottom levels of the angles

Figures 8.5a-d illustrate the variation of strains recorded at all gauge locations that are shown in Fig.8.3 with the shear load in the shear span tested. The curves for gauges #1, #5, #12 and #16 that were affixed at the ends of the angles show the local debonding due to the formation of the diagonal crack at the plate end at a shear load of 107.3 kN. At other locations, the strains increased linearly with the applied load till the complete shear peeling of the angles occurred at a shear load of 138.2 kN, which is marked by the simultaneous drop in strain readings at all locations. The peak strains recorded at the centre of the north angle side and soffit were 650 and 1030 microstrain respectively. The corresponding strains recorded on the south angle were 720 and 1040 microstrains. These magnitudes are much less than the yield strain of the steel angle (1830 microstrains).

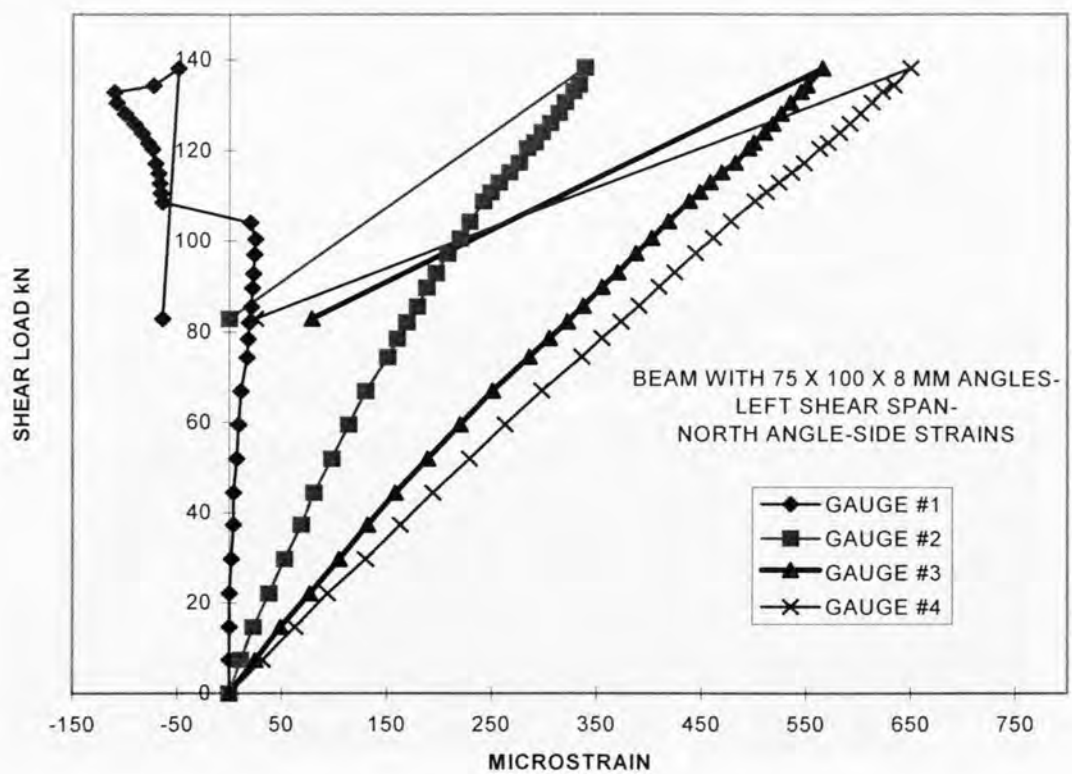

Fig.8.5a. Test-shear-01: Longitudinal strains-Side of north angle

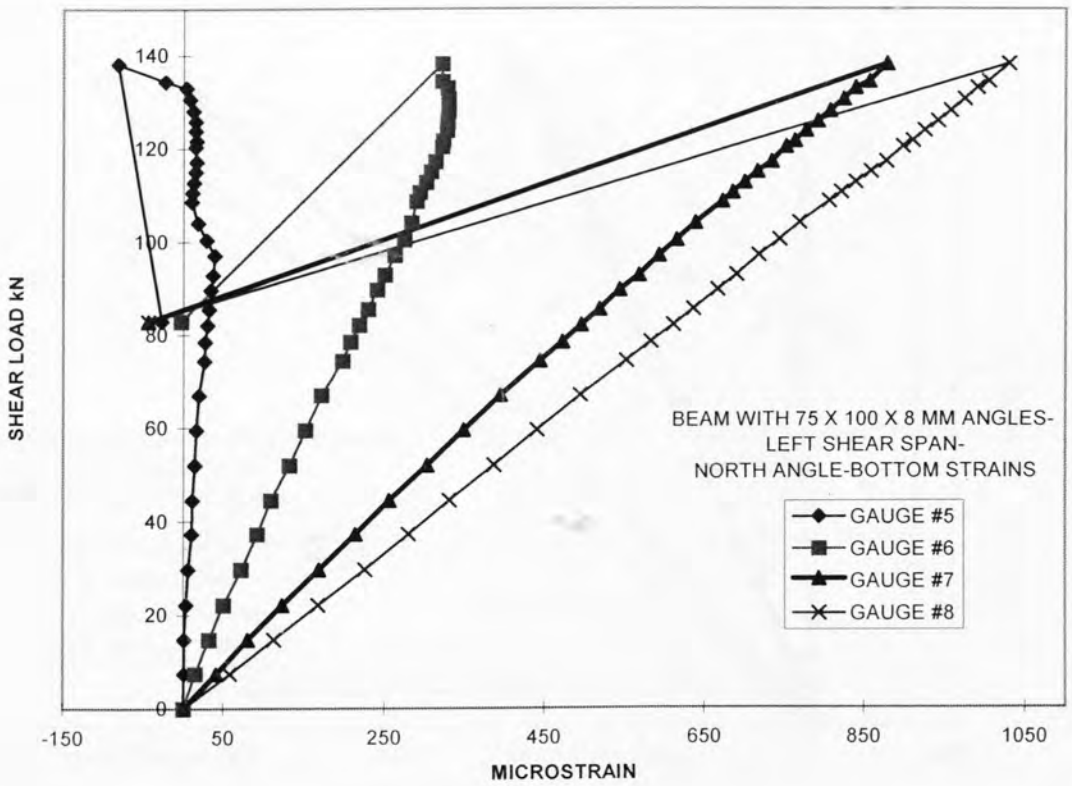

Fig.8.5b. Test-shear-01: Longitudinal strains-Soffit of north angle

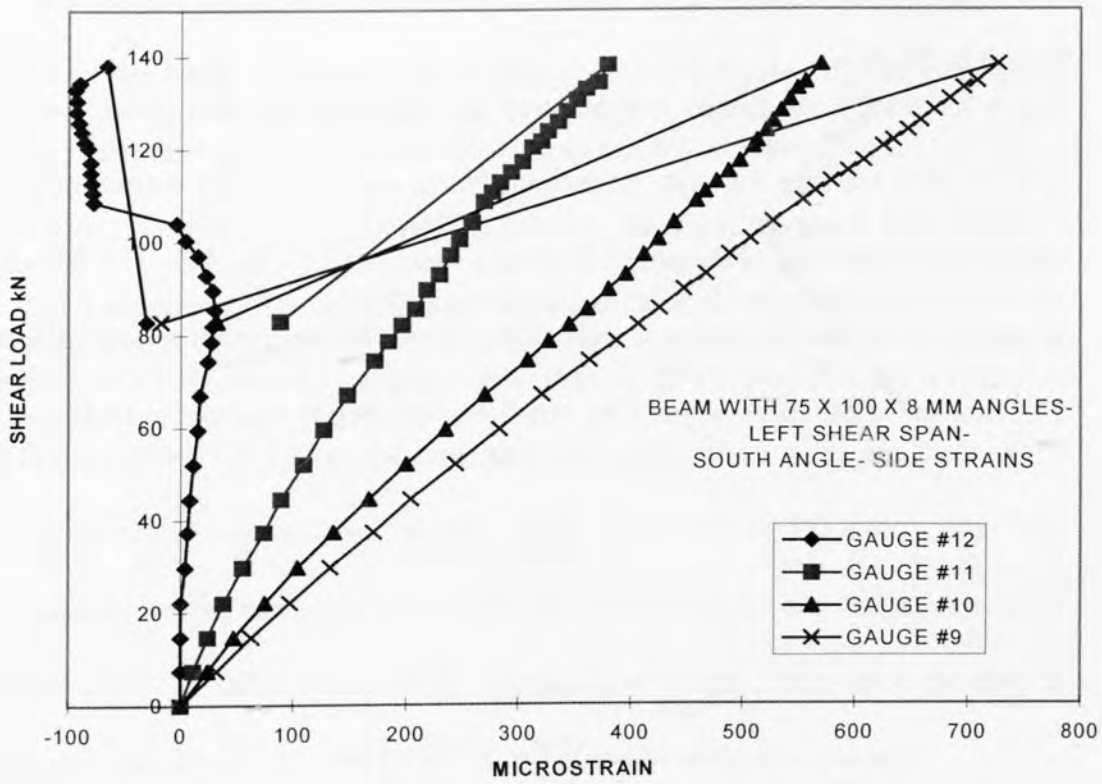

Fig.8.5c. Test-shear-01: Longitudinal strains-Side of south angle

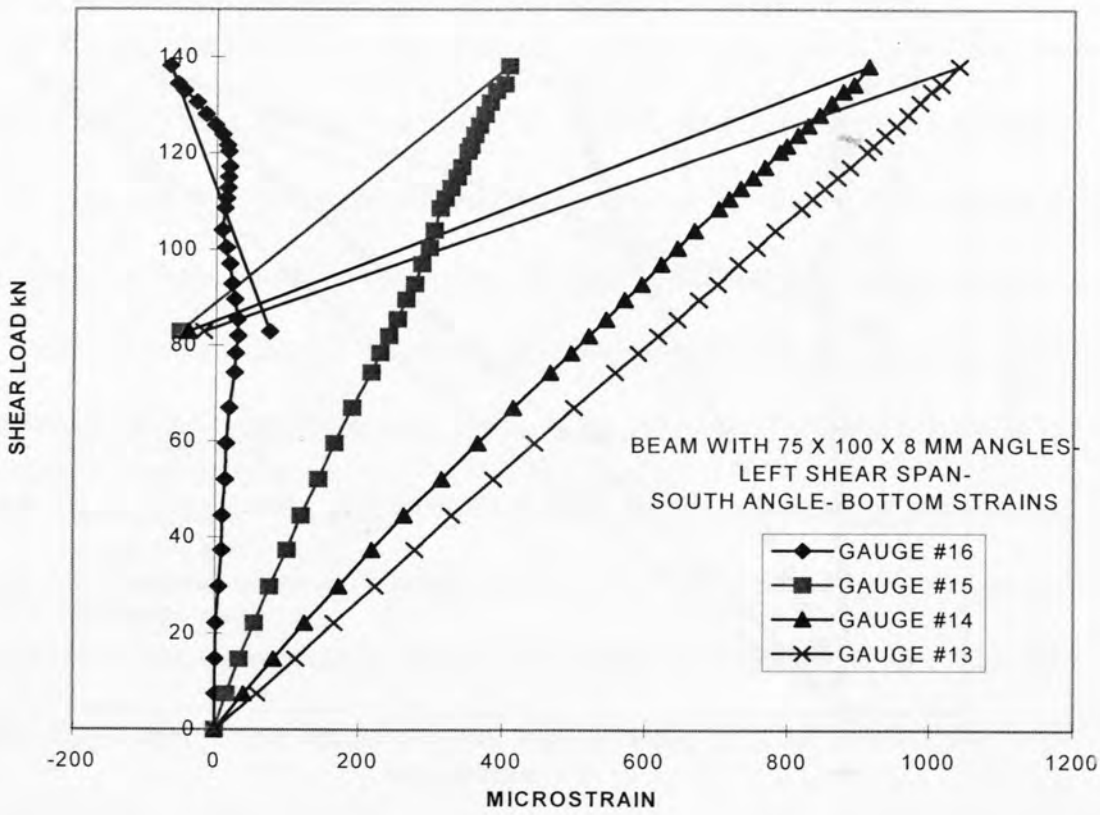

Fig.8.5d. Test-shear-01: Longitudinal strains-Soffit of south angle

8.5.1.3 Deflection

Figure 8.6 depicts the relationship between the deflection recorded at the load point and the shear load for this test. It shows a linear variation of the deflection till the complete shear peeling of the plated beam at a shear load of 138.2 kN. The debonding is marked by the sudden falling branch of the curve. The deflection at debonding was 15.2 mm and at the termination of the test due to the drop in load was at 19.49 mm.

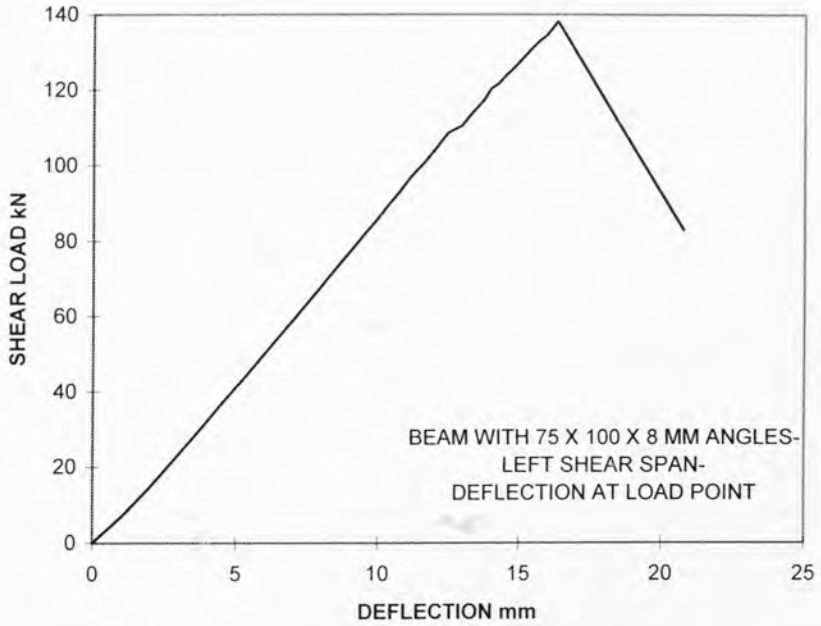

Fig.8.6. Shear-01: Deflection Vs Shear Load

8.5.2 Test Shear-02

Test-Shear-02 was conducted as a confirmatory test for test-shear-01.

8.5.2.1 Crack pattern and failure mode

The crack pattern and failure mode are similar to span-shear-01. At an applied load of 120 kN (V=89.4 kN), a diagonal shear crack appeared from the edge of the support plate as shown in Fig.8.7a and extended upwards as the load was increased. When the load was increased to 164 kN (V =122.2 kN), another crack appeared from the same root and it transformed into a horizontal debonding crack at an applied load of 170 kN (V=126.7 kN). Finally, the complete shear peeling of the plated beam occurred at P=179.6 kN (V=133.8 kN) as the horizontal debonding crack extended beyond the load point along the top edge of the angle, as shown in Fig.8.7b. This was accompanied by the formation of a series of inclined cracks and the separation of concrete cover and the angles from the reinforcement gauge. This led to the drop in load to a magnitude of 107.1 kN (V =79.8 kN) at which the test was ended.

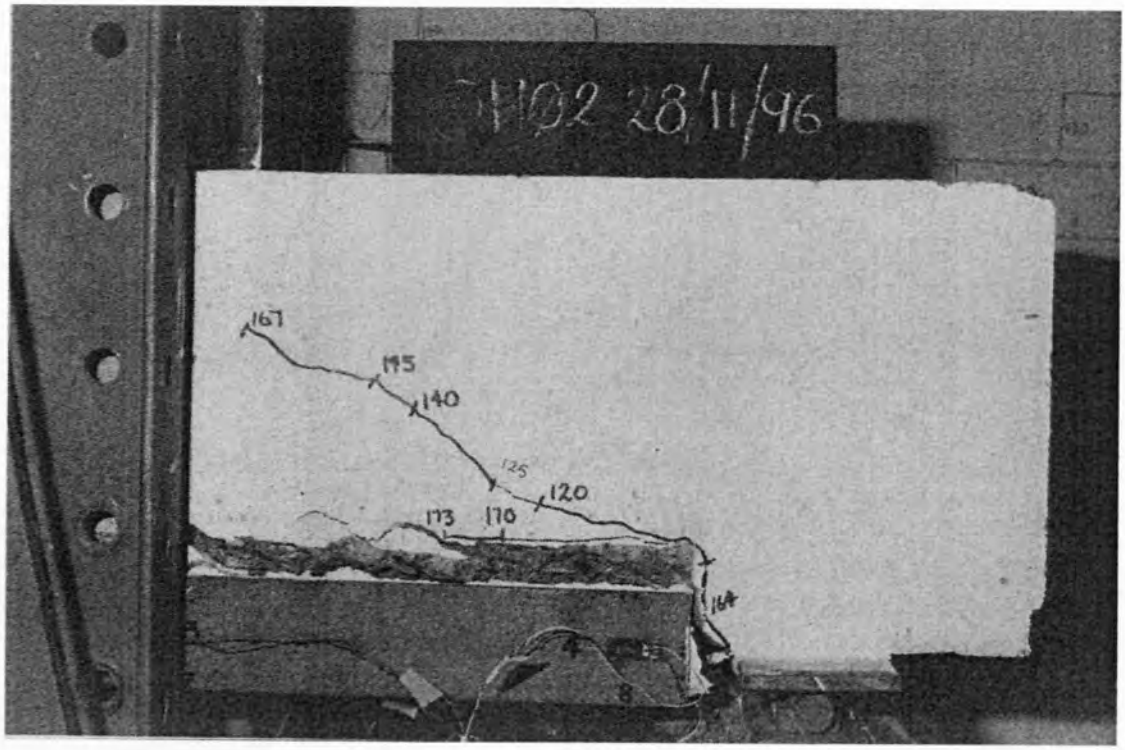

(a) Close view of the diagonal and debonding cracks at the angle end

(b) Complete shear peeling

Fig.8.7. Test-Shear-02 : Crack patterns

8.5.2.2 Longitudinal strains in the sides and bottom levels of the angles

Figures 8.8a-d show the variation of strains recorded at all gauge locations that are shown in Fig.8.3 with the shear load in the shear span tested. It can be seen that the formation of the critical diagonal shear crack in the vicinity of the angle ends at a shear load of 89.4 kN is marked by the slight reduction in strain values at gauge locations #4, #8, #9 and #13 that were affixed very close to the angle ends. Similarly, the initiation of the debonding crack at a shear load of 122 kN is marked by the reduction in strains in gauge locations #3,#7,#10 and #14. Finally, the rapid propagation of the horizontal debonding crack along the top edge of the angle and

subsequent shear peeling is denoted by the rapid drop in strain and load readings at all gauge locations.

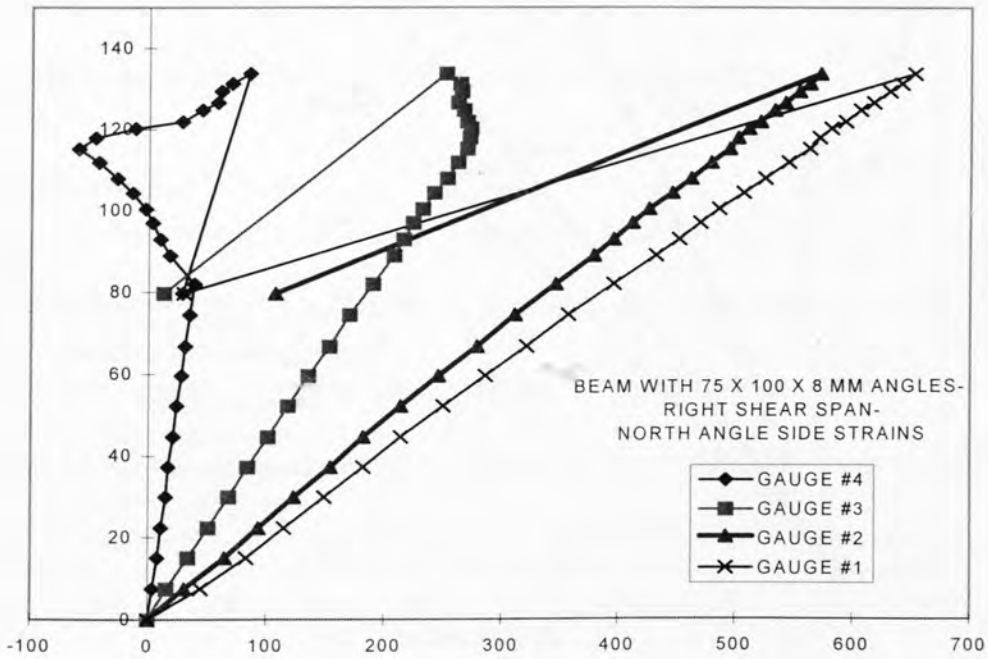

Fig.8.8a. Test-shear-02: Longitudinal strains-Side of north angle

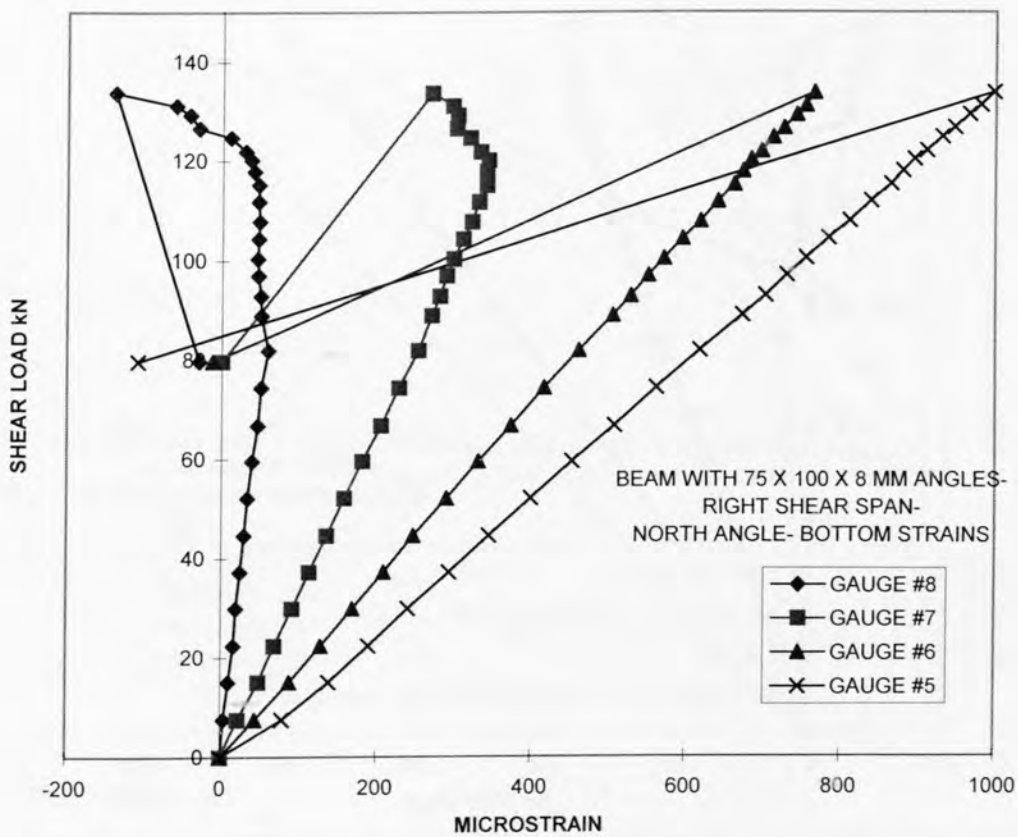

Fig.8.8b. Test-shear-02: Longitudinal strains-Soffit of north angle

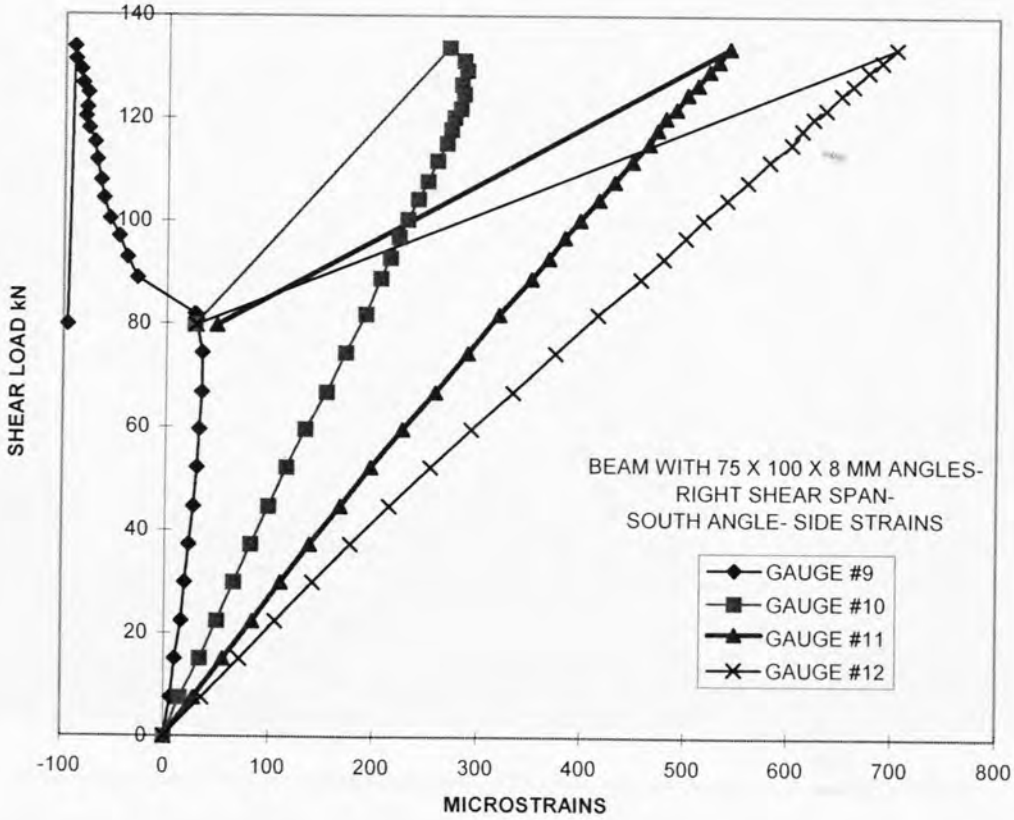

Fig.8.8c. Test-shear-02: Longitudinal strains-Side of south angle

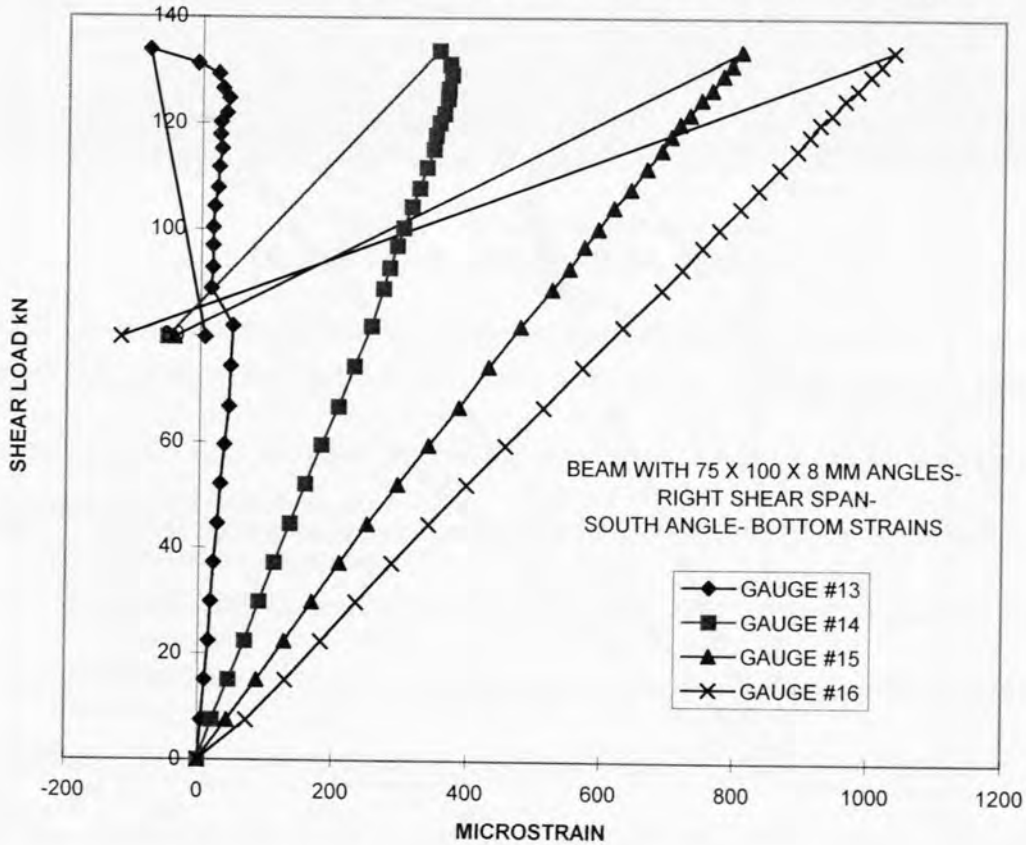

Fig.8.8d. Test-shear-02: Longitudinal strains-Soffit of south angle

The peak strain magnitudes recorded on the side and soffit of the north side angle were 652 and 998 microstrains respectively; the corresponding magnitudes on the south side angle were 702 and 1035 microstrains. This shows that the angle did not yield as the yield strain of the angle plate is 1830 microstrains.

8.5.2.3 Deflection

Figure 8.9 illustrates the relationship between the deflection recorded at the load point and the shear load for this test. It shows that the deflection increased linearly with the applied load till the complete shear peeling of the plated beam occurred at a shear load of 133.8 kN. The debonding is marked by the sudden fall in shear load from 133.8 kN to 79.8 kN. The deflection at debonding was 15.23 mm and at the termination of the test due to the drop in load was 20.04 mm.

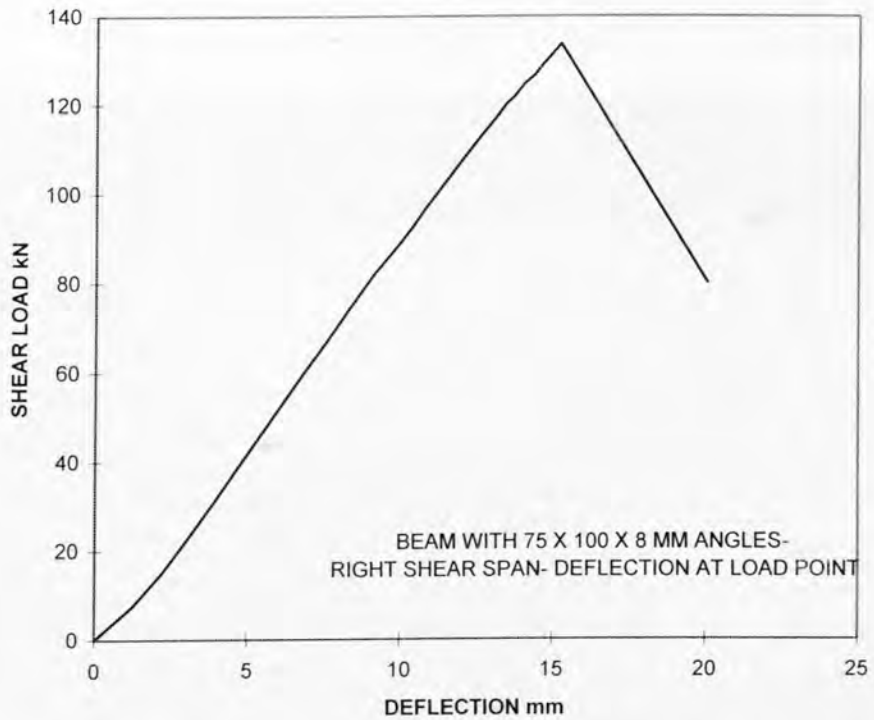

Fig.8.9. Shear-02: Deflection Vs Shear Load

8.5.3 Test Shear-03

Test-shear-03 was conducted on the beam bonded with 150x90x8 mm angles (Fig.8.2b). The shear force (V) in the span tested was 74.5% of the applied load (P).

8.5.3.1 Crack pattern and failure mode

As the angle is 150 mm deep, the shear crack at the angle end formed and extended along the sides of the angle. This happened on the north side when the applied load was 140 kN (V=104.3 kN) and on the south side at 151 kN (V=112.5 kN), as shown in Fig.8.10. This crack propagated diagonally upwards as the load was increased to 148 kN (V=110.3 kN) on the north side. This happened on the south side when the applied load was in the range of 166-172 kN (V = 123.7-128.1 kN). These diagonal cracks extended further with the increased load. Finally, the complete shear peeling of the angles occurred at an applied load of 214 kN (V=159.4 kN), due to the formation of a long horizontal debonding crack that extended from the angle end to the load point and which was accompanied with a series of inclined cracks as shown in Fig.8.11. The load also dropped to 122.2 kN (V= 91 kN), at which the test was ended.

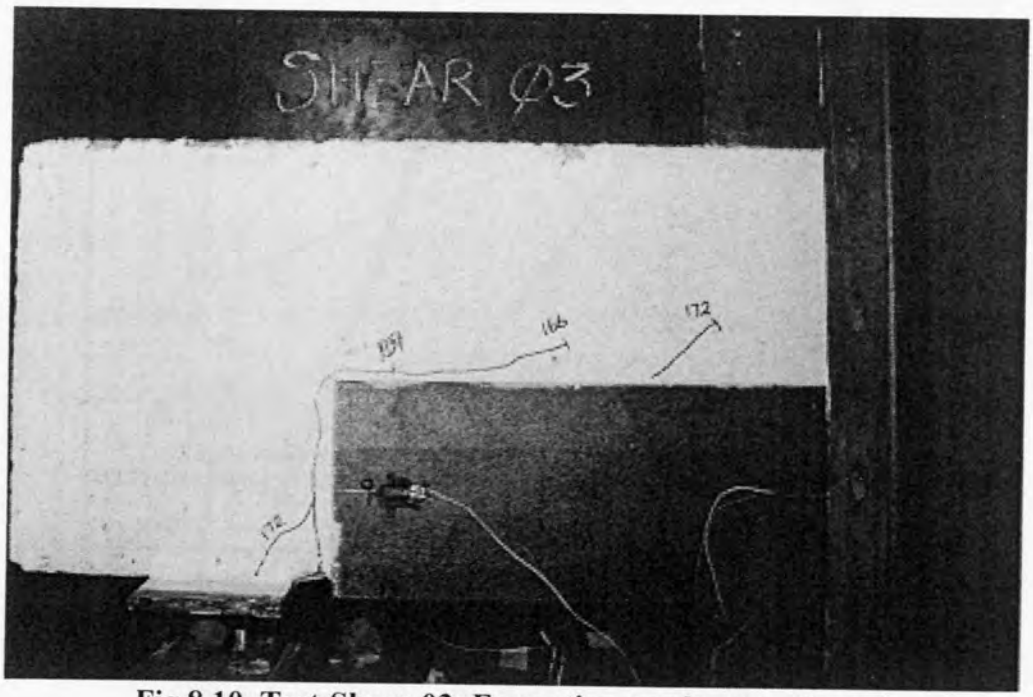

Fig.8.10. Test-Shear-03: Formation cracks at angle end

Fig.8.11. Test-Shear-03: Complete shear peeling

8.5.3.2 Longitudinal strains in the sides and bottom levels of the angles

Figures 8.12a-d depict the variation of strains recorded at all gauge locations that are shown in Fig.8.3 with the shear load in the shear span tested. It can be seen that the formation of the critical shear crack in the vicinity of the angle ends at a shear load of 104.3 kN on the north side is marked by the slight reduction in strain values at gauge locations #4 and #8. Similar reductions at gauge locations #9 and #13 show the formation of the crack at south side at 112.5 kN. Similarly, the initiation of debonding crack is denoted by the kinks in strains in gauge locations #3, #7, #10 and #14. Finally, the rapid propagation of the horizontal debonding crack along the top edge of the angle and subsequent shear peeling at a shear load of 159.4 kN is denoted by the rapid drop in strain and load readings at all gauge locations. The peak strain magnitudes recorded on the side and soffit of the north side angle were 425 and 1333 microstrains respectively; the corresponding magnitudes on the south side angle were 507 and 1328 microstrains. These magnitudes are less than the yield strain of the angle plate (1830 microstrains).

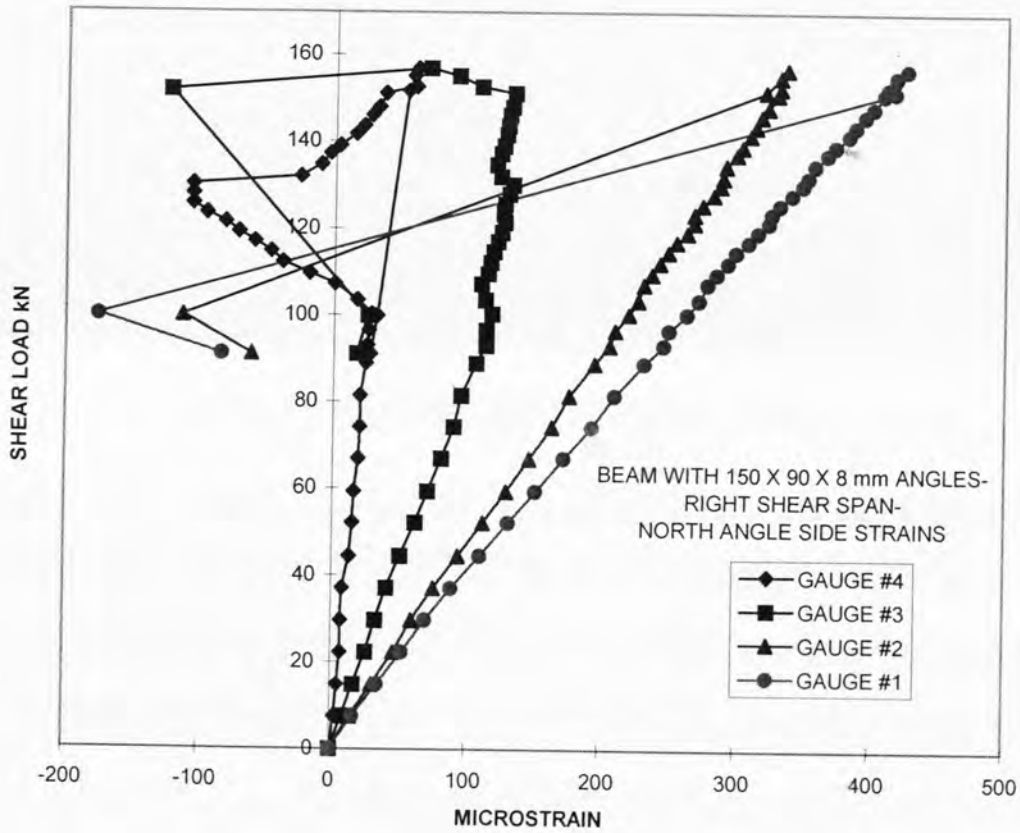

Fig.8.12a. Test-shear-03: Longitudinal strains-Side of north angle

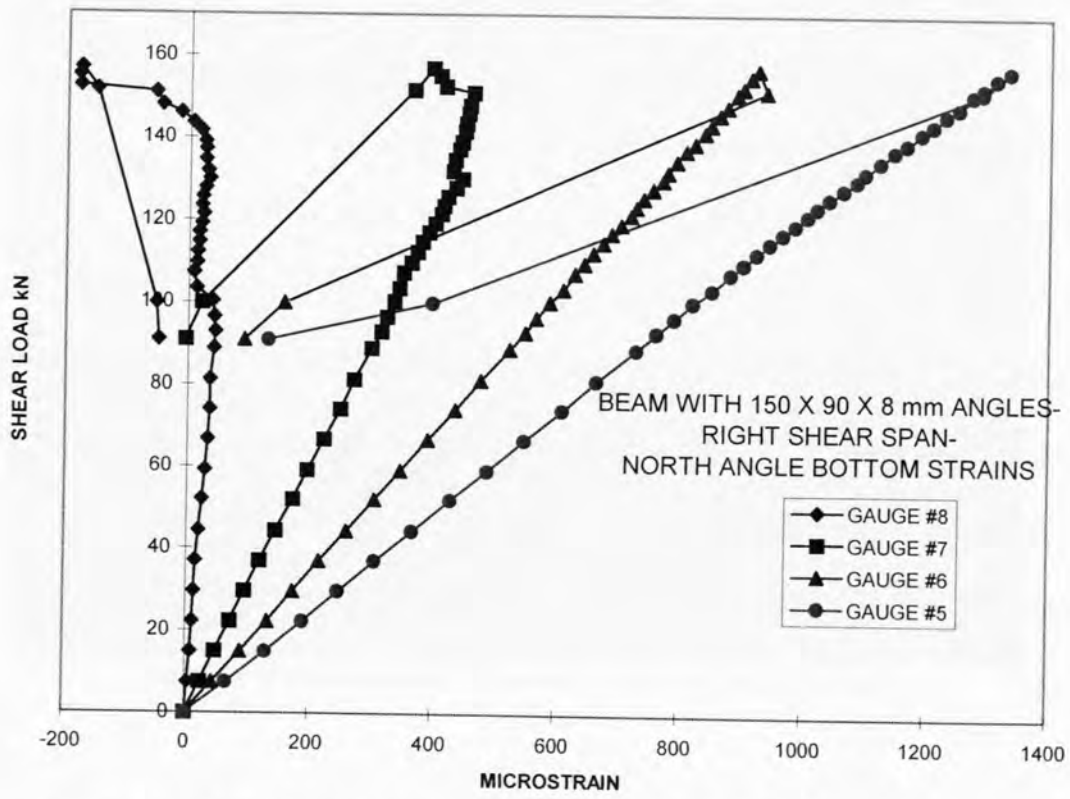

Fig.8.12b. Test-shear-03: Longitudinal strains-Soffit of north angle

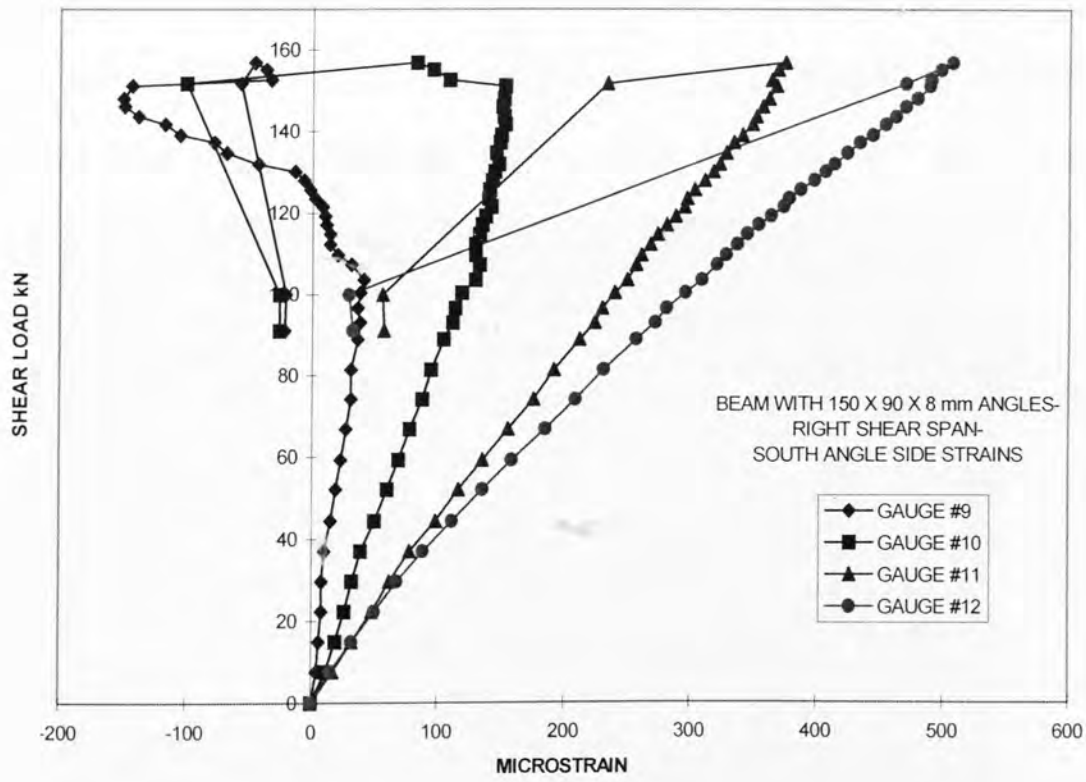

Fig.8.12c. Test-shear-03: Longitudinal strains-Side of south angle

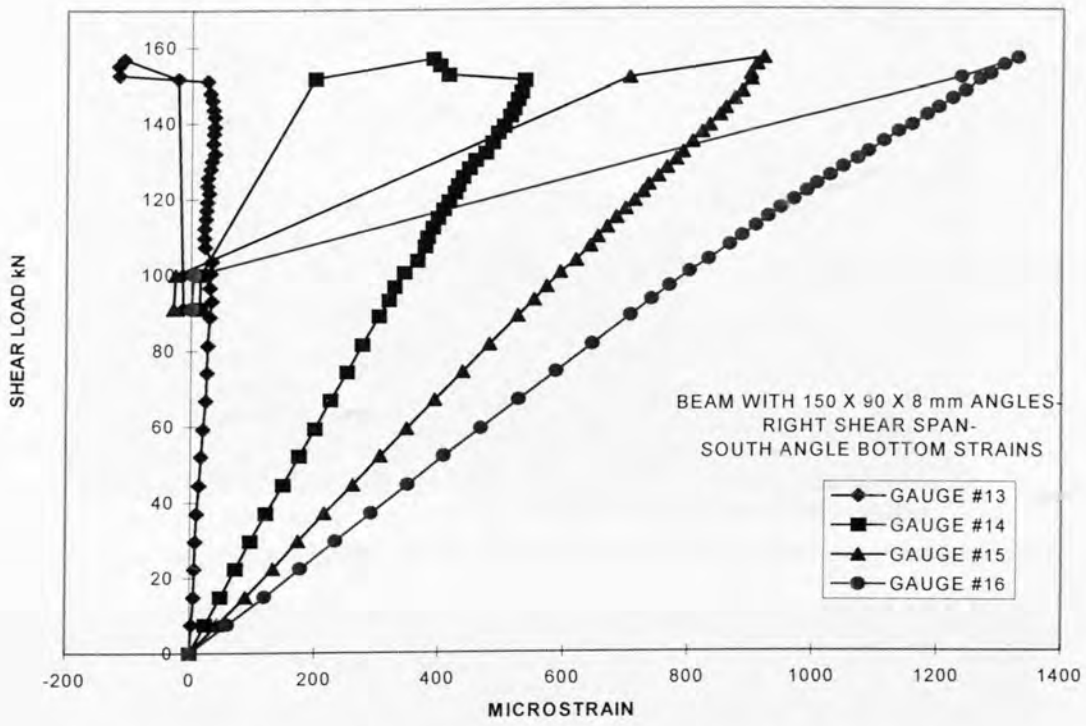

Fig.8.12d. Test-shear-03: Longitudinal strains-Soffit of south angle

8.5.3.3 Deflection

The relationship between the deflection recorded at the load point and the shear load for this test is shown in Fig.8.13. It shows that the deflection increased with the

increase in applied load till the complete shear peeling of the plated beam occurred at a shear load of 159.4 kN. The debonding is marked by the sudden fall in shear load from 159.4 kN to 91 kN. The deflection at debonding was 21.24 mm and it was 24.38 mm at the termination of the test.

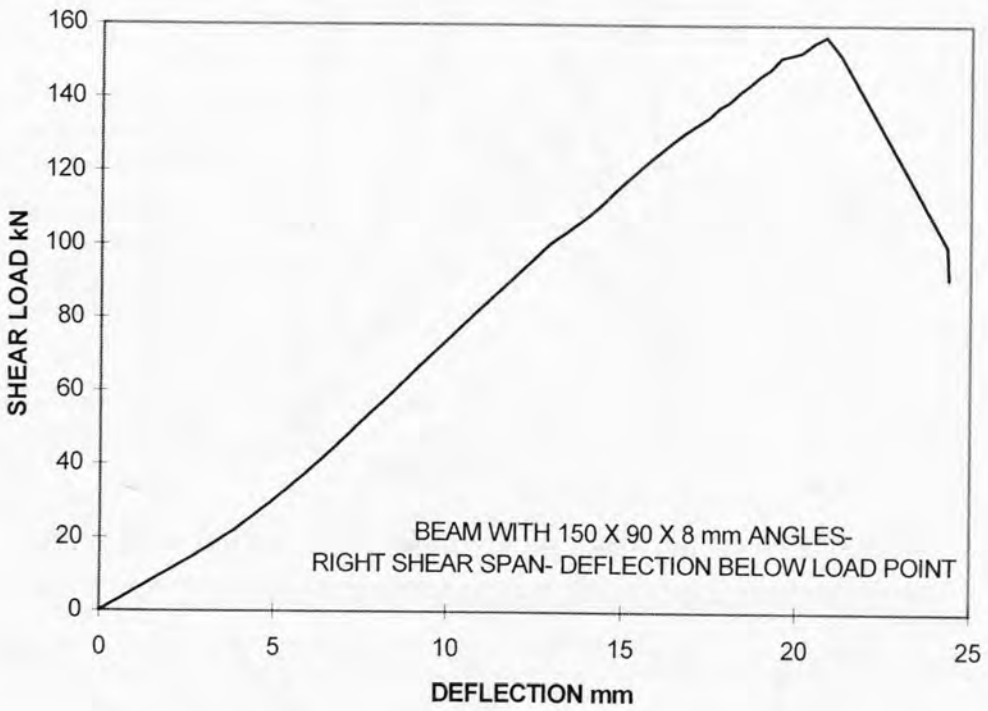

Fig.8.13 Shear-03: Deflection Vs Shear Load

8.5.4 Test Shear-04

This test is same as the test shear-03 and it was conducted to confirm the results from test shear-03.

8.5.4.1 Crack pattern and failure mode

Inclined cracks occurred from the support and extended to the top corner of both angles at an applied load of 158 kN (V=117.7 kN), as shown in Fig.8.14a. The crack extended further when the applied load was 178 kN (V = 132.6 kN). When the applied load was in the range 184 kN-196 kN (V = 137-146 kN), another crack part horizontal-part inclined formed from the corner of the angles as shown in Fig.8.14b. Finally, the beam failed in shear peeling due to the formation of a long horizontal

debonding crack accompanied by a series of inclined cracks as shown in Fig.8.15, at an applied load of 217 kN (V=161.7 kN). Afterwards, the load dropped to 140.7 kN (V = 104.8 kN) and the test was terminated.

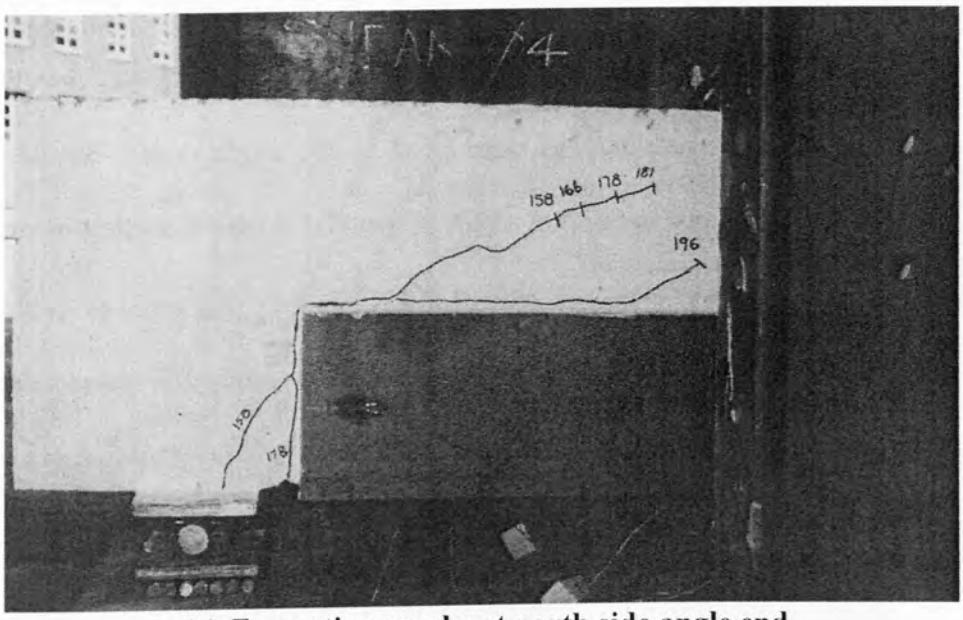

(a) Formation cracks at north side angle end

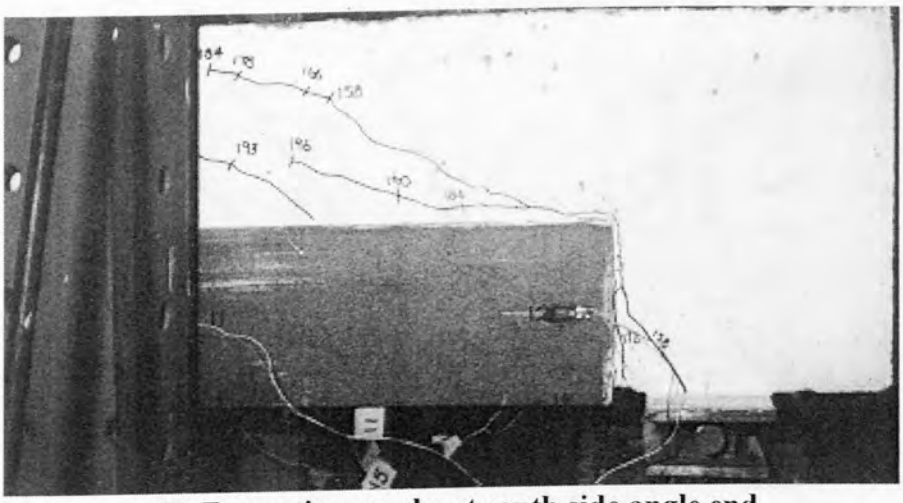

(b) Formation cracks at south side angle end

Fig.8.14. Test-Shear-04 : Crack patterns at angle ends

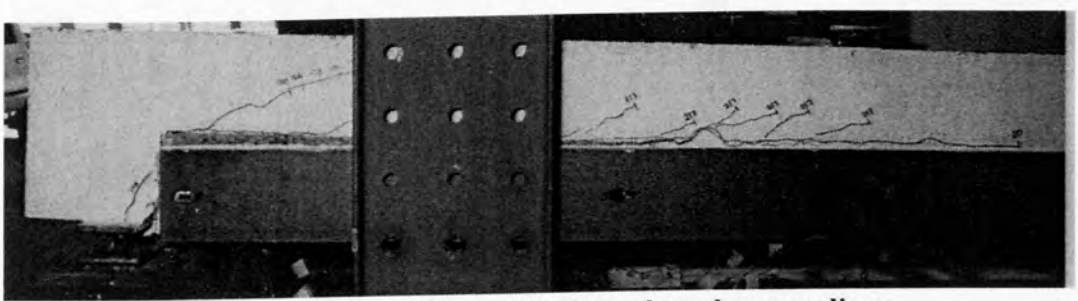

Fig.8.15. Test-Shear-04: Complete shear peeling

8.5.4.2 Longitudinal strains in the sides and bottom levels of the angles

Figures 8.16a-d show the variation of strains recorded at all gauge locations that are shown in Fig.8.3 with the shear load in the shear span tested. It can be seen that the formation of the critical diagonal shear crack in the vicinity of the angle ends at a shear load of 117.7 kN is marked by a reduction in strain values at gauge locations #1, #5 , #12 and #16 that were affixed very close to the angle ends. Similarly, the occurrence of the horizontal debonding crack is denoted by the reduction in strains in gauge locations #2, #6, #11 and #15 at V= 146 kN. Finally, the rapid propagation of the horizontal debonding crack along the top edge of the angle and subsequent shear peeling is denoted by the rapid drop in strain and load readings at all gauge locations at V=161.7 kN.

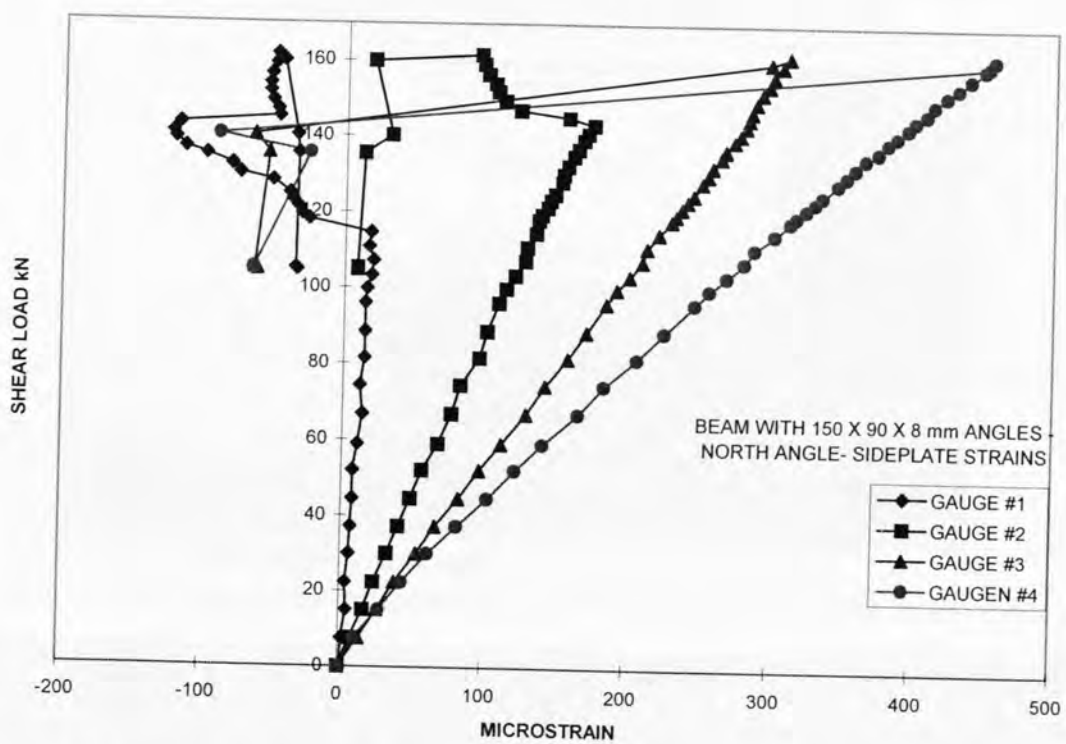

Fig.8.16a. Test-shear-04: Longitudinal strains- Side of north angle

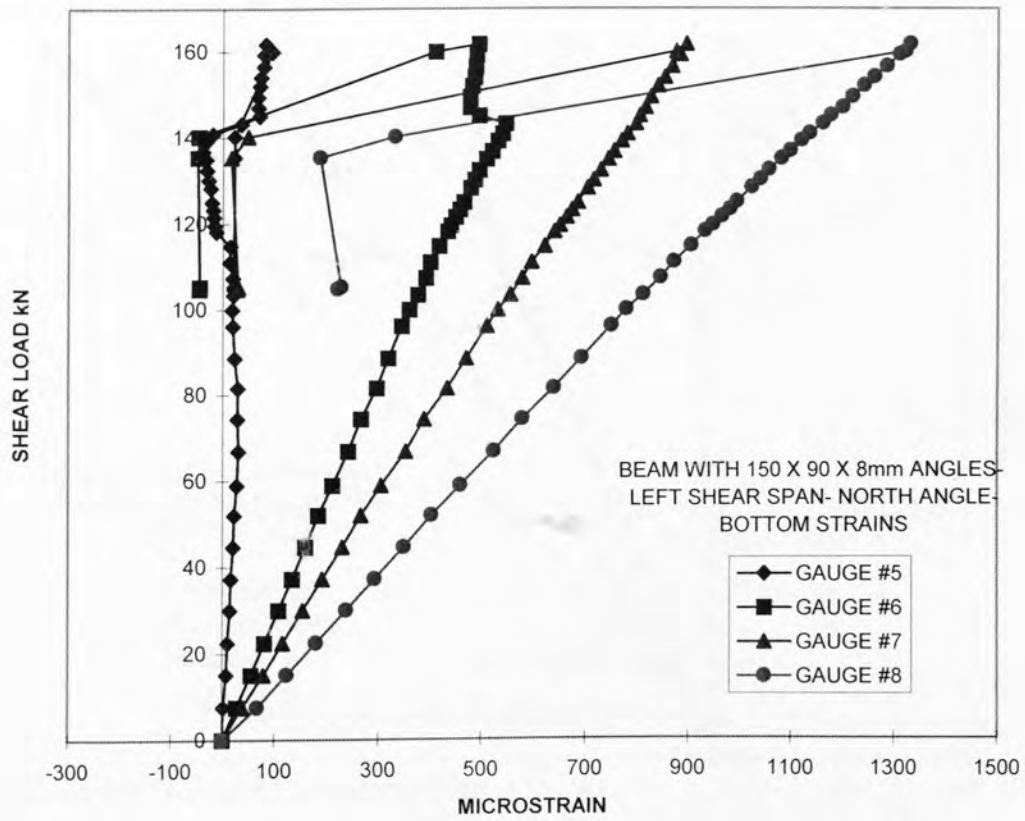

Fig.8.16b. Test-shear-04: Longitudinal strains- Soffit of north angle

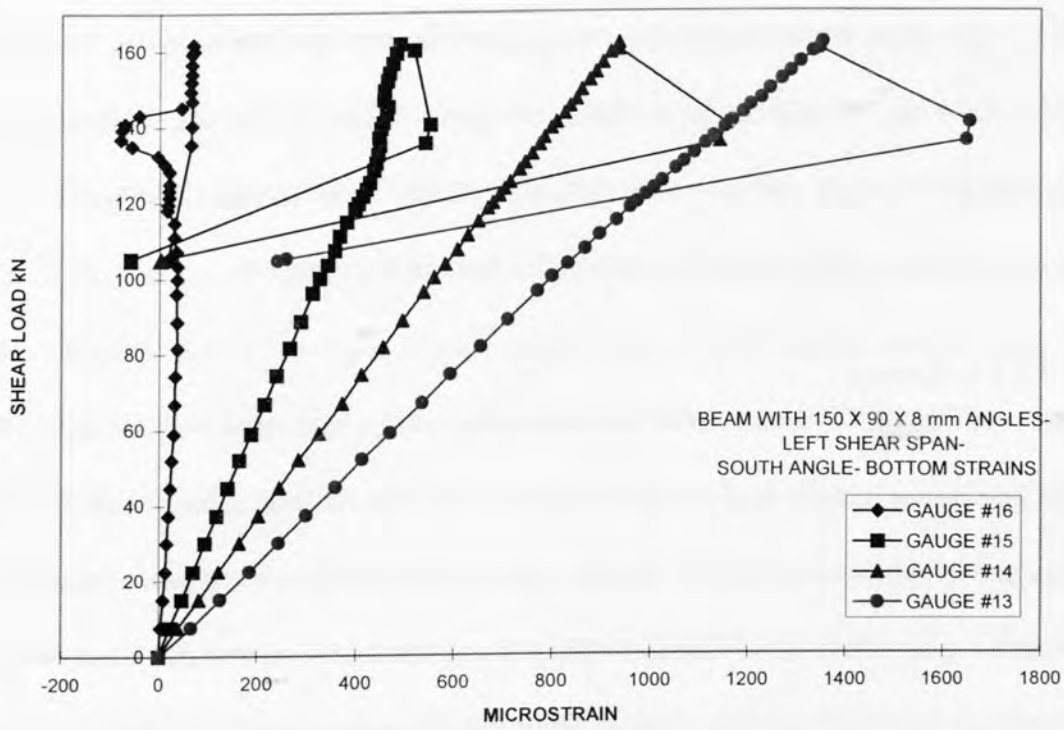

Fig.8.16c. Test-shear-04: Longitudinal strains- Side of south angle

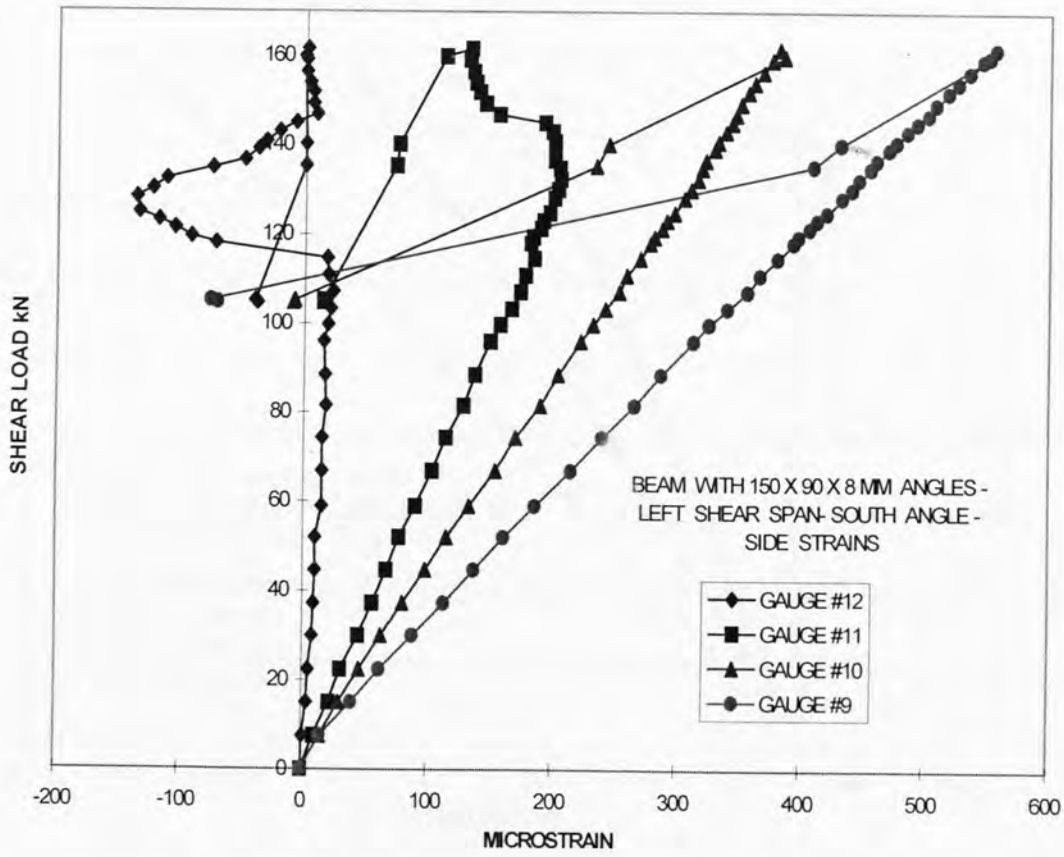

Fig.8.16d. Test-shear-04: Longitudinal strains- Soffit of south angle

The peak strain magnitudes recorded on the side and soffit of the north side angle were 456 and 1331 microstrains respectively; the corresponding magnitudes on the south side angle were 556 and 1655 microstrains. This shows that the angle did not yield as the yield strain of the angle plate is 1830 microstrains.

8.5.4.3 Deflection

The relationship between the deflection recorded at the load point and the shear load for this test is shown in Fig.8.17. It shows that the deflection increased with the increase in applied load till the complete shear peeling of the plated beam occurred at a shear load of 161.7 kN. The debonding is marked by the sudden fall in shear load from 161.7 kN to 104.7 kN. The deflection at debonding was 23.27 mm and at the termination of the test was 25.6 mm.

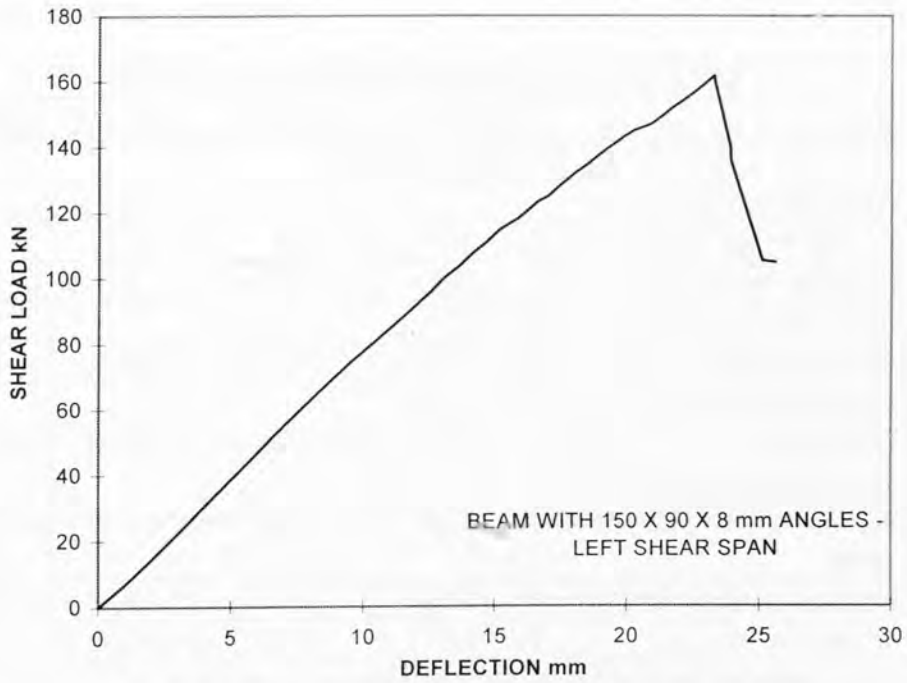

Fig.8.17. Shear-04: Deflection Vs Shear Load

8.6 Discussion of test results

Table-8.5 summarises the outstanding features of the test results obtained from all the four tests. The failure mode of all the four shear spans were similar and can be summarised as follows: first, an inclined shear crack originated from the edge of the support plate and it propagated along the height of angle sides; then a horizontal debonding crack formed from this crack and after a certain increment in shear load, the shear peeling of plated beam occurred as the debonding crack extended rapidly along the top edge of the angles accompanied with a series of parallel, inclined cracks. This led to the quick drop in load. It was also observed that none of the angles recorded strains higher than the yield strain of the angle plate (1830 microstrain). The mean shear peeling strength for shear-01 and shear-02 that were bonded with angles of dimension 75 mm x 100 mm x 8 mm was 136.0 kN. The corresponding value for shear-03 and shear-04 that were bonded with 150 mm x 90 mm x 8 mm angles was 160.55 kN. This represents an increase of 18 % over shear-01 and shear-02, even though the increase in area of external angles was 39 %.

TABLE-8.5: Experimental and analytical results

No.	Item	Shear-01	Shear-02	Shear-03	Shear-04
	TEST RESULTS				
1.	**Angle dimensions**				
	(a) side height (mm)	75	75	150	150
	(b)soffit width (mm)	100	100	90	90
	(c) thickness (mm)	8	8	8	8
	(d) Area (mm^2)	2672	2672	3712	3712
2.	**Shear load (kN) at**				
	(a)formation of shear crack at angle end	107.3	89.4	104.3	117.7
	(b)Initiation of debonding crack	137.0	126.7	104.3	137.0
	(c) total shear peeling	138.2	133.8	159.4	161.7
	(d) end of test	82.9	79.8	91.0	104.8
3.	**Longitudinal strain at peeling in angles (microstrain)**				
	(a) North-side centre	650	652	425	456
	(b) North-soffit centre	1030	998	1333	1331
	(c) South-side centre	720	702	507	556
	(d) South -soffit centre	1040	1035	1328	1655
4.	**Deflection at load point (mm)**				
	(a) at peeling	15.20	15.23	21.24	23.27
	(b) at termination of test	19.49	20.04	24.38	25.60
5.Shear strength of concrete beam as per AS-3600					
a	Shear strength of concrete V_{uc} (kN)	70.3	70.3	70.3	70.3
b	Shear strength of stirrups V_{us} (kN)	164.0	164.0	164.0	164.0
c	Shear capacity of beam (V_{uc}+ V_{us}) (kN)	234.3	234.3	234.3	234.3

As no test was carried out to determine the shear strength of the unplated RC beam, it was estimated using AS-3600 formulae and the magnitudes are shown in Table-8.5. The shear peeling strength in all these tests varied between 200 to 230% of V_{uc} of the basic concrete beam, as can be seen from Table-8.5. However, the shear peeling strength of the angle plated beams (133.8 kN-161.7 kN) were far less than the shear capacity of the reinforced concrete beam (234.3 kN).

8.7 Concluding remarks

1. Tests on reinforced concrete beams bonded with steel angles have shown that the shear peeling is caused by the formation of a critical diagonal crack in the vicinity of the angle ends.
2. The shear peeling occurs well before the internal shear stirrups are fully mobilised. However, the shear peeling strengths were 200 to 230 % higher than the shear strength of concrete beam (V_{uc}) only.
3. The beam with a deeper angle carried about 20% more shear load, even though the total area of angles was about 40% more than the shallow angles.

CHAPTER-9: EXPERIMENTAL INVESTIGATION OF SHEAR PEELING OF COMPRESSION FACE PLATED RC BEAMS

CONTENTS

9.1 Introduction

In practice, plates may have to be bonded to the compression faces of the reinforced concrete beams as in the case of a continuous beam where the tension face plate can be extended beyond a point of contraflexure. This can be explained by referring to the inner span of the plated continuous beam in Fig.2.21a with the applied stress resultants shown in Fig.2.21b. The experimental research and the peeling models described for tension face plated beams in Chapter-2 pertain only to simply supported beams and, hence, only apply directly to the sagging or positive region A-A of the continuous beam, where the stress resultants have the same shape as those in the simply supported beam as shown in Fig.2.5b. A need may arise to extend the plate-ends, say C or F in Fig.2.21a to the compression face region E-D in order to prevent peeling of the tension face plates. In this case, the debonding models for tension face plated beams are not directly applicable to the compression face plated beams. Furthermore, plates may have to be bonded to the compression face in addition to the tension face, to improve the ductility of the over-reinforced tension face plated beams. Hence, the present study was undertaken to investigate the various peeling modes of compression face plated beams so as to develop debonding models as in the case of tension face plated beams.

In this chapter, the test results from the study conducted on the pure shear peeling aspects are presented. The shear peeling behaviour of compression face plated beams are compared with that of tension face plated beams and the salient conclusions are presented. The test results were used to develop and calibrate a mathematical model as described in Chapter-11. The study conducted on the pure flexural peeling of the compression face plates is described in Chapter-12 and the

investigations on the interaction between shear and flexural peeling will be dealt with in Chapter-14.

9.2 Specimens

Three beams were used for this study and they were tested previously for pure flexural peeling of compression or tension face plated beams in FP series in Chapter-12. As the failure plane for the present study is different from the pure flexural peeling failure plane of the previous study, these beams were repaired before bonding new external plates. The beams were tested to fail under shear and the main parameter varied was the thickness of the external plate.

Figure 9.1a shows the details of the basic reinforced concrete beams to which the plates were bonded. A 2300 mm long and 12 mm thick steel plate was adhesively bonded to the half of the compression face beam in Fig.9.1b; the other half of the compression face was bonded with a 6 mm thick plate. This enabled two individual tests to be performed from the same beam. The second beam was similar to the first one except that the plates were bonded to the tension face as shown in Fig.9.1d; this beam served as control specimens for the compression face plated beam. The third beam shown in Fig.9.1f was bonded with a 20 mm thick compression face plate.

A total of five tests were carried out as given below:

1. SP-C6-Shear peeling of a shear span bonded with a 6 mm thick plate to the compression face (Fig.9.1b)
2. SP-C12- Shear peeling of a shear span bonded with a 12 mm thick plate to the compression face (Fig.9.1c)
3. SP-T6- Shear peeling of a shear span bonded with a 6 mm thick plate to the tension face (Fig.9.1d)

4. SP-T12- Shear peeling of a shear span bonded with a 12 mm thick plate to the tension face (Fig.9.1e).

5. SP-C20- Shear peeling of a shear span bonded with a 20 mm thick plate to the compression face (Fig.9.1f)

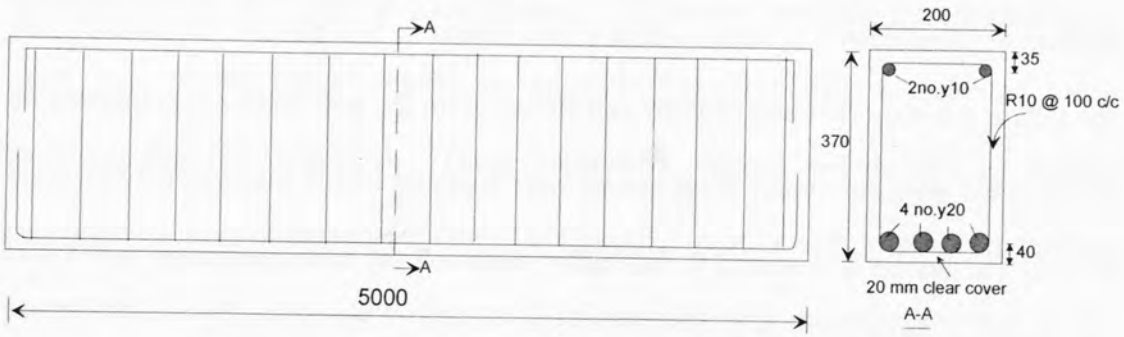

Fig.9.1a. Reinforcement details of basic concrete beam

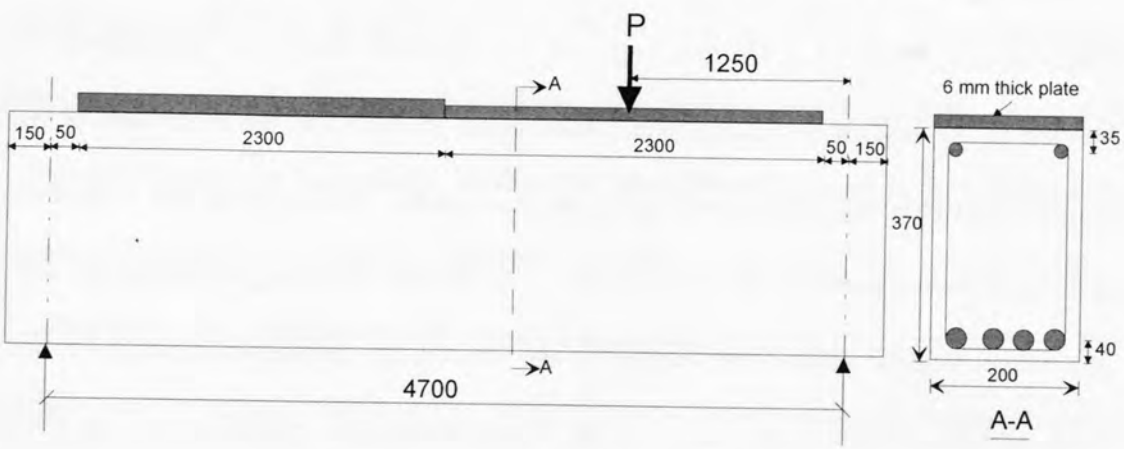

Fig.9.1b. Details of test SP-C6

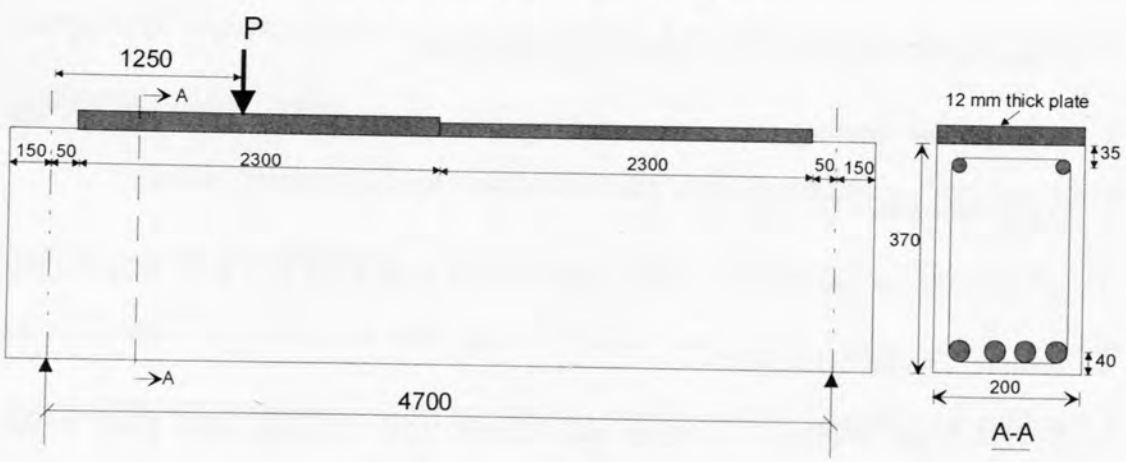

Fig.9.1c. Details of test SP-C12

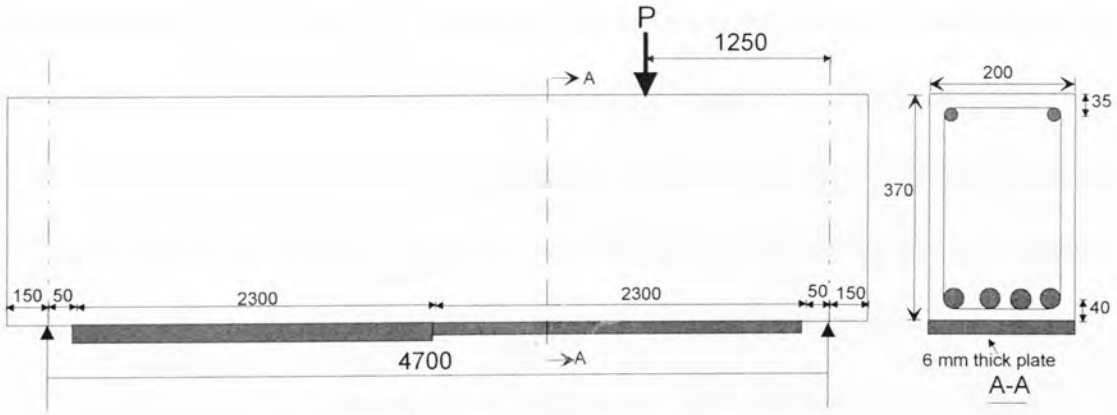

Fig.9.1d. Details of test SP-T6

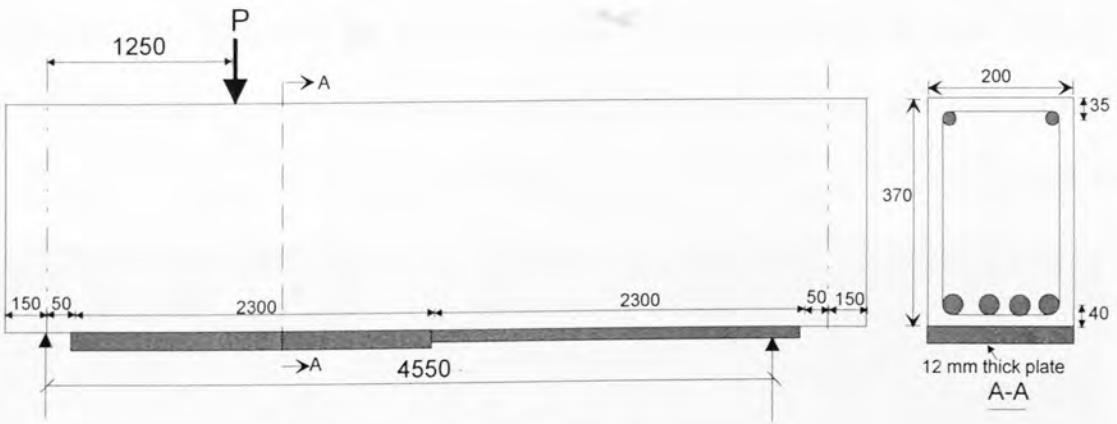

Fig.9.1e. Details of test SP-T12

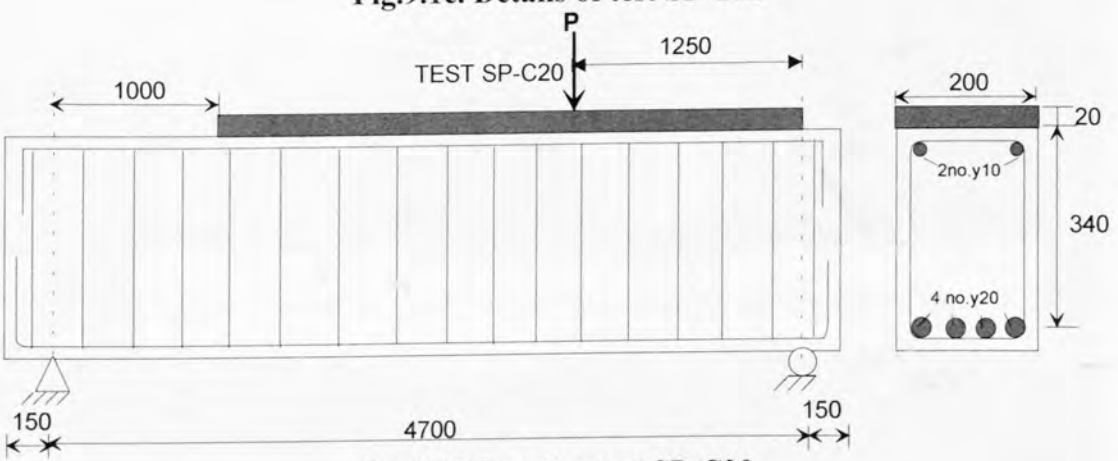

Fig.9.1f. Details otest SP-C20

9.3 Test rig

All the beams were simply supported over an effective span of 4700 mm except for the case of SP-T12 for which the span was 4550 mm. The plate ends were kept 50 mm from the nearest support except for SP-C20 where the plate end was exactly over

the support. The load was applied on the top of the beam by a hand operated hydraulic jack through a load cell and a knife-edge bearing. The two shear spans of the same side plated beam were tested individually; this was achieved by clamping the longer shear span while testing the shorter shear span to failure as shown in Fig.9.2. From the geometry of the loading arrangement, the maximum shear load in the shear span tested is 73.4% of the total load applied in the case of SP-C6, SP-C12 and SP-T6; it was 72.5 % for SP-T12. The ratio of the distance between the position of the applied load and support (1250 mm) and the depth of the beam (370 mm) was kept greater than 3 to avoid the increase in shear strength due to short span tied arching action.

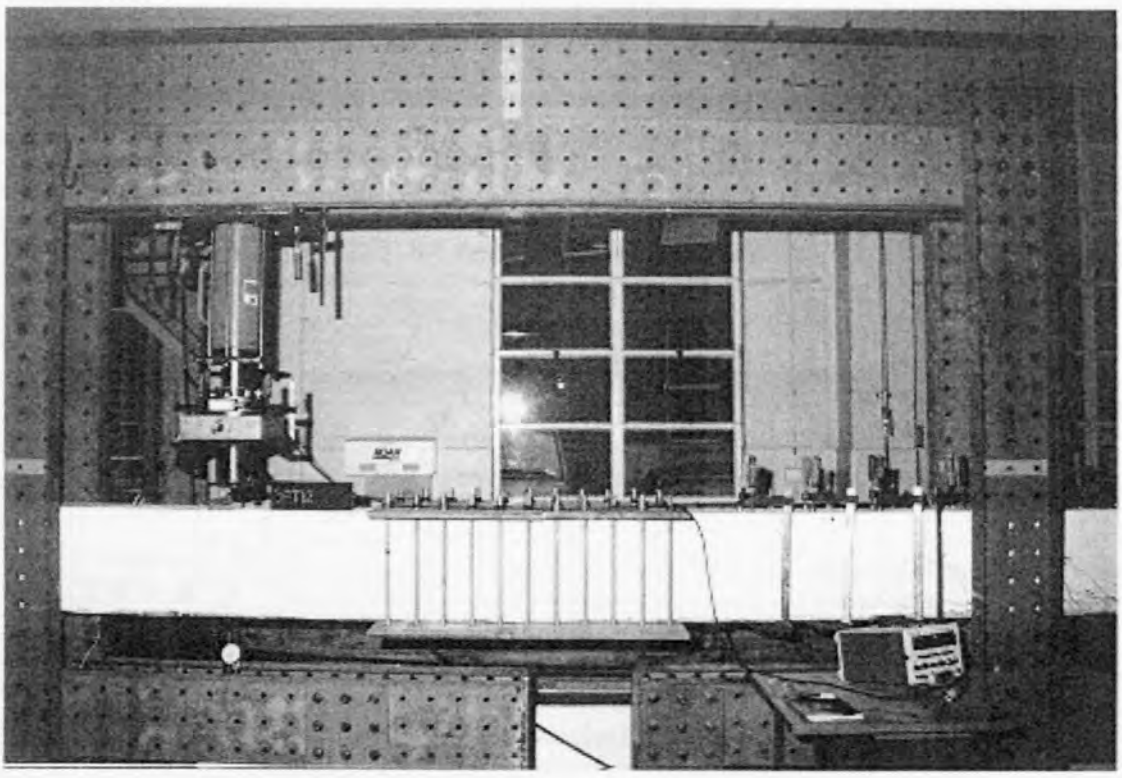

Fig.9.2. Load and clamping arrangement

9.4 Instrumentation

Strain gauges were bonded to the external plates in order to detect the debonding at various sites of the plates. The arrangements of the strain gauges and their numbering

are shown in Figs.9.3a and 9.3b for all the five plated beam tests conducted. The beam deflection at load point was monitored by a dial gauge and also by a transducer.

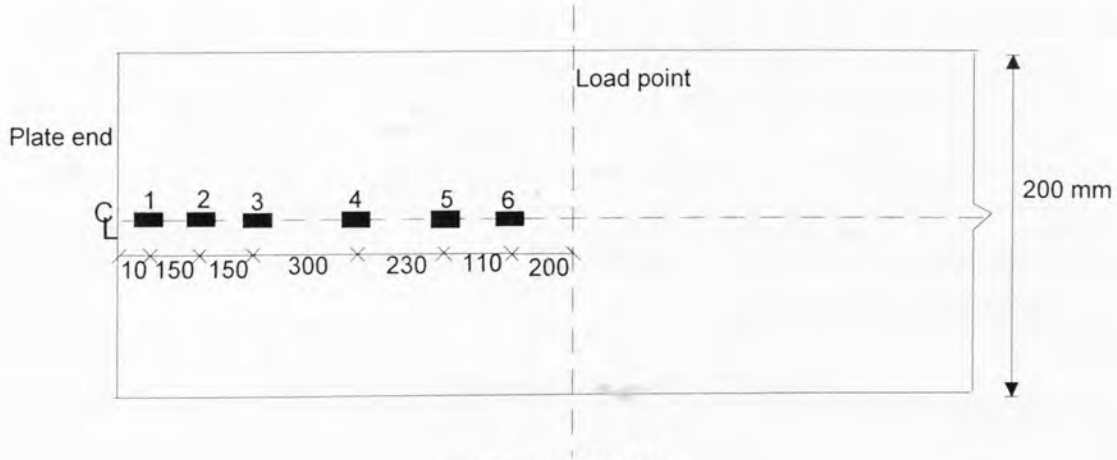

(a) Tests SP-C20

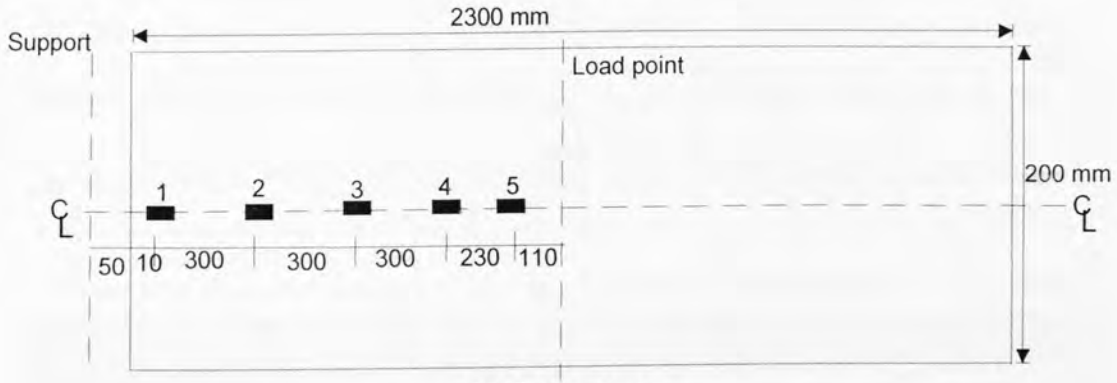

(b) Other tests

Fig.9.3. Arrangement of strain gauges for all the tests (Plan view of plate)

9.5 Material Properties

All the beams were cast in a single pour using ready mixed concrete supplied by a local manufacturer. Material properties of the concrete are shown in Table 1. In this table, the individual values are of each test are given under the "i" column and their mean value under the "m" column. As the beams were tested during a period 253-263 days, the material properties given in Table-9.1 for 248 days are appropriate. Material properties of the steel plates, reinforcing bars and shear stirrups are shown in Table-9.2. The manufacturer's specifications of the material properties of the epoxy glue used for bonding the steel plates are indicated in Table-9.3.

Table-9.1: Material properties of the concrete

Age	E_c (MPa)		f_b (MPa)		f_c (MPa)		f_{cu} (MPa)	
(days)	i	m	i	m	i	m	i	m
248	34425	34283	3.83	3.60	32.66	35.26	35.37	36.47
	34023		3.61		36.90		36.81	
	34203		3.35		36.43		37.24	
	34499				35.07			

where E_c = Elastic modulus of the concrete, f_c = Cylinder compressive strength of the concrete, f_{cu} = Cube compressive strength of the concrete and f_b = Brazilian tensile strength of the concrete.

Table-9.2: Material properties of the steel

Item	f_y (MPa)				f_u (MPa)			
Sample No.	1	2	3	Mean	1	2	3	Mean
Rebar Y20	436.1	429.7	-	432.9	530.0	522.0	-	526.0
Stirrup W10	-	-	-	-	560.2	572.9	-	566.6
6 mm thick plate	360.7	365.7	368.1	364.8	493.6	487.7	490.9	490.7
12 mm thick plate	304.6	298.2	314.6	305.8	513.9	506.4	520.8	513.7

where f_y = Yield strength of the steel and f_u = Ultimate strength of the steel.

Table -9.3: Material properties of the glue Hilti CA 273 after 2 days (as tested by the manufacturer)

Compressive strength (ISO 604)	Tensile strength (ISO 527)	Flexural strength (ISO 178)	Elastic modulus in compression (ASTM-D695)	Tensile bond strength (ISO 527)	Maximum operating temperature
110-120 MPa	30-40 MPa	20-30 MPa	5000-6000 MPa	10-15 MPa	80° C

9.6 Test results

9.6.1 Test SP-T6

This test was carried out on the shear span glued with a 6 mm thick tension face plate (Fig.9.1d) as to provide a datum for SP-C6. The shear force (V) in the span tested was 73.4% of the total applied load (P).

9.6.1.1 Crack propagation and failure model

Two flexural cracks, one when V= 22 kN (P=30 kN) and another when V=29.3 kN (P=40 kN), appeared near the load point as shown in Fig.9.4a. No further cracks were

visible as the load P was increased to 140 kN in increments of 5 kN. When the shear load V was 106.4 kN (P=145 kN), two diagonal cracks appeared; one near the plate end and the other about 300 mm from the plate end, as can be seen in Fig.9.4b. This caused the applied load P to drop from 134 kN. At this stage, the beam was reloaded in increments of 3 kN. As the shear load V was increased to 111.5 kN (P=152 kN), a horizontal debonding crack occurred from the plate end along the concrete cover, triggering off further diagonal cracks. As the shear load was increased slightly to 112.5 kN (P=153.3 kN), the complete shear peeling of the tension face plate occurred due to the extension of a longitudinal crack and the formation of a series of diagonal crack up to the load point as shown in Fig.9.4a. The load P then dropped abruptly to 119.6 kN (V=87.8 kN), at which the test was terminated. Due to shear peeling failure, the concrete cover at the plate end separated from the reinforcement cage, which can be clearly observed in Fig.9.4b.

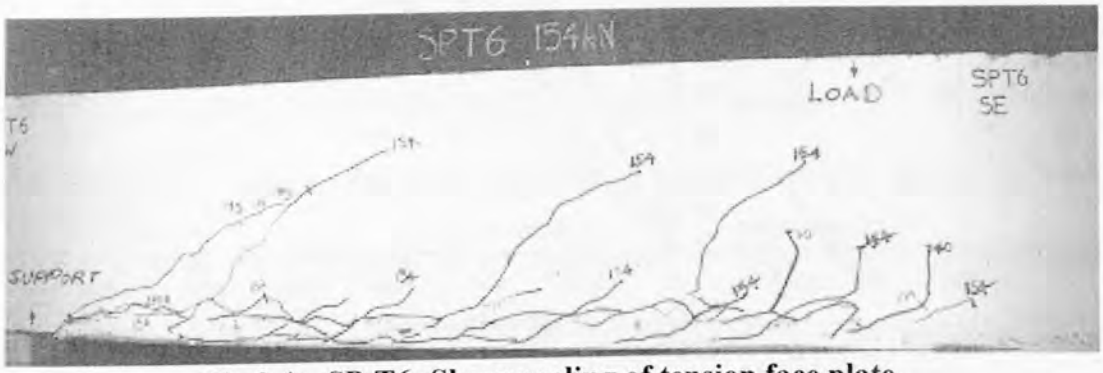

Fig.9.4a. SP-T6: Shear peeling of tension face plate

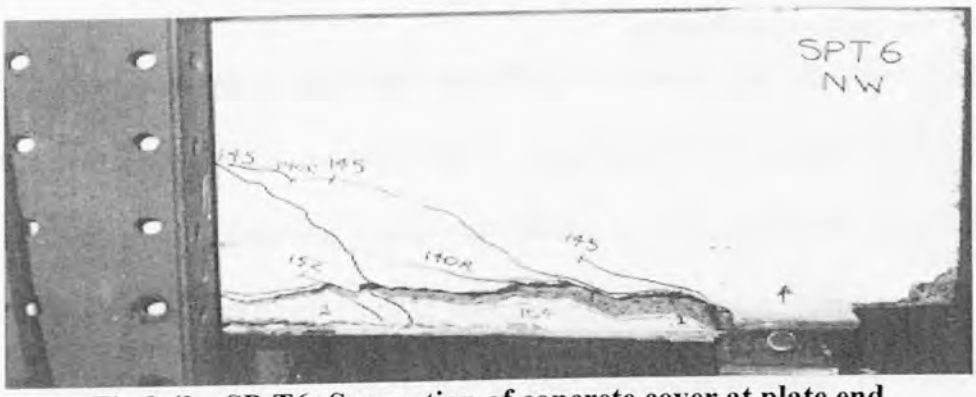

Fig.9.4b. SP-T6: Separation of concrete cover at plate end

9.6.1.2 Longitudinal strains in tension face plate

Figure 9.5 shows the variation of longitudinal strains at all gauge locations (refer Fig.9.3b). The strains increased linearly with the increase in shear force till the formation of diagonal cracks at V= 106.4 kN, which is marked by a small drop in the charts. The complete shear peeling of tension face plate at V=112.5 kN is marked by the sudden drop in both shear force and strain values at all locations. Figure 9.5 also shows that the strains increased progressively from the plate end to the load point. The strain readings did not exceed the yield strain of the plate (1824 microstrain) as the maximum recorded reading just before peeling was 1024 microstrain at gauge #5 that was affixed close to the load point.

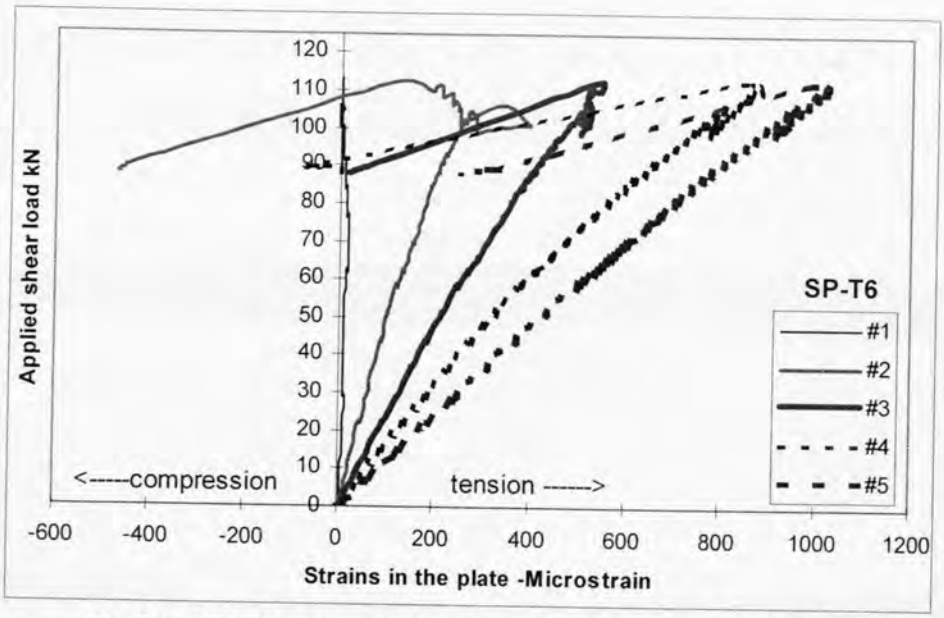

Fig.9.5. SP-T6: Longitudinal strains in tension face plate

9.6.1.3 Variation of deflection

Figure 9.6 depicts the variation of deflection recorded at the load point with the applied shear load in the shear span. The deflection increased linearly with the applied load till V=112.5 kN at which there was a decrease in shear force. It also shows the complete debonding at V=112.5 kN as there was a sudden drop in the chart. The deflection recorded at peeling was 13.9 mm and it was 14.11 mm when the test was terminated at V=87.8 kN.

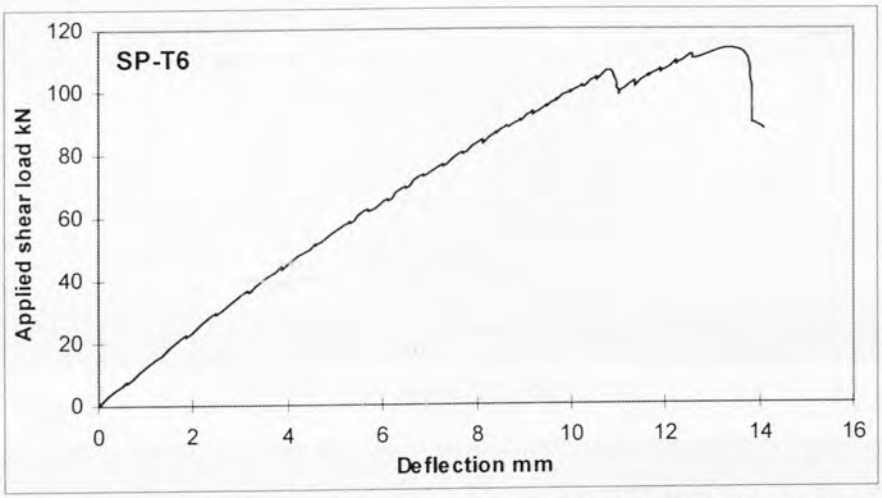

Fig.9.6. SP-T6: Deflection at load point Vs Applied shear load

9.6.2 Test SP-C6

Test SP-C6 was carried out on the shear span bonded with a 6 mm thick compression face plate (Fig.9.1b). The shear force in span V was 73.5% of the total applied load.

9.6.2.1 Crack propagation and failure mode

When the shear force in span (V) was 29.4 kN (P=40 kN), four vertical cracks appeared, one below the load point and the other at regular intervals from the load point as shown in Fig.9.7a. When the shear force V was increased to 44 kN (P=60 kN), another flexural crack appeared adjacent to the load point in the longer shear span. At V=66 kN (P=90 kN), these cracks grew in size and some more vertical cracks appeared between them. When the shear force (V) was increased further to 73.5 kN (P=100 kN), a diagonal crack appeared at 300 mm from the support as shown in Fig.9.7a.

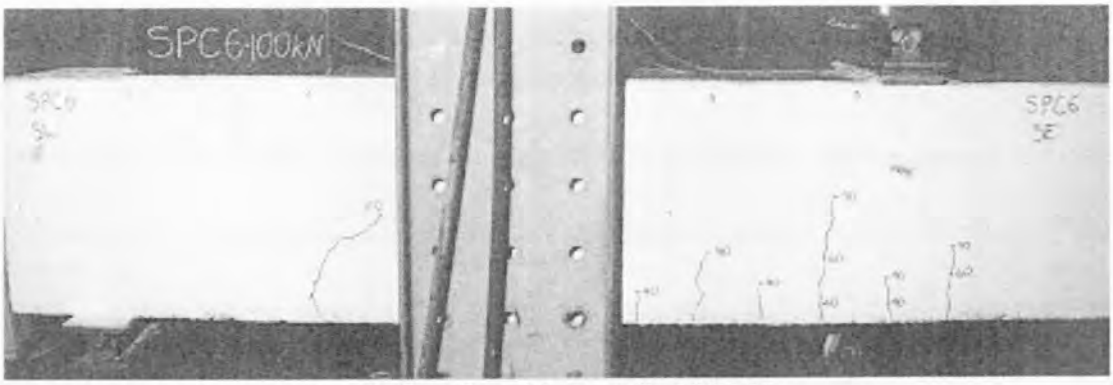

(a) Crack pattern at P=100 kN

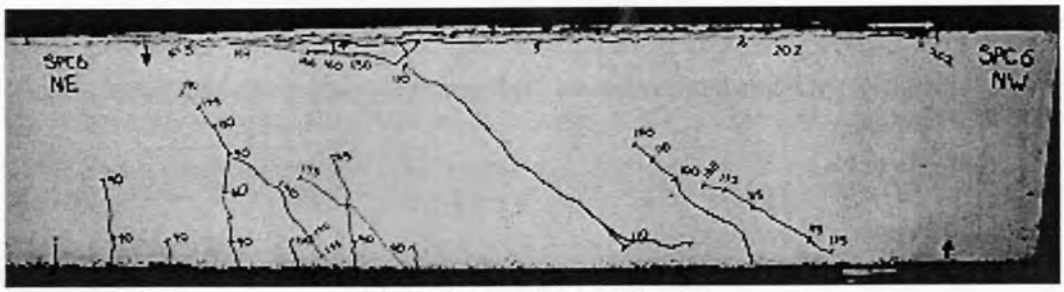

(b) Failure of plated beam

Fig.9.7. Crack patterns of SP-C6

On further application of load, a long diagonal crack whose root was 600 mm from the support and whose tip was about 50 mm from the beam top occurred when V= 80.7 kN (P=110 kN), as can be seen from Fig.9.7b. As the shear force was increased to 103 kN (P=140 kN), this crack started to move towards the load plate. Meanwhile, the flexural cracks adjacent to the load point transformed into flexural shear cracks and the diagonal crack adjacent to the support also propagated rapidly. As the load P was increased from 140 kN to 169 kN (V=103 kN to 124 kN) in increments of 3 kN, the critical diagonal crack touched the edge of the load plate. After this stage, there was no change in crack propagation for the next 30 kN increase in load; the only visible change observed was the bulging of the plated beam top on either side of the load plate due to bearing effect. Finally, when the shear force (V) was 148.2 kN (P=202 kN), long debonding cracks originated from the plate ends and progressed towards the load point; the complete debonding of the compression face

plate also occurred, as shown in Fig.9.7b. The load dropped from 202 kN to 169.7 kN (V=148.2 kN to 24.6 kN) and the test was terminated.

9.6.2.2 Longitudinal strains in the compression face plate

Figure 9.8 illustrates the variation of strains recorded at all strain gauge locations (refer Fig.9.3b) with the applied shear load. The occurrence of a diagonal shear crack near the support is shown by a kink in the chart for gauge #2 at V=73.5 kN, as this crack location corresponds to that of #2. The long, critical diagonal crack that occurred at V=80.7 kN induced the kinks in the charts for #3 and #4. Finally, the plateaus and vertical drop in strain magnitudes at all the five strain gauge locations at V=148.2 kN show the occurrence of debonding of compression face plate. The maximum strain recorded just before debonding was 2352 microstrains and this was higher than the yield strain of the plate (1824 microstrains).

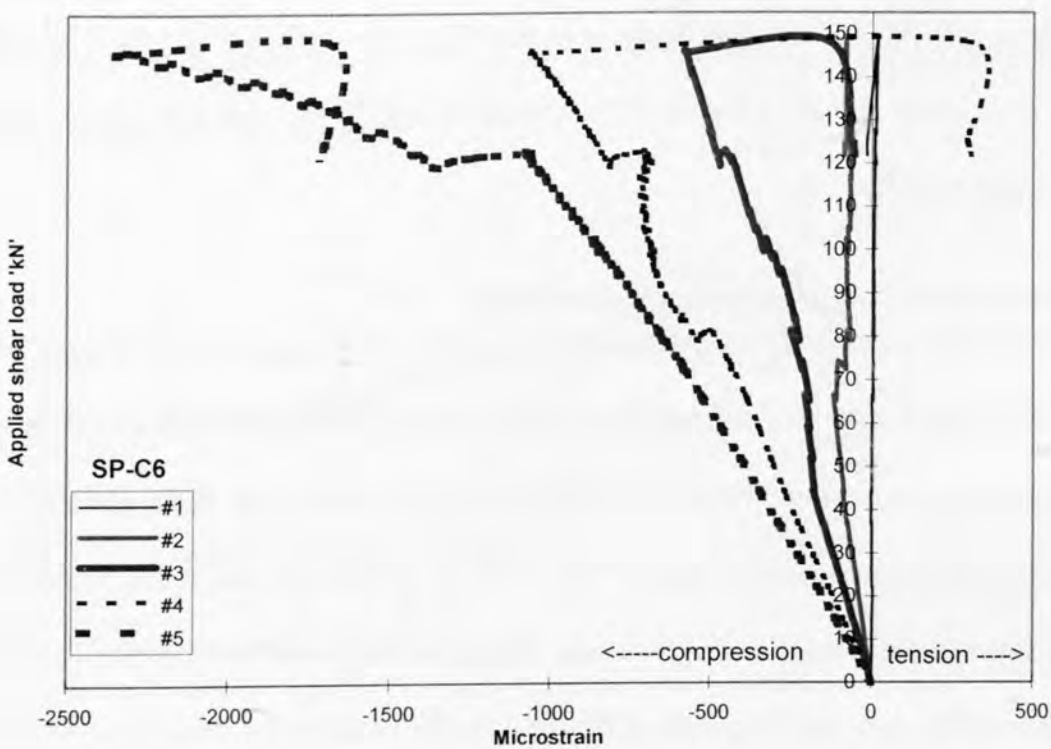

Fig.9.8. SP-C6: Longitudinal strains in compression face plate

9.6.2.3 Variation of deflection

Figure 9.9 depicts the relationship between the deflection at load point and the applied shear load. It can be seen that there is a drop in load at V=148.2 kN, which indicates debonding. The maximum recorded deflection was 21.92 mm.

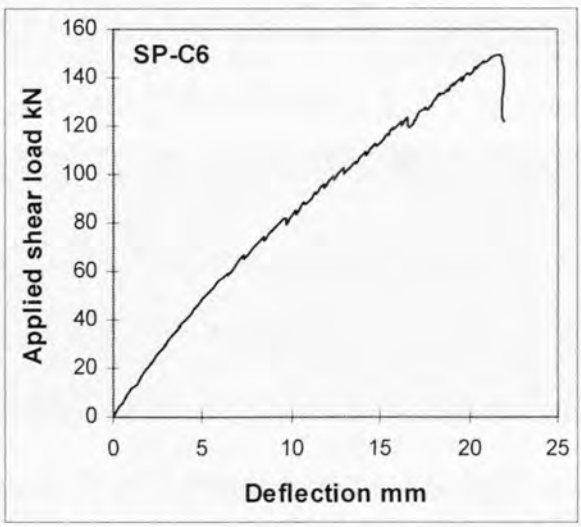

Fig.9.9. SP-C6: Deflection at load point Vs Applied shear load

9.6.3 SP-T12

Shear span SP-T12 was glued with a 12 mm thick tension face plate (Fig.9.1e) and it is the control specimen for SP-C12. The shear load in the span V is 72.5 % of the applied load P.

9.6.3.1 Crack propagation and failure mode

The first flexural shear crack appeared at a distance of 100 mm from load point when V=36.3 kN (P=40 kN) and a flexural shear crack appeared about 300 mm from load point when shear force(V) was 72.5 kN (P=80 kN). Finally, the shear peeling of the tension face plate occurred when V was 112.4 kN (P=155 kN) due to the formation of a diagonal shear crack at the plate end; this led to the formation of a long horizontal debonding crack and a number of diagonal cracks all along the shear span, as shown in Fig.9.10. The shear force (V) dropped suddenly to 68.1 kN (P=93.9 kN) and the

test was terminated at this stage. The concrete cover totally separated from the reinforcement cage as shown in Fig.9.10.

Fig.9.10. SP-T12: Failure mode

9.6.3.2 Longitudinal strains in the tension face plate

Figure 9.11 shows the variation of strains, at the various gauge locations (refer Fig.9.3b) with the applied shear load in the shorter shear span. It can be seen that the strains at all sites increased linearly with applied load till the occurrence of debonding and they dropped drastically after debonding as the beam could not sustain the applied load. The maximum strain for a given load was recorded at the location of gauge #5 and it was 650 microstrains at the peak shear load as compared to the yield stain of the plate, which is 1850 microstrains.

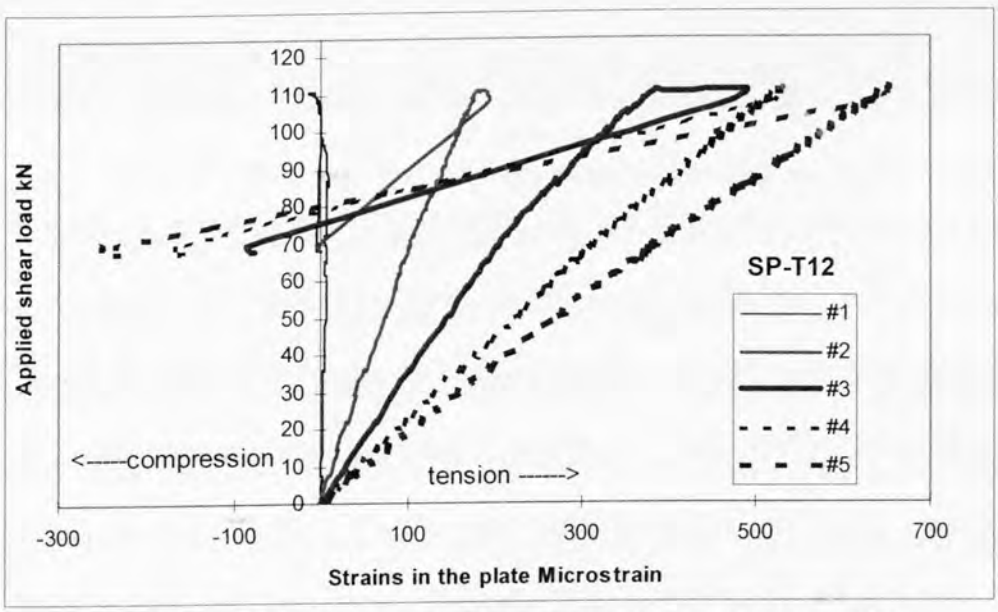

Fig.9.11. SP-T12: Longitudinal strains in tension face plate

9.6.3.3 Deflection variation

Figure 9.12 shows the variation of the deflection at the load- point with the shear force V in the span. The deflection increased linearly till debonding occurred at V=112.4 kN, after which the load dropped suddenly. The maximum deflection recorded was 14 mm.

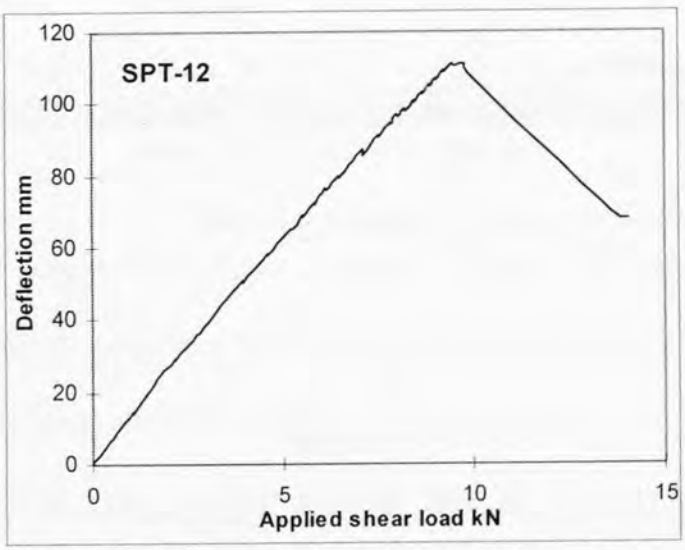

Fig.9.12. SP-T12: Deflection at load point Vs Applied shear load

9.6.4 SP-C12

Shear span SP-C12 was glued with a 12 mm thick compression face plate (Fig.9.1c) and the position of the applied load P was such that the shear force in the span V was 0.734P.

9.6.4.1 Crack propagation and failure mode

A few flexural cracks occurred on both sides of the load point when the shear force V ranged between 22-44 kN (P=30 to 60 kN), as shown in Fig.9.13a. Figure 9.13a also shows the appearance of a web shear crack at a distance 550 mm from the load point, when V=58.7 kN (P=80 kN). It can also be seen that the previously formed flexural crack transformed into a flexural shear crack when the shear force was in the range 73.4-84.4 kN (P=100-115 kN) and it extended towards the load plate at V=88.1 kN (P=120 kN). This caused the beam to shed load and the beam was loaded back to 120

kN. At this stage, a long diagonal crack originated at about 170 mm from the support and instantly extended to the top of the beam as shown in Fig.9.13b. (The load P at this stage is marked as 120R in Fig.9.13b). The beam was loaded further in 3 kN increments and the 120R diagonal crack extended to the load plate along the bottom edge of the compression face plate when V=117.4 kN (P=160 kN).

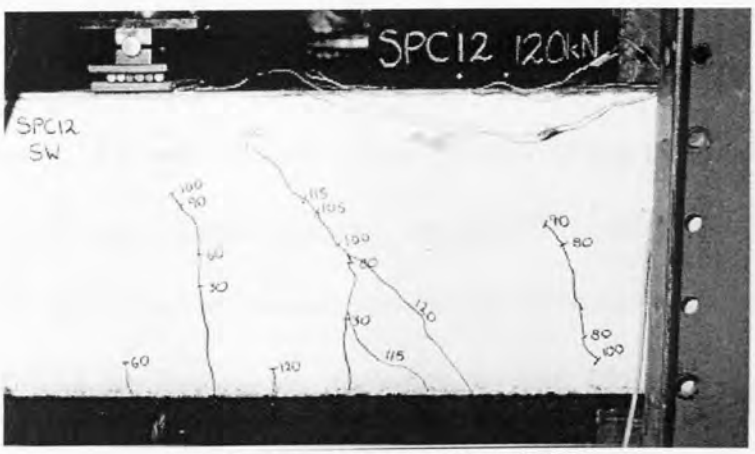

(a) Crack pattern at P=120 kN

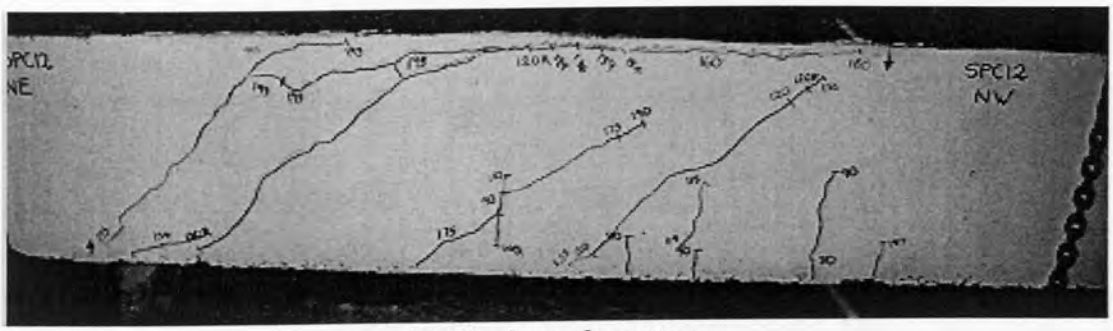

(b) Final crack pattern

Fig.9.13. Test SP-C12: Crack patterns

As the load P was increased further to 190 kN (V=139.5 kN), no further change occurred to this crack and the 80 kN web shear crack was transformed into a full diagonal crack. As the load was increased to 193 kN(V=141.7 kN), the long diagonal crack traversed backwards to the edge of the support plate and another diagonal crack formed from this root and it extended to the top of the beam, i.e. the compression face plate debonded as shown in Fig.9.13b. Thus, the shear peeling

mechanism within the plate ends of the compression face plate was achieved. The load dropped to 177.4 kN (V=130.2 kN) and the test was terminated.

9.6.4.2 Longitudinal strains in the compression face plate

Figure 9.14 illustrates the variation of longitudinal strains recorded at all gauge sites (refer Fig.9.3b) with the shear force in the shear span tested. The charts show the strains increased linearly unto a shear force of 88 kN at which the long diagonal shear crack formed near the support. This is marked by the reduction in strains at gauge location #2,#3, and #4 and the convergence of strains at #2 and #3, which denotes the loss of bond between these two locations. Again the next critical phenomenon, i.e. the extension of the long, diagonal crack towards the load point, is marked by the plateau in gauge locations #2,#3 and #4 and their convergence at V=117.4 kN. The completion of the debonding process is marked by the drop in strains and shear forces at V= 141.7 kN. The maximum strain readings were recorded at gauge #5 and the strain at peak load was 889 microstrains which is less than the yield strain of the 12 mm thick plate (1529 microstrains).

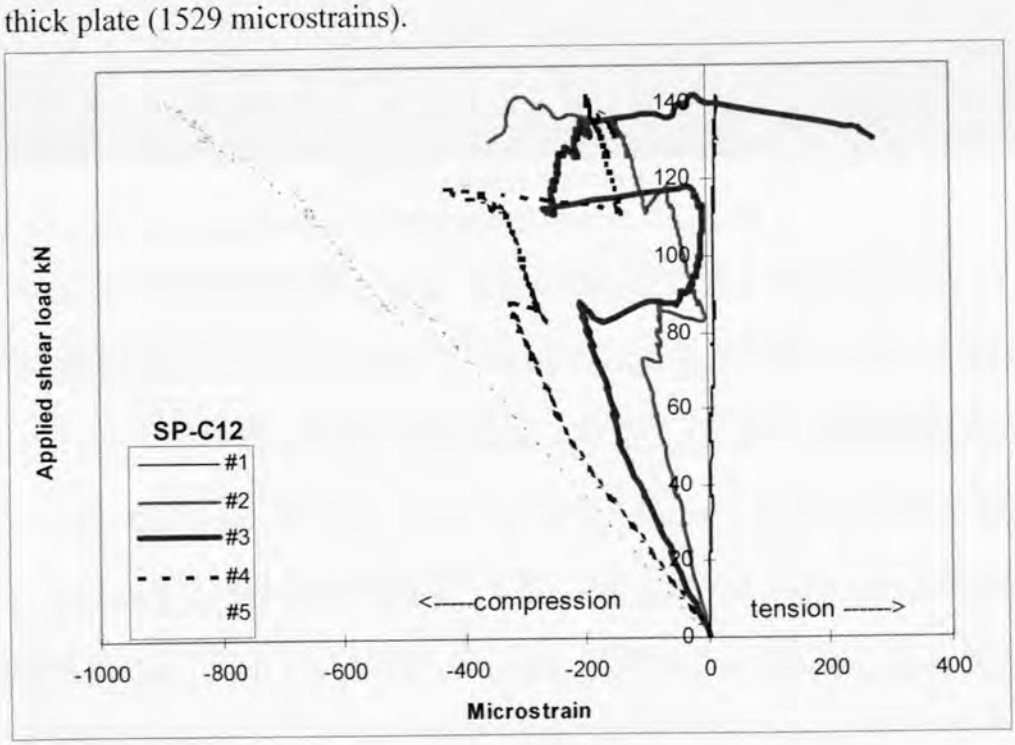

Fig.9.14. SP-C12: Longitudinal strains in compression face plate

9.6.4.3 Deflection

Figure 9.15 depicts the relationship between the deflection recorded at the load point and the shear force in the shear span tested. The deflection increased linearly with the applied load and some drop in load at various stages show the local loss of bond. The maximum recorded deflection at the instance of complete debonding was 20.04 mm.

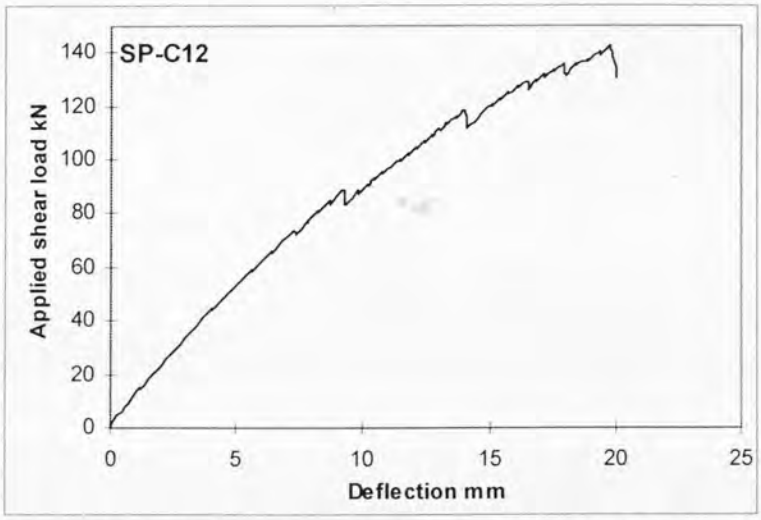

Fig.9.15. SP-C12: Deflection at load point Vs Applied shear load

9.6.5 SP-C20

Shear span SP-C20 (Fig.9.1f) was bonded with a 20 mm thick compression face plate and the position of the applied load P was such that the shear force V in the span was $0.734P$. The plate was terminated in this span exactly over the support so as to keep the bending moment at plate end zero.

9.6.5.1 Crack propagation and failure mode

A few flexural cracks occurred on both sides of the load point when the shear force V ranged between 36.7-73.4 kN (P=50 to 100 kN), as shown in Fig.9.16. Figure 9.16 also shows the appearance of a diagonal shear crack at a distance 230 mm from the support, when V=80.7 kN (P=110 kN). As the beam was further loaded to 115 kN (V= 84.4 kN), this diagonal crack reached the topmost concrete fibre. It then propagated along the bottom side of the compression face plated beam to the load

plate when the shear load V was 94 kN (P=128 kN) as shown in Fig 9.17. Some more flexural shear cracks also occurred when the applied shear load was in the range of 85.1-97.6 kN (P=116-133 kN).

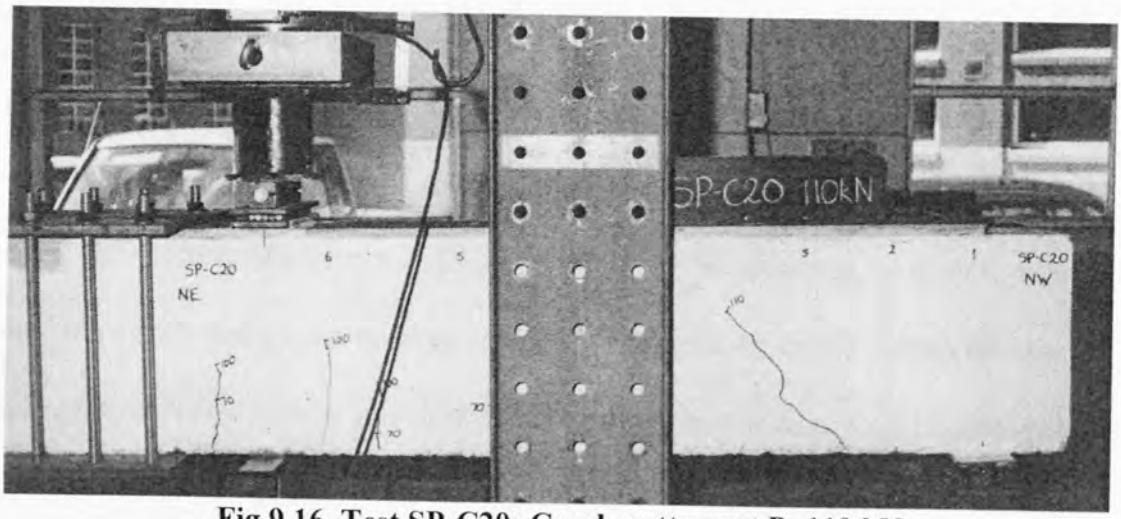

Fig.9.16. Test SP-C20: Crack pattern at P=110 kN

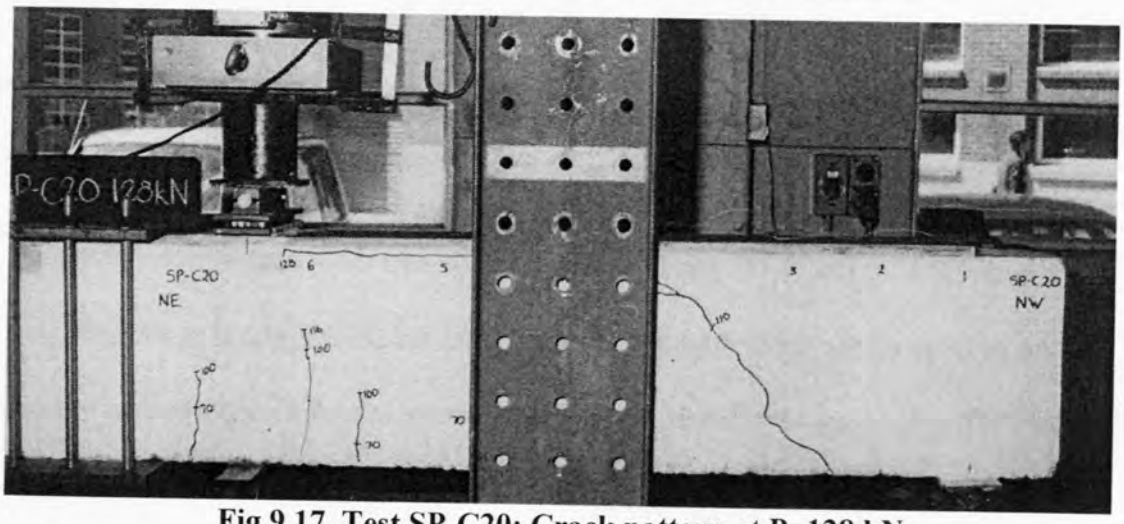

Fig.9.17. Test SP-C20: Crack pattern at P=128 kN

As the load was increased to 212 kN (V=155.6 kN), the long diagonal crack traversed backwards to the edge of the support plate and another diagonal crack formed from this root and it extended to the top of the beam, as shown in Figs.9.18a and 9.18b. This caused the plate to debond from the concrete. It is worth noting from Figs.9.18a and 9.18b that the horizontal peeling crack did not propagate towards the plate end and the crack stopped at a distance 575 mm from the plate end. Thus, the

shear peeling mechanism within the plate ends of the compression face plate was achieved. The load dropped to 208 kN (V=152.6 kN) and the test was terminated.

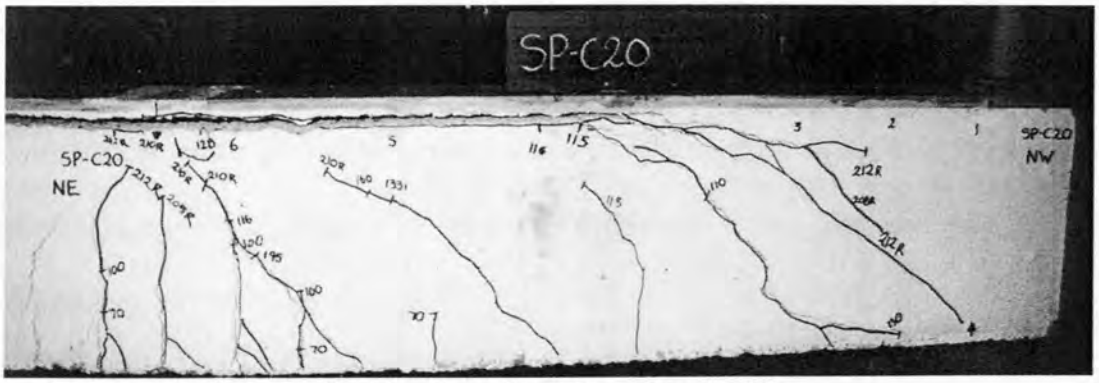

(a) Final crack pattern-North side

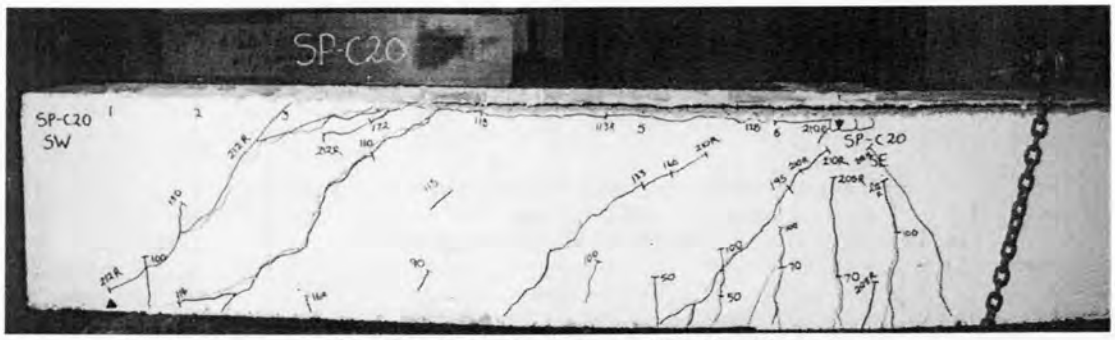

(b) Final crack pattern-South side

Fig.9.18. Test SP-C20: Final crack patterns

9.6.5.2 Longitudinal strains in the compression face plate

Figures 9.19a and 9.19b illustrates the variation of longitudinal strains recorded at all gauge sites (refer Fig.9.3a) with the shear force in the shear span tested. The charts show the strains increased linearly up to a shear force of 80.7 kN at which the long diagonal shear crack formed near the support. This is marked by the reduction in strains at gauge location #2, #3, and #4 and the convergence of strains at #1 and #2, which denotes the loss of bond between these two locations. Again the next critical phenomenon, i.e. the extension of the long, diagonal crack towards the load point, is marked by the plateau in gauge locations #2, #3, #4, #5 and #6 at V=85.1 kN. The completion of the debonding process is marked by the drop in strains and shear forces

at V= 155.6 kN. The maximum strain readings were recorded at gauge #6 and the strain at peak load was 1830 microstrains.

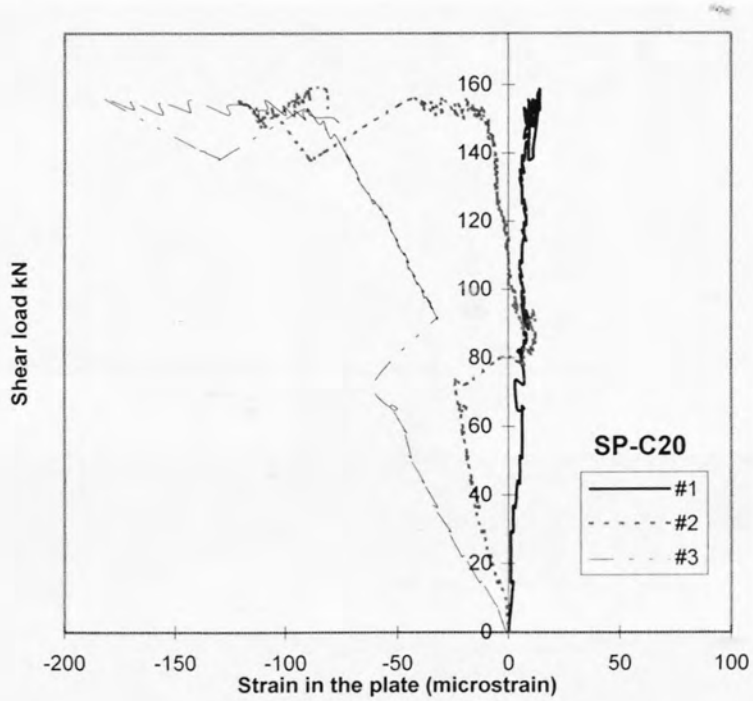

(a)

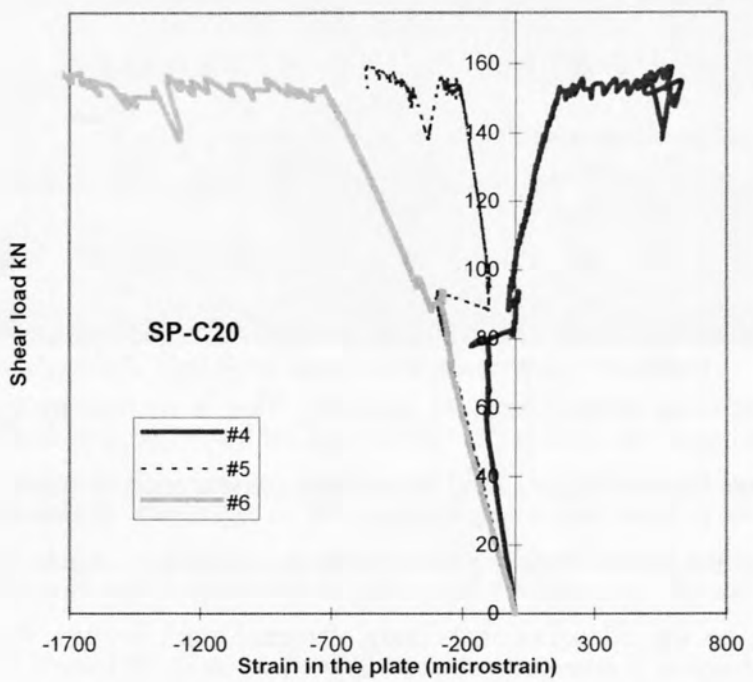

(b)

Fig.9.19. SP-C20: Longitudinal strains in compression face plate

9.6.5.3 Deflection

Figure 9.20 depicts the relationship between the deflection recorded at the load point and the shear force in the shear span tested. The deflection increased linearly with the applied load and some drop in load at various stages show the local loss of bond. The long plateau at the peak shear load shows the ductile nature of the compression face plated beam. The maximum recorded deflection at the instance of complete debonding was 75.2 mm.

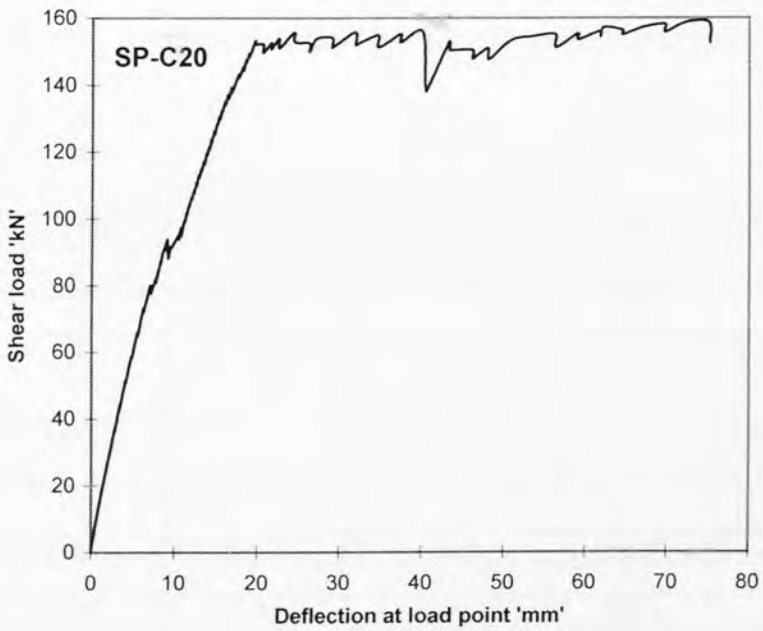

Fig.9.20. SP-C20: Deflection at load point Vs Applied shear load

9.7. Discussion of test results

Table-9.4 gives the salient features of results from all the five tests. As no test was carried out to determine the shear strength of the reinforced concrete beam, the same was computed using the AS-3600 formulae. The theoretical shear strength of the reinforced concrete beam excluding shear reinforcement V_{uc} is 80.7 kN and the shear strength of the beam including shear stirrups V_u is 374.4 kN. In Fig. 9.21, a comparison is made of the shear peeling strengths of all the plated beams and V_{uc} and V_u are also indicated. It can be seen that in all the shear spans tested, whether the plates were bonded to the compression face or tension face, the shear peeling strength

of the beams (112.4-155.6 kN) are far less than the ultimate shear strength of the reinforced concrete beam (V_u =374.4 kN). This shows the presence of internal shear stirrups hardly arrests if at all the propagation of the diagonal shear cracks that causes the peeling. However, the average shear peeling strengths for the tension face plated beams and the compression face plated beams were about 40% and 85% larger than the theoretical shear strength of the concrete beam only (V_{uc}=80.7 kN). Furthermore, the shear peeling strength of the compression face plated beams were about 30% more than the corresponding tension face plated beams, in the case of 6 mm and 12 mm thick plated beams.

Table-9.4: Test Results

	SP-T6	SP-C6	SP-T12	SP-C12	SP-C20
Test results					
External plate	6 mm thick tfp	6 mm thick cfp	12 mm thick tfp	12 mm thick cfp	20 mm cfp
Shear load at first major diagonal crack (kN)	106.4	80.7	112.4	88.1	80.7
Shear load at extension of debonding crack to load point (kN)	-	124.0	-	117.4	94
Shear load at peeling (kN)	112.5	148.2	112.4	141.7	155.6
Max. Moment at peeling (kNm)	140.6	185.3	140.5	177.1	194.5
Maximum strain in plate at debonding	1024×10^{-6} (Plate not yielded)	2352×10^{-6} (Plate yielded)	650×10^{-6} (Plate not yielded)	889×10^{-6} (Plate not yielded)	1830×10^{-6} (Plate yielded)
Failure mode	Shear peeling due to diagonal shear crack formation at plate end	Formation of long diagonal crack at 600 mm from support when V=80.7 kN which caused a horizontal debonding crack extended to load plate at V=124 kN and a long horizontal debonding crack from plate end extending towards load plate at V=148.2 kN	Shear peeling due to diagonal shear crack formation at plate end	Formation of long diagonal crack at 170 mm from support at V=88.1 kN which caused a horizontal debonding crack that extended towards load plate at V=117.4 kN and formation of secondary diagonal crack from the horizontal crack traversing back towards support at V= 141.7 kN	Formation of critical diagonal crack at V=80.7 kN and extension of this crack to the load plate at V=94 kN and formation of secondary diagonal crack from the horizontal crack traversing back towards support at V=155.6 kN causing debonding and secondary diagonal cracks

tfp-tension face plae; cfp-compression face plate

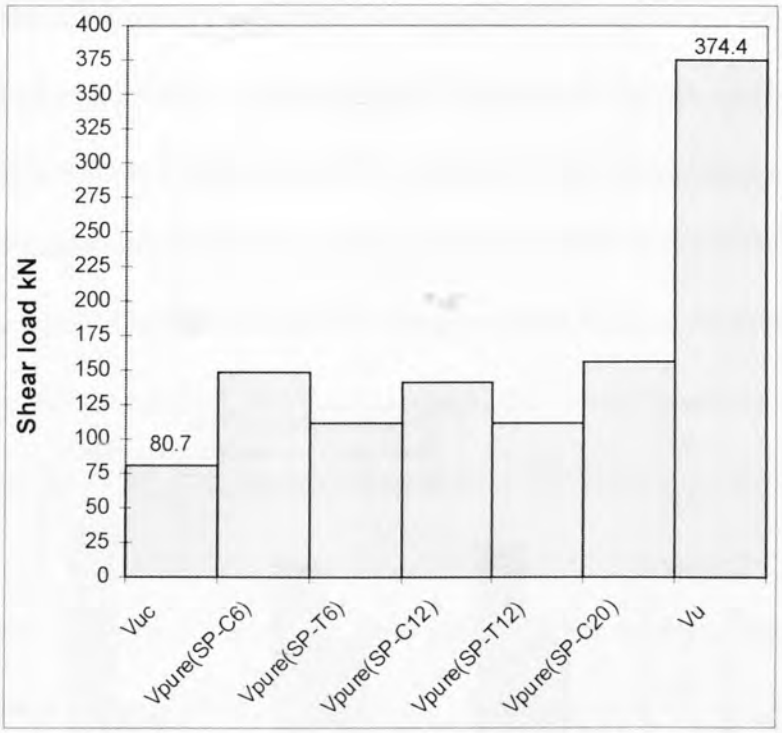

Fig.9.21. Shear peeling strengths of all the plated beams

The shear peeling phenomenon in case of the compression face plated beams occurred at higher shear loads than the corresponding tension face plated beams. Unlike the tension face plated beams, where shear peeling occurred by the formation of a diagonal shear crack in the vicinity of the plate end and its instantaneous propagation towards the load point, the shear peeling of the compression face plated beams was gradual and in stages as follows (Refer Fig.9.22):

(a) First, a shear crack occurred away from the support. The shear loads at which this occurred were varied between 80.7 kN, 88.1 kN and 80.7 kN for the three beams SP-C6, SP-C12 and SP-C20 respectively. This load can be considered to be the shear strength of the beams without shear stirrups, i.e. equal to V_{uc}.

(b) In the second stage, the above mentioned crack propagated along the bottom edge of the plate towards the load point. The shear load at which this occurred in case of SP-C6 ,SP-C12 and SP-C20 are 124 kN, 117.4 and 94 kN respectively.

(c) The stage(b) horizontal debonding crack stabilised on further application of the load. Finally the complete shear peeling of the beam occurred either by the extension of this crack to cover the whole length of the plate as in the case of SP-C6 or the simultaneous extension of the debonding crack and the formation of diagonal cracks originating from the support as happened in SP-C12 and SP-C20.

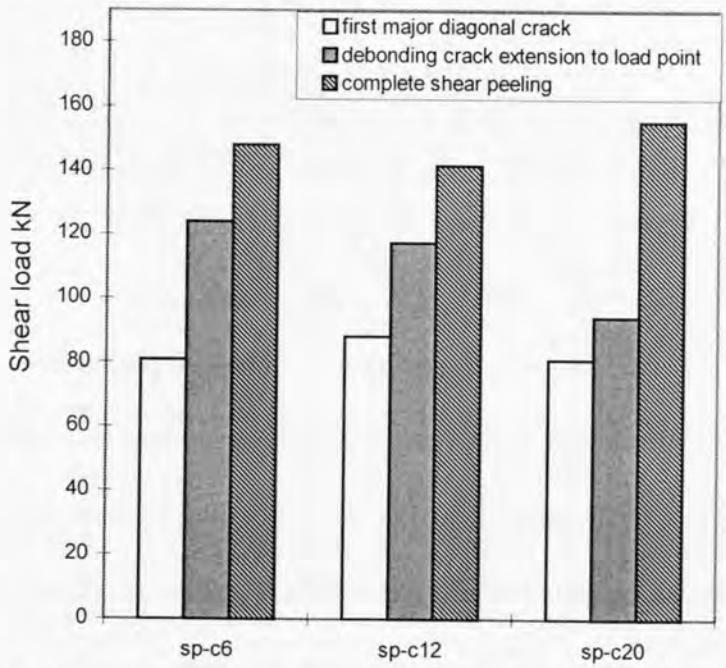

Fig.9.22. Milestones for the shear peeling of compression face plated beams

9.8 Conclusions

1. Tests have shown that shear peeling of tension face plated beams occurs by the formation of a critical diagonal crack in the vicinity of the plated beam and its instantaneous propagation towards the load point. On the other hand, the complete shear peeling of compression face plated beams occurred in three stages: formation of a critical diagonal crack; its extension along the bottom edge of the

plate towards the load point; and the formation of secondary debonding crack from the load point to the plate end for comparatively thin plated beams or the simultaneous extension of the debonding crack and the formation of diagonal cracks originating from the support for thick plated beams.

2. In both tension as well as compression face plated beams, the shear peeling occurred at a shear load less than the ultimate shear strength of the reinforced concrete beam (V_u) but they were 40-85% more than the theoretical shear strength of the concrete beam excluding shear stirrups (V_{uc}).
3. The shear peeling strength of the compression face plated beams were about 30% more than that of the tension face plated beams, for the tests conducted under this study.
4. The effect of plate thickness on the shear peeling strength of the compression face plated beams was negligible.

CHAPTER-10: ENHANCING THE SHEAR PEELING STRENGTH OF TENSION FACE PLATED BEAMS USING SIDE PLATES

CONTENTS

10.1 Introduction

Tests on RC beams strengthened with steel plates bonded to their tension faces have shown that the shear peeling is always caused by the formation of a diagonal shear crack in the vicinity of the plate end and that the presence of internal shear stirrups hardly makes any difference. Therefore, one way of improving the shear peeling strength of the tension face plated beams is to bond additional plates to their sides in the region above the plate ends. This delays the formation and propagation of the critical shear crack at the plate end.

In this report, the experimental study conducted on such beams is summarised first. Then, the improvement in shear peeling strength from these test results is also presented and the inferences from the test results are described. The results from this study are analysed in Chapter-11.

10.2 Specimens

Two beams were used for this study and the basic, unplated reinforced concrete beam is shown in Fig.10.1. Both the beams were bonded with a mild steel plate 6 mm thick and 3620 mm long to the tension face as shown in Figs.10.2a and 10.2b. Whereas one span of a beam had only a tension face plate, the other three shear spans of the beams were additionally bonded with side plates 340 mm deep and 6 mm thick but with varying lengths. Both shear spans of the two reinforced concrete beams were tested individually giving four results. Two shear spans of the same beam were tested individually by applying a single point load at a distance 1200 mm form the support. Premature failure in the longer span was prevented by a suitable clamping arrangement. The designation and details of each shear span tested is as follows.

(a) Test MB-01: This test was carried on the shear span bonded only with a tension face plate 6 mm thick as shown in Fig.10.2a. The tension face plate end was at 200 mm from the support.

(b) Test MB-02: This test was carried on the shear span bonded with a tension face plate 6 mm thick and side plates 340 mm deep, 6 mm thick and 1030 mm long as shown in Fig.10.2b. The tension face plate end was at 450 mm from the support and the side plate end close to the load point was 440 mm from the tension face plate end.

(c) Test MB-03: This test was carried on the shear span bonded with a tension face plate 340 mm deep, 6 mm thick and side plates 1545 mm long as shown in Fig.10.2b. The tension face plate end was at 600 mm from the support and the side plate end close to the load point was 885 mm from the tension face plate end.

(d) Test MB-04: This test was carried on the shear span bonded with a tension face plate 340 mm deep, 6 mm thick and side plates 1830 mm long as shown in Fig.10.2c. The tension face plate end was at 800 mm from the support and the side plate end close to the load point was 1030 mm from the tension face plate end.

The geometric properties of the beams tested are summarised in Table-10.1.

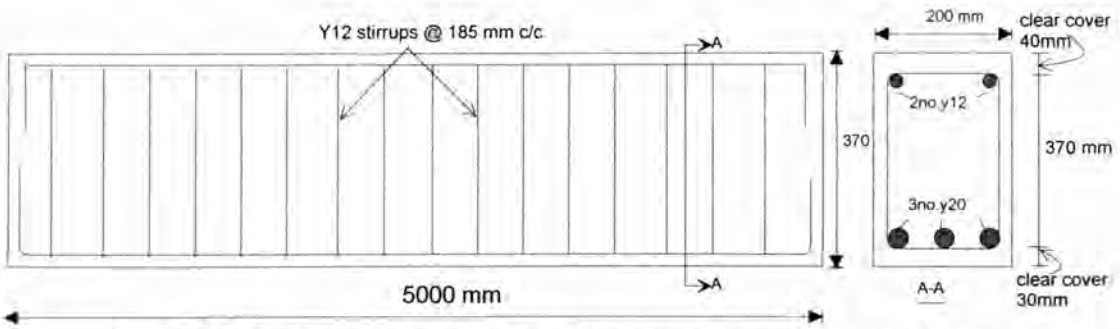

Fig.10.1. Reinforcement details of basic reinforced concrete beam

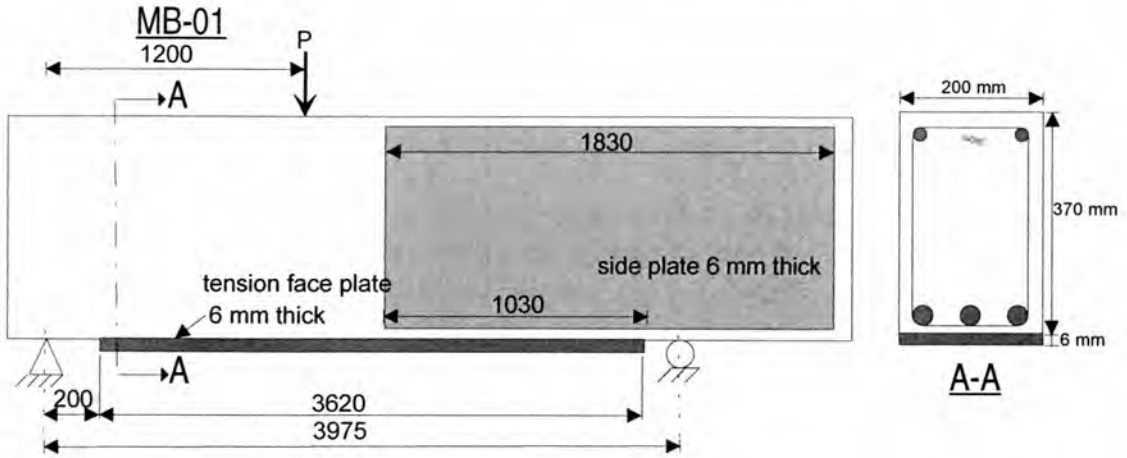

(a) Test MB-01

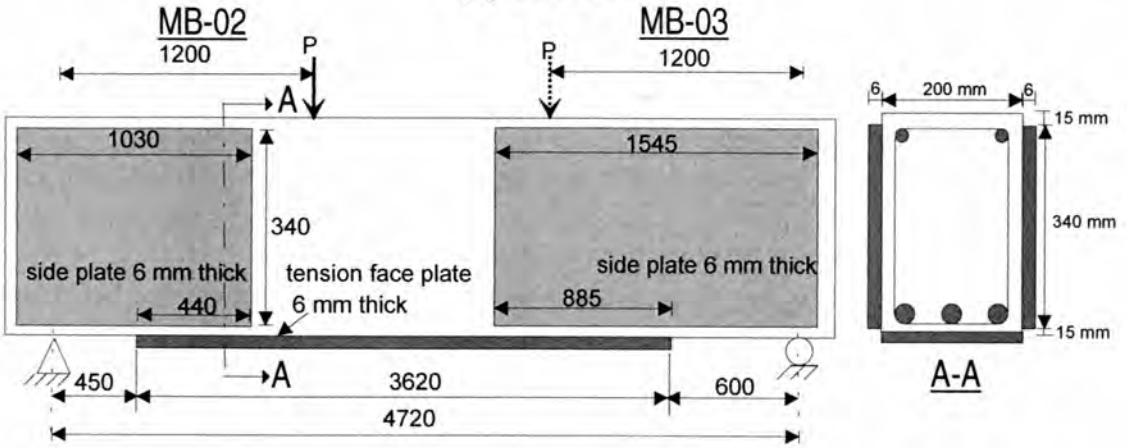

(b) Test MB-02 and Test MB-03

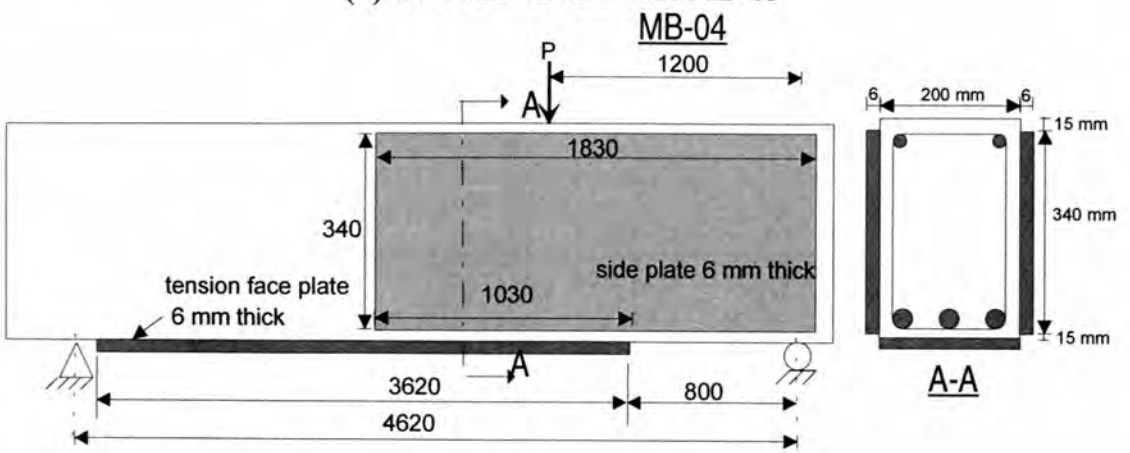

(c)Test MB-04

Fig.10.2. Details of beam tests

TABLE-10.1: Geometric properties

Common properties

Beam- width = 200 mm and depth = 370 mm
Compression reinforcement- Area A_{sc}=226 mm^2 and effective depth d_{sc} = 58 mm
Tension reinforcement - Area A_{st}=942 mm^2 and effective depth d_{st} = 318 mm
Shear stirrups-A_{sv} = 226 mm^2 and spacing s= 185 mm c/c
Total length of the beam = 5000 mm
The beams were simply supported and the length of shear span (a) = 1200 mm
Shear span/ effective depth of the beam (a/ d_{st}) = 3.77
Tension face plate- thickness (t_{tfp}) = 6 mm, width (b_{tfp}) = 200 mm
Area(A_{tfp}) = 1200 mm^2, Length of the plate = 3620 mm
Side plates- thickness (t_{sp}) = 6 mm, depth (d_{sp}) = 340 mm,
Area of two side plates (A_{sp}) = 4080 mm^2

Specific properties

Test	Span of the beam (mm)	Side plate length (mm)	Distance between tfp end & support (mm)	Distance between tfp end & sp end (mm)	Shear load in the span V (kN)	Moment at tfp end (kNm)
MB-01	3920	No sp	200	-	0.6977P	0.1395P
MB-02	4720	1030	450	440	0.7457P	0.3355P
MB-03	4720	1545	600	885	0.7457P	0.4474P
MB-04	4620	1830	800	1030	0.7402P	0.5922P

tfp-tension face plate, sp- side plate, P-applied load (kN)

10.3 Instrumentation

Three strain gauges were bonded to the tension face plate and two gauges to every side plate in order to detect the debonding at various sites of the plates. The arrangements of the strain gauges and their numbering are shown in Figs.10.3a and 10.3b for all the four tests conducted. The beam deflections at a load point were monitored by a dial gauge and also by a transducer.

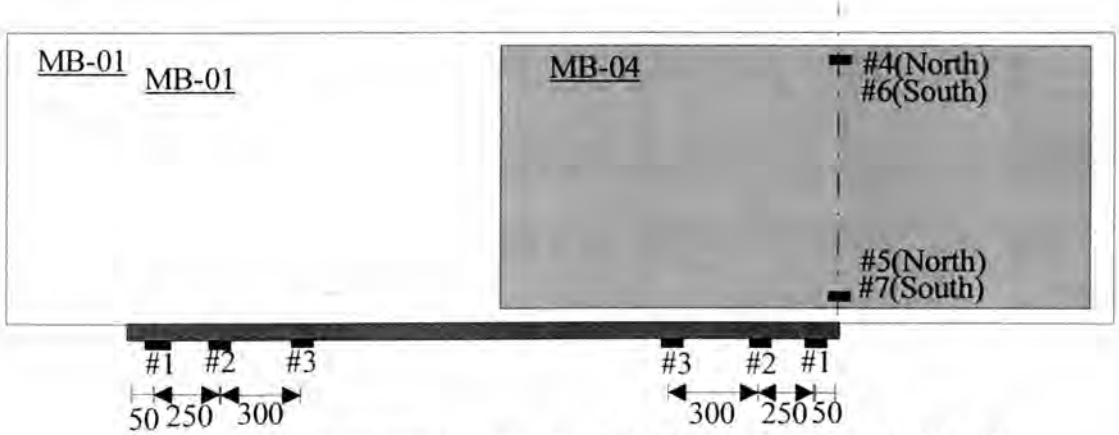

Fig.10.3a. Strain gauge arrangement for Tests MB-01 and MB-04

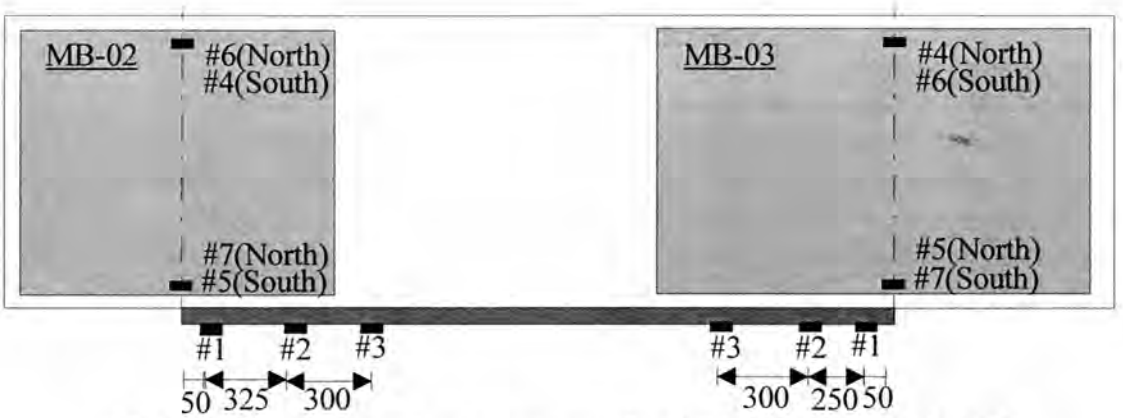

Fig.10.3b. Strain gauge arrangement for Tests MB-02 and MB-03

10.4 Material Properties

All the beams were cast in a single pour using ready mixed concrete supplied by a local manufacturer. The two beams used for this study were unused ones from a previous research project of the University of Adelaide. They were about two years old at the time of load testing. Hence, the material properties of the concrete for 779 days that are shown in Table-10.2 are appropriate for analytical computations. In this table, the individual values of each test are given under the "i" column and their mean value under "m" column.

Table-10.2: Material properties of the concrete

Age	E_c (MPa)		f_b (MPa)		f_c (MPa)		f_{cu} (MPa)	
(days)	i	m	i	m	i	m	i	m
779	34572	35433	3.92	4.05	52.6	51.5	59.5	58.0
	3661		4.06		51.2		52.5	
	36117		4.27		51.0		61.9	
	34381		3.94		51.3			

where, E_c= Elastic modulus of the concrete, f_c = Cylinder compressive strength of the concrete, f_{cu} = Cube compressive strength of the concrete, f_b =Brazilian tensile strength of the concrete, i = individual test results and m = mean value

Material properties of the steel plates, reinforcing bars and shear stirrups are shown in Table-10.3. The manufacturer's specifications of the material properties of the epoxy glue used for bonding the steel plates are indicated in Table-10.4.

Table -10.3: Material properties of the steel

Item	f_y (MPa)				f_u (MPa)			
Sample No.	1	2	3	Mean	1	2	3	Mean
Rebar Y20	478.7	485.1	478.1	480.6	566.3	567.5	565.3	566.4
Rebar& StirrupY12	454.5	458.0	455.3	455.9	552.6	550.9	552.6	552.0
Plate 6 mm thick	360.7	365.7	368.1	364.8	493.6	487.7	490.9	490.7

where f_y = Yield strength of the steel and f_u = Ultimate strength of the steel

Table-10. 4: Material properties of the glue Hilti CA 273 after 2 days (as tested by the manufacturer)

Compressive strength (ISO 604)	Tensile strength (ISO 527)	Flexural strength (ISO 178)	Elastic modulus in compression (ASTM D 695)	Tensile bond strength (ISO 527)	Maximum operating temperature
110-120 MPa	30-40 MPa	20-30 MPa	5000-6000 MPa	10-15 MPa	80° C

10.5 Test results

10.5.1 Test MB-01

Test-MB -01 was conducted on the beam glued only with the tension face plate as shown in Fig.10.2a. The shear force (V) in the span tested was 69.8% of the total applied load (P).

10.5.1.1 Crack pattern and failure mode

The first significant crack to occur was the inclined crack at a distance 400 mm from the load point when the applied load was 146 kN (V =101.9 kN) as can be seen in Fig.10.4a. As the load was increased to 158 kN (V =110.3 kN), a diagonal shear crack occurred in the vicinity of the tension face plate end, as shown in Fig. 10.4a and this caused the load to drop instantly. On reapplication of the load to a magnitude of 150.0 kN (V = 104.7 kN), the shear peeling of the plated beam occurred, as shown in Fig. 10.4b. This was due to the formation of the series of parallel inclined cracks and a long debonding crack along the concrete cover. At this stage, the beam could not sustain the applied load completely and it dropped to 98.6 kN at which the load test

was ended. Therefore, the pure shear peeling strength of tension face plated beam was 110.3 kN.

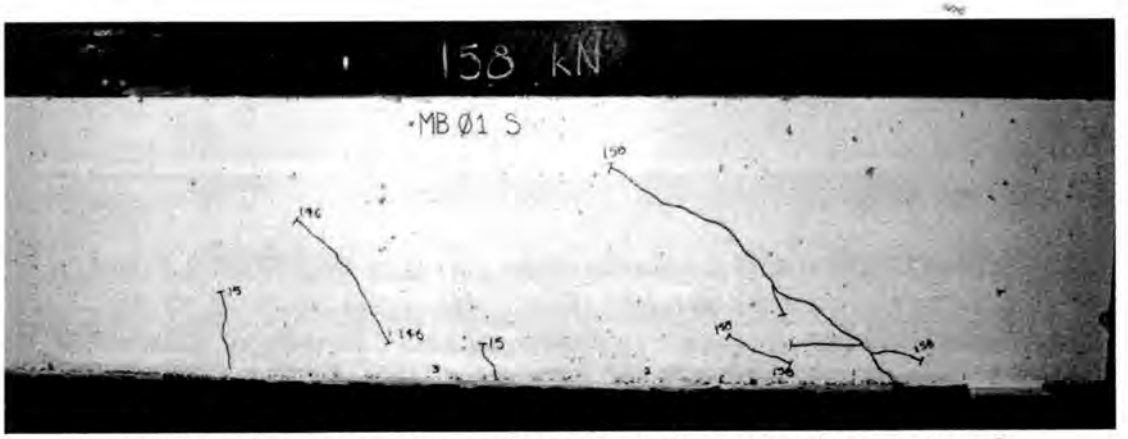

(a) Close view of the diagonal cracks at the tension face plate end

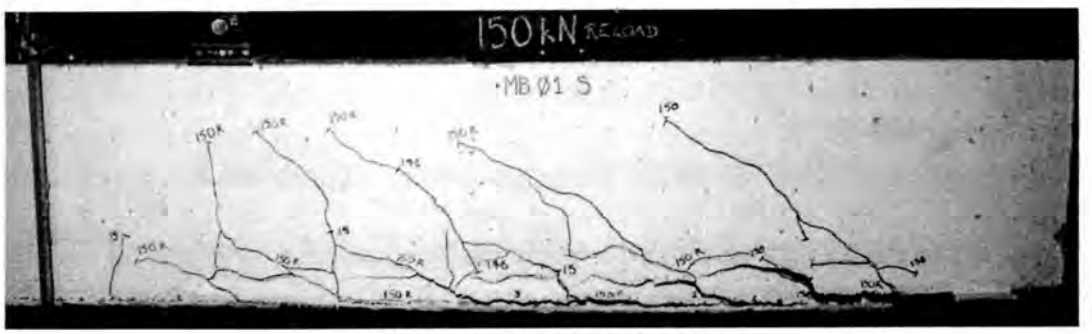

(b) Complete shear peeling

Fig.10.4. Test-MB -01 : Crack patterns

10.5.1.2 Longitudinal strains in the tension face plate and the deflection

Figure 10.5 illustrates the variation of strains recorded at all gauge locations that are shown in Fig.10.3a with the shear load in the shear span tested. It can be seen that the strains increased linearly at all the gauge locations with the applied load till the complete shear peeling of the plate occurred at a shear load of 110.3 kN, which is marked by the simultaneous drop in strain readings at all locations. The maximum magnitudes of strain were recorded at the gauge location #3 and it was 755 microstrains at the instance of the shear peeling. This is approximately 50% of the yield strain of the plate material. Figure 10.6 depicts the relationship between the shear load and the deflection recorded under the load point. The abrupt drop in shear

load shows the debonding of the tension face plated beam. The maximum deflection recorded at the end of the test was 9.72 mm.

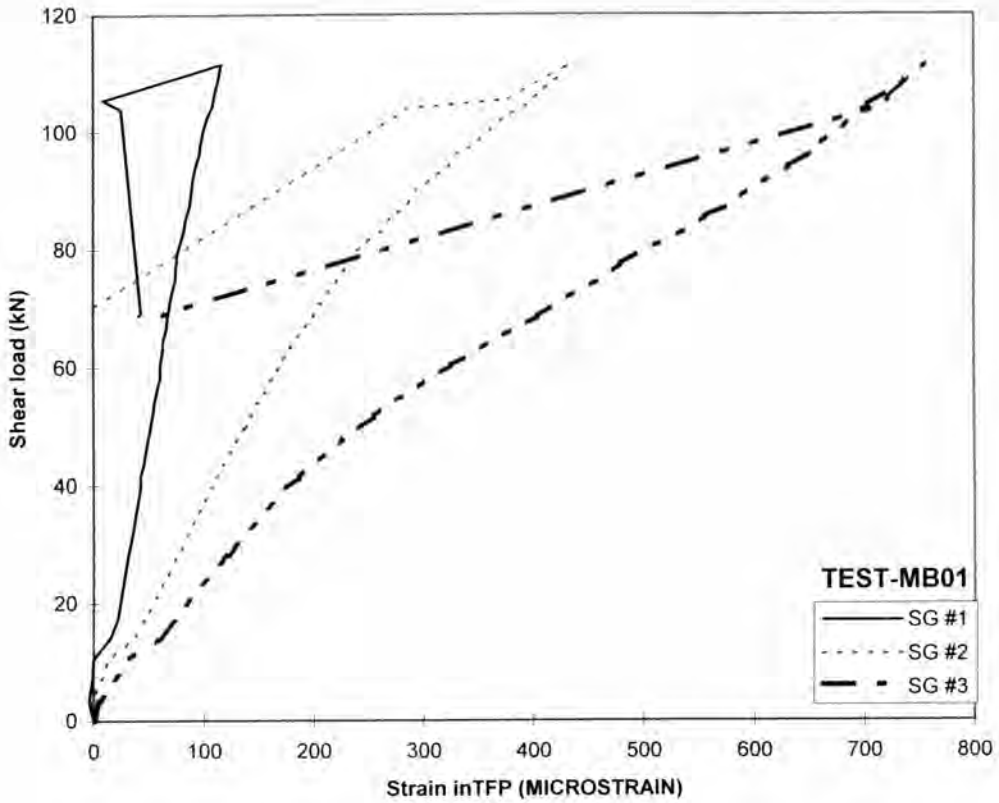

Fig.10.5. Test-MB-01: Strains in the tension face plate

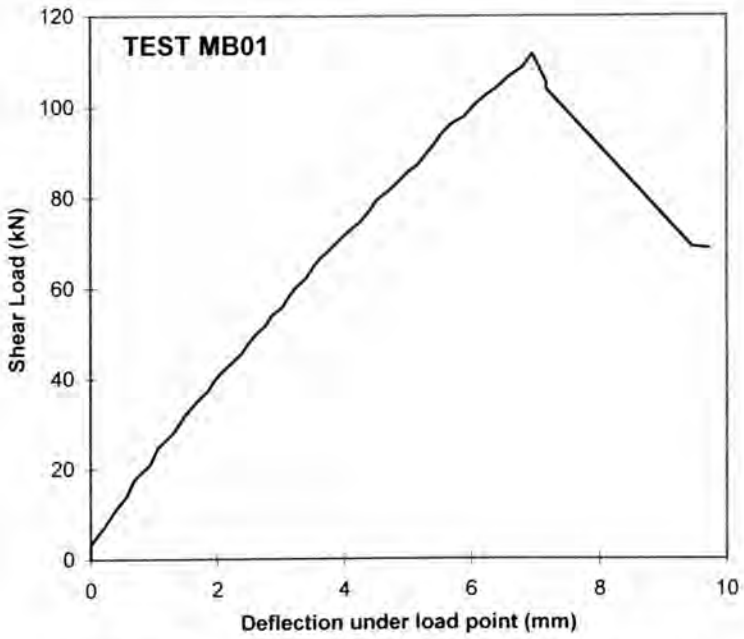

Fig.10.6. Test-MB-01: Deflection Vs Shear load

10.5.2 Test MB-02

Test-MB -02 was conducted on the beam bonded with the tension face plate and also with 1030 mm long side plates, as shown in Fig.10.2b. The shear force (V) in the span tested was 74.6% of the applied load (P).

10.5.2.1 Crack pattern and failure mode

As the side plates were covering the most of the beam depth and also the length of the shear span, the formation of the cracks could not be observed till the debonding of the tension face plate occurred at an applied load of 153 kN (Shear load V=114.1 kN). The correspondng bending moment at the tension face plate end was 51.3 kNm. The peeling of the tension face plate occurred by the separation of the plate from the concrete by long debonding cracks that were preceded by a series of shear cracks as shown in Fig.10.7. This caused the beam to shed the load instantly to 95.3 kN (V=71.1 kN) and hence, the test was terminated.

Fig.10.7. Test MB-02: Peeling of the tension face plate

10.5.2.2 Longitudinal strains in the tension face plate and the deflection

Figures 10.8 and 10.9 illustrate the variation of strains recorded at all gauge locations in the tension face plate and in the side plates, that are shown in Fig.10.3b, with the applied shear load. It can be seen that the strain dropped slightly at the gauge #1 in the tension face plates and the strain curves for the bottom locations in the side plates show a minor plateau, when the shear load was about 60 kN; this indicates the

formation of a crack or minor loss in bond at the tension face plate end. In all other locations, the magnitudes of strain increased linearly with the applied load till the debonding of the tension face plate occurred at a shear load of 114.1 kN, which is marked by the simultaneous drop in strain readings and shear load at all locations. The maximum magnitudes of strain recorded at the gauge locations in the tension face plates were 67 microstrains at #1, 900 microstrains at #2 and 1104 microstrains at #3. In the bottom portion of the side plate, the maximum strains recorded were 437 microstrains at gauge #5 and 489 microstrains at gauge #7. The corresponding magnitudes on the top portion of the side plates were 261(compressive) and 302(compressive) microstrain at the gauge locations #4 and #6. Figure 10.10 depicts the relationship between the shear load and the deflection recorded under the load point. The complete debonding of the tension face plated beam is indicated by the sudden increase in the deflection from 9.3 mm t0 16.9 mm while the shear load dropped from 114.1 kN to 71.0 kN.

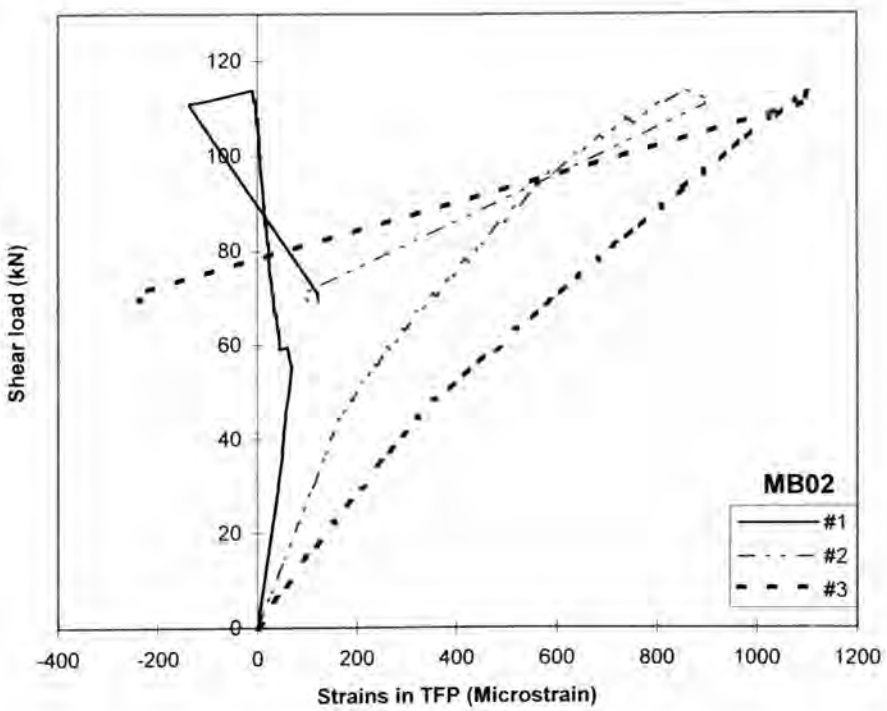

Fig.10.8. Test-MB-02: Strains in the tension face plate

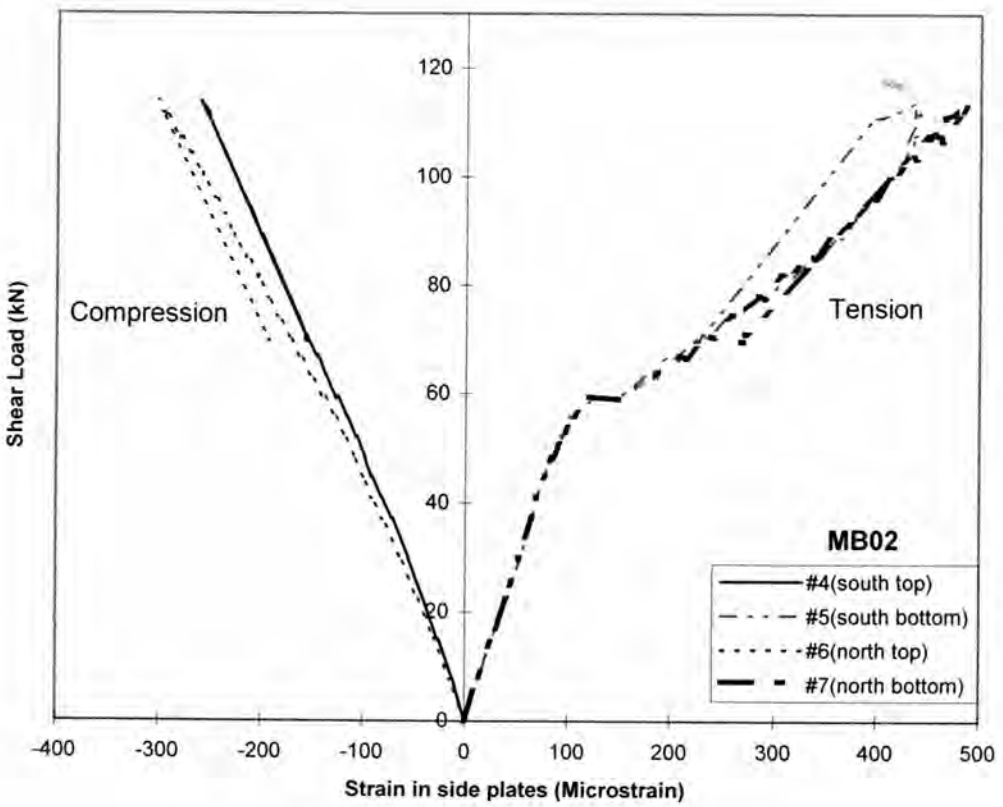

Fig.10.9. Test-MB-02: Strains in the side plates

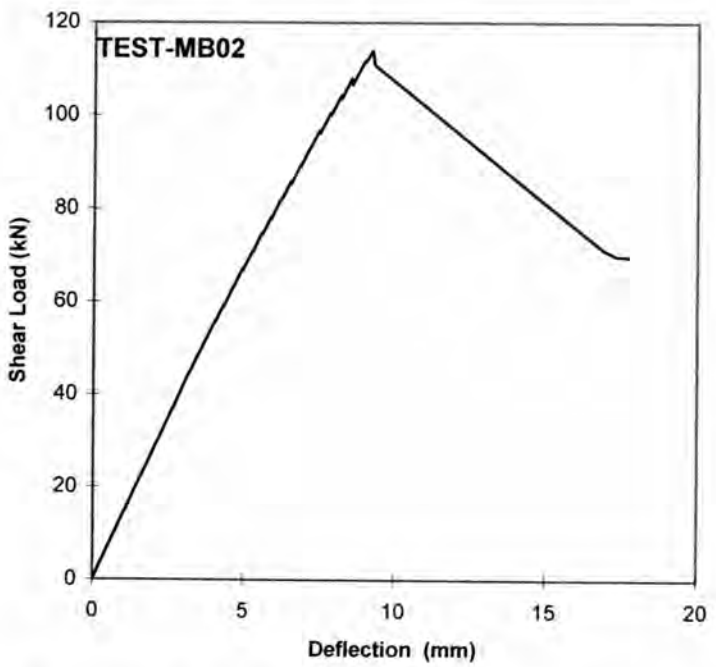

Fig.10.10. Test-MB-02: Deflection Vs Shear load

10.5.3 Test MB-03

Test-MB -03 was conducted on the beam bonded with the tension face plate and also bonded with 1545 mm long side plates, as shown in Fig.10.2b. To avoid any premature flexural failure, additional reinforcement in the form of bolted plates were provided in the long shear span as shown in Fig.10.11. The shear force (V) in the span tested was 74.6% of the applied load (P).

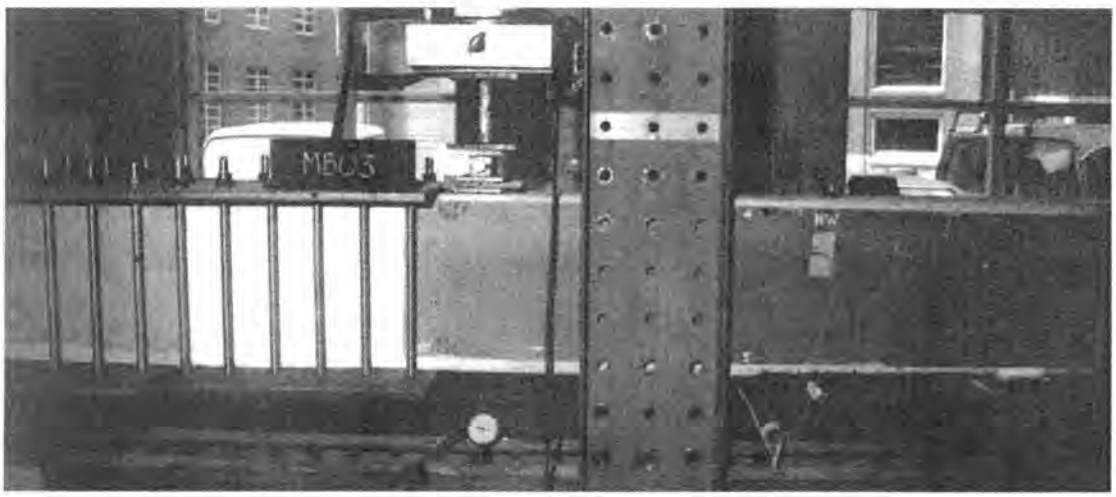

Fig.11 MB-03-Test set-up

10.5.3.1 Crack pattern and failure mode

The first significant crack that could be seen was the debonding crack that extended from the tension face plate end to the bottom corner of the side plate, when the applied load was 145 kN (V=108.2 kN), as shown in Fig.10.12a. As the applied load was increased to 169 kN (V=126.1 kN), this debonding crack further extended upwards along the edges of the side plates to the load point (Fig.10.12a). It can be seen that this caused the peeling of the side plates as well as the tension face plate; the bending moment at the end of the tension face plate at this stage was 75.7 kNm. Figure 10.12b shows the final crack pattern after removing the side plate. It can be seen that the peeling of the tension face plate was caused by the separation of the plate from the

concrete by long debonding cracks. After the peeling of the side plates, the applied load dropped suddenly to 110.7 kN and the load test was terminated.

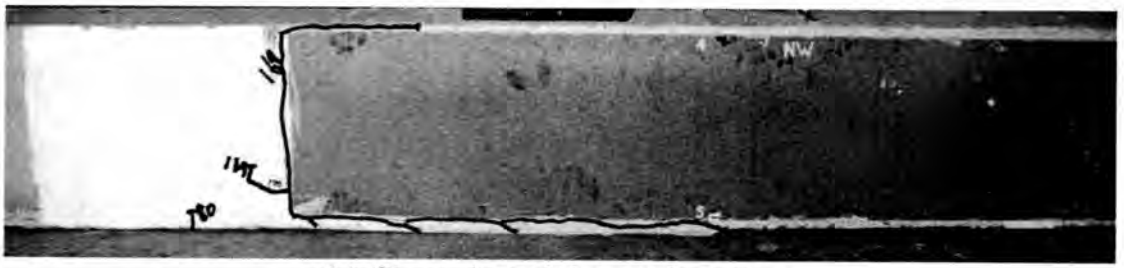

(a) Clear view of the crack pattern

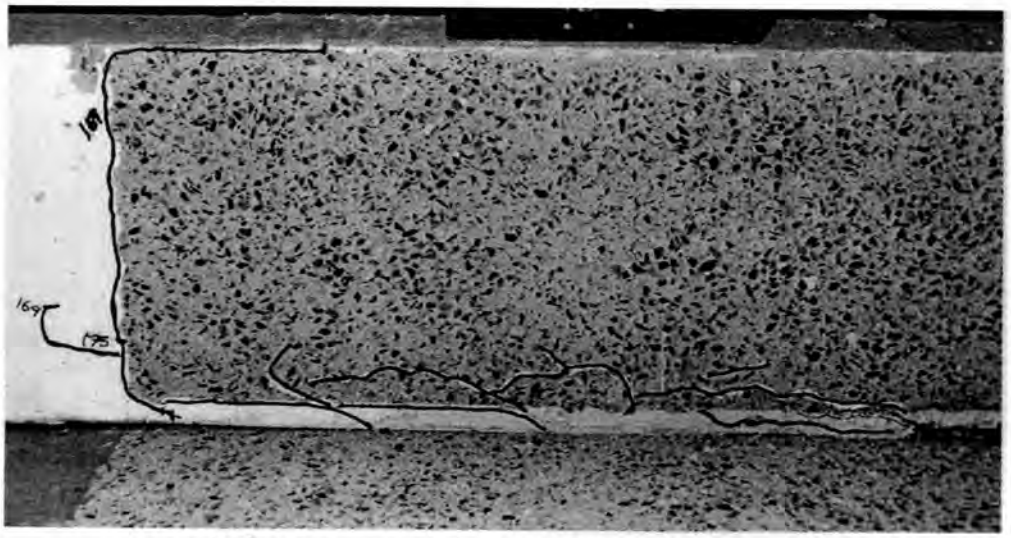

(b) Crack pattern after removing the side plate

Fig.10.12. Test-MB-03: Crack patterns

10.5.3.2 Longitudinal strains in the tension face plate and the deflection

Figures 10.13 and 10.14 show the variation of strains recorded at all gauge locations in the tension face plate and in the side plates, that are shown in Fig.10.3b, with the applied shear load. It can be seen that the strain dropped slightly at the gauge #1 in the tension face plates when the shear load was about 60 kN; this indicates the formation of a crack or minor loss in bond at the tension face plate end. In all other locations, the magnitudes of strain increased linearly with the applied load till the applied shear load was about 100 kN and thereafter the strain magnitudes set to drop gradually in the bottom region of the side plates and the tension face plate. This indicates the propagation of debonding crack along the edges of the side plates.

Finally, the debonding of the tension face plate and the side plates occurred at a shear load of 126.1 kN; this is indicated by the sudden drop in strain readings and shear load at all locations.

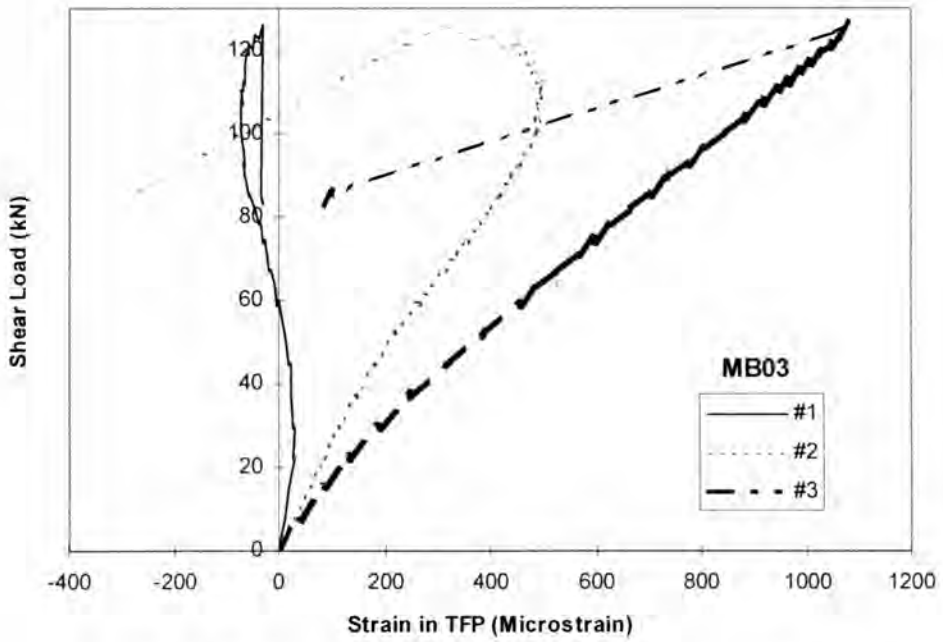

Fig.10.13. Test-MB-03: Strains in the tension face plate

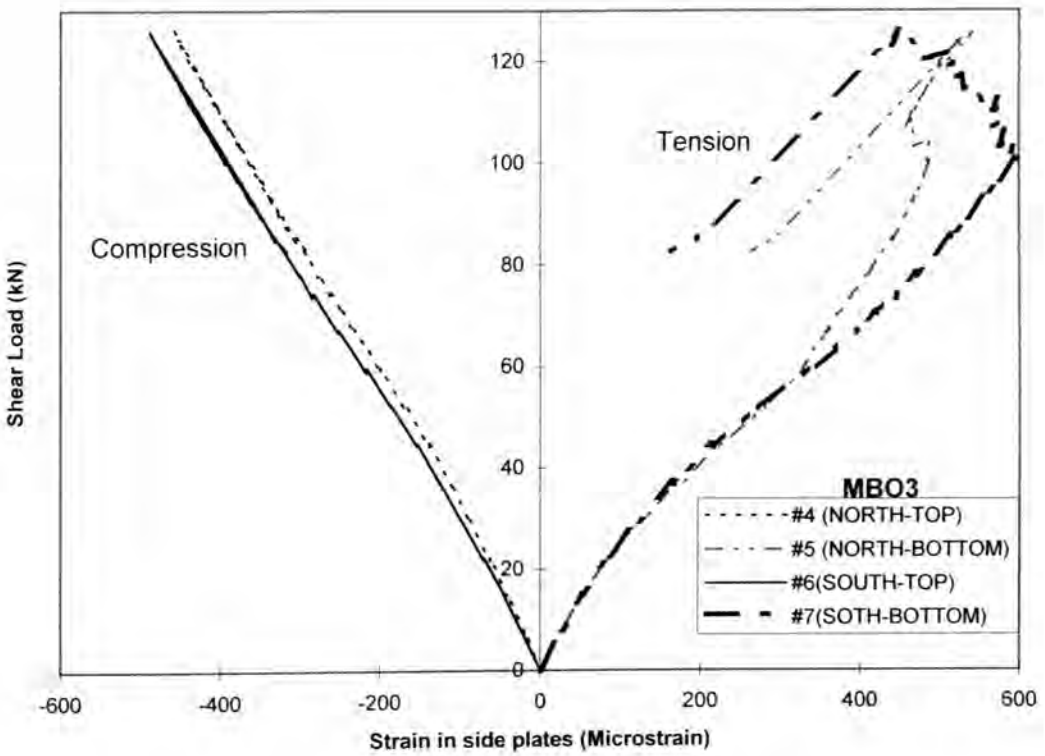

Fig.10.14. Test-MB-03: Strains in the side plates

The maximum magnitudes of strain recorded at the gauge locations in the tension face plates were 29 microstrains, 495 microstrains and 1081 microstrains at the gauge locations #1, #2 and #3 respectively. In the bottom portion of the side plate, the maximum strains recorded were 545 microstrains at gauge #5 and 595 microstrains at gauge #7. The corresponding magnitudes on the top portion of the side plates were 458(compressive) and 489(compressive) microstrains at the gauge locations #4 and #6.

Figure 10.15 depicts the relationship between the shear load and the deflection recorded under the load point. The debonding of plated beam is indicated by the sudden drop in the shear load and the maximum deflection recorded was 12.1 mm.

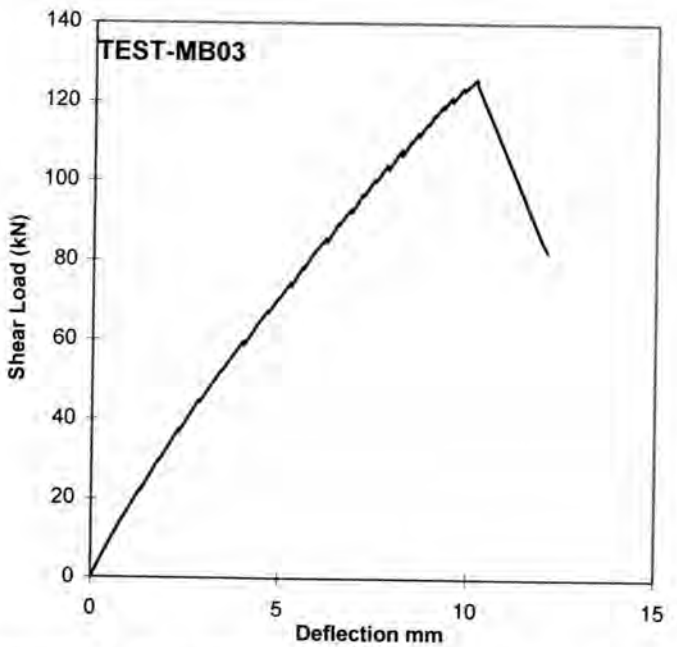

Fig.10.15. Test-MB-03: Deflection Vs Shear load

10.5.4 Test MB-04

Test-MB -04 was conducted on the beam bonded with the tension face plate and also bonded with 1830 mm long side plates, as shown in Fig.10.2c. To avoid any premature flexural failure, additional reinforcement in the form of bolted plates were

provided in the long shear span as shown in Fig.10.16. The shear force (V) in the span tested was 74% of the applied load (P).

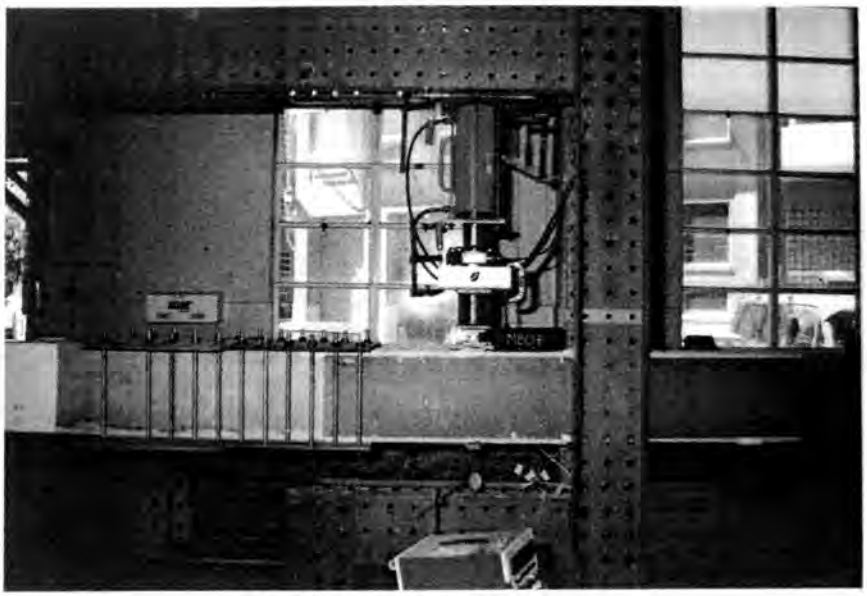

Fig.10.16. MB-04-Test set-up

10.5.4.1 Crack pattern and failure mode

Cracks could be seen beneath the side plates when the applied load was 130 kN (V=96.2 kN). As the applied load was increased to 179.2 kN (V=132.6 kN), the peeling of the tension face plate occurred suddenly due the formation of the long debonding cracks along the edges of the side plate as shown in Fig.10.17a. The bending moment at the tension face plate end at this stage was 106.1 kNm. Figure 10.17b shows the final crack pattern after removing the side plate. It can be seen that the peeling of the tension face plate was caused by the separation of the plate from the concrete by long debonding cracks and they did not encompass the side plates as happened in test MB-03. After the peeling of the tension face plate, the applied load dropped from 179.2 kN to 135.4 kN and therefore, the load test was terminated.

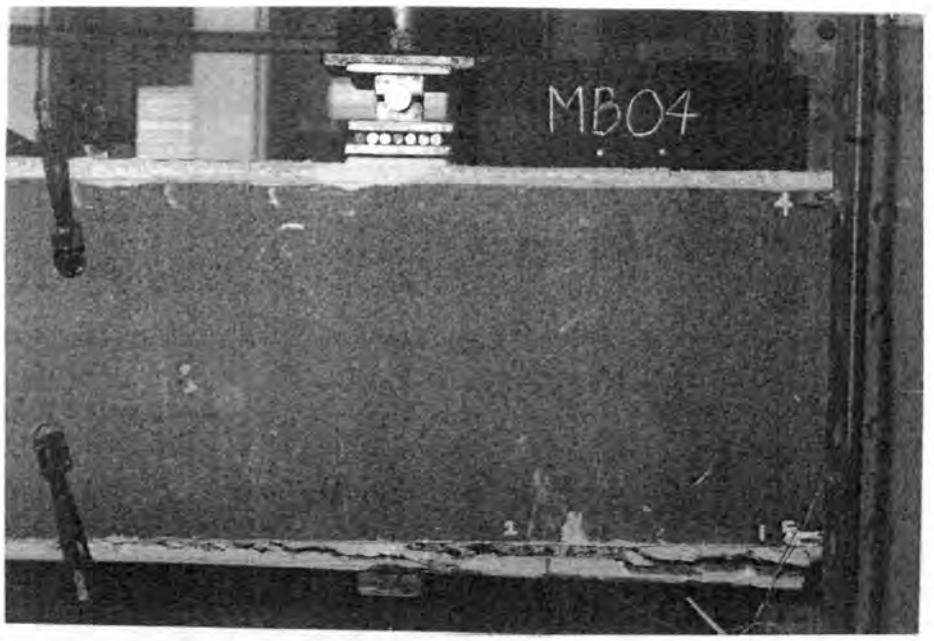

(a) Close view of the debonding of tension face plate

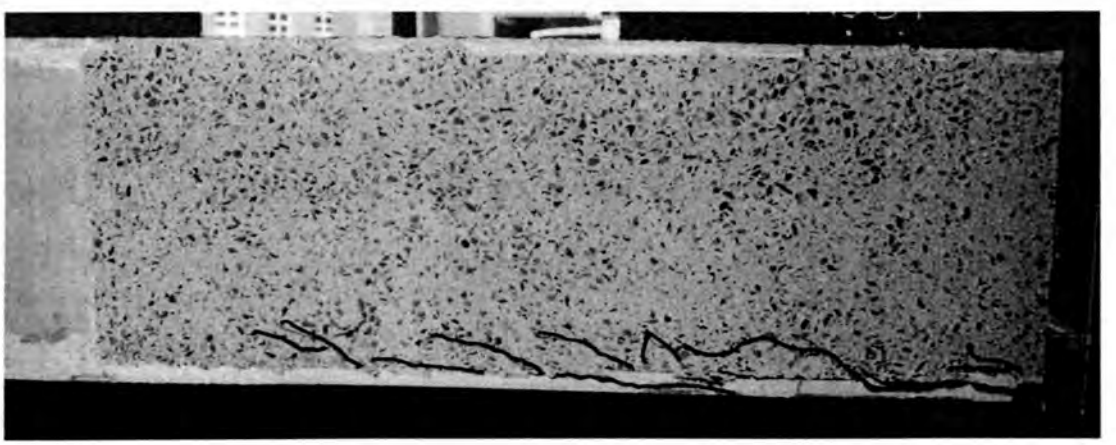

(b) Crack pattern after removing the side plate
Fig.10.17. Test-MB-04: Crack patterns

10.5.4.2 Longitudinal strains in the tension face plate and the deflection

Figures 10.18 and 10.19 show the variation of strains recorded at all gauge locations in the tension face plate and in the side plates, that are shown in Fig.10.3a, with the applied shear load. It can be seen that the strains in the tension face plate increased linearly until the shear load was approximately 100 kN and thereafter they started to reduce smoothly and finally they dropped abruptly due to the debonding of the tension face plate. On the contrary, the strain magnitudes in the side plates increased linearly

till the end of the test, indicating that the bond between the concrete and the long side plates was lost only partially.

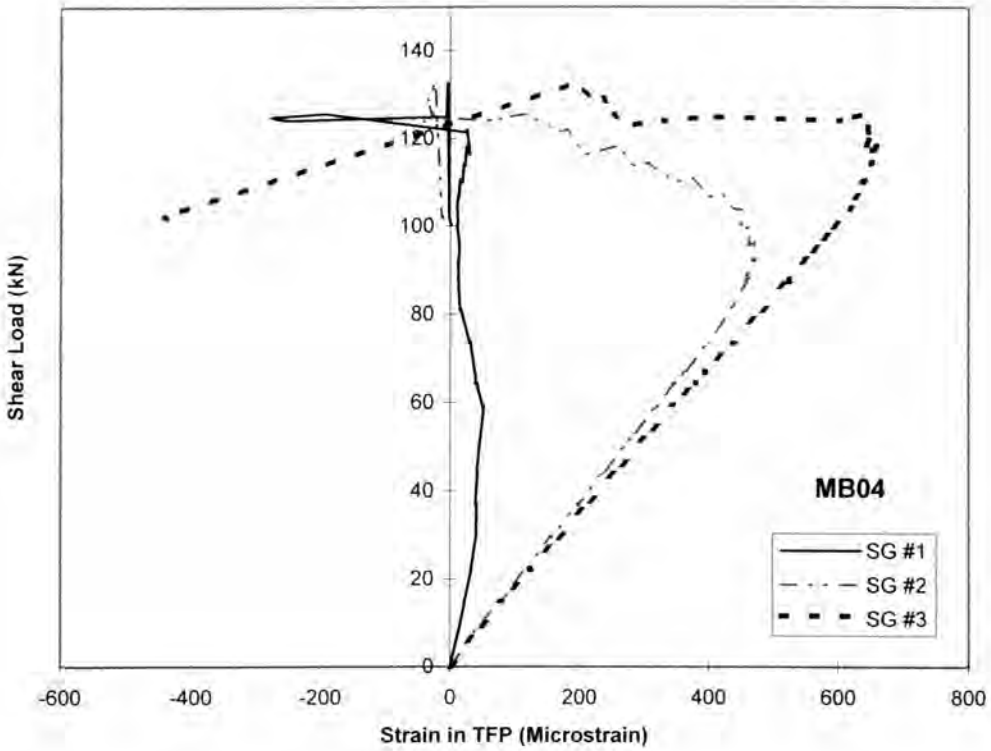

Fig.10.18. Test-MB-04: Strains in the tension face plate

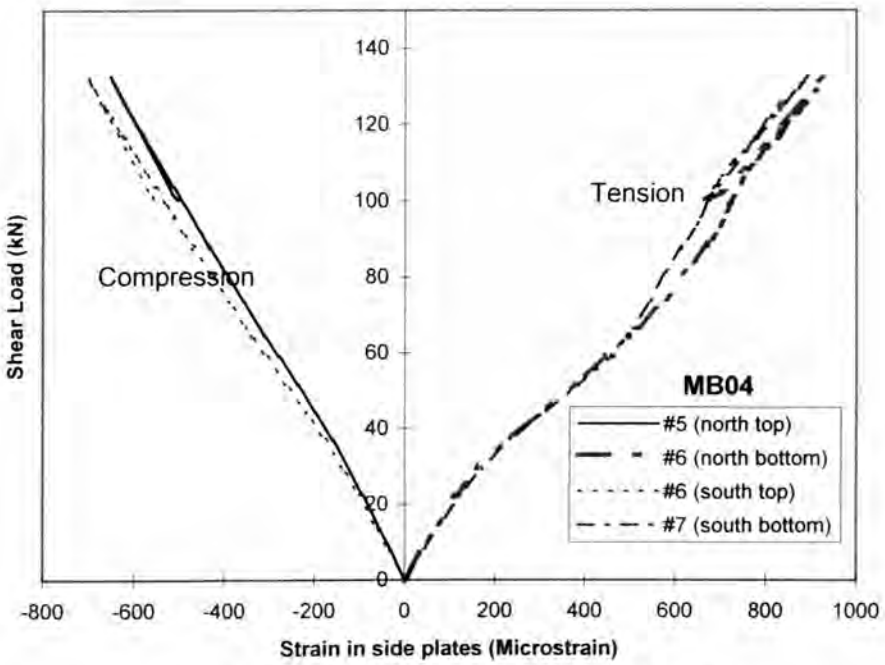

Fig.10.19. Test-MB-04: Strains in the side plates

The maximum magnitudes of strain recorded at the gauge locations in the tension face plates were 50 microstrains, 470 microstrains and 646 microstrains at the gauge locations #1, #2 and #3 respectively. In the bottom portion of the side plate, the maximum strains recorded were 933 microstrains at gauge #5 and 895 microstrains at gauge #7. The corresponding magnitudes on the top portion of the side plates were 653(compressive) and 705(compressive) microstrains at the gauge locations #4 and #6.

Figure 10.20 depicts the relationship between the shear load and the deflection recorded under the load point. The complete debonding of the tension face plated beam is indicated by the sudden increase in the deflection from 12.5 mm to 21.5 mm while the shear load dropped from 132.6 kN to 100.2 kN.

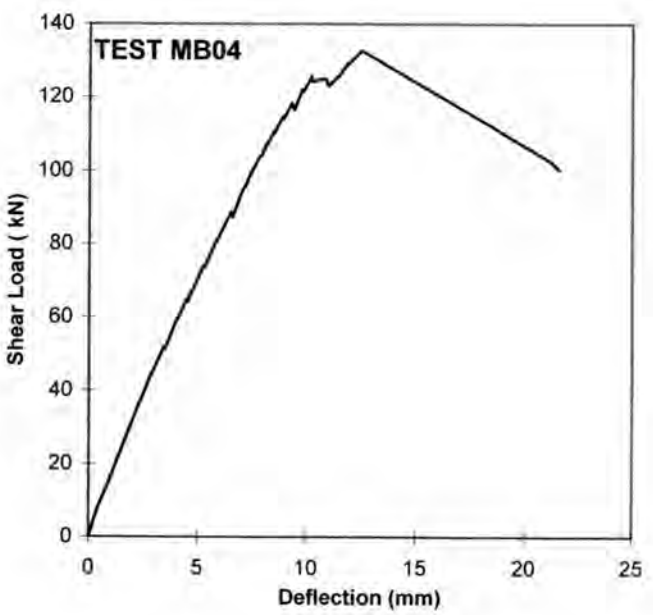

Fig.10.20. Test-MB-04: Deflection Vs Shear load

10.6 Discussion of test results

The salient features of the results from all the four tests are summarised in Table-10.5. It can be seen that the shear peeling strength of the tension face plated beams increased from 110.3 kN for MB-01 without side plates to 132.6 kN for MB-04 that

was bonded with the longest side plates. The increase in shear peeling strength due to side plates looks modest initially. However, it may be noted that the tension face plate end in case of MB-01 was predominantly only under shear but in case of MB-03 and MB-04 they were subjected to considerable moment also, i.e. the moment at the tension face plate end at the instance of peeling was 22.6 kNm for MB-01 while it was 106.1 kNm for MB-04. Therefore, detailed computations have been carried out in Chapter-11 to calculate the pure shear peeling strength and the pure flexural peeling capacity of each beam to study the interaction between moment and shear on peeling. It may also be noted that peeling occurred well before the maximum strains recorded in both the tension face plate and the side plates were less than the yield strain of the steel plate.

Table-10.5: Test results

Test	Side plate length (mm)	Shear load at peeling (kN)	Moment at tfp end at peeling (kNm)	Maximum strain in tfp ($x10^{-6}$)	Maximum strain in sp ($x10^{-6}$)	Failure mode
MB-01	No sp	110.3	22.6	755	-	Shear peeling of tfp
MB-02	1030	114.1	51.3	1104	489	Shear peeling of tfp;no debonding in sp
MB-03	1545	126.1	75.7	1081	595	Debonding crack at tfp end caused both tfp and sp to peel
MB-04	1830	132.6	106.1	646	933	Peeling of tfp due to long debonding cracks at tfp end

tfp-tension face plate, sp- side plate

10.7 Conclusions

In this study, it was shown that the shear peeling strength of the tension face plated beams could be enhanced by bonding additional side plates at the tension face plate end region. Analytical models are needed to study the impact of shear/flexure interaction on shear peeling strength and these are discussed in Chapter-11.

CHAPTER-11: MATHEMATICAL MODELS FOR SHEAR PEELING IN PLATED BEAMS

CONTENTS

11.1 Introduction

This chapter deals with the development and calibration of mathematical models for shear peeling in reinforced concrete beams bonded with different configurations of plates that were studied in Chapters 6 to 10. From these studies that were conducted on the shear peeling aspect, the significance of the formation of the critical shear crack and its impact on debonding was brought out. Only a few models are available for shear peeling in plated beams in the documented literature (Refer Chapters 2 and 3). These are empirical guidelines such as those prescribed by Swamy for tension face plated beams (refer section 2.7.1) and the lower bound approach suggested by Oehlers (Section 2.7.3.1), that the shear peeling strength of a tension face plated beam can be assumed to be the shear strength of the concrete beam excluding the shear stirrups (V_{uc}). Therefore, there is a need to develop and calibrate analytical procedures for a variety of plate configurations.

Keeping this in mind, analytical procedures are developed by using as a basis the shear friction and crack sliding failure concepts explained in Chapter-5. Here, it is stressed that the shear peeling strength is not merely the shear strength of the plated reinforced concrete beam but it has a lot to do with the debonding of the external plates. Therefore, a procedure developed to compute the bond strength between an adhesively bonded steel plate and a concrete element is described first. This procedure is developed by combining the debonding model suggested by Oehlers and Moran (1990) and the available test results on axial peeling of steel plated beams as described in Sections 4.3.2 and 4.4.2.1. The shear peeling models for side plated beams, tension face plated beams, angle plated beams, compression face plated beams and tension face plated beams

bonded with additional side plates are described in the subsequent sections. All the models are calibrated against the test results from the present study and also the test results from other studies. It may be noted that the focus of this chapter is on steel plated beams as the shear peeling tests conducted on FRP plated beams (Chapter-7) were limited in scope.

11.2 Axial force exerted by externally bonded steel plates

11.2.1 Introduction

In developing a model for shear peeling of plated beams, incorporating the contribution of the externally bonded plate into the model is critical. To recognize the restraint provided by the plates against the shear peeling failure, we need to know the force exerted by the plate across a crack plane for a given bond length. However, there is no reliable procedure available to estimate the bond strength between the concrete/steel plate interface, as brought out in Sections 4.13.2 and 4.13.3. Therefore, the test results presented in the literature review on axial peeling of steel plated beams in Chapter-4 are reanalysed to develop a relationship for computing the maximum force that the steel plate can apply across the critical diagonal crack.

11.2.2 Analytical model for axial strength of adhesively bonded plate

The axial force P_b in Fig.11.1b has an upper limit of the yield strength of the plates and it is given as

$$(P_b)_y = A_p f_{yp} \tag{11.1}$$

where A_p is the area of the plate. In the case of two side plates, $A_p=A_{sp}=2t_{sp}d_{sp}$ and for a tension face plate $A_p=A_{tfp}=t_{tfp}b_{tfp}$. Here A_{sp} is the area of two side plates, t_{sp} and d_{sp} are the thickness and depth of the individual side plate respectively; A_{tfp}, t_{tfp} and b_{tfp} are the area, thickness and width of the tension face plate respectively. However the plate may

debond prior to this yield strength being achieved. Finite element analyses performed by Oehlers and Moran(1990) have shown that the direct stresses normal to the bond interface, A-B in Fig.11.1b, has the distribution in Fig.11.1a, where a peak tensile stress occurs at the edge of the concrete slab or beam which causes debonding (Refer to Section 2.7and Fig.2.19).

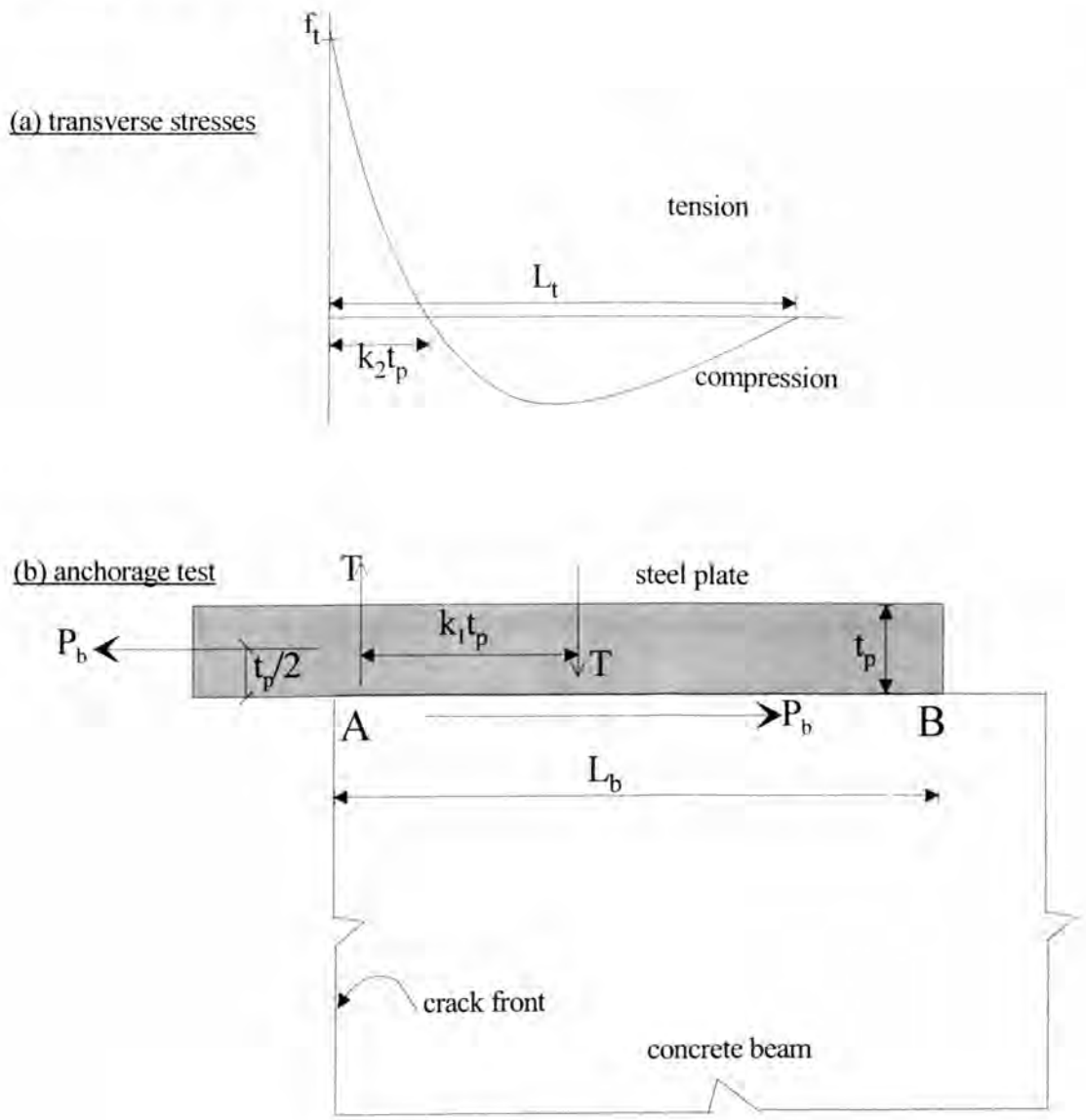

Fig.11.1 Bond stress resultants

It has been shown by Oehlers and Moran (1990) that the only parameter that can affect the lateral stress distribution and lateral force distribution in Figs.11.1a and 11.1b is

the plate thickness t_p subject to the following three conditions. Firstly, the material stiffness of the steel plate and that of the concrete slab or beam should remain constant. Secondly, the plate thickness t_p should be much less than that of the slab or beam and this occurs normally in practice. Finally, the length of the bonded plate L_b is greater than the length of the transverse stress distribution L_t in Fig.11.1. If sf_t is the mean stress in the tensile region k_2t_p in Fig. 11.1a, then we get from rotational equilibrium of the forces in Fig.11.1b

$$P_b = Kf_t t_p b_p \tag{11.2}$$

where the constant $K = 2k_1k_2s$.

By substituting Taljsten's and Swamy's test results (Sections 4.3.2 and 4.4.2.1) for P_b in Eqn.11.2, the variation in K can be derived as shown in Fig.11.2. It can be seen that when the length of the bonded plate L_b is greater than $65t_p$, then K is constant at 71. This is due to the fully fledged development of the stress field shown in Fig.11.1a and hence the magnitude of K is independent of the bond length L_b as $L_b > L_t$. Furthermore, it can be seen in Fig.11.2 that when $L_b < 65t_p$, then K can be assumed to reduce linearly. Therefore, from Eqn.11.2 and the bond failure test results shown in Fig.11.2, the bond strength of a steel plated beam is given by

$$P_b = 71 f_t t_p b_p, \text{ for } L_b > 65t_p \tag{11.3}$$

and

$$P_b = 1.09 L_b f_t b_p, \text{ for } L_b < 65t_p \tag{11.4}$$

where b_p is the width of the plate and bearing in mind that the axial strength is the lesser of P_b and $(P_b)_y$.

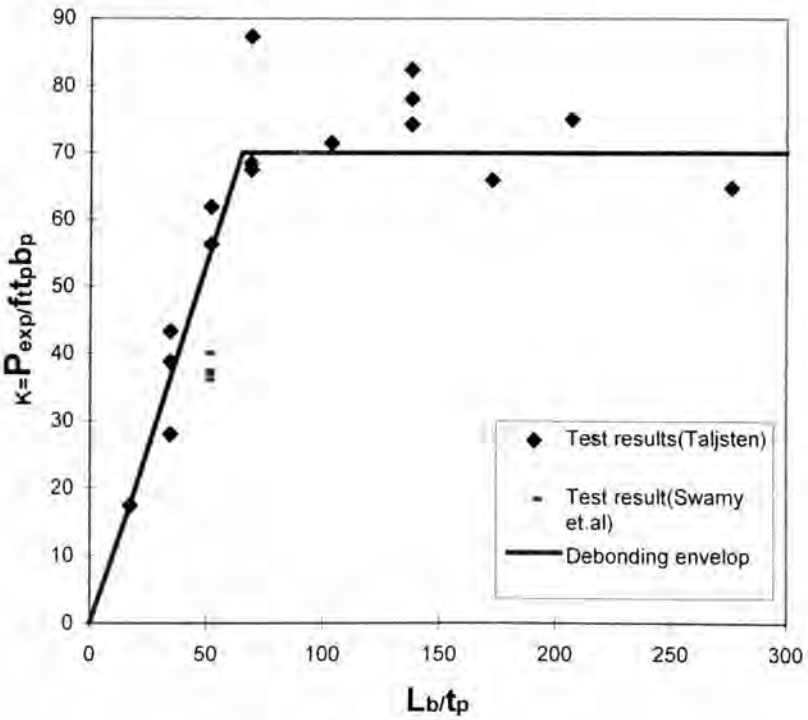

Fig.11.2. Bond failure test results

For the special case of beams with a pair of side plates, P_b is given by

$$P_b = 142 f_t t_{sp} d_{sp}, \text{ for } L_b > 65 t_{sp} \tag{11.5}$$

and

$$P_b = 2.18 f_t L_b d_{sp}, L_b \le 65 t_{sp}. \tag{11.6}$$

In the above equations, t_{sp} and d_{sp} are the thickness and depth of an individual side plate only.

11.3 Mathematical Model for shear peeling of beams bonded with steel plates to the sides

11.3.1 Introduction

The series of tests conducted on the shear peeling aspect of the reinforced concrete beams bonded with plates to the sides led to following three major conclusions (Refer Sections 6.6-6.8): firstly, the shear peeling of plated beams is extremely rapid and it is always

associated with the formation of a critical diagonal crack and the subsequent sliding failure along the crack plane; secondly the location of the critical diagonal crack in side plated beams is different from that of the unplated reinforced concrete beams without shear stirrups; thirdly, the presence of shear stirrups has only a minor effect if any, when the mean strains in the plate are tensile as the opening of the shear crack that is required to stretch the stirrups causes the debonding of the plate. However, shear stirrups do enhance the shear peeling strength when the strain is compressive. The other major conclusion was that the shear peeling resistance depends on the vertical position of the plate. Moreover, these tests confirm that the shear peeling strengths of plated beams are higher than the shear strength of the beams without stirrups and without plates V_{uc}. This shows that V_{uc} can be used as a lower bound for the shear peeling resistance of plated beams as recommended by Oehlers (Section 2.7.3.1). However the use of V_{uc}, as a lower bound value for the shear peeling resistance of plated beams, may severely restrict the application of plating particularly on beams with more than nominal stirrups which, subsequently, require to carry a shear load greater than V_{uc}. Hence it is necessary to develop a model for shear peeling that allows for: any position and geometry of the plate; the possible formation of a critical diagonal crack at any position in the shear span; and the fact that stirrups do not affect the shear peeling resistance when the mean strains in the plates are tensile.

Keeping this in view, the literature on the shear strength of concrete beams was studied to find a suitable model in which the shear strength of the concrete is correlated with the position of the critical diagonal crack. The crack sliding model developed at the Technical University of Denmark by Zhang (Refer to Chapter-5) was found suitable as it

can be modified and adapted for our case. The technique is illustrated in Fig.11.3a and requires that at every possible location of a diagonal crack, such as those shown, it is necessary to determine both the applied shear force required to form the diagonal crack V_{cr} and the applied shear force to fail the cracked section V_u. These shear parameters are plotted and where they intercept gives both the position of the root of the critical diagonal crack from the support $(L_d)_{crit}$ and the strength V_{uc} in case of the unplated beam. For a detailed description of the basic formulations of this model, the reader is referred to Chapter-5 in general and Section 5.3 in particular. This crack sliding model is adapted in the following sections for beams with two side plates, such as those shown in Fig.11.3b, that are subjected to point loads. However, it may be worth noting that the crack sliding model can easily be extended to cover continuous beams and beams with uniformly distributed loads, as discussed in Chapter-5.

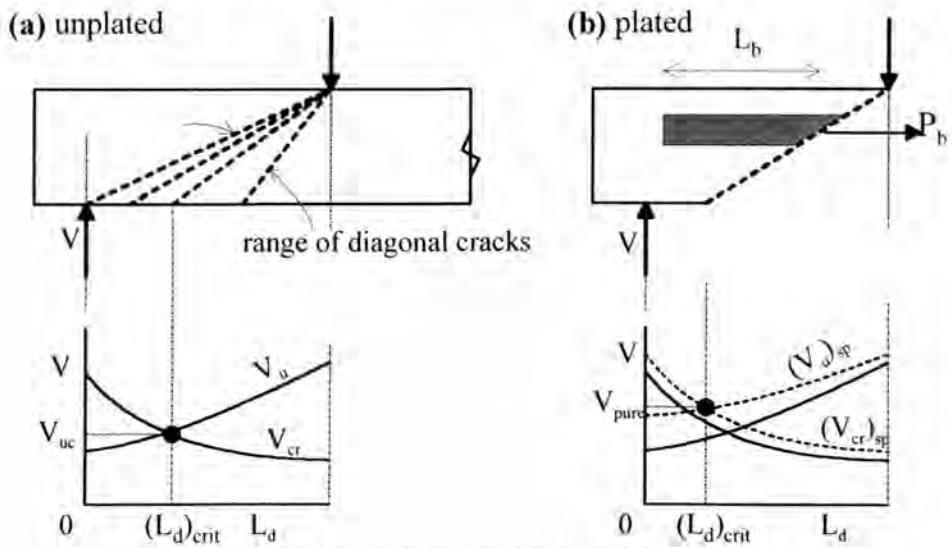

Fig.11.3 Crack sliding model

11.3.2 Shear peeling strength of side plated beams

The shear peeling behaviour of reinforced concrete beams bonded with side plates can be modeled by modifying the crack sliding theory to account for the contribution of side plates towards improving:

(a) the load to cause a diagonal crack at a given location (V_{cr}) and

(b) the shear load (V_u) to cause failure along an existing crack, by transforming the crack into a fully fledged yield line that results in sliding and separation of the critical crack, as shown in Fig.11.3b.

11.3.2.1 Contribution to diagonal cracking load ($V_{cr,sp}$)

The presence of side plates delays the formation and resists the propagation of a diagonal crack at a given location. This can be accounted by the fact that the diagonal crack at a given location occurs when the stress in the concrete equals the direct tensile strength of the concrete f_t corresponding to a strain, say ε_t and hence the side plates are also subjected to a compatible strain ε_t. Figure 11.4 shows the forces that resist the formation of a diagonal crack at a given location; it was drawn from Fig.5.8 for the unplated beam by superimposing the resistance to the formation of diagonal cracks by a pair of side plates which is shown as ΔV_{cr}. It is worth noting that we are dealing with the crack initiation and therefore, we are not concerned with the debonding of the external plates. This component ΔV_{cr} in Fig.11.4 is obtained by multiplying the tensile strength of the concrete and the transformed area of the side plates crossing the inclined plane of the crack (A_{isp}). Therefore,

$$\begin{aligned}\Delta V_{cr} &= mA_{isp}f_t \\ &= 2m\frac{\sqrt{x^2+h^2}}{h}d_{sp}t_{sp}f_t\end{aligned} \tag{11.7}$$

where m= modular ratio (E_p/E_c). Here E_p and E_c are the elastic modulus of side plate and concrete respectively, d_{sp} is the depth of an individual side plate, and t_{sp} is the thickness of an individual side plate, h is the depth of the beam and x is the horizontal projection of

the diagonal crack. The direct tensile strength of the concrete f_t is assumed to be 80% of the Brazilian tensile strength of the concrete f_b.

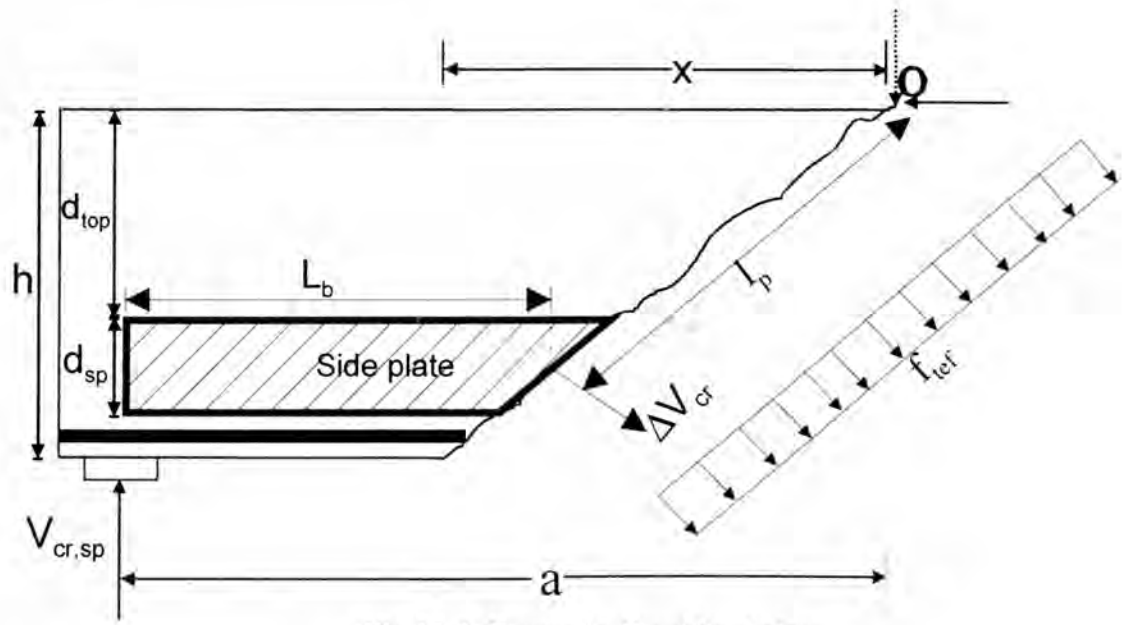

Fig.11.4. Forces in the side plates

Now, the diagonal cracking load of the side plated beam ($V_{cr,sp}$) is obtained by taking moments of all the forces about the point O. (Refer Fig.11.4)

$$\begin{aligned} V_{cr,sp}.a &= \left(f_{tef} b\sqrt{x^2+h^2}.\frac{\sqrt{x^2+h^2}}{2} \right) + \left(\Delta V_{cr} l_p \right) \\ &= \left(\frac{f_{tef} b}{2}\left(x^2+h^2\right) \right) + \left(2mf_t d_{sp} t_{sp} \frac{\sqrt{x^2+h^2}}{h} \frac{\sqrt{x^2+h^2}\,(d_{top}+0.5d_{sp})}{h} \right) \\ &= \left(x^2+h^2\right)\left(\frac{f_{tef} b}{2} + \frac{2mf_t d_{sp} t_{sp}(d_{top}+0.5d_{sp})}{h^2} \right) \end{aligned} \tag{11.8}$$

Therefore,

$$V_{cr,sp} = \left(\frac{x^2+h^2}{-a} \right)\left(\frac{f_{tef} b}{2} + \frac{2mf_t d_{sp} t_{sp}(d_{top}+0.5d_{sp})}{h^2} \right) \tag{11.9}$$

Here a is the shear span and it is approximated as the distance between centre of support plate and edge of load plate, b is the width of the beam, d_{top} is the distance between the

topmost fibre of the beam and the top of the side plate and f_{tef} is the effective tensile strength of the concrete as defined by Eqns.5.30 and 5.31.

11.3.2.2 Contribution to shear strength ($V_{u,sp}$)

When a diagonal crack occurs at a given location, the crack faces are forced to separate and this separation stretches both the reinforcing bars and the side plates crossing the crack plane. This induces a tension force that is balanced by an equal compression force acting across the crack leading to reduced crack widths. Hence the shear resistance to sliding failure along the crack plane is increased. The resistance to shear is also increased by the dowel action of the reinforcement caused by the relative movement of the concrete on the opposite sides of the crack. All these factors are accounted for in Zhang's equation for shear failure strength (Eqn.5.28) for conventionally reinforced concrete beams by the function $f_3(\rho)$ (Eqn.5.27d). It may be noted that this parameter is analogous to the well known passive and active restraining force normal to a crack that allows shear to be transferred across a crack (Oehlers and Bradford 1995 and Mattock and Hawkins 1972). Therefore, it is necessary to find an additional equivalent term for the side plate reinforcement ratio ρ_{sp} to include the increase in shear resistance to sliding provided by the side plates. The following procedure is suggested for this.

1. Calculate the bond strength P_b of the pair of side plates by using Eqn.11.5 or 11.6 and it is always less than $(P_b)_y$ estimated from Eqn.11.1.
2. Find the effective area ($A_{sp.eff}$) that allows for the plate strength less than the yield strength.

$$A_{sp,eff} = \frac{P_b}{f_{yp}} \tag{11.10}$$

and hence

$$\rho_{sp} = \frac{A_{sp,eff}}{bh} * 100 \qquad (11.11)$$

3. The modified equation for $f_3(\rho)$ is

$$f_3(\rho_{sp}) = 0.15(\rho + \rho_{sp}) + 0.58. \quad where\ \rho = \frac{A_s}{bh} * 100\ and\ (\rho + \rho_{sp}) \leq 4.5 \qquad (11.12)$$

The upper limit for the total reinforcement ratio ($\rho+\rho_{sp}$) is still kept at 4.5% as increases in areas above this limit do not mean a proportional increase in shear resistance to sliding failure (Oehlers and Bradford 1995 and Mattock and Hawkins 1972). Therefore, the shear failure strength of the side plated beam is written by modifying Eqn.5.28 for V_u as

$$V_{u,sp} = \frac{1}{2}\gamma_s \gamma_{0,sp} f_c \left(\sqrt{1 + \left(\frac{x}{h}\right)^2} - \frac{x}{h} \right) bh \qquad (11.13)$$

where $\gamma_{0,sp} = \lambda . f_1(f_c) . f_2(h) . f_3(\rho_{sp})$ (11.14)

Here λ = 1.6 for applied concentrated load and the functions $f_1(f_c)$ and $f_2(h)$ are as defined by Eqns.5.27.b and 5.27c and $f_3(\rho_{sp})$ is given by Eqn.11.12.

11.3.2.3 Calculation of shear peeling strength of side plated beam ($V_{pure,sp}$)

The horizontal projection of the critical diagonal crack can be estimated by equating the equations for $V_{cr,sp}$ as given by Eqn.11.9 and $V_{u,sp}$ as given by Eqn.11.13, i.e. solving the following equation will give the magnitude of x.

$$\left(\frac{x^2 + h^2}{a} \right) \left(\frac{f_{tcf} b}{2} + \frac{2 m f_t d_{sp} t_{sp} (d_{top} + 0.5 d_{sp})}{h^2} \right) = \frac{1}{2}\gamma_s \gamma_{o,sp} \left[\sqrt{1 + \left(\frac{x}{h}\right)^2} - \frac{x}{h} \right] bh \qquad (11.15)$$

Eqn.11.15 cannot be solved directly as $\gamma_{o,sp}$ depends on the bond length and hence on the projection of the crack x. Therefore, an iterative procedure has to be used to solve Eqn.11.15, which is tedious. Alternatively, envelopes for equations 11.9 and 11.13 can be drawn for varying x values by using a simple spread sheet and the point of intersection

of the curves will give both the theoretical shear peeling strength ($V_{pure.sp}$) and the location of critical diagonal crack $L_{d.crit}$. This procedure allows for the variation in the bond length L_b in Fig.11.4 with x.

11.3.3 Comparison with test results

In this section, the test beams in Section 6.2 for the side plated beams SP-21,SP-22, SP-31, SP-32, SP-41 and SP-42 along with the unplated beam SPREF are analysed using the present shear peeling model. The model was also used to anlayse the side plated beams tested by Nguyen and Oehlers (Refer Section 2.4.1.1, 2.4.1.2 and Table-2.2).

11.3.3.1 Shear strength of non-plated beam SPREF

Figure 11.5 compares the experimental shear strength of beam SPREF (V_{uc}) that was non-shear reinforced and non-plated with that obtained from Australian code AS -3600 and the crack sliding model. It can be seen that the V_{uc} obtained from crack sliding theory (88.9 kN) compares well with the experimental V_{uc} (85.6 kN). The horizontal projection (x) of critical diagonal crack is 787 mm according to this theory, which compares with the actual projection 700 mm observed from the test. The V_{uc} obtained from AS-3600 is 73.5 kN which is 14% less than the actual value.

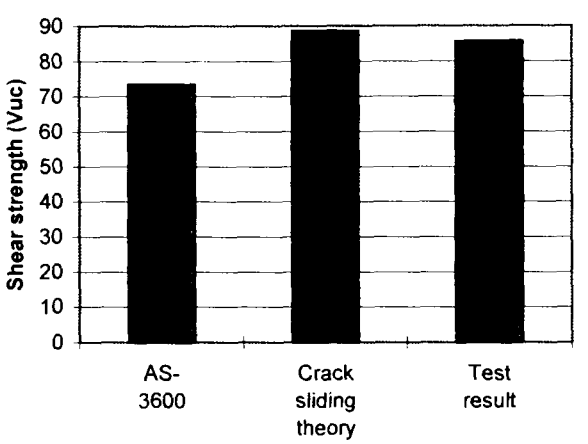

Fig.11.5. Estimation of V_{uc} for SPREF

11.3.3.2 Analysis of side plated beams

A crack sliding analysis of the test specimens in Section 6.2 is shown in Fig.11.6. It can be seen that the shear load to cause diagonal cracking V_{cr} in the case of the beams SP-21 and SP-22 in which the plates were placed near to the tension face of the beam is higher than that of the other side plated beams. In fact, for the beams SP-41 and SP-42 in which the side plates were placed close to the compression face of the beam, there is only a marginal improvement in V_{cr} when compared to the unplated RC beam SPREF. Therefore, the position of the plate significantly affects V_{cr} and the ideal position is to place the plate near to the tension face of the beam. In contrast, the shear load to cause failure of the cracked section $V_{u.sp}$ is hardly affected by the position of the plate for the side plated beams analysed in this section. This is due to the fact that the factor $\gamma_{0.sp}$ in Eqn.11.13 for $V_{u.sp}$ depends on the total reinforcement ratio $(\rho+\rho_{sp})$; ρ_{sp} depends on the bond strength P_b of the external plates which in turn depends on the bond length L_b. For our case, the critical bond length $L_{b.crit}$ (beyond which there is no further increase in bond strength) is 650 mm and it is achieved for the side plates in the beams SP-31and SP-32 when the crack originates at a distance of 150 mm from the support and in the case of beams SP-41 and SP-42, even for the crack that originates from the support, $L_b > L_{b.crit}$ and hence P_b attains the maximum value for most of the crack positions. In the case of the beams SP-21 and SP-22, this happens when the origin of the crack is at a distance 475 mm further than the support. Furthermore, when $L_b > L_{b.crit}$, the ratio $(\rho+\rho_{sp})$ is 4.7 and hence $(\rho+\rho_{sp})$ is limited to 4.5 (Refer Eqn.11.12).

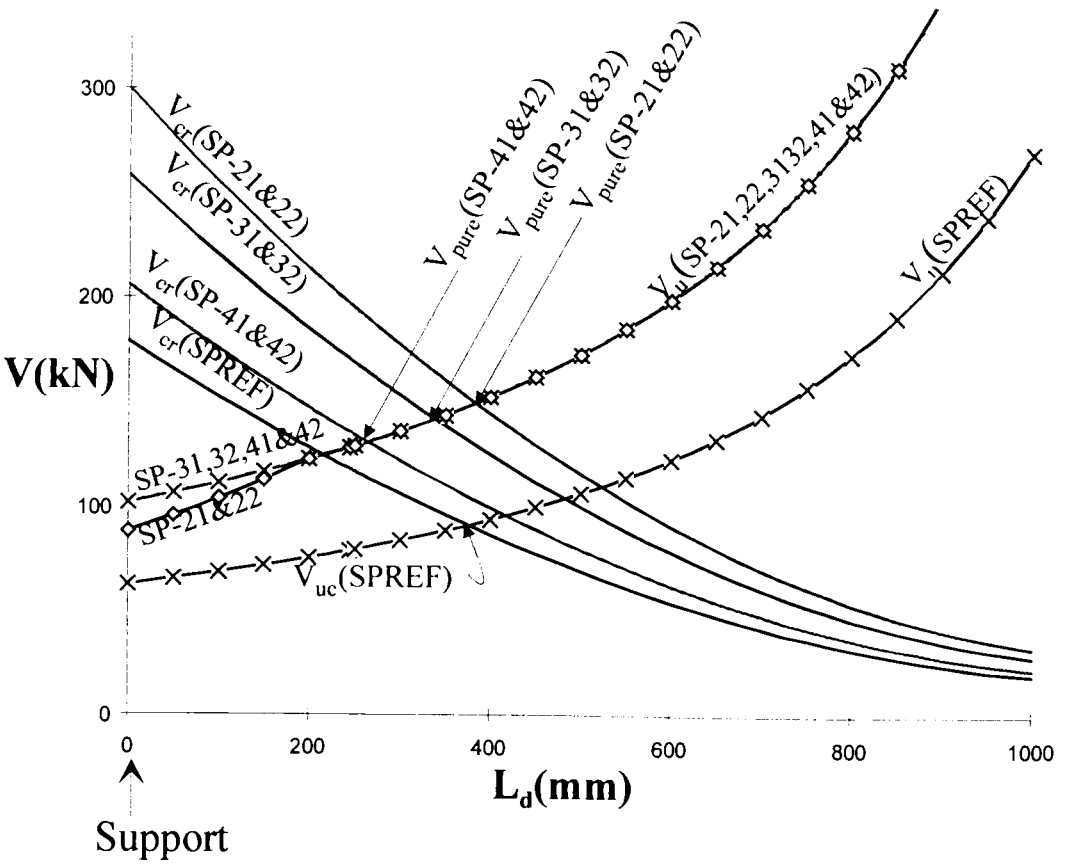

Fig.11.6. Crack sliding analysis of tests

The theoretical results are listed in the first seven rows in Table-11.1. Also listed in the remaining rows are the results from specimens 2a to 2n4 which are the results from beams tested by Nguyen and Oehlers (Refer Sections 2.4.1.1, 2.4.1.2 and Table-2.2). These specimens were the same as the beam in Fig.6.1b except that the plates were 65 mm deep and 5 mm or 8 mm thick and there were substantially more stirrups in the beams, i.e. they had two legged 10 mm diameter stirrups at a spacing of 150 mm. It is worth noting in Table-11.1 that the shear failure strengths V_{uc} of tests SPREF and 2a of 86 kN and 85kN in column 4 are remarkably close to those predicted by Zhang of 89 kN and 88 kN in column 5.

Table-11.1: Comparison of results

Specimen (1)	Plates d_{sp} x t_{sp} (mm) (2)	d_{top}/h	Stirrups (3)	$(V_{pure})_{exp}$ (kN) (4)	$(V_{pure})_{theory}$ (kN) (5)	$(V_{pure})_{exp}/(V_{pure})_{theory}$ (6)	$(V_{pure})_{exp}/(V_{uc})_{exp}$ (7)
SPREF	unplated	-	No	86(V_{uc})	89(V_{uc})	0.97	1
SP21	130x10	0.58	No	157	149	1.05	1.83
SP22	130x10	0.58	Yes	162	149	1.09	1.88
SP31	130x10	0.32	No	169	141	1.20	1.97
SP32	130x10	0.32	Yes	166	141	1.18	1.93
SP41	130x10	0.07	No	96	130	0.74	1.12
SP42	130x10	0.07	Yes	132	130	1.02	1.53
2a	unplated	-	No	85(V_{uc})	88(V_{uc})	0.97	1
2n1	65x5	0.72	No	103	95	1.08	1.21
2n2	65x5	0.72	Yes	126	95	1.33	1.48
2n3	65x8	0.72	No	109	110	0.99	1.28
2n4	65x8	0.72	Yes	127	110	1.15	1.49

11.3.3.3 Comparison between test and analytical results

The results in Table-11.1 are plotted in Fig.11.7. The shear peeling experimental strengths $(V_{pure})_{exp}$ are plotted along the abscissa as a proportion of the experimental shear strength of the beam without stirrups $(V_{uc})_{exp}$. It can be seen that the addition of side plates can substantially increase the resistance to peeling; for specimen SP31 it has almost doubled the shear load at the formation of a critical diagonal crack from V_{pure} = V_{uc} = 89 kN, when there are no side plates, to V_{pure} = 169 kN with side plates. Hence the addition of side plates can substantially improve the shear peeling resistance. All the results in Fig.11.7 are virtually on the line $(V_{pure})_{exp}/(V_{pure})_{th}$ = 1 or above the line. This shows that the equations for shear peeling of side plated beams developed from Zhang's theory form a good lower bound to the test results. The only exception is test SP41 where the plates were placed in the compression zone in a beam without stirrups. However, it is worth noting that specimen SP42, which had identical plates in a beam with nominal stirrups, was in very good agreement with the theoretical results. It is, therefore, suggested that the design rules should be restricted to rehabilitation of beams

with at least nominal amounts of shear stirrups or with plates only in the tension zone. The mean experimental peeling strength of the plated beams, except SP41, is 12% greater than the theoretical peeling strength as shown in Fig. 11.7 and has a standard deviation of 0.105 and a coefficient of correlation of 0.923. Therefore, the mathematical model developed for estimating the shear peeling strength of beams glued with side plates can be used with confidence.

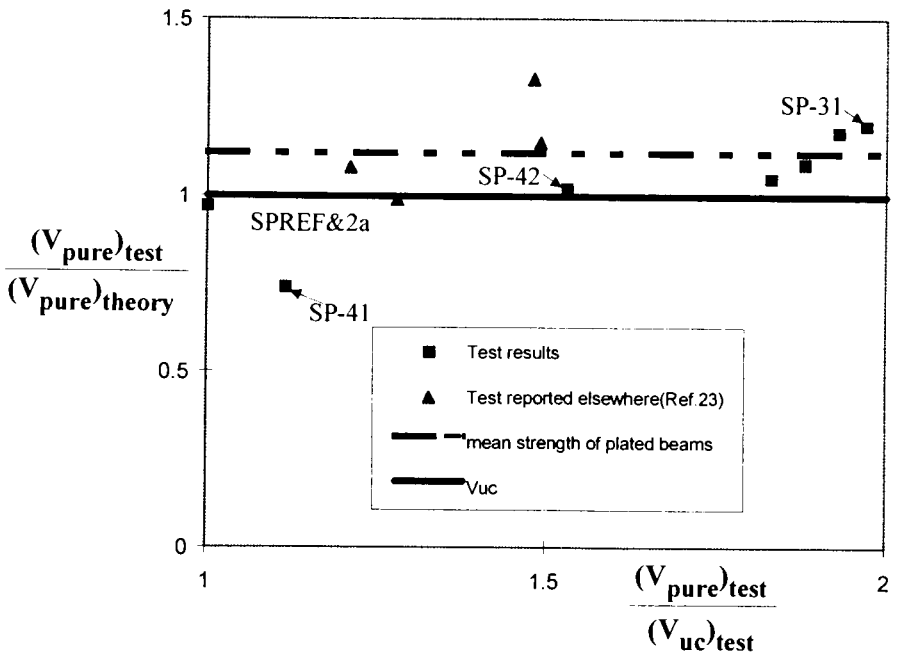

Fig.11.7. Side plated beams and unplated beams- Comparison between test and theoretical results

11.4 Procedure for estimating the shear peeling strength of tension face plated beams

The method developed for side plates can be extended to determine the shear peeling strength of the beams bonded with tension face plates by affecting some modifications as explained below.

11.4.1 Diagonal cracking load of the tension face plated beams ($V_{cr,tfp}$)

The expression for the diagonal cracking load of tension face plated beams ($V_{cr,tfp}$) can be derived in the same way as the Eqn.11.9 for $V_{cr,sp}$ for the side plated beams and it is given as

$$V_{cr,tfp} = \left(\frac{x^2 + h^2}{a}\right)\left(\frac{f_{tcf} b}{2} + \frac{m f_t b_{tfp} t_{tfp} (h + 0.5 t_{tfp})}{h^2}\right) \tag{11.16}$$

where b_{tfp} and t_{tfp} are the width and the thickness of the tension face plate respectively.

11.4.2 Expression for shear strength ($V_{u,tfp}$)

As in the case of the side plated beams, it is necessary to find an additional equivalent tension face plate reinforcement ratio ρ_{tfp} to allow for the increase in the shear resistance to sliding provided by the tension face plate. The following procedure is developed for this purpose.

1. Calculate the bond force P_b in the tension face plate using the following equations derived from Eqns.11.3 and 11.4.

$$P_b = 71 f_t t_{tfp} b_{tfp} \quad \text{where } P_b \le (P_b)_y \tag{11.17}$$

when $L_b > 65 t_{tfp}$, otherwise

$$P_b = 1.09 L_b f_t b_{tfp} \quad \text{where } P_b \le (P_b)_y \tag{11.18}$$

2. Find the effective area ($A_{tfp,eff}$) that allows for the plate strength less than the yield strength.

$$A_{tfp,eff} = \frac{P_b}{f_{yp}} \tag{11.19}$$

and hence

$$\rho_{tfp} = \frac{A_{tfp,eff}}{bh} * 100 \tag{11.20}$$

3. The modified equation for $f_3(\rho)$ is

$$f_3(\rho_{tfp}) = 0.15(\rho + \rho_{tfp}) + 0.58. \quad where\ \rho = \frac{A_s}{bh} * 100 \ and\ (\rho + \rho_{tfp}) \leq 4.5 \qquad (11.21)$$

Therefore, the shear failure strength of the tension face plated beam is given by

$$V_{u,tfp} = \frac{1}{2}\gamma_s \gamma_{o,tfp} f_c \left(\sqrt{1 + \left(\frac{x}{h}\right)^2} - \frac{x}{h} \right) bh \qquad (11.22)$$

where $\gamma_{0,tfp} = \lambda . f_1(f_c) . f_2(h) . f_3(\rho_{tfp})$. (11.23)

11.4.3 Estimating the shear peeling strength of the tension face plated beam ($V_{pure,tfp}$)

As in the case of the side plated beams, the envelopes of Eqn.11.16 for $V_{cr.tfp}$ and Eqn.11.21 for $V_{u.tfp}$ can be drawn for varying x values by using a simple spread sheet and the point of intersection of the curves will give the shear peeling strength ($V_{pure.tfp}$) as well as the location of critical diagonal crack.

11.4.4 Correlation with test results

11.4.4.1 Analysis of tension face plated beams

The above described procedure was used to estimate the shear peeling strength of the tension face plated beam SP01 (Refer Section 6.6.2); SP-T6 and SP-T12 that were tested as reference beams for the study of the shear peeling of compression face plated beams (Refer Sections 9.6.1 and 9.6.3); and the beams tested by Oehlers (1992). Figures 11.8 and 11.9 show the envelopes drawn for equations 11.16 and 11.21 for the beams SP-01, and SP-T6 and SP-T12. The envelopes for the corresponding non-plated, non-shear reinforced concrete beams are also shown in these diagrams and the theoretical shear strength of the non-plated beams are 88.9 kN for SP-01 and 80 kN for the non-plated beams of SP-T6 and SP-T12.

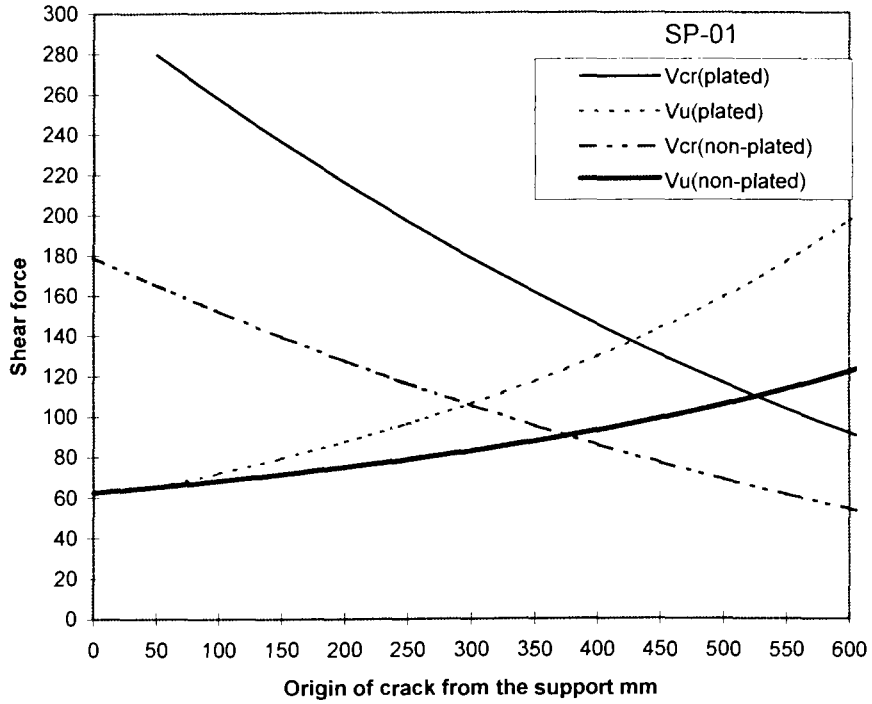

Fig.11.8. Envelopes for shear loads-SP01

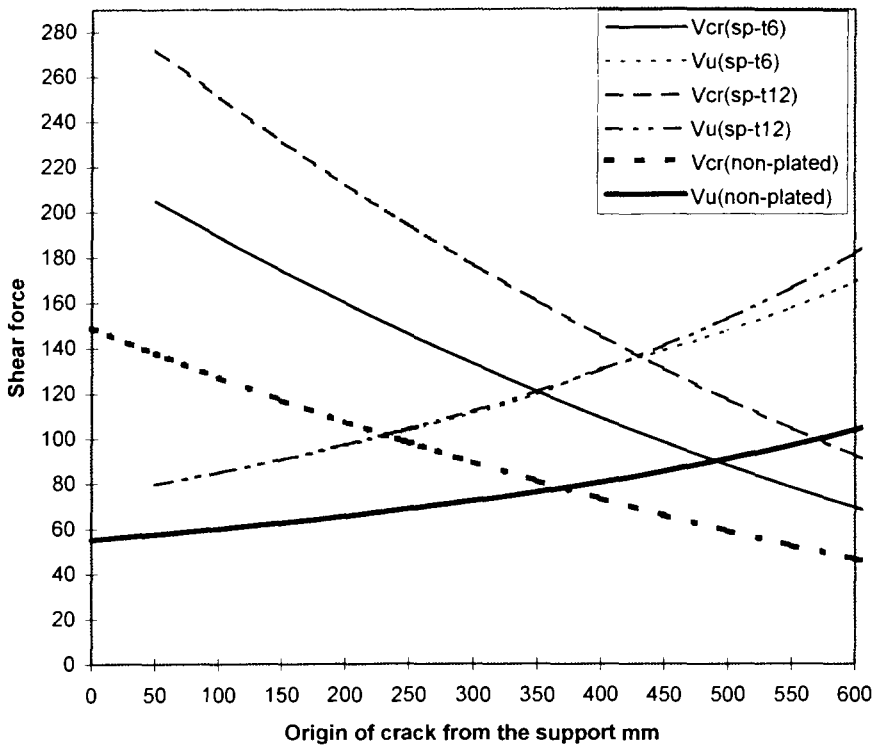

Fig.11.9. Envelopes for shear loads-SP-T6 and SP-T12

Table -11.2 gives the details of the geometric properties of all the beams considered for the analysis and Table-11.3 summarises the analytical and test results.

Table-11.2: Tension face plated beam-Geometric properties

Specimen	b mm	h mm	stirrups	t_{tfp} m m	f_c MPa	a mm	L_{end} mm
(1)	(2)	(3)	(4)	(5)	(6)	(7)	(8)
1. SP01	200	370	minimal	10	48.9	1150	50
2. SPT6	200	370	10mm/100*	6	35.3	1200	50
3. SPT12	200	370	10mm/100	12	35.3	1200	50
Tests done by Oehlers(1992)							
4. 1/4/S	130	175	minimal	5	42	500	50
5. 1/2/N	130	175	minimal	5	42	500	150
6. 2/1/S	130	175	minimal	5	47	500	75
7. 2/2/S	130	175	4 mm/75	5	47	500	75
8. 2/3/S	130	175	6 mm/75	5	47	500	75
9. 2/4/S	130	175	6 mm/45	5	47	500	75
10. 5/1/S	130	175	6 mm/45	5	49	500	150

t_{tfp} = thickness of tension face plate, L_{end} = distance between centre of support plate and plate end
*10 mm/100 mm denotes the provision of 10 mm diameter stirrups at 100 mm spacing.

Table-11.3: Test and analytical results

Specimen	V_{pure} (test) kN	V_{pure} (theory) kN	V_{pure}(test)/ V_{pure}(theory)	V_{uc}(theory) kN	V_{pure}(test)/ V_{uc}(theory)
(1)	(2)	(3)	(4)	(5)	(6)
1. SP01	140.0	137	1.02	88.9	1.57
2. SPT6	112.5	121	0.93	80.0	1.41
3. SPT12	112.4	139	0.81	80.0	1.41
4. 1/4/S	41.0	44.5	0.92	35.5	1.15
5. 1/2/N	32.5	34.5	0.94	35.5	0.92
6. 2/1/S	40.1	48.5	0.83	35.0	1.14
7. 2/2/S	42.5	48.5	0.88	35.0	1.21
8. 2/3/S	39.3	48.5	0.81	35.0	1.12
9. 2/4/S	41.3	48.5	0.85	35.0	1.18
10. 5/1/S	37.3	37.5	0.99	35.0	1.06

Now, the analytical results of the beams SP-T6 and SP-T12 will be diagonised in detail. In Fig.11.9, the loads to cause the shear crack V_{cr} is always greater for the 12 mm thick plated beam (SP-T12) than the 6 mm thick plated beam. This is due to the fact that when all the other parameters are fixed, $V_{cr.tfp}$ in Eqn.11.16 increases proportionally to the thickness of the tension face plate t_{tfp}. However, the load to cause shear failure V_u for

both the plated beams is almost the same for the crack origin between 0-425 mm, as can be seen in Fig.11.9. This can be explained with the help of Figs.11.10 and 11.11. In Fig.11.10 and 11.11, the bond strengths P_b of both the beams are almost identical for the crack origin between 0-400 mm. This is due to the fact that the critical bond length for the 6 mm thick plate is 390 mm whereas it is 780 mm for the 12 mm thick plated beam (Refer Eqns.11.3 and 11.4). Furthermore, the factor γ_0 remains constant for the unplated RC beam while $\gamma_{0.tfp}$ in Eqn.11.21 for $V_{u.tfp}$ is affected by the tension face plate ratio ρ_{tfp} which in turn depends upon the bond strength. Hence, there is not much appreciable changes in $\gamma_{0.tfp}$ in Fig.11.11 and hence in $V_{u.tfp}$ in Fig.11.9 for SP-T6 and SP-T12 for the crack origin upto 400 mm.

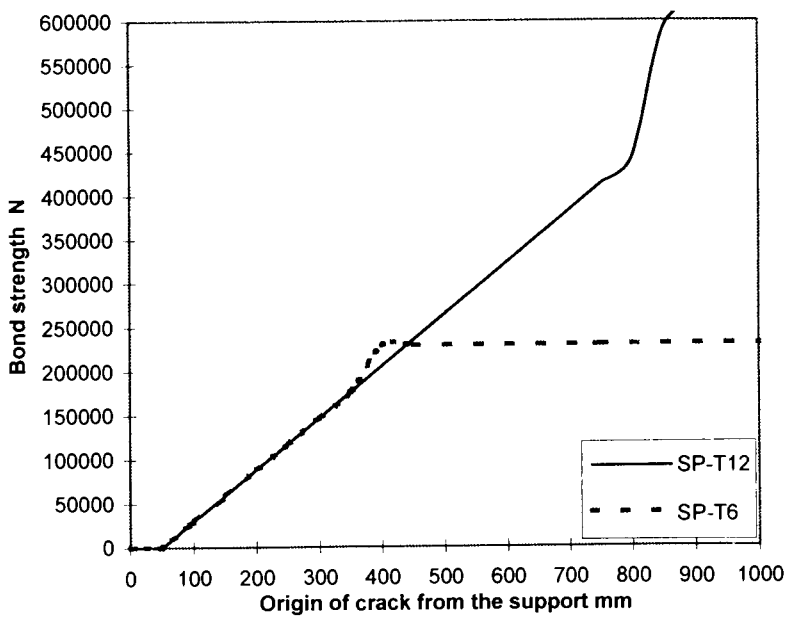

Fig.11.10. Variation of bond strength in Beams-SP-T6 and SP-T12

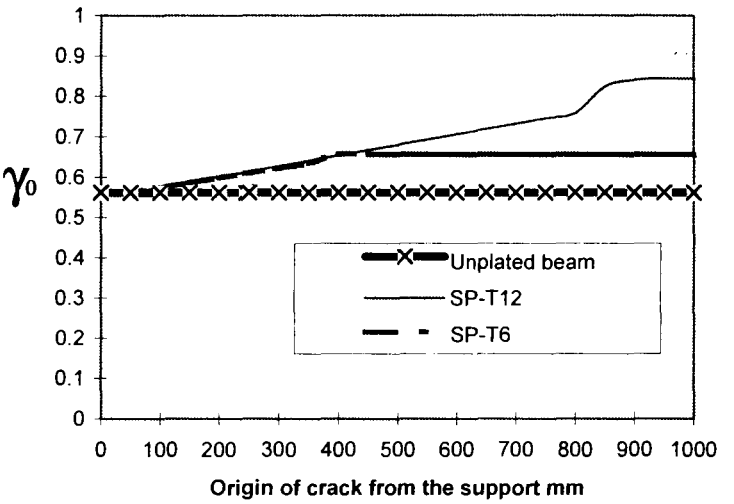

Fig.11.11. Variation of γ_0 in Beams-SP-T6 and SP-T12

Figure 11.12 compares the test results with that obtained from the analysis. On an average, the actual shear peeling strength is 89.8% that of the theoretical shear peeling strength with a standard deviation of 0.072. It may be noted that the test results pertain to large variation of plate thickness (5-12 mm), concrete strength (35-50 MPa) and the amount of shear stirrups (minimal to large quantum). The most significant factor that affects the shear peeling resistance of the tension face plated beam is the location of the plate end and for the present set of test data L_{end} ranged between 50-150 mm. Hence, the procedure can be used with confidence. It is suggested to scale down the theoretical shear peeling strength of the tension face plated beams as obtained from this procedure by 10%, which will lead to a safe estimation.

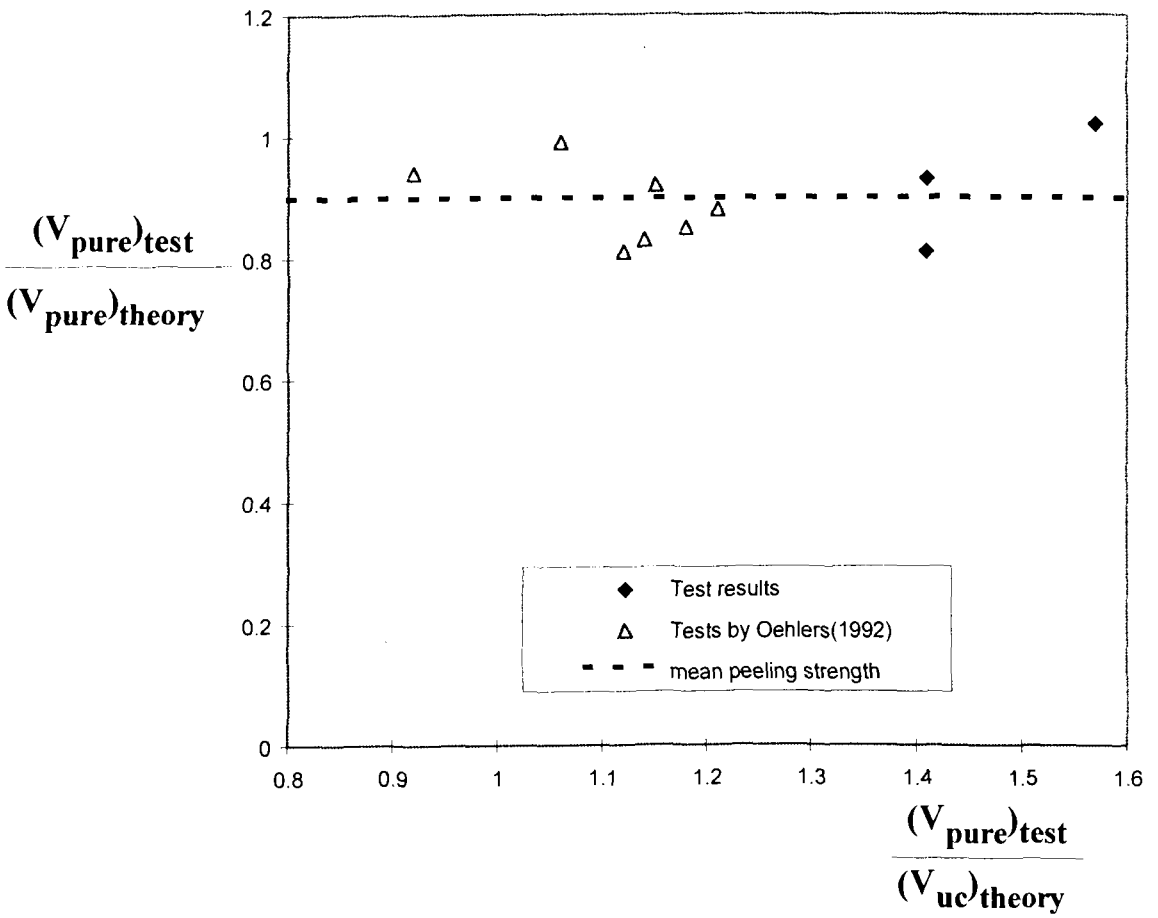

Fig.11.12. Tension face plated beams: Comparison of test and theoretical results

11.5 Alternative simple procedure for estimating the shear peeling strength of beams bonded with nearly full length tension face plates

11.5.1 Equation for shear peeling strength

Tests have shown that the shear peeling in simply supported RC beams bonded with nearly full tension face plates occurred at the plate ends after the formation of critical crack in the vicinity of the plate ends. Therefore, the behaviour of simply supported plated beams that are subjected to concentrated loads and in which the plate ends are terminated in a region of predominant shear forces is similar to that of the non-shear reinforced and non-plated beams but for the location of the critical diagonal crack, as shown in Fig.11.13a and 11.13b.

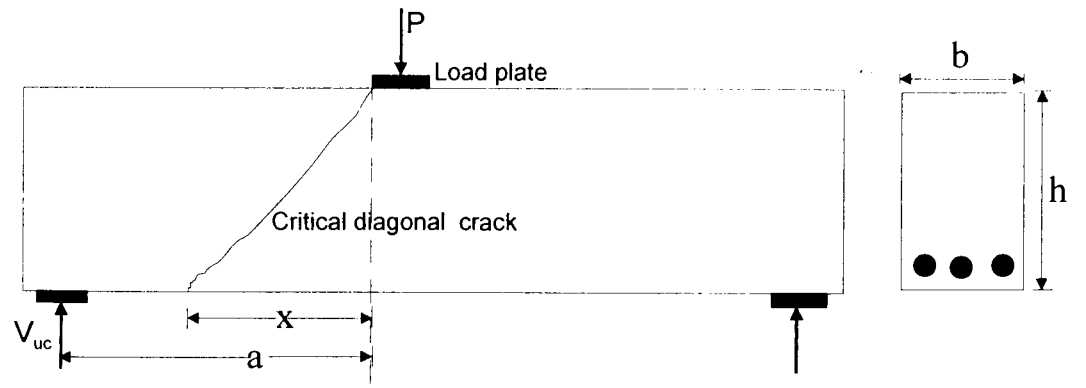

(a)Non-shear reinforced and non-plated beam (*x* unknown)

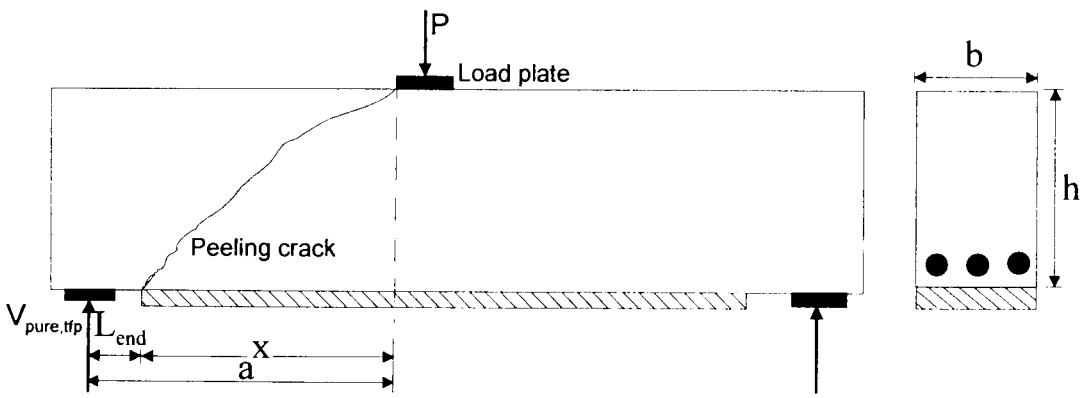

(b) Tension face plated beam (*x* known)

Fig.11.13. Location of critical diagonal crack

Whereas the critical diagonal shear crack in the case of plated beams occurs always near or at the plate ends, the same is not the case with the non-plated beams as shown in Fig.11.13. Hence, the shear peeling strength of the tension face plated beam can be approximated as the load to cause a critical diagonal crack at the plate end and can be written by modifying Eqn.5.29 as

$$V_{pure,tfp} = 0.5.f_{tef}\frac{b}{a}(x_{crit}^{\ 2} + h^2) \tag{11.24}$$

As the projection of the critical diagonal crack $x_{crit} = a\text{-}L_{end}$ from Fig.11.13b, then

$$V_{pure,tfp} = 0.5 f_{tef}\frac{b}{a}\left[(a - L_{end})^2 + h^2\right] \tag{11.25}$$

where L_{end} is the distance between the support and the plate end.

11.5.2 Correlation with test results

11.5.2.1 Analysis of test results

Equation 11.25 was used to estimate the shear peeling strength of the ten tension face plated beams listed in Table-11.2 and the results are summarised in Table 11.4.

Table-11.4: Test and analytical results

Specimen (1)	V_{pure}(test) kN (2)	V_{pure}(theory) kN (3)	V_{pure}(test)/ V_{pure} (theory) (6)
1. SP01	140.0	164.9	0.85
2. SPT6	112.5	137.8	0.82
3. SPT12	112.4	137.8	0.82
4. 1/4/S	41.0	48.3	0.85
5. 1/2/N	32.5	31.7	1.03
6. 2/1/S	40.1	47.2	0.85
7. 2/2/S	42.5	47.2	0.90
8. 2/3/S	39.3	47.2	0.83
9. 2/4/S	41.3	47.2	0.88
10. 5/1/S	37.3	35.2	1.06

11.5.2.2 Comparison of test results

The experimental shear peeling strengths and the theoretical shear peeling strengths obtained from Eqn.11.25 are compared in Fig.11.14. The ratio between $V_{ure..tfp}$*(test) and* $V_{pure.tfp}$*(theory)* has a mean value of 0.89 with standard deviation of 0.08 and this compares well with the results obtained from the exact procedure. Now, Eqn.11.25 can be modified for better prediction as follows; the ranges of the test results used for calibrating the model are also specified.

$$V_{pure,tfp} = 0.45 f_{tef} \frac{b}{a}\left[(a - L_{end})^2 + h^2\right] \tag{11.26}$$

$$\text{subject to} \quad \frac{a}{h} \geq 2.85 \; and \; \frac{L_{end}}{h} \leq 0.85 \tag{11.27}$$

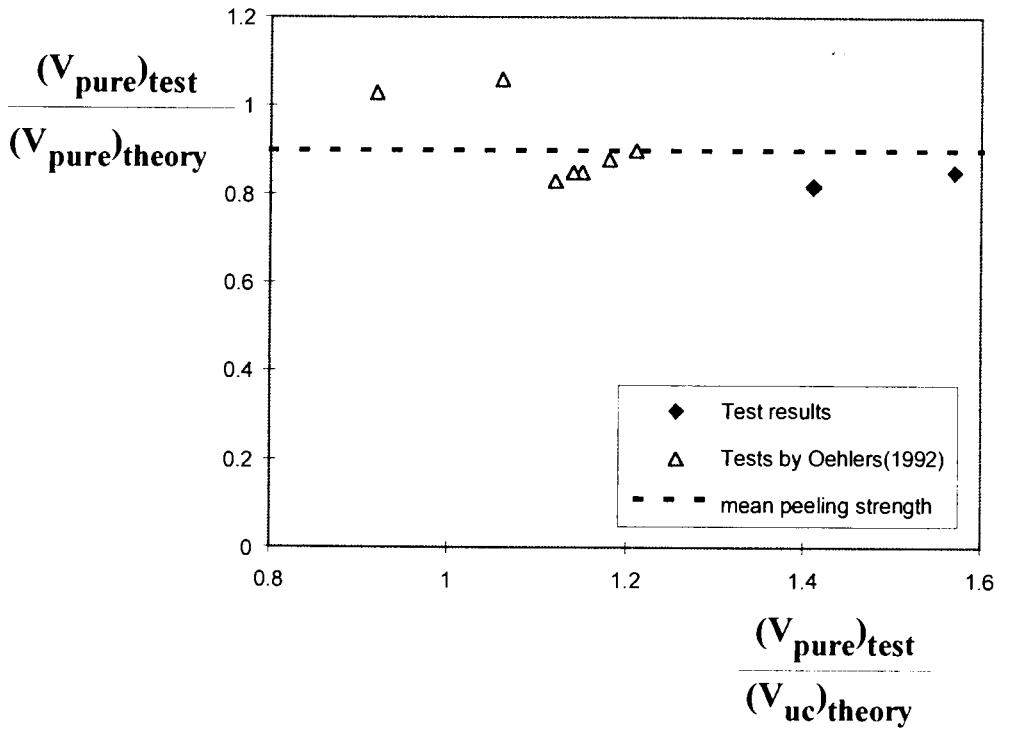

Fig.11.14. Tension face plated beams: Comparison of test and theoretical results

11.6 Model for shear peeling in reinforced concrete beams bonded with steel angles to their sides and tension faces

Tests, as described in Chapter-8, on reinforced concrete beams bonded with steel angles have shown that the shear peeling is always caused by the formation of a critical diagonal crack. Furthermore, debonding occurs well before the internal shear stirrups are fully mobilised. However, the shear peeling strengths were 200 to 230% higher than the shear strength of the unplated reinforced concrete beam excluding the shear stirrups (V_{uc}). As this behaviour is comparable to the side plated beams, the beams bonded with angles were modelled in a similar fashion and the formulation of the procedure is described subsequently.

11.6.1 Contribution to diagonal cracking load ($V_{cr,angle}$)

The contribution to the diagonal cracking load by the angles (ΔV_{cr}) is calculated by considering the component $\Delta V_{cr,sp}$ resisted by the area of side plates crossing the crack

plane and the component $\Delta V_{cr.sof}$ resisted by the inclined area of the soffit plates crossing the crack plane, as shown in Fig.11.15. Therefore, the final equation for computing load to cause a diagonal crack at a location for the beams bonded with angles ($V_{cr.angle}$) is derived in a similar manner for $V_{cr.sp}$ (Eqn.11.9) and $V_{cr.tfp}$ (Eqn.11.16) and it is given as

$$V_{cr.angle} = \left(\frac{x^2 + h^2}{a} \right) \left(\frac{f_{tef} b}{2} + \frac{2mf_t}{h^2} \{ d_{sp} t_{sp} (d_{top} + 0.5 d_{sp}) + b_{sof} t_{sof} (h + 0.5 t_{sof}) \} \right) \qquad (11.28)$$

where d_{top} is the distance between the beam top to the topmost fibre of the angle, d_{sp} and t_{sp} are the depth and thickness of the side plate of an individual angle and b_{sof} and t_{sof} are the width and thickness of the soffit plate of an individual angle, as shown in Fig.11.16.

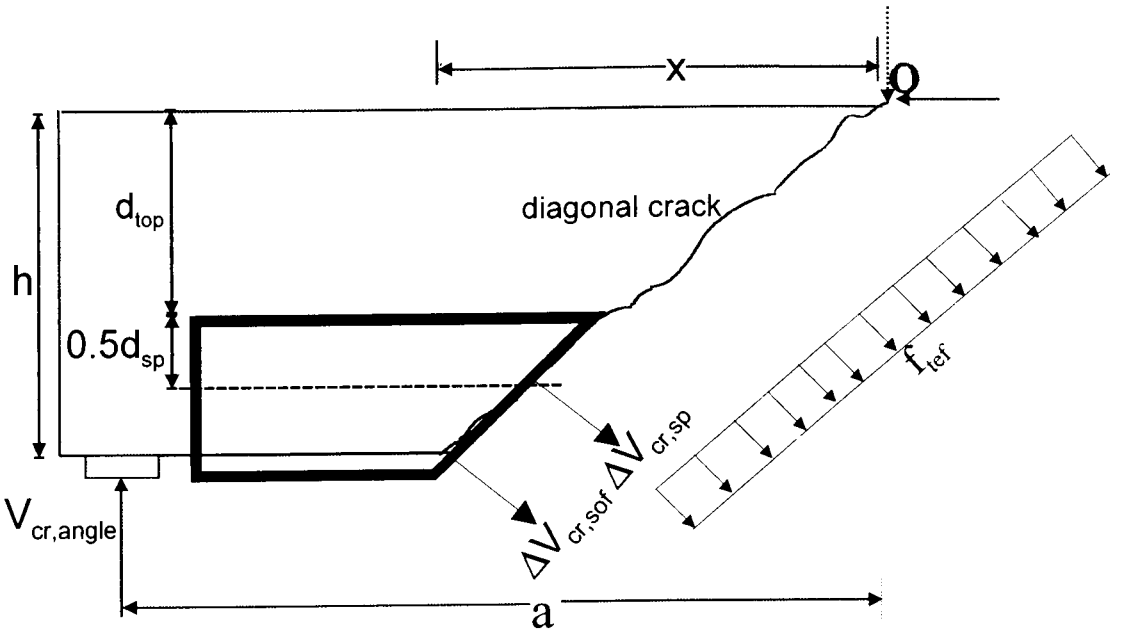

Fig.11.15. Forces in the diagonally cracked beam

11.6.2 Contribution to shear strength ($V_{u,angle}$)

The basic equation for the shear strength (V_u) has to be modified to include the contribution from the angles. This can be done in the same way as for the side plates where the only modification that is needed is for the function $f_3(\rho)$. For the beams bonded with angles, the bond force (P_b) consists of two components: (1) $P_{b,sp}$ acting on

the side plates of the angles and (2) $P_{b,sof}$ acting on the soffit plates of the angles, as shown in Fig.11.16. The corresponding bond lengths $L_{b,sp}$ and $L_{b,sof}$ are measured along the centre of the side plate and the soffit plate respectively.

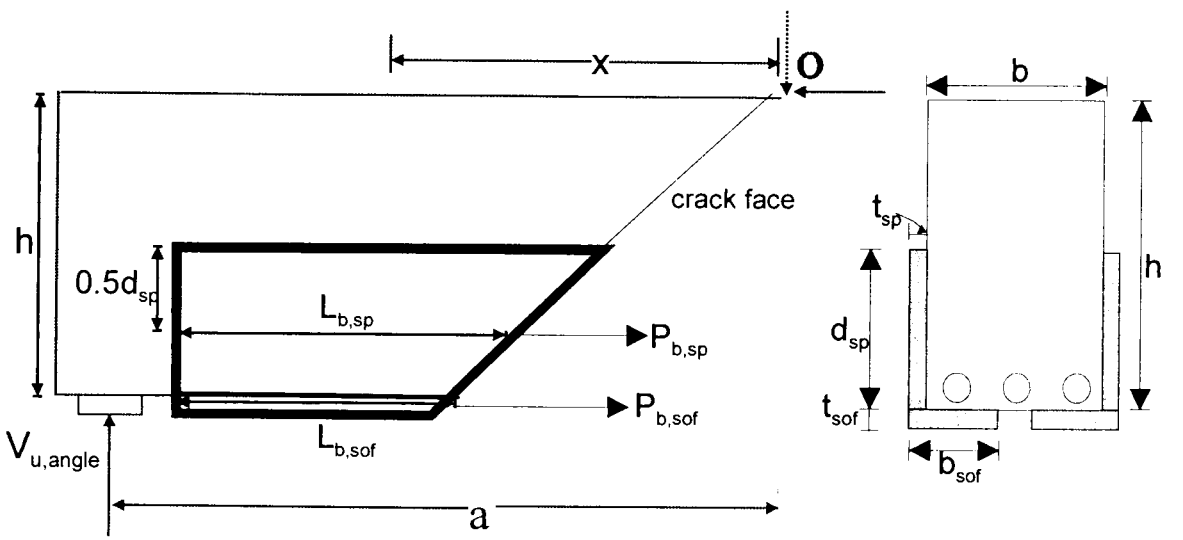

Fig.11.16. Bond forces in the angle

The procedure for calculating $V_{u,angle}$ is as follows:

1. Calculate the bond force $P_{b,sp}$ in the side plates and ensure that this is lower than the axial yield strength of the plates ($A_{sp}.f_{yp}$) where f_{yp} is the yield strength of the plate material.

$$P_{b,sp} = 2.18 L_{b,sp} t_{sp} d_{sp} f_t \quad \text{for} \frac{L_{b,sp}}{t_{sp}} \le 65$$

$$= 142 t_{sp} d_{sp} f_t \quad \text{for} \frac{L_{b,sp}}{t_{sp}} > 65 \qquad (11.29)$$

subject to $P_{b,sp} \le 2 t_{sp} d_{sp} f_{yp}$

Here, d_{sp} and t_{sp} are the depth and the thickness of the side plate of an individual angle and $L_{b,sp}$ is measured as shown in Fig.11.16.

2. Calculate the bond force $P_{b,sof}$ in the soffit plates and ensure that this is lower than the axial yield strength of the plates .

$$P_{b,sof} = 2.18 L_{b,sof} t_{sof} b_{sof} f_t \quad \text{for} \frac{L_{b,sof}}{t_{sof}} \le 65$$

$$= 142 t_{sof} b_{sof} f_t \quad \text{for} \frac{L_{b,sof}}{t_{sof}} > 65 \tag{11.30}$$

$$subject\ to\ P_{b,sof} \le 2 t_{sof} b_{sof} f_{yp}$$

Here, b_{sof} and t_{sof} are the width and the thickness of the soffit plate of an individual angle.

3. Find the effective area of the side plate ($A_{sp,eff}$) and the soffit plate($A_{sof,eff}$) that allows for partial anchorage.

$$A_{sp,eff} = \frac{P_{b,sp}}{f_{yp}} \text{ and hence } \rho_{sp} = \frac{A_{sp,eff}}{bh} * 100 \tag{11.31}$$

$$A_{sof,eff} = \frac{P_{b,sof}}{f_{yp}} \text{ and hence } \rho_{sof} = \frac{A_{sof,eff}}{bh} * 100 \tag{11.32}$$

4. The modified equation for $f_3(\rho)$ is

$$f_3(\rho_{angle}) = 0.15(\rho + \rho_{sp} + \rho_{sof}) + 0.58.$$
$$where\ \rho = \frac{A_s}{bh} * 100\ and\ (\rho + \rho_{sp} + \rho_{sof}) \le 4.5 \tag{11.33}$$

(5) Finally, the shear failure strength of the beam bonded with the angles is given by modifying Eqn.11.13 for $V_{u,sp}$ as

$$V_{u,angle} = \frac{1}{2} \gamma_s \gamma_{0,angle} f_c \left(\sqrt{1 + \left(\frac{x}{h}\right)^2} - \frac{x}{h} \right) bh \tag{11.34}$$

where $\gamma_{0,angle} = \lambda . f_1(f_c) . f_2(h) . f_3(\rho_{angle})$ (11.35)

11.6.3 Calculation of shear peeling strength ($V_{pure,angle}$)

As in the case of side plated beams, the envelopes for $V_{cr,angle}$ (Eqn.11.28) and $V_{u,angle}$ (Eqn.11.34) can be drawn for varying x values by using a simple spread sheet and the

point of intersection of the curves will give both the theoretical shear peeling strength ($V_{pure,angle}$) and the projection of the critical diagonal crack x_{crit}.

11.6.4 Correlation with test results

11.6.4.1 Analysis of test results

Figure 11.17 illustrates the envelopes drawn both for the shear cracking load and the shear failure load for all the beams bonded with angles (Refer Chapter-8) and also the corresponding RC beam excluding the plates and stirrups.

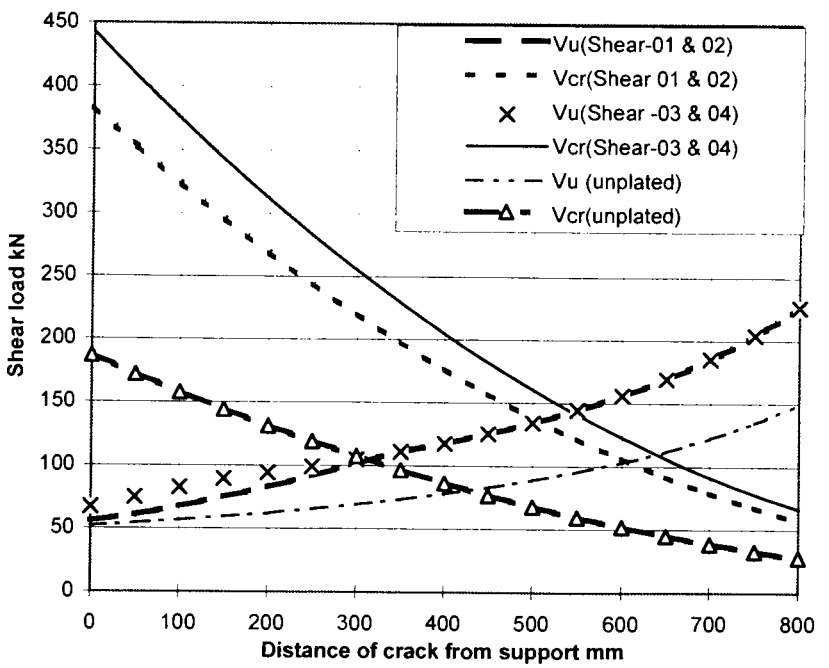

Fig.11.17. Envelops for shear cracking and shear failure loads

It can be seen in Fig.11.17 that the beams with the deeper angles (Shear 03 and Shear-04) are predicted to have more resistance to the formation of diagonal shear cracks than the beams bonded with shallow angles (Shear-01 and Shear-02). However, the resistance to shear failure is nearly the same for both cases due to the 4.5% limit placed on the reinforcement ratio ρ_{angle}. The predicted shear peeling strength for spans shear-01 and shear-02 was 136 kN and the corresponding value for shear spans shear-03 and

shear-04 was 143.5 kN. These magnitudes compare well with the test values as can be seen from Table-11.5.

TABLE-11.5: Experimental and analytical results

Item	Shear-01	Shear-02	Shear-03	Shear-04
1.Angle dimensions				
(a) side plate height d_{sp} (mm)	67	67	142	142
(b)soffit plate width b_{sof} (mm)	100	100	90	90
(c) thickness of plates (mm)	8	8	8	8
(d) Area (mm^2)	2672	2672	3712	3712
2.Test shear peeling strength $(V_{pure})_{test}$	138.2	133.8	159.4	161.7
3.Shear strength of concrete V_{uc} (kN) (theory)	81.0	81.0	81.0	81.0
4.Shear strength of stirrups V_{us} (kN) (theory)	164.0	164.0	164.0	164.0
5.Shear capacity of beam (V_{uc} + V_{us}) (kN) (theory)	245.3	245.3	245.3	245.3
6.Shear peeling strength (theory) $(V_{pure})_{theory}$(kN)	136.0	136.0	143.5	143.5
7.$(V_{pure})_{test}/(V_{pure})_{theory}$	1.02	0.98	1.11	1.12
8.$(V_{pure})_{test}/(V_{uc})_{theory}$	1.96	1.90	2.26	2.30
9.Shear stress due to longitudinal shear flow (MPa)	1.46	1.41	1.59	1.62

The theory predicts the shear strength of the concrete beam V_{uc} as 81 kN. It can be seen from row-8 of Table-11.5 that the experimental shear peeling strength of the plated beams $(V_{pure})_{test}$ were about 190 to 230% higher than shear strength of the concrete beam V_{uc} as determined from the theory. The ninth row of Table-11.5 also shows the magnitudes of the elastic interface shear stresses obtained using a cracked plated section at the instance of shear peeling for all the cases. The magnitudes vary between 1.41-1.62 MPa and they are much less than the Brazilian tensile strength of concrete (f_b=4.4 MPa). This shows, the debonding is not due to shear flow forces.

11.6.4.2 Comparison between test and analytical results

Figure 11.18 shows a comparison between the test and analytical shear peeling strengths. The test strengths were on an average 1.07 times that of the predicted peeling strengths. Therefore, the model developed for angle plated beams can be adopted with confidence.

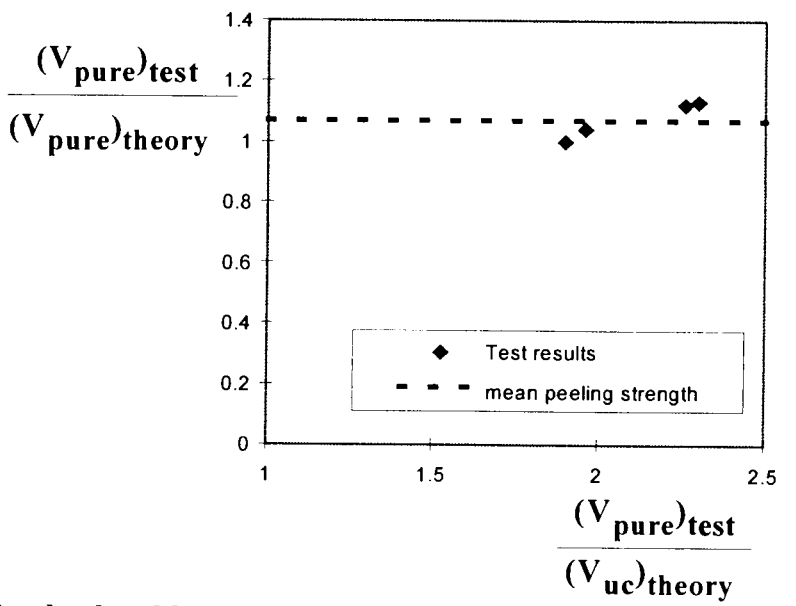

Fig.11.18. Angle plated beams - Comparison between test and theoretical results

11.7 Model for shear peeling of compression face plated reinforced concrete beams

11.7.1 Sequence of shear peeling

As discussed in Section 9.7, the shear peeling of compression face plated beams occurs in the three stages shown in Figs.11.20a-c. This is unlike the instantaneous shear peeling of tension face plated beams due to the formation of a critical diagonal crack, as shown in Fig.11.19.

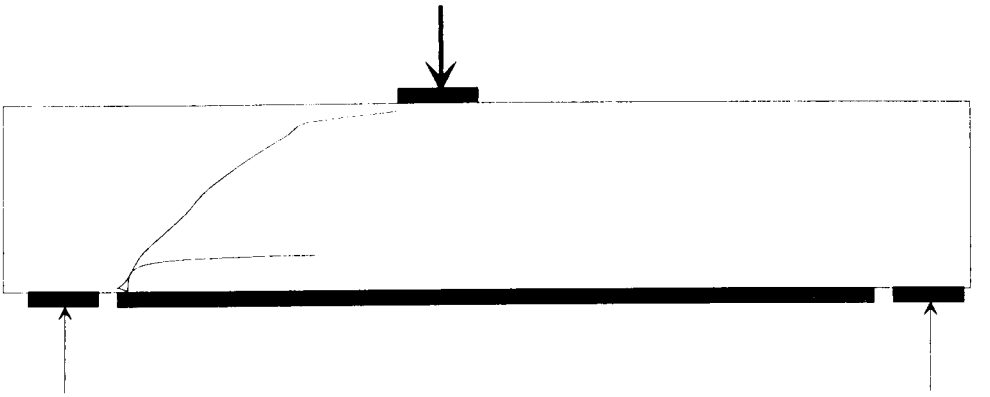

Fig.11.19. Instantaneous shear peeling in tension face plated beams

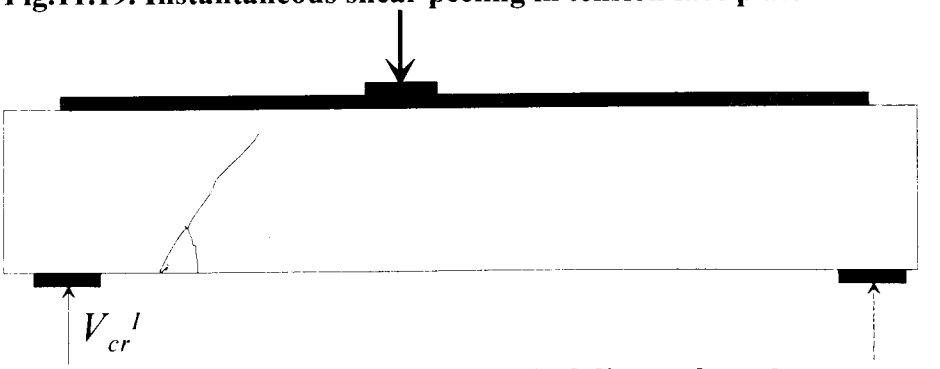

(a) Stage I-Formation of critical diagonal crack

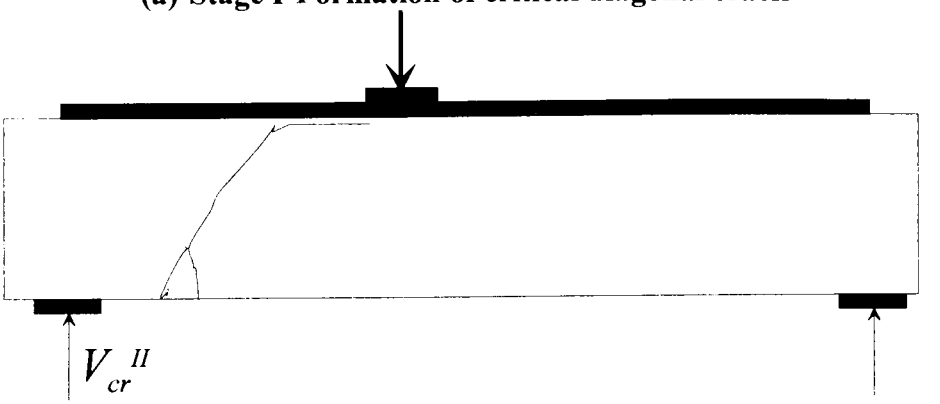

(b) Stage II-Extension of diagonal crack to load point

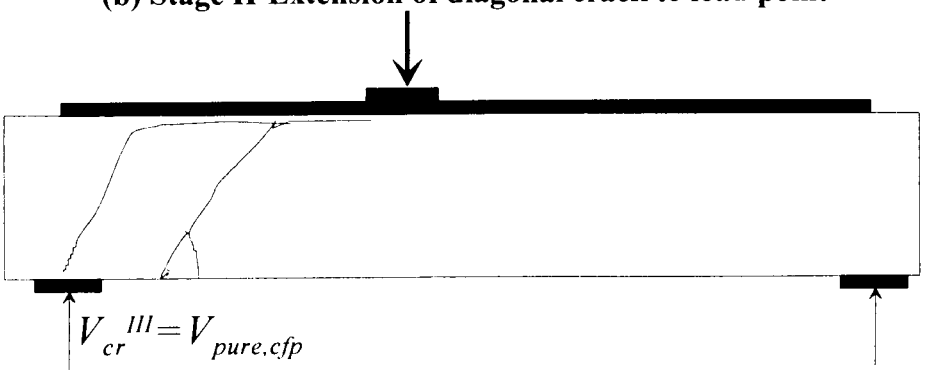

(c) Stage III-Formation of diagonal crack from support and complete peeling

Fig.11.20. Shear peeling in compression face plated beams

In stage I in Fig.11.20a, a critical diagonal crack forms at a distance from the support as shown in Fig.11.20a and the shear load needed to cause this crack is termed as V_{cr}^{I}. In stage II, a debonding crack forms from the tip of the stage I crack and propagates along the bottom edge of the plate to the load point, as shown inn Fig.11.20b; the shear load required to cause this crack is termed as V_{cr}^{II}. In stage III, the shear peeling of the plated beam is completed due to the formation of a long diagonal crack from the support to the load point as shown in Fig.11.20c; the shear load needed to cause this crack is termed V_{cr}^{III} which is also the shear peeling resistance of the compression face plated beam, $V_{pure,cfp}$, i.e. $V_{pure,cfp} = V_{cr}^{III}$.

11.7.2. Proposed model for shear peeling

Based on the tests on compression face plated beams, the following procedure is suggested to analyse the three different stages of shear peeling.

11.7.2.1 Equation for stage I (V_{cr}^{I})

The load to cause the critical shear crack can be assumed to be the shear strength of the unplated reinforced concrete beam without shear stirrups (V_{uc}) as given in national codes of practice or calculated using Zhang's crack sliding model as described in Section 5.3.

$$V_{cr}^{I} = V_{uc} \tag{11.36}$$

11.7.2.2 Equation for stage II (V_{cr}^{II})

The stage-II behaviour of the compression face plated beam can be compared to that of the beam bonded with tension face plates as described in Section 11.4. Therefore, V_{cr}^{II}

can be computed by carrying out a crack sliding failure analysis, as depicted in Fig.11.21.

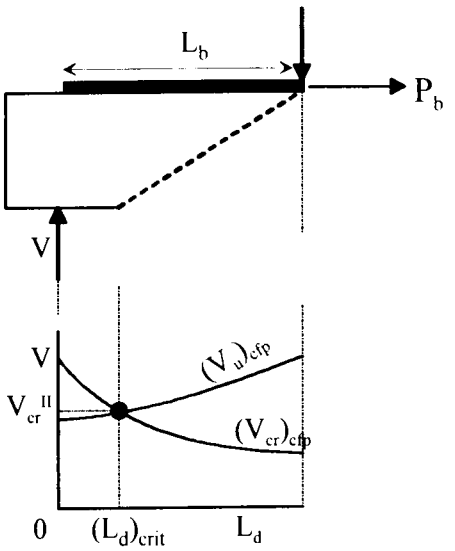

Fig.11.21. Crack sliding approach for stage-II shear load (V_{cr}^{II})

The critical diagonal crack is approximated to be a straight line as shown in Fig.11.21 so that Eqn.11.16 to compute the load to cause shear crack V_{cr} applies to Fig.11.21 and hence becomes

$$V_{cr,cfp} = \left(\frac{x^2+h^2}{a}\right)\left(\frac{f_{tcf}\,b}{2} + \frac{mf_t b_{cfp} t_{cfp}(0.5t_{cfp})}{h^2}\right) \tag{11.37}$$

where b_{cfp} and t_{cfp} are the width and the thickness of the compression face plate respectively. Similarly, the load to cause failure along a diagonal crack $V_{u.cfp}$ can be calculated in the same manner as for the tension face plated beam (refer section 11.4.2) and hence Eqn.11.22 becomes

$$V_{u,cfp} = \frac{1}{2}\gamma_s \gamma_{o,cfp} f_c \left(\sqrt{1+\left(\frac{x}{h}\right)^2} - \frac{x}{h}\right) bh \tag{11.38}$$

In Eqn.11.38 $\gamma_{0.cfp}$ is estimated similar to in Eqn.11.22 by changing the subscript 'tfp' in Eqns.11.17-22 with the subscript 'cfp'. The solution of Eqns.11.37 and 11.38 gives both the location of the critical crack $L_{d.crit}$ and V_{cr}^{II} as shown in Fig.11.21.

11.7.2.3 Equation for stage III-complete shear peeling ($V_{cr}^{III} = V_{pure.cfp}$)

In the third stage, when complete debonding occurs by the formation of a diagonal crack from the support as shown in Fig.11.17c, the shear peeling resistance of the compression face plated beam ($V_{pure.cfp}$) can be written by substituting $x = a$ in Eqn.11.37 as the position of the diagonal crack is now fixed.

$$V_{pure.cfp} = V_{cr}^{III} = \left(\frac{a^2 + h^2}{a}\right)\left(\frac{f_{tef}\, b}{2} + \frac{0.5 m f_t b_{cfp} t_{cfp}^2}{h^2}\right) \tag{11.39}$$

11.7.3 Analysis and comparison of test results

All the salient test and analytical results are summarised in Table-11.6. It can be seen that the shear peeling strengths of the beams $V_{pure.cfp}$ are far less than the shear strength of the unplated reinforced concrete beam including stirrups (V_u = 365.1 kN) as calculated from AS-3600 formulae. This shows that the presence of internal shear stirrups does not arrest the propagation of the diagonal shear cracks that cause peeling. However it is worth noting that complete shear peeling occurred at shear loads about 183-200% of the theoretical shear strength of the unplated RC beam excluding the stirrups V_{uc} (Refer Section 9.7). Furthermore, the shear stresses at the interface that were calculated from the standard $VAy/I_p b_p$ formula for all the three beams (0.98-1.89 MPa) are much less than the tensile strength of the concrete (f_b =3.6 MPa). Hence, the possibility of shear flow debonding can be ruled out. The analytical results are summarised in Table-11.6 and they are compared with test results subsequently.

Table-11.6: Test and analytical results for compression face plated beams

Item/Specimen	SP-C6	SP-C12	SP-C20
t_{cfp} (mm)	6	12	20
$V_{cr}^{I}(Expt)$ kN	80.7	88.1	80.7
$V_{cr}^{I}(Theory)$ kN	77.5	77.5	77.5
$V_{cr}^{I}(Expt/theory)$	1.04	1.14	1.04
$V_{cr}^{II}(Expt)$ kN	124.0	117.4	100.0
$V_{cr}^{II}(Theory)$ kN	88.0	100.0	103.0
$V_{cr}^{II}(Expt/theory)$	1.41	1.17	0.97
$V_{pure.cfp}(Expt)$ kN	148.2	141.7	155.6
$V_{pure.cfp}(Theory)$ kN	149.1	151.2	155.3
$V_{pure.cfp}(Expt/Theory)$	0.99	0.94	1.00
$V_{pure.cfp}(Expt)/V_{uc}$	1.91	1.83	2.00
Shear stress at the interface (MPa)	0.98	1.34	1.89

11.7.3.1 Stage I-V_{cr}^{I}

The first major shear crack occurred at shear load that varied between 80.7-88.1 kN as shown in Table-11.6. This compares well with the shear strength of the non-plated and non-shear reinforced beam (V_{uc} = 77.5 kN as per AS:3600 formula). On an average, the test strengths were 1.07 times higher than the theoretical strength.

11.7.3.2 Stage II-V_{cr}^{II}

In the second stage, the major shear crack propagated along the bottom edge of the plate towards the load point. To compute V_{cr}^{II}, the envelopes for V_u and V_{cr} were drawn for the three compression face plated beams as well as for the non-plated beam and they are shown in Fig.11.22. It can be seen that the presence of the compression face plate has virtually no effect on the load to cause the shear crack ($V_{cr.cfp}$). The difference in strengths comes from the shear loads to cause shear failure along an existing crack ($V_{u.cfp}$). On an average, the experimental strengths for stage II were 1.18 times the theoretical strength.

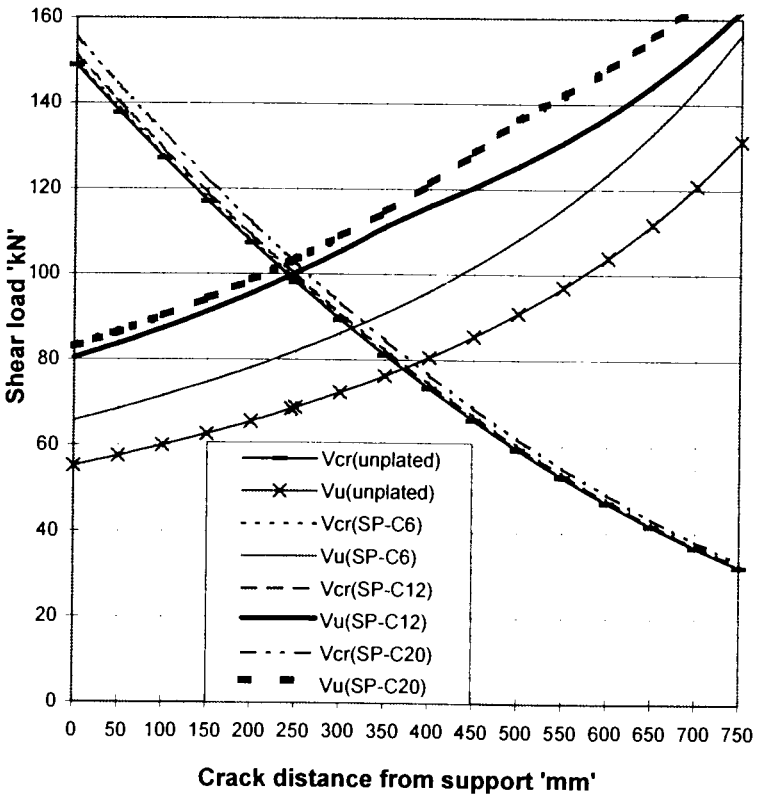

Fig.11.22. Analysis of compression face plated beams using crack sliding model

11.7.3.2 Stage III-$V_{pure,cfp} = V_{cr}^{III}$

The stage-II horizontal debonding crack stabilised on further application of the load. Finally, shear peeling of the beam occurred either by the extension of this crack to cover the whole length of the plate as in the case of SP-C6 or by the simultaneous extension of the debonding crack and the formation of diagonal cracks originating from the support as happened in SP-C12 and SP-C20 (Refer Section 9.7). Therefore, the shear load to cause complete failure of the compression face plated beam ($V_{pure,cfp}$) was predicted using Eqn.11.39; the theoretical and test results are compared in Table-11.6 and they are plotted as shown in Fig.11.23. The mean predicted peeling strengths are almost equal to the mean test strength. Hence, this procedure can be adopted with confidence.

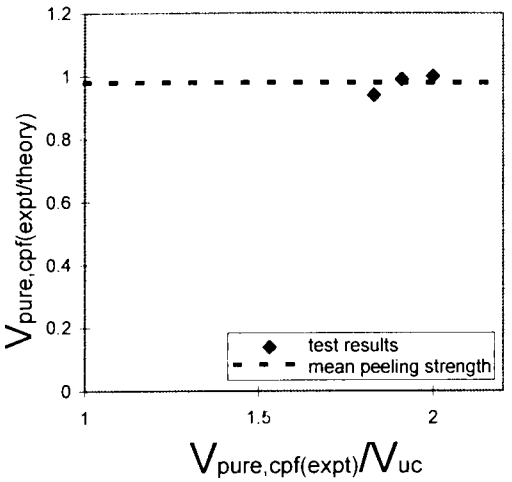

Fig.11.23. Comparison between shear peeling strengths of compression face plated beams

11.8 Mathematical model for enhancing the shear peeling strength of the tension face plated beams by side plates

11.8.1 Introduction

In this section, mathematical models are developed to analyse the improvement in the shear peeling strength of tension face plated beams by bonding additional side plates. The most comprehensive experimental study on this aspect was carried out by Weimin-Luo (1993) at the University of Adelaide and the test results given in Table-2.4 were discussed in detail in Section 2.5. Here, firstly, the improvement in shear peeling strength from these test results is quantified by two empirical methods, namely the element strength approach and the shear strength approach (Oehlers,Ali and Weimin-Luo 1998). Then, a mathematical model based on the crack sliding theory is presented and it is calibrated against the test results from Weimin-Luo's study.

11.8.2 Empirical methods

11.8.2.1 Discussion of test results by Weimin-Luo(1993)

The aim of these tests was to determine directly through experimental testing the increase in the pure shear peeling capacity ΔV_{pure} that the side plates provided.

$$\Delta V_{pure} = V_{pure.wsp} - V_{pure.nsp} \tag{11.40}$$

where $V_{pure.nsp}$ is the pure shear peeling capacity with no side plates and $V_{pure.wsp}$ is the pure shear peeling capacity with side plates. The pure shear peeling capacity of beams with no side plates $V_{pure\cdot nsp}$ was determined from tests of beams with only tension face plates and it was the shear at which the tension face plates debonded. Similarly, the pure shear peeling capacity of beams with side plates $V_{pure\cdot wsp}$ was the shear at which the tension face plates debonded. The first plate to debond is listed in Column 8 of Table-11.7. In most cases the tension face plate (tfp) debonded completely before the side plate (sp) showed signs of debonding, and in some cases it was difficult to determine which plate debonded first and this has been referred to as (both) in Table-11.7.

The shear loads in these beams when the strains in the tension face plates sudden reduced due to debonding are listed as V_{pure} in Column 6 in Table-11.7. The increase in the pure shear peeling capacity ΔV_{pure} is given in Column 7. In deriving ΔV_{pure} for Series 1, the shear peeling strength with no side plates $V_{pure\cdot nsp}$ was taken as the average of V_{pure} for tests S1B1L and S1B2L. However in Series 2 and 3, each beam had a shear span without a side plate and this was taken as $V_{pure\cdot nsp}$ for the shear span with the side plate. For the definitions of the notations used in Table-11.7, the reader is referred to Section 2.5.1.

TABLE- 11.7: Beam tests by Weimin-Luo

	GEOMETRIC PROPERTIES				TEST RESULTS			ANALYTICAL RESULTS		
Shear span (1)	L_{in} mm (2)	L_{out} mm (3)	t_{sp} mm (4)	A_{st} mm^2 (5)	V_{pure} kN (6)	$\Delta Vpure$ kN (7)	first plate (8)	τ_{tfp} N/mm^2 (9)	$\frac{\Delta Vpure}{P_b}$ (10)	$\frac{\Delta Vpure}{P_p}$ (11)
Series-1: Varying lengths of side plates										
S1B1L	0	0	4.0	402	33.4	0	tfp	1.24	0	0
S1B2L	0	0	4.0	402	26.4	0	tfp	0.98	0	0
S1B3L	45	45	4.0	402	30.8	0.9	sp	0.99	0.0154	0.0023
S1B2R	90	90	4.0	402	37.0	7.1	sp	1.18	0.0609	0.0202
S1B4R	135	135	4.0	402	35.0	5.1	both	1.12	0.0292	0.0144
S1B1R	180	180	4.0	402	43.2	13.3	both	1.38	0.0570	0.0381
S1B3R	270	270	4.0	402	50.0	20.1	tfp	1.60	0.0574	0.0577
S1B4L	345	345	4.0	402	60.6	30.7	tfp	1.94	0.0687	0.0877
Series-2: Varying tension reinforcing bars										
S2B5L	0	0	0	157	33.0	0	tfp	1.43	0	0
S2B5R	270	420	4.0	157	62.8	29.8	tfp	2.28	0.0852	0.0854
S2B6L	0	0	0	628	31.5	0	tfp	1.06	0	0
S2B6R	270	420	4.0	628	69.8	38.3	tfp	2.07	0.1095	0.1096
Series:3-Varying thickness of side plates										
S3B7L	0	0	0	402	27.9	0	tfp	1.03	0	0
S3B7R	335	915	1.0	402	54.6	26.7	tfp	1.90	0.0536	0.2044
S3B8L	0	0	0	402	33.1	0	tfp	1.23	0	0
S3B8R	335	915	2.0	402	64.7	33.4	tfp	2.16	0.0769	0.1495
S3B9L	0	0	0	402	33.0	0	tfp	1.23	0	0
S3B9R	335	915	3.0	402	72.6	39.6	tfp	2.35	0.0951	0.1195

11.8.2.2 Analysis of experimental work

The shear stresses τ_{tfp} between the tension face plate and the reinforced concrete beam at the shear peeling load(V_{pure}) are listed in Column 9 in Table-11.7. These shear stresses were derived from elementary linear elastic theory using the well known $VAy/I_p b_p$ formula. They were derived from the second moment of area of the cracked plated section I_{cp} in which the tensile strength of the concrete is assumed to be zero and, hence, should over estimate the magnitude of the shear stress. It can be seen that debonding of the tension face plates occurred over a very wide range of shear stresses from 0.98 N/mm^2 to 2.34 N/mm^2 and, hence, these shear stresses cannot be used to account for the variations in the shear peeling strength V_{pure}. Furthermore, the shear stresses τ_{tfp} in Column 9 are always much less than the tensile strength of the concrete f_b

= 3.60 N/mm^2 and it is, therefore, unlikely to have caused debonding in any of the tests. The aim of this experimental research is to quantify the increase in the shear peeling strength of the tension face plates ΔV_{pure}.

11.8.2.3 Element Strength Approach

Let us define the bond strength between a side plate and the reinforced concrete beam as $L_{min} d_{sp} f_b$ where L_{min} is the minimum of the bond lengths L_{in} and L_{out} that are shown in Figs.2.14-16. Therefore, the bond strength P_b between both plates, on either side of the beam, and the reinforced concrete beam is

$$P_b = 2L_{\min} d_{sp} f_b \tag{11.41}$$

Furthermore, let us define the axial yield strength of both side plates $(P_b)_y$ as

$$(P_b)_y = A_{sp} f_{yp} = 2 d_{sp} t_{sp} f_{yp} \tag{11.42}$$

where A_{sp} = cross-sectional area of both plates on either side of the beam, and f_{yp} = yield strength of the side plate.

As the shear strength of a reinforced concrete beam without stirrups and, hence, the shear peeling strength, is an extremely complex problem it can be assumed that the increase in the shear peeling strength ΔV_{pure} is a function of the bond strength P_b and plate strength $(P_b)_y$. The experimentally determined values of $\Delta V_{pure} / P_b$ and $\Delta V_{pure} / (P_b)_y$ are listed in Columns 10 and 11 in Table-11.7 and are plotted in Fig.11.24.

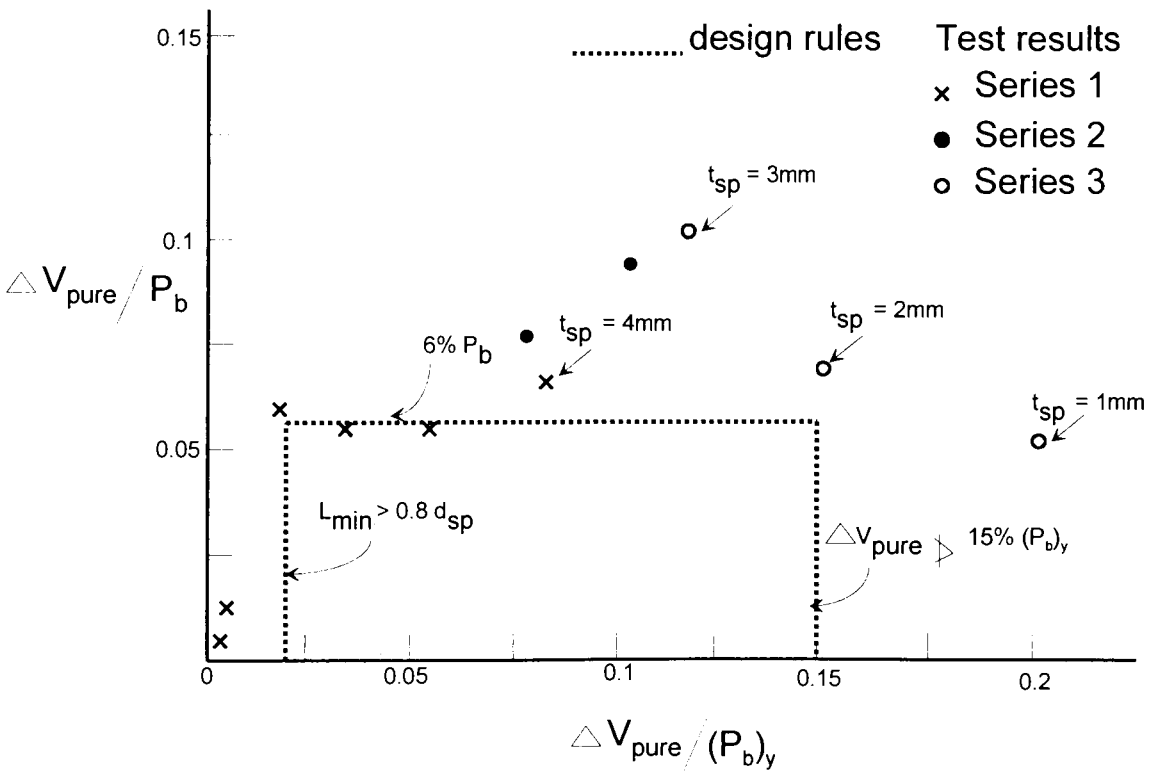

Fig.11.24. Element strength approach

Consider the results from Series 1 in Fig.11.24 in which the bond length L_{min} (minimum of L_{in} and L_{out} in Table-11.7, shown in Figs.2.14-16) was gradually increased within the series. Apart from the two results at low values of $\Delta V_{pure}/(P_b)_y$ in Fig.11.24 in which the bond length was less than $0.75d_{sp}$, the increase in the shear peeling strength is fairly constant at about 6% of P_b. It is felt that these two low results may have been due to debonding of the side plate prior to debonding of the tension face plate as shown in Column 8 in Table-11.7. The plates had a small aspect ratio L_{min}/d_{sp} and, hence, it would appear that premature debonding of the side plate could be prevented by ensuring that $L_{min} \geq 0.8d_{sp}$. Furthermore, as there is no reduction in the bond strength of 6% P_b with increasing $(P_b)_y$ in Series 1, it would appear that the bond strength P_b controlled the increase in the shear peeling strength in this series of tests and not the plate strength $(P_b)_y$.

The horizontal line at 6% of P_b appears to form a lower bound to Series 2 and, hence, also copes with the variation in the area of the tension reinforcing bars.

The Series 1 result in Fig.11.24 marked with 't_{sp} = 4 mm' can be considered to be part of Series 3 as it had almost the same bond length as the tests in Series 3. However, the plates in Series 3 were folded round the edge of the beam as shown in Fig.2.16. This fold would probably have increased the bond strength in much the same way as a bend in a reinforcing bar increases its anchorage strength. This may explain the increase in bond strength when the plate thickness t_{sp} was reduced from 4 mm to 3 mm and then 2 mm in Series 3. The bond strength $\Delta V_{pure} / P_b$ for the result with t_{sp} = 1 mm is probably also slightly overestimated because of the bend as explained previously. It is felt that the reduction in strength from the 2 mm plate to the 1 mm plate and the low value of the bond strength for the 1 mm plate, both signify the transition from the bond strength P_b controlling the increase in the shear peeling strength to the plate strength $(P_b)_y$ controlling the increase. It will be assumed that the transition point occurs at the result for the 2 mm plate where ΔV_{pure} is 15% of the yield strength of the plate $(P_b)_y$.

The design rules proposed above are shown as dotted lines in Fig.11.24. In order to ensure that they are not applied beyond the parameters of the tests, it is also suggested that the bond length should not be greater than twice the depth of the plate. The design rules for a reinforced concrete beam with the same size side plates on both sides of the beam can, therefore, be summarised as

$$\Delta V_{pure} = 0.06 P_b = 0.12 L_{\min} d_{sp} f_b \qquad (11.43a)$$

$$\Delta V_{pure} \le 0.15 A_p f_{yp} = 0.30 d_{sp} t_{sp} f_{yp} \qquad (11.43b)$$

$$0.8 d_{sp} \le L_{\min} \le 2 d_{sp} \qquad (11.43c)$$

This approach is purely empirical and based on the strengths of the bond and plate elements and no attempt has been made to simulate the extremely complex failure mechanism that is associated with shear peeling. However, the complexity of the problems associated with shear strength is illustrated in the following section where an attempt is made to adapt accepted rules for the shear strength of reinforced concrete beams without stirrups to allow for side plates.

11.8.2.4 Shear Strength Approach

The shear capacity of a reinforced concrete beam without stirrups V_{uc} (N) can be written in the following form (Zsutty 1968)

$$V_{uc} = k(b_w d_o)^{2/3}(A_{st})^{1/3} \tag{11.44}$$

where k is a constant, b_w = width of the web of the reinforced concrete beam (mm); d_o = distance from the extreme compressive fibre to the outermost tensile reinforcing bar (mm); and A_{st} = area of the fully anchored tensile reinforcement (mm^2). The $(b_w d_o)^{2/3}$ parameter in Eqn.11.44 can be visualised as the effective area of the concrete element of the beam through which the shear is transferred, and the $(A_{st})^{1/3}$ parameter as the dowel action of the reinforcement that contributes to the shear strength.

To be able to include the area of the side plate A_{sp} into Eqn.11.44, it is necessary to ensure that either the side plates are fully anchored, as this is a prerequisite for the tension reinforcing bars, or use an effective area $A_{sp,eff}$ that allows for partial anchorage. This can be achieved by equating Eqns.11.41 and 11.42 so that

$$A_{sp,eff} = \frac{2L_{\min} d_{sp} f_b}{f_{yp}} \tag{11.45a}$$

$$A_{sp,eff} \le A_{sp} \tag{11.45b}$$

If the side plates have a total effective area $A_{sp,eff}$, then the effective area of the beam can be assumed to increase by $m\,A_{sp,eff}$ where $m = E_s/E_c$, and the dowel contribution can be assumed to increase by $A_{sp,eff}$. Therefore Eqn.11.44 becomes

$$\begin{aligned}(V_{uc})_{sp} &= k\left(b_w d_o + mA_{sp,eff}\right)^{2/3}\left(A_{st} + A_{sp,eff}\right)^{1/3} \\ &= kV_{uc}\left(1+\frac{mA_{sp,eff}}{b_w d}\right)^{2/3}\left(1+\frac{A_{sp,eff}}{A_{st}}\right)^{1/3}\end{aligned} \tag{11.46}$$

We know from Eqn.2.4, $V_{pure,nsp}=V_{pure,tfp}=V_{uc}$; furthermore $V_{pure,wsp}=(V_{uc})_{sp}$. Therefore, the increase in shear peeling strength due to side plates ΔV_{pure} is given by

$$\begin{aligned}\Delta V_{pure} &= V_{pure,wsp} - V_{pure,nsp} = (V_{uc})_{sp} - V_{uc} \\ &= V_{pure,nsp}\left[\left(1+\frac{A_{sp,eff}}{A_{st}}\right)^{1/3}\left(1+\frac{mA_{sp,eff}}{b_w d_o}\right)^{2/3} - 1\right]\end{aligned} \tag{11.47}$$

The experimental results from Column 7 in Table-11.7 are compared in Fig.11.25 with the theoretical results from Eqn.11.47. Results adjacent to the diagonal line signify good correlation between theory and experiment and those to the left signify an under estimation. It can be seen that Eqn.11.47 considerably overestimates the increase in the shear peeling strength at low values of ΔV_{pure} and severely underestimates the increase in strength at high values of ΔV_{pure}. It is felt that the cause of the large scatter is the cubic exponent in Eqn.11.47, which makes the equation highly sensitive to small changes. It is worth noting that Eqn.11.47 suggests that ΔV_{pure} is not sensitive to the effective area parameter $\left(1+\frac{mA_{sp.eff}}{b_w d_o}\right)^{2/3}$ as this parameter tends to unity. This was confirmed by linear elastic theory, which showed that the increase in the transformed area due to plating as a proportion of the transformed area of the non-side plated section was

considerably less than $\Delta V_{pure} / V_{pure.nsp}$. Hence, this factor could not be used to account for the increase in the shear peeling strength.

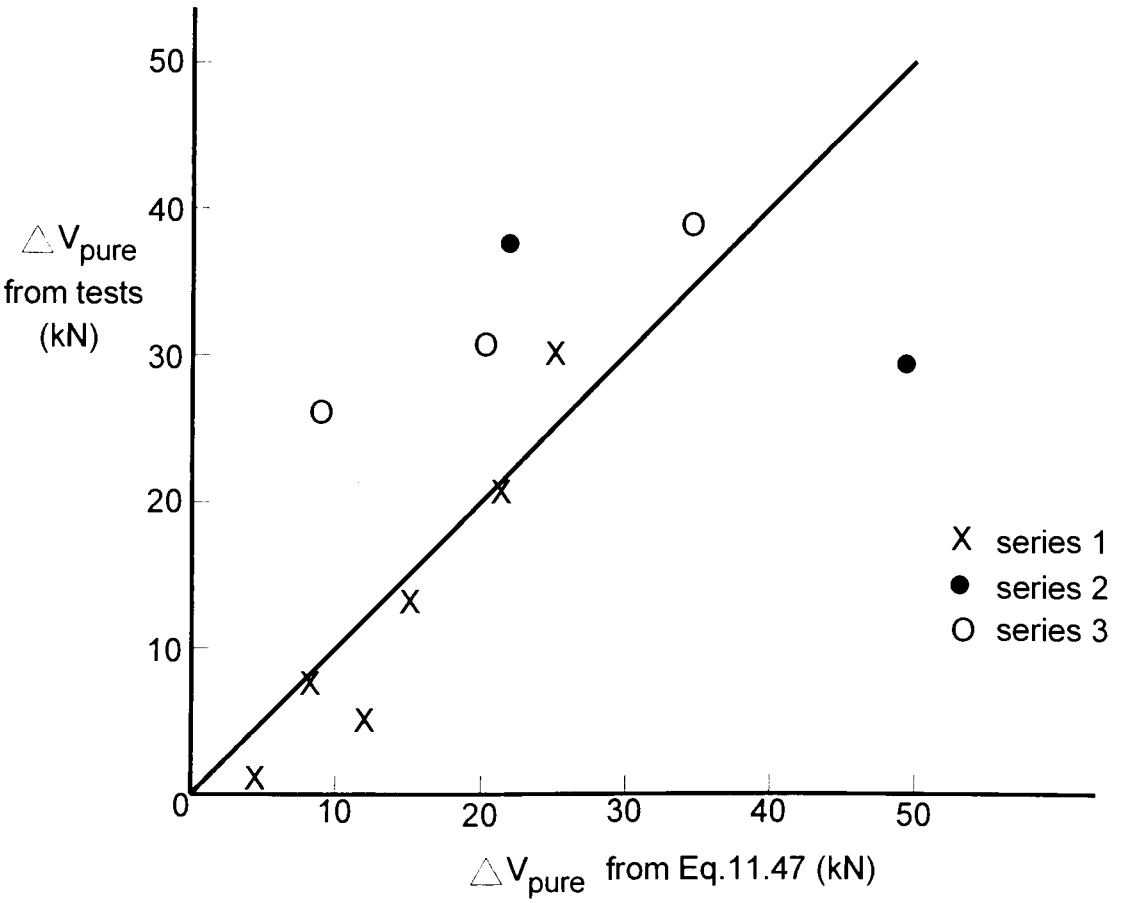

Fig.11.25. Shear strength approach

11.8.3 Model based on diagonal cracking load approach

11.8.3.1 Model formulation

From the preceding discussion, it is evident that the element strength approach prescribes useful design guidelines along with some restrictions placed to cater for the critical parameters of the experimental study that were used to calibrate the model. The shear peeling strength of tension face plated beams cannot also be quantified by these empirical approaches. Therefore, the diagonal cracking load approach can be modified as follows to cater for variations such as the dimension of the side plates.

Test results have shown that the shear peeling of tension face plated beams with side plates is due to the formation of a critical diagonal crack close to the tension face plate end, similar to that which occurs in beams bonded with tension face plate only, as shown in Fig.11.26. Furthermore, the research in Section 11.5 shows that this could be simplified to a crack emanating from the plate end. The only difference is the increase in the shear peeling strength due to the presence of the side plates that depends upon the bond length and the dimensions of the side plates. Therefore, the shear peeling strength of tension face plated beams with side plates $V_{pure,wsp}$ can be considered as the load to cause a diagonal crack at the end of the tension face plate, as shown in Fig.11.27. This figure is similar to Fig.11.4 for the beams bonded only with side plates but the length of side plate to the right side of the crack is L_{in} and the position of the crack is now assumed to be fixed at the end of tension face plate end.

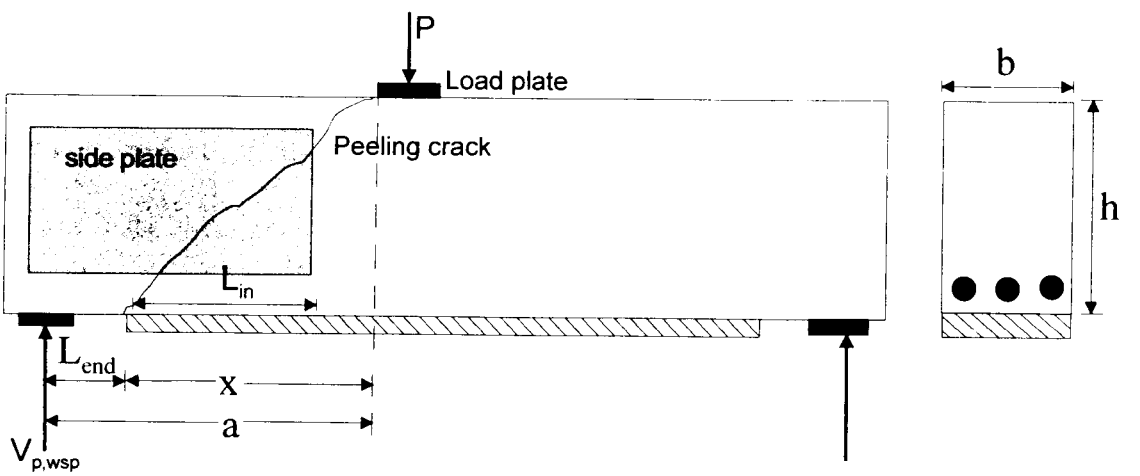

Fig.11.26. Shear peeling in tension face plated beams with side plates

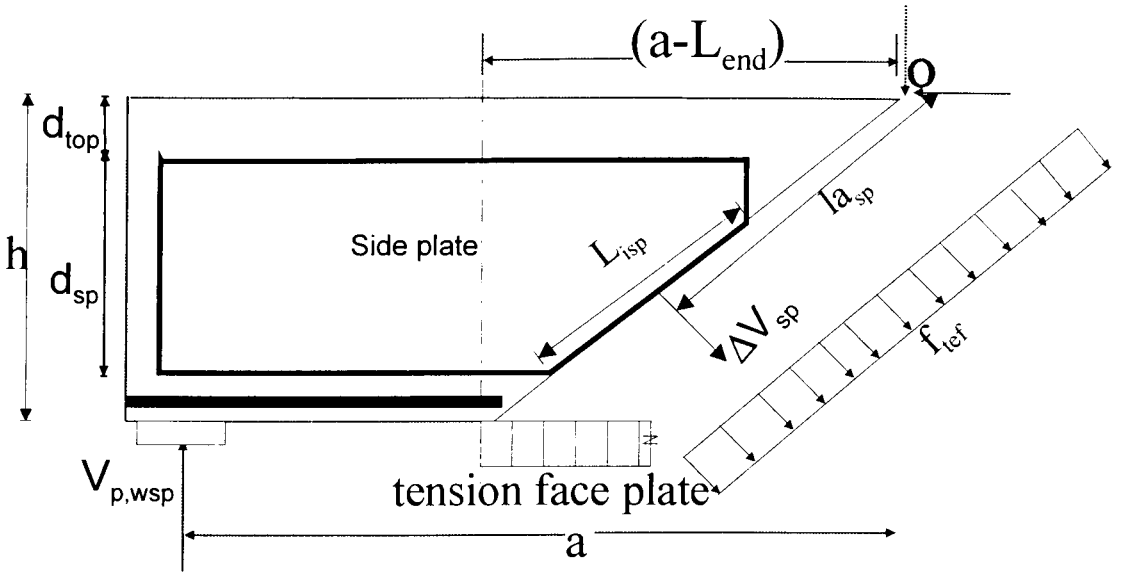

Fig.11.27. Model for determining diagonal cracking load

The length of the side plate crossing the inclined crack plane (L_{isp}) in Fig.11.27 is

$$L_{isp} = \frac{L_{in}}{x}\sqrt{x^2 + h^2}, \; if \; L_{in} \le x \tag{11.48a}$$

or

$$L_{isp} = \frac{d_{sp}}{h}\sqrt{x^2 + h^2}, \; if \; L_{in} > x \tag{11.48b}$$

Here, L_{in} is the distance between the end of the tension face plate and the end of the side plate lying within the shear span, and x=a-L_{end}. Therefore, the area of both the side plates crossing the inclined crack plane (A_{isp}) is

$$A_{isp} = 2t_{sp}\frac{L_{in}}{x}\sqrt{x^2 + h^2}, \; if \; L_{in} \le x \tag{11.49a}$$

or

$$A_{isp} = 2t_{sp}\frac{d_{sp}}{h}\sqrt{x^2 + h^2}, \; if \; L_{in} > x \tag{11.49b}$$

The component force ΔV_{sp} exerted by the side plate across the crack can be derived in the same way as for ΔV_{cr} of the beams bonded only with side plates (Refer

Eqn.11.7). This component ΔV_{sp} is obtained by multiplying the tensile strength of the concrete and the transformed area of the side plates crossing the inclined plane of the crack (A_{isp}).

$$\Delta V_{sp} = mA_{isp}.f_{ct} = \left(2m\frac{\sqrt{x^2+h^2}}{x} L_{in} t_{sp} \right) f_t, \ if \ L_{in} \le x \tag{11.50a}$$

or

$$\Delta V_{sp} = mA_{isp}.f_t = 2mt_{sp}\frac{d_{sp}}{h}\sqrt{x^2+h^2}\, f_t, if \ L_{in} > x \tag{11.50b}$$

where m= modular ratio (E_{sp}/E_c). Here E_{sp} and E_c are the elastic modulus of side plate and concrete respectively, d_{sp} is the depth of side plate, and t_{sp} is the thickness of side plate. The direct tensile strength of the concrete (f_t) is assumed to be 80% of the Brazilian tensile strength of the concrete (f_b).

The force ΔV_{sp} acts at a distance of la_{sp} from the point 'O' shown in Fig.11.24 and is given by

$$\begin{aligned} la_{sp} &= \frac{\sqrt{x^2+h^2}}{h}\left(d_{top} + d_{sp} - \frac{1}{2}\left\{ \frac{hL_{in}}{x} - d_{bot} \right\} \right) \ if \ L_{in} \le x \\ &= \frac{\sqrt{x^2+h^2}}{h}\left(d_{top} + 0.5d_{sp} \right), \ if \ L_{in} > x \end{aligned} \tag{11.51}$$

Now, the diagonal cracking load of the tension face plated beam with side plates ($V_{p.wsp}$) is obtained by taking moment of all the forces about the point O. (Refer Fig.11.27)

$$V_{p.wsp}.a = \left(f_{tef} b\sqrt{x^2+h^2}.\frac{\sqrt{x^2+h^2}}{2} \right) + \left(\Delta V_{sp} la_{sp} \right) \tag{11.52}$$

Therefore, substituting the values of ΔV_{sp} and la_{sp} into Eqn.11.52 and simplifying, we get the following equation for $V_{p.wsp}$.

$$V_{p,wsp} = \left(\frac{x^2+h^2}{a}\right)\left(\frac{f_{tef}\,b}{2} + \frac{2mf_t L_{in} t_{sp}\left[d_{top} + d_{sp}\left\{1 - \frac{0.5L_{in}}{x}\right\}\right]}{xh}\right), \; if \;\; L_{in} \le x \qquad (11.53a)$$

and

$$V_{p,wsp} = \left(\frac{x^2+h^2}{a}\right)\left(\frac{f_{tef}\,b}{2} + \frac{2mf_t d_{sp} t_{sp}(d_{top} + 0.5d_{sp})}{h^2}\right), \; if \;\; L_{in} > x \qquad (11.53b)$$

Note that the horizontal projection of the diagonal crack x in the above equations is (a-L_{end}). Here a is the distance between the centre of support plate and edge of load plate, L_{end} is the distance between the end of the tension face plate and the centre of support plate and d_{top} is the distance between the topmost fibre of the beam and the top of the side plate. It may be noted that Eqn.11.53a was derived for the case when the bottom edge of the side plate coincides with the bottom of the concrete beam and Eqn.11.53b is a general one. However when there is a gap of d_{bot} between the bottom of the side plate and bottom of the concrete beam, the following general equation should be used in stead of Eqn.11.53a, when $L_{in} \le x$.

$$V_{p,wsp} = \left(\frac{x^2+h^2}{a}\right)\left(\frac{f_{tef}\,b}{2} + \frac{2mf_t t_{sp}\left(\frac{L_{in}}{x} - \frac{d_{bot}}{h}\right)\left(d_{top} + d_{sp} - \frac{1}{2}\left\{\frac{hL_{in}}{x} - d_{bot}\right\}\right)}{h}\right), \; L_{in} \le x$$

.....(11.54)

11.8.3.2 Correlation with test results

The experimental and the theoretical shear peeling strengths of tension face plated beams with side plates from Series 1,2 and 3 (Section 2.5) are summarised in Table-11.8. The experimental results are compared with that obtained from Eqns.11.53a and 11.53b. in Fig.11.28. It shows the existence of very good correlation with the ratio of the predicted

strength to the actual strength being 1.04 with a standard deviation of 0.17, even though the ratio between the minimum bond length and thickness of side plate had a wide range of 0-430.

Table-11.8:Comparison of test and theoretical results

Shear span	V_{pure}(test) kN	V_{pure} (Theory) kN	V_{pure} *(test/Theory)*
S!B1L	33.4	28.3	0.847
S1B2L	26.4	28.3	1.072
S1B3L	30.8	33.5	1.09
S1B2R	37	38.1	1.03
S1B4R	35	41.9	1.2
S1B1R	43.2	45	1.04
S1B3R	50	49	0.98
S1B4L	60.6	50.1	0.83
S2B5L	33.0	39.6	0.83
S2B5R	62.8	61	0.97
S2B6L	31.5	39.6	0.80
S2B6R	69.8	61	0.87
S2B7L	27.9	39.6	0.70
S2B7R	54.6	47.3	0.87
S2B8L	33.1	39.6	0.84
S2B8R	64.7	55	0.85
S2B9L	33.0	39.6	0.83
S2B9R	72.6	62.7	0.86

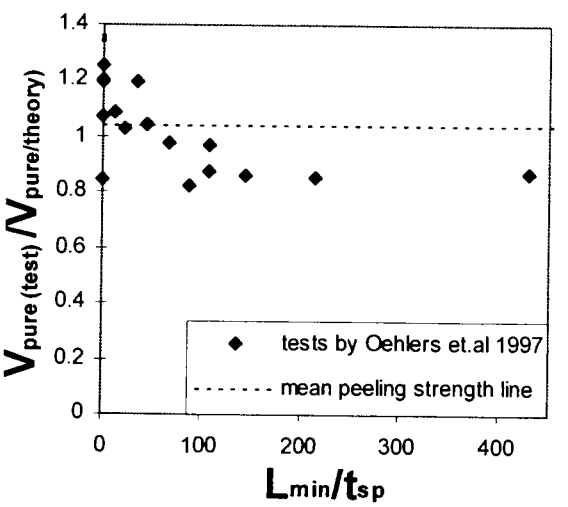

Fig.11.28. Theoretical and experimental shear peeling strengths for beams with tfp and side plates

11.9 Enhancing the shear peeling strength of the tension face plated beams by side plates (Results from Chapter-9)

The test results from Weimin-Luo (Section 2.5) pertain to the beams in which the tension face plate ends were predominantly under shear with negligible moments. On the contrary, for the beams tested in Chapter-9 the tension face plate ends were in a region of shear and flexure. Hence, the method developed in section 11.8.3 cannot be applied. To overcome this difficulty, the pure shear peeling strength as well as the pure flexural peeling capacity of each beam was calculated to study the interaction between moment and shear on peeling.

11.9.1 Analysis of test results

Figures 11.29a and 11.29b show the curves for shear cracking load (V_{cr}) and sliding strength (V_u) of all the four plated beams. Figure 11.29a also shows the curves for the unplated reinforced concrete beam without stirrups and also for a hypothetical beam that is plated with full length tension face plate and full length side plates. The analysis gives the pure shear peeling strength of MB-01, 02, 03 and 04 as 118 kN, 150 kN, 153 kN and 153 kN respectively. The theoretical shear strength of the unplated beam is obtained as 93 kN whereas the theory predicts the shear peeling strength of the beam bonded with full length side plates and tension face plate to be 178 kN. This shows that the maximum increase in shear peeling strength that can be achieved with additional bonding of side plates is twice that of the shear strength of the concrete beam without stirrups (V_{uc}). This limited increase may be attributed to the fact that in calculating the shear failure strength V_u of the plated beams, an upper limit of 4.5% is placed on the equivalent amount of the internal reinforcement and the external plates that can resist the sliding of the crack front (Refer to Eqns.11.21).

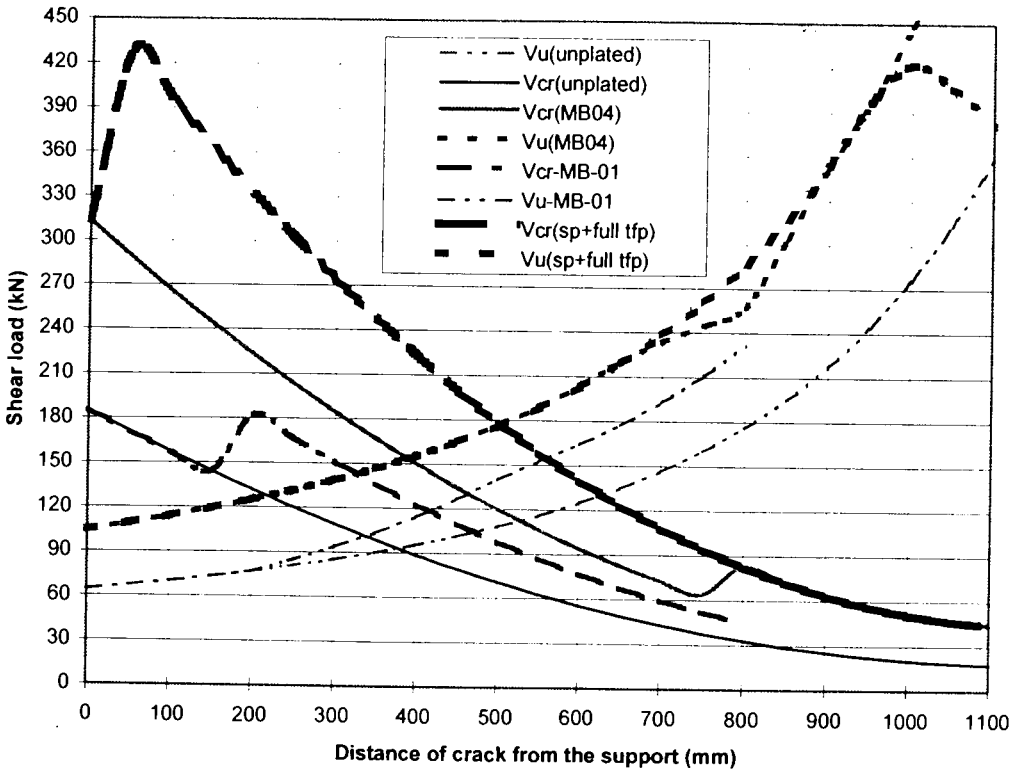

(a)

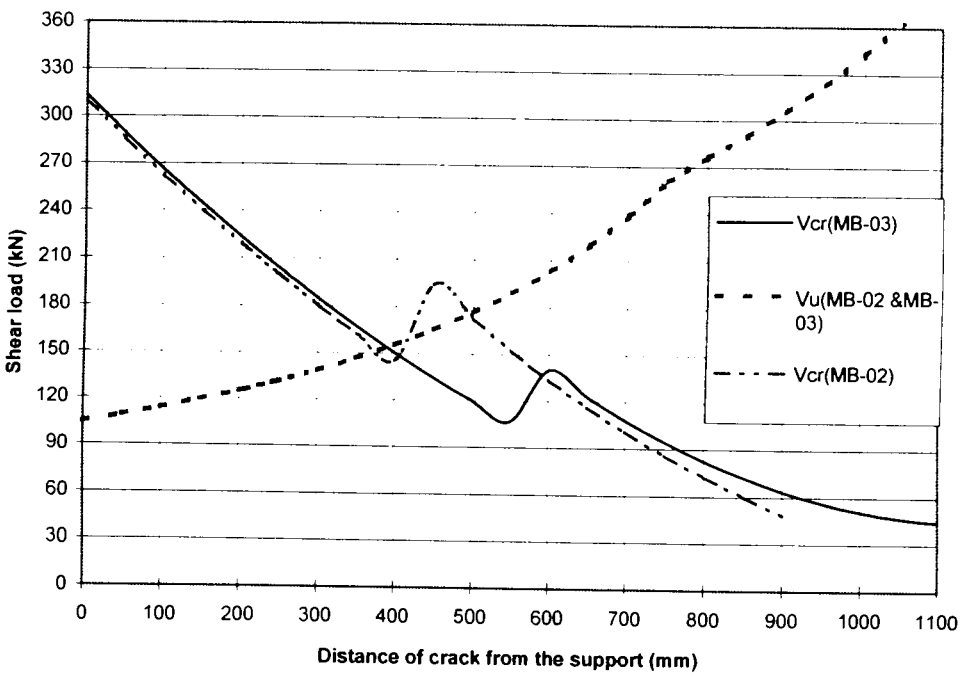

(b)

Fig.11.29. Envelops for the calculation of shear peeling strengths

Similarly, the moment required to peel off the tension face plate when no shear force is acting at the ends of the plate end ($M_{pure.tfp}$) was estimated using Oehlers and Moran's Equation (Refer Eqn.2.5); the area of cross-sections of both the side plates and the tension face plates were included in the computation. It was 183 kNm for MB-01 and 233 kNm for MB-02, MB-03 and MB-04. All these results are tabulated in Table-11.9. It may be noted that the magnitudes of theoretical shear peeling strength in Table-11.9 are scaled down by 10% to account for the overestimation, as discussed in Section 11.4.4 (Refer Eqns.11.24 and 11.25). Figure 11.30 is the interaction diagram that depicts the relationship between the ratios ($M_{tfp\text{-}end}/M_{pure.tfp}$) and ($V_{tfp\text{-}end}/V_{pure.theory}$).

Table-11.9: Analytical and experimental results

Specimen	$V_{tfp\text{-}end}$ (test) (kN)	V_{pure} (theory) (kN)	$M_{tfp\text{-}end}$ (test) (kNm)	$M_{pure.tfp}$ (theory) (kNm)	$V_{tfp\text{-}end}/V_{pure}$	$M_{tfp\text{-}end}/M_{pure.tfp}$
MB-01	111.6	106.2	22.3	181.8	1.051	0.123
MB-02	113.9	135.0	51.3	233	0.843	0.220
MB-03	126.0	137.7	75.6	233	0.915	0.324
MB-04	132.6	137.7	106.1	233	0.963	0.455

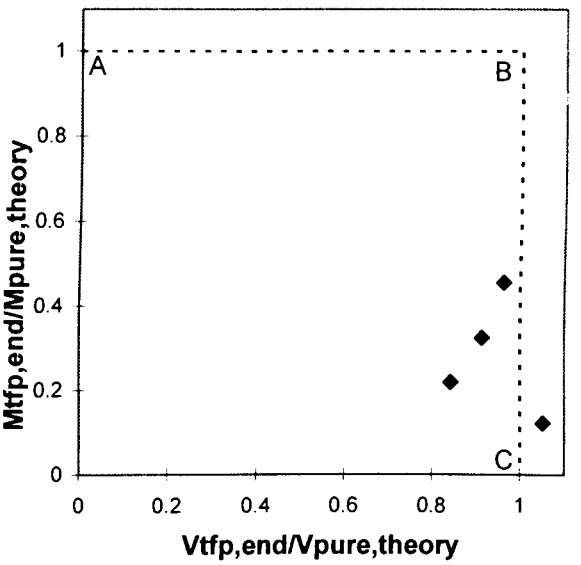

Fig.11.30. Interaction diagram

It can be seen from Fig. 11.30 that there is a negligible interaction between flexure and shear as the parameter $V_{tfp\text{-}end}/V_{pure,theory}$ has a mean value of 0.943 and all the results are centred around the pure shear peeling line BC in Fig.11.30 .

11.10 Shear peeling in beams bonded with FRP plates to the sides- Analysis of test results

11.10.1 Introduction

The tests conducted on the beams bonded with external plates show that the beams bonded with steel plates (test SP-S5 in Section 7.7.2 and test SP-S8 in Section7.7.3) and the carbon FRP plate (test SP-C in Section 7.7.4) failed by shear peeling in a similar manner. The shear loads to cause debonding were substantially lower than the ultimate shear strength of the unplated, reference beam. In the case of the beam bonded with avery flexible FRP plates like the one used in test SP-CG (Section 7.7.5), the shear peeling mechanism was similar to the beams bonded with stiffer plates. However, the shear peeling of the beam SP-CG occurred almost at the same shear strength as that of the unplated beam.

The present study on shear peeling of FRP plated beams is very limited in nature and as we have only one useful FRP plated beam result (test SP-C). The carbon and glass FRP plate used in test SP-CG had a very low elastic modulus and hence cannot be used in practice for strengthening. Further, a generic model on the bond forces sustained by FRP plates is lacking due to the wide range of material properties of FRP plates. A few available models such as Triantafillou's effective strain method (Section 3.5.3.3) and the other methods described in Section 3.5 either involve empirical constants pertaining to a single type of FRP material or the test results used to calibrate the model involved very thin plates and the depth of the plate is equal to the depth of web. Therefore, Eqns.11.9

and 11.13 derived for steel side plated beams will be used for analysing the beam SP-C. It is worth noting that the equation to predict the shear load to shear crack $V_{cr.sp}$ (Eqn.11.9) can be applied to beams bonded with any type of plate. However, Eqn.11.13 for the load to cause shear failure $V_{u.sp}$ in general and the function $f_3(\rho_{sp})$ (Eqn.11.12) in particular were developed specifically for steel plated beams. As a starting point, the quantity $\rho + \rho_{sp}$ in Eqn.11.12 was always set equal to 4.5 while analysing the carbon FRP plated beam.

11.10.12 Analytical results

Figure 11.31 shows the envelopes for the shear cracking load and shear sliding failure load as obtained from the shear cracking model approach for all the beams except beam SP-CG. The strength of the unplated beam without shear stirrup (V_{uc}) is 45 kN as per this model. The shear peeling strength of the plated beams SP-S5, SP-S8 and SP-C are 53 kN, 55 kN and 51 kN respectively. The corresponding experimental shear peeling strength at which the first plate debonded were 62.3, 68.3 and 71.3 kN respectively. The discrepancies in analytical results can be attributed to the fact that the beams used for the present study were cast originally for studying the flexural peeling mechanism in FRP plated beams (Chapter-13). Therefore, they were provided with large amount of internal reinforcement and stirrups to avoid unintended flexural and shear failures. In fact, the longitudinal tension reinforcement ratio in these beams was 4.2%. This lead to a maximum contribution of only 0.3% from the external side plates in computing $f_3(\rho_{sp})$. Therefore, there is only a negligible difference in the shear loads to cause failure by sliding along an existing crack V_u between the plated beams and the unplated beam, as can be seen in Fig.11.31.

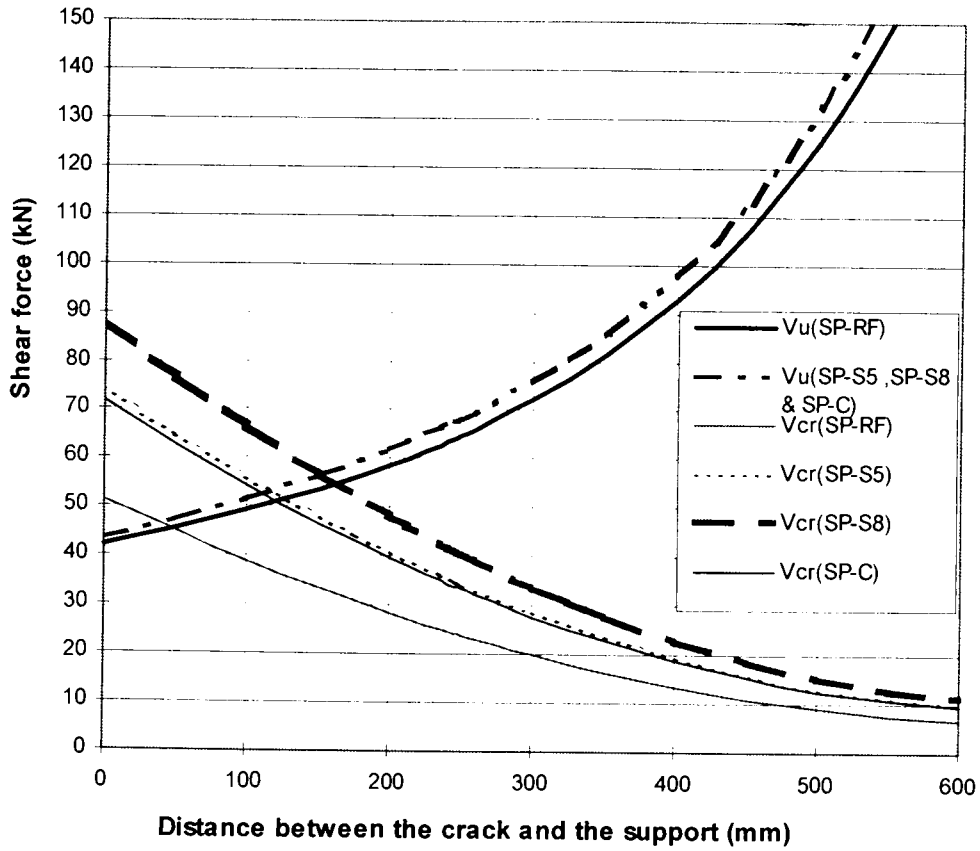

Fig.11.31. Analysis of the beams as per shear cracking model approach

11.11 Modifications suggested for beams subjected to uniformly distributed loads

11.11.1 Beam bonded with side plates

The expression for the ultimate load for side plated beams under a uniformly distributed load ($V_{u.sp.udl}$) can be derived by modifying Eqns.11.13 and 11.14 pertaining to concentrated load cases in accordance with the Eqns.5.36 and 5.38 given in Section 5.4.

$$V_{u,udl} = \frac{1}{2}\gamma_s \gamma_{0,sp,udl} f_c \frac{\left(\sqrt{1+\left(\frac{x}{h}\right)^2} - \frac{x}{h}\right)(L+L_o)bh}{(L-2a_o)} \tag{11.55}$$

where $\gamma_{o,sp,udl} = 1.2.f_1(f_c).f_2(h).f_3(\rho_{sp})$ (11.56)

The equation for the diagonal cracking shear load $(V_{cr.sp.udl})$ is obtained by modifying Eqn.11.9 for $V_{cr.sp}$ and Eqn.5.41 for $V_{cr.udl}$.

$$V_{cr.sp.udl} = \frac{x^2 + h^2}{(a_o + 0.5L_o)\left(1 - \frac{(a_o + 0.5L_o)}{(L + L_o)}\right)}\left(\frac{1}{2} f_{tcf} b + \frac{2mf_{ct} d_{sp} t_{sp} (d_{top} + 0.5d_{sp})}{h^2}\right) \qquad (11.57)$$

As in the previous cases, the envelopes for $V_{cr.sp.udl}$ and $V_{u.sp.udl}$ can be drawn and the point of intersection will give both the shear peeling load and the critical crack location.

11.11.2 Beam bonded with tension face plate

The shear peeling strength of tension face plated beams subjected to uniformly distributed load $(V_{pue.tfp.udl})$ is assumed as 90% of the load needed to form a diagonal crack at the plate end. Therefore, $V_{p.tfp.udl}$ can be derived from Eqn.5.41 by setting $x = (a_o - L_{end})$ where L_{end} is the distance between the centre of the support and the plate end.

$$V_{pure.tfp.udl} = 0.45 f_{tcf} \frac{\left[(a_o - L_{end})^2 + h^2\right] b(L + L_o)}{(L + L_o)\left(a_o + \frac{L_o}{2}\right) - \left(a_o + \frac{L_o}{2}\right)^2}. \qquad (11.58)$$

It may be noted that the above equation is applicable only when the plate ends are placed in a region of high shear force and negligible bending moment.

11.12 Conclusions

1. In this chapter, a series of mathematical models was developed to analyse the shear peeling phenomenon in steel plated beams of any configurations. The procedures were developed for simply supported beams subject to a single concentrated point load and they can easily be extended to apply to uniformly distributed loads and different support conditions. All the models were calibrated using the test results from the present study and the literature.

2. As the shear peeling resistance in plated beams critically depends on the bond strength of the plates, a procedure was developed to quantify the same. This was achieved by calibrating Oehlers and Moran's model for stress distributions in concrete-plate interfaces against the available test results. This procedure in conjunction with the crack sliding model for the shear strength of non-shear reinforced concrete beams were used to develop a series of mathematical models for a variety of steel plated beams. This hybrid procedure recognizes the significance of the formation of a critical diagonal shear crack that can occur anywhere in the beam and the subsequent failure by sliding along the plane of the critical crack. It also incorporates the resistance provided by the external plates both to the crack formation and to the failure and the resulting debonding along the crack plane.
3. The shear peeling model for side plated beams are capable of accurate predictions of the shear peeling strength irrespective of the location of the plate along the depth of the beam. The only restriction placed is that the plate should be either under predominantly tensile region or else a nominal amount of internal shear stirrups should be present which is the normal case.
4. Two procedures were developed to quantify the shear peeling strength of the tension face plated beams. The first one is a normal procedure similar to the one developed for side plated beams and it can be used for any location of the plate end. The other one is a simple procedure which recognizes the fact that when the tension face plate ends are terminated very close to the support, the shear load to cause peeling is nothing but the shear load to cause a diagonal crack at the plate end. The constraints in the test data used for calibrating the second procedure were also stated.

5. The procedure for angle plated beams considers an angle to consist of a side plate and a soffit plate. Therefore, the equations developed for side and tension face plated beams were used to develop final equations. The method shows a good correlation with the test results.
6. As shear peeling of compression face plated beams involves three stages, a procedure was developed to predict the shear load to cause these three milestones. Firstly, the shear load to cause the formation of a main diagonal crack away from the support was modelled as the shear strength of the unplated beam. Secondly, the shear load at the propagation of the main diagonal crack along the bottom edge of the plate to the load point can be obtained by adopting a similar procedure developed for tension face plated beams. Finally, the shear load at the completion of debonding was found to be the shear load to cause a diagonal crack from support to the load point.
7. The improvement in the shear peeling strength of tension face plated beams due to bonding additional side plates were quantified by two empirical procedures, namely, the element strength approach and the shear strength approach. Based on a comprehensive test data, the improvement in the shear peeling strength was found to lie between 6% of the bond strength and 15% of the axial strength of the two side plates, when the minimum bond length lies within 80-200% of the depth of the side plates. However, the shear strength approach that tries to modify the equation for V_{uc} in most codes of practice was found to be unsuitable. To overcome the limits of the empirical methods, the sliding crack model approach was used to develop a general analytical procedure. In this method, the improvement in the shear peeling strength due to side plates was quantified as the resistance by the side plates to the propagation

of a diagonal crack that originates at the tension face plate end that is predominantly under shear. The theoretical formulation was found to have excellent correlation with test results.

8. The effect of additional side plates on the peeling strength when the tension face plates are terminated in shear/flexure region was studied by computing both the pure flexural peeling capacity and the pure shear peeling resistance. An interaction diagram was drawn and the interaction between shear and flexure was found to be negligible.
9. The validity of the models developed in this chapter for steel side plated beams and the other procedures in the literature were checked for the very limited test data on the FRP side plated beams. It was found that there is no generic model to compute the bond strength of FRP plates and this is an impediment in extending the existing models. The methods in the literature on FRP plated beams were calibrated with test data on thinner plates and in which the depth of the plate and the depth of the web are equal. Furthermore, some methods involve empirical constants restricting their application.
10. Finally, it was shown that the procedures developed for beams under concentrated loads can be modified for beams subject to uniformly distributed loads. This was demonstrated for side plated beams as well as tension face plated beams.

References

AS3600 (1994). Australian Standard- Concrete Structures, Standards Australia, 1994.
Mattock,A.H. and Hawkins, N.M.(1972). Shear transfer in reinforced concrete-research. Precast Concrete Institute Journal, March-April 1975, pp.55-75.
Oehlers, D.J. and Bradford,M.A. (1995). Composite steel and concrete structural members-Fundamental behaviour. Pergamon,Oxford(U.K.).p.549.

Oehlers,D.J.(1992). Reinforced concrete beams with plates glued to their soffits. Journal of Structural Engineering (ASCE), 1992, Vol.118, No. 8, Aug.: 2023-2039.

Oehlers, D.J., Mohamed Ali,M.S., and Wemin-Lou. (1998). Upgrading continuous reinforced concrete beams by gluing steel plates to their tension faces. Journal of Structural Engineering (ASCE), V0l.24, No.3, March 1998. Pp.224-232.

Oehlers,D.J.and Moran,J.P.(1990). Premature failure of externally plated reinforced concrete beams. Journal of Structural Engineering (ASCE), 1990, Vol.116, No. 4, April: 978-995

Wemin-Lou. (1993). "Strengthening of post-tensioned and reinforced concrete beams strengthened by steel plates." Thesis Submitted to the University of Adelaide, Jan.1993.

Zsutty,T.C. (1968). " Beam shear strength prediction by analysis of existing data."Journal ACI, Vol.65, Novomber,1968. pp 943-951.

PART-IV: FLEXURAL PEELING

CHAPTER-12: FLEXURAL PEELING OF STEEL PLATES BONDED TO THE COMPRESSION FACE OF REINFORCED CONCRETE BEAMS

CONTENTS

12.1 Introduction

One of the major areas of thrust of the present research project is to understand the debonding behaviour of compression face plated beams and to model the peeling mechanism mathematically. Keeping this in mind, a series of tests was performed on the pure shear peeling, the pure flexural peeling and the interaction between flexure and shear peeling of compression face plated beams. This chapter deals with the pure flexural peeling aspect. The tests that were conducted on large beams to compare the flexural peeling behaviour of compression face plated beams with that of the tension face plated beams is first discussed. Then, the tests conducted at the University of Adelaide on microbeams, as a pilot study before undertaking the large beam tests, are then presented. Finally, the test results are used to develop a procedure to quantify the flexural peeling strength of compression face plated beams on the same line with that developed by Oehlers and Moran for tension face plated beams (Refer Section 2.7.3.1).

12.2 Large Beams (FP series)

12.2.1 Test specimens

In this study, a series of simply supported reinforced concrete beams with plates bonded to their compression faces were subjected to debonding under pure flexural peeling. Beams with tension face plates of the same thickness were tested as control specimens so as to calibrate the Oehlers-Moran model for pure flexural peeling for compression face plated beams.

The specimens used for studying flexural peeling of compression face plated beams are shown in Figs.12.1a-e. They consisted of four reinforced concrete beams with steel plates 920 mm long that were glued either to the tension face or

compression face of the beams. This arrangement was used to compare directly the performance of the compression face plated beams with those of the tension face plated beams for which the analytical procedure is well documented and hence, reduce the scatter of the results. The only parameter varied for this study was the thickness of the plates. A total of four tests were performed and these tests are denoted as FP-T20, FP-C20, FP-T25 and FP-C25; as an example of the notations used, FP-T20 denotes that the beam was bonded with a plate of 20 mm on the tension face and FP-C25 stands for the beam with a 25 mm plate on its compression face. Details of various beams tested are shown in Figures 12.1a to 12.1e and these four beams are identified as the FP series.

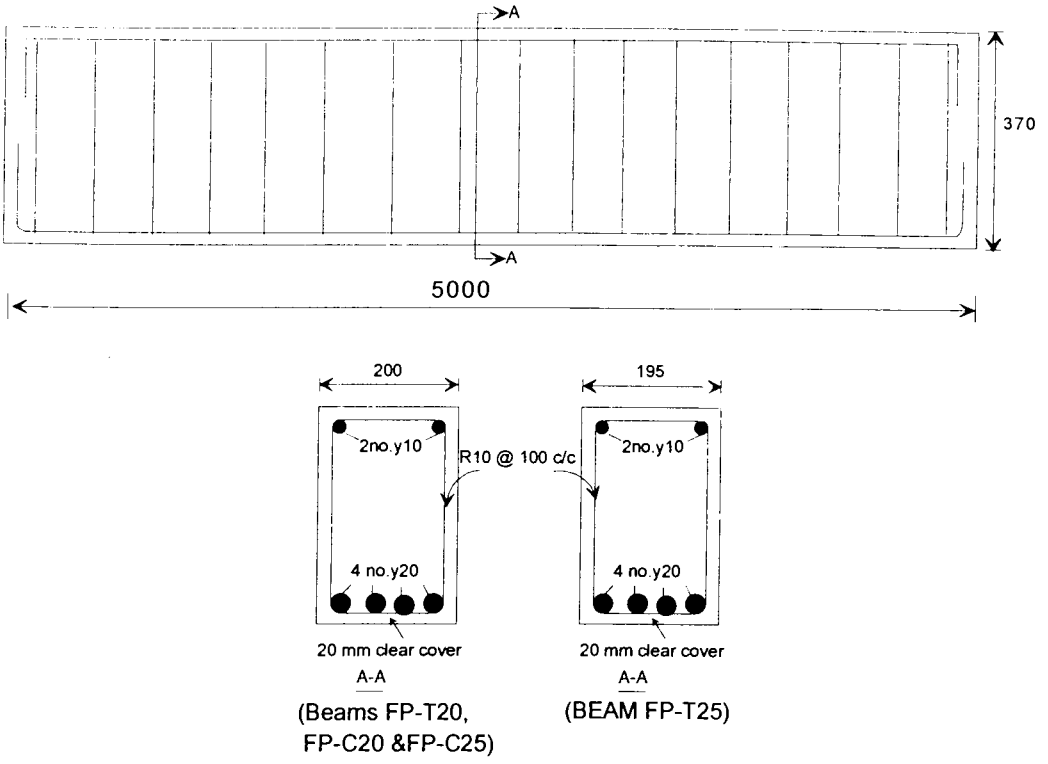

Fig.12.1(a). Reinforcement details

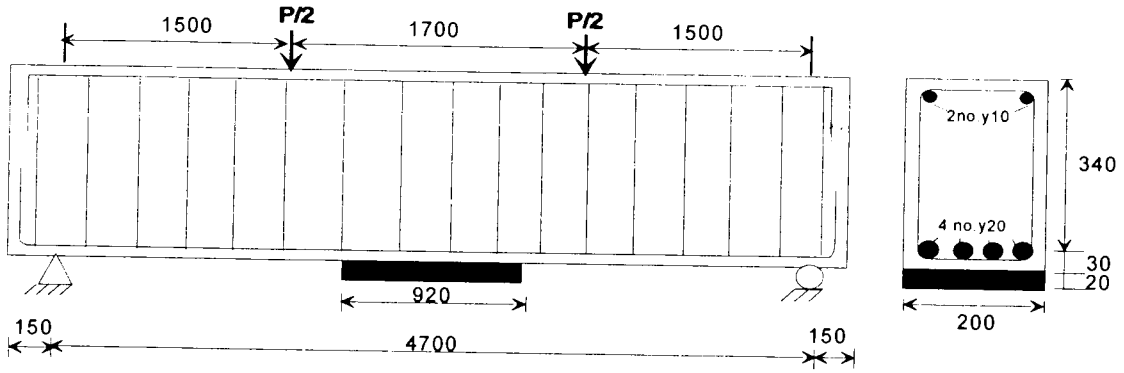

Fig.12.1(b).Beam FP-T20

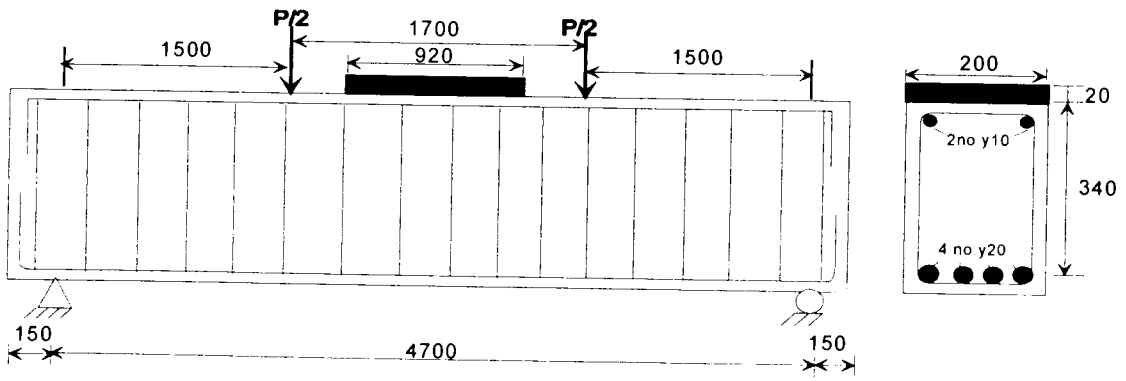

Fig.12.1(c). Beam FP-C20

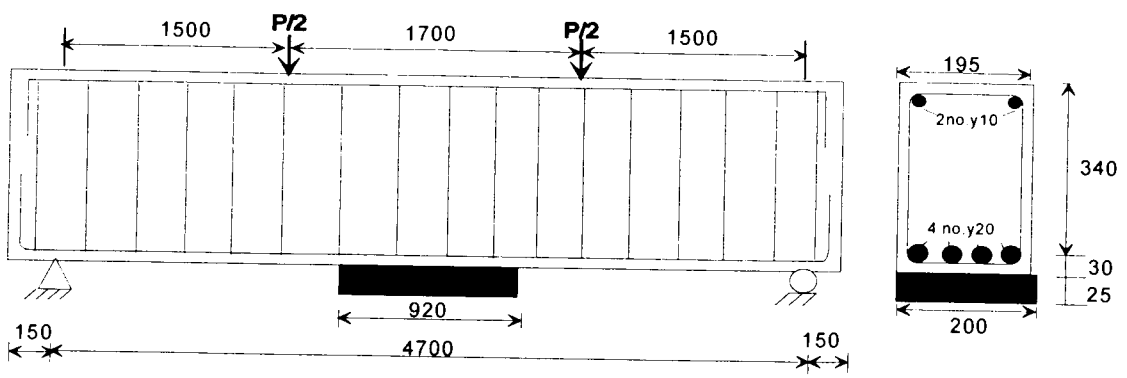

Fig.12.1(d). Beam FP-T25

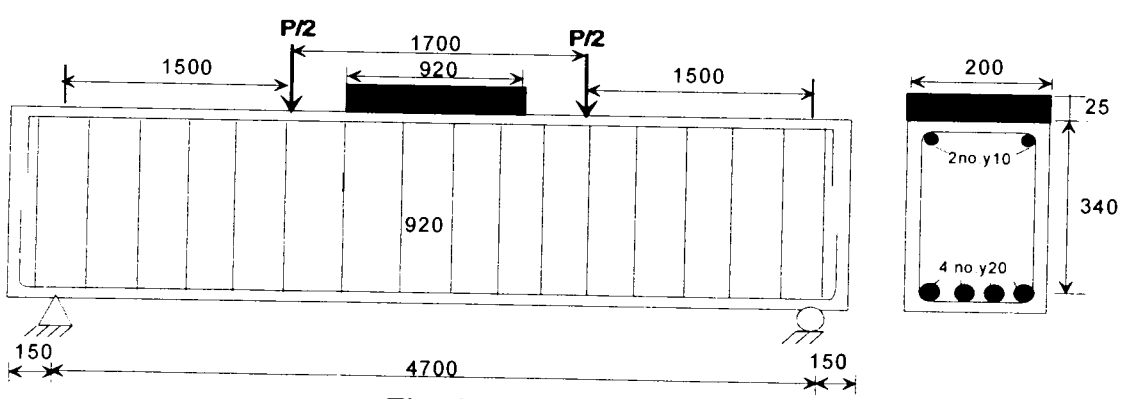

Fig.12.1(e). Beam FP-C25

Fig.12.1. General details of beams -FP series

12.2.2 Test rig

The beams were simply supported over an effective span of 4700 mm as shown in Fig.12.1(b) and the load was applied on the top of the beam by a hand operated hydraulic jack through a load cell, spreader joist and a pair of knife edge bearings. The geometry of the loading arrangement for all the beams in Fig.12.2 was such that the ends of the plates were in a constant bending moment and hence, zero vertical shear region.

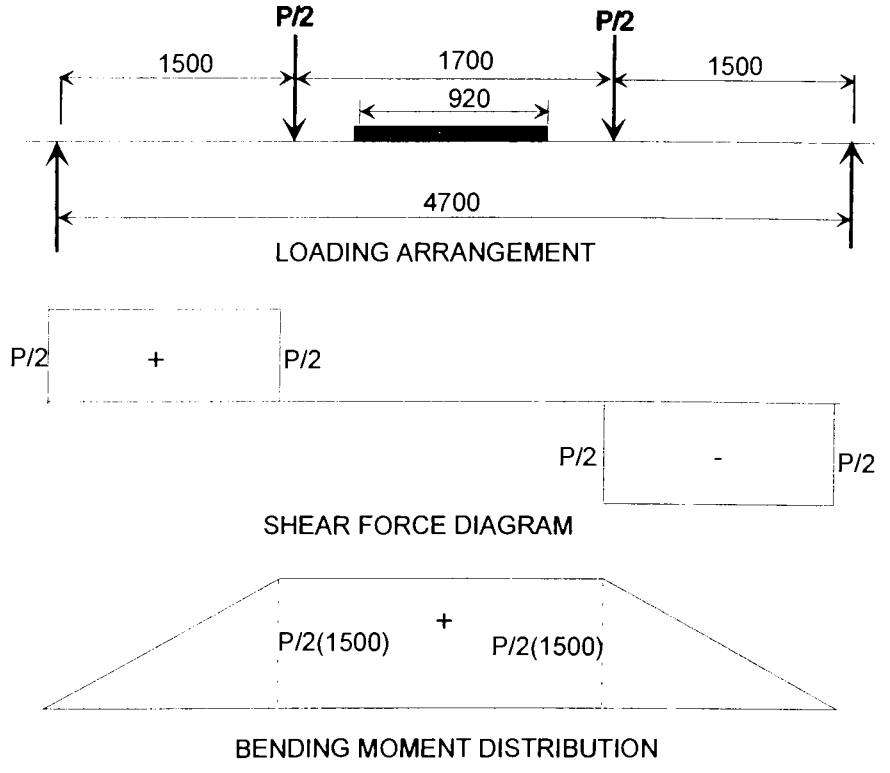

Fig.12.2. Loading arrangement for the beams tested (FP series)

12.2.3 Instrumentation (FP series)

Strain gauges were bonded to the external plates in order to detect the debonding at various sites of the plates. The arrangements of the strain gauges and their numbering are shown in Fig.12.3. The beam deflection at mid-span was monitored by both a dial gauge and a transducer.

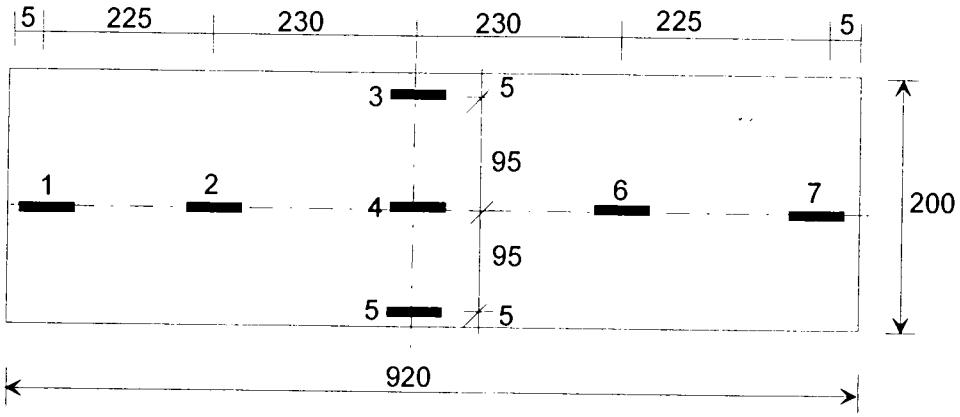

Fig.12.3. Strain gauges arrangement (FP-series)

12.2.4 Test procedure (FP series)

For each test, the beam was first loaded in steps of 5 kN and the cracks were marked and photographically recorded. The corresponding micro-strains at the various sites of the external plate were measured by strain gauges and were recorded at every load step though a data-logging system. The load step was reduced to 3 kN when there was a fall in strain at any site of the plate. The test was terminated when the plate peeling was total, ie when all of the strain gauges recorded reducing magnitudes of strains; the pure flexural peeling moment of the plated beam corresponds to the bending moment at this stage.

12.2.5 Material Properties (FP series)

All the beams were cast in a single pour using ready mixed concrete supplied by a local manufacturer. Material properties of the reinforcing bars and shear stirrups are shown in Table-12.1. The manufacturer's specifications of the material properties of the epoxy glue used for bonding the steel plates are indicated in Table-12.2.

Table-12.1. Material properties of the steel

Item	f_y (MPa)			f_u (MPa)		
Sample No.	1	2	Mean	1	2	Mean
Rebar Y20	436.1	429.7	432.9	530.0	522.0	526.0
Stirrup W10	-	-	-	560.2	572.9	566.6

where f_y = Yield strength of the steel and f_u = Ultimate strength of the steel.

Table-12.2. Material properties of the glue Hilti CA 273 after 2 days (as tested by the manufacturer)

Compressive strength (ISO 604)	Tensile strength (ISO 527)	Flexural strength (ISO 178)	Elastic modulus in compression (ASTM D 695)	Tensile bond strength (ISO 527)	Maximum operating temperature
110-120 MPa	30-40 MPa	20-30 MPa	5000-6000 MPa	10-15 MPa	80° C

Material properties of the concrete are shown in Table-12.3. In this table, the individual values of each test are given under the "i" column and their mean value under "m" column.

Table-12.3. Material properties of the concrete

Age	E_c (MPa)		f_b (MPa)		f_c (MPa)		f_{cu} (MPa)	
(days)	i	m	i	m	i	m	i	m
248	34425	34282	3.83	3.60	32.66	35.26	35.37	36.47
	34023		3.61		36.90		36.81	
	34203		3.35		36.43		37.24	
	34499				35.07			

where E_c is the elastic modulus, f_c is the cylinder compressive strength, f_{cu} *is* cube compressive strength and f_b is the Brazilian tensile strength of the concrete.

12.3 Test results (FP series)

12.3.1 Beam FP-T20

This beam was provided with a 20 mm thick steel plate at its tension face. The initial crack formation for this beam is shown in Fig.12.4. It can be seen that a flexural crack first occurred in the unplated region at an applied moment of 22.5 kNm (that is an applied load P=30 kN) and a small crack also appeared adjacent to the north-west and south west plate ends simultaneously. The minor plate end cracks were transformed into fully fledged debonding cracks at both plate ends as the moment was increased from 30 kNm to 49.5 kNm (P= 40 kN to 66 kN). The complete flexural peeling of the plate is considered to have occurred at 46.4 kNm (P = 61.9 kN) when all the strain readings showed a falling trend. The test was terminated at 51.1 kNm (P = 68.1 kN). Figure 12.5 shows the final crack pattern of this beam.

Fig.12.4. FP-T20: Initial flexural crack pattern

Fig.12.5. FP-T20: Crack pattern near plate ends at debonding

The results from beam FP-T20 are given in Table-12.4. The strain gauges in Fig.12.3 are listed in column 1 in Table-12.4, and they have been grouped in column 2 according to their longitudinal position. The loads in column 3 are the applied loads at which the strains in the corresponding gauges reduced having reached their maximum values which are listed in column 4; this was interpreted as the load at which debonding occurred in the region adjacent to the strain gauge. The corresponding debonding moments are given in column (5). The variation of longitudinal strains with applied moment is illustrated in Fig.12.6.

TABLE-12.4: Test results of Beam FP-T20

Strain-gauge Level & No. (1)	Strain-gauge Position group (2)	Total Applied Load P(kN) (3)	Maximum Strain (micro-strain) (4)	Moment (kNm) (5)
Middle (No.1)	Plate end	55.0	-15	41.3
Middle(No.7)		59.7	-13	44.8
Middle (No.2)	Intermediate	34.9	43	26.2
Middle (No.6)		47.1	60	35.3
Edge(No.3)		59.2	108	44.4
Middle (No.4)	Centre	61.9	114	46.4
Edge(No.5)		61.9	109	46.4

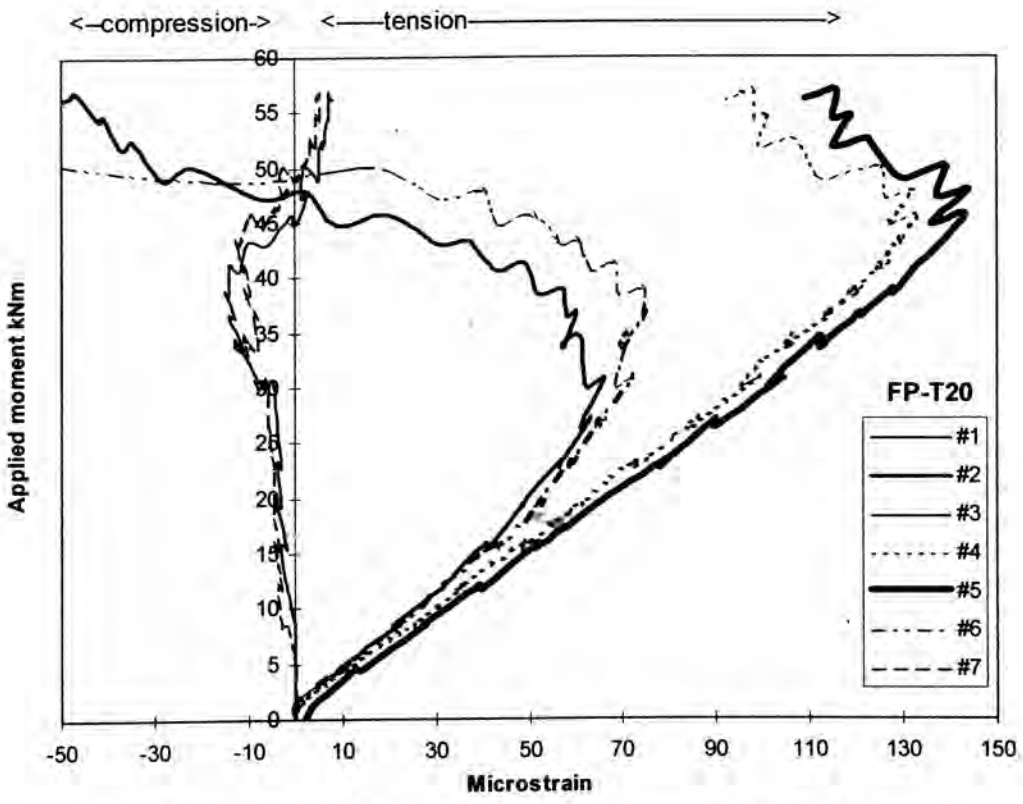

Fig.12.6. FP-T20: Longitudinal strain variation in plate

On loading, the strains shown in Fig.12.6 at the plate ends become compressive; this indicates some form of stress concentration was present. The rate at which debonding occurred along the plate length can be visualised by comparing the strains at debonding in Table-12.4. Gauge No.2 indicated that debonding occurred at that site at 26.2 kNm. The next gauge to indicate debonding was No.6 at 35.3 kNm which was followed by No.1 at 41.3 kNm. Finally, the central part of the plate debonded at 46.4 kNm. Therefore, it can be inferred that even though the debonding process commenced at a lower moment, it stabilised until there was very rapid crack propagation at the maximum peeling moment. The relationship between the deflection at mid-span and the applied moment is shown in Fig.12.7. It can be seen that the beam is still elastic at the instance of maximum peeling moment, as the relationship is still linear.

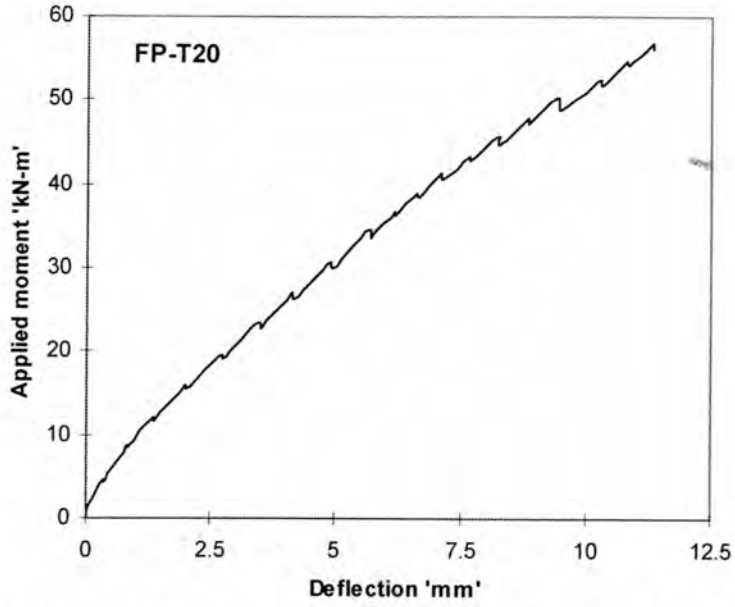

Fig.12.7. FP-T20: Mid-span deflection Vs Applied moment

12.3.2 Beam FP-T25

Beam FP-T25 was bonded with a 25 mm thick plate to the tension face; the width of this beam happened to be only 195 mm as against 200 mm for other beams due to a minor construction error. The initial flexural crack occurred at a distance 300 mm from the plate end and also a debonding crack occurred adjacent to the eastern end of the plate at an applied moment of 27.3 kNm (P=36.3 kN) as shown in Fig.12.8. The debonding cracks propagated in an inclined fashion until 38.5 kNm (P=51.3 kN); thereafter they turned horizontally along the concrete cover until the moment was 47.4 kNm (P=63.2 kN) by which time the debonding process was complete as shown in Fig.12.9. The load test was terminated at 57.2 kNm (P=76.2kN).

Fig.12.8. FP-T25: Initial flexural crack near plate ends

Fig.12.9. FP-T25: Crack pattern near plate ends at debonding

The results from this test are given in Table-12.5. From Table-12.5 and from Fig.12.10, which depicts the strain distribution along the plate with the applied moment, it can be seen that residual compressive stresses were present in the plate at plate ends and also under intermediate strain gauges. The debonding process was smooth, as the moments corresponding to peak strains recorded for each level of strain gauges were different. The debonding first occurred at the plate ends, then under gauges No.2 and No.6 and then the central region of the plate debonded. Figure 12.11 shows the variation of deflection at mid-span with applied moment.

TABLE -12.5: Test results of Beam FP-T25

Strain-gauge Level & No. (1)	Strain-gauge Position group (2)	Total Applied Load P(kN) (3)	Maximum Strain (micro-strain) (4)	Moment (kNm) (5)
Middle (No.1)	Plate end	33.4	-8	25.1
Middle(No.7)		42.3	-12	31.7
Middle (No.2)	Intermediate	42.3	40	31.7
Middle (No.6)		48.4	60	36.3
Edge(No.3)	Centre	63.2	108	47.4
Middle (No.4)		63.2	114	47.4
Edge(No.5)		63.2	109	47.4

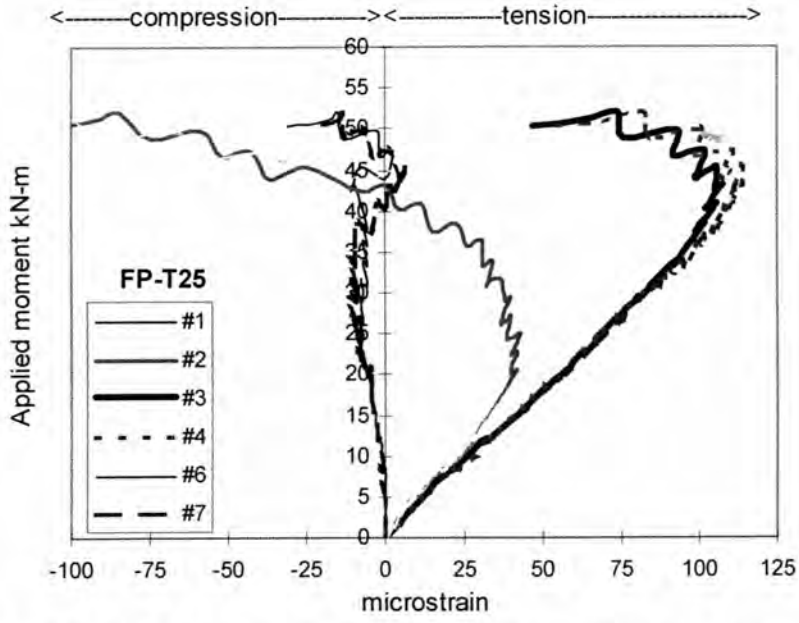

Fig.12.10. FP-T25: Longitudinal strain variation in plate

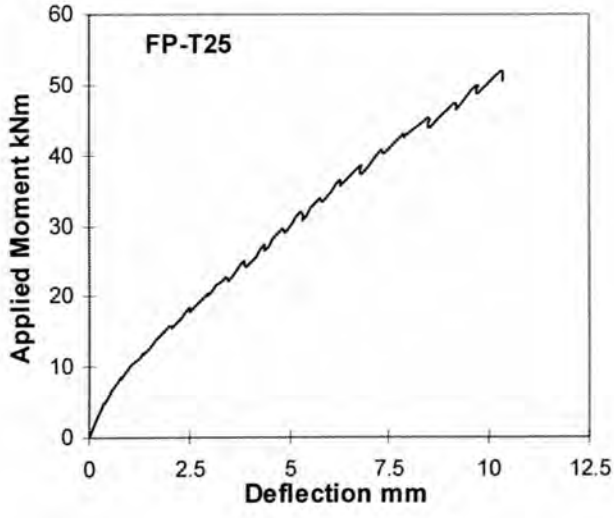

Fig.12.11. FP-T25: Midspan deflection Vs Applied moment

12.3.3 Beam FP-C20

This beam was bonded with a 20 mm thick plate to its compression face. The first flexural cracks occurred in the constant bending moment region at a moment of 22.5 kNm (P=30 kN) and they stabilised at 41.3 kNm (P=55 kN) as can be seen in Fig.12.12. At 45.1 kNm (P=60 kN), a long debonding crack occurred below the centre point of the plate extending towards one end of the plate as shown in Fig.12.12;

a small increase in applied load corresponding to 47.3 kNm (P=63.1 kN).caused the plate to debond completely as the debonding crack propagated all around the bottom edge of the compression face plate as shown in Fig.12.13. Table-12.6 gives the results obtained from this test.

Fig.12.12. Long debonding crack in FP-C20

Fig.12.13. View after removing plate from concrete-FP-C20

TABLE-12.6: Test results of Beam FP-C20

Strain-gauge Level & No. (1)	Strain-gauge Position group (2)	Total Applied Load P(kN) (3)	Maximum Strain (micro-strain) (4)	Moment (kNm) (5)
Middle (No.1)	Plate end	61.2	22	45.9
Middle(No.7)		61.2	29	45.9
Middle (No.2)	Intermediate	62.0	-158	46.5
Middle (No.6)		63.1	-168	47.3
Edge(No.3)	Centre	61.2	-155	45.9
Middle (No.4)		61.2	-145	45.9
Edge(No.5)		61.2	-140	45.9

Figure 12.14 shows the variations of longitudinal strains and the applied moments. It can be seen from Fig.12.14 and Table-12.6 that the debonding of the

compression face plate initiated from the middle region then propagated towards the end of the plate and it occurred in a narrow range of load, i.e. from 61.2 to 63.2 kN. This is in contrast with the corresponding beam with the tension face plate (FP-T20) where the debonding crack initiated from the plate ends and progressed at a steady rate towards the centre of the plate. Another feature is that the small magnitudes of strains recorded near the plate ends by gauges No. 1 and 7 are tensile in nature unlike the other sites in the plate where the strains are compressive. The strain distribution in Fig.12.14 as compared to that in Fig.12.6 corresponds to a reversal of the stress distribution in Fig.2.18, ie the tensile stress now occurs away from the plate end. Figure 12.15 illustrates the relationship between the deflection recorded at the mid-span with the applied moment.

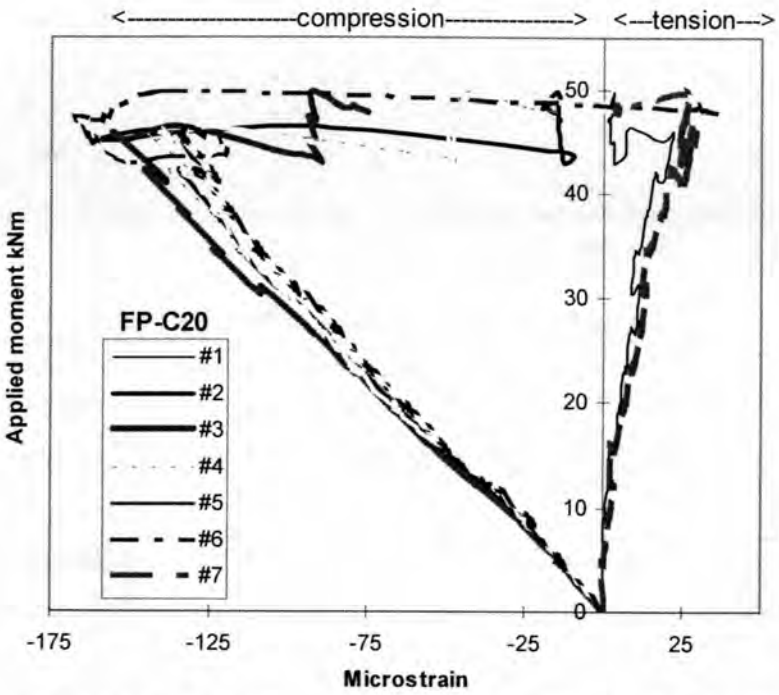

Fig.12.14. FP-C20: Longitudinal strain variation in plate

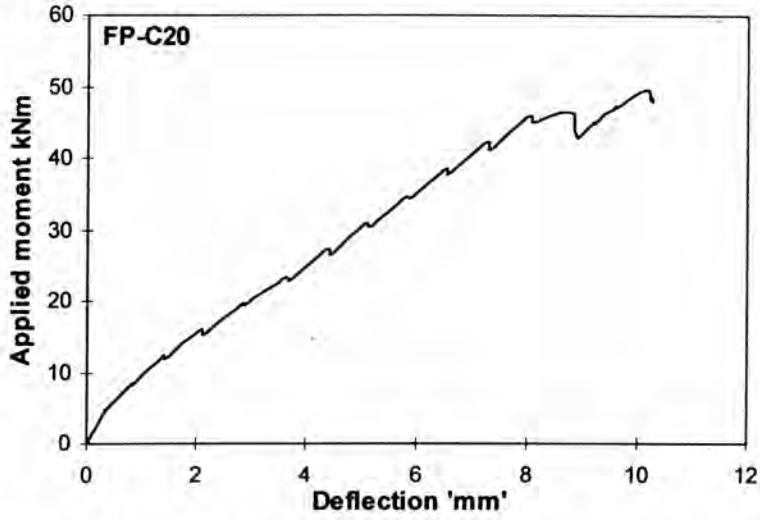

Fig.12.15. FP-C20: Mid-span deflection Vs Applied moment

12.3.4 Beam FP-C25

This beam was bonded with a 25 mm thick steel plate to its compression face. A number of flexural cracks appeared and propagated within the constant bending moment region between 22.5 kNm and 56 kNm (P =30 to 75 kN). At 56.8 kNm (P=75.7 kN), a debonding crack extended from the plate end to the centre as shown in Fig.12.16 and the load dropped to 73 kN. Upon further application of the original moment of 56.8 kNm (P=75.7 kN), the debonding crack propagated to the other plate end and thus complete debonding of the plate occurred as shown in Fig.12.16. Figure 12.17 depicts the scene after the plate was removed from the concrete and it shows that the failure did not occur along the adhesive layer.

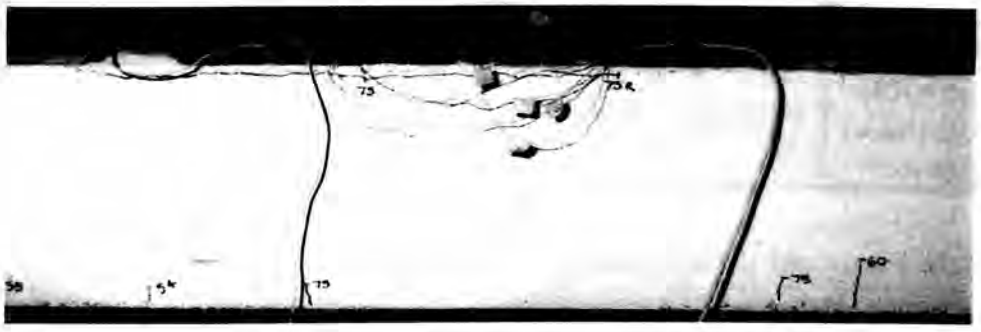

Fig.12.16. Long debonding crack in FP-C25

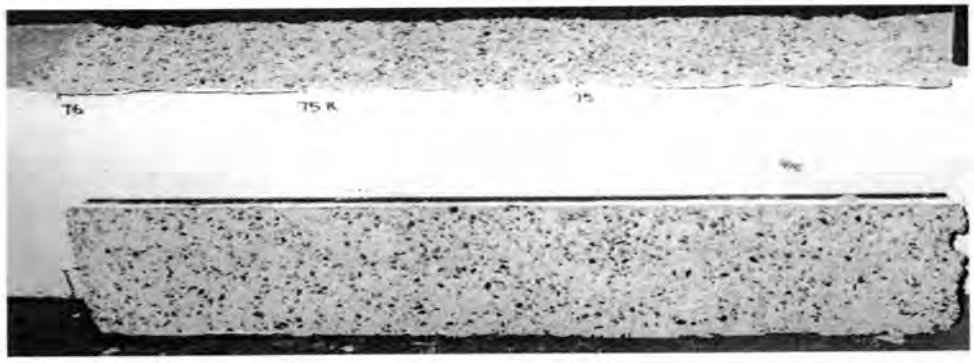

Fig.12.17. View after removing plate from concrete in FP-C25

Table-12.7 summarises the results obtained for this beam. Figure 12.18 illustrates the variation of longitudinal strains along the plate length with applied moment. It can be seen from Table-12.7 and Fig.12.18 that debonding of the compression face plate occurred simultaneously at 56.8 kNm (P=75.7 kN), which is unlike the corresponding beam bonded with the tension face plate of the same thickness (FP-T25) where debonding occurred at different regions and at different loads. Furthermore, the strains recorded near the plate ends were tensile unlike the other sites where the recorded strains were compressive. Figure 12.19 shows the variation of deflection recorded at mid-span with applied moment.

TABLE –12.7: Test results of Beam FP-T25

Strain-gauge Level & No. (1)	Strain-gauge Position group (2)	Total Applied Load P(kN) (3)	Maximum Strain (micro-strain) (4)	Moment (kNm) (5)
Middle (No.1)	Plate end	75.7	27	56.8
Middle(No.7)		75.7	26	56.8
Middle (No.2)	Intermediate	75.7	-175	56.8
Middle (No.6)		75.7	-182	56.8
Edge(No.3)	Centre	75.7	-191	56.8
Middle (No.4)		75.7	-181	56.8
Edge(No.5)		75.7	-201	56.8

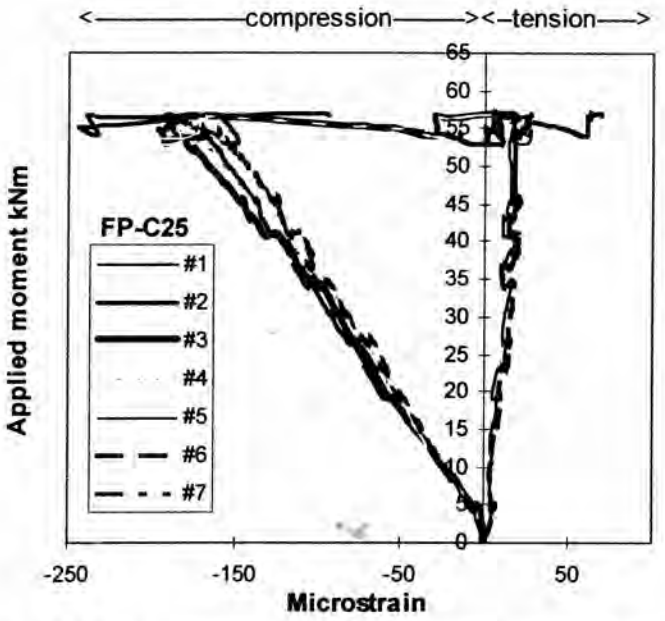

Fig.12.18. Longitudinal strain variation in plate

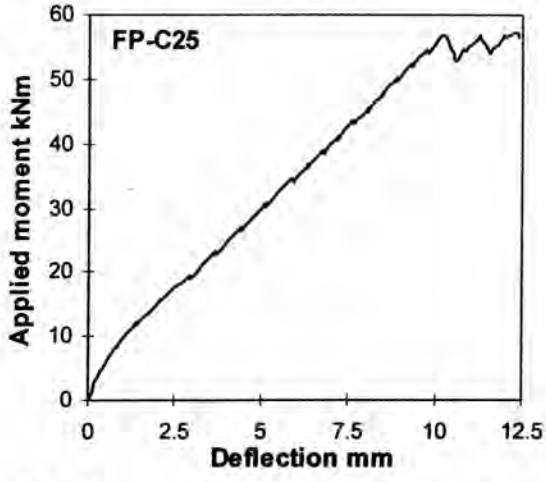

Fig.12.19 Midspan deflection Vs Applied moment

12.4 Tests on microbeams (Microseries)

12.4.1. Test program

Tests were also conducted at the University of Adelaide on small sized reinforced concrete beams by Malla, Song, and Yong (1997) as a precursor to the study on large scale beams and they referred to these tests as the Microseries. The details of the basic, unplated RC beam are shown in Fig. 12.20 and that of the four plated beams are shown in Fig.12.21-12.24. The beams were simply supported over a span of 1350 mm; they were 100 mm in width and 125 mm in depth and reinforced with 2-Y16

tensile bars and 2-R6 compressive bars. All the beams were bonded with a 10 mm thick mild steel plate and their designations are as follows: MICRO 1: 250 mm long plate on tension face, MICRO 2: 250 mm long plate on compression face, MICRO 3: 450 mm long plate on tension face andMICRO 4: 450 mm long plate on compression face. For details regarding instrumentation, loading and material properties pertaining to the Microseries, the report by Malla, Song and Yong (1997) can be referred to.

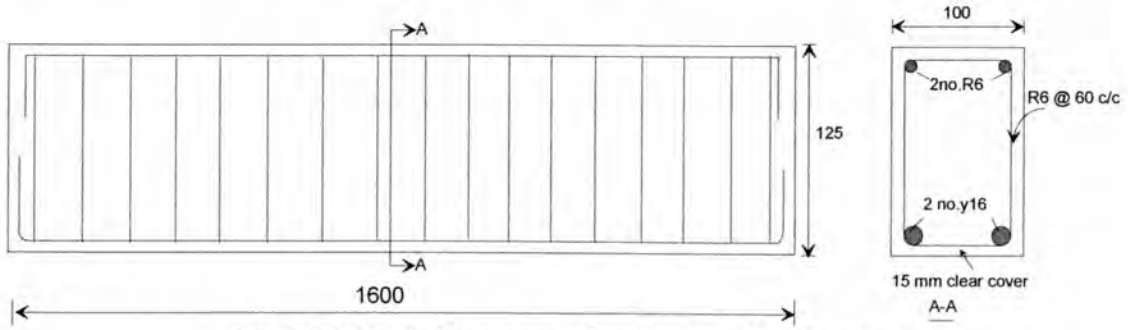

Fig.12.20 Reinforcement details for microbeams

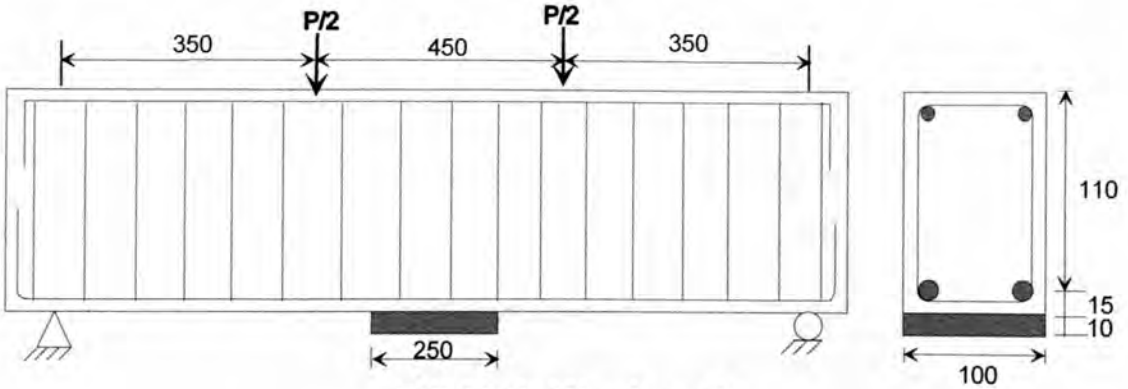

FIG.12.21. Microbeam 1

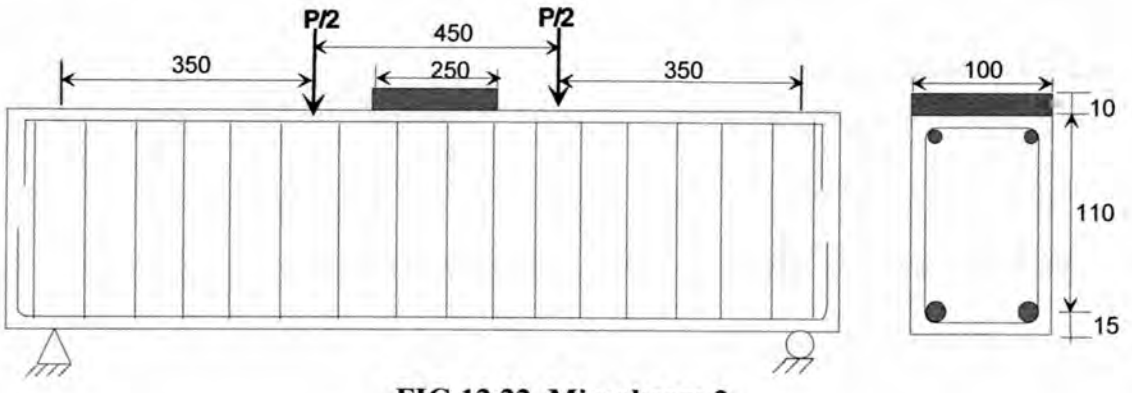

FIG.12.22. Microbeam 2

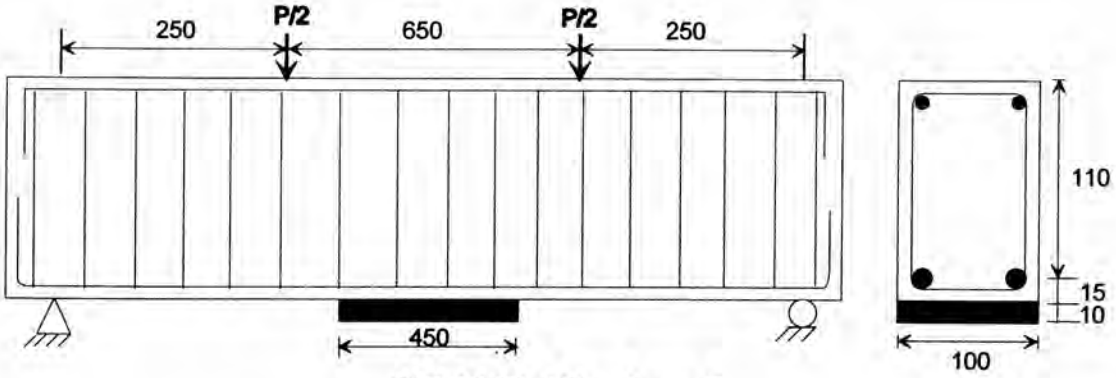

FIG.12.23. Microbeam 3

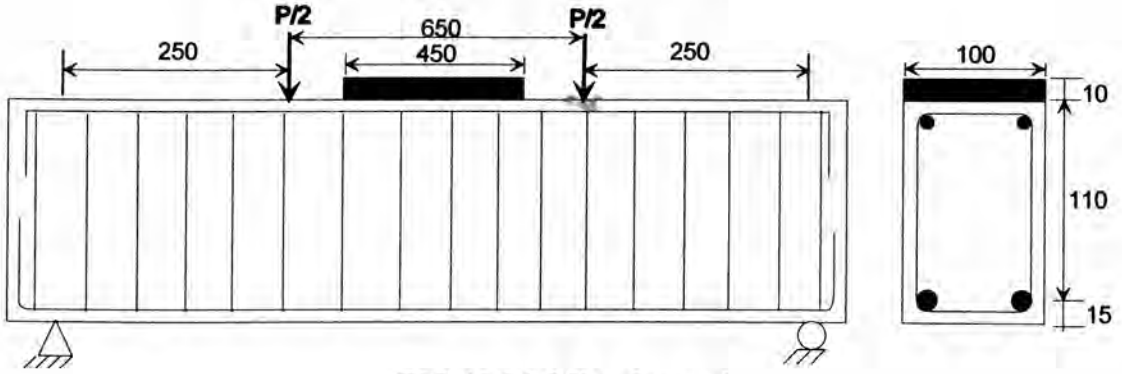

FIG.12.24. Microbeam 4

12.4.2 Test results from Microseries

The flexural peeling patterns in the microbeams were similar to the corresponding full-scale beams in the FP series. The flexural peeling in the tension face plated beams was initiated by the formation of flexural cracks in the vicinity of plate ends and progressed towards the middle of the plate. In the case of the compression face plated beams, the flexural peeling was accompanied by long debonding cracks that encompassed the plates. Table-12.8 summarises the results obtained for the tests on the microbeams.

TABLE-12.8: Test results of Microbeams

Micro-Beam no	Plate dimensions length x thick (mm x mm)	f_b (MPa)	Maximum strain at peeling (με)	Peeling moment (kNm)
1	250 x 10 (tfp)	3.00	98	3.94
2	250 x 10 (cfp)	3.03	326	6.24
3	600 x 10 (tfp)	3.34	225	4.95
4	600 x 10 (cfp)	3.34	471	6.95

12.5 Development of analytical procedure

12.5.1 Proposed model

In this section, the model prescribed for flexural peeling in tension face plated beams by Oehlers and Moran (1990) and described in section 2.7.3.2 will be modified for compression face plated beams. It may be recalled that the stress distribution as shown in Fig.2.18 used for developing the procedure by Oehlers and Moran (1990) is applicable to any plate configuration as it is generic in nature. Hence, it can be used for plates placed in the compression face also. The following equation (Vide Eqn.2.5) was suggested for computing the pure flexural peeling capacity of the tension face plated beams

$$M_{pure,tfp} = \frac{(EI)_{cp} f_b}{k_{tfp} E_p t_{tfp}} \qquad (12.1).$$

Here, k_{tfp} stands for the empirical constant relevant to the tension face plated beams and by putting k_{tfp}=0.474, we get the mean $M_{pure,tfp}$ value and for k_{tfp}=0.901 we get the 5% characteristic design value. It is worth remembering that these constants were obtained from the calibration of a large pool of test data catering for a wide range of variables generated by Oehlers and Moran (1990). Therefore, it is appropriate for our case of compression face plates to adopt the above model but to derive the empirical constant k_{cfp} as discussed below. Equation 12.1 can be modified for beams bonded with compression face plates as follows:

$$M_{pure,cfp} = \frac{(EI)_{cp} f_b}{k_{cfp} E_s t_{cfp}} \qquad (12.2)$$

12.5.2 Analysis of test results and calibration of the model

Equations 12.1 and 12.2 were used to analyse the results obtained from the tests; as M_{pure} is known experimentally, the magnitudes of k_{cfp} and k_{tfp} can be calculated. The results obtained from the analysis are shown in Table 12-9. Figure 12.25 shows the

relationship between the thickness of plate and the ratio k_{tfp}/k_{cfp}. It can be seen that the test results represent a wide range of parameters such as thickness of plate varying from 10 mm to 25 mm and moment of inertia of cracked plated section ranging between 2.2 x 10^7 mm^4 and 159 x 10^7 mm^4. The mean value of k_{tfp}/k_{cfp} is 2.295 with a corresponding standard deviation value of 0.22. This implies that the mean flexural peeling value of compression face plated beam will be about 2.295 times that of the beam bonded with a tension face plate of same thickness and elastic modulus. As Oehlers and Moran (1990) suggested a mean value of k_{tfp} to be 0.474, the mean value of k_{cfp} will be 0.474/2.295=0.206 and characteristic value of k_{cfp} will be 0.901/2.295=0.393. Substituting in Eqn.12.2, we get

$$M_{pure,cfp}(mean) = \frac{(EI)_{cp} f_b}{0.206 E_s t_{cfp}} \tag{12.3}$$

and

$$characteristic\ M_{pure,cfp} = \frac{(EI)_{cp} f_b}{0.393 E_s t_{cfp}} \tag{12.4}$$

TABLE-12.9: Analytical Results

Specimen	t_p (mm)	M_{pure} (kN-m)	$I_{cp}/10^7$ (mm^4)	E_c (MPa)	f_b (MPa)	k_{tfp}	k_{cfp}	k_{tfp}/k_{cfp}
Results from FP-series								
FP-T20	20	46.4	144.0549	34282.5	3.6	0.9579	-	2.05
FP-C20	20	47.3	70.4907	34282.5	3.6	-	0.4674	
FP-T25	25	47.4	159.1274	34282.5	3.6	0.8304	-	2.58
FP-C25	25	56.8	74.0489	34282.5	3.6	-	0.3218	
Results from Microbeams								
MICRO 1	10	3.94	3.77	27100	3	0.388		2.33
MICRO 2	10	6.24	2.49	27571	3.03		0.166	
MICRO 3	10	4.95	3.55	30797	3.34	0.369		2.22
MICRO 4	10	6.95	2.24	30797	3.34		0.166	

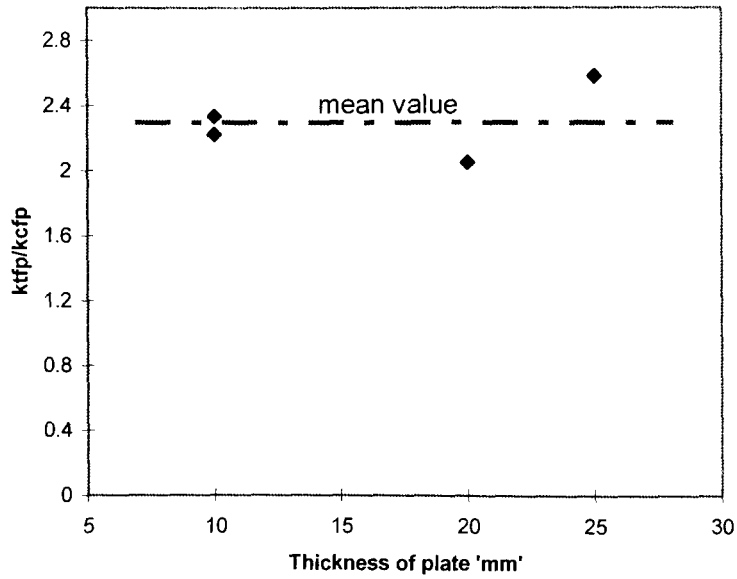

Fig.12.25. Thickness of plate Vs k_{tfp}/k_{cfp}

12.6 Conclusion

Tests conducted on beams bonded with steel plates to their compression faces show that the plated beams are vulnerable to flexural peeling when the plate ends are terminated in regions where the bending moment is predominant and shear forces are negligible. The pure peeling moments have been quantified and it was established that compression face plated beams are about 2.3 times stronger in pure flexural peeling than the corresponding tension face plated beams.

References

Malla, A.P., Song, P.Y., and Yong, J.W. (1997). "Debonding of steel plates glued to the tension and compression faces of beams and slabs". Student Project Report, Dept.of Civil and Environmental Engg., University of Adelaide, Adelaide, Novomber 1997. Pp.B1-B50.

Oehlers, D.J., and Moran,J.P. (1990). "Premature failure of externally plated reinforced concrete beams." Journal of Structural Engg.,(ASCE). Vol.116, No.4,.978-995.

CHAPTER-13: PURE FLEXURAL PEELING OF FIBRE REINFORCED PLASTIC PLATES BONDED TO THE TENSION FACE OR SIDES OF REINFORCED CONCRETE BEAMS

CONTENTS

13.1 Introduction

The objective of the present study is to compare the flexural peeling behaviour of RC beams bonded with FRP plates to that of conventional steel plated RC beams. The present study will be used to check the applicability of the mathematical models that were developed for steel tension face and side plated beams to FRP plated beams. The major parameter varied in this study was the stiffness of the plate. This was varied by using different thicknesses of plate that ranged from 5 mm-32 mm and five different plate materials in which the elastic moduli ranged from 8,800-200,000 MPa.

This chapter is divided into three major parts. Firstly, tests conducted on tension face plated beams are discussed. Secondly, tests conducted on side plated beams are described. Finally, the test results are compared and calibrated to produce an analytical procedure.

13.2 Test specimens

A total of eight plated beams were tested in this study. The basic beam used was 3000 mm long, 150 mm wide and 250 mm deep as shown in Fig.13.1. The target compressive strength of the concrete was chosen as 20 MPa and sufficient longitudinal and transverse reinforcement was provided to avoid premature flexural or shear failure of the beam.

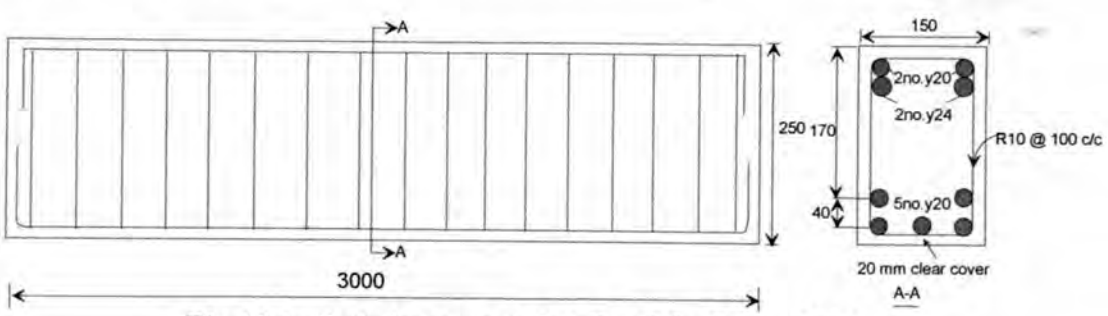

Fig.13.1. Reinforcement details of the basic RC beam

13.3 Group-I Tension face plated beams (FP series)

Out of the eight beams that were cast for this study, five beams were bonded with plates to the tension face as shown in Figures 13.2a-e. The designation and the geometric properties of all the tested beams are summarised in Table-13.1.

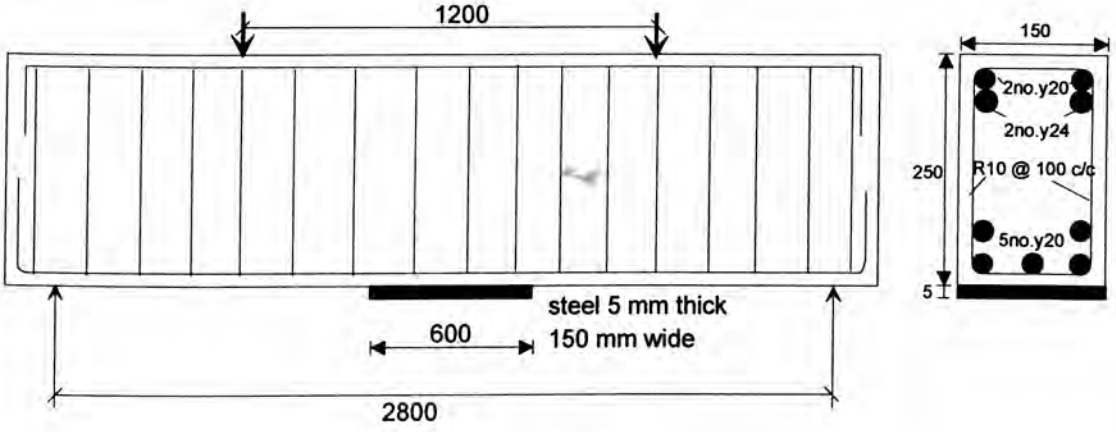

Fig.13.2a. FP-S5

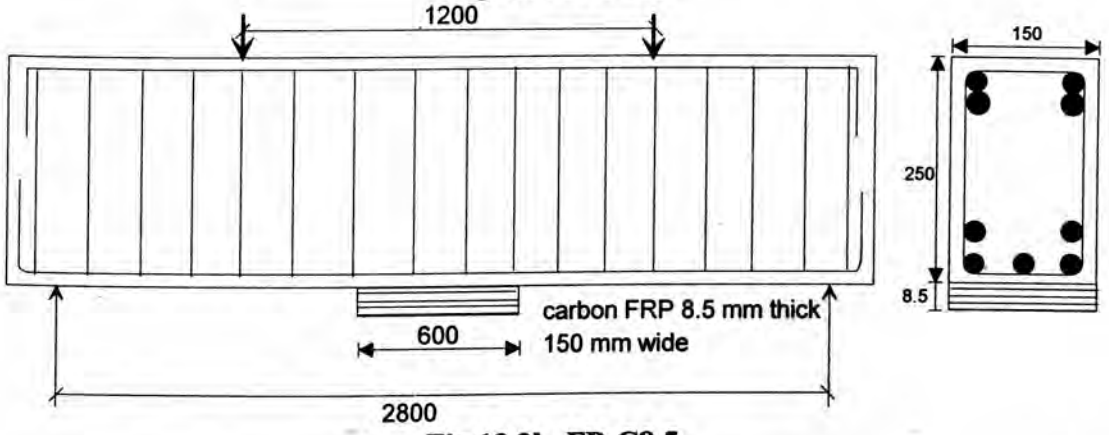

Fig.13.2b. FP-C8.5

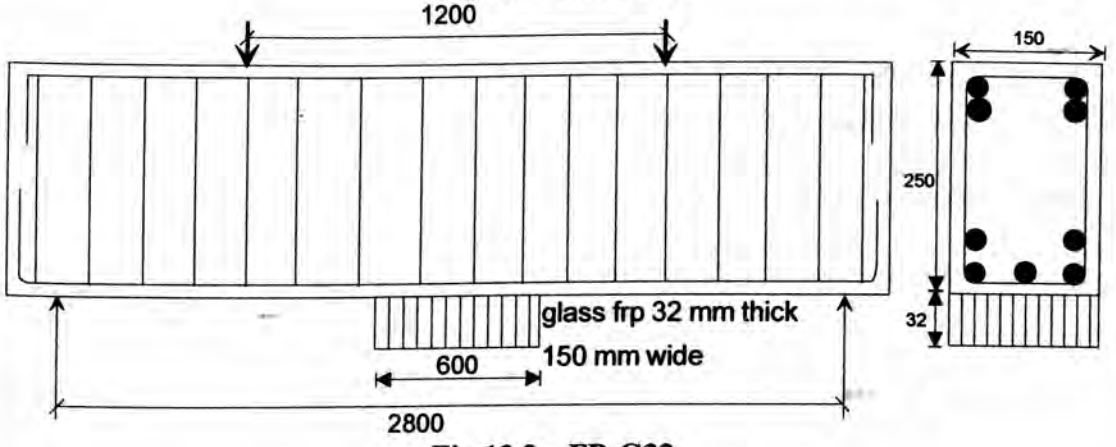

Fig.13.2c. FP-G32

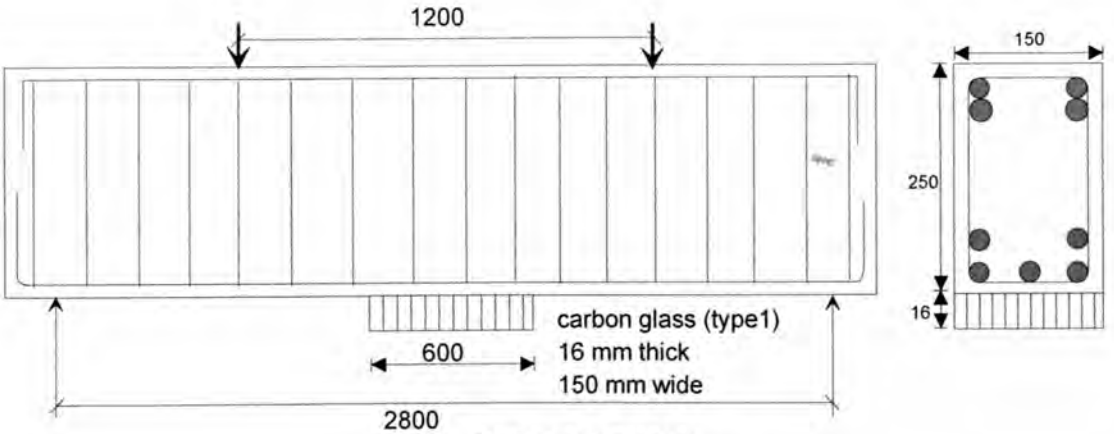

Fig.13.2d. FP-CG16

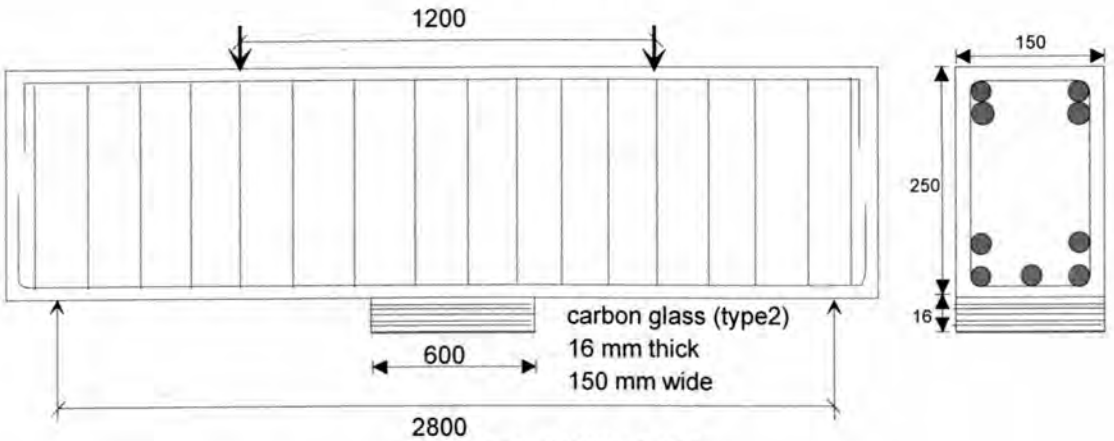

Fig.13.2e. FP-CG2-16

Fig.13.2. Details of tension face plated beam tests

Table-13.1: Geometric properties

Common properties

Breadth of beam (b)=150 mm, depth of beam (h) = 250 mm

Tension reinforcement: number of layers =2, total area (A_{st})=1570 mm^2

Effective depth (d_{st}): first layer = 170 mm second layer = 210 mm

Area: first layer = 942 mm^2, second layer = 628 mm^2

Compression reinforcement: number of layers =2, total area (A_{sc})=1533 mm^2

Effective depth (d_{sc}): first layer = 40 mm, second layer = 62 mm

Area: first layer = 905 mm^2, second layer = 628 mm^2

Shear reinforcement: area = 157 mm^2, spacing = 100 mm

Tension face plate: Length = 600 mm, width = 150 mm

Specific properties

Sl.No	Designation	Tension face plate		
		Plate type	t_{tfp} (mm)	$E_{p,long}$ (MPa)
1	FP-S-5	Steel	5	200,000
2	FP-C-8.5	Carbon FRP	8.5	130,550
3	FP-G-32	Glass FRP	32	10,200
4	FP-CG-16	Carbon & Glass FRP	16	8,800
5	FP-CG2-16	Carbon & Glass FRP	16	42,110

t_{tfp}= thickness of tension face plate, $E_{p,long}$ = elastic modulus of tension face plate along the longitudinal axis.

13.3.1 Test rig

The beams were simply supported over an effective span of 2800 mm as shown in Fig.13.3 and the load was applied on the top of the beam by a hand operated hydraulic jack through a load cell, spreader joist and a pair of knife edge bearings. The geometry of the loading arrangement for all the beams in Fig.13.3 was such that the ends of the plates were in a constant bending moment region and hence, in a zero vertical shear region.

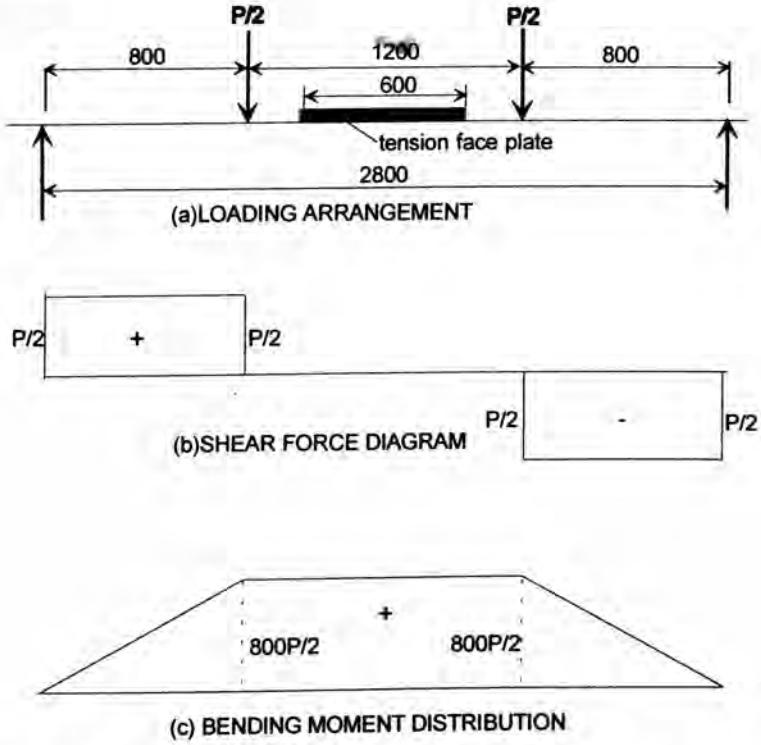

Fig.13.3. Loading arrangement for the tension face plated beams

13.3.2 Instrumentation

Strain gauges were bonded to the external plates in order to detect the debonding at various sites of the plates. The arrangements of the strain gauges and their numbering are shown in Fig.13.4. The beam deflection at mid-span was monitored by both a dial gauge and a transducer.

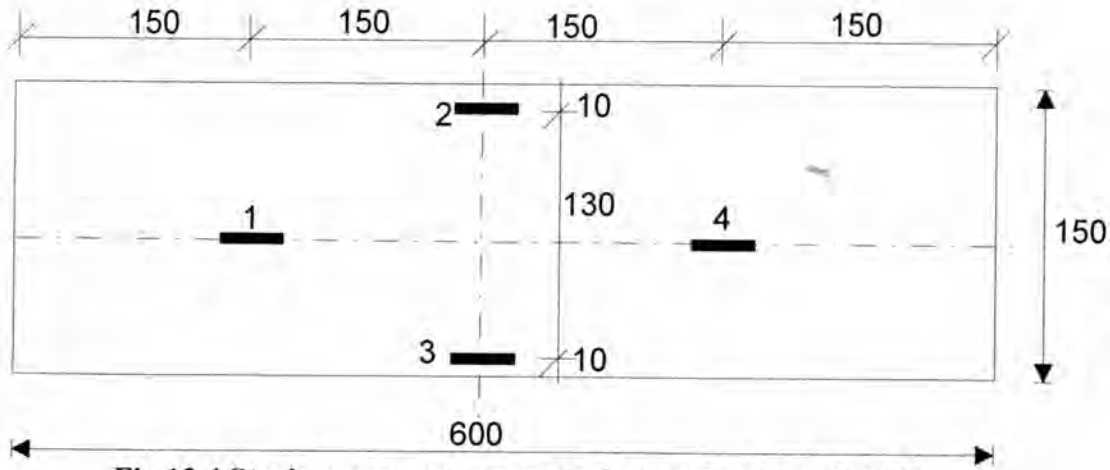

Fig.13.4 Strain gauge arrangement for tension face plated beams

13.3.3 Test procedure

For each test, the beam was first loaded in steps of 5 kN and the cracks were marked and photographically recorded. The corresponding micro-strains at the various sites of the external plate were measured by strain gauges and were recorded at every load step though a data-logging system. The load step was reduced to 3 kN when there was a fall in strain at any site of the plate. The test was terminated when the plate peeling was total, i.e. when all of the strain gauges recorded reducing magnitudes of strains with increasing applied load; the pure flexural peeling moment capacity of the plated beam corresponded to the bending moment at this stage.

13.3.4 Material Properties

All the beams were cast in a single pour using ready mixed concrete supplied by a local manufacturer. Material properties of the concrete are shown in Table-13.2. In this table, the individual values of each test are given under the "i" column and their mean value under "m" column. Material properties of the reinforcing bars and shear stirrups are shown in Table-13.3. The manufacturer's specifications of the material properties of the epoxy glue used for bonding the steel plates are indicated in Table-13.4.

Table-13.2: Material properties of the concrete

Age	E_c (MPa)		f_b (MPa)		f_c (MPa)		f_{cu} (MPa)	
(days)	i	m	i	m	i	m	i	m
141	29863	30081	2.67	2.55	19.6	19.8	22.0	21.6
	28659		2.63		20.2		20.8	
	30286		2.26		19.6		22.0	
	29713		2.65					
	31886							

where E_c = Elastic modulus of the concrete, f_c = Cylinder compressive strength of the concrete, f_{cu}= Cube compressive strength of the concrete and f_b = Brazilian tensile strength of the concrete.

Table-13.3: Material properties of the steel

Item	f_y (MPa)			f_u (MPa)		
Sample No.	1	2	Mean	1	2	Mean
Rebar Y20	436.1	429.7	432.9	530.0	522.0	526.0
Stirrup W10				560.2	572.9	566.6

where f_y = Yield strength of the steel and f_u = Ultimate strength of the steel.

Table-13.4. Material properties of the glue Hilti CA 273 after 2 days (as specified by the manufacturer)

Compressive strength (ISO 604)	Tensile strength (ISO 527)	Flexural strength (ISO 178)	Elastic modulus in compression (ASTM D 695)	Tensile bond strength (ISO 527)	Maximum operating temperature
110-120 MPa	30-40 MPa	20-30 MPa	5000-6000 MPa	10-15 MPa	80° C

13.3.5 Test results (FP series)

13.3.5.1 Beam FP-S5

Beam FP-S5 was bonded with a steel plate of 5 mm thickness to its tension face (Fig.13.2a); it was tested to serve as a reference for the other beams bonded with FRP plates. The applied load (P kN) was such that the moment at the end of the plate (M_{end}) was $0.4P$ kNm in all the beams tested.

The initial crack formation for this beam is shown in Fig.13.5. It can be seen that a number of flexural cracks first occurred in the unplated region at an applied moment of 12.0 kNm (that is an applied load P=30 kN) and a small crack also appeared adjacent to the northwest plate end simultaneously. Flexural cracks occurred at the remaining plate ends as the moment at the plate end was increased to 18 kNm (P=45 kN). The minor plate end cracks were transformed into fully fledged debonding cracks at both plate ends as the moment was increased from 22.0 kNm to 30.0 kNm (P=55 kN to 75 kN). The complete flexural peeling of the plate is

considered to have occurred at 26.3 kNm (P=61.9 kN) when all the strain readings showed a falling trend. The test was terminated at 51.1 kNm (P=65.6 kN). Figures 13.6a and 13.6b show the final crack pattern of this beam.

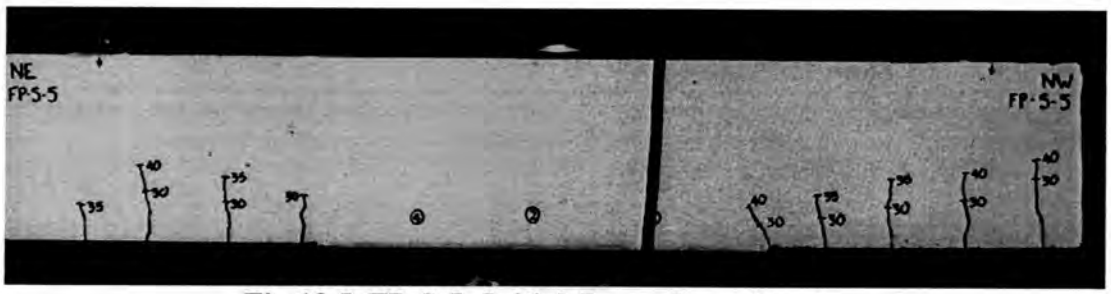

Fig.13.5. FP-S-5: Initial flexural crack pattern

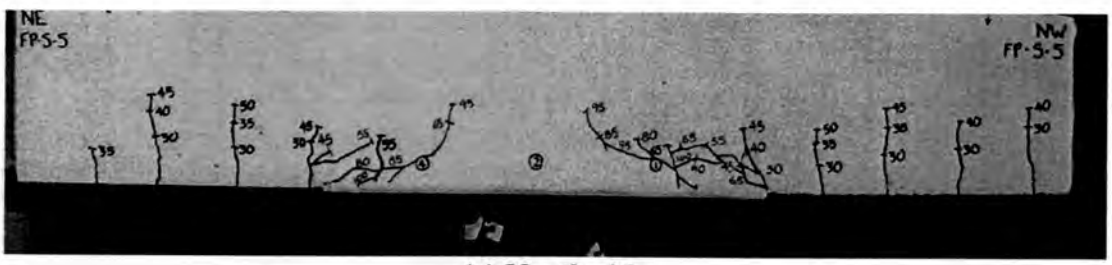

(a) North side

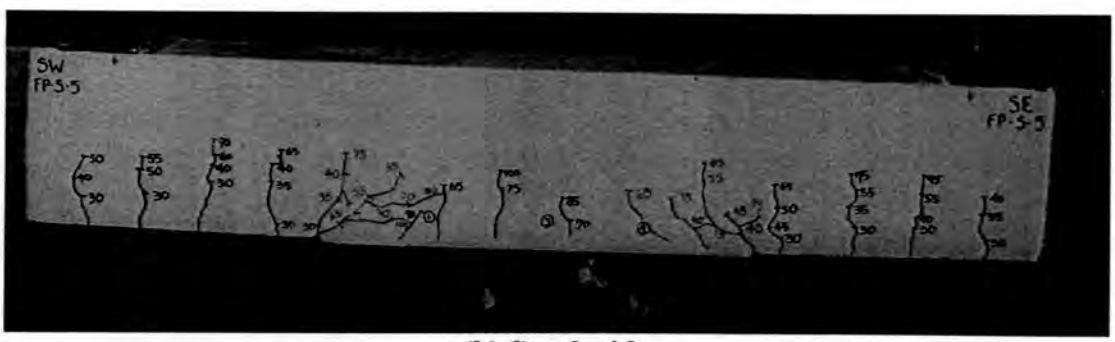

(b) South side

Fig.13.6. FP-S-5: Crack pattern near plate ends at debonding

The results from beam FP-S-5 are given in Table-13.5. The strain gauges in Fig13.4 are listed in column (1) in Table-13.5, and they have been grouped in column (2) according to their longitudinal position. The loads in column (3) are the applied loads at which the strains in the corresponding gauges reduced having reached their maximum values which are listed in column (5); this was interpreted as the load at which debonding occurred in the region adjacent to the strain gauge. The corresponding debonding moments are given in column (4).

TABLE-13.5: Test results of Beam FP-S-5

Strain-gauge Level & No. (1)	Strain-gauge Position group (2)	Total Applied Load P(kN) (3)	Moment (kNm) (4)	Maximum Strain (micro-strain) (5)
Middle(No.1)	Quarter	55.7	22.3	223
Middle(No.4)		50.5	20.2	179
Edge(No.2)	Centre	65.6	26.3	325
Edge(No.3)		65.6	26.3	303

The variations of the longitudinal strains with applied moment are illustrated in Fig.13.7. The rate at which debonding occurred along the plate length can be visualized by comparing the strains at debonding in Table-13.5. Gauge No.4 indicated that debonding occurred at that site at 20.2 kNm. The next gauge to indicate debonding was No.1 at 22.3 kNm. Finally, the central part of the plate debonded at 26.3 kNm. Therefore, it can be inferred that even though the debonding process commenced at a lower moment, it stabilised until there was very rapid crack propagation at the maximum peeling moment. It can be seen that the maximum strain recorded at the instance of the complete flexural peeling was 325 microstrain, i.e. only a fraction of the strain to cause yielding of the steel plate material.

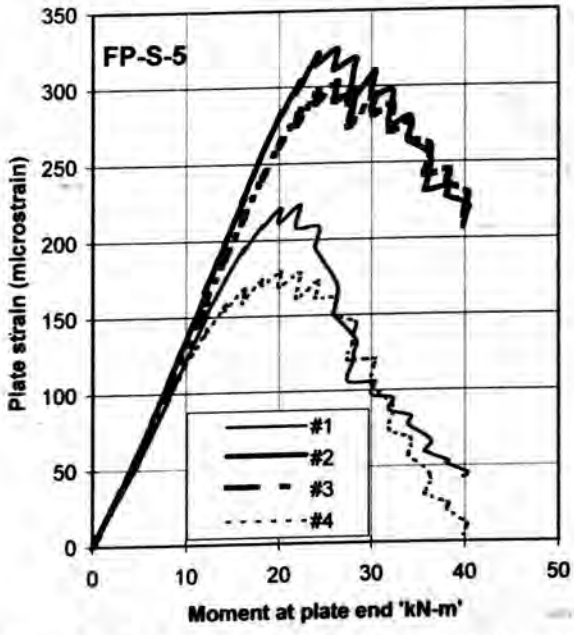

Fig.13.7. FP-S-5: Longitudinal strain variation in plate

The relationship between the deflection at mid-span and the applied moment is shown in Fig.13.8. It can be seen that the beam is still elastic at the instance of maximum peeling moment, as the relationship is still linear.

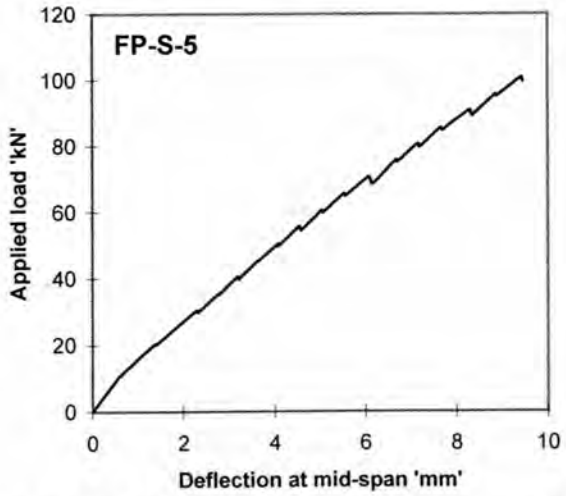

Fig.13.8. FP-S-5: Mid-span deflection Vs Applied moment

13.3.5.2 Beam FP-C-8.5

Beam FP-C-8.5 was bonded with a carbon fibre reinforced plastic plate of 8.5 mm thickness to its tension face (Fig.13.2b). The plate as supplied by the manufacturer was 1.8 mm thick and 80 mm wide. The plate used for our study was fabricated at the University of Adelaide by bonding four layers of 1.85 mm thick plates using a standard epoxy resin (Sikadur-30).

The crack patterns for this beam are shown in Figs.13.9 and 13.10a-c. It can be seen in Fig.13.9 that a number of flexural cracks first occurred in the unplated region at an applied moment range of 8.0-12.0 kNm (P=20-30 kN) and a small crack also appeared adjacent to the north-west plate end simultaneously. Vertical cracks occurred at the plate ends as the moment was increased to 16 kNm (P=40 kN). Figures 13.10a-c show that the minor plate end cracks were transformed into fully fledged debonding cracks as new cracks branched out from the plate ends, propagating along the concrete cover as the moment was increased from 20.0 kNm to

38.0 kNm (P=50 kN to 95 kN). The complete flexural peeling of the plate is considered to have occurred at 28.1 kNm (P=70.3 kN) when all the strain readings showed a falling trend, as illustrated by Fig.13.11. The test was terminated at 38.0 kNm (P=95.0 kN).

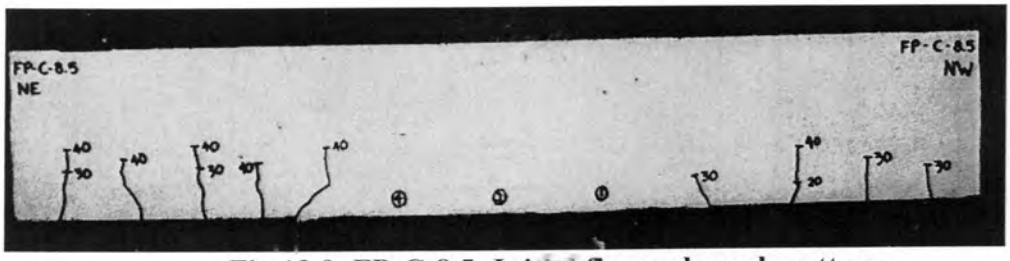

Fig.13.9. FP-C-8.5: Initial flexural crack pattern

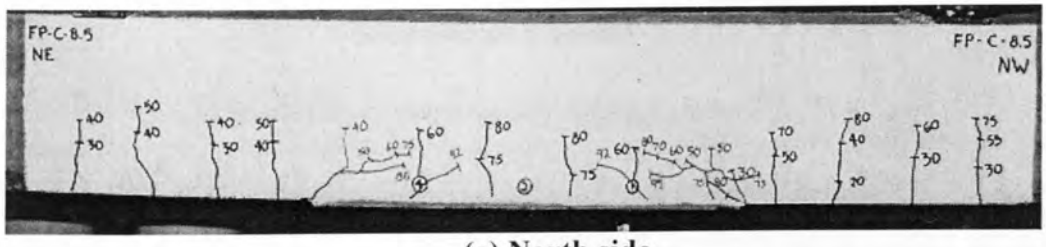

(a) North side

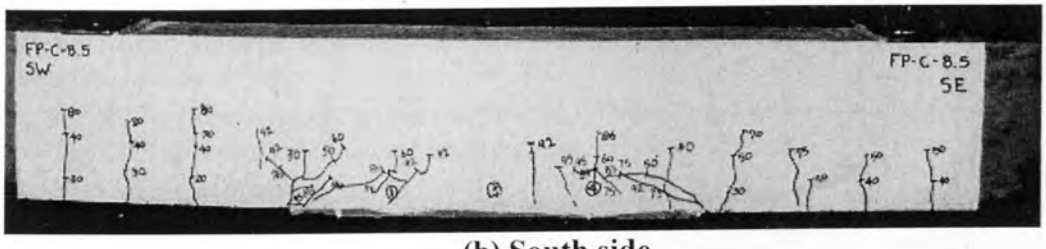

(b) South side

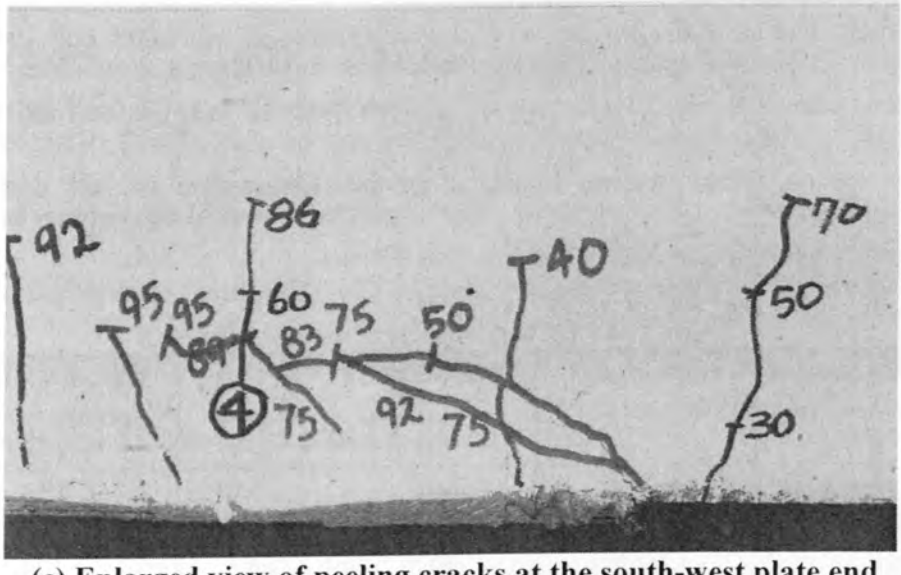

(c) Enlarged view of peeling cracks at the south-west plate end

Fig.13.10. FP-C-8.5: Crack pattern near plate ends at debonding

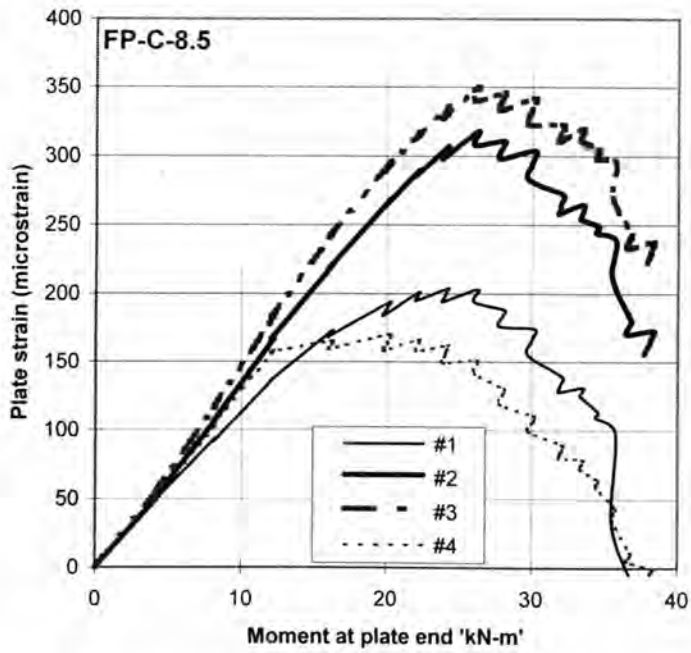

Fig.13.11. FP-C8.5: Longitudinal strain variation in plate

The results from beam FP-C-8.5 are given in Table-13.6. The rate at which debonding occurred along the plate length can be visualized by comparing the strains at debonding in Table-13.6. It can be inferred that even though the debonding process commenced at a lower moment (22.3 kNm) at the quarter point of the plate, it propagated towards the middle region of the plate as the moment was increased to 28.1 kNm. The maximum strain recorded at the instance of complete peeling was 342 microstrain. The relationship between the deflection at mid-span and the applied moment is shown in Fig.13.12. It can be seen that the beam is still elastic at the instance of maximum peeling moment, as the relationship is still linear. The deflection recorded at the end of the test was 8.9 mm.

TABLE-13.6: Test results of Beam FP-C-8.5

Strain-gauge Level & No. (1)	Strain-gauge Position group (2)	Total Applied Load P(kN) (3)	Moment (kNm) (4)	Maximum Strain (micro-strain) (5)
Middle(No.1)	Quarter	64.7	26.0	194
Middle(No.4)		55.3	22.3	166
Edge(No.2)	Centre	70.3	28.1	304
Edge(No.3)		70.3	28.1	342

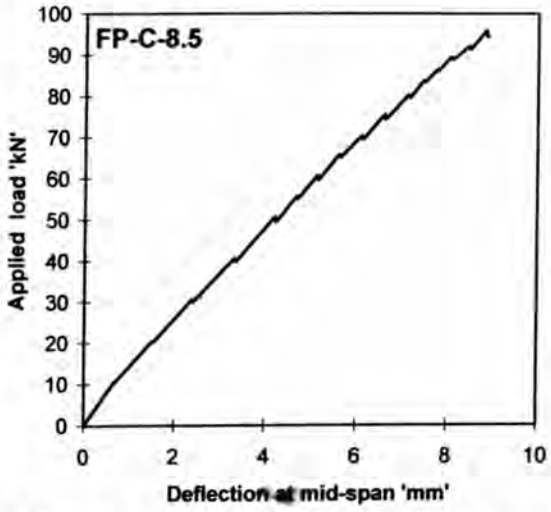

Fig.13.12. FP-C-8.5: Midspan deflection Vs Applied moment

13.3.5.3 Beam FP-G-32

Beam FP-G-32 was bonded with a glass fibre reinforced plastic plate of 32 mm thickness to its tension face (Fig.13.2c). The plate was fabricated by bonding together two plates of 16 mm thick using a standard epoxy resin (Sikadur-30). The FRP plate is quite flexible as the elastic modulus of the FRP plate along the longitudinal axis of the beam is approximately one-twentieth that of the steel plate.

The initial crack formation for this beam is shown in Figs.13.13a and 13.13b. A number of flexural cracks occurred and propagated upwards in the whole constant bending moment region of the beam at an applied moment range of 12.0-20.0 kNm (P=30-50 kN). Cracks also appeared at the plate ends simultaneously. These minor plate end cracks were transformed into fully fledged peeling cracks as new cracks branched out from the plate ends, propagating along the concrete cover as the moment was increased from 20.0 kNm to 44.0 kNm (P= 50 kN to 110 kN) as shown in Figs.13.14a and 13.14b. The complete flexural peeling of the plate occurred at 40.4 kNm (P =101.0 kN) when all the strain readings showed a falling trend, as illustrated by Fig.13.15. The test was terminated at 46.0 kNm (P =115.0 kN).

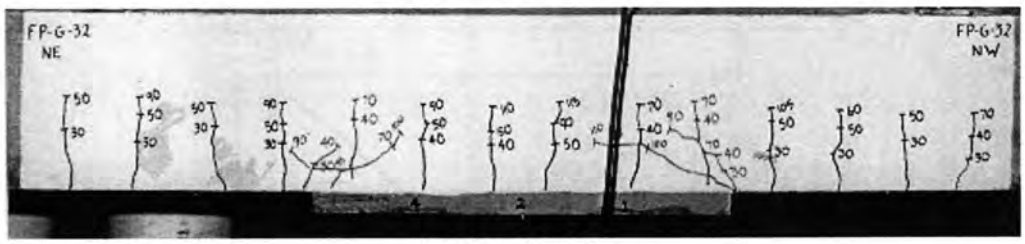

(a) North side

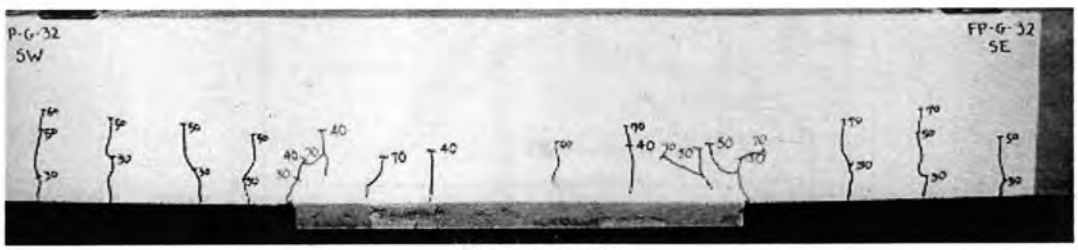

(b) South side

Fig.13.13. FP-G-32: Initial flexural crack pattern

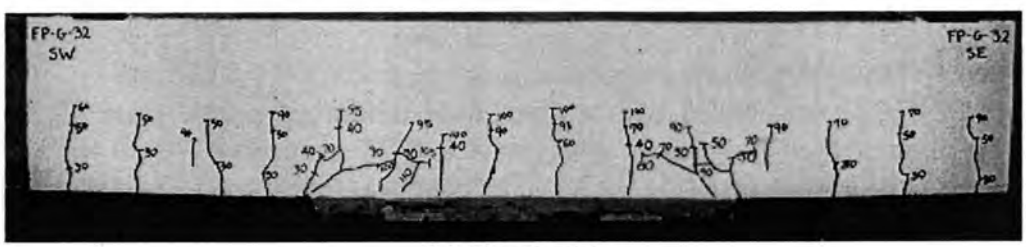

(a) North side

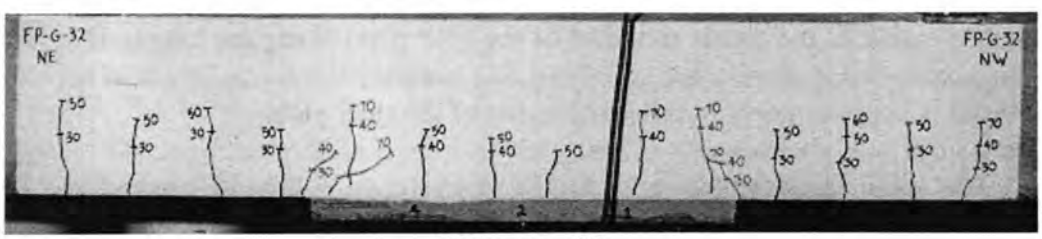

(b) South side

Fig.13.14. FP-G-32: Crack pattern near plate ends at debonding

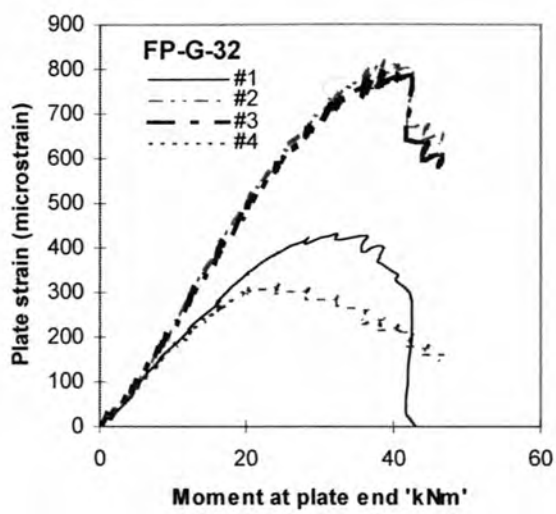

Fig.13.15. FP-G-32: Longitudinal strain variation in plate

The test results for beam FP-G-32 are summarised in Table-13.7. Table-13.7 shows that the flexural peeling process commenced at a lower moment (24.2 kNm) at the quarter point of the plate and it stabilised until there was very rapid crack propagation at the maximum peeling moment of 40.4 kNm at the middle region of the external plate. The maximum strain recorded at the instance of complete peeling was 806 microstrain. The relationship between the deflection at mid-span and the applied moment is shown in Fig.13.16. It can be seen that the beam is still elastic at the instance of maximum peeling moment, as the relationship is still linear.

TABLE-13.7: Test results of Beam FP-G-32

Strain-gauge Level & No. (1)	Strain-gauge Position group (2)	Total Applied Load P(kN) (3)	Moment (kNm) (4)	Maximum Strain (micro-strain) (5)
Middle(No.1)	Quarter	80.4	32.2	433
Middle(No.4)		60.4	24.2	315
Edge(No.2)	Centre	101.1	40.4	809
Edge(No.3)		101.1	40.4	786

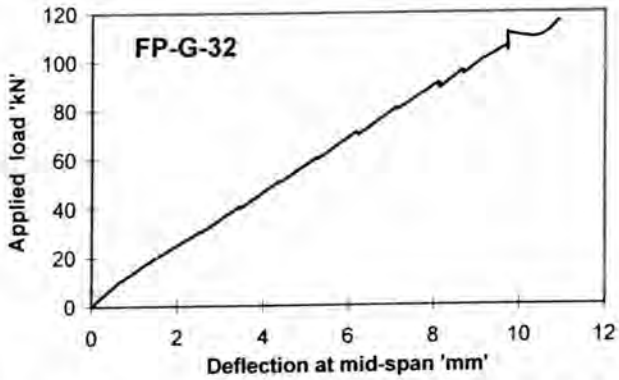

Fig.13.16. FP-G-32: Midspan deflection Vs Applied moment

13.3.5.4 Beam FP-CG-16

Beam FP-CG-16 was bonded with a combined carbon and glass fibre reinforced plastic plate of 16 mm thickness to its tension face (Fig.13.2d). The plate was fabricated by bonding together two plates of 8 mm thick using a standard epoxy resin (Sikadur-30). The FRP plate was bonded in such a way that its weaker axis was

parallel to the longitudinal axis of the beam. It is quite flexible along its weaker axis as the elastic modulus of the FRP plate along the longitudinal axis of the beam is only 4.4% that of the steel plate.

The initial crack formation for this beam is shown in Figs.13.17a and 13.17b. It can be observed that a number of flexural cracks occurred at regular spacings in the non-plated region when the applied moment was 12.0 kNm (P=30 kN). Cracks also appeared at the plate ends and within the plate ends as the moment was increased to 20.0 kNm (P=50 kN). Peeling cracks branched out from the minor plate end cracks and they propagated gradually along the concrete cover as the moment was increased from 20.0 kNm to 65.2 kNm (P= 50 kN to 163 kN) as shown in Figures 13.18a and 13.18b. The complete flexural peeling of the plate occurred at 62.1 kNm (P =155.3 kN) when all the strain readings showed a falling trend, as can be seen in Fig.13.19. The test was terminated when the moment was 66.0 kNm (P =165.0 kN).

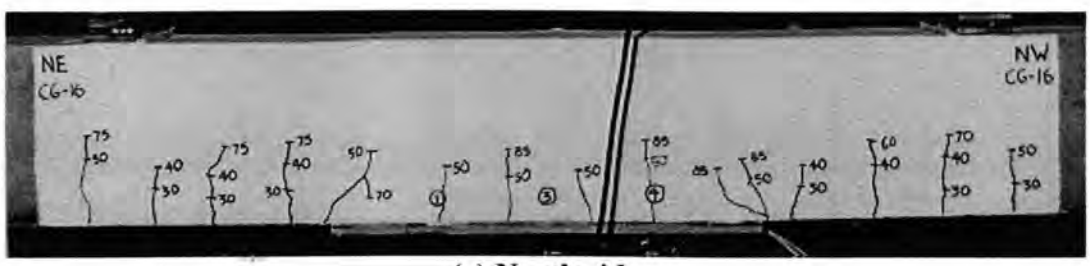

(a) North side

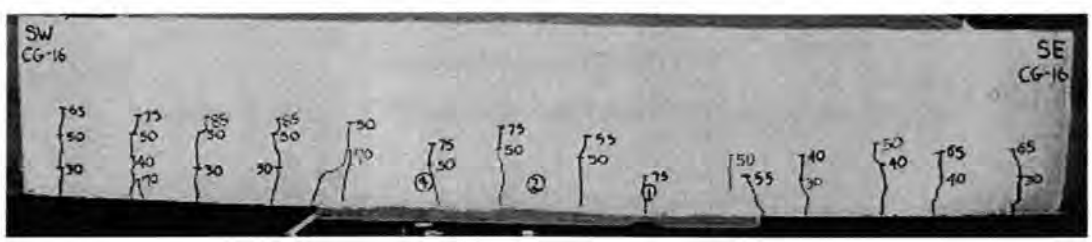

(b) South side

Fig.13.17. FP-CG-16: Initial flexural crack pattern

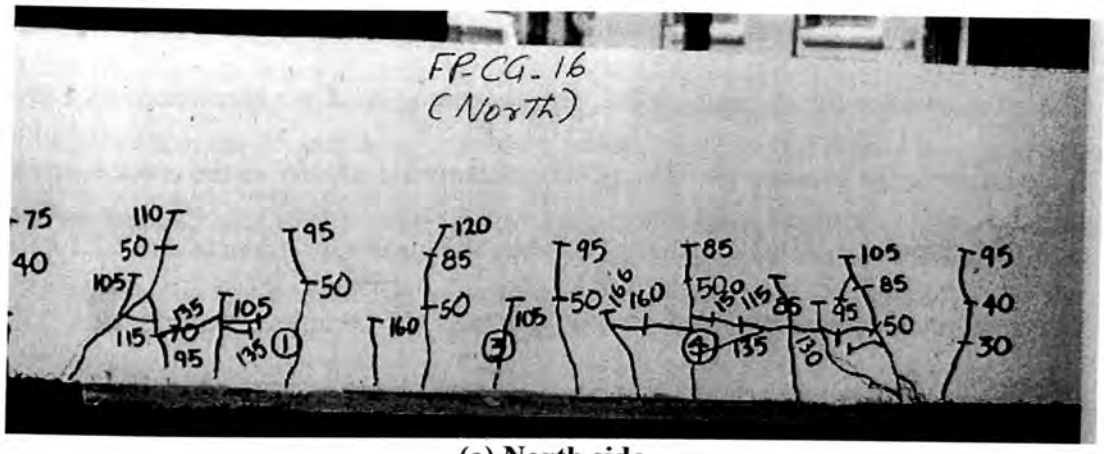

(a) North side

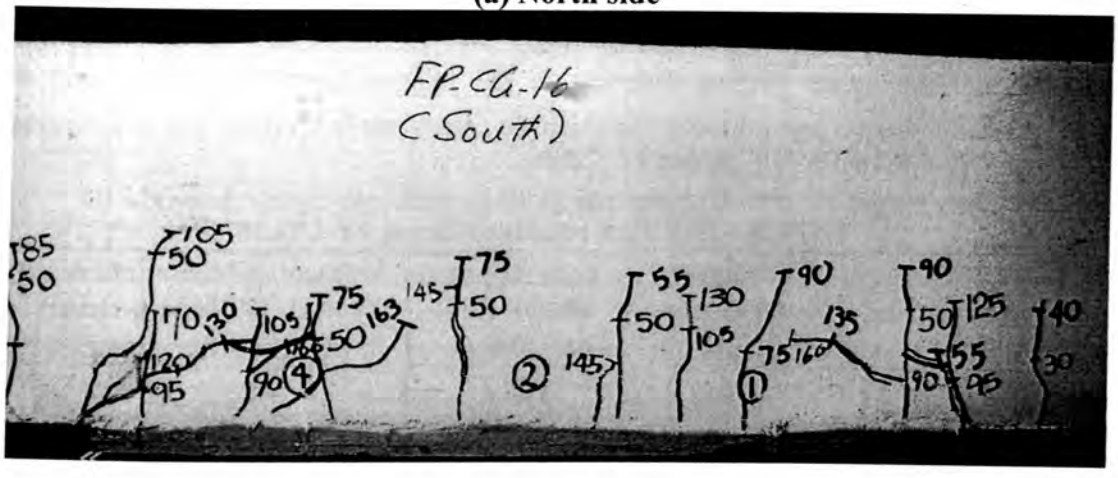

(b) South side

Fig.13.18. FP-CG-16: Crack pattern near plate ends at debonding

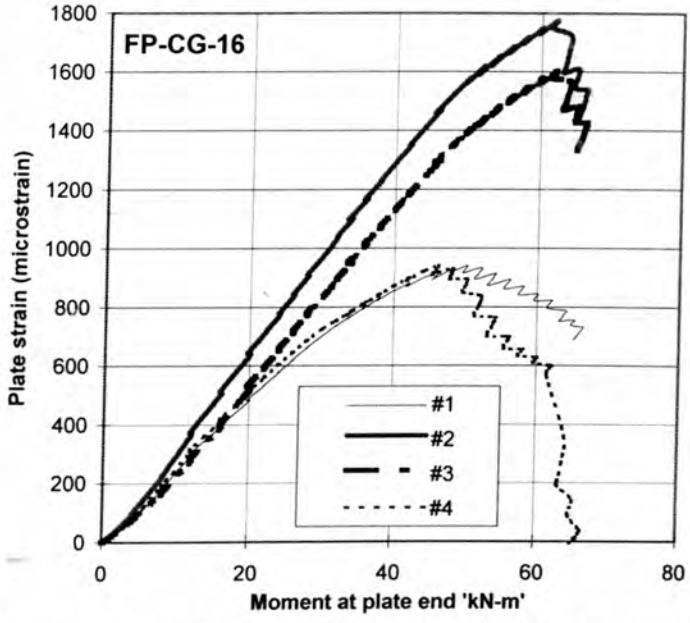

Fig.13.19. FP-CG-16: Longitudinal strain variation in plate

The salient features of the test results for beam FP-CG-16 are given in Table-13.8. It shows that the flexural peeling process commenced at a moment of 48.1 kNm at the strain gauge location #4. The peeling occurred gradually as the crack extended to the middle region of the external plate when the maximum moment was 62.1 kNm. The maximum strain recorded at the instance of complete peeling was 1775 microstrain. The relationship between the deflection at mid-span and the applied moment is shown in Fig.13.20. It can be seen that the beam is still elastic at the instance of maximum peeling moment as the relationship is still linear and the maximum deflection recorded was 17.2 mm.

TABLE –13.8 Test results of Beam FP-CG.16

Strain-gauge Level & No. (1)	Strain-gauge Position group (2)	Total Applied Load *P* (kN) (3)	Moment (kNm) (4)	Maximum Strain (micro-strain) (5)
Middle(No.1)	Quarter	130.2	52.1	934
Middle(No.4)		120.3	48.1	931
Edge(No.2)	Centre	155.3	62.1	1775
Edge(No.3)		155.3	62.1	1601

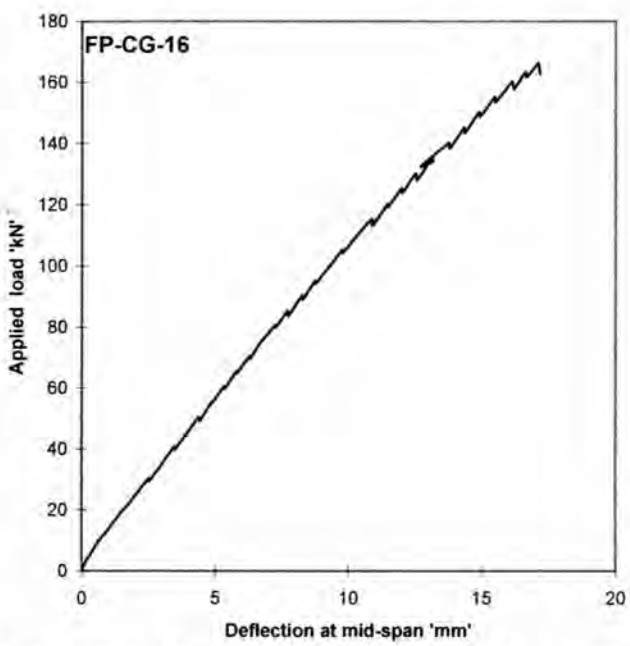

Fig.13.20. FP- FP-CG-16: Mid-span deflection Vs Applied moment

13.3.5.5 Beam FP-CG2-16

Beam FP-CG2-16 was similar to beam FP-CG-16; the only difference being that the stronger axis of the 16 mm thick combined carbon and glass FRP plate was parallel to the longitudinal axis of the beam (Fig.13.2e). In this case, the elastic modulus of the FRP plate along the longitudinal axis of the beam is about 21% that of the steel plate.

The initial crack formation for this beam is shown in Figs.13.21a and 13.21b. It can be observed that a number of flexural cracks occurred at regular spacing in the non-plated region when the applied moment was 8.0 kNm (P =20 kN). Cracks also appeared in the vicinity of the plate end when the moment was increased to 16 kNm (P = 40 kN) and within the plate ends as the moment was increased to 20.0 kNm (P=50 kN). Peeling cracks branched out from the minor plate end cracks and they propagated gradually along the concrete cover as the moment was increased from 20.0 kNm to 40.0 kNm (P= 50 kN to 100 kN) as shown in Figures 13.22a and 13.22b. The complete flexural peeling of the plate occurred at 62.1 kNm (P =155.3 kN) when all the strain readings showed a falling trend, as can be seen in Fig.13.23. The test was finished when the moment dropped to 28.0 kNm (P = 69.6 kN).

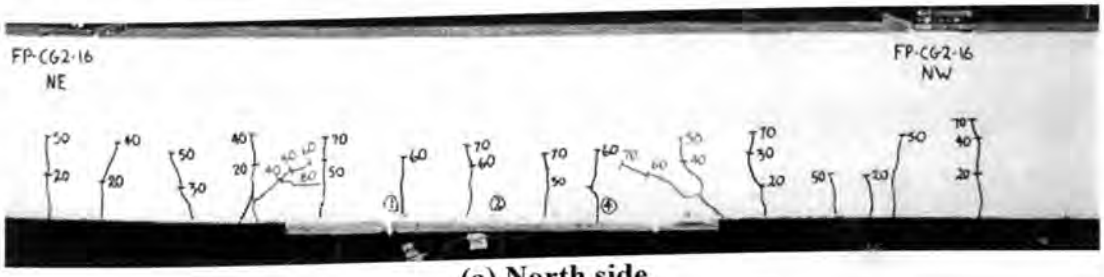

(a) North side

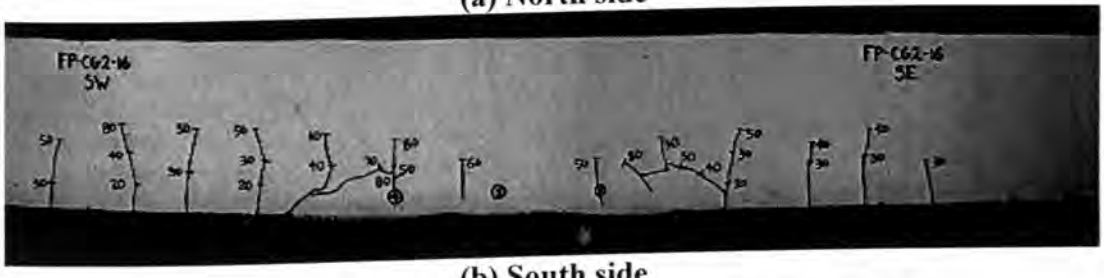

(b) South side

Fig.13.21. FP -CG2-16: Initial flexural crack pattern

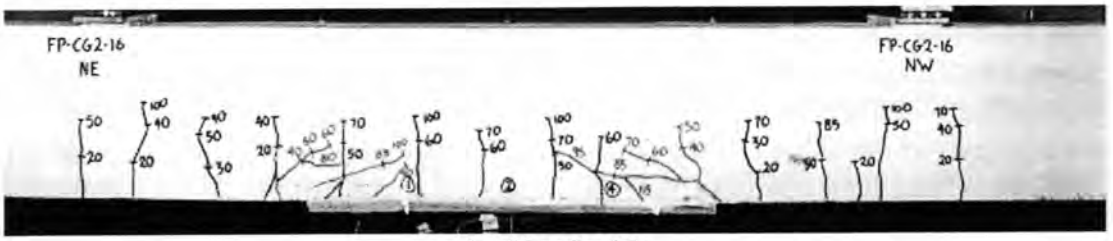

(a) North side

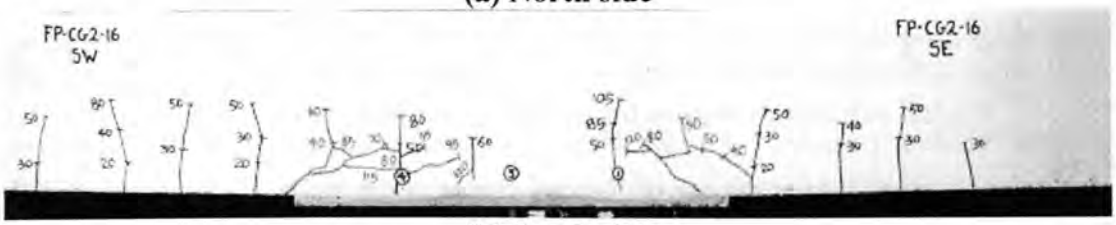

(b) South side

Fig.13.22. FP-CG2-16: Crack pattern near plate ends at debonding

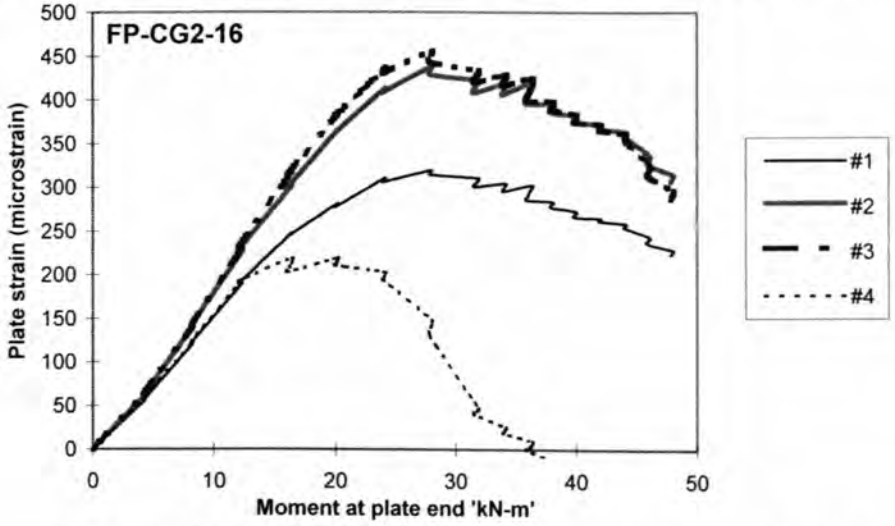

Fig.13.23. FP- CG2-16: Longitudinal strain variation in plate

The salient features of the test results for beam FP-CG2-16 are given in Table-13.9. It shows that the flexural peeling process commenced at a moment of 20.1 kNm at the strain gauge location #1. The peeling was complete when the strain magnitudes declined at all other gauge locations when the maximum moment was 28.0 kNm. The maximum strain recorded at the instance of complete peeling was 455 microstrain. The relationship between the deflection at mid-span and the applied moment is shown in Fig.13.24. It can be seen that the beam is still elastic at the instance of maximum peeling moment as the relationship is still linear and the maximum deflection recorded was 11.8 mm.

TABLE- 13.9: Test results of Beam FP-CG2-16

Strain-gauge Level & No. (1)	Strain-gauge Position group (2)	Total Applied Load P(kN) (3)	Moment (kN-m) (4)	Maximum Strain (micro-strain) (5)
Middle(No.1)	Quarter	69.6	28.0	320
Middle(No.4)		50.5	20.2	219
Edge(No.2)	Centre	69.6	28.0	438
Edge(No.3)		69.6	28.0	455

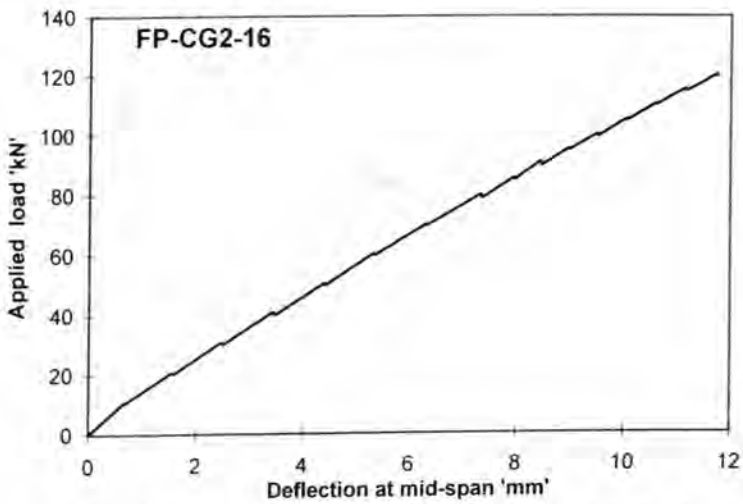

Fig.13.24. FP-CG2-16: Mid-span deflection Vs Applied moment

13.3.6 Discussion of test results

The tests carried on the beams that were bonded with different plate material to their tension faces have shown that flexural peeling is initiated by the formation of flexural cracks in the vicinity of the plate end. The peeling process was completed as the plate end cracks propagated along the concrete cover towards the centre of the plate as the applied load was increased. Table-13.10 summarises the moment at the plate end and also the strain recorded in the plate when the complete flexural peeling occurred, i.e. when the strain readings started to fall at all the strain gauge locations.

Table-13.10: Test results-tension face plated beams

No.	Designation	t_{tfp} (mm)	$E_{p,long}$ (MPa)	M_{pure} (kNm)	Maximum microstrain
1	FP-S-5	5	200,000	26.3	325
2	FP-C-8.5	8.5	130,550	28.1	342
3	FP-CG2-16	16	42,110	28.0	455
4	FP-G-32	32	10,200	40.4	809
5	FP-CG-16	16	8,800	62.0	1775

It can be seen from Table-13.10 that the pure flexural peeling capacities (M_{pure}) of the plated beams does not show any trend for the change in the elastic modulus of the plates for beams FP-S-5, FP-C-8.5 and FP-CG2-16, as the magnitudes of M_{pure} for this three cases are nearly the same. However, for flexible plates such as FP-G-32 and FP-CG-16, there was a marked increase in peeling moment capacities. Moreover, debonding occurred over a wide range of plate strains, i.e. 325-1775 microstrain. Hence controlling the strain in the plate cannot be used to control flexural peeling. As the raw data does not show any meaningful trend, the following analysis was carried out and its implications are discussed.

13.3.7 Analysis of test results

According to the study conducted by Oehlers and Moran (Sections 2.3.2 and 2.7.3.2), the flexural peeling of steel tension face plated beams is caused by the curvature of the concrete beam. Therefore, the pure flexural peeling capacity M_{pure} is directly proportional to the flexural rigidity of the concrete beam based on cracked plated section (E_cI_{cp}). The resistance to flexural peeling also depends on the stiffness of the plate, as stiffer plates are more vulnerable to peeling. Hence, M_{pure} is inversely proportional to the plate stiffness represented by E_pt_p. Table-13.11 shows the analytical results. The following coefficient k_{tfp} is defined as the coefficient in the basic equation of Oehlers and Moran for M_{pure} in Eqn.2.5.

$$k_{tfp} = \frac{(E_cI_{cp})f_b}{E_pt_{tfp}M_{pure}(test)} \tag{13.1}$$

Fig.13.25 illustrates the relationship between the ratio of the axial stiffness of the plate (E_pt_{tfp}) to that of the steel plate (E_st_{steel}) and the ratio between the flexural peeling moment capacities of all the beams tested (M_{pure}) and that of the steel plated beam

FP-S5($M_{pure(steel)}$). Figure 13.26 is a similar graph for the relationship between the flexural peeling capacities and the flexural rigidity of the cracked plated section. Both figures show the existence of an exponential relationship defined by the following equations.

$$\frac{M_{pure(steel)}}{M_{pure}} = \left(\frac{E_s t_{steel}}{E_p t_{tfp}} \right)^{-0.41} \tag{13.2}$$

$$\frac{M_{pure(steel)}}{M_{pure}} = \left(\frac{(E_c I_{cp})_{steel}}{E_c I_{cp}} \right)^{-1.96} \tag{13.3}$$

Table-13.11: Test results-tension face plated beams

No.	Designation	M_{pure}(test) (kNm)	$E_c I_{cp}$ (kNm^2)	$E_p.t_{tfp}$ (kN/mm)	k_{tfp}
1	FP-S-5	26.3	8236	1000	0.217
2	FP-C-8.5	28.1	8617	1109.7	0.218
3	FP-CG2-16	28.0	5530	673.8	0.23
4	FP-G-32	40.4	7429	326.4	0.92
5	FP-CG-16	62.0	6192	140.8	2.73

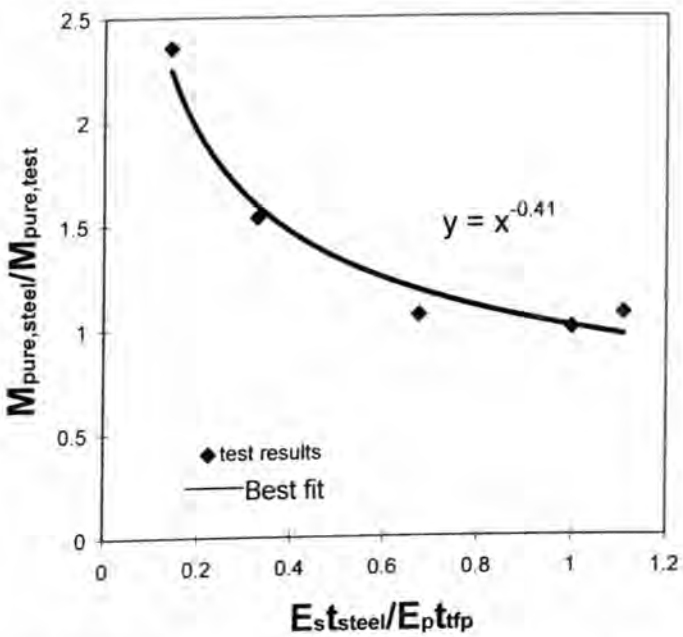

Fig.13.25. Variation of M_{pure} with plate stiffness

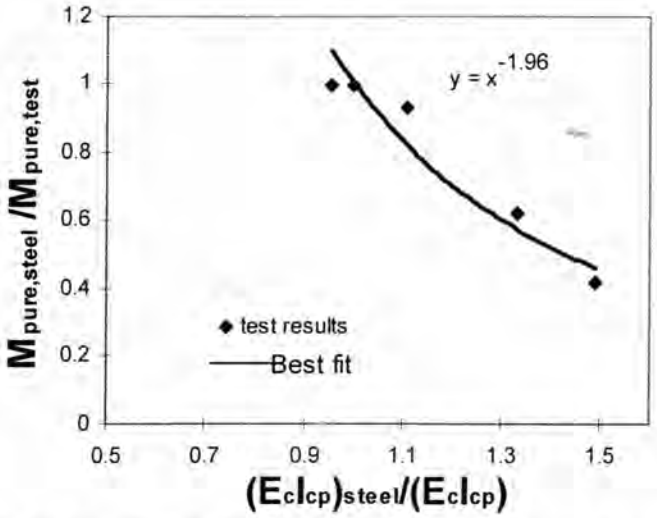

Fig.13.26. Variation of M_{pure} with flexural rigidity of plated beam

Figure 13.27 shows the variation the empirical coefficient k_{tfp} with the elastic modulus of the plates.

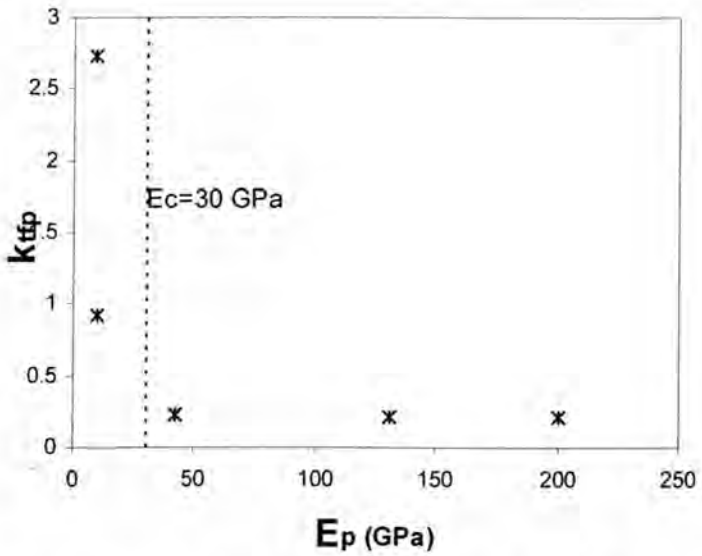

Fig.13.27. Variation of k_{tfp} with elastic modulus of plates

It can be seen from Fig.13.27 and Tables-13.10 and 13.11 that the three plated beams in which the elastic modulus of external plates were greater than the elastic modulus of concrete (E_c=30081 MPa), the magnitude of k_{tfp} is nearly the same. There is also only a negligible difference in the flexural peeling capacity of these three beams. The tension face plated beams with a very low elastic modulus carried higher moments but they are only of academic interest and they cannot be used for

strengthening in actual practice. Therefore, the models developed by Oehlers and Moran for flexural peeling in steel plated beams can be extended confidently to the FRP plated beams. However, further research is needed to evaluate the empirical constant k_{tfp} as it has a wide scatter even for steel plated beams.

13.4 Group-II Side plated beams (FPS series)

13.4.1 Specimens

Out of the eight beams that were cast for this study, three beams were bonded with plates to the sides as shown in Figures 13.28a-c. The designation and the geometric properties of all the tested beams are summarised in Table-13.12.

Table-13.12: Geometric properties

Common properties: same as given in Table -13.1; omit the details on tension face plates.

Specific properties

No.	Designation	Side plate				
		Plate type	Length (mm)	depth d_{sp}(mm)	thickness t_{sp}(mm)	$E_{p,long}$ (MPa)
1	FPS-S-5	Steel	600	75	5	200,000
2	FPS-C-8.5	Carbon FRP	600	80	8.5	130,550
5	FPS-CG-24	Carbon & Glass FRP	350	75	24	42,110

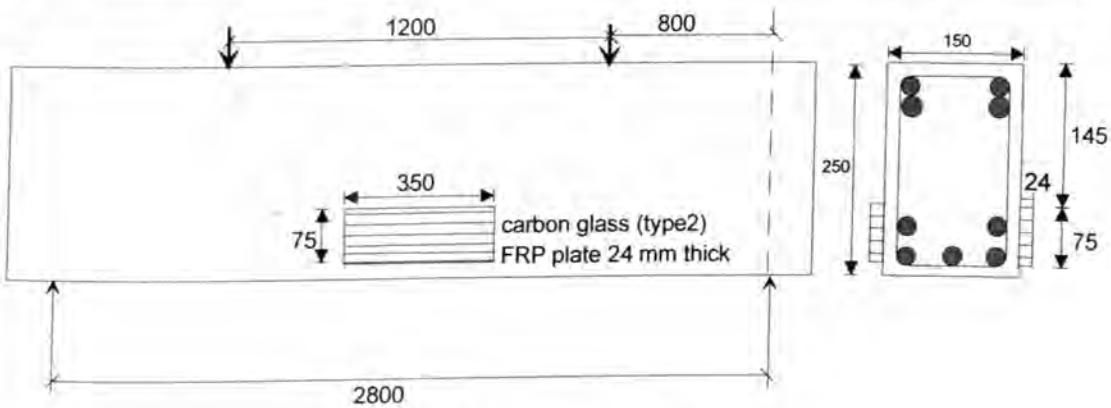

Fig.13.28(a). FPS-S-5

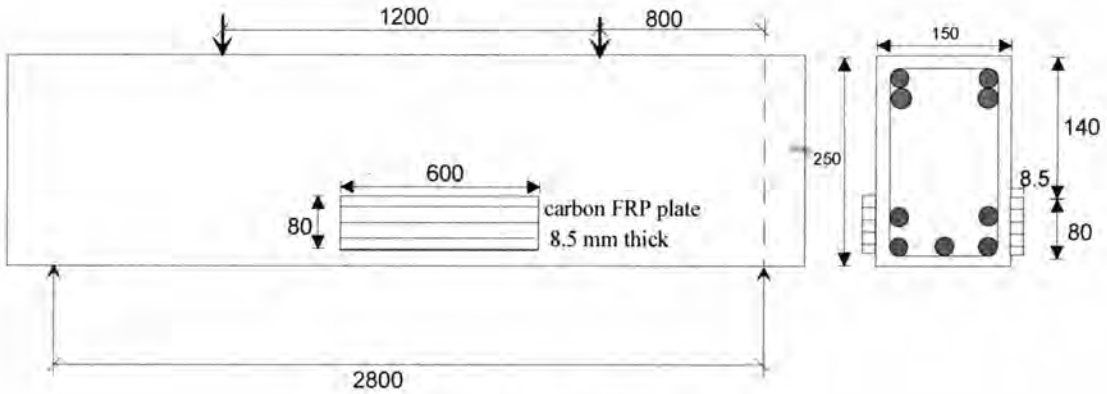

Fig.13.28(b). FPS-C-8.5

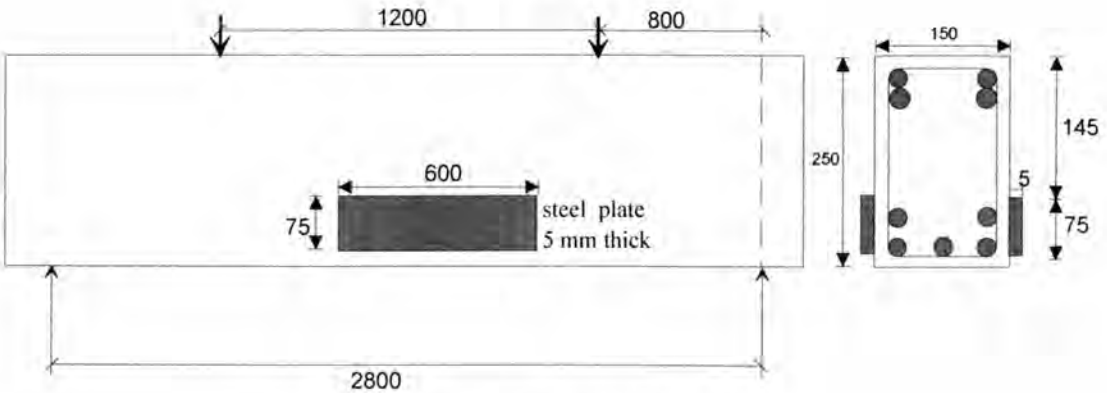

Fig.13.28(c). FPS-CG-24
Fig.13.28. Details of side plated beams

13.4.2 Test rig

Test rig and loading arrangement were the same to that used for Group-I beams (FP series).

13.4.3 Instrumentation

Strain gauges were bonded to the external plates in order to detect the debonding at various sites of the plates. The arrangements of the strain gauges and their numbering are shown in Figs.13.29a and 13.29b. The beam deflection at mid-span was monitored by both a dial gauge and a transducer.

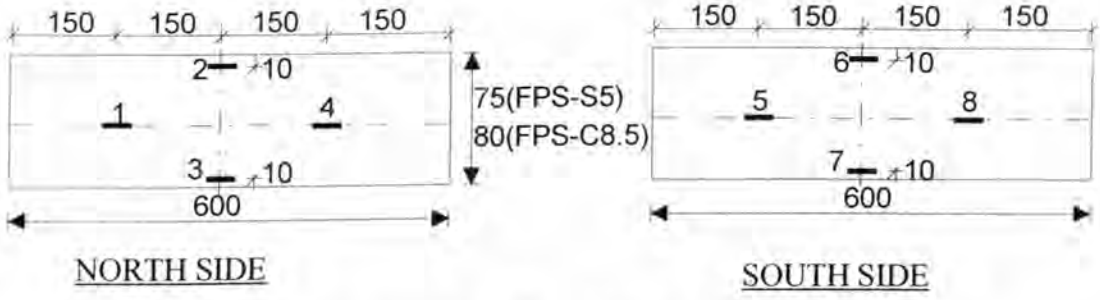

(a) FPS-S-5 and FP-C-8.5

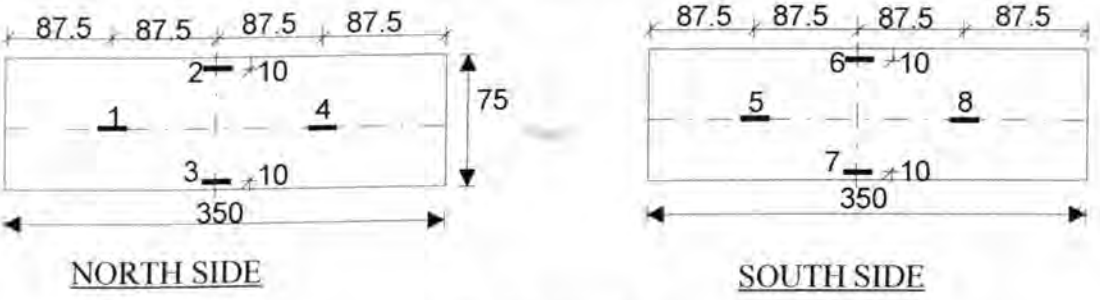

(b) FP-CG-24

Fig.13.29. Strain gauge arrangement

13.4.4 Test procedure

A typical side plated beam ready-to-test is shown in Fig.13.30. For each test, the beam was first loaded in steps of 5 kN and the cracks were marked and photographically recorded. The corresponding micro-strains at the various sites of the external plate were measured by strain gauges and were recorded at every load step though a data-logging system. The load step was reduced to 3 kN when there was a fall in strain at any site of the plate. The test was terminated when the plate peeling was total, i.e. when the strain at the centroid of the side plates set to fall. The pure flexural peeling moment capacity of side plated beam corresponds to the bending moment at this stage. It may be noted that the strain at the centroid is the mean value of the readings recorded at the gauge locations #2 and #3 on the north side of the beam and at #6 and #7 on the south side of the beam in Fig.13.29. The fall in the strain value at the centroid is used for indicating the peeling as part of the change in strains at other locations occurs due to change in flexural stresses.

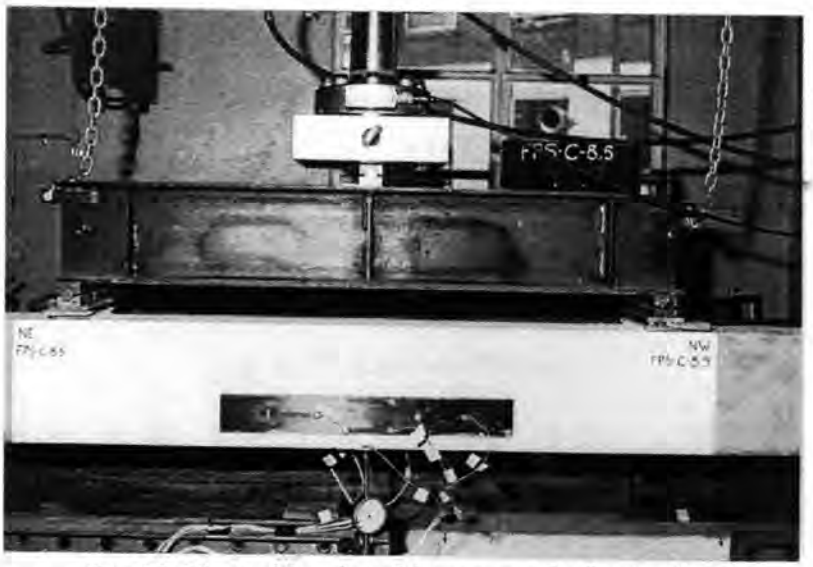

Fig.13.30. A side plated beam ready for testing

13.4.5 Material Properties

Material properties are same as given for Group-I beams (Section 13.3.4).

13.4.6 Test results (FPS series)

13.4.6.1 Beam FPS-S-5

Beam FPS-S5 was bonded with steel plates 600 mm long, 75 mm deep and 5 mm thick to the sides (Fig.13.28a); it was tested to serve as a reference for the other beams bonded with FRP plates. The applied load (P kN) was such that the moment at the end of the plate (M_{end}) was $0.4P$ kNm in all the beams tested.

A number of flexural cracks first occurred in the unplated region as the applied moment was in the range 8.0 kNm-16.0 kNm (that is an applied load P=20-40 kN) as shown in Figs.13.31a and 13.31b. These figures also show the occurrence of several flexural cracks below the side plates when the applied moment was varied from 16.0 kNm to 20.0 kNm (P=40-50 kN). The next significant cracks to occur were the ones that formed in the vicinity of the plate ends, when the moment was increased to 28.0 kNm (P=70.0 kN) as shown in Figs.13.31a and 13.31b. Further application of the load caused the plate end cracks first to extend to the top corners of the side plates and then to propagate gradually along the top edge of the side plates, as shown in

Figs.13.32a and 13.32b. Moreover, new cracks also branched out from these horizontal peeling cracks. All these phenomena occurred over wide range of applied moment of 32.0-67.0 kNm (P = 80-165 kNm). The test was terminated at 72.0 kNm (P=180 kN), as no further propagation in peeling cracks was observed. The complete flexural peeling of the plate is considered to have occurred at 48.0 kNm (P=120.1 kN) when the strain magnitudes at the centroid of both the side plates started to fall, as shown in Fig.13.33c.

(a) North side

(b) South side

Fig.13.31. FPS-S-5: Initial flexural crack pattern

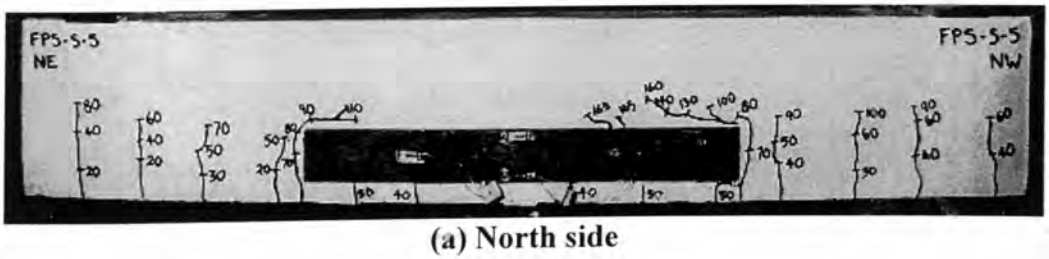

(a) North side

(b) South side

Fig.13.32. FPS-S-5: Crack pattern near plate ends at debonding

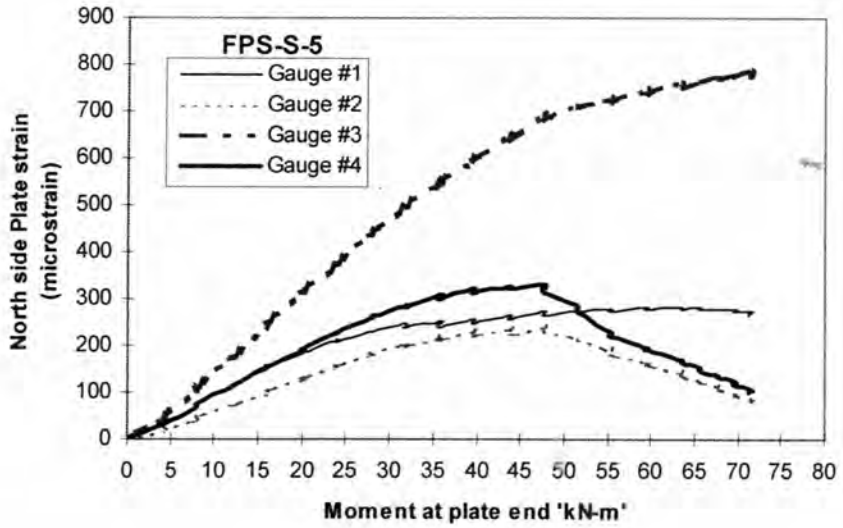

(a) North side

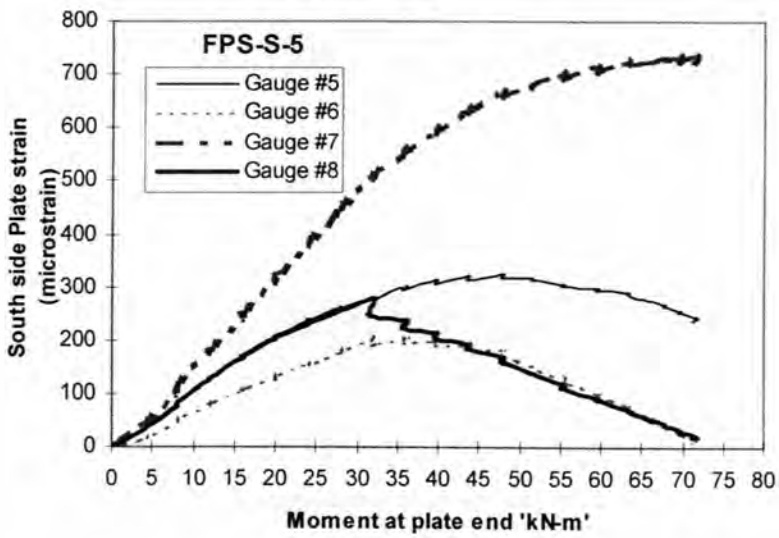

(b) South side

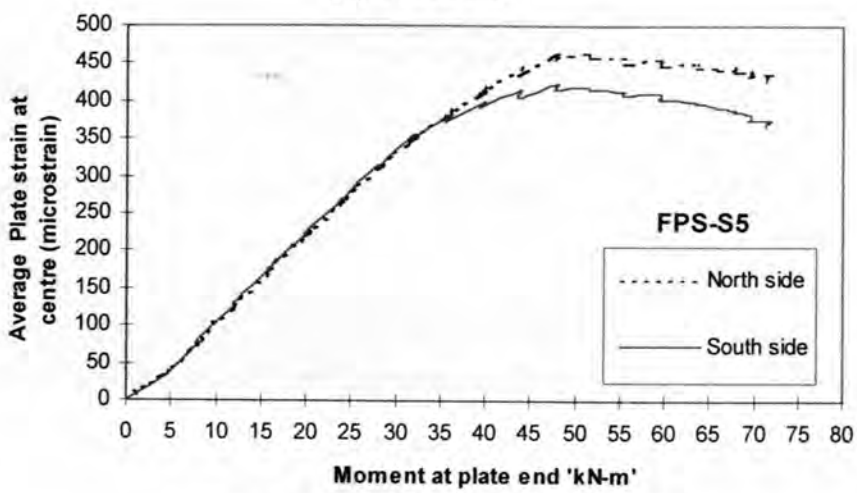

(c) Strain at the centroid of the plate

Fig.13.33. FPS-S-5: Longitudinal strain variation in plate

The results from the present test are given in Table-13.13. The strain gauges shown in Fig.13.29a are listed in column(1) in Table-13.13, and they have been grouped in column(2) according to their longitudinal position. The loads in column(3) are the applied loads at which the strains in the corresponding gauges reduced having reached their maximum values which are listed in column(4); this was interpreted as the load at which debonding occurred in the region adjacent to the strain gauge. The corresponding debonding moments are given in column(4). The strain magnitude and the corresponding moment at the centroid of the side plates are also indicated.

TABLE-13.13: Test results of Beam FPS-S-5

Position group (1)	Strain-gauge Level & No. (2)	Total Applied Load P(kN) (3)	Moment (kNm) (4)	Maximum Strain (micro-strain) (5)
North side plate				
Quarter	Middle(No.1) Middle(No.4)	159.2 120.1	63.5 48.0	283 329
Centre	Top (No.2) Bottom (No.3)	120.1 179.5	48.0 71.8	238 786
Centroid	Mean of #2&#3	120.1	48.0	464
South side plate				
Quarter	Middle(No.5) Middle(No.8)	120.1 80.3	48.0 32.1	329 278
Centre	Top (No.6) Bottom (No.7)	120.1 179.5	48.0 71.8	329 734
Centroid	Mean of #6&#7	120.1	48.0	425

The variation of longitudinal strains in the side plates with applied moment is illustrated in Figs.13.33a-c. It can be seen that the strain magnitudes at the quarter points and at the top fibre at the centre point shows a falling trend due to the propagation of peeling cracks at the plate ends. However, the corresponding strain readings at the bottom fibre (i.e. gauge locations #3 and #7) increased linearly with the applied load and they did not show any fall. Only the rate of increase in strain was

slowed down due to the propagation of the debonding cracks and the strain profile flattened out at this stage.

Fig.13.33c shows that the slope of the falling branch of the strain profile at the centroid of the side plates is not steep. Therefore, the flexural peeling of the side plated beam FPS-S-5 can be considered as smooth and gradual. Figure 13.34 illustrates the relationship between the applied load and the deflection at the mid-span of the beam. The maximum deflection recorded at the end of the test was 18.7 mm.

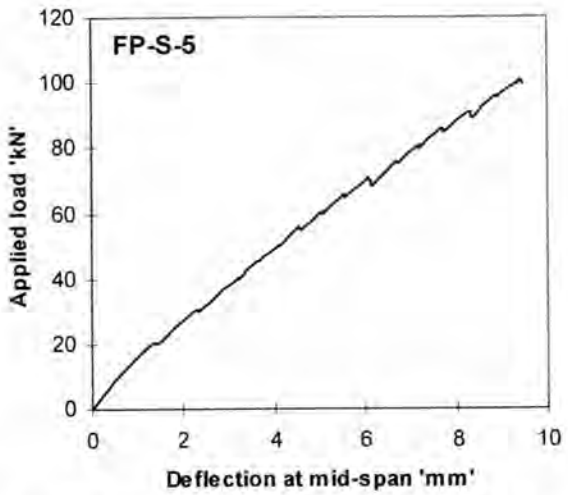

Fig.13.34. FPS-S-5: Mid-span deflection Vs Applied moment

13.4.6.2 Beam FPS-C-8.5

Beam FPS-C-8.5 was bonded with carbon FRP plates 600 mm long, 80 mm deep and 8.5 mm thick to the sides. The elastic modulus of this plate is about 65% that of the steel plate.

Several flexural cracks first occurred in the unplated region as the applied moment was in the range 8.0 kNm-16.0 kNm (that is an applied load P=20-30 kN) as shown in Fig.13.35. Flexural cracks also appeared below the side plates when the applied moment was varied from 16.0 kNm to 20.0 kNm (P=40-50 kN). The next significant cracks to occur were the ones that formed in the vicinity of the plate ends, when the moment was increased to 22.0 kNm (P=55.0 kN) as shown in Fig.13.35. The plate end cracks first extended to the top corner of the side plates and then propagated

gradually along the top edge of the side plates on further application of the load, as shown in Figs.13.36a and 13.36b. Moreover, the plate end crack extended below the side plate on the north-eastern side. All these phenomena occurred over wide range of applied moment of 28.0-48.0 kNm (P = 70-120 kNm). The test was terminated at 68.0 kNm (P = 170 kN), as no further propagation in peeling cracks was observed. The complete flexural peeling of the plate is considered to have occurred at 64.2 kNm (P = 160.6 kN) when the strain magnitudes at the centroid of both the side plates started to fall, as given in Table-13.14.

Fig.13.35. FPS-C-8.5: Initial flexural crack pattern

(a) North side

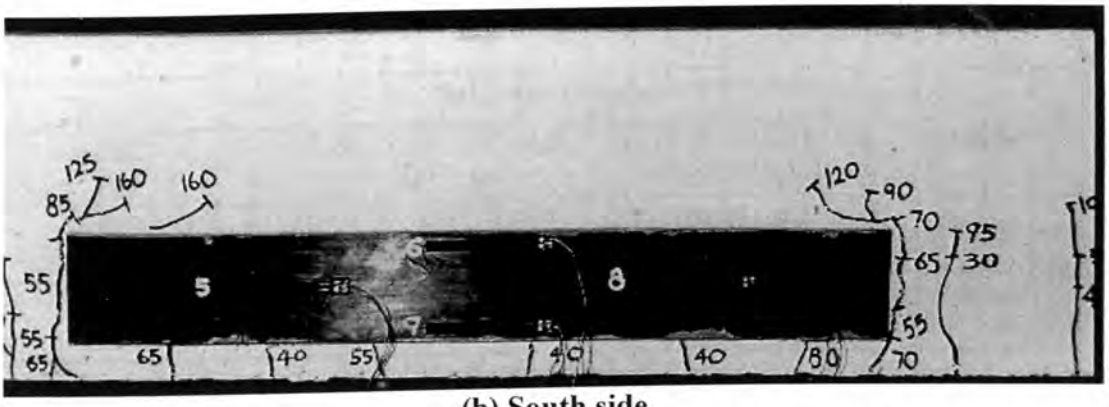

(b) South side

Fig.13.36. FPS-C-8.5: Close view of final crack pattern

The variation of longitudinal strains in the side plates with applied moment is illustrated in Figs.13.37a-c. It can be seen that the strain magnitudes at the quarter points and at the top fibre at the centre point show a smooth, gradual falling trend due to the propagation of peeling cracks at the plate ends. However, the corresponding strain readings at the bottom fibre (i.e. gauge locations #3 and #7) increased with the applied load and they did not show any fall. Fig.13.37c shows that there was no abrupt fall in the strain profile at the centroid of the side plates. Therefore, the flexural peeling of the side plated beam FPS-C-8.5 can be considered as smooth and gradual. Figure 13.38 illustrates the relationship between the applied load and the deflection at the mid-span of the beam. The maximum deflection recorded at the termination of the test was 17.8 mm.

TABLE-13.14: Test results of Beam FPS-C-8.5

Position group (1)	Strain-gauge Level & No. (2)	Total Applied Load *P*(kN) (3)	Moment (kNm) (4)	Maximum Strain (micro-strain) (5)
North side plate				
Quarter	Middle(No.1) Middle(No.4)	80.6 140.1	32.2 56.3	256 307
Centre	Top (No.2) Bottom (No.3)	125.7 160.2	50.3 64.2	174 820
Centroid	Mean of #2&#3	160.6	64.2	477
South side plate				
Quarter	Middle(No.5) Middle(No.8)	140.7 125.7	56.3 51.3	202 271
Centre	Top (No.6) Bottom (No.7)	130.0 169.6	52.0 67.8	209 880
Centroid	Mean of #6&#7	160.6	64.2	529

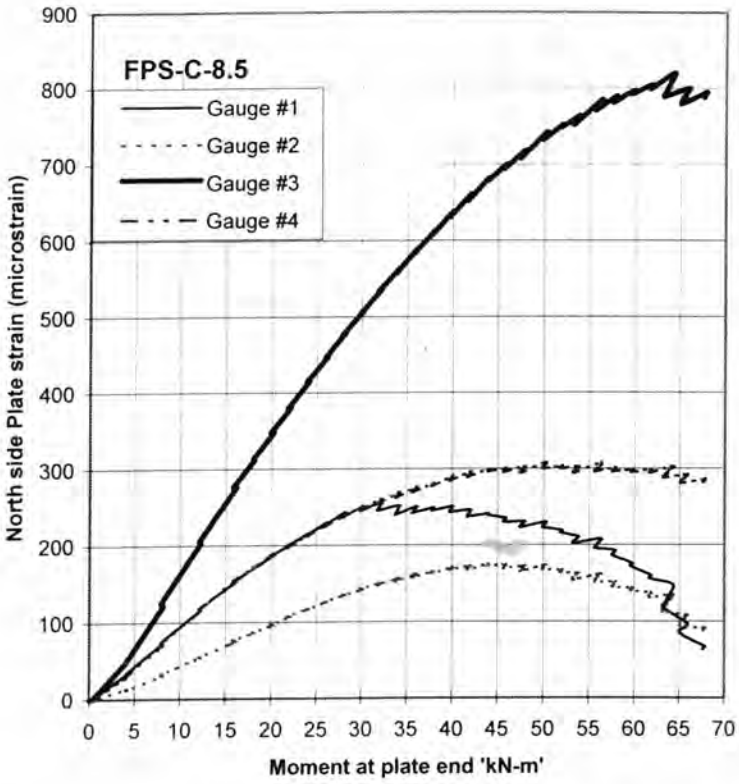

Fig.13.37(a). North side

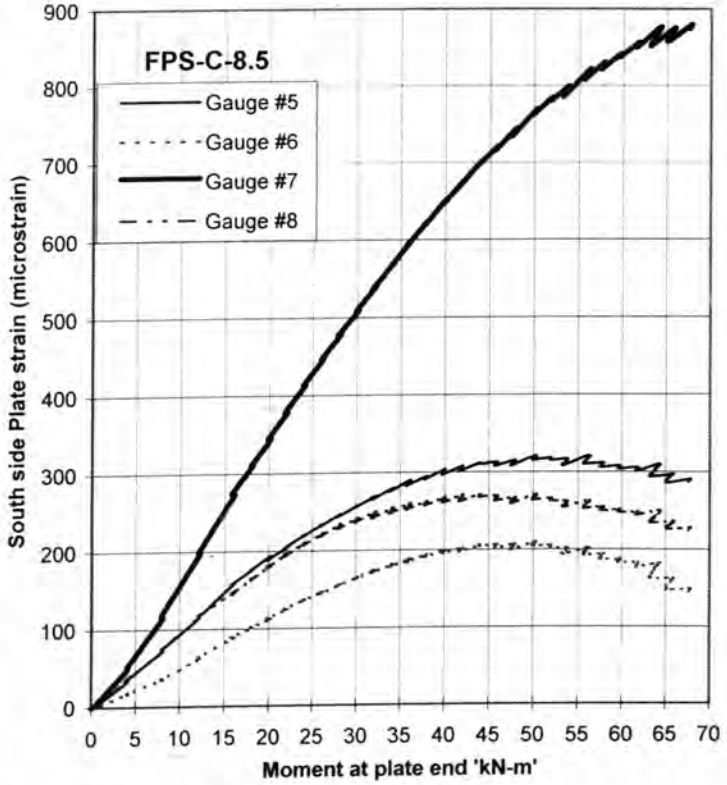

Fig.13.37(b). South side

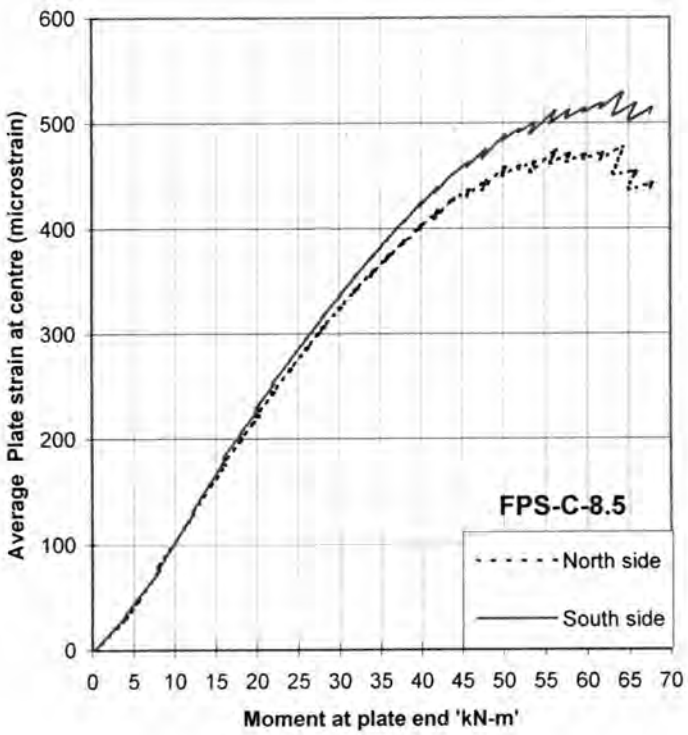

Fig.13.37(c). Strain at the centroid of the plate
Fig.13.37. FPS-C-8.5: Longitudinal strain variation in plate

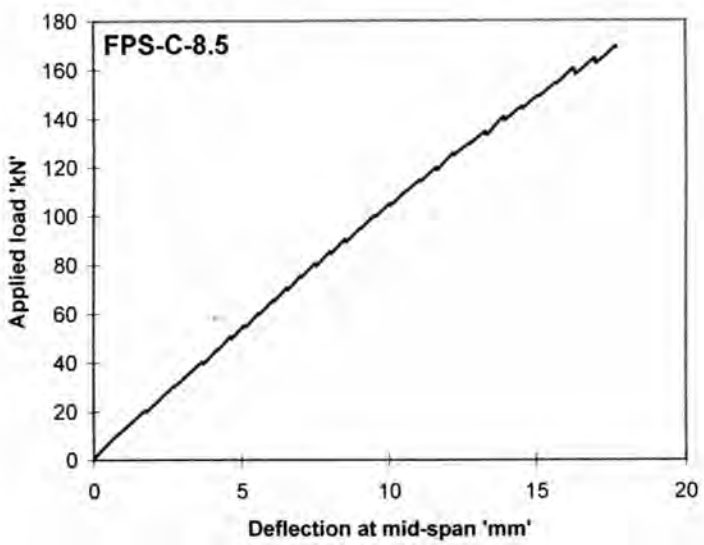

Fig.13.38. FPS-C-8.5: Mid-span deflection Vs Applied moment

13.4.6.3 Beam FPS-CG-24

Beam FPS-CG-24 was bonded with carbon and glass FRP plates 350 mm long, 75 mm deep and 24 mm thick to the sides. The elastic modulus of this plate is about one-fifth that of the steel plate. Several flexural cracks were observed in the unplated

region as the applied moment was in the range 8.0 kNm-16.0 kNm (that is an applied load P=20-30 kN) as shown in Figs.13.39a and 13.39b.

(a) North side

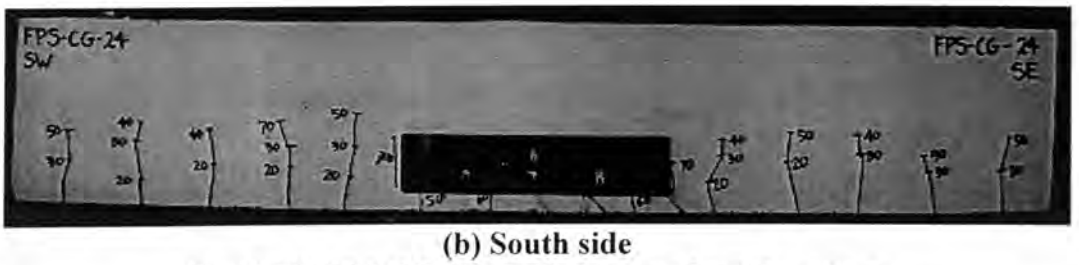

(b) South side

Fig.13.39. FPS-CG-24: Initial flexural crack pattern

Flexural cracks also appeared below the side plates when the applied moment was varied from 20.0 kNm to 24.0 kNm (P=50-60 kN). The next significant cracks to occur were the ones that formed in the vicinity of the plate ends, when the moment was increased to 28.0 kNm (P=70.0 kN) as shown in Figs.13.39a and 13.39b. The plate end cracks first extended to the top corner of the side plates when the applied moment was increased to 32.0 kNm (P=80.0 kN). They propagated along the top edge of the side plates only to a small extent and then they branched out upward on further application of the load, as shown in Figs.13.40a and 13.40b. Moreover, the plate end crack could also be seen extending below the side plate also. All these phenomena occurred over wide range of applied moment of 32.0-60.0 kNm (P=80-150 kNm). The test was ended at 72.0 kNm (P=180 kN), as no further appreciable propagation of peeling cracks could be observed. The complete flexural peeling of the plate is considered to have occurred at 36.3 kNm (P=90.6 kN) when the strain magnitudes at the centroid of both the side plates started to fall, as shown in Table-13.15.

(a) North side

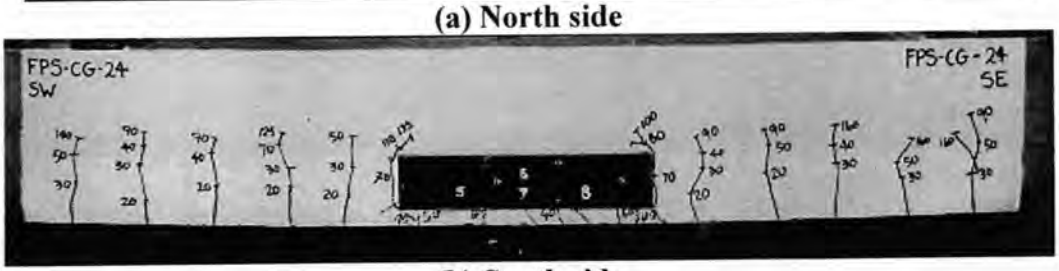

(b) South side

Fig.13.40. FPS-CG-24: Final crack pattern

TABLE-13.15: Test results of Beam FPS-CG-24

Position group (1)	Strain-gauge Level & No. (2)	Total Applied Load P(kN) (3)	Moment (kNm) (4)	Maximum Strain (micro-strain) (5)
North side plate				
Quarter	Middle(No.1) Middle(No.4)	60.7 50.6	24.3 20.2	58 65
Centre	Top (No.2) Bottom (No.3)	50.6 160.7	20.2 64.4	43 346
Centroid	Mean of #2&#3	90.6	36.3	155.5
South side plate				
Quarter	Middle(No.5) Middle(No.8)	50.6 50.6	20.2 20.2	88 74
Centre	Top (No.6) Bottom (No.7)	50.6 161.1	20.2 64.4	55 375
Centroid	Mean of #6&#7	90.6	36.3	170

The variation of the longitudinal strains in the side plates with applied moment is illustrated in Figs.13.41a- c. It shows that the strain magnitudes at the quarter points and at the top fibre at the centre point shows a steep falling trend due to the propagation of the plate end peeling cracks. However, the corresponding strain readings at the bottom fibre (i.e. gauge locations #3 and #7) increased with the applied load and they did not show any abrupt fall. Fig.13.41c shows that there was steep fall

in the strain profile at the centroid of the side plates due to the propagation of plate end debonding crack.

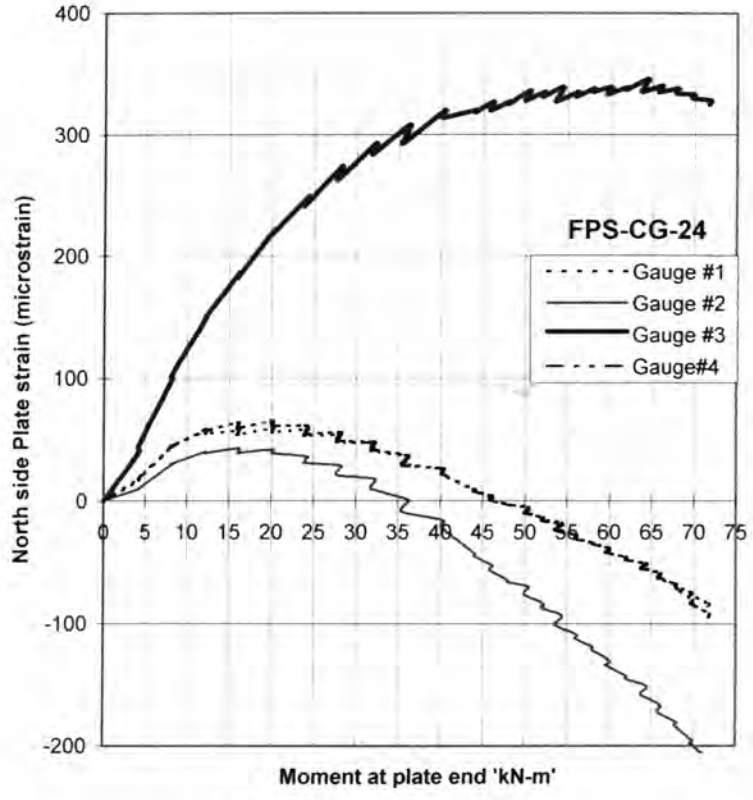

Fig.13.41(a). North side

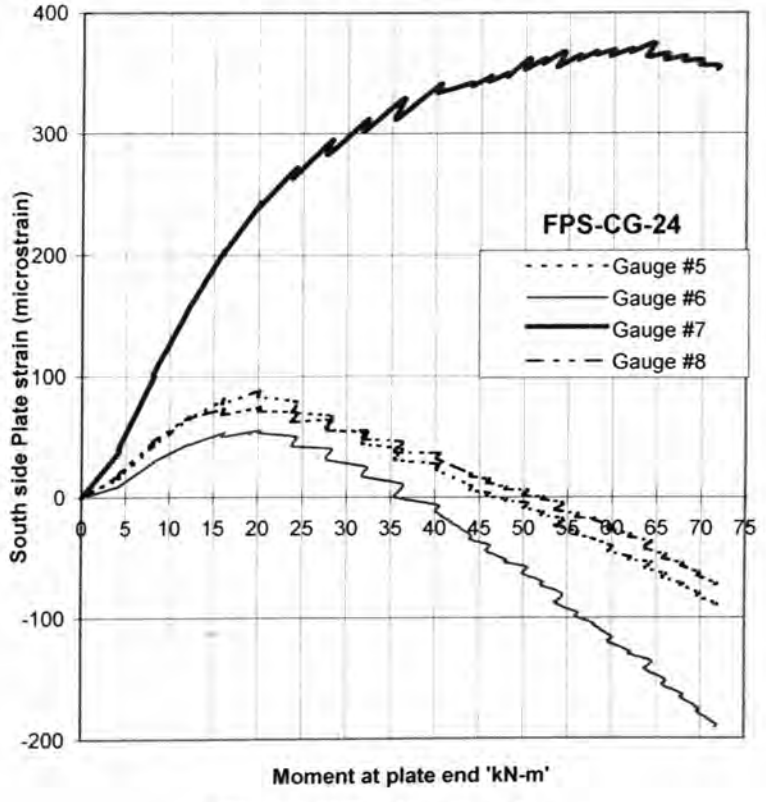

Fig.13.41(b). South side

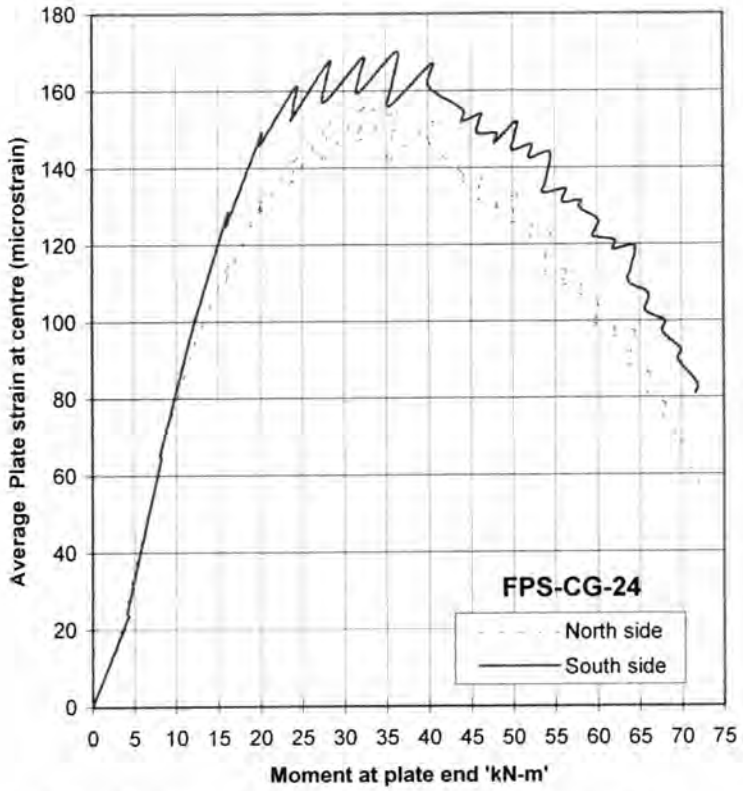

Fig.13.41(c). Strain at the centroid of the plate
Fig.13.41. FPS-CG-24: Longitudinal strain variation in plate

Figure 13.42 illustrates the relationship between the applied load and the deflection at the mid-span of the beam. The maximum deflection recorded at the termination of the test was 19.35 mm.

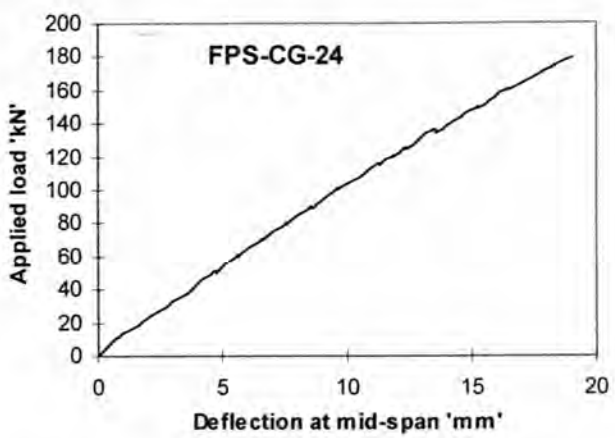

Fig.13.42. FPS-CG-24: Mid-span deflection Vs Applied moment

13.4.7 Discussion of test results from side plated beams

The sequence of flexural peeling in the tests carried on the beams bonded with different plate materials to their sides can be summarised as follows. Firstly, flexural cracks appeared at very low applied loads in the unplated region and a slight increase in applied load caused cracks to appear in the concrete below the side plates also. In the next stage, cracks appeared in the vicinity of the plate ends and they extended upwards to the top corners of the side plates. Next, these cracks propagated by a small length along the top side of the plates. This led to the drop in strain readings in the central portion of the plates. These debonding cracks did not immediately propagate towards the centre of the plates but stabilised for considerable increase in the application of load. However, some more cracks branched out upwards from the corners of the side plates. In some cases, there was a minor, downward extension of the plate end crack along the bottom corner of the side plates. The flexural peeling mechanism in side plated beams can be considered as smooth and gradual as the fall in strain readings occurred over a range of applied moment. Furthermore, the plate end cracks that impair the bond between the plate and the concrete propagated steadily and stabilised for a long period before the end of the tests. The other significant observation was that the peeling mechanism in the FRP plated beams was similar to the steel plated beam even though the elastic modulus of the carbon and glass FRP plate and carbon FRP plate were one-fifth and one-third that of the steel plate respectively. Table-13.16 summarises the salient features of the results from this series of tests.

Table-13.16: Test results (FPS series)

No	Designation	t_{sp} (mm)	d_{sp} (mm)	E_p (MPa)	stiffness $E_p t_{sp}$(kN/mm)	M_{pure} (kNm)	Max. strain
1	FPS-S-5	5	75	200,000	2000	48.0	786×10^{-6}
2	FPS-C-8.5	8.5	80	130,550	2219.4	64.2	880×10^{-6}
3	FPS-CG-24	16	75	42,110	1347.5	36.3	375×10^{-6}

Figure 13.43 shows the variation of the pure flexural peeling moment capacity of the beam with that of the axial stiffness of both the side plates. It shows an increase in capacity with the increase in axial stiffness of the side plates.

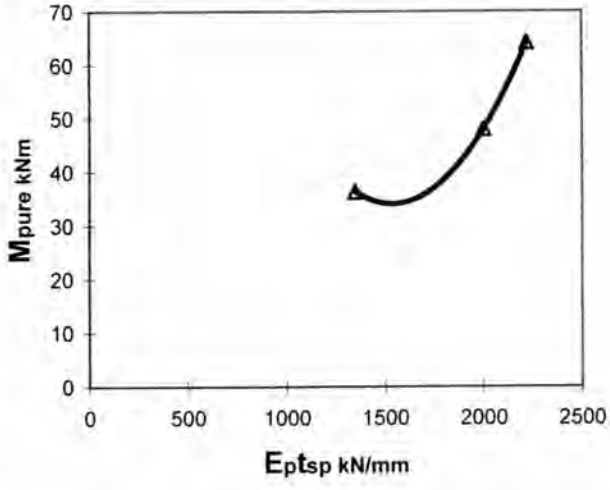

Fig.13.43. Experimental flexural peeling moment Vs Axial stiffness

13.5 Analysis of all test results

Presently, the only equations available to quantify the pure flexural peeling moment capacity of tension face plated beams or side plated beams are the ones developed by Oehlers and his team (Sections 2.7.3.2 and 2.8.1.1). However, these equations were derived for and calibrated against the test results obtained from steel plated beams. Besides, the basic equations themselves have inherent scatter. The objective of the present limited parametric study on FRP plated beams is to probe the possibility of extending the existing analytical approaches for the conventional steel plated beams. Therefore, the test results obtained in this study are brought to the same platform as those of the steel plated beam as explained subsequently.

Table-13.17 summarises and compares the analytical results with the test results. Column(2) shows the ratio between the elastic modulus of the FRP plate and the steel plate. Column(3) gives the pure flexural peeling capacities of the beams obtained from tests and column(4) shows the theoretical values obtained from the equations for

the mean flexural peeling capacities (Eqn.2.5 for tension face plates and Eqn.2.7a for side plates using the FRP plate stiffness). Column(5) removes the scatter between the test results and the theoretical results so that the variation can be derived later. To achieve this, the test M_{pure} for the steel plate is made equal to the corresponding theoretical magnitudes and for the FRP plated beams, all the test results were multiplied by the coefficient ($M_{pure,test(steel)}/M_{pure,theory(steel)}$). Here $M_{pure,test(steel)}$ and $M_{pure,theory(steel)}$ are the pure flexural peeling capacity of the steel plated beam FP-S-5 that was obtained from the test and theory respectively. Column(6) gives the theoretical mean flexural peeling strength of the beam plated with a steel plate having the same thickness as that of the FRP plate. Column(7) is the ratio between the adjusted test strength in Column(5) and the theoretical strength of the equivalent steel plated beam in Column(6).

TABLE-15.17: THEORETICAL AND TEST RESULTS

Designation (1)	E_p/E_s (2)	$M_{pure,test}$ (kNm) (3)	$M_{pure,theory}$ (kNm) (4)	$M_{pure,test}$ *(adjusted)* (kNm) (5)	$M_{pure,steel\text{-}theory}$ *(Equivalent)* (kNm) (6)	$M_{pure,test(adj)}/M_{pure,steel(Eqv)}$ (7)
Tension face plated beams						
FP-S-5	1.0	26	46	46	46	1.0
FP-C-8.5	0.653	26	43.5	46	28.4	1.62
FP-CG2-16	0.211	28	61.6	49.6	9.9	5.01
FP-G-32	0.051	42	106.1	74.3	5.4	13.76
FP-CG-16	0.044	62	219.2	109.7	9.66	11.36
Side plated beams						
FPS-S-5	1.0	55	35.6	35.6	35.6	1.0
FPS-C-8.5	0.653	60	43.7	38.8	28.5	1.36
FPS-CG-24	0.211	40	47.0	25.9	9.9	2.61

Fig.13.45 shows the relationship between the quantities $M_{pure,test}/M_{pure,theory}$ and E_p/E_s. The best fit curve is described by the following Eqn.13.4 and the coefficient of correlation is 0.55.

$$\frac{M_{pure,test}}{M_{pure,theory}} = \left(\frac{E_p}{E_s}\right)^{-0.35} \qquad (13.4)$$

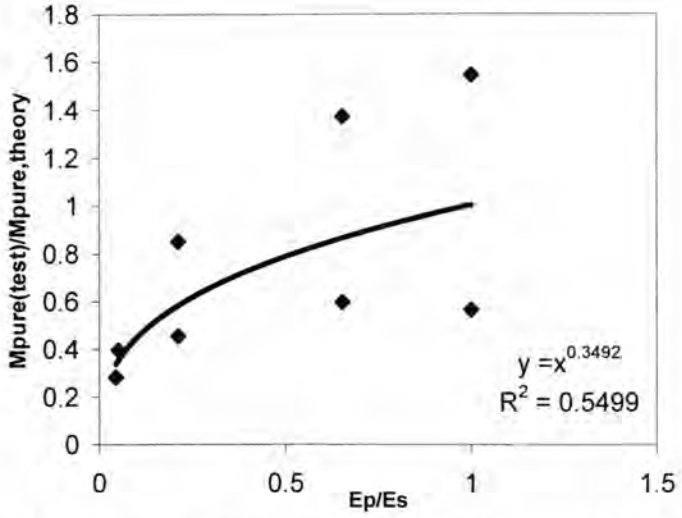

Fig. 13.45 Relationship between $M_{pure,test}/M_{pure,theory}$ and E_p/E_s

As the relationship defined by the Eqn.13.4 has a wide scatter as can be seen from Fig.13.45, it was considered to establish a relationship between the quantities $M_{pure,test}(adjusted)/M_{pure,theory}$ and E_p / E_s as shown in Fig.13.46.

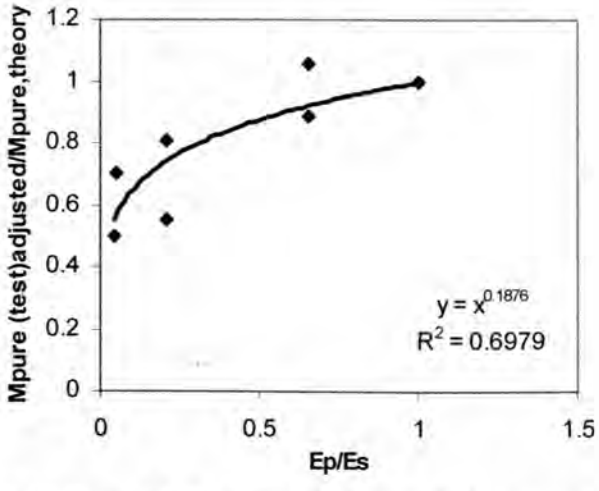

Fig. 13.46. Relationship between $M_{pure,test}/M_{pure,theory}$ and E_p/E_s

The new relationship is defined by the following equation 13.5 and it has a coefficient of correlation of 0.7.

$$\frac{M_{pure,test,adjusted}}{M_{pure,theory}} = \left(\frac{E_p}{E_s}\right)^{-0.19} \qquad (13.5)$$

From Eqn.13.5, we can write the pure flexural peeling capacity of FRP plated beam $M_{pure,frp}$ as

$$M_{pure,frp} = M_{pure,theory}\left(\frac{E_p}{E_s}\right)^{-0.19} \tag{13.6}$$

In Eqn.13.6, the coefficient $\left(\frac{E_p}{E_s}\right)^{-0.19}$ caters for the difference in stiffness of the FRP plated beams and steel plated beam as $M_{pure,theory}$ was derived from the stress distribution shown in Fig.11.1a. It is worth noting that while the shape of the peeling stress distribution in Fig.11.1a was derived from finite element analysis, the actual model was calibrated against the test results from steel plated beams. Furthermore, the stress distribution depends on the stiffness of the plate, when the thickness of the plate is fixed.

Although the relationship defined by Eqn.13.5 has less scatter than the relationship defined by Eqn.13.4, it was decided to establish a relationship between the quantities E_p / E_s and the coefficient in the column(7) of Table-15 to see whether the scatter can be reduced further. Figure 13.47 shows the existence of an exponential relationship between these two quantities with a very good coefficient of correlation (0.96). The equation that defines the relation between them is given as

$$\frac{M_{pure,test,adjusted}}{M_{pure,steel,eqv}} = \left(\frac{E_p}{E_s}\right)^{-0.82} \tag{13.7}$$

Therefore, the following Eqn.13.8 derived from Eqn.13.7 is recommended tentatively for practice to predict the pure flexural peeling capacities of reinforced concrete beams bonded with FRP plates ($M_{pure,frp}$) of elastic modulus E_{frp}.

$$M_{pure,frp} = M_{pure,steel,eqv}\left(\frac{E_{frp}}{E_s}\right)^{-0.82} \tag{13.8}$$

It is worth noting that Eqns.13.6 and 13.8 are empirical and tentative in nature and further research is needed to improve them.

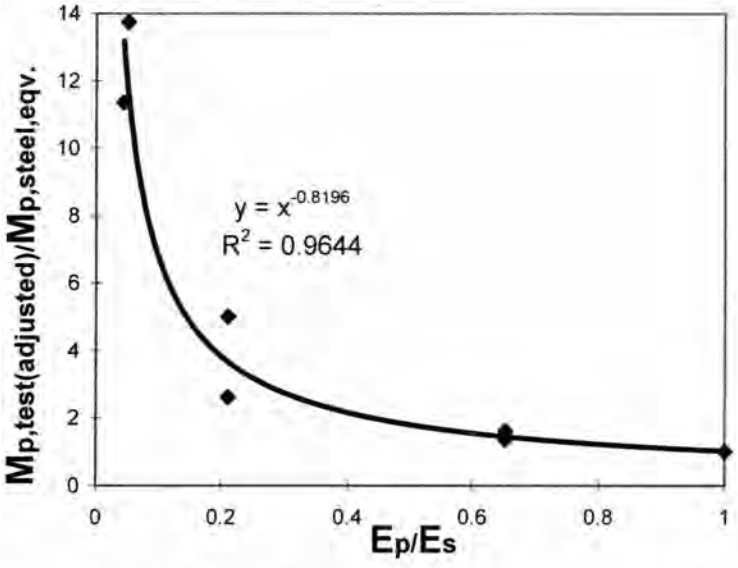

Fig.13.47. Relationship between $M_{pure,test,adjusted}/M_{pure,steel,theory(Equivalent)}$ and E_p/E_s

13.6 Conclusion

1. The tests carried on beams with plates of different materials that were bonded to their tension faces or sides have shown that flexural peeling is initiated by the formation of flexural cracks in the vicinity of the plate end. The peeling mechanism is the same both for steel plated beams and FRP plated beams.
2. The flexural peeling mechanism in side plated beams can be considered as smooth and gradual as the fall in strain readings occurred over a range of applied moment. Furthermore, the plate end cracks that impair the bond between the plate and the concrete propagated steadily and stabilised for a long period before the end of the tests. The other significant observation was that the peeling mechanism in the FRP plated beams was similar to that in the steel plated beam even though the elastic modulus of the carbon and glass FRP and carbon FRP plates were one-fifth and one-third that of the steel plate.

3. In this study, the validity of the model proposed by Oehlers and Moran(1990) was investigated for the FRP sides plated as well as tension face plated beams. Two tentative relationships were derived for computing the $M_{pure,frp}$ as $M_{pure,frp} = M_{pure,theory}\left(\frac{E_p}{E_s}\right)^{-0.19}$ and $M_{pure,frp} = M_{pure,steel,eqv}\left(\frac{E_{frp}}{E_s}\right)^{-0.82}$. Here $M_{pure,steel,eqv}$ is the pure flexural peeling capacity of a plated beam with a steel plate of the same size as the FRP plated beam. These equations will have the same scatter in results as the original equation for the steel plated beams.

References

Oehlers, D.J., and Moran,J.P. (1990). "Premature failure of externally plated reinforced concrete beams." Journal of Structural Engg.,(ASCE). Vol.116, No.4,.978-995.

PART-V: INTERACTION BETWEEN FLEXURAL AND SHEAR PEELING

CHAPTER-14: INTERACTION BETWEEN SHEAR AND FLEXURAL PEELING OF COMPRESSION FACE PLATED REINFORCED CONCRETE BEAMS

CONTENTS

14.1 Introduction

The objective of this series of tests is to study the peeling behaviour of compression face plated beams when the plate ends are terminated in a region where both shear force and bending moment are present. The study was further divided into two groups as follows:

(a) Group-I: Beams in which the plate ends under bending compression are subjected to the least bending moment than in the other regions of the plate under bending compression as in the case of the plate end C of the plate CD in Fig.14.1a.

(b) Group-II: Beams in which the plate ends under bending compression are at a higher moment than in the other locations of the plates under bending compression as in the case of the plate end F of the plate EF in Fig.14.1a.

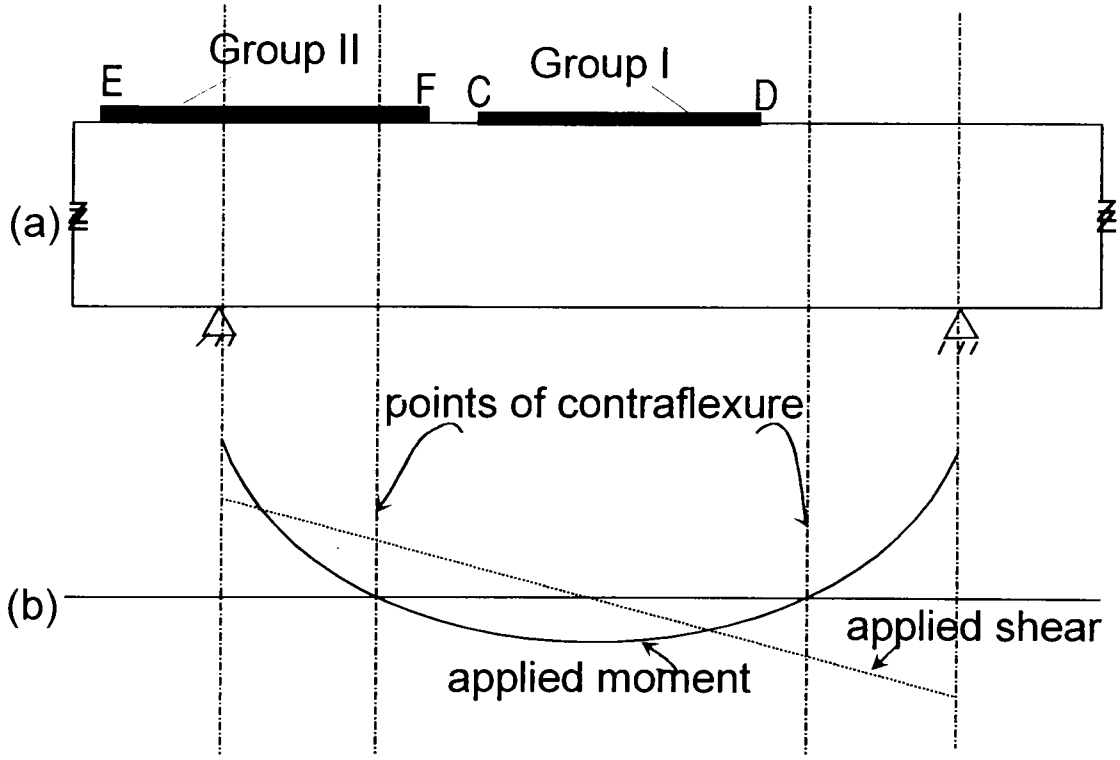

Fig.1 Group-I and Group-II beams

The beams used for preparing the test specimens were earlier tested for pure flexural peeling of tension face plated beams in FP series (Section 12.2). The plates

were removed and the concrete was repaired before preparing the specimen for the present test series. All the beams were bonded with 20 mm thick steel plates to their compression faces. The only parameter varied was the point of termination of the plate end from the support so as to place the plate ends in region of varying ratios of moment to shear force. The material properties are the same as given in Section 12.2.5.

14.2 Group I Beams

14.2.1 Test specimens

The reinforcement details of the basic, unplated reinforced concrete beam are given in Fig.12.1a (Section 12.2.1). In this series, two RC beams (Fig.12.1a) were used to prepare four test specimens as shown in Fig.14.2a-c. Both shear spans of the beam were tested individually. The longer shear span was clamped suitably while testing the short span. The details of the four test specimens are as follows:

(a) Test SP-C20: The plate end was terminated exactly over the support so that the plate end will be under pure shear force with zero moment (Fig.14.2a). This test gives the pure shear peeling strength of the plated beams tested in this series. Test SP-C20 was discussed in detail in Section 9.6.5. It may be recalled that the test FP-C20 gives the pure flexural peeling capacity for this series of tests (Refer Section 12.3.3).

(b) Test SF-C1: The plate end was located 250 mm from the nearest support (Fig.14.2b).

(c) Test SF-C2: The plate end was located 500 mm from the nearest support (Fig.14.2c).

(d) Test SF-C3: The plate end was located 1000 mm from the nearest support (Fig.14.2d).

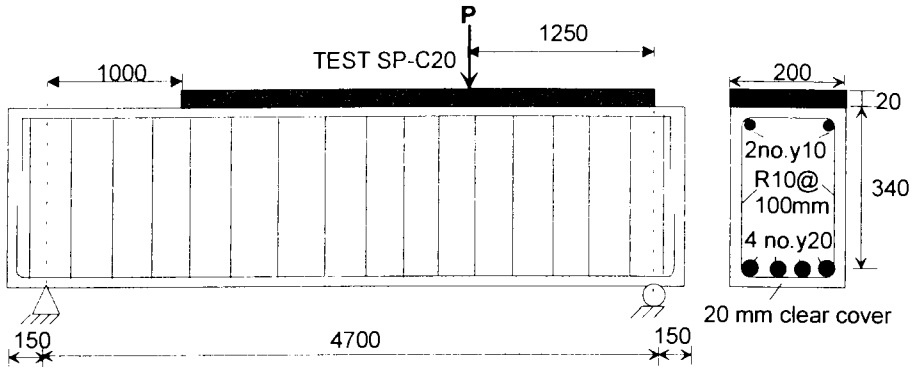

(a) Test SP-C20

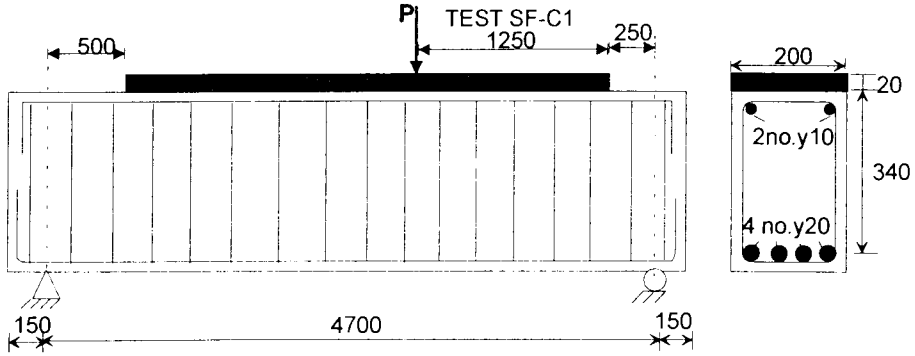

(b) Test SF-C1

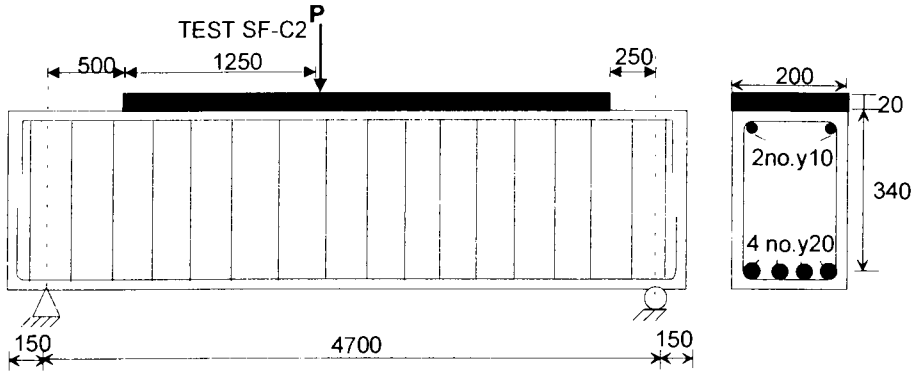

(c) Test SF-C2

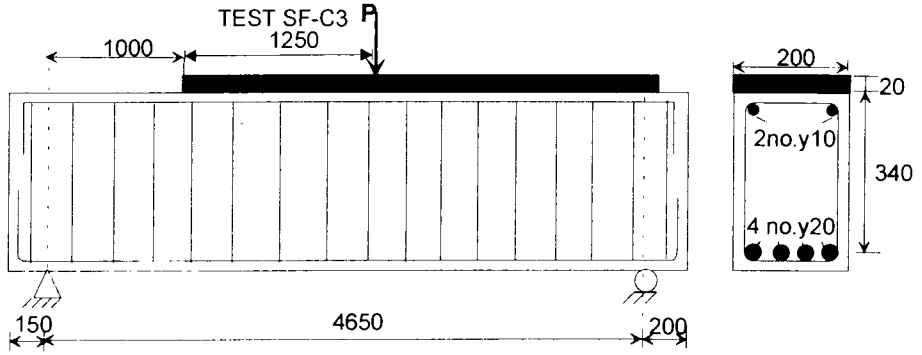

(d) Test SF-C3

Fig.14.2. Group-I beams

All the beams were simply supported over an effective span of 4700 mm except for the case of SF-C3 for which the span was 4650 mm. The load was applied on the top of the beam by a hand operated hydraulic jack through a load cell and a knife-edge bearing. The load point was kept at a distance of 1250 mm from the plate end for all the beams tested; this is to eliminate any local stiffening effect on the peeling behaviour due to the concentrated applied load. The ratio of the distance between the position of the applied load and the support (>1250 mm) and the depth of the beam (370 mm) was kept greater than 3 to avoid the increase in shear strength due to short span tied arching action.

14.2.2 Material properties

Matreial properties are the same for the beams tested in FP series and hence refer to Section 12.2.5.

14.2.3 Instrumentation

Strain gauges were bonded to the external plates in order to detect debonding at various sites of the plates. The arrangements of the strain gauges and their numbering are shown in Figs.14.3 and 14.4 for all the tests conducted. The beam deflection at the load point was monitored by both a dial gauge and a transducer.

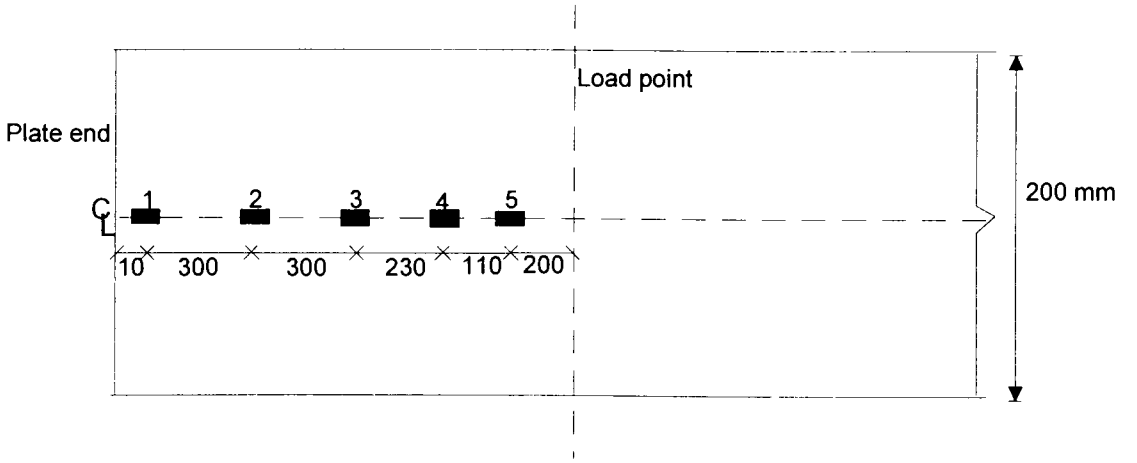

Fig.14.3. Strain gauge arrangement for Test SF-C3

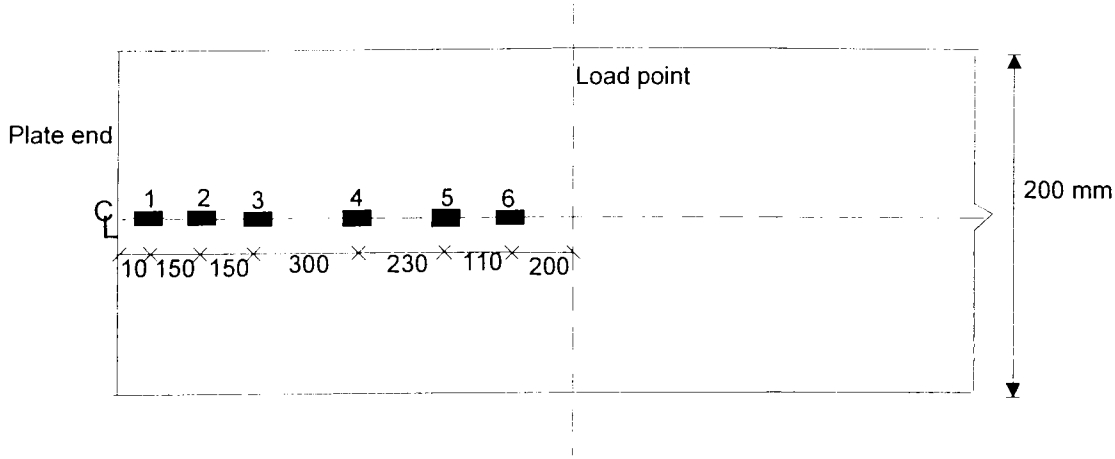

Fig.14.4. Strain gauge arrangement for Tests SP-C20, SF-C1, and SF-C2

14.3 Test results for Group I beams

14.3.1 SP-C20

A detailed description of test results of beam SP-C20 can be found in Section 9.6.5.

14.3.2 SF-C1

Test SF-C1 was carried on the shear span in which the 20 mm thick compression face plate was terminated at a distance 250 mm from the support, as shown in Fig.14.2b. The position of the applied load P was such that the shear force V in the span was 0.681P kN and the moment at the plate end was $0.17P$ or $0.25V$ kNm.

14.3.2.1 Crack propagation and failure mode

A few flexural cracks were noticed below the load point when the applied load was 50 kN (V=34 kN). Two diagonal shear cracks, one at a distance of 470 mm from the support at an applied load of 100 kN (V=68.1 kN) and another at a distance of 1200 mm from the support at an applied load of 110 kN (V=74.9 kN), appeared in the shear span being tested as shown in Fig.14.5. As the load was increased to 130 kN (V=88.5 kN), another diagonal shear crack occurred near the support as shown in Fig.14.6. This caused the applied load to drop to 125.3 kN. On reapplying the load, the two diagonal cracks close to the support propagated rapidly upwards, joined together and then propagated parallel to the bottom edge of the plate till the horizontal portion of the crack reached the load plate at 140 kN (V=95.3 kN) as can be seen in Fig.14.6.

This led to the sudden drop of the applied load from 140 kN to 122 kN. A flexural shear crack appeared when the applied load was 150 kN (V=102.1 kN). When the applied load was 175 kN (V=119.1 kN), the long horizontal debonding crack traversed back to the support as shown in Figs.14.7 and 14.8. The load also dropped to 155 kN (V=105.5 kN) at which the load test was terminated. Thus, the complete debonding of the compression face plate occurred.

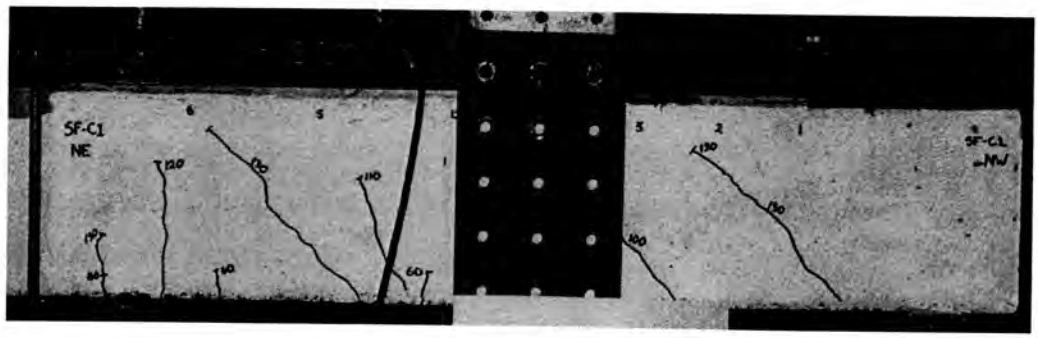

Fig.14.5. Test SF-C1: Crack pattern at P=110 kN

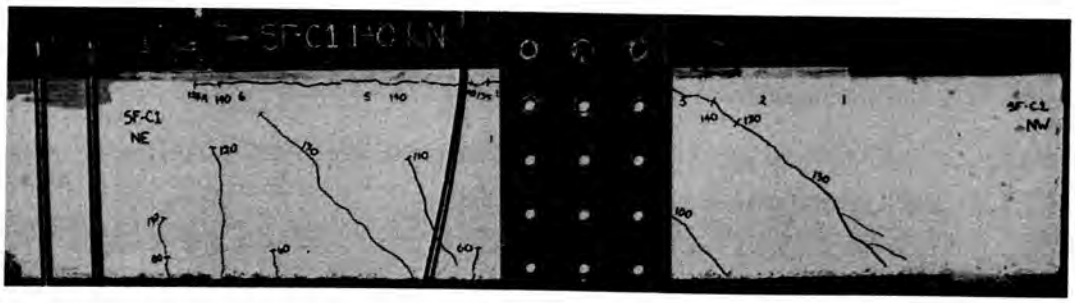

Fig.14.6. Test SF-C1: Crack pattern at P=140 kN

Fig.14.7. Test SF-C1: Final crack pattern-North side

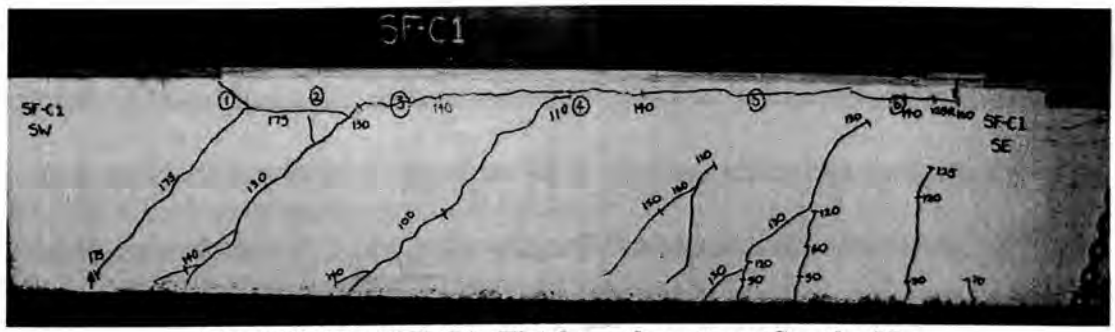

Fig.14.8. Test SF-C1: Final crack pattern-South side

14.3.2.2 Longitudinal strains in the compression face plate

Figure 14.9 shows the variation of longitudinal strains recorded at all gauge sites in the compression face plate (refer Fig.14.4) with the shear force in the shear span tested. The occurrence of the diagonal shear cracks close to the support at a shear load of 68.1 kN can be observed from Fig.14.9 by the drop in strain readings and kinks the in the strain charts for the gauges #1, #2, #3, and #4.

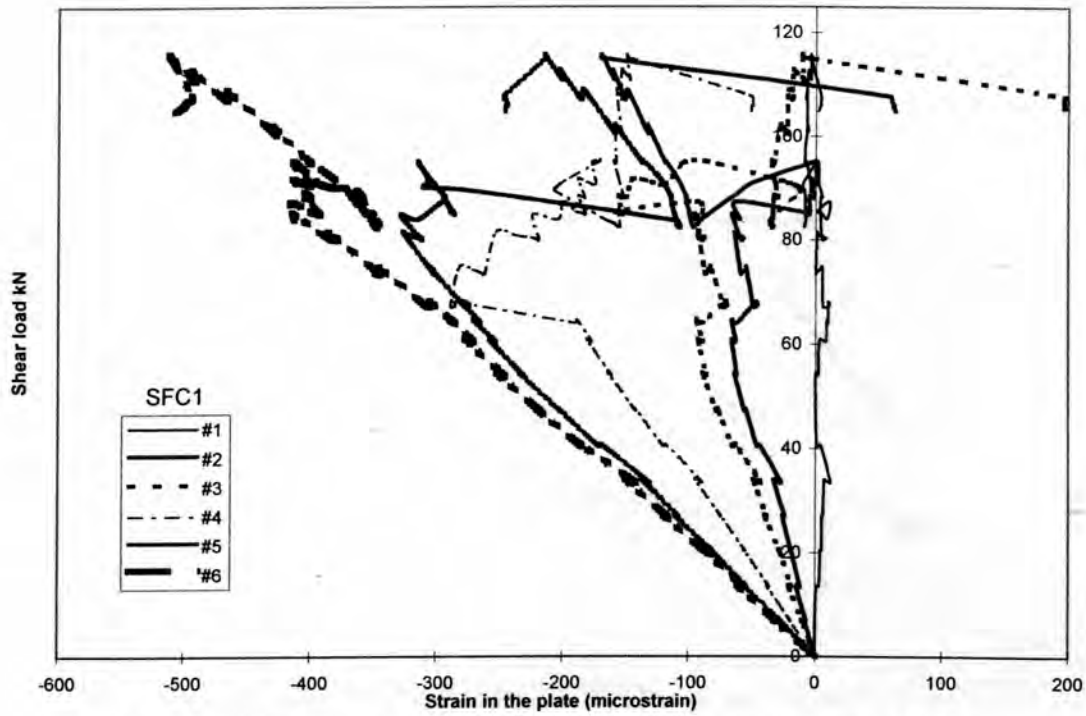

Fig.14.9. SF-C1: Longitudinal strains in compression face plate

The propagation of the horizontal debonding crack that emanated from these diagonal cracks at the shear load of 95.3 kN is marked by the long plateau in the strain charts for the gauges #2, #3, #4, and #5. The strain curves also intersect with one

another at this level indicating the loss of bond due to the propagation of debonding crack towards the load point. Finally, the complete debonding is denoted by the drop in both shear load and strain readings at all the gauge locations at the shear load of 119 kN. The maximum strain recorded in the plate was 510 microstrains, which is well below the yield strain of the plate.

14.3.2.3 Deflection

Figure 14.10 illustrates the relationship between the deflection recorded at the load point and the shear force in the shear span tested. The deflection increased linearly with the applied load and some drop in load at various stages indicates the propagation of the debonding crack and local loss of bond. The maximum recorded deflection at the instance of complete debonding was 28.1 mm.

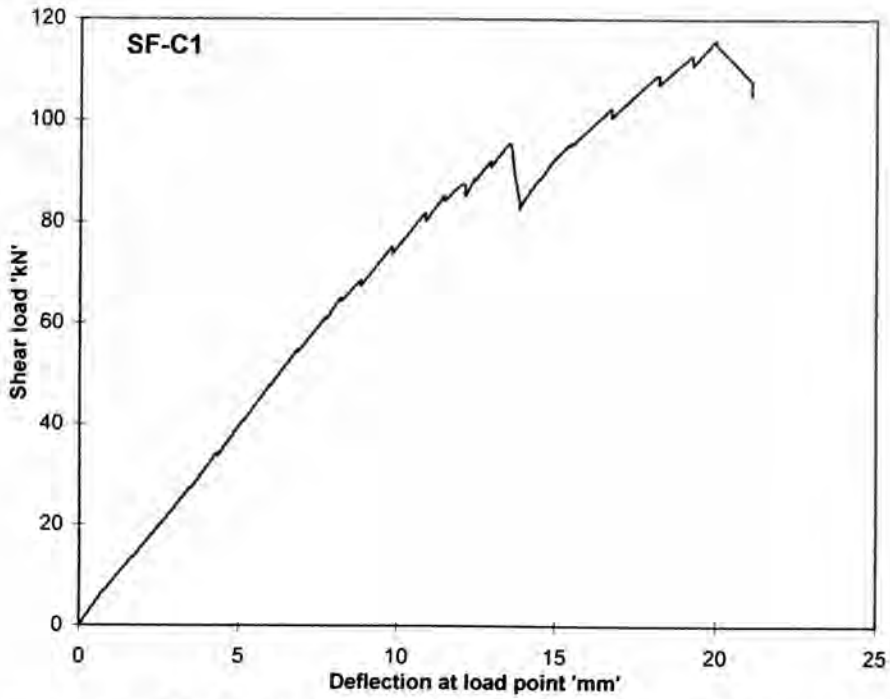

Fig.14.10. SF-C1: Deflection at load point Vs Applied shear load

14.3.3 SF-C2

Test SF-C2 was carried on the shear span in which the 20 mm thick compression face plate was terminated at a distance 500 mm from the support, as shown in Fig.14.2c.

The position of the applied load P was such that the shear force V in the span was $0.628P$ kN and the moment at the plate end was $0.314P$ or $0.5V$ kNm.

14.3.3.1 Crack propagation and failure mode

Two flexural cracks could be observed on either side of the load point when the applied load was in the range of 90-100 kN (V=56.5-62.8 kN). When the applied load was 125 kN (V=78.5 kN), a flexural shear crack formed from the root of an existing minor flexural crack that was at 900 mm from the support, as can be seen from Fig.14.11. As the load was increased to 140 kN (V=87.87 kN), a new diagonal crack appeared in the vicinity of the support. On increasing the applied load to 150 kN (V=94.1 kN), the flexural shear crack propagated along the bottom edge of the plate, as shown in Fig.14.12. This caused the formation of a long horizontal debonding crack that propagated towards the plate end and causing the plate to completely debond as shown in Figs.14.12 and 14.13. The applied load dropped to 110 kN (V=69.0 kN) at which the load test was terminated.

Fig.14.11. SF-C2: Formation of diagonal and flexural shear crack

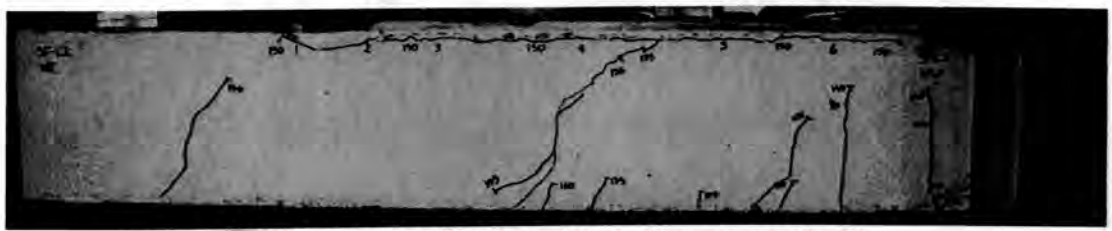

Fig.14.12. SF-C2: Plate debonding on north side

Fig.14.13. SF-C2: Plate debonding on south side

14.3.3.2 Longitudinal strains in the compression face plate

Figure 14.14 depicts the variation of longitudinal strains recorded at all gauge sites in the compression face plate (refer Fig.14.4) with the shear force in the shear span tested. The occurrence of the flexural shear crack at a shear load of 78.5 kN can be observed from Fig.14.14 by the change in shape of the strain curves for the gauges #3, and #4.

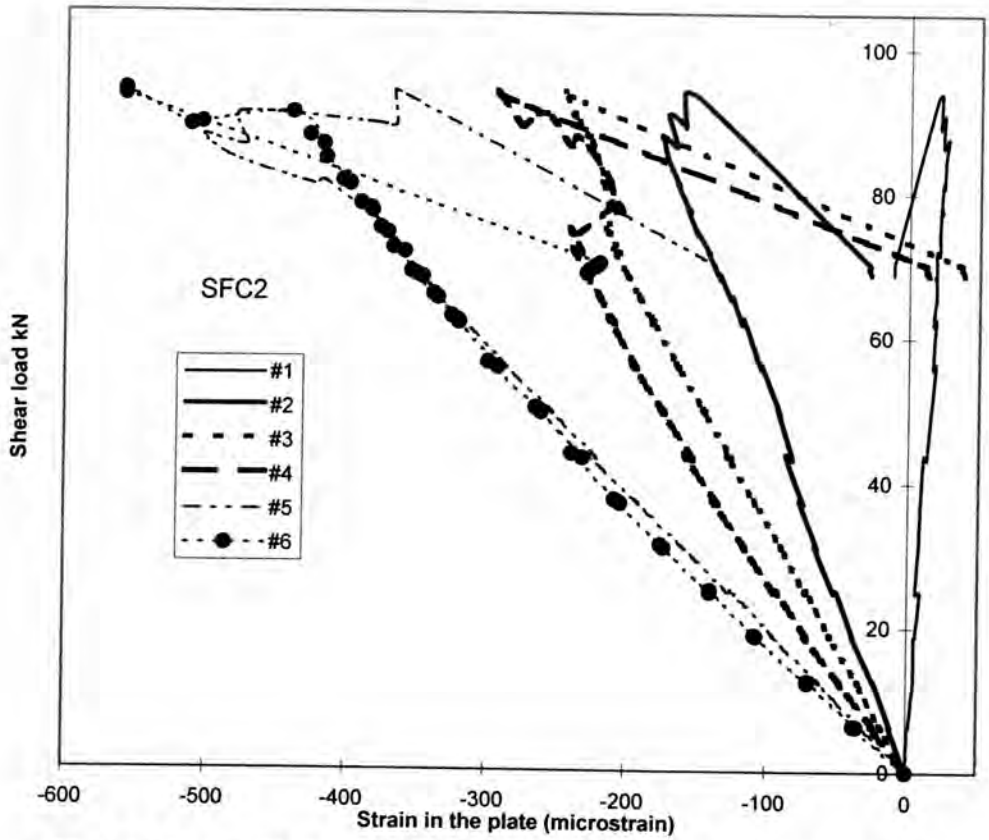

Fig.14.14. SF-C2: Longitudinal strains in compression face plate

The complete debonding of the compression face plate due to the sudden formation of the long, horizontal debonding crack is denoted by the drop in both shear

load and strain readings at all the gauge locations at the shear load of 94.1 kN (Fig.14.14). The maximum strain recorded in the plate was 560 microstrains which is less than the yield strain of the plate.

14.3.3.3 Deflection

Figure 14.15 shows the variation of the deflection recorded at the load point with the shear force in the shear span tested. The deflection increased linearly with the applied load and the sudden drop in load at 94.1 kN denotes the complete debonding of the plate. The maximum recorded deflection at the instance of complete debonding was 15.6 mm .

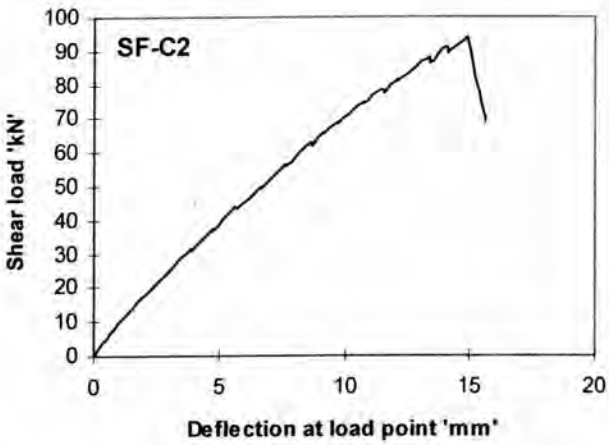

Fig.14.15. SF-C2: Deflection at load point Vs Applied shear load

14.3.4 SF-C3

Test SF-C3 was carried on the shear span in which the 20 mm thick compression face plate was terminated at a distance 1000 mm from the support, as shown in Fig.14.2c. The position of the applied load P was such that the shear force V in the span was $0.523P$ kN and the moment at the plate end was $0.523P$ kNm.

14.3.4.1 Crack propagation and failure mode

A few minor flexural cracks were visible when the applied load was 80 kN (V=42.1 kN). When the applied load was increased to 100 kN (V=52.7 kN), a horizontal debonding crack originating in the vicinity of the load point propagated along the

bottom edge of the plate rapidly towards the plate end. This caused the plate to completely debond from the concrete as shown in Fig.14.16. The corresponding moment at the plate end at debonding was 52.7 kNm. The load also rapidly dropped to 70 kN (V=36.9 kN) and the test was terminated.

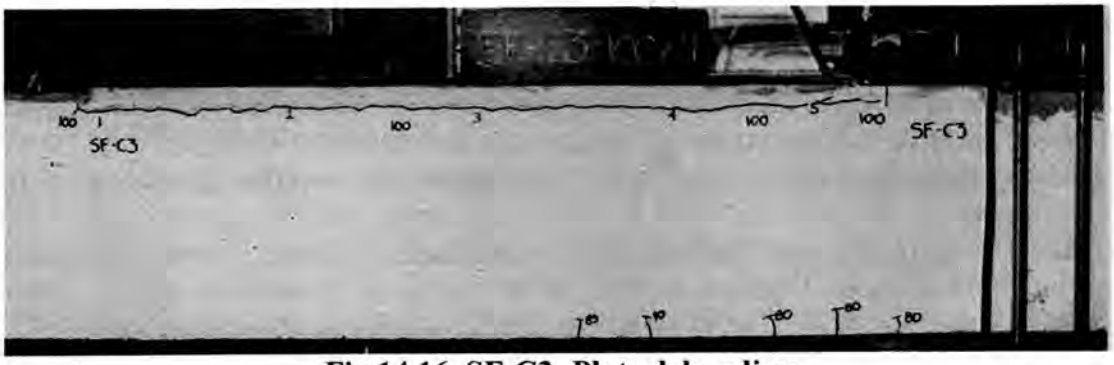

Fig.14.16. SF-C3: Plate debonding

14.3.4.2 Longitudinal strains in the compression face plate

Figure 14.17 shows the variation of longitudinal strains recorded at all gauge sites in the compression face plate (refer Fig.14.3) with the shear load in the shear span tested.

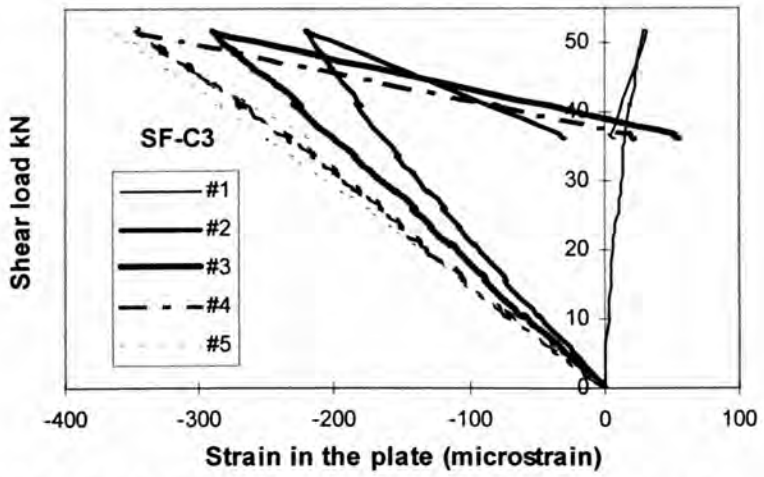

Fig.14.17. SF-C3: Longitudinal strains in compression face plate

It can be seen in Fig.14.17 that the strains varied linearly at all gauge locations till the debonding of the plate at the shear load of 52.7 kN; the debonding is marked by the sudden drop in load as well as strain readings in all the gauge locations.

14.3.4.3 Deflection

Figure 14.18 shows the variation of the deflection recorded at the load point with the shear force in the shear span tested. The deflection increased linearly with the applied

load and the sudden drop in load at 52.7 kN reveals the complete debonding of the plate. The maximum recorded deflection at the instance of complete debonding was 10.5 mm.

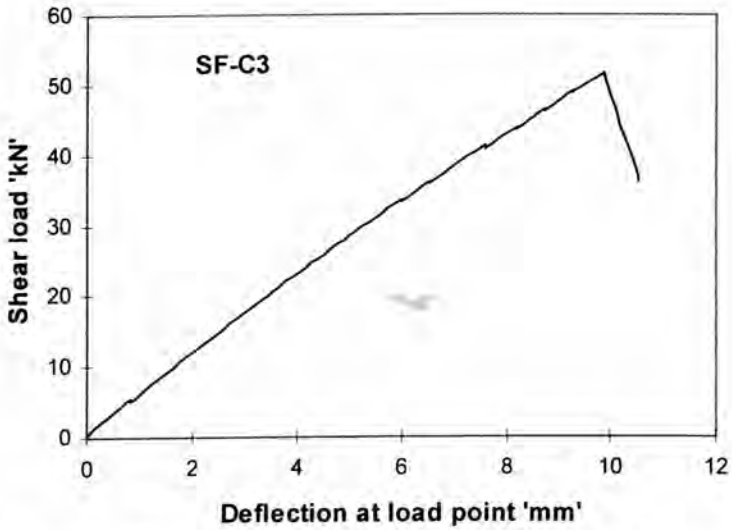

Fig.14.18. SF-C3: Deflection at load point Vs Applied shear load

14.4 Discussion of test results from Group I beams

Table-14.1 summarises the results obtained from all the tests. The failure mode of all the beams are given in Table-14.2. In Tales-14.1 and 14.2, the test results for the pure shear peeling test (SP-C20 from Section 9.6.5) and for the pure flexural peeling test (FP-C20 from Section 12.3.3) are also given.

Table-14.1: Test results

Test	L_{end}/h	M_{end} (kNm)	V_{end} kN	$\varepsilon_{p,max}$	Δ_{max} mm
SP-C20	0	0	155.6	-1830×10^{-6}	75.2
SF-C1	0.68	29.8	119.1	-510×10^{-6}	28.1
SF-C2	1.35	47.05	94.1	-560×10^{-6}	15.6
SF-C3	2.70	52.7	52.7	-363×10^{-6}	10.52
FP-C20	5.1	47.3	0	-168×10^{-6}	10.3

L_{end}= distance between plate end and support, h= depth of the beam,
M_{end}, V_{end} = Moment and shear force at the plate end at the instance of peeling,
$\varepsilon_{p,max}$, Δ_{max} = maximum plate strain and maximum deflection recorded at the instance of peeling

Table-14.2: Mode of Peeling

Test	Sequence of peeling
SP-C20	Formation of critical diagonal crack at V=80.7 kN. Extension of this crack to the load plate at V=94 kN along the bottom edge of the compression face plate. Propagation of this horizontal crack backwards towards the support at V=155.6 kN causing debonding and secondary diagonal cracks, but a portion of plate 575 mm from plate end did not debond.
SF-C1	Formation of critical diagonal crack at V=68.1 kN and extension of this crack to the load plate at V=95.3 kN along the bottom edge of compression face plate. Propagation of this horizontal crack backwards towards the support at V=119.1 kN causing debonding and secondary diagonal cracks. Debonding encompassed the whole plate length from load plate to the plate end.
SF-C2	Formation of critical flexural shear crack at V=78.5kN and extension of this crack to the load plate at V=87.8 kN along the bottom edge of compression face plate. Propagation of this horizontal crack backwards towards the plate end at V=94.1 kN causing debonding that encompassed the whole plate length from load plate to the plate end. No secondary diagonal cracks formed.
SF-C3	At V=52.7 kN, a long horizontal debonding crack from load plate to plate end propagated causing instantaneous debonding. No diagonal crack formed.
FP-C20	At 45.1 kNm (P=60 kN), a long debonding crack occurred below the centre point of the plate extending towards the one end of the plate appeared. At 47.3 kNm(P=63.1 kN) the debonding crack propagated all around the bottom edge of the compression face plate causing complete peeling of the plate.

From the test results, it was observed that as the plate end is terminated away from the support as in test SF-C3, the peeling of the plate ends occur at a moment approximately equal to that of the pure flexural peeling moment as estimated from test FP-C20. For the shear span SF-C1 that had its plate end terminated closer to the support, the peeling failure occurred as indicated by the formation of diagonal shear crack and subsequent long horizontal debonding crack along the bottom edge of the plate. In fact, the diagonal shear crack extended to the load point at a shear load of 95.3 kN, as given in Table-14.2. This compares well with the corresponding shear load 94 kN for the pure shear peeling test specimen SP-C20. Therefore, the debonding failure in the case of SF-C1 is entirely due to the shear crack and not due to the applied moment. In the case of SF-C2, the results are apparently seems to be mixed as the moment at the plate end at debonding (52.7 kNm) is only slightly greater than the pure flexural peeling capacity of the beam FP-C20 (47.3 kNm). However, the debonding was still caused by the formation of a shear crack at a shear load of

68.1 kN that propagated along the bottom edge of the plate to the load plate at a shear load of 87.8 kN. This compares well with the test results for SP-C20 and SF-C1. Therefore, the interaction between shear and flexure seems to be negligible at this stage for Group-I beams and further analysis of the test results is presented in Section 14.8.

14.5 Group-II beams

14.5.1 Test specimens

In this series of tests, the behaviour of reinforced concrete beams in which the plate ends under bending compression are at a higher moment than the other locations of the plates under bending compression is studied. Four shear spans were prepared from two beams that were previously tested for pure flexural peeling after carrying out proper repairs. All the spans were bonded with a 20 mm thick steel plate and the only parameter varied was the distance of the plate end from the nearest support, as shown in Figs.14.19a-f. The details are as follows.

(a) Test SF-C4: The plate end was located at 500 mm from the nearest support.

(b) Tests SF-C5(a)&(b): The plate end was located at 750 mm from the support.

(c) Tests SF-C6 (a)&(b): The plate end was located at 1000 mm from the support.

(d) Tests SF-C7(a),(b)&(c): The plate end was located at 1500 mm from the support.

It is worth noting that the reinforced concrete beams used in these tests had the same internal reinforcement details shown in Fig.12.1a (Section 12.2.1).

14.5.2 Sequence of testing

A total of eight tests were carried out in this series by varying the relative positions of the load points. First, tests SF-C5(a) and SF-C6(a) were carried out simultaneously by applying a single concentrated load that was at 1250 mm from both the plate ends, as shown in Fig.14.19a. As the desired debonding behaviour was not obtained by this

method, it was decided to test the shear spans SF-C5 and SF-C6 individually by placing the load at 400 mm from the end of the plate, as shown in Figs.14.19b and 14.19c. These tests were designated as SF-C5(b) and SF-C6(b).

Shear spans SF-C4 and SF-C7 were also tested individually by placing the load at 400 mm from the end of the plate, as shown in Figs.14.19d and 14.19e and these tests were called test SF-C4 and test SF-C7(a). In case of test SF-C7(a), the unplated portion of the beam was damaged and therefore it was reinforced with an external plate and clamps and the test was repeated as test SF-C7(b). After completing the test SF-C7(b), the shear span SF-C7 was tested further by placing the load at 75 mm from the plate end as shown in Fig.14.19f to extract more useful information and this test was designated as test SF-C7(c).

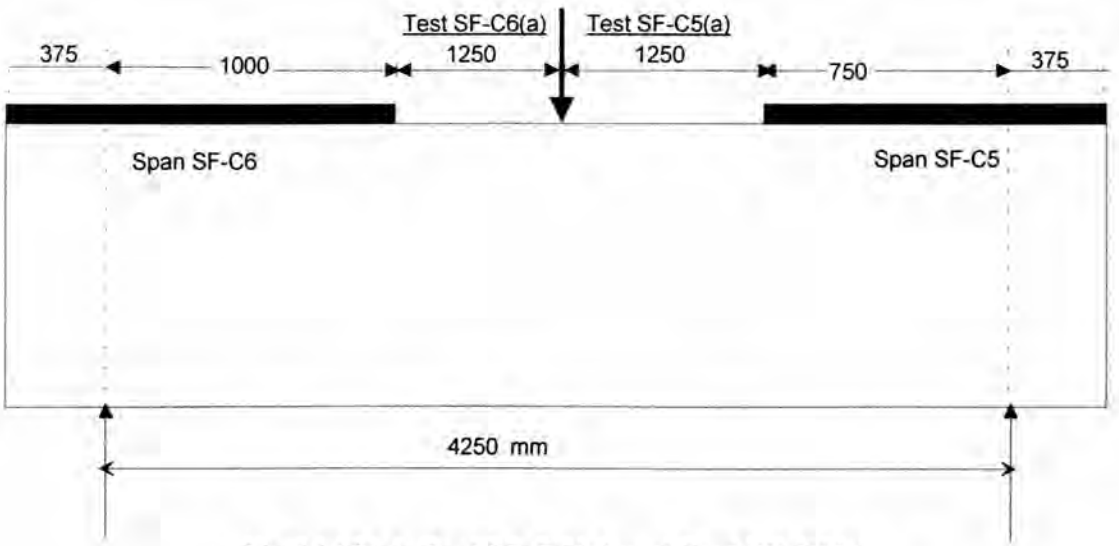

Fig.14.19(a). Test SF-C5(a) and Test SF-C6(a)

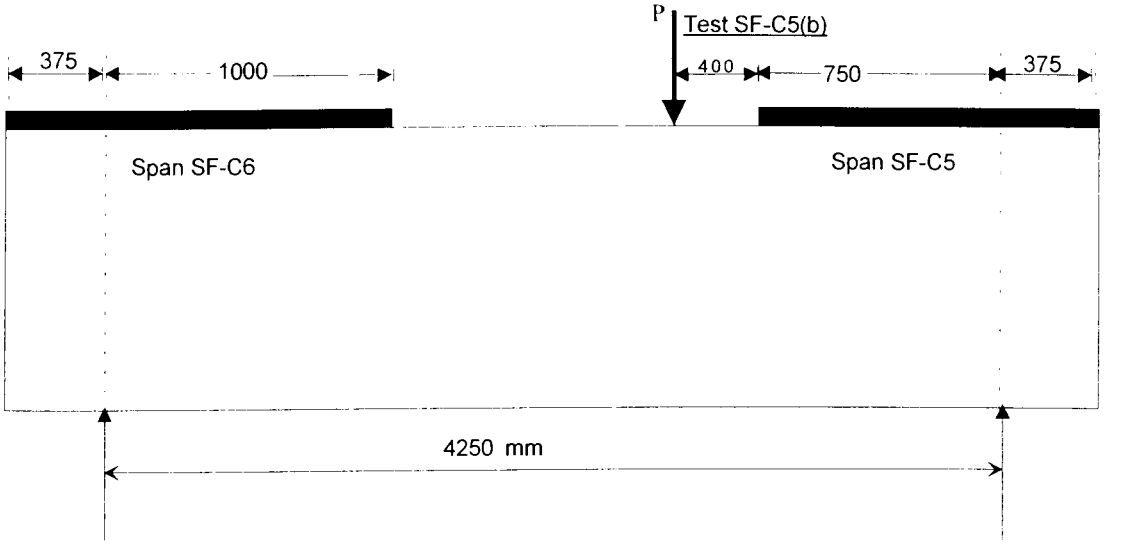

Fig.14.19(b). Test SF-C5(b)

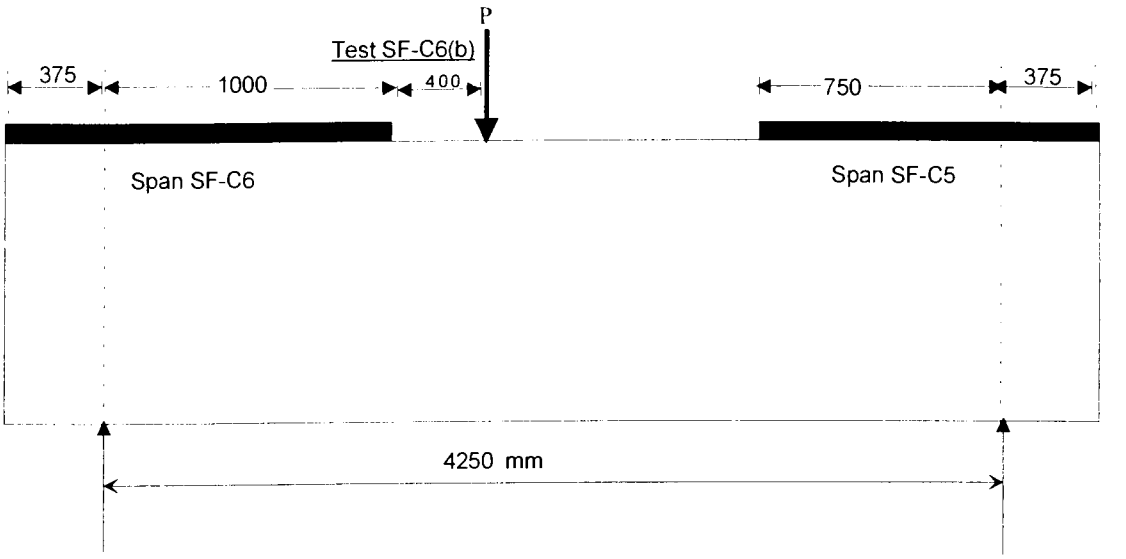

Fig.14.19(c). Test SF-C6 (b)

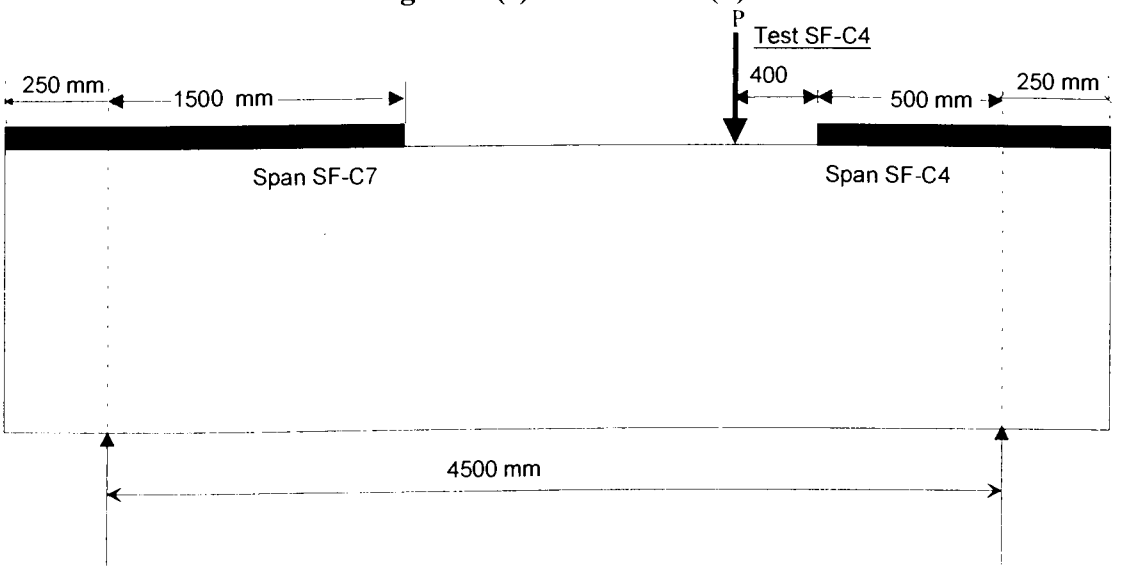

Fig.14.19(d). Test SF-C4

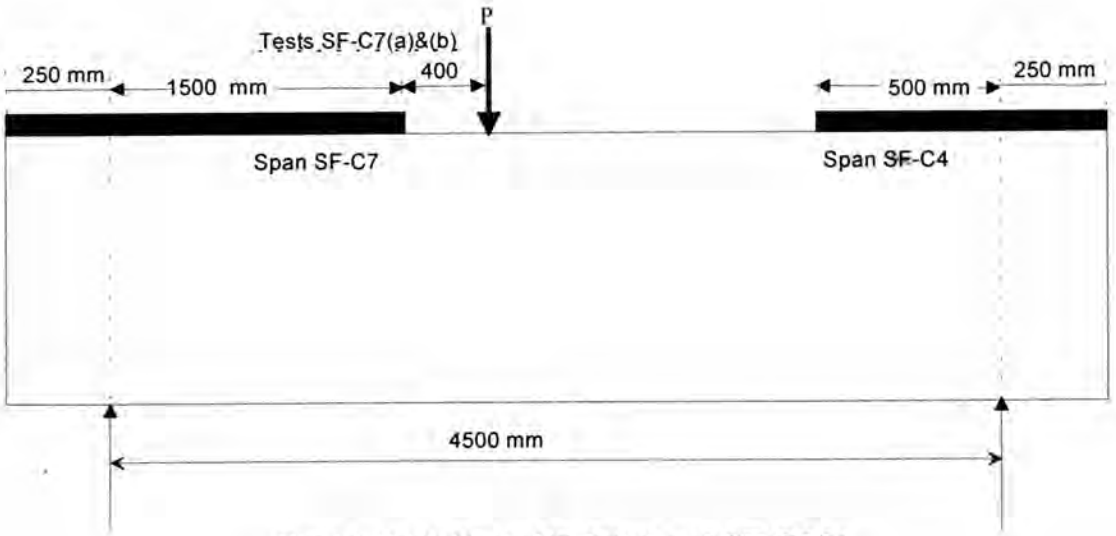

Fig.14.19(e). Tests SF-C7(a) and SF-C7(b)

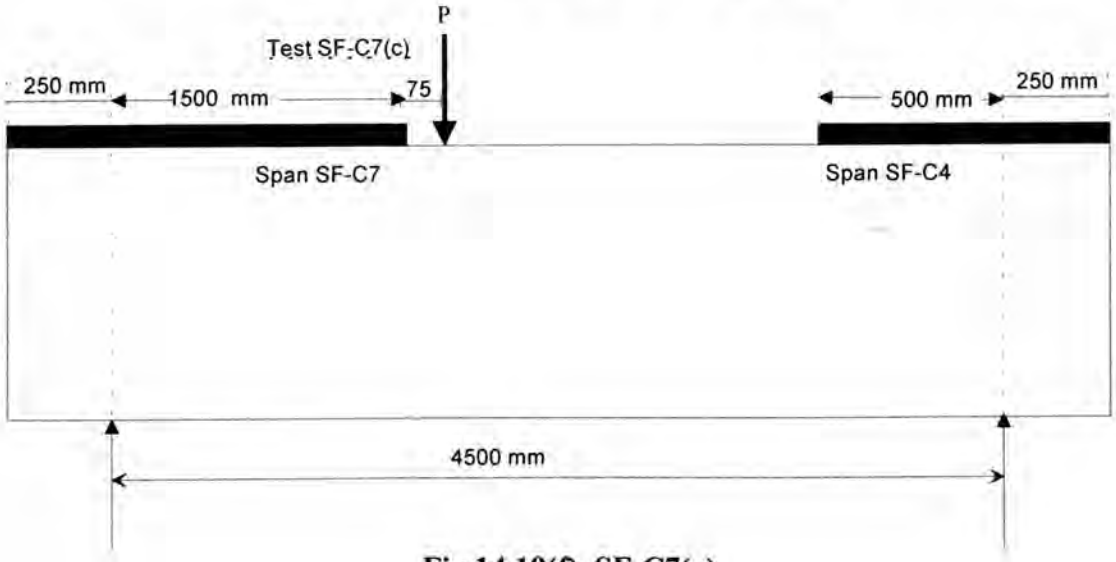

Fig.14.19(f). SF-C7(c)

Fig.14.19. Group II beams: Schematic detail of all the beams tested

14.5.3 Instrumentation

Strain gauges were bonded to the external plates in order to detect the debonding at various sites of the plates. The arrangements of the strain gauges and their numbering are shown in Figs.14.20a-d for all the plated beam tests conducted. The beam deflection at the load point was monitored by a dial gauge and also by a transducer.

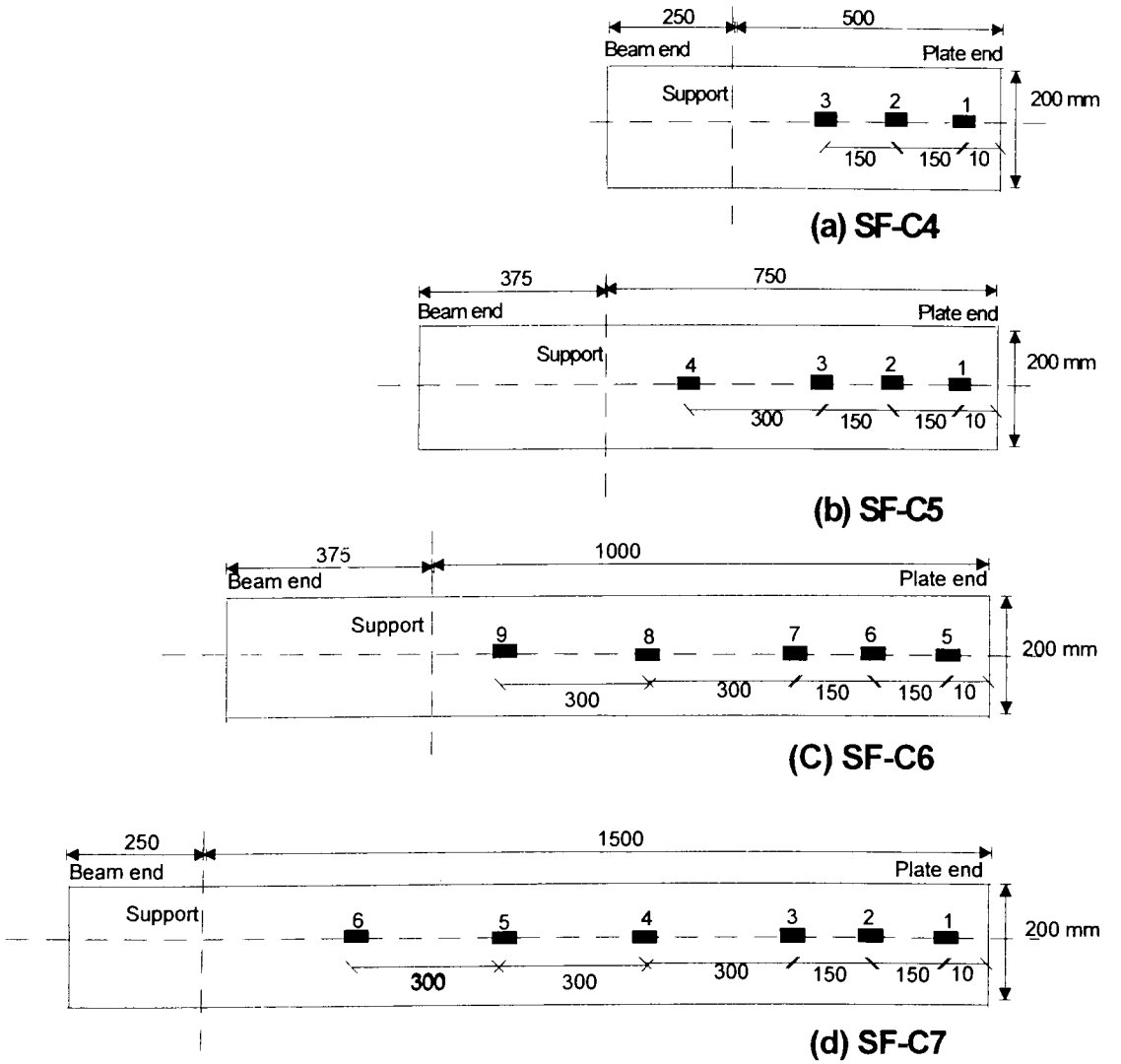

Fig.14.20. Strain gauge arrangement for Group II beams

14.5.4 Material properties

Matreial properties are the same for the beams tested in FP series and hence refer to Section 12.2.5.

14.6 Test results for Group II beams

14.6.1 Test SF-C4

Test SF-C4 was carried on the shear span in which the 20 mm thick compression face plate was terminated at a distance 500 mm from the support, as shown in Fig.14.19d and Fig.14.21 illustrates the test set up for this beam. The position of the applied load P was such that the shear force V in the span was $0.8P$ kN and the moment at the plate end was $0.4P$ kNm.

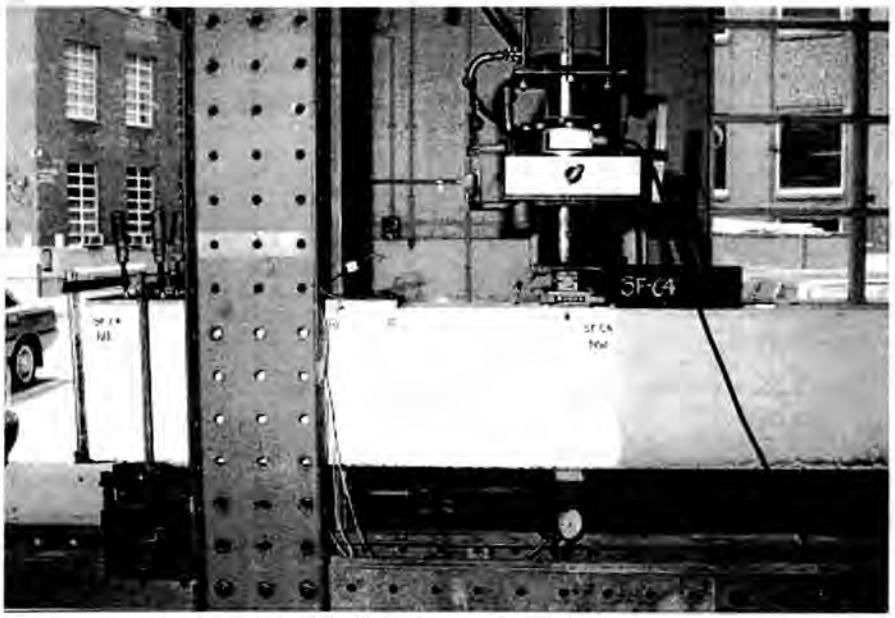

Fig.14.21.Test-up for SF-C4

14.6.1.1 Crack propagation and failure mode

A few flexural cracks appeared beneath the load point at an applied load of 60 kN as can be seen in Figs.14.22a and 14.22b. When the applied load was increased to 85 kN (V=68 kN), a diagonal crack appeared at a distance 320 mm from the support. This crack propagated rapidly upwards for a slight increase in applied load to 100 kN (V=80 kN) as shown in Figs.14.22a and 14.22b. Another diagonal crack formed close to the support at a distance of 105 mm when the applied load was 105 kN (V=84 kN) and it joined with the long diagonal crack. A flexural shear crack at a distance 550 mm from the support also occurred at an applied load of 170 kN (V=136 kN). The inclined cracks propagated further towards the load point and they stabilised at an applied load of 210 kN (V=168 kN). When the applied load was increased to 230.3 kN (V=184.2 kN), crushing of concrete under load plate could be observed and the load dropped to 221.5 kN (V=179.8 kN). The load test was terminated at this juncture as further damage could jeopardise the load testing of the second shear span SF-C7. It is worth noting that the compression face plate was intact and no debonding crack was initiated at the plate end. This is due to the fact that plate end did not interfere with the path of the critical diagonal crack as can be seen from Figs.14.22a and 14.22b.

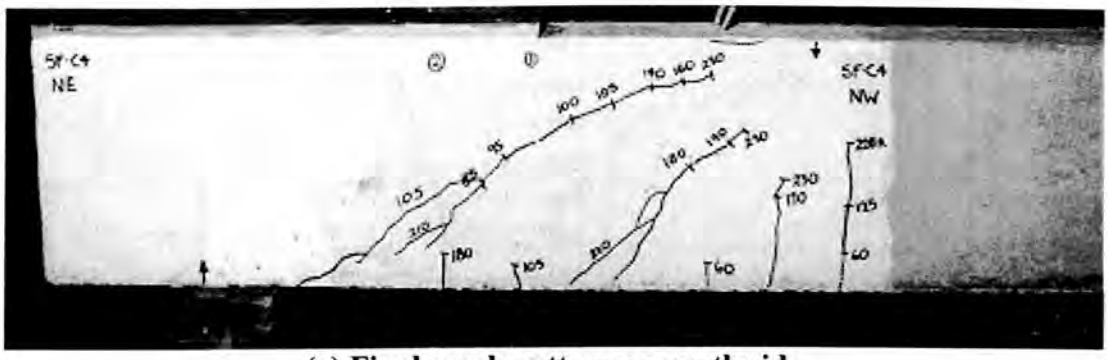

(a) Final crack pattern on north side

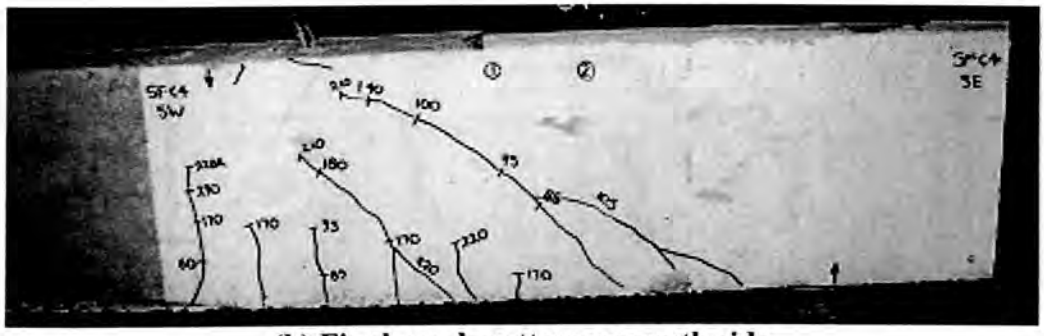

(b) Final crack pattern on south side

Fig.14.22. Test SF-C4: Final crack pattern

14.6.1.2 Longitudinal strains in the compression face plate

Figure 14.23 illustrates the variation of longitudinal strains recorded at all gauge sites (refer Fig.14.20a) with the shear force in the shear span tested. The charts show the strains increased linearly up to a shear force of 60 kN after which the long diagonal shear crack formed near the support. This is marked by the reduction in strains at gauge location #2, and #3 and the convergence of strains at #1 and #2 at a shear force of 76 kN. The strain gauge readings show that the strains in the plate change from compression to tension after the formation of the diagonal shear crack and the strains remained tensile even though the beam was able to sustain a maximum shear force of 178.8 kN. The crushing of concrete is indicated by the slight fall in the shear load from 184 kN to 177 kN at the closure of the test. The maximum strain readings were recorded at gauge location #3 and the maximum recorded strain was 30 microstrains (compressive) which is appreciably lower than the yield strain of the mild steel plate.

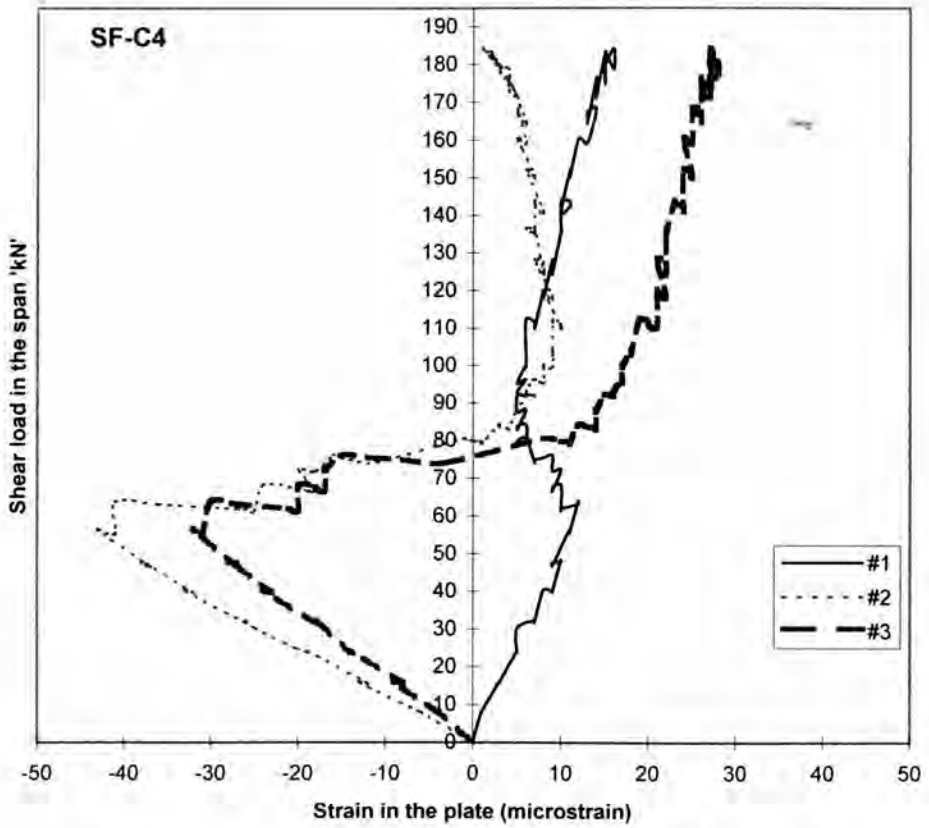

Fig.14.23. Longitudinal strains in compression face plate

14.6.1.3 Deflection

Figure 14.24 depicts the relationship between the deflection recorded at the load point and the shear force in the shear span tested. The deflection increased linearly with the applied load and a small plateau could be observed at the maximum shear load. The maximum recorded deflection at the termination of the test was 26.1 mm.

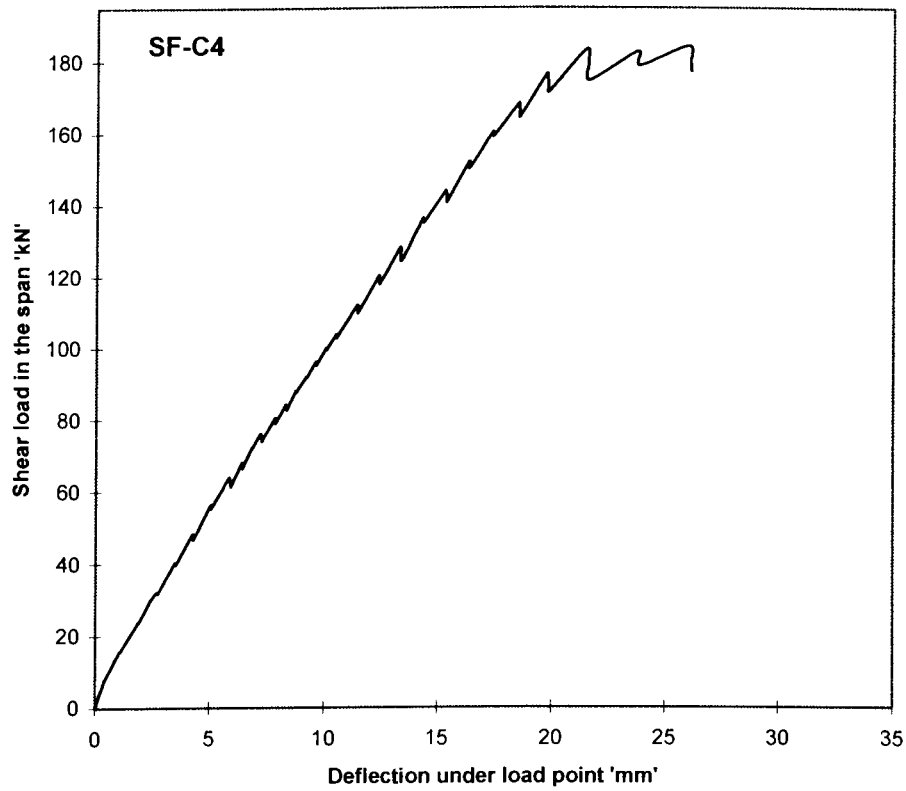

Fig.14.24. SF-C4: Deflection at load point Vs Applied shear load

14.6.2 Test SF-C5(a)

Test SF-C5(a) was carried on the shear span in which the 20 mm thick compression face plate was terminated at a distance 750 mm from the support, as shown in Fig.14.19a. It may be recalled that tests SF-C5(a) and SF-C6(a) were carried out simultaneously. The position of the applied load P was such that the shear force V in the span was $0.5294P$ kN and the moment at the plate end was $0.397P$ kNm.

14.6.2.1 Crack propagation and failure mode

A few flexural cracks appeared in the region beneath the plate end when the applied load was 80-111 kN (V=42.4-58.8 kN) as shown in Fig.14.25. Two web shear cracks occurred; one at an applied load of 132 kN (V=69.9 kN) and the other at 150 kN (V=79.4 kN). As the load was increased to 152.6 kN (V=80.8 kN), the concrete below the load plate started crushing and the load dropped to 143.7 kN (V=76.1 kN) at which the load test was terminated. Since the aim of this test is to observe the

debonding behaviour of the plated beam, it was decided to test each shear span separately by suitably strengthening the unplated section. The distance between the load point and support was also reduced to decrease the maximum bending moment in the span so as to avoid premature flexural failure of the unplated portion of the beam.

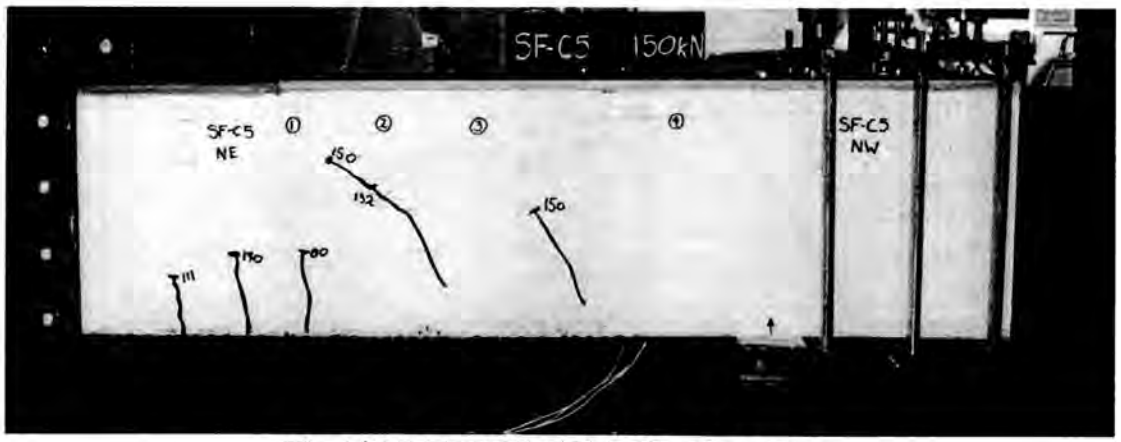

Fig.14.25. Test SF-C5(a): Crack pattern

14.6.2.2 Longitudinal strains in the compression face plate

Figure 14.26 illustrates the variation of longitudinal strains recorded at all gauge sites (refer Fig.14.20b) with the shear force in the shear span tested. The charts show the strains increased linearly unto a shear force of 50 kN. The formation of the web shear cracks is marked by the kink and the change of slope in the curves, when the shear load range was 50-70 kN. Finally, the crushing of concrete is indicated by the fall in the shear load from 81 kN to 76 kN. The maximum strain readings were recorded at gauge location #2 and the maximum recorded strain was 137 microstrains (compressive) which is lower than the yield strain of the steel plate.

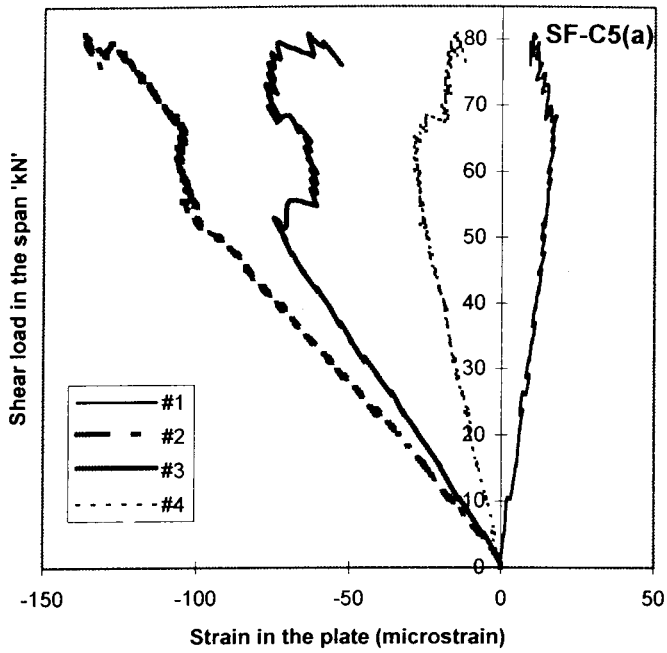

Fig.14.26. SF-C5(a): Longitudinal strains in compression face plate

14.6.2.3 Deflection

Figure 14.27 illustrates the relationship between the deflection recorded at the load point and the shear force in the shear span tested. The deflection increased linearly with the applied load till the test was ended due to the onset of concrete crushing. The maximum recorded deflection at the termination of the test was 27.1 mm.

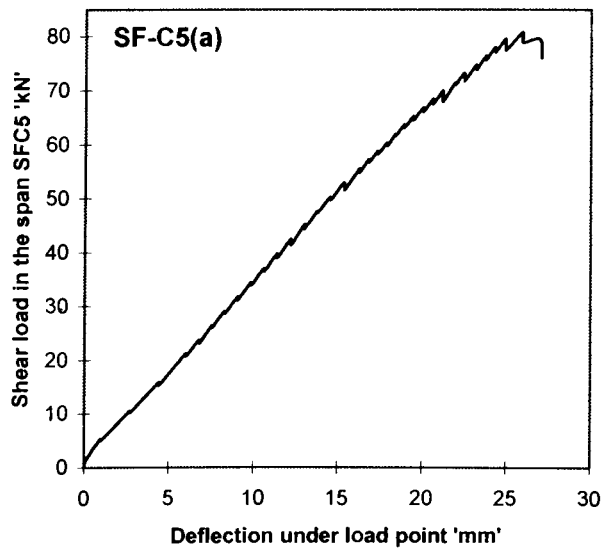

Fig.14.27. SF-C5(a): Deflection at load point Vs Applied shear load

14.6.3 Test SF-C5(b)

Test SF-C5(b) is a repeat test on the shear span SF-C5 as depicted in Fig.14.19b. As the desired debonding failure of the compression face plated beam could not be realised in Test SF-C5(a), the distance between the load point and support was also reduced from 1250 mm to 400 mm. This was done to decrease the maximum bending moment in the span so as to avoid premature flexural failure of the unplated portion of the beam and also to increase the shear load in the span being tested. This will facilitate the occurrence of debonding cracks. The other precautionary measures taken were to test each shear span separately and provide extra temporary reinforcement for the unplated section. The position of the applied load P was such that the shear force V in the span was $0.7294P$ kN and the moment at the plate end was $0.547P$ kNm.

14.6.3.1 Crack propagation and failure mode

Figures 14.28a and 14.28b depict the crack patterns observed on the north and south side of the beam. The crack pattern from the previous test SF-C5(a) conducted on the same beam is also shown on these figures. The crack pattern from the present test is distinguished by marking the load with suffix 'N' such as 120N and 140N. The two web shear cracks from test SF-C5 reappeared and transformed into fully fledged diagonal cracks when the applied load was 110-120 kN (V=80.2-87.5 kN) as shown in Figs.14.28a and 14.28b. As the load was increased to 140 kN (V=102.1 kN), a horizontal debonding crack appeared along the bottom edge of the plate end. It was about 95 mm long on the north side of the plate and 160 mm long on the north side of the plate. There was no further propagation of this debonding crack till the termination of the test. Afterwards a few more flexural shear cracks occurred in the region between the plate end and the load point, when the applied load was in the range 145-185 kN (V=105.8-134.9 kN). The long diagonal shear crack close to the

support propagated backwards at an applied load of 195 kN (V=142.2 kN). As there was no further propagation of the debonding crack was observed, the test was finished when the applied load was 206.8 kN (V=150.8 kN).

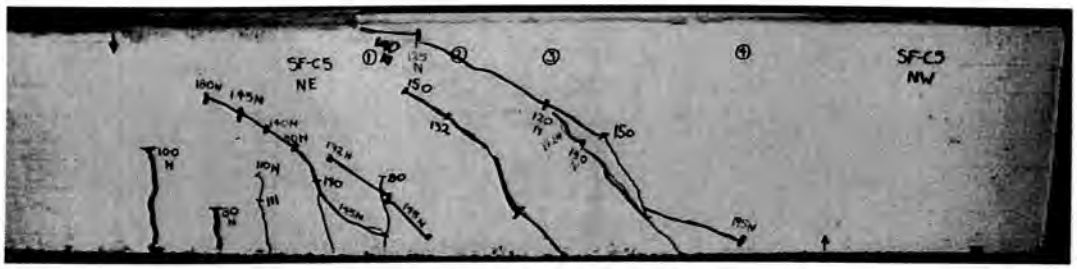

(a) Crack pattern on north side

(b) Crack pattern on south side

Fig.14.28. Test SF-C5(b): Crack pattern

14.6.3.2 Longitudinal strains in the compression face plate

Figure 14.29 illustrates the variation of longitudinal strains recorded at all gauge sites (refer Fig.14.20b) with the shear force in the shear span tested. The notable features that can be seen from this figure is the plateau in the curves for the gauges #2 and #3 and drop in strains in all gauge location when the shear load was in the range 90-110 kN. This corresponds to the rapid propagation of shear cracks and the formation of debonding crack at the plate end. The charts show that the strains increased linearly up to a shear force of 50 kN. The formation of the web shear cracks is marked by the kink and the change of slope in the curves when the shear load range was 50-70 kN. Finally, the crushing of concrete is indicated by the fall in the shear load from 81 kN to 76 kN. Figure 14.29 also shows that despite steep increase in the applied load and hence the shear load in the span tested, the strain readings kept on falling. The maximum strain readings were recorded at gauge location #2 and the maximum

recorded strain was 157 microstrains (compressive) which is lower than the yield strain of the steel plate.

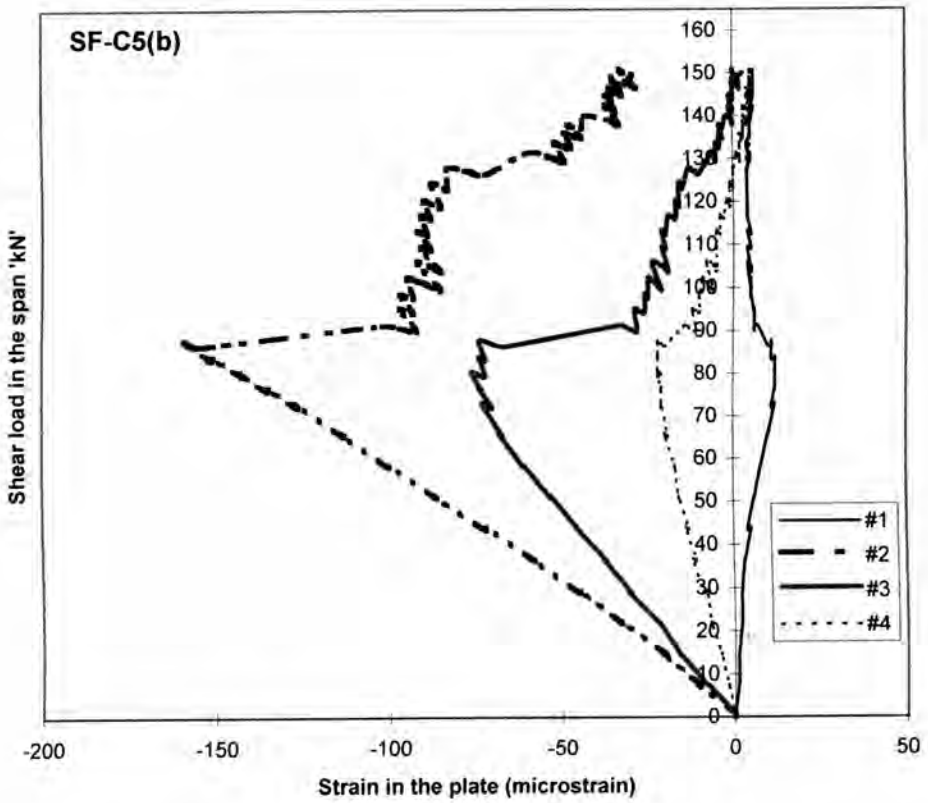

Fig.14.29. SF-C5(b): Longitudinal strains in compression face plate

14.6.3.3 Deflection

Figure 14.30 illustrates the relationship between the deflection recorded at the load point and the shear force in the shear span tested. The deflection increased linearly with the applied load just before the closure of the test. As the shear load approached the value of 150.2 kN, there was about 5 mm increase in deflection only for a small load increment of about 2 kN. The maximum recorded deflection at the termination of the test was 27.21 mm.

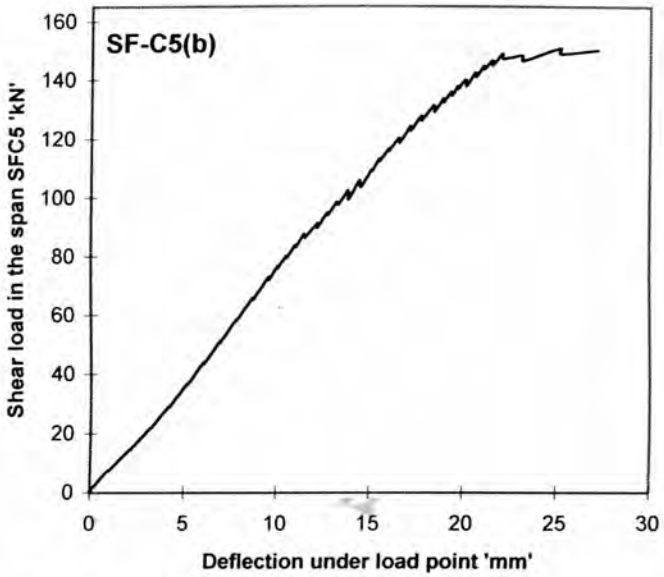

Fig.14.30. SF-C5(b): Deflection at load point Vs Applied shear load

14.6.4 Test SF-C6(a)

Test SF-C6(a) was carried on the shear span in which the 20 mm thick compression face plate was terminated at a distance 1000 mm from the support, as shown in Fig.14.19a. It may be recalled that tests SF-C5(a) and SF-C6(a) were carried out simultaneously as shown in Fig.14.31. The position of the applied load P was such that the shear force V in the span was $0.4706P$ kN and the moment at the plate end was $0.4706P$ kNm.

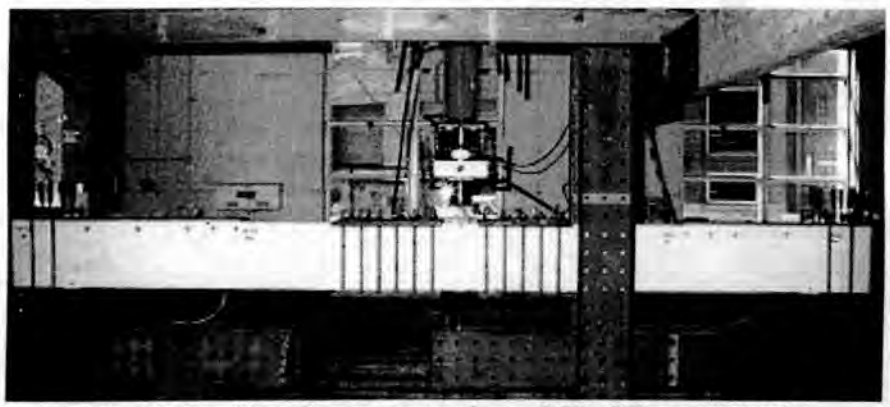

Fig.14.31. Simultaneous testing of SF-C5 and SF-C6

14.6.4.1 Crack propagation and failure mode

Figures 14.32 and 14.33 show the crack pattern observed on both sides of the shear span during test SF-C6(a). Figure 14.32 shows the appearance of several flexural

cracks in the region between the plate end and the load point on the north side of the beam when the applied load was in the range 100-138 kN (V=47-64.9 kN). On the south side of the beam, two flexural shear cracks; one at 132 kN (V=62.1 kN) and another at 138 kN (V= 64.9 kN), occurred as can be seen in Fig.14.33.

The crucial debonding crack at the plate end occurred first at the north side at 138 kN (V= 64.9 kN). It was 185 mm long at this stage and extended by another 40 mm when the load was increased to 141 kN (V=66.4 kN). At this stage, the debonding crack extended on the south side of the plate end for a length of 155 mm as shown in Fig.14.33. As the load was increased to 152.6 kN (V=71.8 kN), the concrete below the load plate started crushing and the load dropped to 143.7 kN (V=67.6 kN) at which the load test was terminated. The debonding crack did not propagate further. In order to gain more useful information on the debonding behaviour of the plated beam, the test was repeated by suitably strengthening the unplated section and by reducing the distance between the load point and support. The new test SF-C6(b) will be described later.

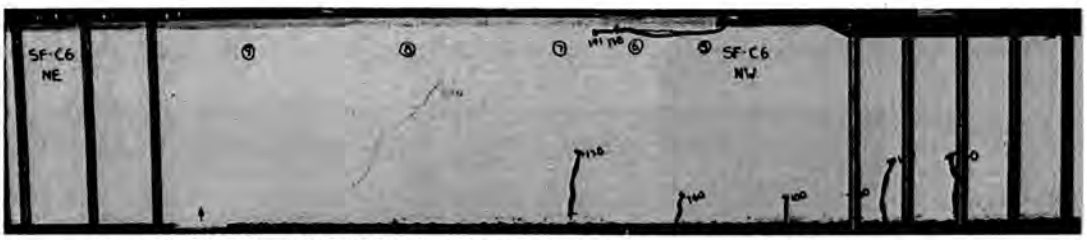

Fig.14.32. Test SF-C6(a): Crack pattern on north side

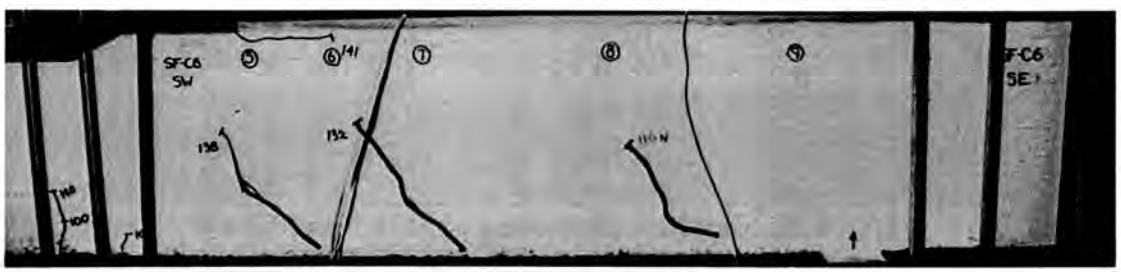

Fig.14.33. Test SF-C6(a): Crack pattern on south side

14.6.4.2 Longitudinal strains in the compression face plate

Figure 14.34 illustrates the variation of the longitudinal strains recorded at all gauge sites (refer Fig.14.20c) with the shear force in the shear span tested. It can be seen from Fig.14.34 that the strain magnitudes increased linearly at all gauge locations till the debonding crack propagated when the shear load was about 65 kN. The readings in gauge locations #6 and #7 started falling at this stage. The crushing of concrete at the termination of the test is marked by the fall in strain magnitudes and also the shear load at all the gauge locations. The maximum strain readings were recorded at gauge location #2 and the maximum recorded strain was 159 microstrains (compressive) which is lower than the yield strain of the steel plate.

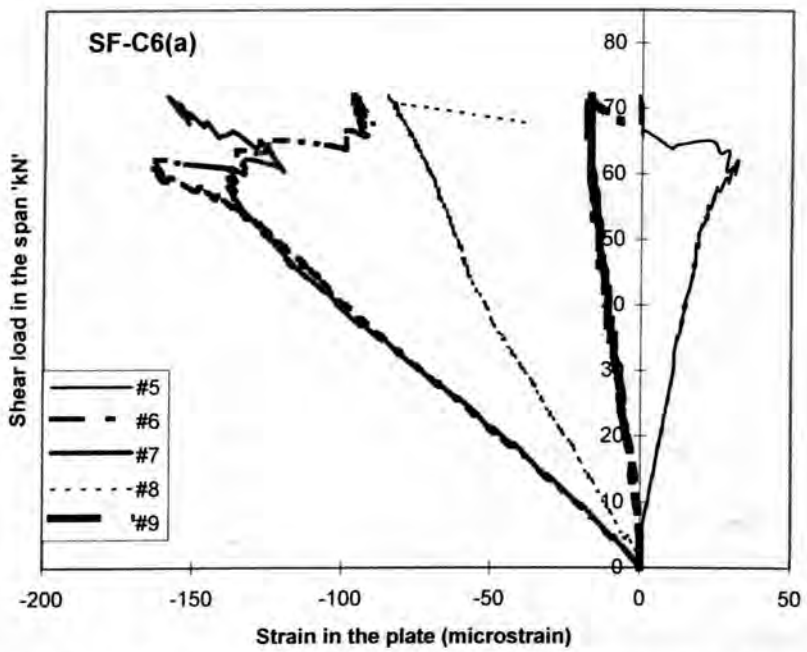

Fig.14.34. SF-C6(a): Longitudinal strains in compression face plate

14.6.4.3 Deflection

Figure 14.35 illustrates the relationship between the deflection recorded at the load point and the shear force in the shear span tested. The deflection increased linearly with the applied load till the test was ended. The maximum recorded deflection at the termination of the test was 27.21 mm.

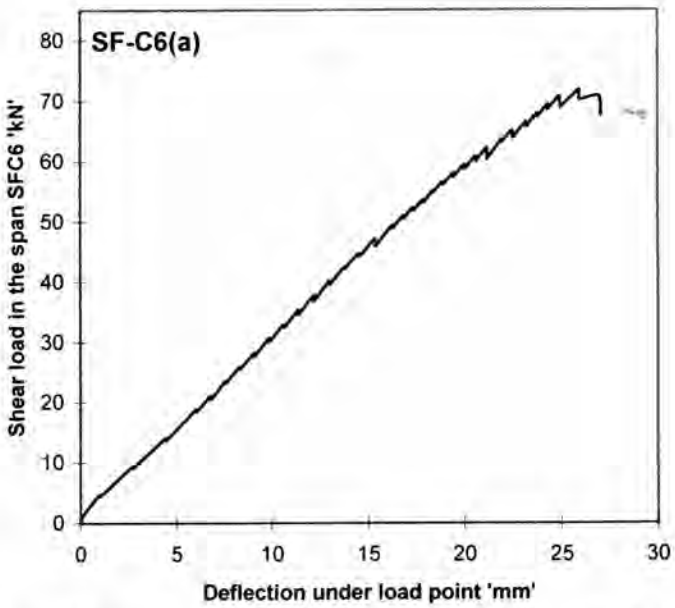

Fig.14.35. SF-C6(a): Deflection at load point Vs Applied shear load

14.6.5 Test SF-C6(b)

Test SF-C6(b) is a repeat test on the shear span SF-C6(a) as depicted in Fig.14.19c. As the debonding crack at the end of the compression face plated beam did not propagate to the desired level in Test SF-C6(a), the distance between the load point and support was also reduced from 1250 mm to 400 mm. This test was carried out for the same reason stated for test SF-C5(b). The position of the applied load P was such that the shear force V in the span was $0.6706P$ kN and the moment at the plate end was $0.6706P$ kNm.

14.6.5.1 Crack propagation and failure mode

Figures 14.36a and 14.36b depict the crack patterns observed on the north and south side of the beam. The crack pattern from test SF-C6(a) is also shown on these figures. The crack pattern from the present test is distinguished by marking the load with suffix 'N' such as 120N and 140N. The first significant change to occur was the formation of a long diagonal shear crack at a distance of 230-250 mm from the support when the applied load was 110 kN (V=73.8 kN). This crack propagated gradually upwards with the applied load and joined with the debonding crack at the

plate end from the previous test at an applied load of 130 kN (V=87.2 kN). At this stage the length of the horizontal debonding crack was 255 mm on the north side and 425 mm on the south side. As the load was increased, new flexural shear cracks formed either adjacent to the existing cracks or from their roots as can be seen in Figs.14.36a and 14.36b.

(a) Crack pattern on north side

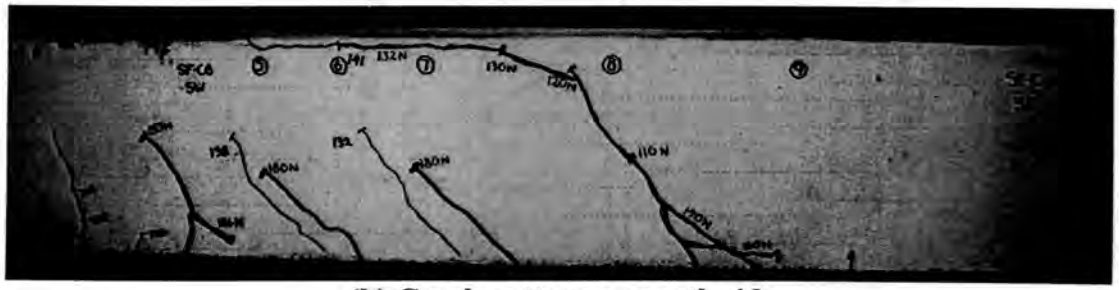

(b) Crack pattern on south side

Fig.14.36. Test SF-C6(b): Crack pattern

When the applied load was 185 kN, no other changes were noticed in the crack pattern and the beam was unable to sustain further increments in the load. Hence, the load increments were applied to produce a 2 mm change in the deflection under load point. Finally, the test was ended at 188 kN (V=126.1 kN) as the beam was undergoing large deformations without any significant change to the debonding crack.

14.6.5.2 Longitudinal strains in the compression face plate

Figure 14.37 shows the variation of longitudinal strains recorded at all gauge sites (refer Fig.14.20c) except gauge #5 with the shear force in the shear span tested. Zero readings were recorded at gauge #5 due to the presence of debonding crack at the plate end from the previous test. The strain magnitudes increased linearly at all gauge locations till the long diagonal shear crack propagated upwards and joined with the

debonding crack when the shear load 92.7 kN. This is marked by the sudden fall in strain magnitudes and they kept falling for further increases in applied load indicating the loss of bond at all gauge sites. The maximum strain readings were recorded at gauge location #8 and the maximum recorded strain was 137 microstrains (compressive) which is lower than the yield strain of the steel plate.

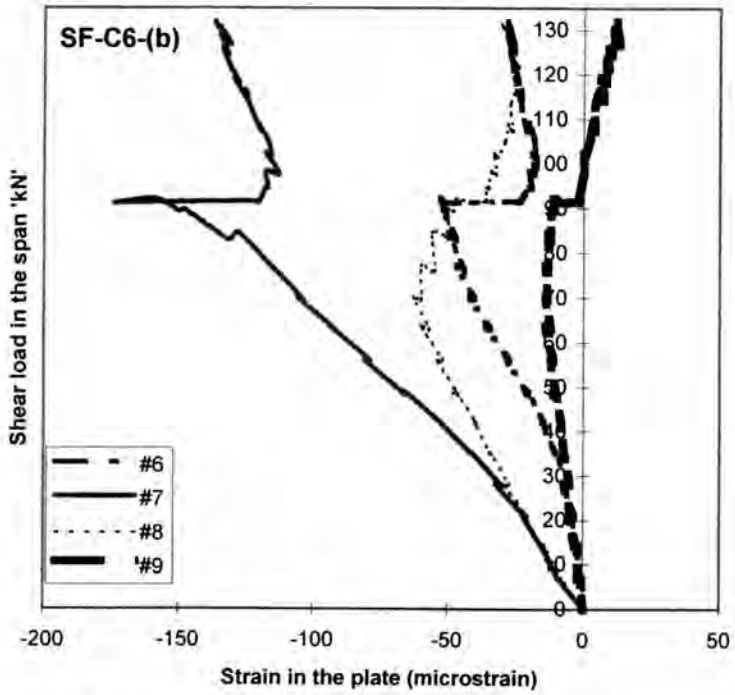

Fig.14.37. SF-C6(b): Longitudinal strains in compression face plate

14.6.5.3 Deflection

Figure 14.38 illustrates the relationship between the deflection recorded at the load point and the shear force in the shear span tested. The deflection increased linearly with the applied load till the test was ended. It also shows when the shear load was about 130 kN, the deflection magnitudes increased appreciably for small increase in load. The maximum recorded deflection at the termination of the test was 33.3 mm.

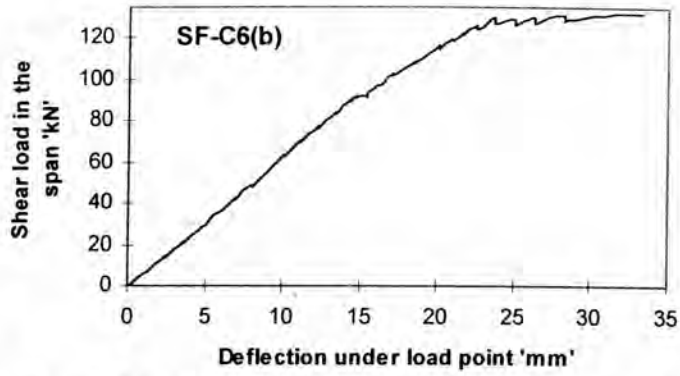

Fig.14.38. SF-C6(b): Deflection at load point Vs Applied shear load

14.6.6 Test SF-C7(a)

Test SF-C7(a) was carried on the shear span in which the 20 mm thick compression face plate was terminated at a distance 1500 mm from the support, as shown in Fig.14.19e. The position of the applied load P was such that the shear force V in the span was $0.578P$ kN and the moment at the plate end was $0.867P$ kNm.

14.6.6.1 Crack propagation and failure mode

A few flexural cracks and flexural shear cracks appeared at regular intervals in the shear as can be seen in Figs.14.39a and 14.39b. These cracks propagated with the increase in applied load. The notable feature of this test was the formation of the horizontal debonding crack at an applied load of 85 kN (V=49.1 kN) and its further propagation with the applied load as shown in Fig.14.39b. It may be noted that the debonding crack originated and extended independent of the occurrence and propagation of other cracks. The debonding crack did not propagate further beyond an applied load of 135 kN (V=78 kN) as can be seen from Figs.14.41 and 14.42. Two diagonal shear cracks also occurred close to the support when the applied load was 140 kN (V=80.9 kN). As the load was increased to 145 kN (V=83.8 kN), the beam was unable to sustain further load and it dropped to 142.2 kN at which the test was terminated. The beam was totally unloaded; the unplated region was clamped with additional reinforcement. The test was repeated as SF-C7(b) and it is described in

Section 14.6.7. The rate at which the debonding crack propagated with the applied load are indicated in Figs.14.40 and 14.41 and this data is summarised in Table-14.3.

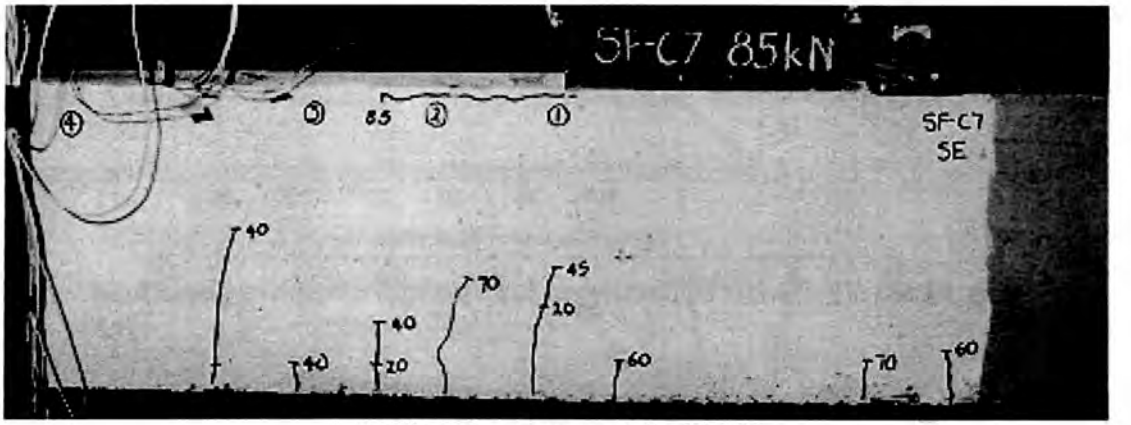

(a) Crack pattern at P=85 kN

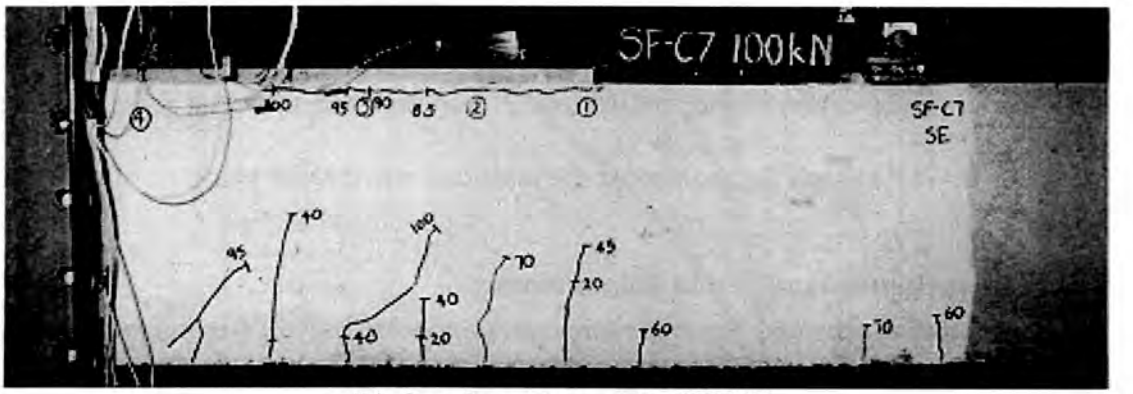

(b) Crack pattern at P=100 kN

Fig.14.39. Test SF-C7(a): Crack pattern

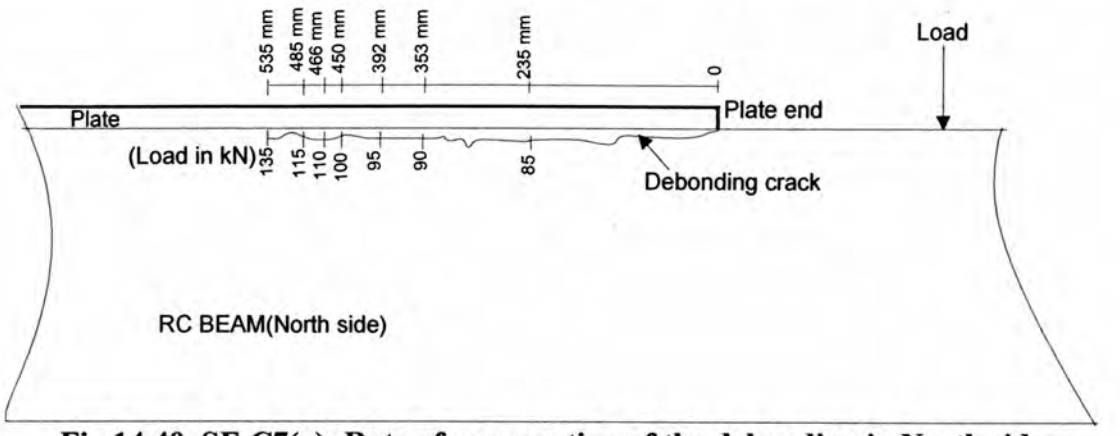

Fig.14.40. SF-C7(a): Rate of propagation of the debonding in North side

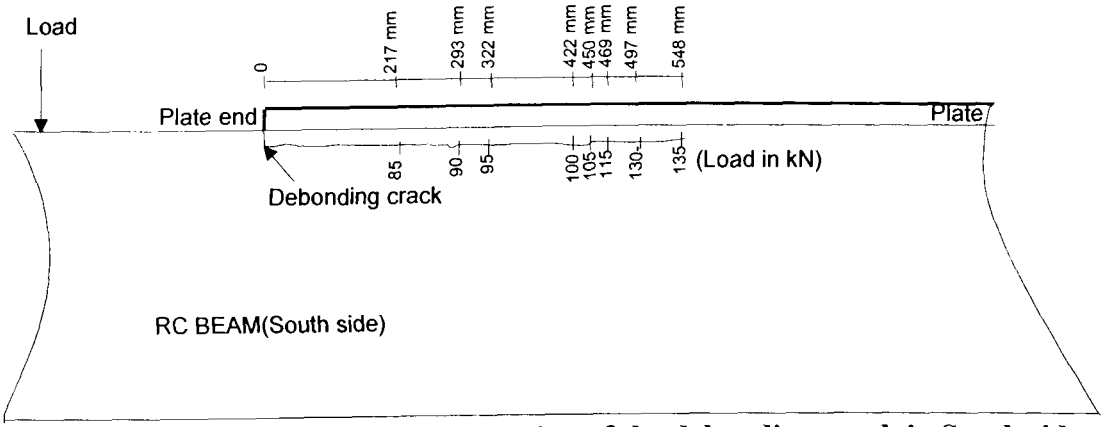

Fig.14.41. SF-C7(a): Rate of propagation of the debonding crack in South side

Table-14.3: Rate of propagation of debonding crack for test SF-C7(a)

Load (kN)	Crack position (mm)		M_{end} (kNm)	V_{end} (kN)
	origin	end		
North side				
85	0	235	42.6	28.4
90	235	353	65.8	52.0
95	353	392	63.0	54.9
100	392	450	64.0	57.8
110	450	466	66.8	63.6
115	466	485	68.8	66.5
135	485	535	79.2	78.0
South side				
85	0	217	42.6	28.4
90	217	293	66.7	52.0
95	293	322	66.3	54.9
100	322	422	68.1	57.8
105	422	450	65.4	60.7
115	450	469	69.8	66.5
135	469	548	80.4	78.0

Note: M_{end}, V_{end} = Bending moment and shear force acting at the plate end respectively. But, once the portion of a plate is debonded, they are calculated from the origin of the intact portion of the plate (this position is shown as the origin of the crack for a given load in the table).

14.6.6.2 Longitudinal strains in the compression face plate

Figure 14.42 shows the variation of longitudinal strains recorded at all gauge sites (refer Fig.14.20d) with the shear force in the shear span tested. The strain magnitudes increased linearly at all gauge locations till the occurrence of debonding crack at the plate end when the shear load was 49 kN. This is marked by the sudden fall in strain magnitudes of gauges #1 and #2 that were bonded closer to the plate end. The gradual progression of the debonding crack with the applied load is indicated by the fall in

strain values of different gauge locations for varying shear loads. The maximum strain readings were recorded at gauge location #4 and the maximum recorded strain was 247 microstrains (compressive) which is lower than the yield strain of the steel plate.

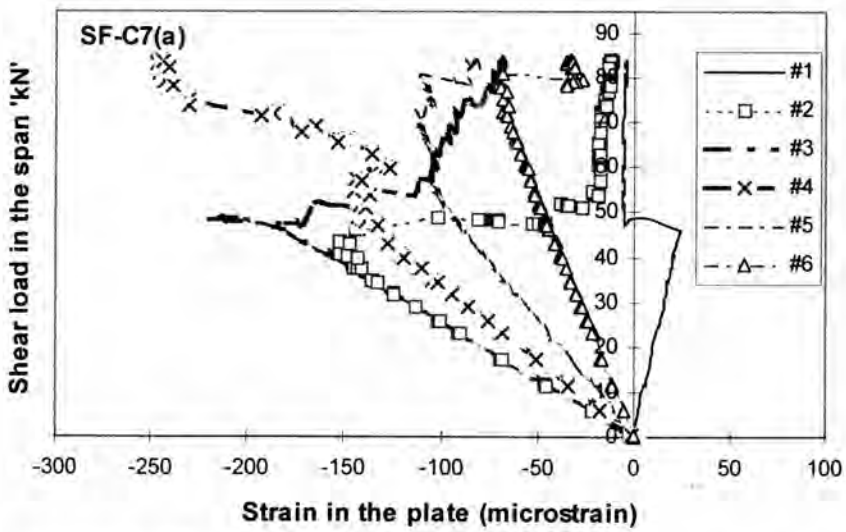

Fig.14.42.SF-C7(a): Longitudinal strains in compression face plate

14.6.6.3 Deflection

Figure 14.43 illustrates the relationship between the deflection recorded at the load point and the shear force in the shear span tested. The deflection increased linearly with the applied load till the test was ended. The maximum recorded deflection at the termination of the test was 28.63 mm.

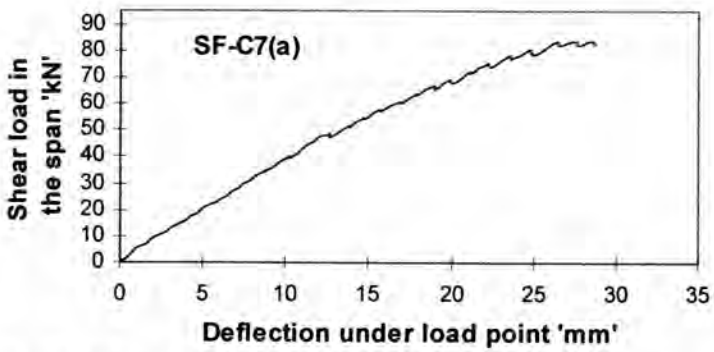

Fig.14.43. SF-C7(a): Deflection at load point Vs Applied shear load

14.6.7 Test SF-C7(b)

Test SF-C7(b) is a repeat test of the test SF-C7(a). In this case, the portion between the plate end and load point in the shear span SF-C7 was provided with additional reinforcement in the form of plates clamped both on top and bottom of the beam as shown in Fig.14.44. It may be noted that the clamped plates were not connected to the bonded plate and hence they did not affect the peeling behaviour of the compression face plate. They were used to prevent premature flexural failure of the concrete beam. The position of the applied load P was kept the same as in test SF-C7(a) and hence, the shear force V in the span was $0.578P$ kN and the moment at the plate end was $0.867P$ kNm.

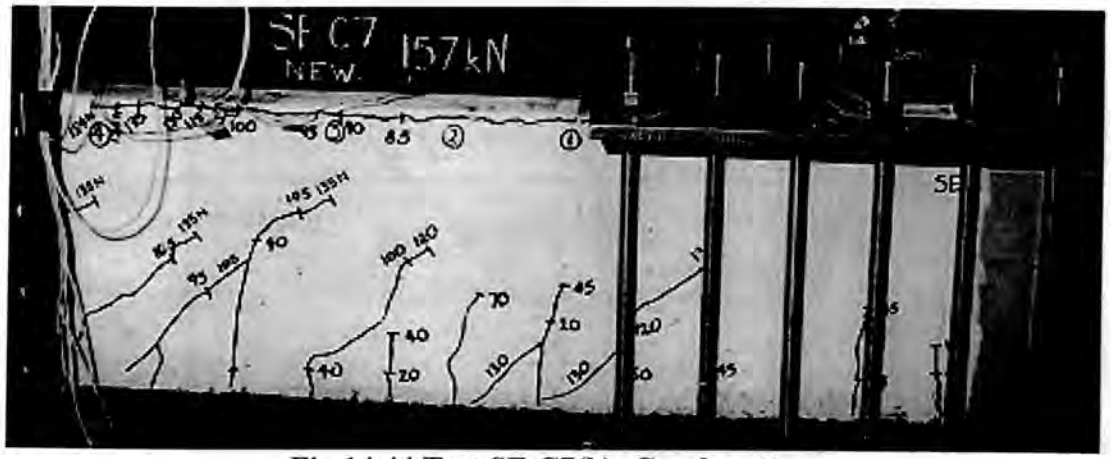

Fig.14.44 Test SF-C7(b): Crack pattern

14.6.7.1 Crack propagation and failure mode

Figure 14.44 depicts the crack pattern observed in this test. The crack pattern from test SF-C5 is also shown on these figures. The crack pattern from the present test is distinguished by marking the load with suffix 'N' such as 135N and 150N. The only change in the debonding crack to occur in the present test was the extension of the existing debonding crack by about 46 mm on the north side when the applied load was 150 kN (V=86.7 kN) as shown in Fig.14.45a. On the south side, it extended by 95 mm when the applied load was 154 kN (V=89 kN) as shown in Fig.14.45b. The beam was able to sustain a maximum load of 157 kN (V=90.7 kN) and the concrete

started crushing in the unplated portion. This led to the drop in load to 151.5 kN (V=87.6 kN) at which the test was finished. The rate at which the debonding crack propagated with the applied load is indicated in Figs.14.45a and 14.45b and this data is summarised in Table-14.4.

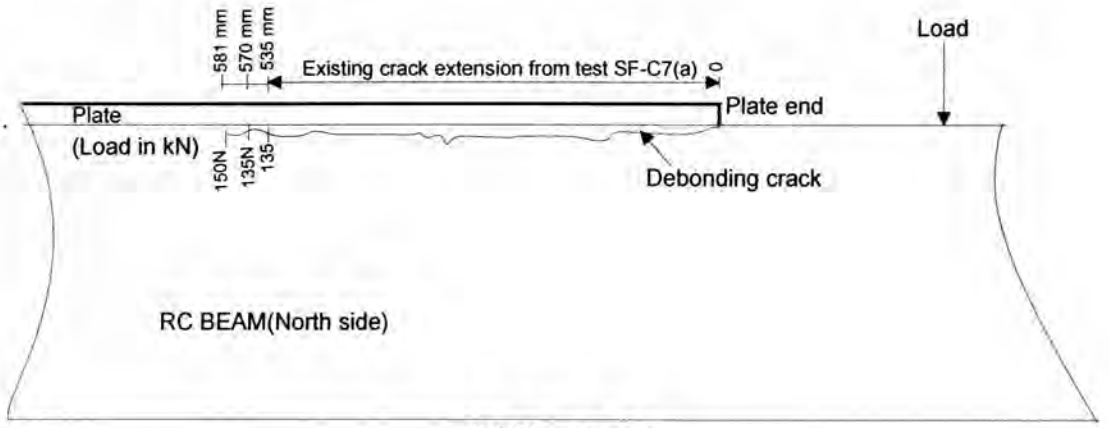

(a) North side

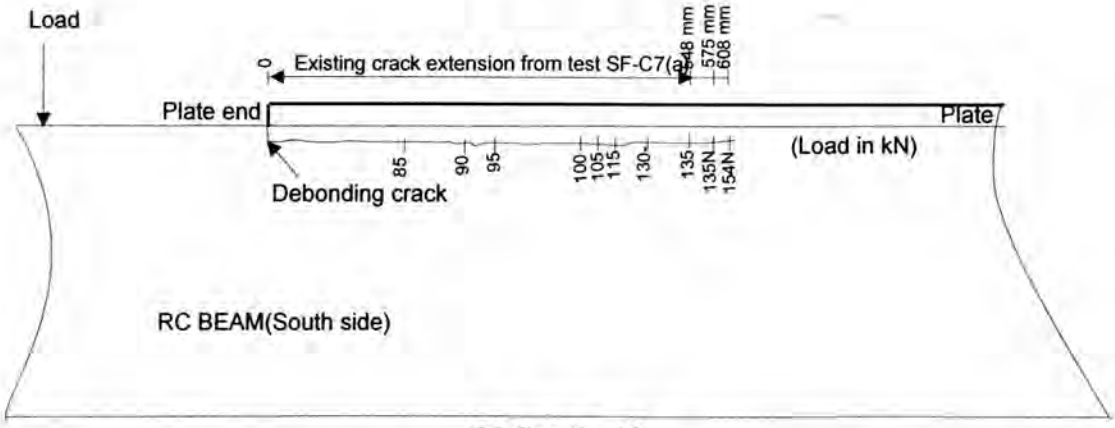

(b) South side

Fig.14.45. SF-C7(b): Rate of propagation of the debonding crack

Table-14.4: Rate of propagation of debonding crack for test SF-C7(b)

Load (kN)	Crack position (mm)		M_{end} (kNm)	V_{end} (kN)
	origin	end		
North side				
135	535	570	75.2	78.0
150	570	581	80.6	86.7
South side				
135	548	575	74.3	78.0
154	575	608	82.3	89.0

14.6.7.2 Longitudinal strains in the compression face plate

Figure 14.46 shows the variation of longitudinal strains recorded at all gauge sites (refer Fig.14.20d). Zero readings were recorded at gauge #5 due to the presence of debonding crack at the plate end from the previous test. The strain magnitudes increased linearly at all gauge locations till the beam was unable to sustain further load beyond 157 kN (V=90.7 kN). This is marked by the fall in strain and shear load magnitudes in Fig.14.46. The maximum strain readings were recorded at gauge location #4 and the maximum recorded strain was 190 microstrains (compressive) which is lower than the yield strain of the steel plate.

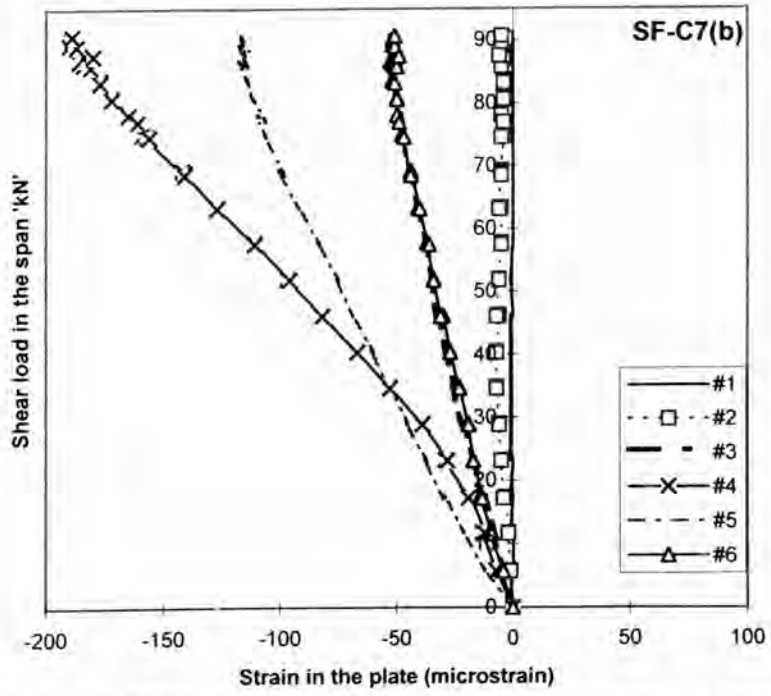

Fig.14.46. SF-C7(b): Longitudinal strains in compression face plate

14.6.7.3 Deflection

Figure 14.47 illustrates the relationship between the deflection recorded at the load point and the shear force in the shear span tested. The deflection increased linearly with the applied load till the test was ended. It also shows when the shear load was about 89 kN, the deflection magnitudes increased appreciably for small increase in load. The maximum recorded deflection at the termination of the test was 33.53 mm.

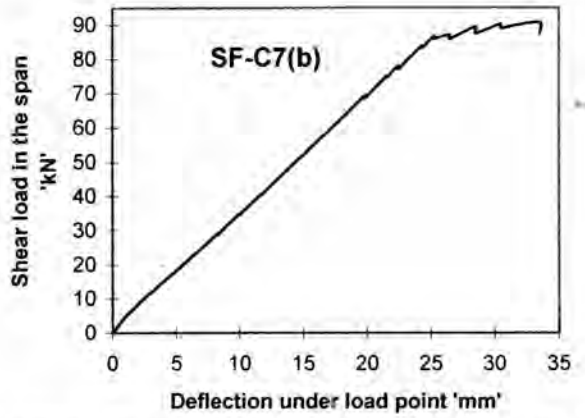

Fig.14.47. SF-C7(b): Deflection at load point Vs Applied shear load

14.6.8 Test SF-C7(c)

Test SF-C7(c) was conducted on the shear span SF-C7 after performing test SF-C7(b) as depicted in Fig.14.19f. In this test, the distance between the load point and the plate end was reduced from 400 mm to 75 mm. This was done to decrease the maximum bending moment in the span so as to avoid premature flexural failure of the unplated portion of the beam. This also caused an increase in the shear load and a corresponding increase in the moment at the plate end that will assist the formation of debonding cracks. The position of the applied load P was such that the shear force V in the span was $0.65P$ kN and the moment at the plate end was $0.975P$ kNm.

14.6.8.1 Crack propagation and failure mode

Figures 14.48a and 14.48b depict the crack patterns observed on the north and south side of the beam. The existing crack patterns from tests SF-C7(a) and SF-C7(b) are also shown on these figures. The crack pattern from the present test is distinguished by marking the load with suffix 'N2' such as 157N2 and 140N2.

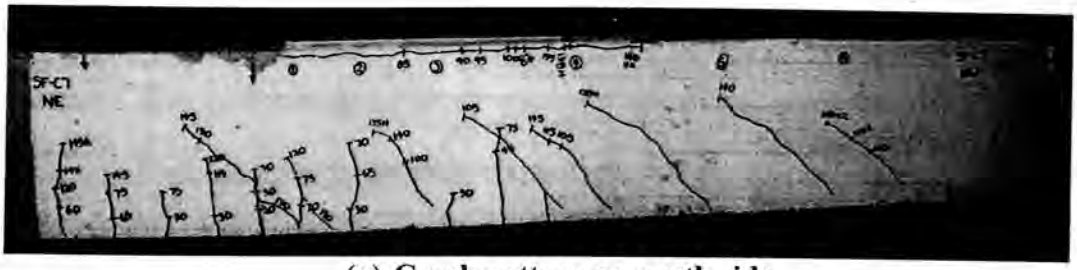

(a) Crack pattern on north side

(b) Crack pattern on south side

Fig.14.48. Test SF-C7(c): Crack pattern

The rate at which the debonding crack propagated with the applied load is indicated in Figs.14.49a and 14.49b. The information is also summarised in Table-14.5. The change in the debonding crack that occurred in this test was the extension by 131 mm on the north side when the applied load was 160 kN (V=104 kN) as shown in Fig.14.49a. On the south side, the existing diagonal crack at 280 mm from the support rapidly propagated towards the bottom edge of the plate when the applied load was 100 kN (V=65kN) as shown in Fig.14.48b. Then the debonding crack extended by 62 mm when the applied load was increased to 160 kN (V=104 kN) as shown in Fig.14.49b. At this stage, the beam shed some amount of load. On reapplication of the load, the debonding crack on the south side extended by another 60 mm. The load at this stage was 157 kN (V=102 kN); the debonding crack which combined together with the diagonal shear crack, as shown in Fig.14.48b, was able to sustain a maximum load of 157 kN (V=90.7 kN) and the concrete started crushing in the unplated portion. The maximum load sustained by the beam was 161.6 kN (V=105 kN) at which the concrete under load point started failing. This led to the drop in load to 159 kN (V=103.4 kN) and the test was terminated.

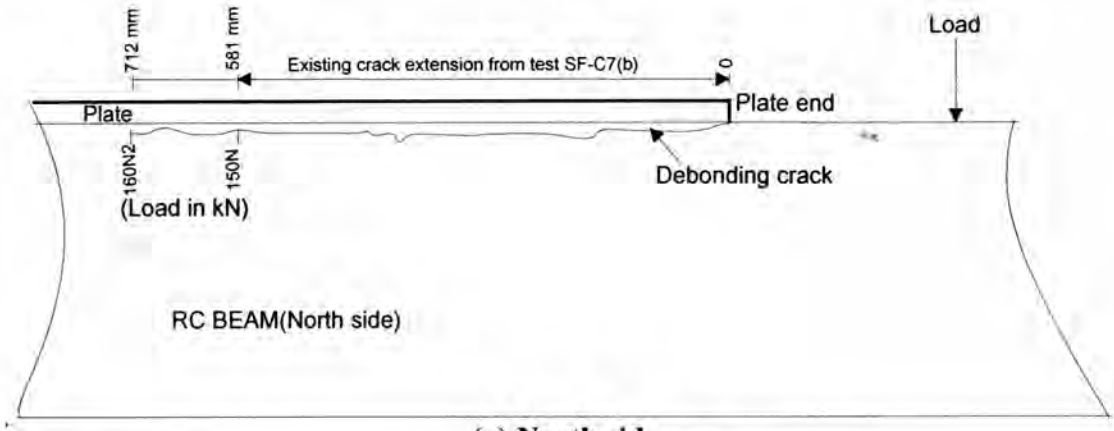

(a) North side

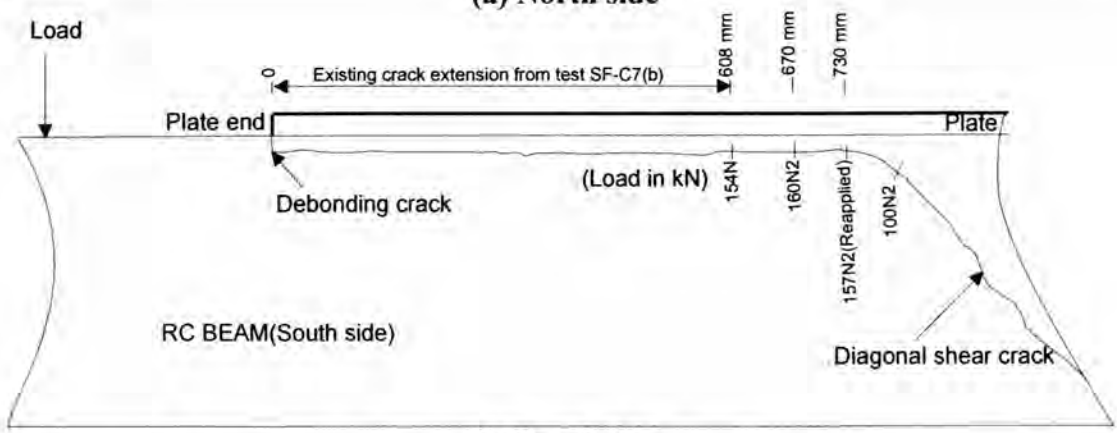

(b) South side

Fig.14.49. SF-C7(c): Rate of propagation of the debonding crack with applied load

Table-14.5: Rate of propagation of debonding crack for test SF-C7(New2)

Load (kN)	Crack position (mm)		M_{end} (kNm)	V_{end} (kN)
	origin	end		
North side				
160	581	712	95.6	104.0
South side				
160	608	670	92.8	104.0
157(reapplied)	670	730	84.7	102.0

14.6.8.2 Longitudinal strains in the compression face plate

Figure 14.50 shows the variation of longitudinal strains recorded at all gauge sites (refer Fig.14.21d). The strain magnitudes increased linearly at all gauge locations till the extension of the existing debonding crack occurred at a shear load of 104 kN. This is marked by the fall in strain and shear load magnitudes at gauges #4 and #5 that were corresponded to the new position of the debonding crack. Finally, the slight fall in load and subsequent termination of the load test due to the failure of unplated

section can be observed by the drop in load and strain magnitude in every gauge location. The maximum strain readings were recorded at gauge location #4 and the maximum recorded strain was 198 microstrains (compressive) which is lower than the yield strain of the steel plate.

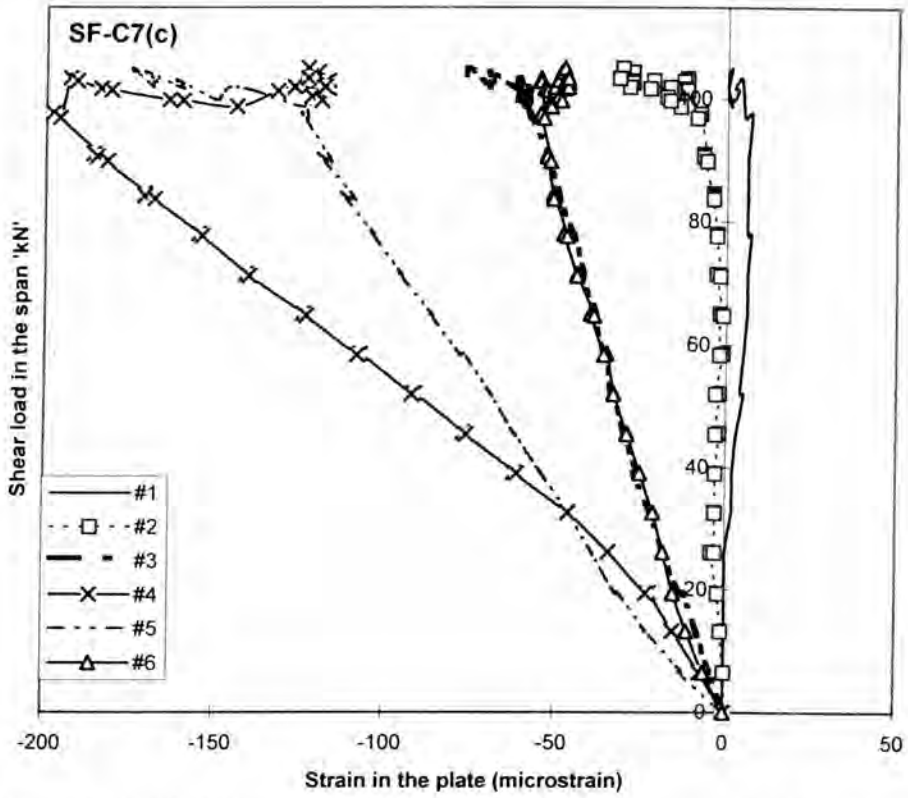

Fig.14.50. SF-C7(c): Longitudinal strains in compression face plate

14.6.8.3 Deflection

Figure 14.51 illustrates the relationship between the deflection recorded at the load point and the shear force in the shear span tested. The deflection increased linearly with the applied load till the test was ended. It also shows when the shear load was about 104 kN, the deflection magnitudes increased appreciably for small increase in load. The maximum recorded deflection at the termination of the test was 34.65 mm.

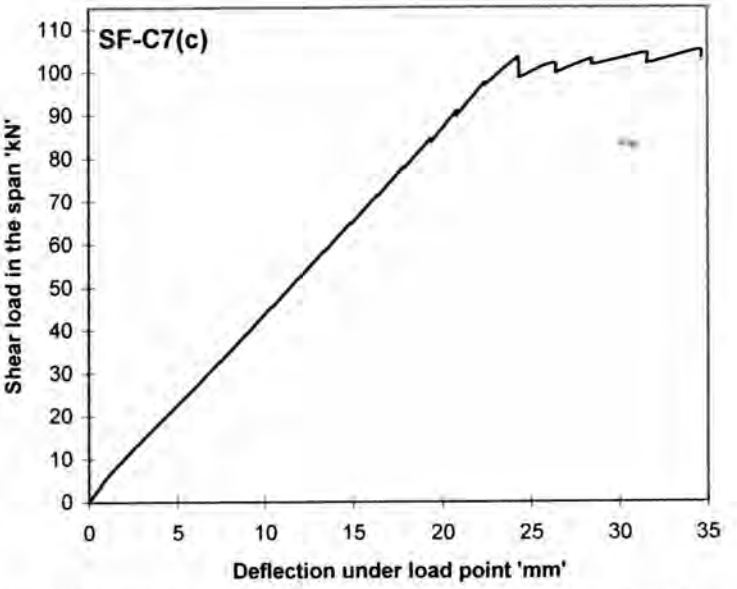

Fig.14.51. SF-C7(c): Deflection at load point Vs Applied shear load

14.7 Discussion of test results from Group II beams

The test results are summarised in Table-14.6 and the sequence of events leading to failure of the beam is shown in table-14.7.

Table-14.6: Test results (Group II)

Test	L_{end}/h	a/h	span (mm)	M_{end} (kNm)	V_{end} kN	$\varepsilon_p(max)$ (microstrain)	Δ_{max} (mm)
SF-C4	1.35	2.4	4500	92.1*	184.2*	30	26.1
SF-C5(a)	2.0	5.4	4250	60.6*	80.8*	137	27.1
SF-C5(b)	2.0	3.1	4250	76.6	102.1	157	27.2
SF-C6(a)	2.7	6.1	4250	66.4	66.4	159	27.2
SF-C6(b)	2.7	3.8	4250	87.2	87.2	137	33.3
SF-C7(a)	4.1	5.1	4500	79.2	78.0	247	28.6
SF-C7(b)	4.1	5.1	4500	80.6	86.7	190	33.5
SF-C7(c)	4.1	4.3	4500	84.7	102.0	198	34.7

a= shear span, L_{end}= distance between plate end and support h= depth of the beam,
M_{end} ,V_{end} = Moment and shear force at the plate end at the final extension of debonding crack (refer to the footnote at Table-14.3 also) but * mark denotes the maximum moment and shear force sustained as no debonding occurred in these tests,
$\varepsilon_{p(max)}$, Δ_{max} = maximum plate strain and maximum deflection recorded at the instance of peeling

It may be noted that when the plate end distance from support L_{end} to depth of beam ratio (L_{end}/h) is lower as in the case of beams SF-C4 and SF-C5(a), the formation of the diagonal shear cracks did not cause the formation of debonding crack along the plate edges. The failure in these beams occurred by the crushing of concrete beneath the load plate. In the case of tests SF-C5(b), SF-C6(a) and SF-C6(b), the debonding crack occurred at the plate end but they did not extend further with the

applied load. The final failure in these tests was also due to crushing of concrete in the vicinity of the load plate. However, for tests SF-C7(a), (b) and (c)in which L_{end}/h was larger, the debonding cracks extended progressively with the applied load.

Table-14.7: Mode of failure (Group II)

Test	Sequence of failure
SF-C4	Formation of diagonal crack at V=68.0 kN and extension of this crack to the beam top at V=80.0 kN. No debonding cracks formed. Final failure by concrete crushing at V=179.8 kN.
SF-C5(a)	Formation of two web shear cracks at V=69.9 kN. No debonding cracks formed. Final failure by concrete crushing at V=80.8 kN.
SF-C5(b)	Formation of fully fledged diagonal cracks at V=87.5 kN, 95 mm long debonding crack at the plate end at V=102.1 kN, which did not extend any further till concrete crushing at V=150.8 kN
SF-C6(a)	Formation of two flexural shear cracks at V=62.1 kN and V=64.5 kN, formation of 185 mm long debonding crack at the plate end at V=102.1 kN, which extended by another 40 mm at V=66.4 kN. Finally concrete crushing at V=71.8 kN
SF-C6(b)	Formation of long diagonal crack at V=77.1 kN and joined with the existing debonding crack from SF-C6(a) at V=87.2 kN, no further change till end of test at V=126.1 kN as the beam experienced large deformations.
SF-C7(a)	Formation of horizontal debonding crack at V=49.1 kN and its progressive extension with applied load till V=78.0 kN.
SF-C7(b)	Extension of existing debonding crack from SF-C7(a) at V=86.7 kN on the north side of the beam and at V=89.0 kN on the south side. Finally, concrete crushing at load point at V=90.7 kN
SF-C7(c)	Extension of existing debonding crack from SF-C7(a) and SF-C7(b) at V=104.0 kN on the north side of the beam and at V=65.0 kN on the south side and this process continued till V=102.0 kN, at which the debonding crack joined with the diagonal crack. Finally, concrete crushing at load point at V=105.0 kN

The notable feature of this series of tests is that the moment at the plate end, either when the debonding crack occurred or when a diagonal shear crack close to the plate end occurred, was always greater than the pure flexural peeling moment capacity as estimated from the test FP-C20 (Section-12.3.3). This is due to the fact that once a diagonal crack occurred in Group-II beams, the flexural stresses are relieved in the plate ends and hence the possibility of peeling was vastly reduced. This explains why the debonding crack that started at the plate end did not progress rapidly as in the case of Group I beams. The shear loads at the plate end at the final stage of the debonding cracks were also lower than the pure shear peeling strength V_{pure} as determined from test SP-C20. Table-14.6 also indicates that the maximum strains recorded in the plate in all the cases were only a fraction of the yield strain of the plate material.

14.8 Analysis of test results from Group I and Group II beams

Table-14.8 shows the analysis of the test results from Group I and Group II beams in which debonding cracks were observed. The analytical results are plotted in Fig.14.52 to draw the failure envelope for the interaction between shear and flexural peeling modes for compression face plated beams.

Table-14.8: Analysis of test results (Group I and Group II)

Test	L_{end}/h	M_{end} (kNm)	V_{end} kN	M_{end}/M_{pure}	V_{end}/V_{pure}	$V_{end}/V_{pure}+M_{end}/M_{pure}$
SP-C20	0	0	155.6	0	1	1
SF-C1	0.68	29.8	119.1	0.630	0.765	1.395
SF-C2	1.35	47.05	94.1	0.995	0.605	1.599
SF-C3	2.70	52.7	52.7*	1.114	0.339	1.453
SF-C5(b)	2.0	76.6	102.1	1.622	0.656	2.278
SF-C6(a)	2.7	66.4	66.4	1.404	0.427	1.831
SF-C6(b)	2.7	87.2	87.2	1.844	0.56	2.404
SF-C7(a)	4.1	79.2	78.0	1.674	0.501	2.176
SF-C7(b)	4.1	80.6	86.7	1.704	0.559	2.351
SF-C7(c)	4.1	84.7	102.0	1.791	0.656	2.446
FP-C20	5.1	47.3	0	1	0	1

* no diagonal crack formed in this case.
M_{pure} = pure peeling moment capacity when no shear force acting at the plate end i.e. M_{end} of FP-C20
V_{pure}= pure shear peeling strength when no moment acting at the plate end i.e. V_{end} of SP-C20

It can be seen from Fig.14.52 that all of the test results from Group-II beams lie outside the envelop ABC in Fig.14.52 and the maximum moment at the plate end M_{end} is about 1.4 to 1.85 times the pure flexural peeling capacity M_{pure}. This is due to the fact that once a diagonal crack occurred in Group-II beams, the flexural stresses are relieved in the plate ends and hence the possibility of peeling was vastly reduced. In the case of Group-I beams, two test results lie around the pure flexural peeling line AB and one test result is closer to the pure shear peeling line BC in Fig.14.52. Therefore, the interaction between flexure and shear is negligible for both group I and II as shown by the failure envelop ABC in Fig.14.52. and it can be defined by the following Equations.

$$\left(\frac{M_{end}}{M_{pure}}\right)+\left(\frac{V_{end}}{V_{pure}}\right)=2.0, \qquad (14.1a)$$

where

$$M_{end} \leq M_{pure}, \tag{14.1b}$$

and

$$V_{end} \leq V_{pure}, \tag{14.1c}$$

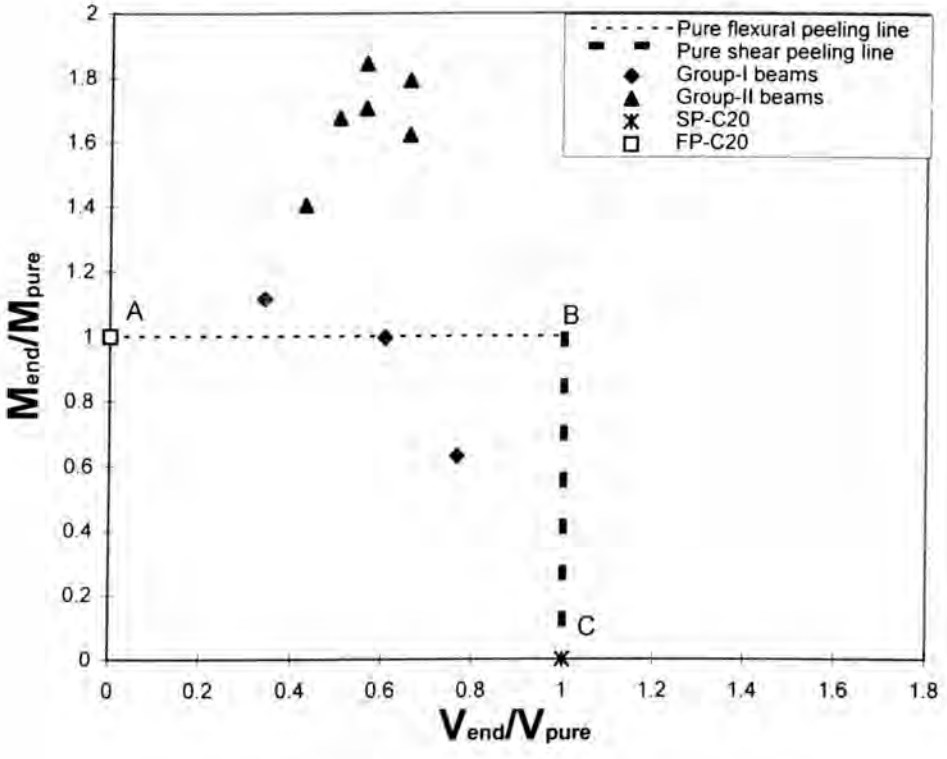

Fig.14.52. Interaction envelop for Group I & II beams

14.9 Conclusion

1. In this study, the peeling behaviour of compression face plated beams when the plate ends are terminated in a region where both shear force and bending moment are present was investigated. The study was conducted in two groups. Group I in which the plate ends are subjected to the least bending moment than in the other regions of the plate and this represents the case of simply supported beams. In GroupII, the plate ends were at a higher moment than in the other locations of the plates and this represents the case of hogging region moments in continuous beams where the plates are extended to the sagging moment region.

2. In Group I beams, it was found that as the plate end is terminated away from the support, the peeling of the plate ends occur at a moment approximately equal to that of the pure flexural peeling capacity of the plated beam. On the contrary, when the plate end was terminated closer to the support, peeling failure occurred as indicated by the formation of a diagonal shear crack and a subsequent long horizontal debonding crack along the bottom edge of the plate
3. In Group II beams, when the plate end distance from support L_{end} to depth of beam ratio (L_{end}/h) was less than 3, the formation of a diagonal shear crack did not cause the formation of a debonding crack along the plate edges. The failure in these beams occurred by crushing of concrete beneath the load plate. In the case of beams where L_{end}/h was between 3 and 4, a debonding crack of limited length occurred at the plate end but they did not extend further with the applied load. The final failure in these tests was also due to crushing of concrete in the vicinity of the load plate. However, for beams in which L_{end}/h was larger, the debonding cracks extended progressively with the applied load.
4. The notable feature of Group II tests is that the moment at the plate end either when the debonding crack occurred or when the strain readings showed a decline was always greater than the pure flexural peeling capacity. This is due to the fact that once a diagonal crack occurred in Group-II beams, the flexural stresses are relieved in the plate ends and hence the possibility of peeling was vastly reduced. This explains why the debonding crack that started at the plate end did not progress rapidly as in the case of Group I beams. Furthermore, the shear loads at the plate end at the final stage of the debonding cracks were lower than the pure shear peeling strength V_{pure} as determined from test SP-C20. The maximum

strains recorded in the plate in all the cases were only a fraction of the yield strain of the plate material.

5. The analysis of the test results gives the equation for the failure envelop as $\left(\frac{M_{end}}{M_{pure}}\right)+\left(\frac{V_{end}}{V_{pure}}\right)=2.0$, where $M_{end} \le M_{pure}$,and $V_{end} \le V_{pure}$. It was conclusively shown that the interaction between flexure and shear is negligible for compression face plated beams.

CHAPTER-15: FLEXURE/SHEAR INTERACTION IN SIDE PLATED BEAMS

CONTENTS

15.1 Introduction

In this chapter, the interaction between the shear and flexural peeling of side plated beams is investigated using the test results of Oehlers, Nguyen and Bradford as described in Section 2.4.3. It may be recalled that the combination of stress resultants to cause peeling is given by the failure envelope shown in Fig.2.20. The equation derived by Oehlers et.al for shear/flexure interaction is (Refer Eqn.2.8. in Section 2.8.1.2)

$$\left[\frac{M_{end}}{M_{pure,sp}(mean)}\right]+\left[\frac{V_{end}}{V_{pure,sp}}\right]\leq 1.28. \qquad (15.1)$$

In this equation, the mean pure flexural peeling capacity $M_{pure,sp}$ was calculated using Eqn.2.7a. However, as there was no reliable model for computing the pure shear peeling resistance $V_{pure,sp}$ available to Oehlers et.al, they used the actual shear peeling resistance of the beam 2n4 in the analysis (Refer Table-2.2 in Section 2.4.1.2). Furthermore, M_{end} and V_{end} indicate the bending moment and shear force at the plate end. It may be noted that the side plates were terminated over the support in case of 2n4 and hence the M_{end} was zero for this beam. Now that mathematical models have been developed to compute $V_{pure,sp}$ in the present study for any location of the plate end, it is appropriate to reanalyse the test results in Table-2.3 that were used for calibrating the interaction equation 2.8. This will lead to a refined model for shear/flexure interaction for side plated beams.

15.2 Analysis of test results from section 2.4.3

15.2.1 Shear and flexural peeling strengths

The mathematical model for side plated beams as described in section 11.3 was used to compute the shear peeling strength of the side plated beams $V_{pure,sp}$. The envelops for the shear load to cause shear crack V_{cr} and the shear load load to cause failure along an

existing crack V_u for all the beams are shown in Fig.15.1. It may be noted that for all the tests in Table-2.3 except test-3c, the shear peeling strength of the plated beams are equivalent to the shear strength of the unplated reinforced concrete beam excluding the stirrups V_{uc}. This is due to the fact that the critical crack location for the unplated beam is about 575 mm from the support , whereas the plate ends except for 2c are 900 mm or more from the support. Hence, the side plates have negligible effect on the shear peeling resistance as they can neither offer resistance to the formation of the critical diagonal shear cracks nor can they prevent the failure along the critical shear cracks. The present analysis gives $V_{pure,sp}$ for tests 3c1N, 3c1S, 3c2N and 3c2S to be 101 kN and for all the other tests, the magnitude is 78 kN, as summarised in Table-15.1. Furthermore, Eqn.2.7a was used to compute mean $M_{pure,sp}$ and it is found to be 78 kNm for all the beams.

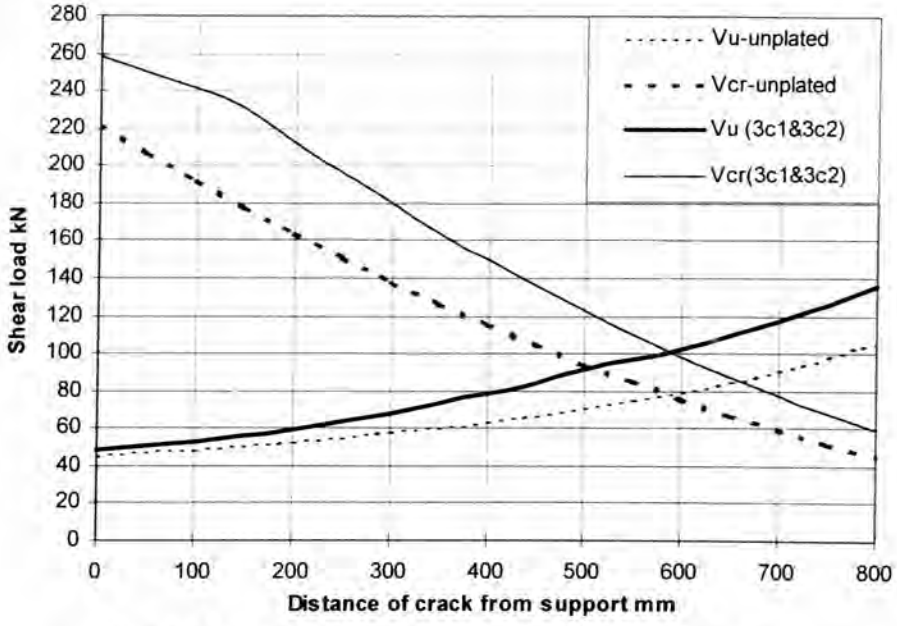

Fig.15.1. Shear peeling analysis of all test results

15.2.2 Interaction equation

Table-15.1 summarises both test and analytical results and Fig.15.2 illustrates the interaction failure envelope. It can be seen from Fig.15.2 that most of the test results are

scattered around either the pure flexural peeling failure line AB or the pure shear peeling failure line BC. Only three results lie outside the failure envelope ABC and even in this case, the moment at the instance of the peeling M_{end} is about 30% more than the pure flexural peeling capacity M_{pure}. This shows that the interaction between shear and flexure is weak unlike that suggested by Eqn.2.8. The present analysis gives the three equations that define the failure envelope ABC as

$$\left[\frac{M_{end}}{M_{pure,sp}(mean)}\right]+\left[\frac{V_{end}}{V_{pure,sp}}\right]\leq 2 \qquad (15.2a)$$

where

$$V_{end}\leq V_{pure,sp} \qquad (15.2b)$$

$$M_{end}\leq M_{pure,sp}(mean) \qquad (15.2c)$$

Table-15.1: Analysis of test results

Tests	L_{end} (mm)	V_{end} (kN)	M_{end} (kNm)	$V_{pure,sp}$ (kN)	$M_{pure,sp}$ (kNm)	$V_{end}/V_{pure,sp}$	$M_{end}/M_{pure,sp}$	$V_{end}/V_{pure,sp}$ + $M_{end}/M_{pure,sp}$
3c1N	300	103.1	30.9	101	78	1.021	0.3962	1.417
3c1S	300	103.1	30.9	101	78	1.021	0.3962	1.417
3c2N	300	104.5	31.3	101	78	1.035	0.4013	1.436
3c2S	300	104.5	31.3	101	78	1.035	0.4013	1.436
3d1N	910	74.7	68	78	78	0.958	0.8718	1.829
3d1S	910	72.6	66.1	78	78	0.931	0.8474	1.778
3d2N	910	87.5	79.6	78	78	1.122	1.0205	2.142
3d2S	910	76.9	70	78	78	0.986	0.8974	1.883
3e1N	2740	40.3	110.3	78	78	0.517	1.4141	1.931
3e1S	2740	36.2	99.3	78	78	0.464	1.2731	1.737
3e2N	2395	42.1	100.9	78	78	0.54	1.2936	1.833
3e2S	2395	28.6	68.6	78	78	0.367	0.8795	1.246
3f1N	1200	65.2	78.3	78	78	0.836	1.0038	1.84
3f1S	1200	52	62.4	78	78	0.667	0.8	1.467
3f2N	1200	55.7	66.9	78	78	0.714	0.8577	1.572
3f2S	1200	55.7	66.9	78	78	0.714	0.8577	1.572

L_{end}= distance between the plate end and the support

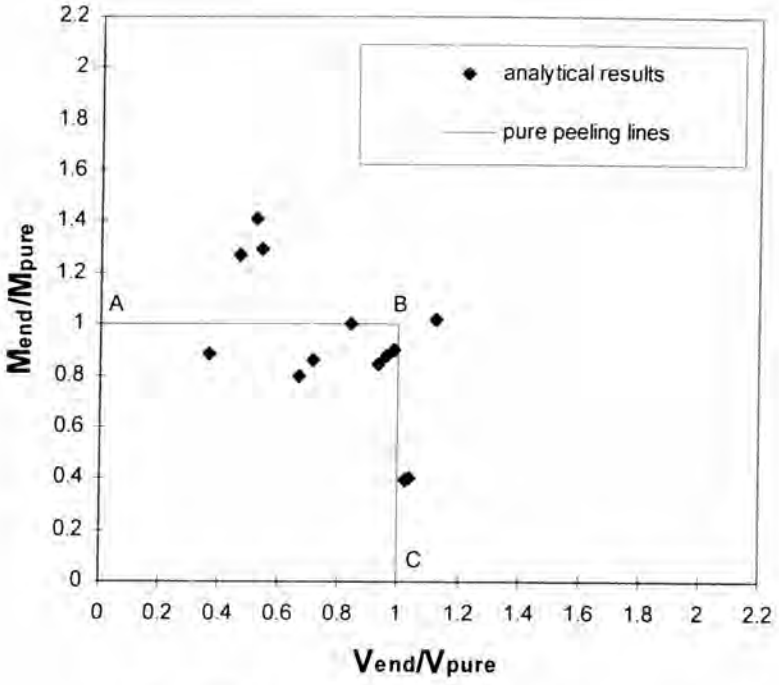

Fig.15.2. Interaction failure envelope

15.3 Conclusion

In this study, the interaction between the shear and flexural peeling failure modes for side plated beams was investigated and the interaction was shown to be very weak, unlike that originally proposed by Oehlers, Nguyen and Bradford (Refer Section 2.8.1.2). The mean failure line for interaction was defined by the following three equations:

$$\left[\frac{M_{end}}{M_{pure,sp}(mean)}\right]+\left[\frac{V_{end}}{V_{pure,sp}}\right]\leq 2,\ V_{end}\leq V_{pure,sp},\ \text{and}\ M_{end}\leq M_{pure,sp}(mean).$$

PART-VI: AXIAL PEELING

CHAPTER-16: AXIAL PEELING WITHIN PLATE ENDS OF R C BEAMS BONDED WITH STEEL PLATES TO THEIR SIDES

CONTENTS

16.1 Introduction

This chapter deals with the axial peeling of steel side plated beams that occurs within the plate ends. Unlike shear or flexural peeling that occurs in the vicinity of plate ends, the axial peeling occurs when a flexural shear crack crosses the plane of the plate resulting in debonding crack along the edges of the plate. As no instantaneous debonding occurs as in the shear peeling at the plate ends, the plates will be subjected to infinite strains. The large amount of strains has to be accommodated at the point where the crack crosses the plate inducing the debonding cracks that propagate away from the flexural cracks, as shown in Fig.4.1 (Section 4.1). The primary objective of this study is to investigate the axial peeling behaviour in beams bonded with considerably deep steel side plates. The phenomenon is first observed through studies and then the test results are analysed for various modes of debonding. Finally, useful guidelines are presented to determine the capacity of side plated beams susceptible to axial peeling.

16.2 Specimen and test rig

The specimens consisted of three reinforced concrete beams with steel plates bonded to both the sides of the beams. The basic, unplated reinforced concrete cross section of all the three beams is the same and is shown in Fig.16.1a. In this series of tests, a total of three tests were carried out; whereas beams 2B and 2D were tested under two concentrated loads, beam 2C was subjected to a single concentrated load, as shown in Figs.16.1b-d. The only parameter varied in the study was the depth of the side plates, which were bonded and spanned from support to support of the simply supported beams.

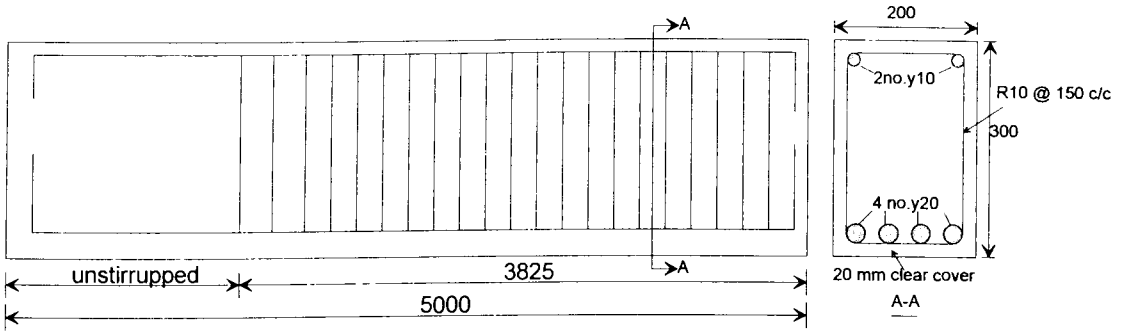

(a) Reinforcement details of unplated beam

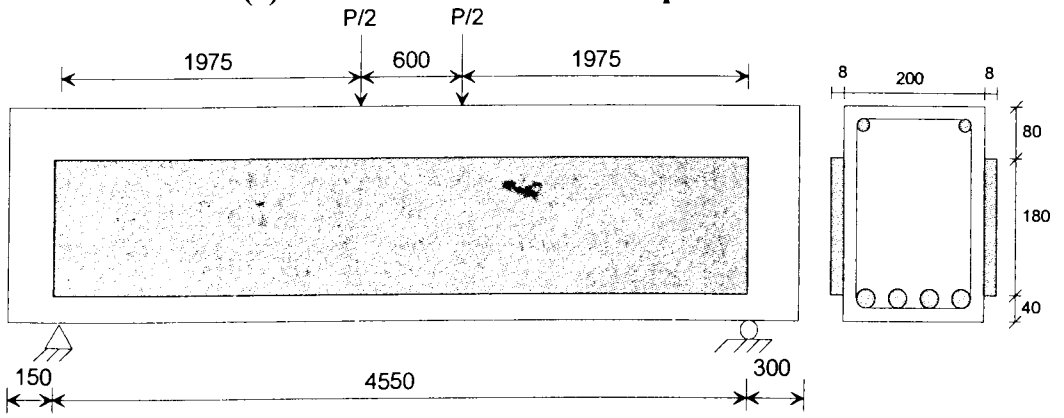

(b) Details of beam 2B

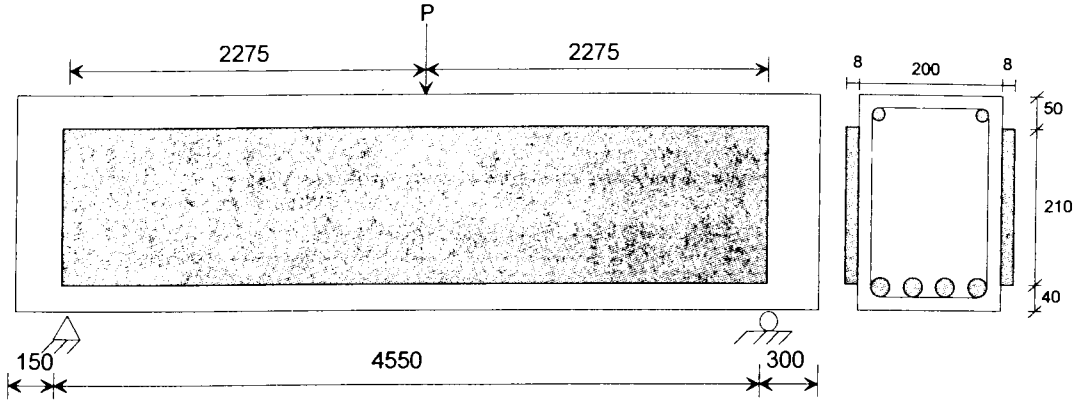

(c) Details of beam 2C

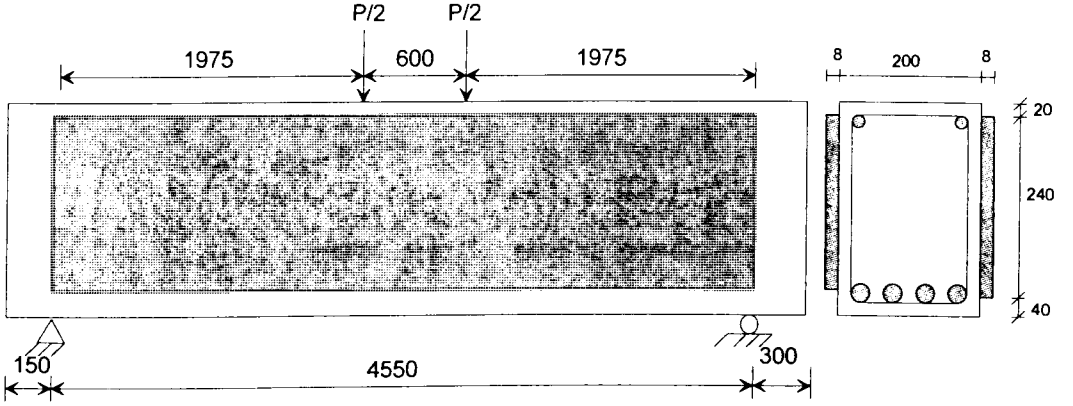

(d) Details of beam 2D

Fig.16.1. Schematic details of beams tested

16.3 Instrumentation

Strain gauges were bonded to both side plates in order to detect the debonding at various sites of the plates and also to study the behaviour under flexure. The arrangements of the strain gauges and their numbering are shown in Figs. 16.2a-c for all the three beams tested. The beam deflections at mid-span were monitored by a dial gauge and also by a transducer.

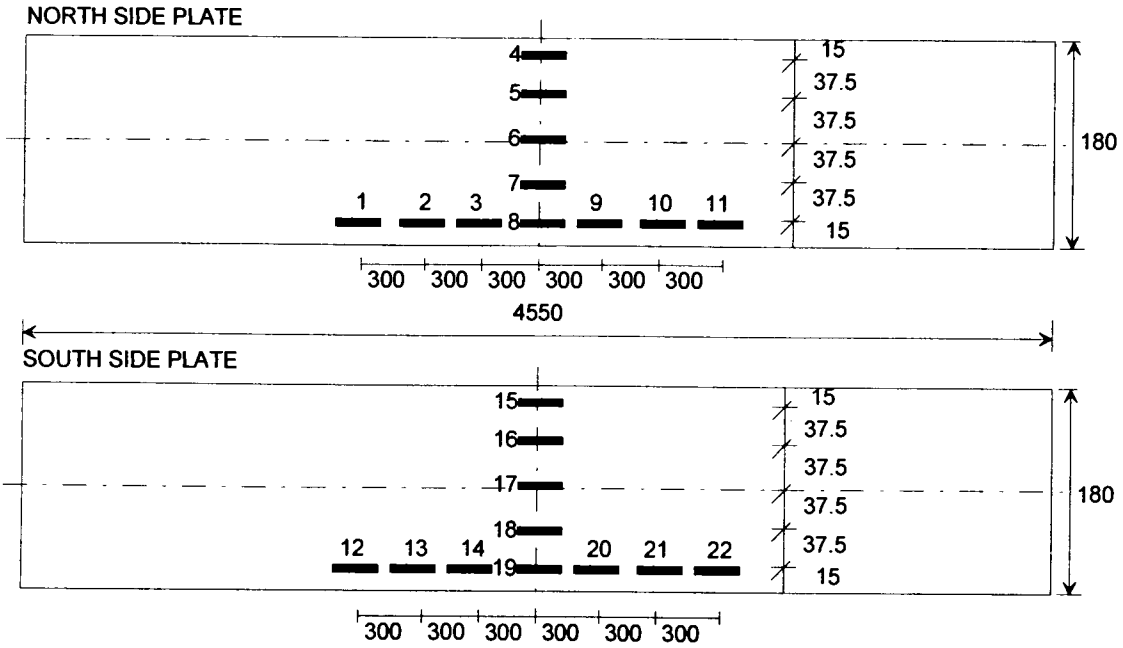

Fig.16.2a. Strain gauge arrangement for Beam 2B

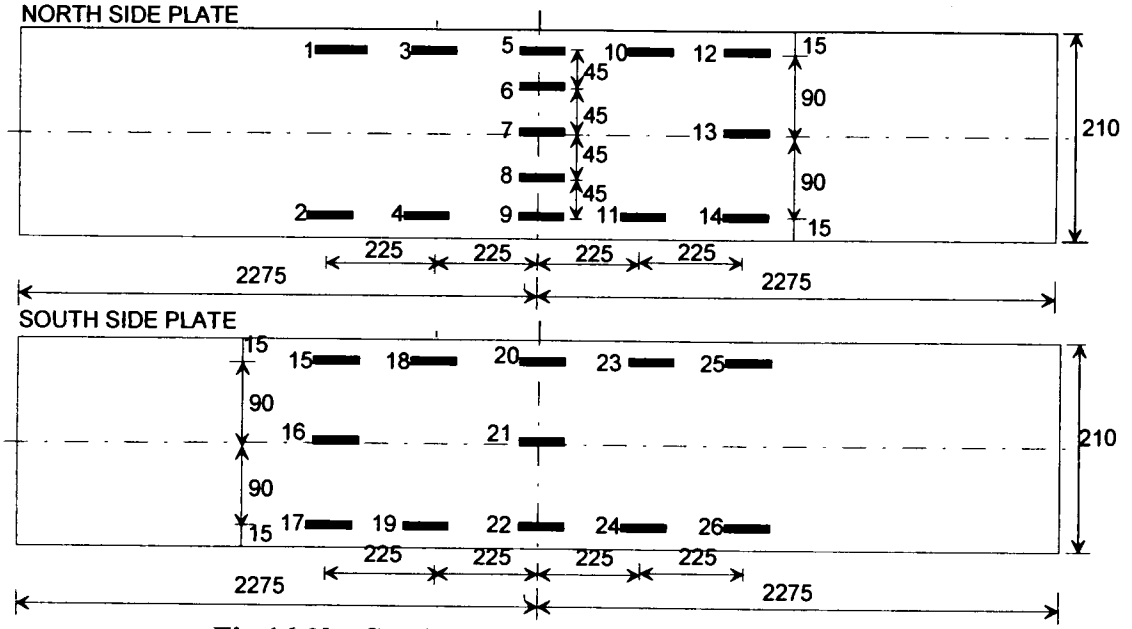

Fig.16.2b. Strain gauge arrangement for Beam 2C

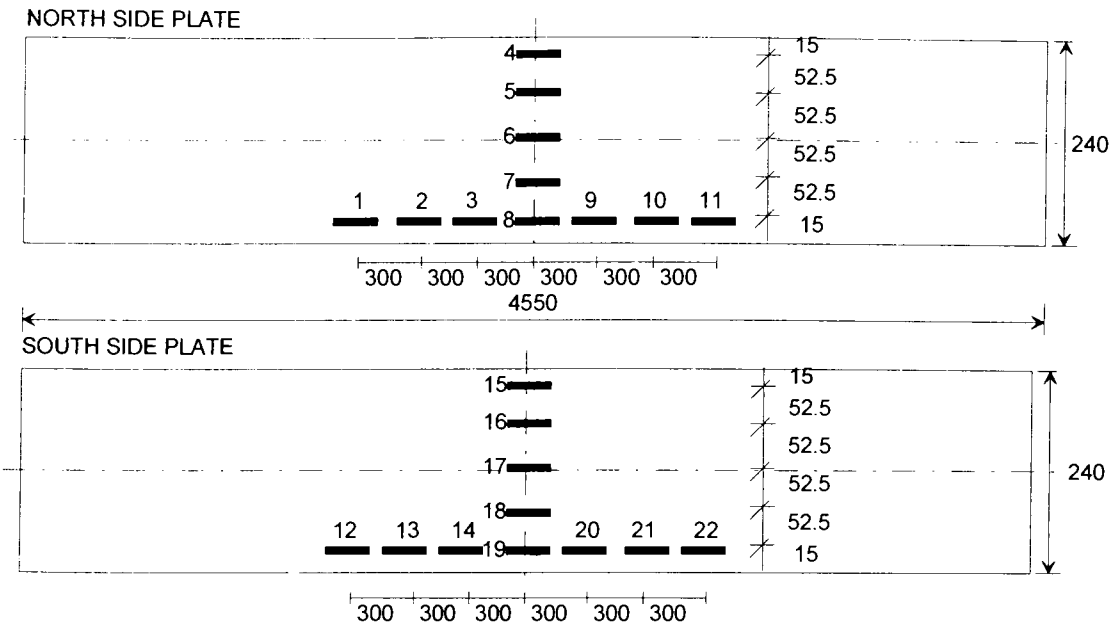

Fig.16.2c. Strain gauge arrangement for Beam 2D

16.4 Material properties

All the beams were cast in a single pour using ready mixed concrete supplied by a local manufacturer. Material properties of the concrete are shown in Table-16.1. As the beams were tested during a period 170-175 days, the material properties given in Table-16.1 for 179 days were used for analysing the test results. Material properties of the steel plates, reinforcing bars and shear stirrups are shown in Table-16.2. In this table, the individual values are of each test are given under the "i" column and their mean value under "m" column. The manufacturer's specifications of the material properties of the epoxy adhesive used for bonding the steel side-plates are indicated in Table-16.3.

Table-16.1: Material properties of the concrete

Age	E_c (MPa)		b_f (MPa)		f_{tbm} (MPa)		f_c (MPa)		f_{cu} (MPa)	
(days)	i	m	i	m	i	m	i	m	i	m
28	33876		3.71		6.29		46.7		54.9	
	32869	33329	4.51		5.79	6.03	45.3	46.9	55.5	55.7
	33240		4.62	4.23	6.00		48.7		56.6	
			3.92							
			4.38							
179	38641		4.42		8.18		59.5		61.8	
	36353	38182	4.47	4.54	7.95	8.07	54.2	57.9	63.1	64.0
	39551		4.73		8.10		59.9		67.1	

Where, E_c = Elastic modulus of the concrete, f_c= Cylinder compressive strength of the concrete, f_{cu}=Cube compressive strength of the concrete, f_b= Brazilian tensile strength of the concrete and f_{tbm} = Beam tensile strength of the concrete.

Table-16.2. Material properties of the steel

Item	f_y (MPa)				f_u (MPa)			
Sample No.	1	2	3	Mean	1	2	3	Mean
Rebar Y20	457.4	453.6	450.7	453.9	547.2	544.3	549.1	546.9
Stirrups R10	-	-	-	-	570.9	582.5	581.4	576.7
Side-plates- 8 mm	302.6	298.0	302.7	301.1	460.05	456.6	457.0	457.9

where f_y = Yield strength of the steel and f_u = Ultimate strength of the steel

Table-16.3. Material properties of the glue Hilti CA 273 after 2 days (as tested by the manufacturer)

Compressive strength (ISO 604)	Tensile strength (ISO 527)	Flexural strength (ISO 178)	Elastic modulus in compression (ASTM D 695)	Tensile bond strength (ISO 527)	Maximum operating temperature
110-120 MPa	30-40 MPa	20-30 MPa	5000-6000 MPa	10-15 MPa	80° C

16.5 Test procedure

A total of three tests were carried out in this series to study the behaviour under flexure of the side plated beams. Whereas beams 2B and 2D were subjected to two point loading, beam 2C was tested under a single point load applied at mid-span as shown in Figs.16.1b, 16.1c and 16.1d.

For each test, the beam was first loaded in steps of 10 kN and the cracks were marked and photographically recorded. The corresponding micro-strains at the various sites of the side plates (Figs.16.2a-c) were monitored by strain gauges and the readings at each load step were recorded through a data logging system. The beam deflection at the mid-span at each load step was also recorded by means of both a transducer and also a dial gauge. The load increment was reduced to 5 kN when a debonding crack was observed and later to 3 kN as the beam was heading towards failure. Each test took about 4 hours to complete.

16.6 Test results

16.6.1 Beam 2B

Beam 2B was bonded with plates of dimension 180x8 mm on both sides, as shown in Fig.16.1b. It was tested to failure by a two-point load such that the magnitude of the bending moment in the constant moment region (M) in kNm was 0.9875 times the total applied load (P) in kN.

16.6.1.1 Crack propagation and mode of failure

At a total applied load of 30 kN (Maximum moment (M) = 29.62 kNm), flexural hair line cracks at a regular interval of 150 mm occurred in the region between the strain gauges #1 and #9, as can be seen in Fig.16.3a.

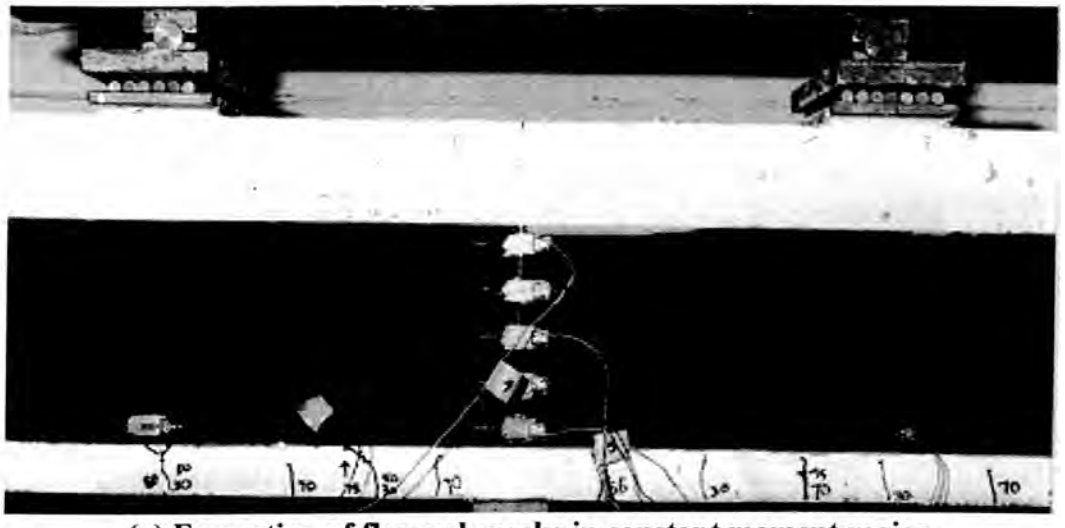

(a) Formation of flexural cracks in constant moment region

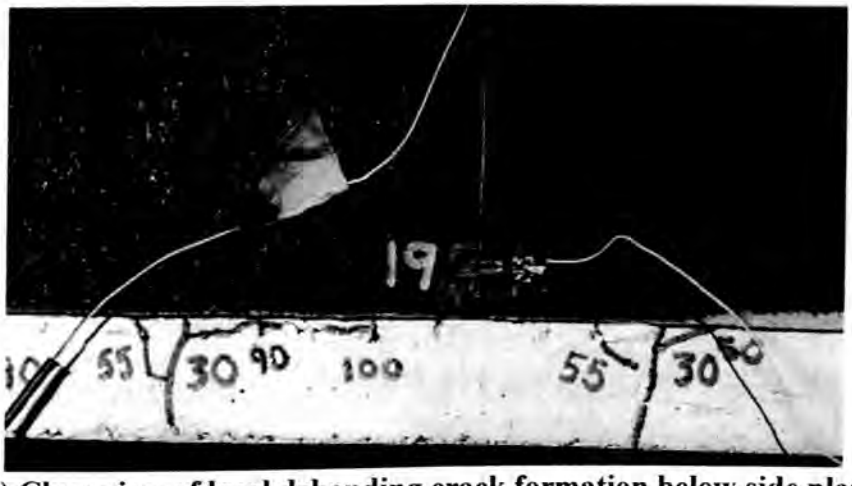

(b) Close view of local debonding crack formation below side plate

Fig.16.3. Test-2B: Crack patterns

When the applied load was increased to 40 kN (M=39.5 kNm), new flexural cracks became visible below the gauges #10 and #11. As the load was further increased to 55 kN (M = 54.3 kNm), the flexural cracks extended further upwards and then the cracks propagated along the bottom edge of the plates. At an applied load of 70 kN (M=69.1 kNm), new flexural cracks were observed in the constant bending moment region between the existing cracks, as shown in Fig.16.3a. Moreover, the existing cracks started to join with the adjacent cracks and this eventually led to the formation of horizontal debonding cracks along the bottom edge of the side plates at higher applied loads, as shown in Fig.16.3b. As the load was increased to 95 kN (M=93.8 kNm), debonding cracks appeared in the region beneath strain gauges #1, #2, and #3.

As further increments of loads were applied, other debonding cracks also propagated gradually, as shown in Fig.16.4a. When the load was increased to 183 kN (M=180.7 kNm), a chunk of concrete under compression in the central region got crushed, as shown in Fig.16.4a. This led to a sudden drop in load from 183 kN to 167 kN (M=180.7 kNm to 164.9 kNm). Still, the beam was able to carry further load as the steel plates were carrying the reduced load and undergoing large magnitude of strains. At this stage the concrete was unable to carry further loads due to crushing as shown in Fig.16.4b and the large compressive stresses were transferred to the top fibres of the plate. Finally, the south side plate debonded from the concrete at a load of 147 kN (M=145.2 kNm) due to the formation of long, horizontal debonding crack along the top edge of the plate. Subsequently, the north side plate also debonded in a similar fashion and the load test was terminated when the load was 121.7 kN (M=119.5 kNm).

(a) Onset of concrete crushing and extension of debonding cracks

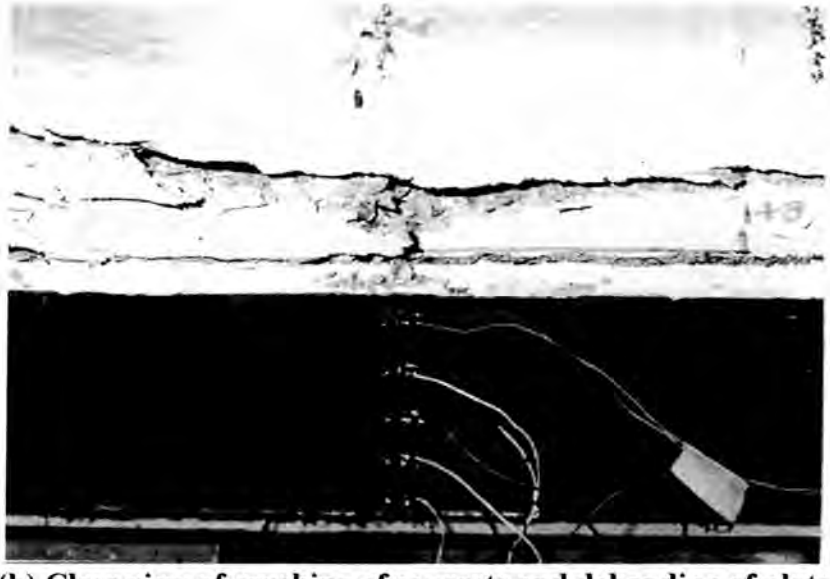

(b) Close view of crushing of concrete and debonding of plate

Fig.16.4. Test-2B: Final crack patterns

16.6.1.2 Longitudinal strains in side plates

The side plates of beam 2B were bonded with electrical resistance strain gauges and were numbered as shown in Fig.16.2a. The strain magnitudes at the middle cross section for north and south side plates are shown in Figs.16.5a and 16.5b respectively. It can be observed that the plate strains increased gradually with the applied moment and the bottom fibre of the plates yielded, i.e. strain magnitudes were greater than 1500 microstrains at an applied moment of 138.2 kNm for the plate on the south side and 148.1 kNm for the plate on the north side. Once the concrete crushed leading to a sudden drop in applied moment from 180.7 kNm to 164.9 kNm, the plates started

carrying more load as the concrete was unable to carry the load. The long plateau of the strain diagram shows the beneficial effect of side plates in improving the ductility of the plated beam.

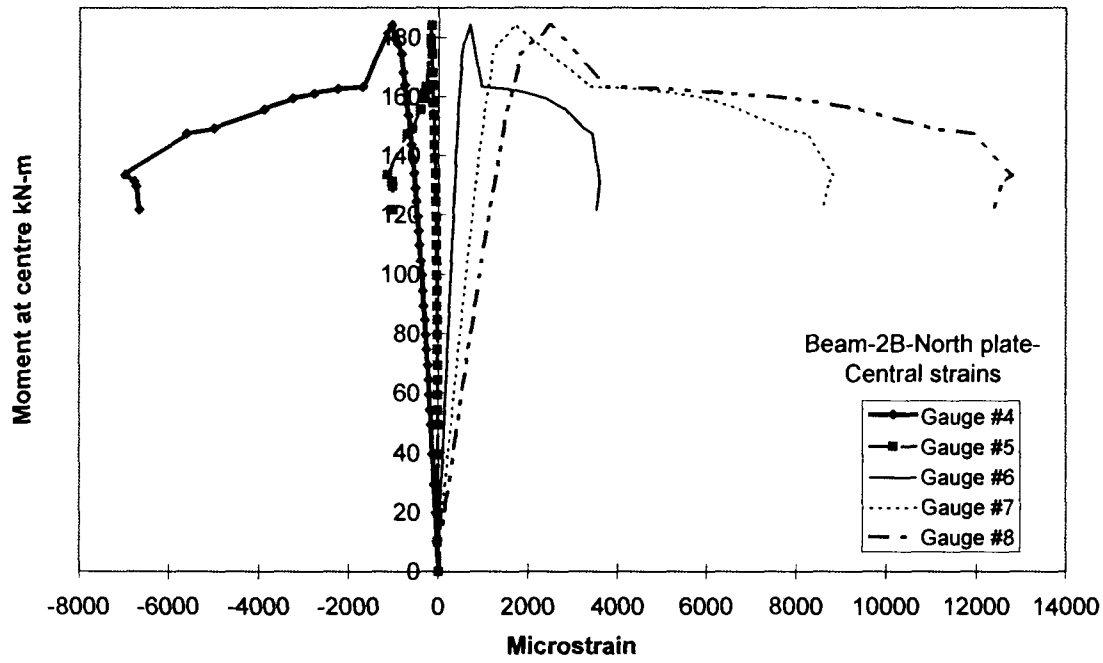

Fig.16.5a. Beam-2B: North side plate-strains at centre

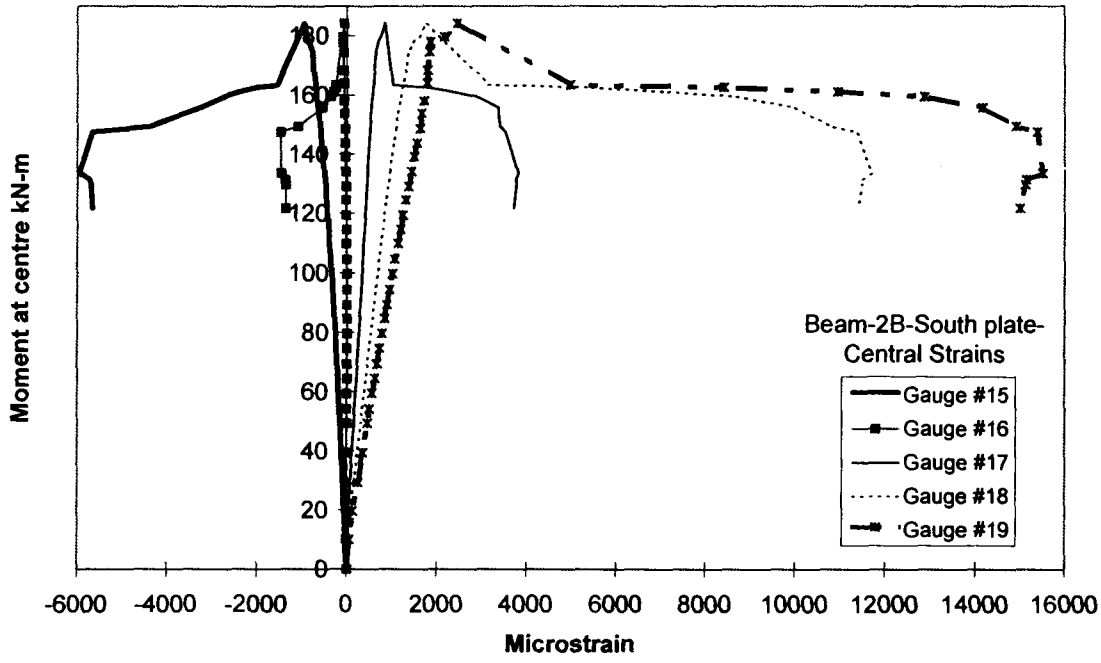

Fig.16.5b. Beam-2B: South side plate-strains at centre

Figures 16.6a and 16.6b show the strains recorded along the bottom level of both the plates, except the gauges placed at the mid-span. Figure 16.7 shows the

variation of strain recorded on the top fibres of the plates with the maximum applied moment. These figures reveal that the strain magnitudes at all the locations increased linearly with the maximum moment until the maximum moment was 180.7 kNm. When the maximum moment was 180.7 kNm, a chunk of concrete under compression in the central region crushed and this led to a sudden drop in moment from 180.7 kNm kN to 164.9 kNm and this is shown by a fall in the relationship. However, the ductile nature of the plated beam is shown by the large increase in the strain magnitudes in the strain gauges bonded in the mid-span. It can be observed that the gauges #2, #3, #9 and #10 in the north side in Fig.16.6a and #13, #14, #20 and #21 in the south side in Fig.16.6b recorded values well above the yield strain of the plate material. The diagrams also show the debonding of the side plates by showing the sudden drop in strain values.

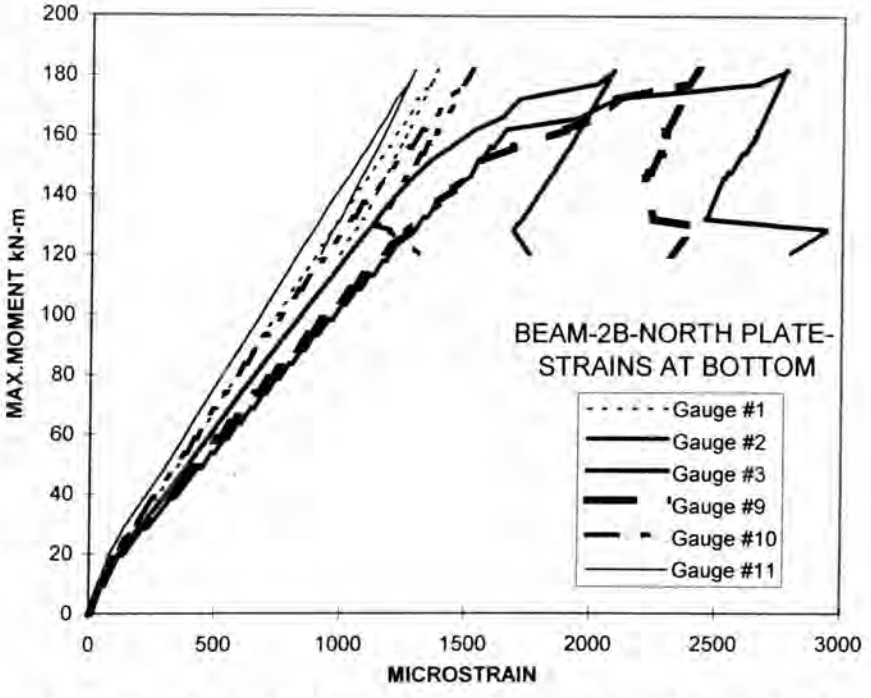

Fig.16.6a. Beam-2B: North side plate-strains at bottom level

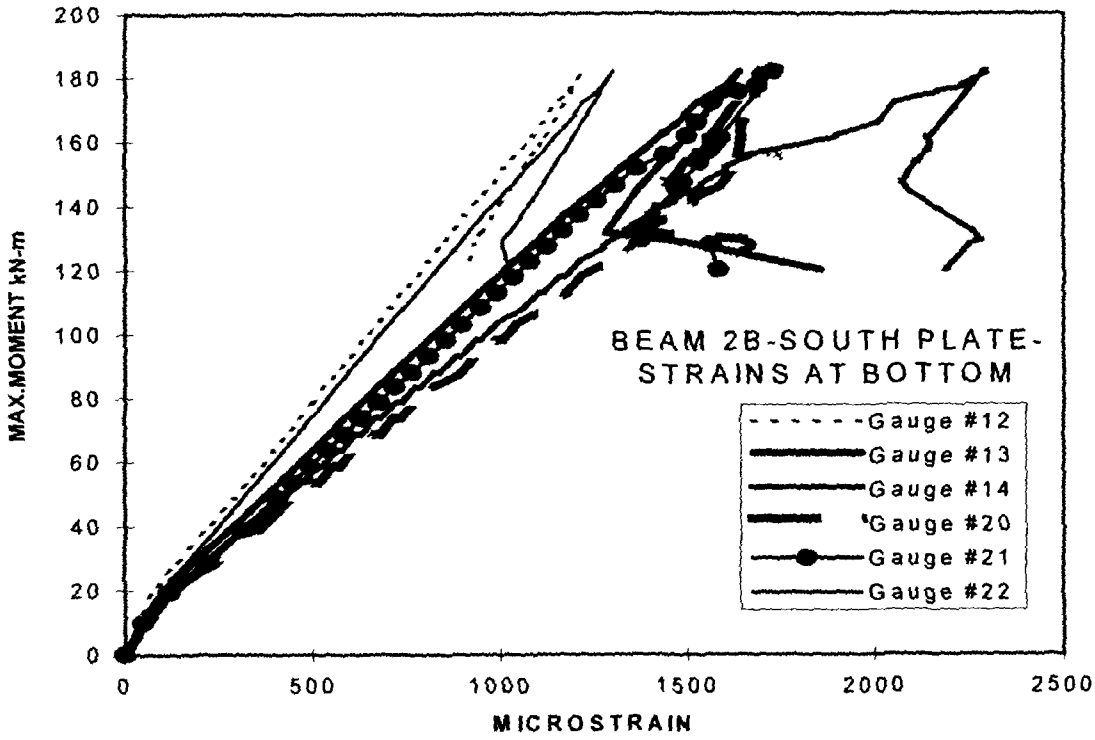

Fig.16.6b. Beam-2B: South side plate-strains at bottom level

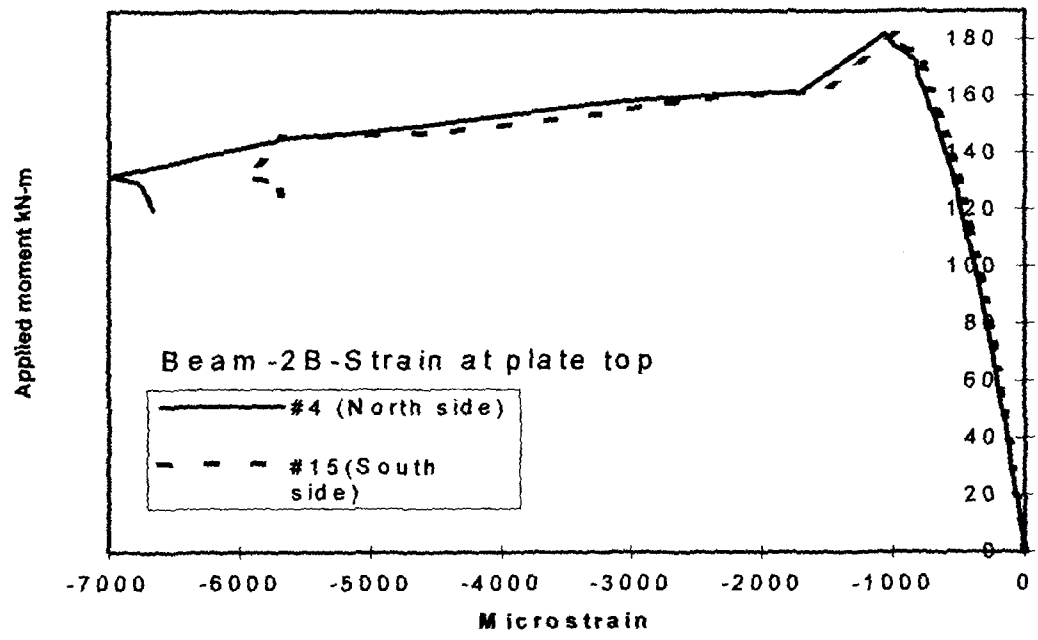

Fig.16.7. Beam-2B: North and South side plates-strains at top level

Table-16.4 summarises the maximum strains recorded in the plate at the three significant stages of the test, i.e. when the beam carried the maximum moment, the immediate fall in moment due to onset of concrete crushing and the failure due to

complete debonding of side plates. It can be seen that the maximum strains recorded at the bottom fibres of the plate at the maximum moment level is about 900 microstrains more than the yield strain of the plate (1505 microstrains). It may be noted that the yield strain of the internal tension reinforcement is 2250 microstrains. Furthermore, as the reinforcement strains were not measured directly, the plate bottom strain can be assumed to correspond to the reinforcement strain before the occurrence of any major debonding cracks. This is due to the centroid of the reinforcement and the bottom level of the side plates being the same. Therefore, the strain in the internal reinforcement can be assumed to have just yielded at this stage. As the concrete started crushing at the maximum moment, the stresses were transferred to the external plates. This is revealed by the quantum jump in strain magnitudes at the onset of concrete crushing. Finally, the maximum tensile strain recorded in the plate at complete debonding was 15000 microstrains, which is about 10 times the yield strain. The maximum recorded compressive strain is about 6000 microstrains, which is about 4 times the yield strain. This shows the ductile nature of failure.

Table-16.4: Beam-2B: Maximum plate strains

Event	Moment (kNm)	Recorded strain (Microstrains)			
		North side		South side	
		Top	Bottom	Top	Bottom
At maximum applied moment	180.7	-1056	2471	-956	2456
At sudden drop in moment due to concrete crushing	164.9	-1654	3706	-1516	4808
At failure (complete debonding)	119.5	-6988	12799	-6270	15712

Note: (-ve)compressive and (+ve) tensile strains.

16.6.1.3 Deflection

Fig.16.8 illustrates the relationship between the deflection recorded at the mid-span and the maximum applied moment. It depicts the improved ductility of the plated

beam as the deflection value at concrete crushing was only 40 mm while it was about 60 mm when the debonding of the plate occurred.

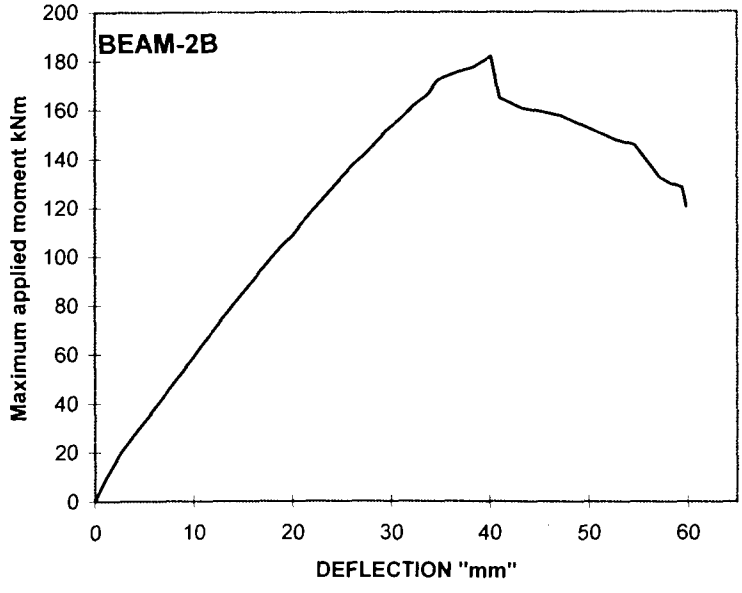

Fig.16.8. Deflection at mid-span in Beam-2B

16.6.2 Beam-2C

Beam-2C was bonded with two side-plates of 210 mm deep and 8 mm thick, as shown in Fig.16.1c. It was tested to failure by applying the load at its centre such that the magnitude of bending moment at the centre (M) in kNm was 1.1375 times the total applied load (P) in kN.

16.6.2.1 Crack propagation and mode of failure

At an applied load of 20 kN (M = 22.75 kNm), hairline cracks could be observed in the concrete at the middle region below the plates and they propagated further on increasing the applied load, as shown in Fig.16.9. At about 50 kN (M=56.9 kNm), the cracks extended to the bottom edge of the plates and they started branching into multiple cracks and propagated parallel to the bottom level of the side plates. This process continued and the cracks tended to join with each other so as to form long debonding cracks at higher loads as shown in Fig.16.9. At about 130 kN (M=147.9

kNm), new flexural cracks were formed between the existing cracks in the central region.

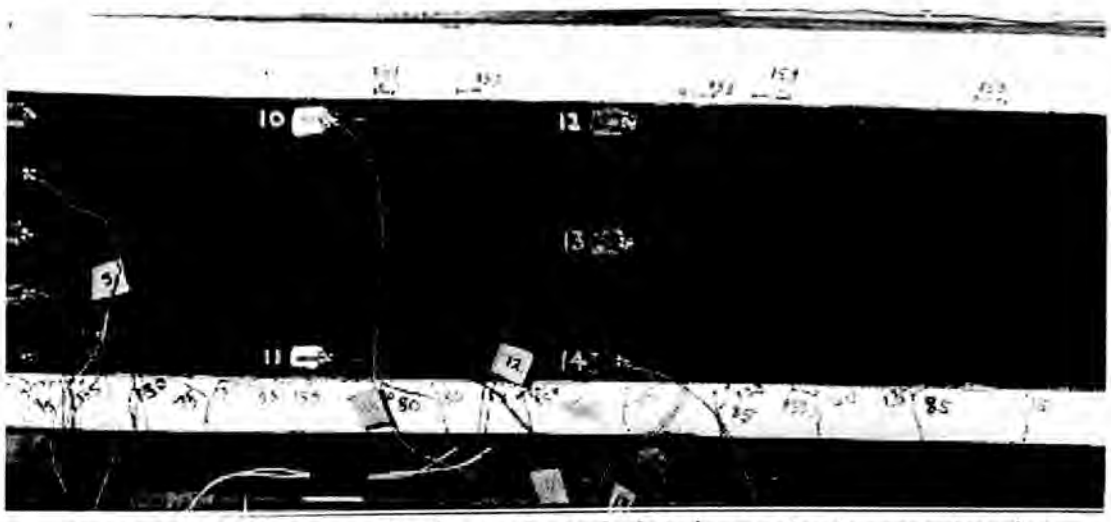

Fig.16.9. Debonding cracks beneath steel plate in constant moment region

At an applied load of 153 kN (M=174 kNm), the extreme top fibre concrete beneath the load point started crushing gradually, as shown in Fig.16.10. This process continued till the load was 175 kN (M=199 kNm) at which the compressive concrete failed completely and the load suddenly dropped to 164 kN (M=186.6 kNm). Further application of displacement increased the magnitude of the applied load to 170.2 kN (M=193.6 kNm) but the beam could not sustain the applied load fully and it dropped to 167.8 kN (M=190.8 kNm). The applied load started decreasing rapidly thereafter. During this interval, long debonding cracks occurred along the top level of the plates and the north side plate debonded accompanied by buckling at a reapplied load of 140.3 kN (M=159.6 kNm), as shown in Fig.16.11a. The south side plate also completely debonded in a similar fashion at a reapplied load of 119.4 kN (M=135.8 kNm), at which the test was terminated as can be seen in Fig.16.11b.

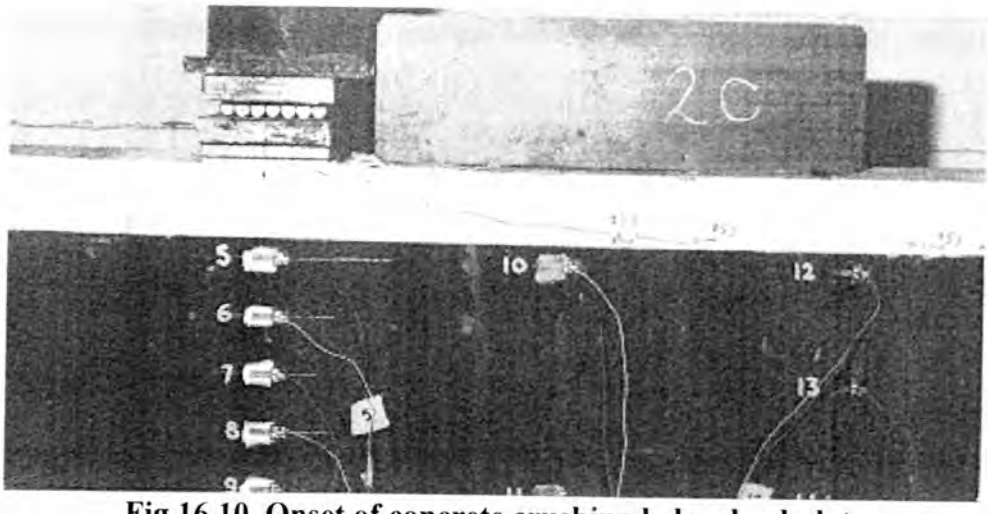

Fig.16.10. Onset of concrete crushing below load plate

(a) Extension of debonding crack and local buckling of north side plate

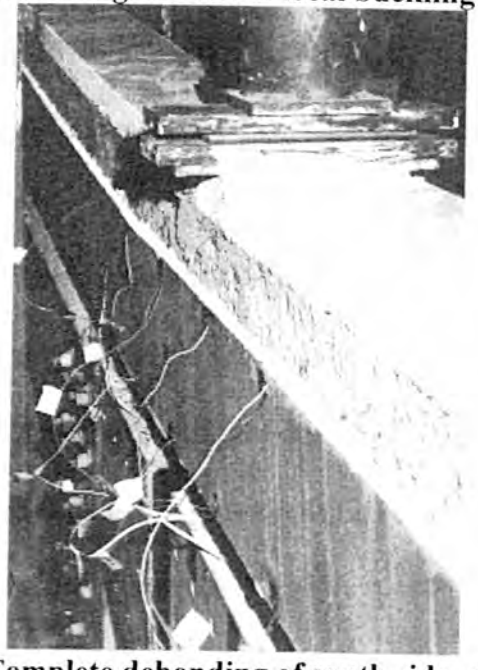

(b) Complete debonding of south side plate

Fig.16.11. Beam-2C: Crack pattern and failure mode

16.6.2.2 Longitudinal strains in the side plates

Figures 16.12-16.15 illustrate the relationship between the longitudinal strain distribution recorded at various gauge locations (Refer Fig.16.2b) and the maximum applied bending moment. The strain diagrams for the significant gauge locations show three distinguished features. Firstly, there was a linear variation of strain till there was visible sign of concrete crushing at which there was a minor drop in the applied moment. Secondly, the stresses were transferred to the external plates due to the onset of concrete crushing. This is indicated by long plateaus in the relationship. Thirdly, the plate debonding due to long debonding cracks along the top edge of the plates and the associated local buckling of the plates are indicated by the steep drop in both the applied moment and the strain.

Figures 16.12a and 16.12b show the strain distribution across the plate sections in north and south sides at the mid-span. It shows the maximum strain in tension at the point of maximum moment was about 6000 microstrains in the north side-plate and 7000 microstrains in the south side-plate. The respective values for compression are about 4200 and 3500 microstrains. This implies that the strain magnitudes in both the plate top and bottom fibres far exceeded the yield strain. The diagrams also reveal that the plates yielded well before the concrete started crushing.

The strain distribution along the top level of the north side-plate and the south side plate are shown in Figs.16.13a and 16.13b and that along the bottom level are shown in Figs. 16.14a and 16.14b. Several gauges both on the top and bottom levels recorded strain readings exceeding the yield strains; this shows the plate yielding occurred over a considerable length, thereby improving the ductility of the plated section. Figure 16.15a depicts the strain distribution across a section 450 mm to the left of the centre of the north side plate; a similar distribution for the south side plate

is shown in Fig.16.15b. At these cross-sections also, the plates yielded both at the top and bottom levels.

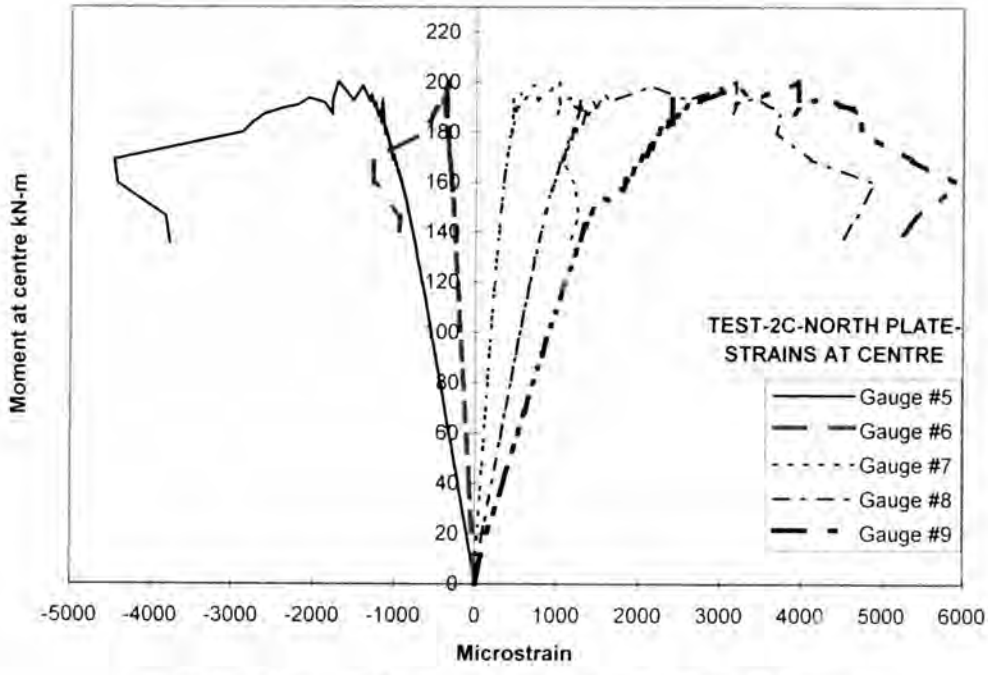

Fig.16.12a Beam-2C: North side plate-strains at centre

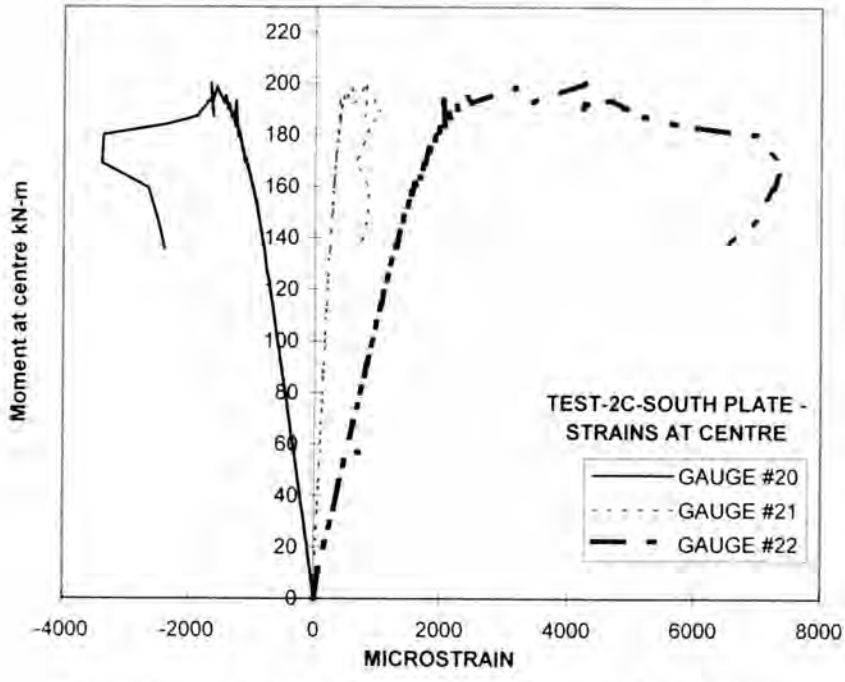

Fig.16.12b. Beam-2C: South side plate-strains at centre

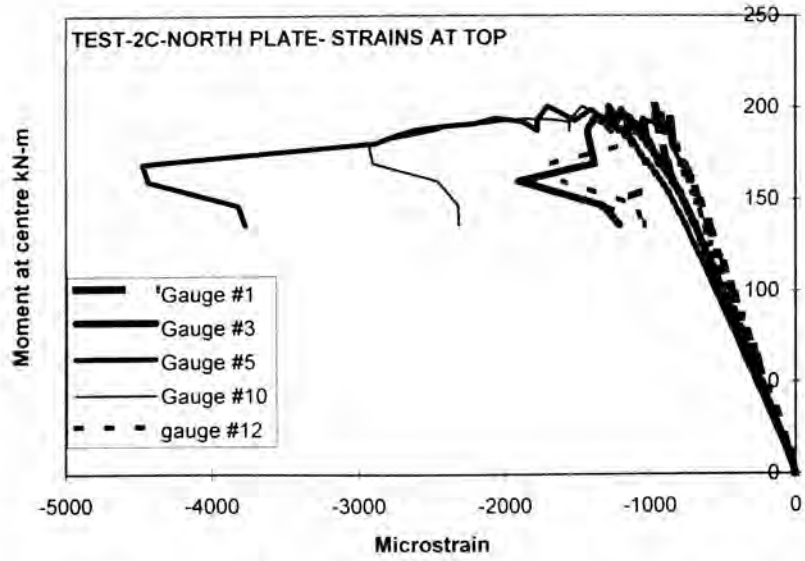

Fig.16.13a. Beam-2C: North side plate-strains at top level

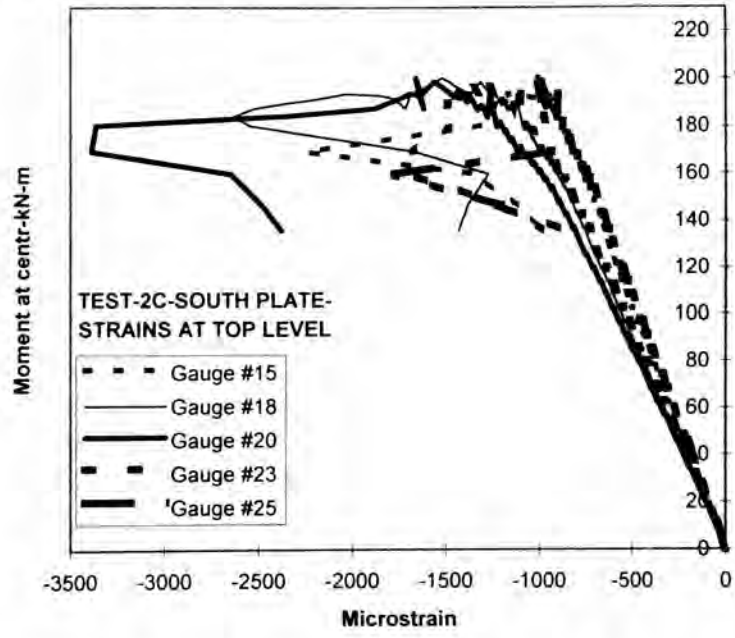

Fig.16.13b Beam-2C: South side plate-strains at top level

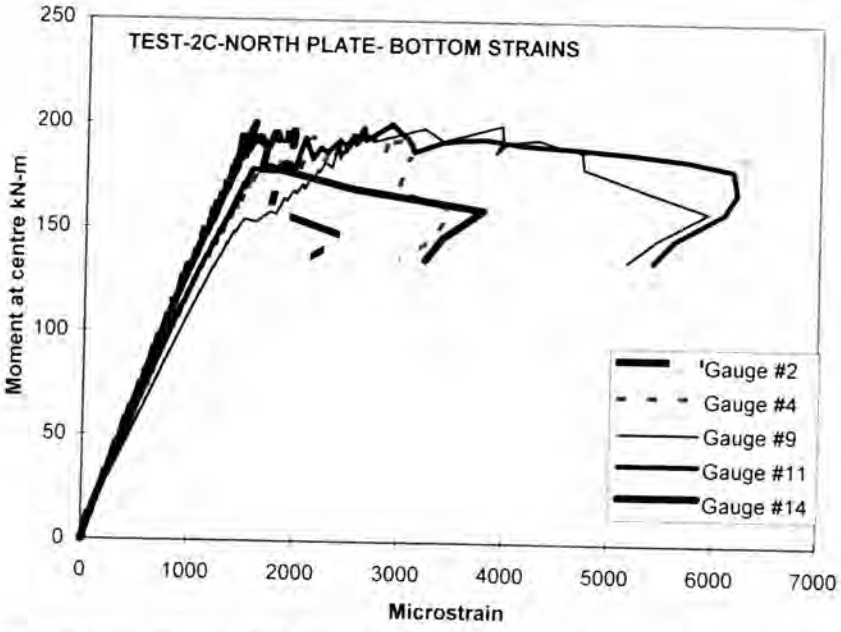

Fig.16.14a. Beam-2C: North side plate-strains at bottom level

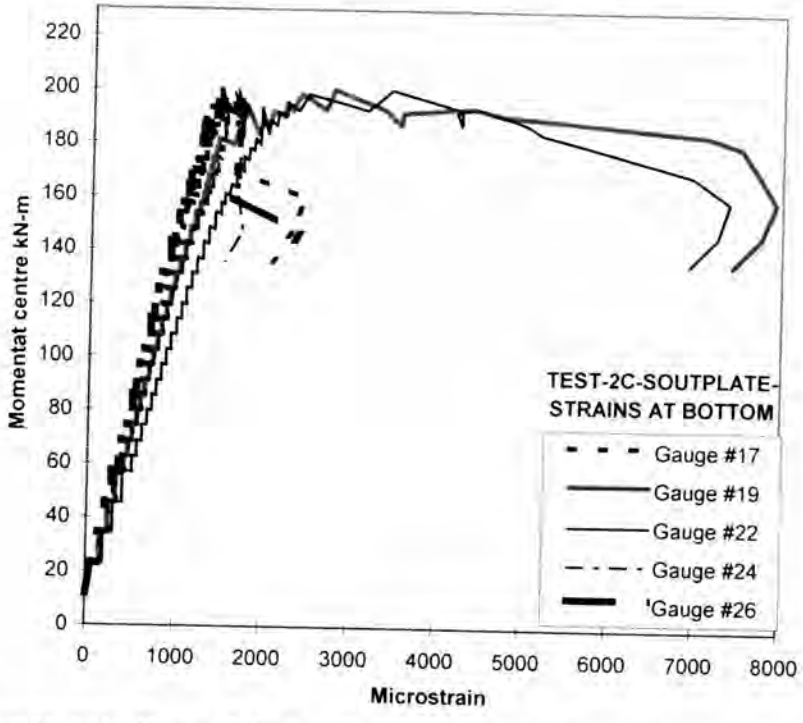

Fig.16.14b. Beam-2C: South side plate-strains at bottom level

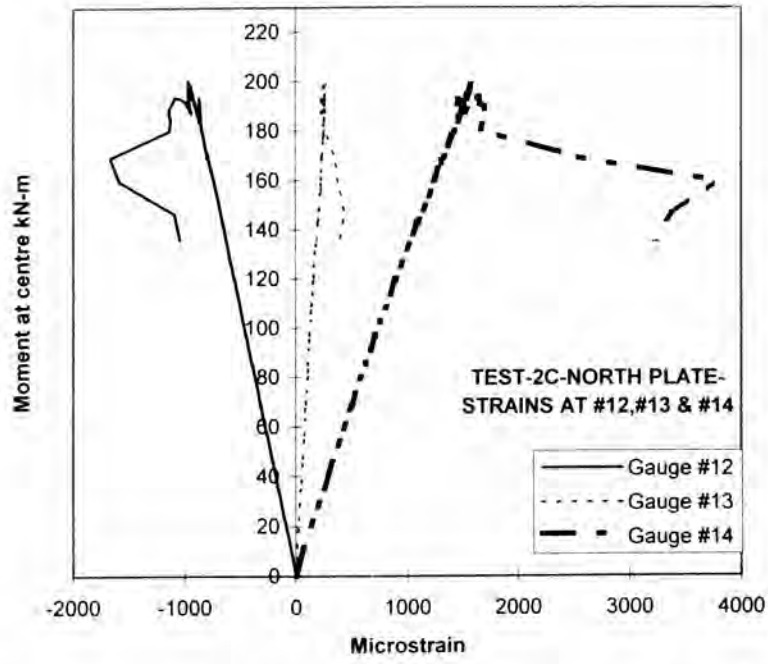

Fig.16.15a. Beam-2C: North side plate-strains at #12,#13 & #14.

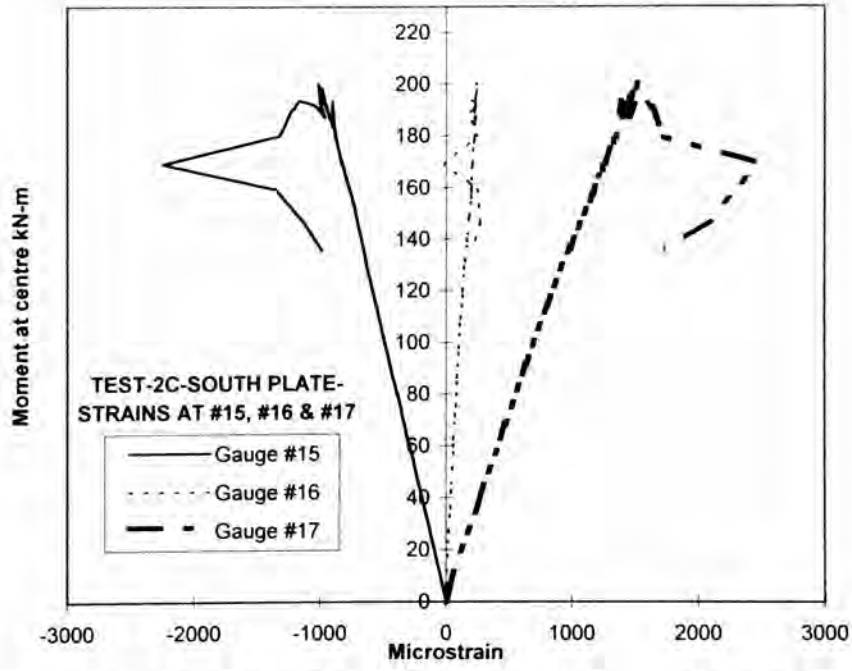

Fig.16.15b. Beam-2C: South side plate-strains at #15,#16 &#17

Table-16.5 summarises the maximum strains recorded in the plate at the three significant stages of the test-2C, as discussed for beam-2B (Section16.6.1.2). It can be seen that the concrete crushing was initiated when the maximum strains recorded at the bottom fibres of the plate was about 600 microstrains more than the yield strain of

the plate (1505 microstrains). The strain in the internal reinforcement can be assumed to have just yielded at this stage (2277 microstrains). However, the onset of concrete crushing did not impair the load carrying capacity of the plated beam unlike in Beam-2B. The applied moment could be increased to a maximum of 199 kNm and at this stage the maximum strain recorded was about 275% of the plate yield strain. Finally, the maximum tensile strain recorded in the plate at complete debonding was 7925microstrain, which is about 5 times the plate yield strain. The maximum recorded compressive strain is about -4472 microstrains, which is about 3 times the yield strain. This shows the ductile nature of failure.

Table-16.5: Beam-2C: Maximum plate strains

Event	Moment (kNm)	Maximum strain (Microstrains)			
		North side		South side	
		Top	Bottom	Top	Bottom
At starting of concrete crushing	174.0	-1063	2147	-1158	1804
At maximum applied moment	199.0	-1463	3947	-1518	4255
At failure (complete debonding)					
(a) North side plate	159.6	-4472	6203		
(b) South side plate	135.8			-2620	7925

Note: (-ve)compressive and (+ve) tensile strains.

16.6.2.3 Deflection

The variation of the deflection at mid-span with the maximum applied moment for the beam-2C is shown in Fig.16.16. The beam deflected by 37 mm when the crushing of concrete occurred and by 66 mm just before the plates debonded; this shows the improved ductility due to side plates.

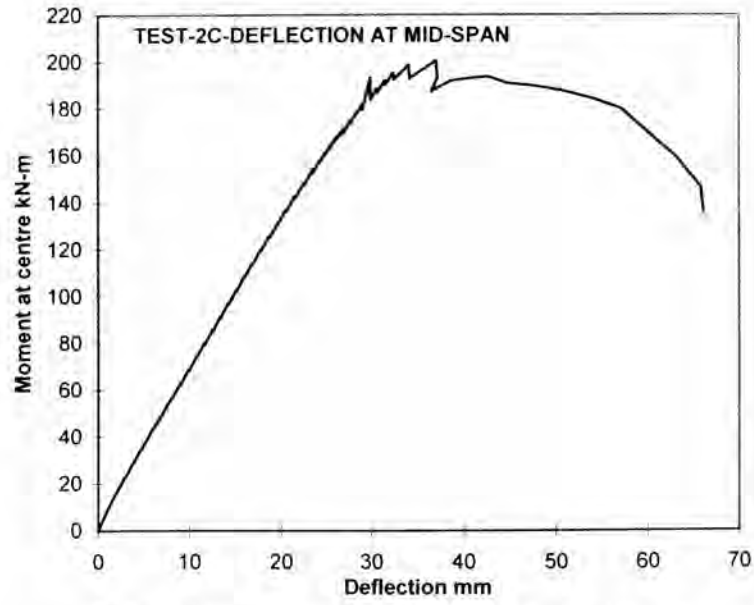

Fig.16.16. Beam-2C: Deflection at mid-span

16.6.3 Beam-2D

Beam-2D was bonded with side-plates of 240 mm deep and 8 mm thick, as shown in Fig.16.1d. It was tested to failure by two point loads such that the magnitude of the bending moment in the constant moment region (M) in kNm was 0.9875 times the total applied load (P) in kN. The test was interrupted when the total applied load was 140 kN as the computer system unexpectedly crashed. At this stage, the recorded deflection at mid-span was 23.16 mm. The beam was unloaded and after repairing the computer system; it was gradually reloaded from 0 kN to 140 kN and the deflection observed this time was 23.54 mm. As the difference in deflection (set) was negligible, the load testing of the beam was continued till the final debonding of the side plates occurred.

16.6.3.1 Crack Propagation

The crack propagation in case of beam-2D was similar to that of beam-2C. A typical crack pattern in the constant moment region of beam-2D is shown in Fig.16.17. At a total applied load of 30 kN (M=29.6 kNm), hairline flexural cracks were visible in the

constant bending moment region. These cracks started to spread vertically, then branched out into multiple cracks from the same root and then propagated horizontally along the bottom edge of the side plates, as shown in Fig.16.17. New flexural cracks also started appearing between the existing ones in the central region. This process continued till the applied load was about 145 kN (M= 143.2 kNm). Then the bottom most fibre of the plate yielded at a load of 150 kN (M= 148.1 kNm) and the horizontal cracks beneath the plates tended to join with each other.

As the load was increased to 203.4 kN (M=200.8 kNm), the concrete fibres above the side plates in the constant bending moment region started crushing. This led to the formation of long debonding cracks along the top of the plate, as shown in Fig.16.17; the load suddenly dropped to 196.7 kN (M=194.2 kNm). As the concrete started crushing, further application of the load caused the compressive force to be transferred to the side plates. This eventually led to the local buckling of the south side plate when the reapplied load was 167.8 kN (M=165.7 kNm), as can be seen in Fig.16.18b. Finally, both the plates debonded from the concrete when the recorded load was 132.8 kN (M=131.1 kNm) and this is illustrated by the Figs.16.18a and 16.18b.

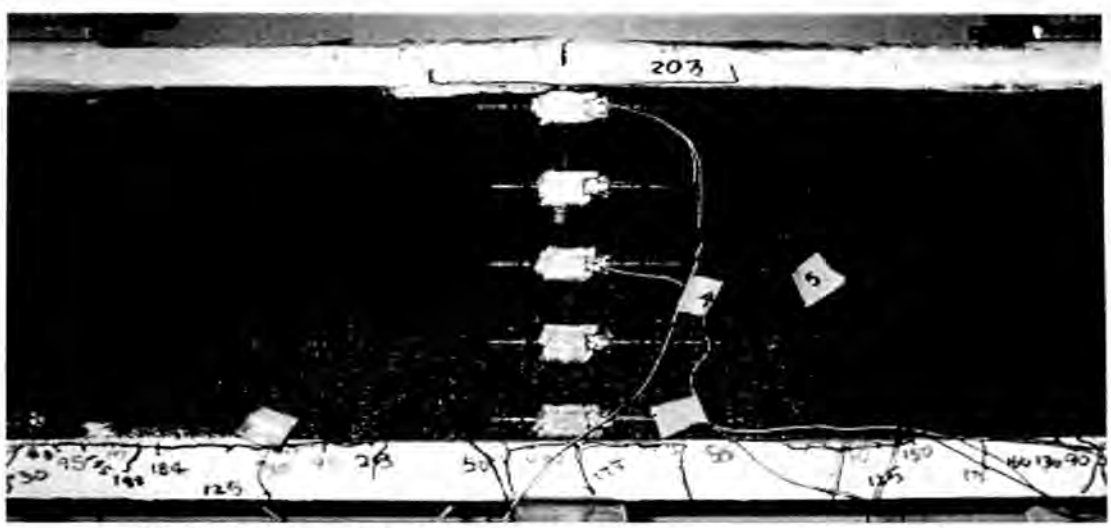

Fig.16.17. Test-2D: Crack pattern in constant moment region

(a) North side plate

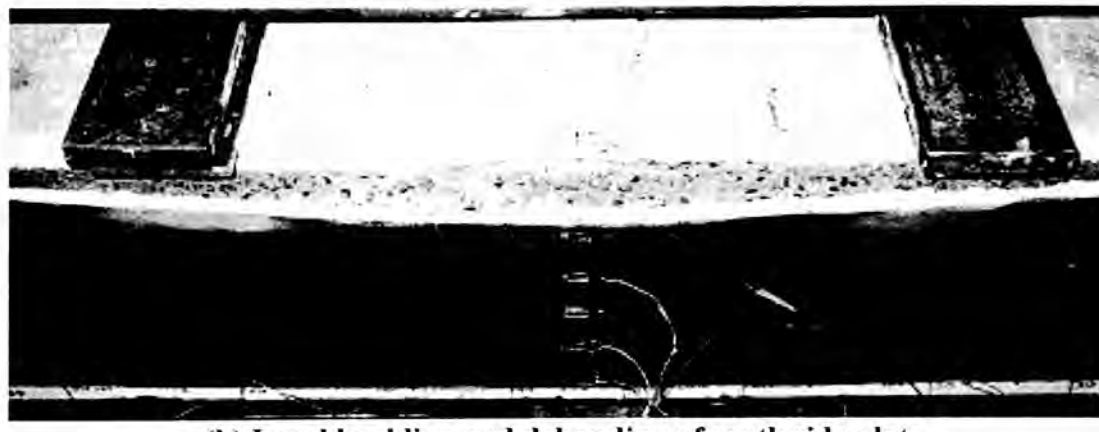

(b) Local buckling and debonding of south side plate

Fig.16.18. Test-2D: Debonding of side plates

16.6.3.2 Longitudinal strains in side plates

Figures 16.19 and 16.20 depict the relationship between the longitudinal strain distribution recorded at various gauge locations (Refer Fig.16.2c) and the maximum applied bending moment. The strain diagrams for the significant gauge locations show some distinguished features. Firstly, there was a linear variation of strain until the maximum moment was reached in all the gauge locations. Then, the strains recorded in the mid-spans in the side plates increased rapidly even though there was a slight drop in the applied moment due to the crushing of concrete and the subsequent formation of horizontal debonding cracks. This feature is indicated by the long flat

region for the strain gauge locations such as #7, #8 and #19 that were bonded along the bottom fibres of the plate. Finally, the plate debonding due to long debonding cracks along the top edge of the plates and the associated local buckling of the plates are indicated by the steep drop in both the applied moment and the strain. The local buckling of the plate and the subsequent debonding is quite demarcated by successive drops in both the applied moment and the strain magnitudes in case of the strain gauges that were bonded along the top fibres of the plates such as gauges #4, #5, #15 and #16.

Figures 16.19a and 16.19b show the strain distribution across the plate sections in the north and south sides at the mid-span. It shows the maximum strain in tension at the point of maximum moment was about 11000 microstrains in the north side-plate and 13500 microstrains in the south side-plate. The respective values for compression are about 5500 and 8500 microstrains. This implies that both the plate top and bottom fibres far exceeded the yield strain of the plate material. The diagrams also reveal that the plates were subjected to strains higher than the yield strain of the plate material well before the concrete started crushing. The strain distribution along the bottom fibres of the north side-plate and the south side plate are shown in Figs.16.20a and 16.20b. Several gauges both on the top and bottom levels recorded strain readings exceeding the yield strains; this shows the plate yielding occurred over a considerable length, thereby improving the ductility of the plated section.

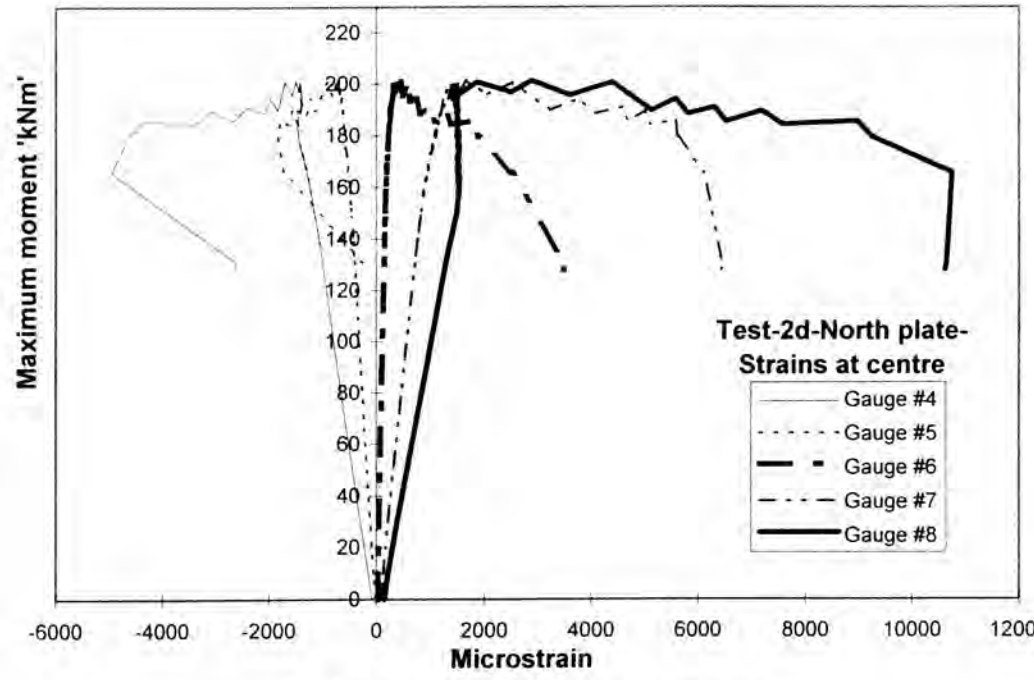

(a) North side plate-strains at centre

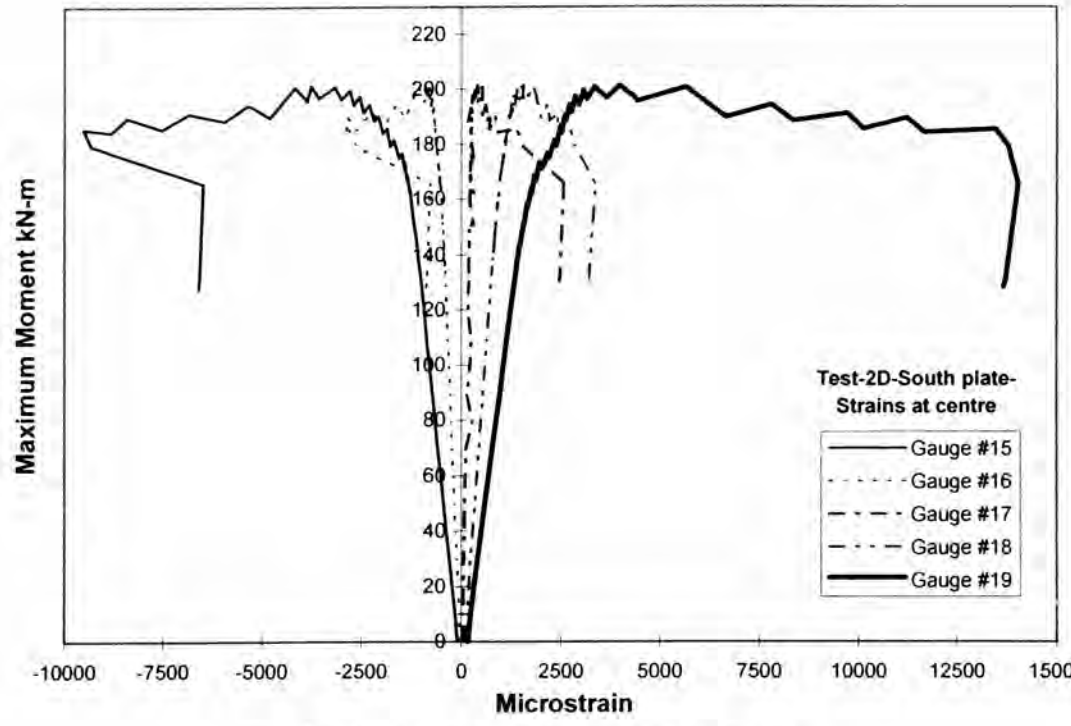

(b) South side plate-strains at centre

Fig.16.19. Test-2D: Strains recorded at the mid-span

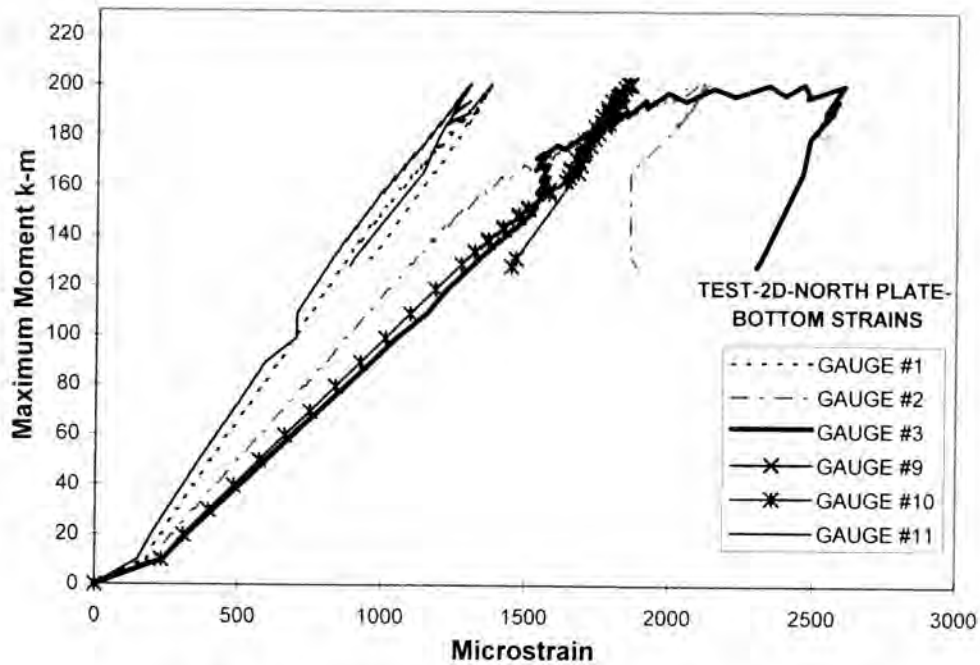

(a) North side plate-strains at bottom level

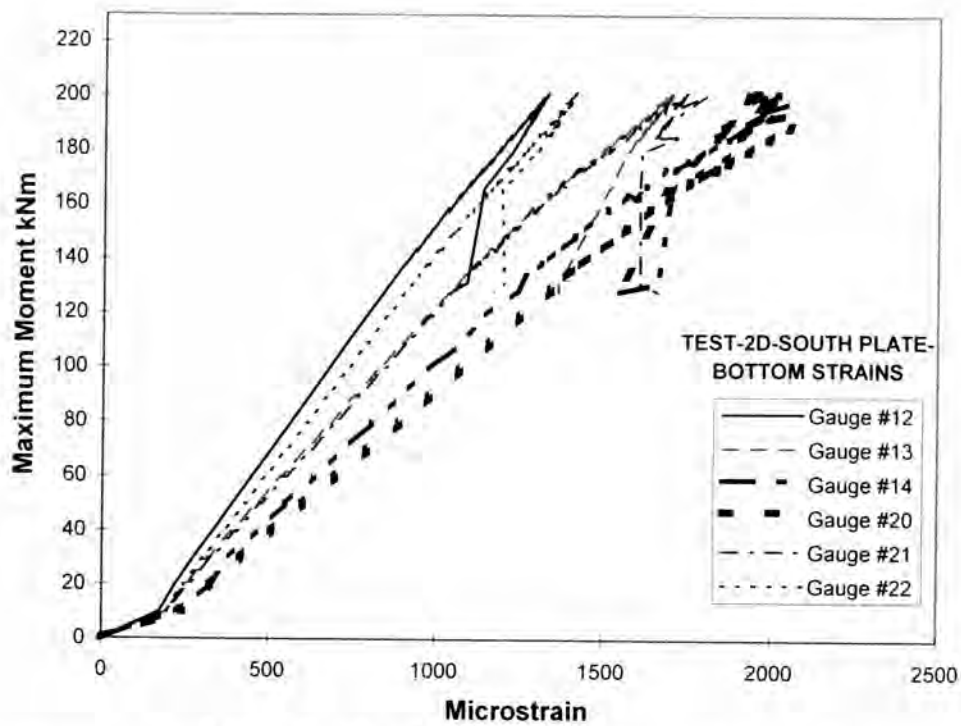

(b) South side plate-strains at bottom level

Fig.16.20. Beam-2D: Longitudinal strain variation in the side plates

Table-16.6 summarises the maximum strains recorded in the plate at the three significant stages of the test, i.e. when the beam carried the maximum moment, the immediate fall in moment due to onset of concrete crushing and the failure due to

complete debonding of side plates. It can be seen that the maximum strains recorded at the bottom fibres of the plate at the maximum moment level are about twice the yield strain of the plate (1505 microstrains). The strain in the internal reinforcement can be assumed to be about 500 microstrains greater than its yield strain. As the concrete started crushing at the maximum moment, the stresses were transferred to the external plates. This is accompanied by very large increases in strain magnitudes at the onset of concrete crushing, even though the moment dropped by a small amount only. Finally, the maximum tensile strain recorded in the plate at complete debonding was 14000 microstrains, which is about 10 times the yield strain. The maximum recorded compressive strain is about 9323 microstrains, which is about 6 times the yield strain. This shows the ductile nature of failure.

Table-16.6: Beam-2B: Maximum plate strains

Event	Moment (kNm)	Maximum strain (Microstrains)			
		North side		South side	
		Top	Bottom	Top	Bottom
At maximum applied moment	200.8	-1423	2340	-3170	3350
At sudden drop in moment due to concrete crushing	194.2	-1976	5588	-5341	7809
At failure (complete debonding)	131.1	-4954	10755	-9323	14034

Note: (-ve)compressive and (+ve) tensile strains.

16.6.3.3 Deflection

The relationship between the moment and deflection at mid-span for the beam-2D is illustrated in Fig.16.21. The beam deflected by 39.1 mm when the crushing of concrete occurred and by 55.7 mm just before the plates debonded; this shows the enhanced ductility due to side plates.

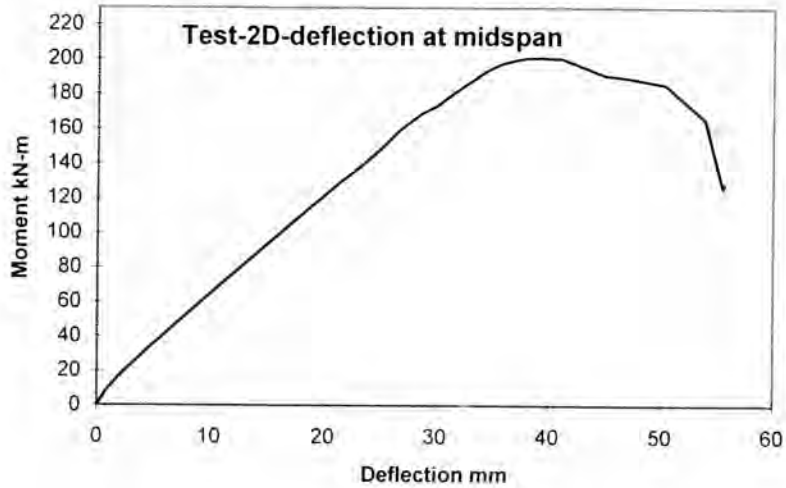

Fig.16.21. Beam-2D: Deflection at mid-span

16.7 Discussion of test results

The salient features of the test results are summarised in Table-16.7.

Table-16.7: Test results

Item		Beam-2B	Beam-2C	Beam-2D
Plate dimensions (depth(mm) x thickness (mm))		180x8	210x8	240x8
(a)Maximum moment (kNm) (ie at onset of concrete crushing)		180.7	199.0	200.8
(b) Moment after concrete crushing		164.9	186.6	194.2
Maximum shear load (kN)		91.5	87.5	101.7
Bending Moment at debonding of plate ie after concrete crushing (kNm)	North side	143.3	159.5	131.1
	South side	120.1	135.8	131.1
Maximum strain in side plates at starting of concrete crushing (microstrains)				
(1)tensile	North	2775	3379	2888
	South	2471	3438	3987
(2) compressive	North	-1056	-1512	-1496
	South	-956	-1637	-3765
Maximum strain in side plates at plate debonding (microstrains)				
(1) tensile	North	12616	6203	10755
	South	15508	7925	14037
(2) compressive	North	-6750	-4472	-4954
	South	-5948	-3387	-6588
deflection (mm)				
(1) at concrete crushing		40.13	34.26	39.1
(2) at debonding of plate		59.81	66.1	55.7

It can be seen from Table-16.7 that the flexural capacity of the side plated beams could be increased only marginally, i.e. 10% by increasing the depth of the side plate from 180 mm (Beam-2B) to 210 mm(Beam-2C). This is due to the debonding of the plate concrete crushing and the resulting local buckling of the plates. However, the concrete crushing and subsequent drop in applied load occurred smoothly in

beams 2C and 2D unlike beam 2B, the drop in load was abrupt, as shown in Fig.16.22. It is worth mentioning that the Beam-2C had a slightly different loading arrangement than that of the other two beams but all the beams had the same span. The relationship between the maximum tensile and compressive strains recorded with the applied moment for the three beams are compared in Figs. 16.23a and 16.23b. From the results in Figs.16.22, 16.23a and 16.23b, it can be seen that the ductility of the plated beam could be improved by increasing the depth of the plate. This is revealed by the large magnitudes of maximum strains recorded both in the top and bottom fibres of the side plates. In the case of beams 2B and 2D, the maximum strain magnitudes recorded were about ten times that of the yield strain of the plate material.

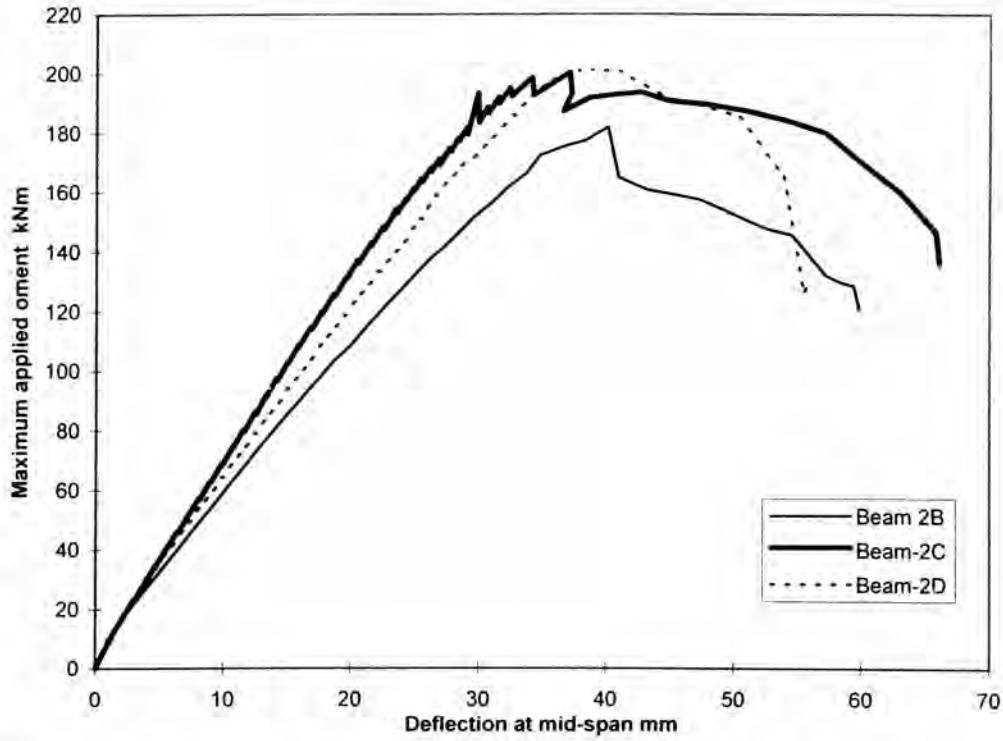

Fig.16.22. Relationship between deflection at mid-span and maximum applied moment

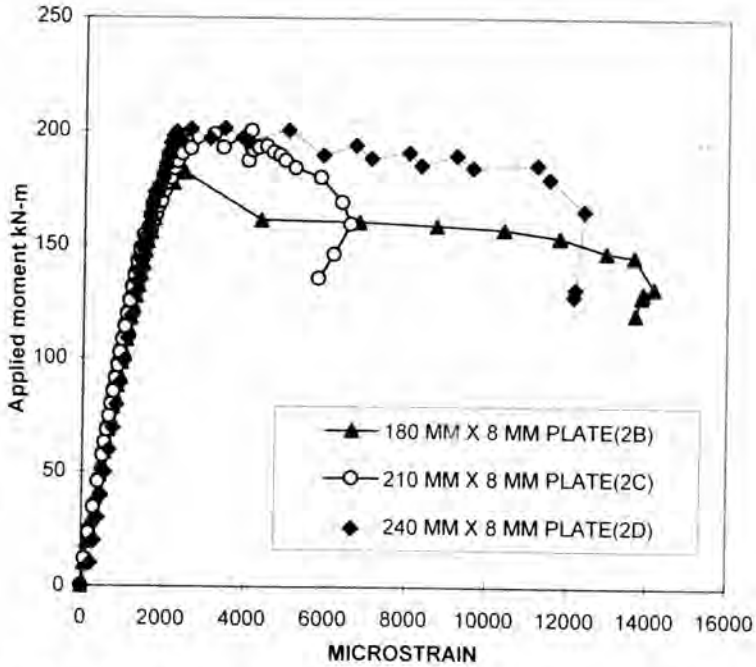

Fig.16.23a. Maximum tensile strains recorded in the side plates

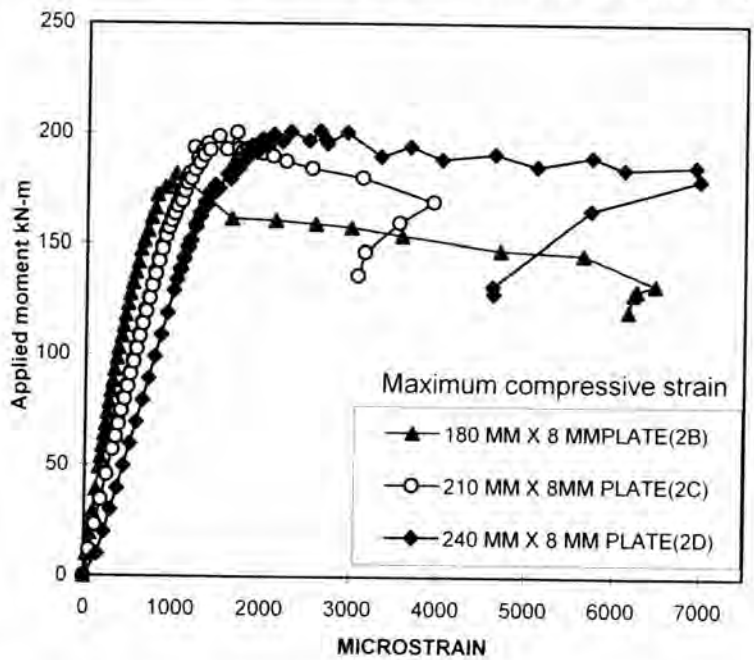

Fig.16.23b. Maximum compressive strains recorded in the side plates

16.8 Analysis of test results-Bond force

From the strains recorded across the middle section of the side plates, the compression and tension forces in the side plates were calculated for all the three beams using the appropriate stress-strain relationship. The net force in the side plates is termed the longitudinal bond force and the variation of the bond force with the maximum applied

moment for all the beams are shown in Figs.16.24-26. Table-16.8 compares the net tensile, compressive and bond forces in the three beams at significant stages of the tests. In the case of beams 2B and 2C, the bond force increased linearly with the applied moment and then set to decrease with the decreasing moment after the concrete crushing and also at debonding of the side plates. However, Fig.16.26 shows the gradual reduction in bond force in the case of beam 2D as the applied moment was increased beyond 160 kNm; this indicates the debonding process was steady and gradual.

Table-16.8: Longitudinal bond forces

Event	2B			2C			2D		
	T	*C*	*B*	*T*	*C*	*B*	*T*	*C*	*B*
At maximum applied moment	436.4	123.6	312.8	569.0	225.1	343.9	523.4	386.6	136.8
At sudden drop in moment due to concrete crushing	500.3	196.5	303.8	576.6	237.9	338.6	605.8	411.1	194.6
At failure (complete debonding)	496.4	271.8	224.6	540.2	348.2	192.0	607.7	456.9	184.3

T- Net Tensile force (kN), *C*-Net Compressive force (kN) and *B*-Bond force (kN).

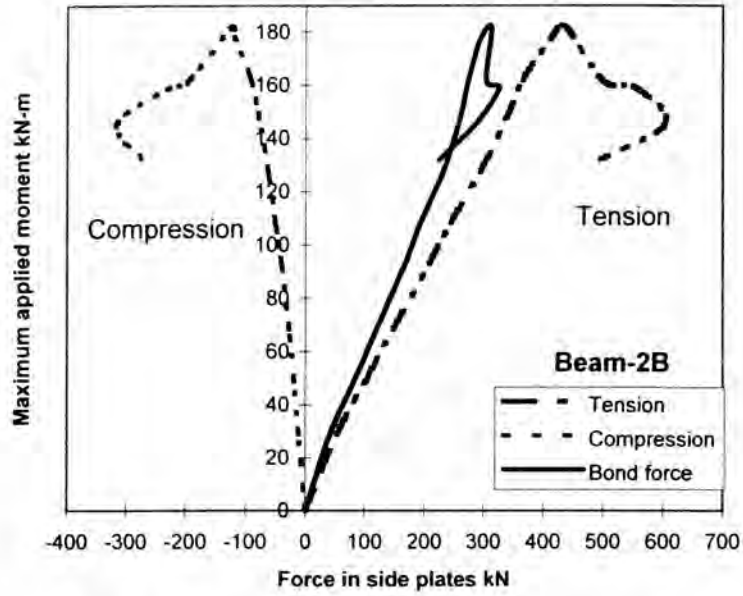

Fig.16.24. Beam-2B: Bond force in side plates

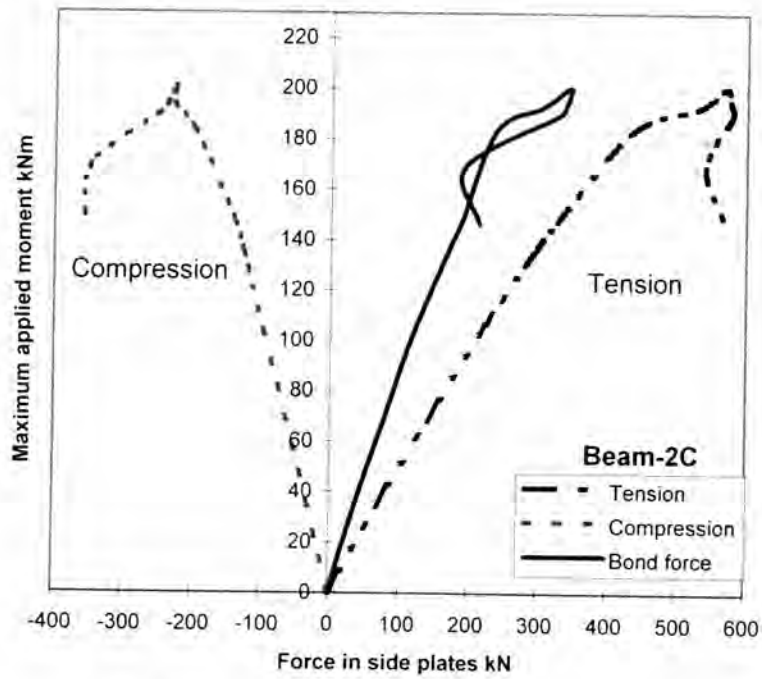

Fig.16.25.Beam-2C: Bond force in side plates

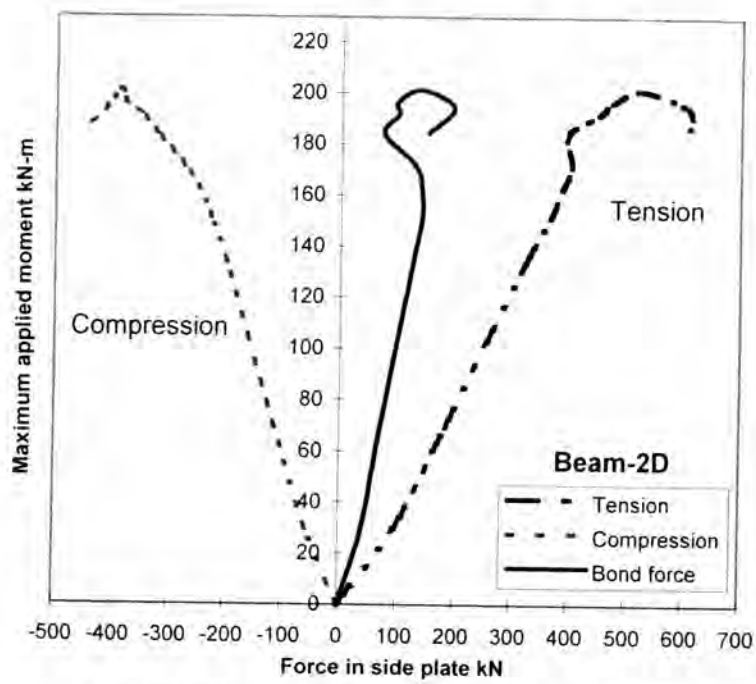

Fig.16.26.Beam-2D: Bond force in side plates

16.9 Flexural capacity of strengthened beams- Analytical results

The three beams strengthened were analysed by two different methods as described in the following sections. In both the methods, full interaction is assumed between the reinforced concrete beam and the side plates.

16.9.1 Rigid plastic analysis

Rigid plastic analysis is a simple technique that is used to estimate the maximum flexural capacity of the composite plated beam, as shown in Fig.16.27. In this method, all the components of the plated beam are assumed to be at their plastic stage. The following stress distributions are assumed in this method.

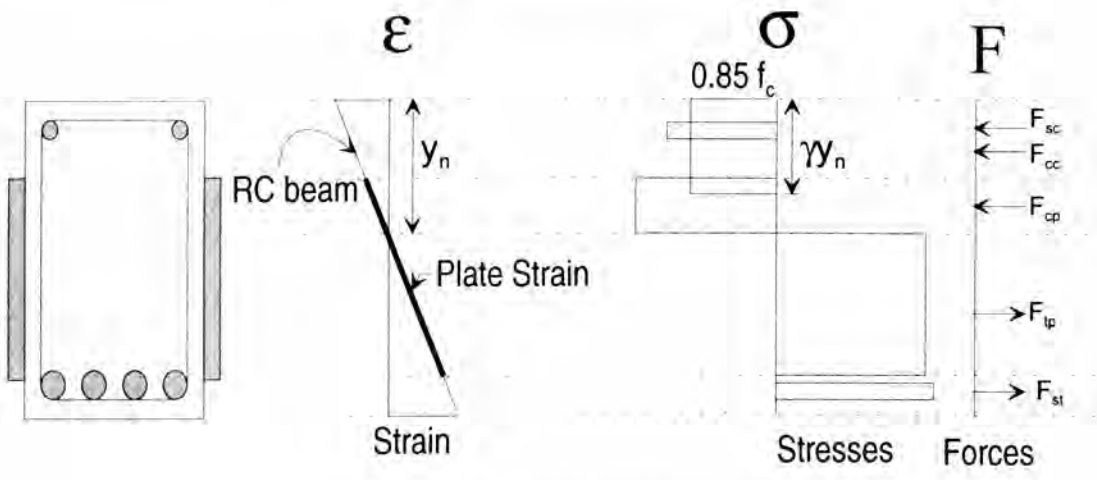

Fig.16.27. Rigid plastic analysis

(i) For the concrete under compression, a rectangular stress distribution with a width of $0.85f_c$ and a depth of γy_n is assumed. Here, f_c is the cylindrical compressive strength of the concrete, y_n is the depth of neutral axis from the topmost compressive fibre of the concrete beam and γ is the neutral axis depth factor. It is given in AS 3600-1994 as

$$\gamma = 0.85-0.007(f_c-28) \leq 0.85 \text{ and } \geq 0.65 \qquad (16.1a)$$

and Ahmed (1996) derived the following formula for the full interaction analysis of bolted plated sections.

$$\gamma = 0.935\text{-}0.00191(f_c\text{-}28) \leq 0.85 \text{ and } \geq 0.65 \qquad (16.1b)$$

It may be noted that analyses were carried out separately using the two different values of γ given by Eqns.16.1a and 16.1b. Now, the compressive force in the concrete section is given by,

$$F_{cc}=0.85 f_c \gamma y_n b. \qquad (16.2a)$$

where b is the width of the beam.

(ii) The compression steel is assumed to have yielded and the force F_{sc} exerted by compression steel is given by

$$F_{sc}=(f_{ysc}\text{-}0.85f_c)A_{sc} \qquad (16.2b)$$

where are f_{ysc} and A_{sc} the yield strength and area of cross section of the compression steel.

(iii) The tension steel is assumed to have yielded and the force F_{st} in the tension steel is given by

$$F_{st}=f_{yst}A_{st} \qquad (16.2c)$$

where are f_{yst} and A_{st} the yield strength and area of cross section of the tension steel.

(iv) All the fibres in the side plates are assumed to have yielded. Therefore, the compressive force F_{cp} and the tensile force F_{tp} in both the side plates are given by

$$F_{cp} =2(y_n\text{-}d_{top})t_{sp}f_{yp} \qquad (16.2d)$$

and

$$F_{tp} =2(d_{sp}\text{-}y_n\text{+}d_{top})t_{sp}f_{yp} \qquad (16.2e)$$

where are d_{sp} and t_{sp} are the depth and thickness of an individual side plate, f_{yp} is the yield strength of the plate and d_{top} is the distance between the top of the beam and the top of the side plate.

(v) For equilibrium, the sum of the compressive forces is equated to the sum of the tensile forces. Hence,

$$F_{cc} + F_{sc} + F_{cp} = F_{st} + F_{tp} . \tag{16.3}$$

(vi) Substituting the terms for the forces from Eqns.16.2a-e into Eqn.16.3 and upon manipulating, we get the depth of neutral axis as

$$y_n = \frac{f_{st}A_{st} - (f_{ysc} - 0.85f_c')A_{sc} + 2f_{yp}(d_{sp} + 2d_{top})t_{sp}}{0.85f_c\gamma + 4f_{yp}t_{sp}} \tag{16.4}$$

(vii) Taking moments about the topmost compressive fibre of concrete, we get the ultimate moment capacity of the beam M as

$$M = F_{st}d_{st} + F_{tp}\left(\frac{d_{sp} + y_n + d_{top}}{2}\right) - F_{cc}\left(\frac{\gamma y_n}{2}\right) - F_{sc}d_{sc} - F_{cp}\left(\frac{d_{top} + y_n}{2}\right) \tag{16.5}$$

where d_{st} and d_{sc} are the distance between the centroids of tension and compression reinforcements from the topmost compression fibre of the concrete beam.

The rigid plastic analysis (using the magnitude of γ as obtained from Eqn.16.1a) estimates the moment capacities of the three beams 2B, 2C and 2D as 209.6 kNm, 216.1 kNm and 225.8 kNm respectively. The corresponding test values from Table-16.7 are 180.7 kNm, 199.0 kNm and 200.8 kNm. This implies that the rigid plastic analysis overestimates the flexural strength of the three beams by about 12%.

16.9.2 Numerical analysis

In this method, the plated section is modeled by subdividing the beam cross-section into a number of slices. The strain distribution across the slices is analysed as a series

of idealised linear functions. The force in each slice is calculated from the material stress-strain relationships.

16.9.2.1 Stress-strain relationship for concrete in compression

For our case, the concrete in compression is modeled with a non-linear stress-strain relationship as recommended by Warner(1969) for normal-density concrete. The relationship has been represented by using a non-dimensionalised stress S and a normalised strain ε_{nor}. The non-dimensionalised stress S is given by

$$S = \frac{\sigma}{\sigma_u} \tag{16.6}$$

where σ is the specified compressive stress in concrete and σ_u is the compressive strength of concrete in 28 days. The normalised strain ε_{nor} is given by

$$\varepsilon_{nor} = \frac{\varepsilon}{\varepsilon_u} \tag{16.7}$$

where ε is the specified strain in concrete and ε_u is the strain in concrete at σ_u. The following equations are used to represent the relation between the stress and strain for monotonically increasing strain.

$$\varepsilon_{nor} < 0; \qquad S = 0 \tag{16.8a}$$

$$0 \le \varepsilon_{nor} \le 0; \qquad S = \gamma_1 \varepsilon_{nor} + (3 - 2\gamma_1)\varepsilon_{nor}^2 + (\gamma_1 - 2)\varepsilon_{nor}^3 \tag{16.8b}$$

$$1.0 \le \varepsilon_{nor} \le \gamma_2; \qquad S = 1 - \frac{1 - 2\varepsilon_{nor} + \varepsilon_{nor}^2}{1 - 2\gamma_2 + \gamma_2^2} \tag{16.8c}$$

$$\varepsilon_{nor} > \gamma_2; \qquad S = 0 \tag{16.8d}$$

The factors γ_1 and γ_2 in Eqns.16.8a-d are shown in Fig.16.28 and they define the shape of the loading and unloading portions of the curves respectively. The initial slope γ_1 is fixed by the initial elsatic modulus of concrete E_c and it is given by

$$\gamma_1 = \frac{E_c \varepsilon_c}{\sigma_u} \tag{16.9}$$

The factor γ_2 is assumed to be equal to 3 (Burnet 1998).

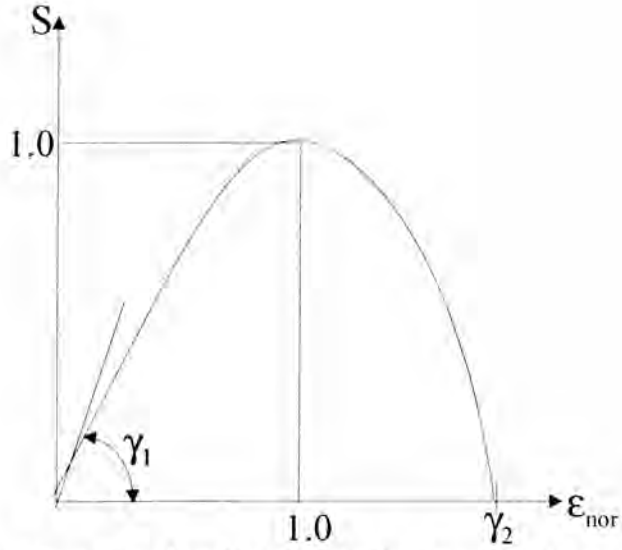

Fig.16.28. Stress-strain relationship for concrete in compression

16.9.2.2 Stress-strain relationship for concrete in tension

The stress-strain curve for concrete in tension (Burnet 1998) is shown in Fig.16.29. The concrete is assumed to behave linearly upto the tensile strength of the concrete f_t till cracking strain ($\varepsilon_{crack} = f_t/E_c$). Once the concrete tensile strength has been exceeded, the stress in the concrete diminishes with increasing strain upto a strain ten times the cracking stain as shown in Fig.16.29.

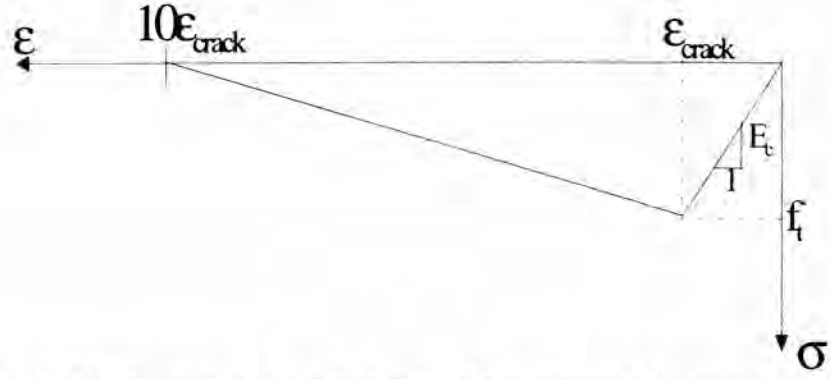

Fig.16.29. Stress-strain relationship for concrete in compression

16.9.2.3 Stress-strain relationship for steel reinforcement and plates

The stress-strain relationship for steel reinforcement and plates is idealised as shown in Fig.16.30. The stress is assumed to increase linearly with the strain until the yield stress f_y is reached, at a yield strain of ε_y of f_y/E_s. Further straining is assumed to results in plastic flow with no increase in stress until the strain hardening strain ε_{sh}. Here ε_{sh} is assumed to be ten times the yield strain. For strains greater than ε_{sh}, the stress in steel is assumed to be zero.

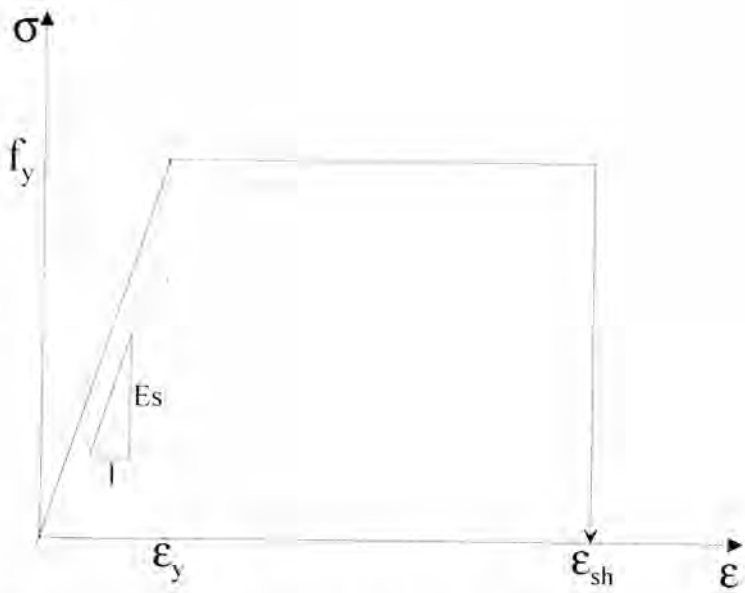

Fig.16.30. Stress-strain relationship for steel reinforcement and plate

16.9.2.4 Formulation of analytical procedure

The numerical technique is only practicable by computer and hence a computer program was developed to analyse each beam configuration as discussed below. The basic formulation of the method is as follows.

The concrete beam is divided into a number of slices as shown in Fig.16.31a.

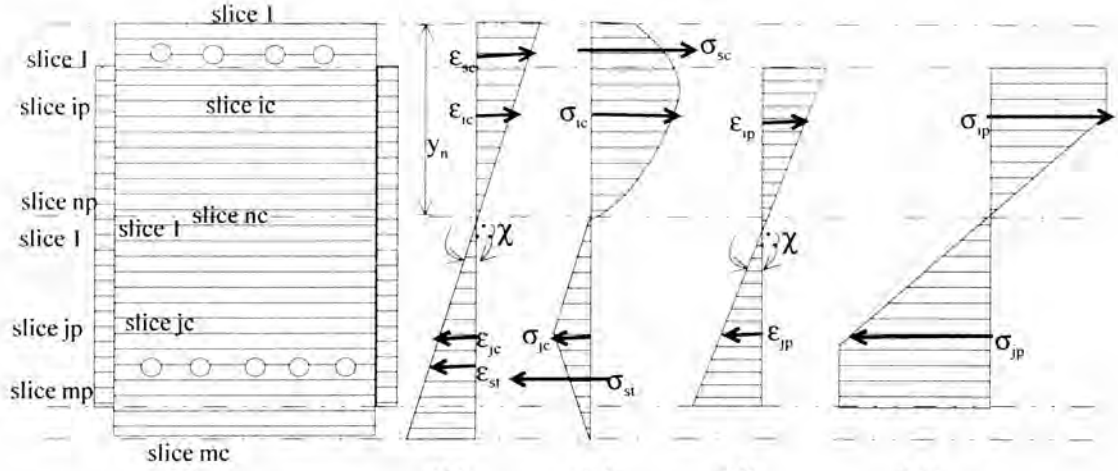

Fig.16.31. Strain and stress distribution in different components

If the thickness of each slice is t_s and h is the depth of the beam, then the number of slices in the concrete beam is $ns=h/t_s$. The section of the beam above the neutral axis is assumed to be under bending compression. If y_n is the neutral axis depth from the topmost fibre, then the number of slices in the concrete beam above the neutral axis nc is (y_n/ t_s) and the number of slices below the neutral axis mc is *(ns-nc)*. Similarly, the side plates are also divided into np and mp number of slices. The strain distribution in the concrete beam and the side plates are shown in Figs.16.31b and 16.31d. It may be noted that the curvature in both the concrete cross section and the side plates χ is the same as no slip is assumed to exist between the concrete and side plates. The coordinate axes are set up at the top of the cross-section and the strain is evaluated at the mid-height of each slice. The step by step procedure for analysis is described as below.

Step-1: For a given curvature χ, assume a neutral axis depth of y_n.

Step-2: Calculate the strain at the middle of each slice in the concrete beam. For the slices above the neutral axis,

$$\varepsilon_{ic} = (y_n - y_{ic})\chi \qquad (16.10)$$

and for a slice below the neutral axis

$$\varepsilon_{jc} = (y_{jc} - y_n)\chi \tag{16.11}$$

where y_{ic} and y_{jc} are the depth of the slices from the top of the cross section. For these strain magnitudes, we can find out the corresponding stresses in the slices σ_{ic} and σ_{jc} from the stress-strain relationship. Therefore, the force in each slice is given by

$$F_{ic} = \sigma_{ic} b t_s \tag{16.12}$$

$$F_{jc} = \sigma_{jc} b t_s \tag{16.13}$$

Therefore, the total compressive force F_{cc} and the total tensile force F_{tc} in the concrete cross section is given by summing up the forces in the individual slices.

$$F_{cc} = \sum_{ic=1}^{nc} F_{ic} \tag{16.14}$$

$$F_{tc} = \sum_{jc=1}^{mc} F_{jc} \tag{16.15}$$

Step-3: Compute the strain at the centroid of the compression reinforcement ε_{sc}.

$$\varepsilon_{sc} = (y_n - d_{sc})\chi \tag{16.16}$$

where d_{sc} is the distance between the top of the beam to the centroid of the compression reinforcement. The corresponding stress σ_{sc} can be determined from the stress-strain relationship for the steel reinforcement. Hence, the force F_{sc} in the compression reinforcement is given as

$$F_{sc} = \sigma_{sc} A_{sc} \tag{16.17}$$

Step-4: Compute the strain at the centroid of the tensile reinforcement ε_{st}.

$$\varepsilon_{st} = (d_{st} - y_n)\chi \tag{16.18}$$

where d_{st} is the distance between the top of the beam to the centroid of the tension reinforcement. The corresponding stress σ_{st} can be determined from the stress-strain

relationship for the steel reinforcement. Hence, the force F_{st} in the tensile reinforcement is given as

$$F_{st} = \sigma_{st} A_{st} \tag{16.19}$$

Step-5: Calculate the strain at the middle of each slice in the side plates. For the slices above the neutral axis,

$$\varepsilon_{ip} = (y_n - y_{ip})\chi \tag{16.20}$$

and for a slice below the neutral axis

$$\varepsilon_{jp} = (y_{jp} - y_n)\chi \tag{16.21}$$

where y_{ip} and y_{jp} are the depth of the slices from the top of the cross section. For these strain magnitudes, we can find out the corresponding stresses in the slices σ_{ic} and σ_{jc} from the stress-strain relationship. Therefore, the force in each slice is given by considering two side plates.

$$F_{ip} = 2\sigma_{ip} t_{sp} t_s \tag{16.22}$$

$$F_{jp} = 2\sigma_{jp} t_{sp} t_s \tag{16.23}$$

Therefore, the total compressive force F_{cp} and the total tensile force F_{tp} in the side plates is given by summing up the forces in the individual slices.

$$F_{cp} = \sum_{ip=1}^{np} F_{ip} \tag{16.24}$$

$$F_{tp} = \sum_{jp=1}^{mp} F_{jp} \tag{16.25}$$

Step-6: The total compressive force F_c and the total tensile force F_t in the plated beam are calculated as

$$F_c = F_{cc} + F_{sc} + F_{cp} \tag{16.26}$$

$$F_t = F_{tc} + F_{st} + F_{tp} \tag{16.27}$$

If F_c=F_t , then the equilibrium condition is satisfied and the assumed neutral axis depth is correct. Otherwise, assume a new value for y_n and repeat steps 1-6 till equilibrium condition is satisfied within acceptable accuracy.

Step-7: Once the neutral axis depth is fixed for a particular curvature, the moment is determined by algebraically summing the individual compressive and tensile forces times about their moment arms about the topmost concrete fibre and it is given by

$$M = \sum_{ic=1}^{mc} F_{ic} y_{ic} + \sum_{ip=1}^{mp} F_{ip} y_{ip} + F_{st} d_{st} - \sum_{ic=1}^{nc} F_{ic} y_{ic} - \sum_{ip=1}^{np} F_{ip} y_{ip} - F_{sc} d_{sc} \qquad (16.28)$$

16.9.2.5 Data required for program

The above procedure was codified into a computer program. All the dimensions of the beam (width, depth, effective depth to steel and plates, external plate dimensions) must be known. The complete stress-strain relationships of the internal steel, external plate, and the concrete must also be known.

16.9.2.6 Iterative computer program

First, a curvature and a corresponding neutral axis depth are assigned and therefore, the strains in the concrete are known. The entire depth of the concrete cross section is divided into 250 slices and the side plates into 150 slices. Using the average strain for each slice, the compression and tension stresses in concrete and external plates can be can be found from the corresponding stress-strain curve. Multiplying this by the area of the slice gives the compressive or tensile force. A similar approach is used to find the compressive or tensile forces in the internal steel. The neutral axis depth is then adjusted until equilibrium is achieved, i.e. the sum of all the compressive forces equals the sum of all the tensile forces. Thus, the entire moment-curvature relationship for the beam configuration can be generated by repeating the above process for different magnitudes of the curvatures.

16.9.2.7 Validating the program

As no RC beam without side plates was tested, the program was validated for a RC beam designated as A21 and tested by Marfique(1996). The ultimate bending moment as per the computer program is 129 kNm whereas the rigid plastic analysis yields 128.3 kNm. The actual flexural capacity of this beam was 113.41 kNm.

16.9.3 Ultimate bending moment capacity

The ultimate bending moment capacity of the beams obtained from the analysis are given in Table-16.9.

TABLE- 16.9: Flexural capacity (kNm) by different methods

Beam	Test result	RPA- AS:3600 Gamma value	RPA- Marfique's Gamma value	Numerical analysis
Unplated	-	134.0	139.98	139.2
2b	180.7	209.6	214.50	219.4
2c	199.0	216.1	220.32	226.2
2d	200.8	225.8	229.45	235.9

The rigid plastic analysis generally tends to overestimate the ultimate flexural capacity by 10% as all the fibres of the side plates are assumed to have yielded. The numerical modelling should have estimated more accurately but for the following facts:

(a) The numerical analysis assumes a full interaction between the reinforced concrete beam and the external plates, whereas the bond between the concrete and the side plates is weakened progressively due to the propagation of debonding cracks.

(b) The strain and stress distributions in the side plates at the ultimate moment as determined from the numerical analysis are shown in Figs.16.32a-c. The strains computed for the side plates are considerably higher than the experimentally recorded strains that are shown in Figs.16.33a-c. Moreover, the analysis shows a greater area

of the side plates to have yielded than that was observed in the test. This difference is due to the onset of debonding of the plates.

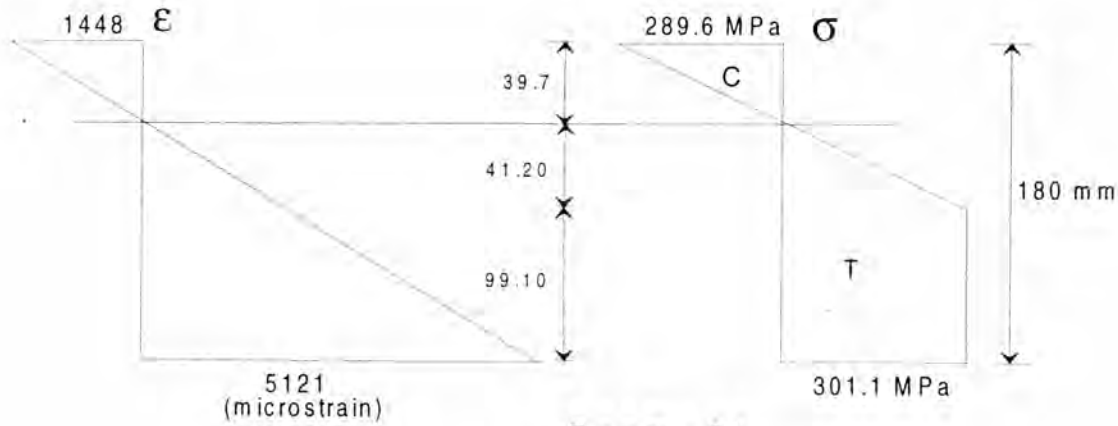

Beam - 2b

(a)

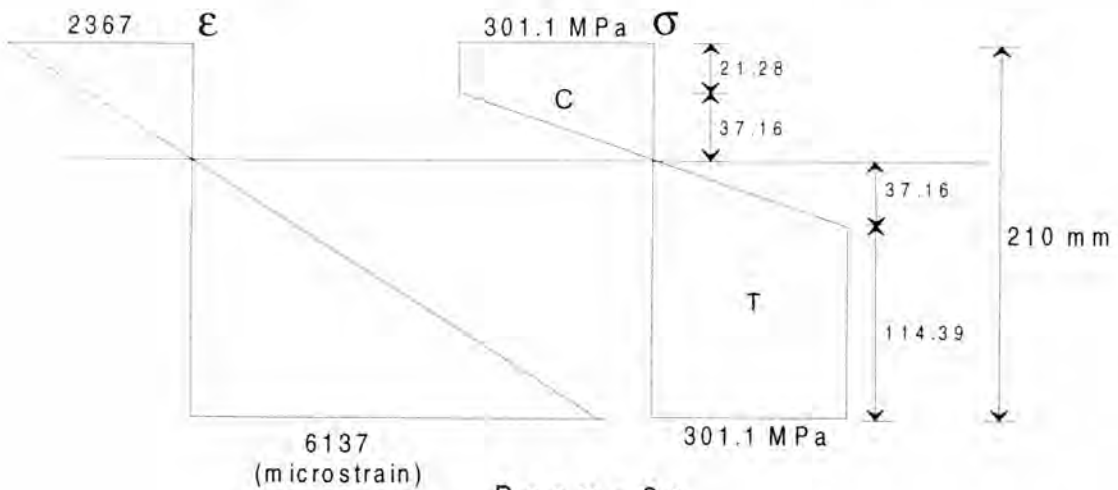

Beam - 2c

(b)

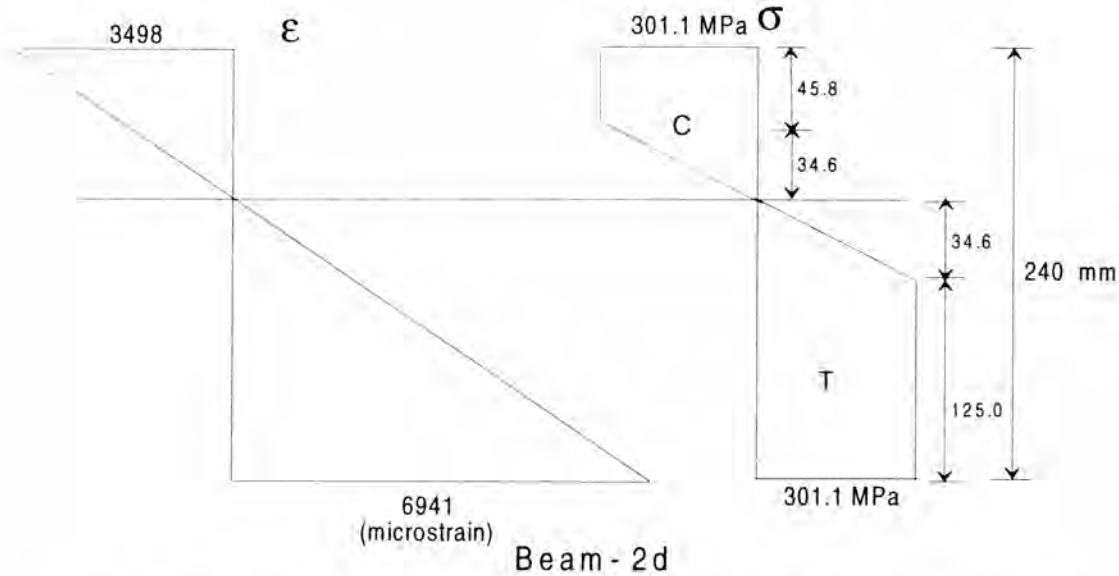

(c)

Fig.16.32. Theoretical strain and stress distribution in the side plates at the ultimate moment

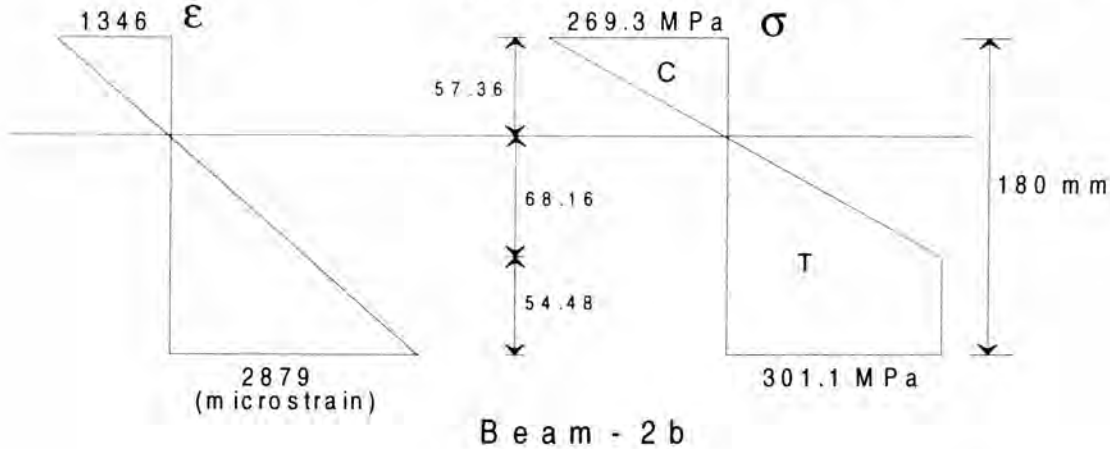

(a)

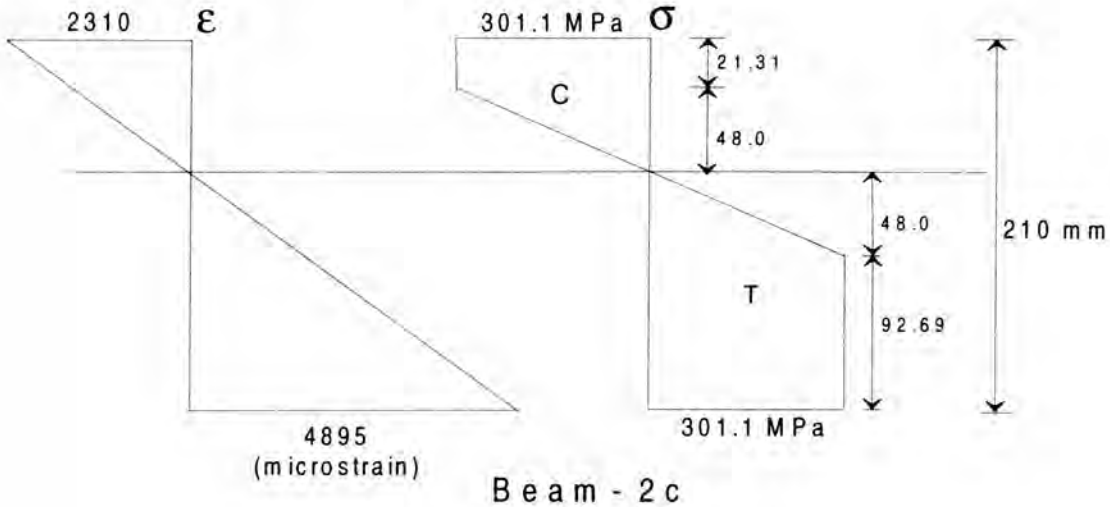

(b)

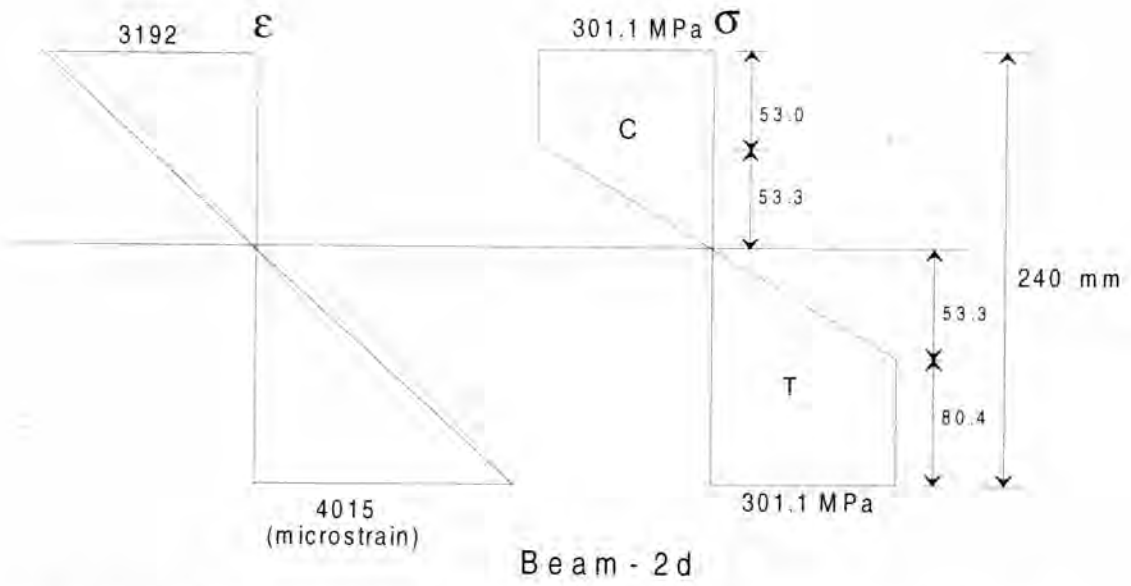

(c)

Fig.16.33. Experimental strain and stress distribution in the side plates at the maximum moment

The moment-curvature relationship obtained from the numerical analysis with that obtained from the test strain distribution are compared in Figs.16.34-36. It can be seen that there is generally a good agreement between the test results and the numerical procedure, till the maximum test moment. However, the discrepancy sets in after this stage and the numerical procedure overestimates the curvature and moment values. This is due to the fact that the actual failure of the beams occurred due to the crushing of concrete followed by the local buckling of external plates and the subsequent debonding. All these factors are ignored in the numerical analysis.

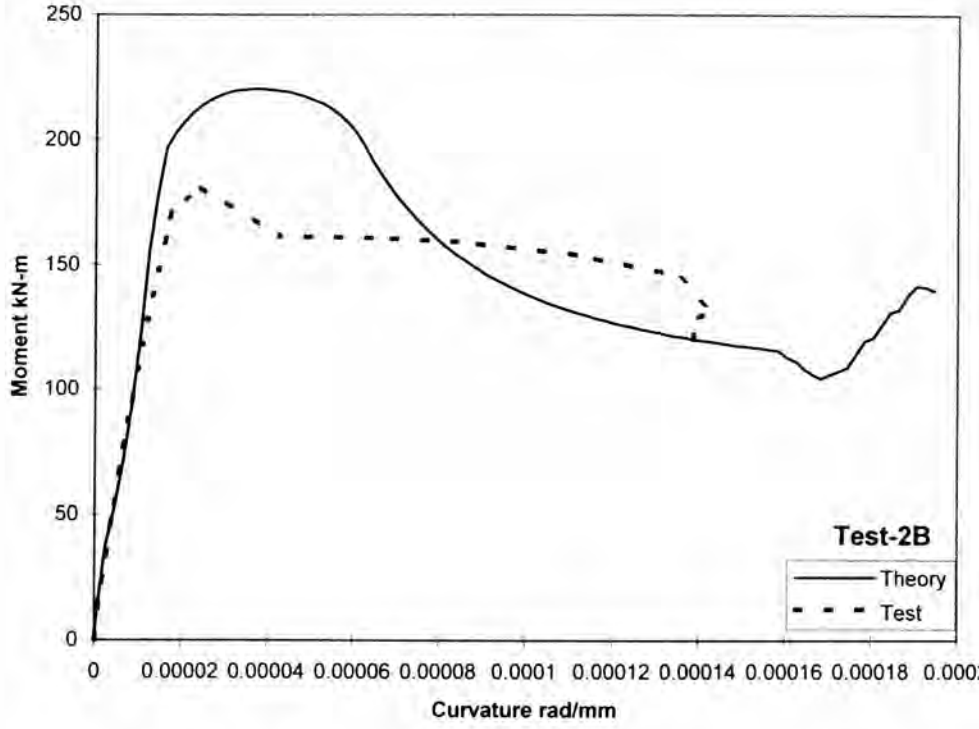

Fig.16.34. Moment-curvature relationship for Beam-2B

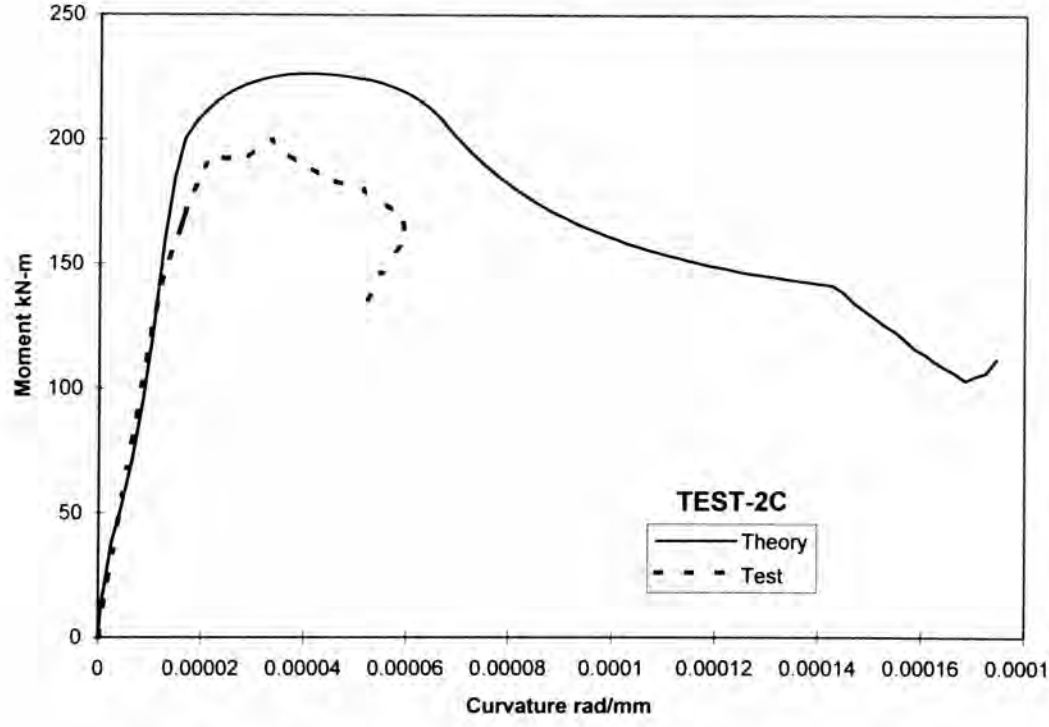

Fig.16.35. Moment-curvature relationship for Beam -2C

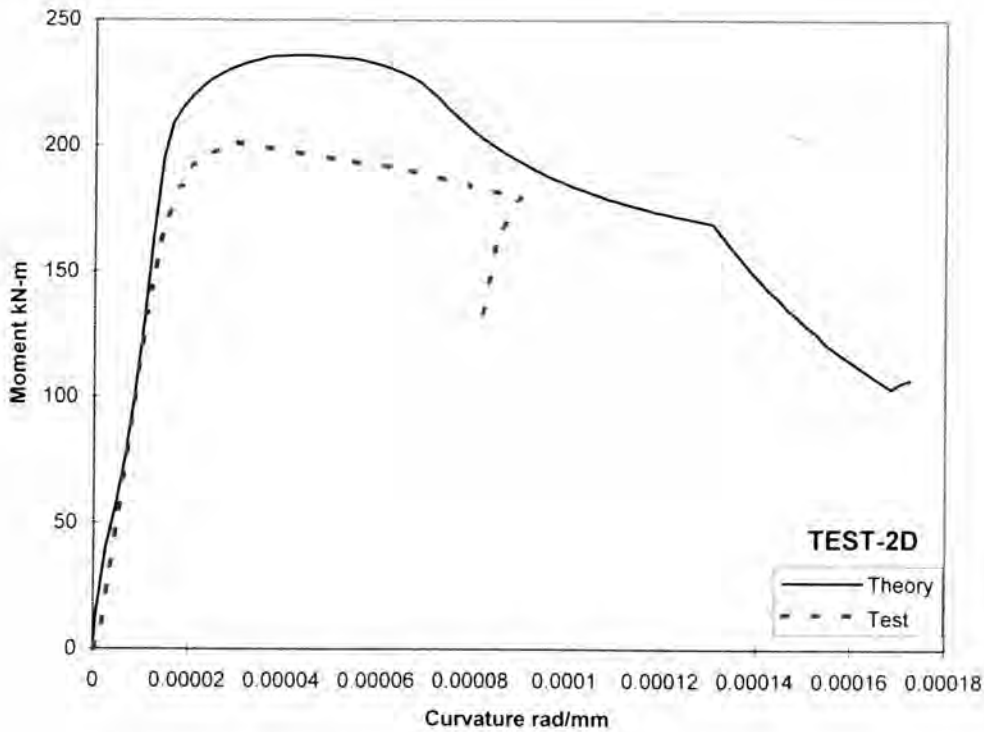

Fig.16.36. Moment-curvature relationship for Beam –2D

Figure 16.37 shows the variation of strain in the internal tensile steel reinforcement with the moment as calculated from the numerical analysis. The theoretical moment corresponding to the reinforcement yield strain (2215 microstrain) were 190 kNm, 192 kNm and 198 kNm for the beams 2B, 2C and 2D respectively. This compares well with the corresponding maximum applied moments of the beams before concrete crushing and subsequent plate debonding, which are 182 kNm, 199 kNm and 201 kNm. Therefore, it can be assumed that for the side plated beams tested in this study, the yielding of internal reinforcement is a crucial factor for determining the flexural capacity and the subsequent debonding.

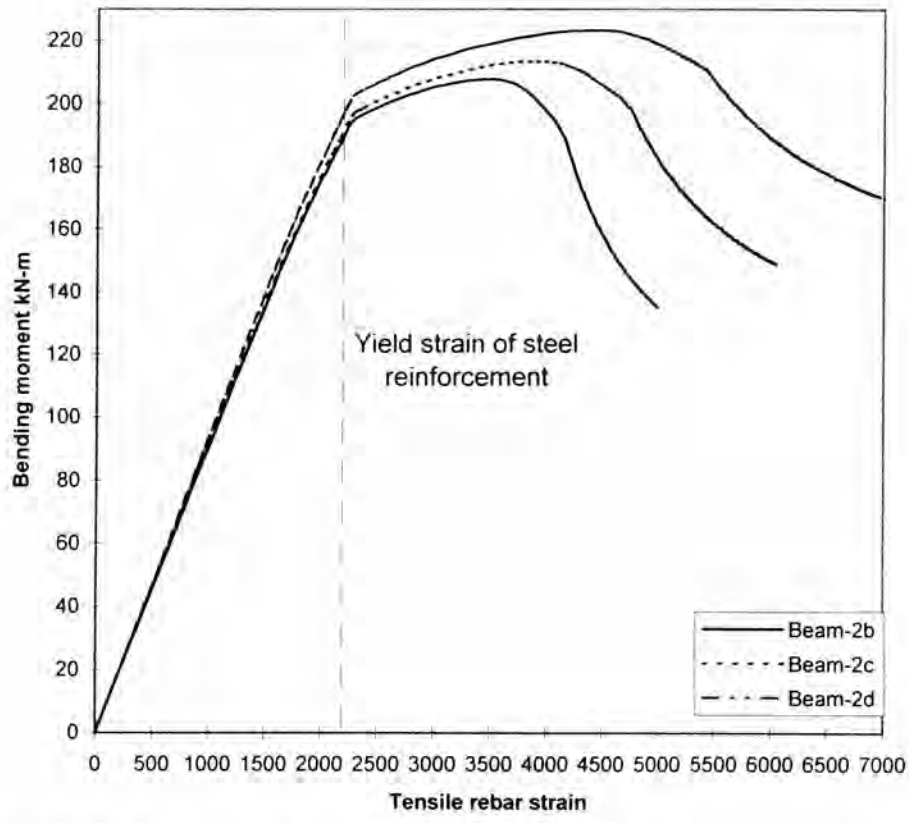

Fig.16.31. Variation of analytical strain in the reinforcement with the moment

16.9.4 Shear strength and shear peeling strength calculations

The crack sliding model was adapted to calculate the shear strength of the non-plated, non-shear reinforced beam cross section (Refer Section 5.3) and the shear peeling strength of the three side plated beams (Refer Section11.3). The envelopes for beams 2B and 2D are shown in Fig.16.32 and for beam-2C are shown in Fig. 16.33. The shear strength of the reinforced concrete beam (V_{uc}) is estimated to be 73.5 kN. The shear peeling strength for the beams 2B, 2C and 2D are 108 kN, 108 kN and 110 kN respectively. The calculated shear peeling strengths are greater than the shear load at which the debonding of the plates occurred (Refer table-16.7). Further, the analysis shows that the critical shear crack will occur at a distance of about 1100 mm from the support. This means, the debonding of such long plates of 1100 mm would occur only by plate yielding and the same was observed in the tests also. Hence, the possibility

of debonding due to shear could be ruled out for plated beams such as tested in this study with high ratios of shear span to depth.

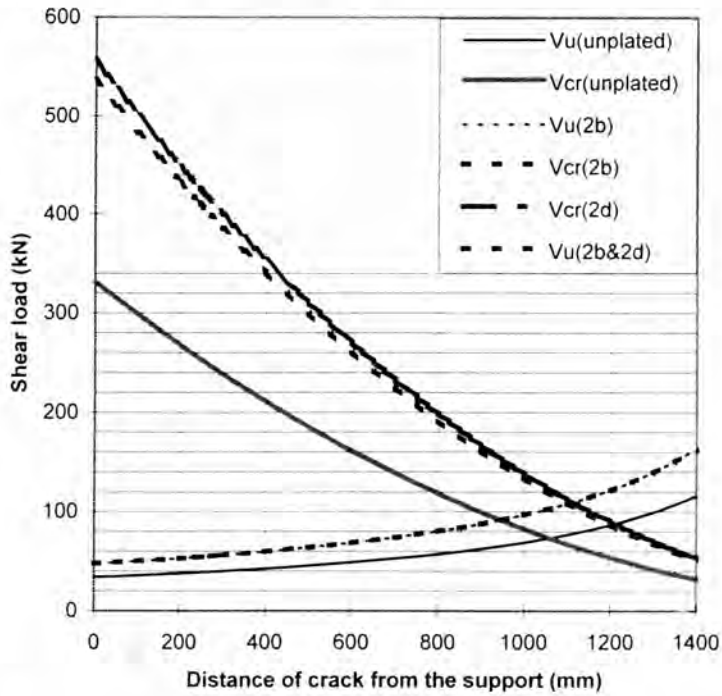

Fig.16.32. Shear strength and shear peeling strength: Beams-2B and 2D

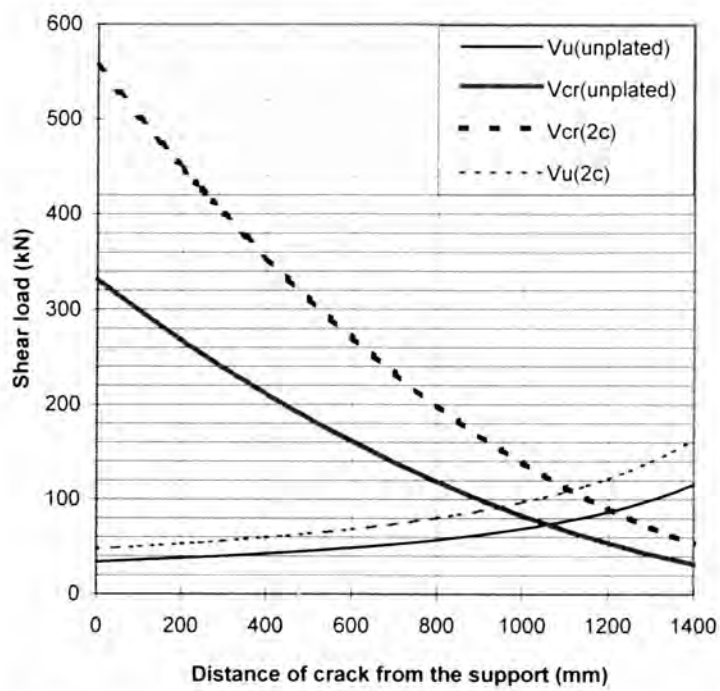

Fig.16.33. Shear strength and shear peeling strength: Beam-2C

16.9.5 Shear stresses due to longitudinal shear flow

The interface shear stresses computed from the standard $VAy/I_p b_p$ formula for the three beams 2B, 2C and 2D at the instance of the maximum applied shear loads were 0.124 MPa, 0.154 MPa and 0.179 MPa. These magnitudes are only a fraction of the tensile strength of the concrete. Hence, the possibility of shear flow debonding is ruled out.

16.10 Concluding remarks

The present study on the reinforced concrete beams bonded with full length, very deep side plates has shown that the axial peeling of beams bonded with deep side plates is a gradual process. It develops in various stages such as during the formation of extensive flexural and flexural shear cracks, crushing of concrete and the subsequent transfer of large compressive forces to the side plates. This build up of compressive forces leads to the formation of debonding cracks along the top edges of the plate and the accompanying local buckling caused the complete debonding of the plates. Adequate warning of the impending debonding was available as the strains recorded at the instance of debonding were in the order of 8000-15000 microstrains. Therefore, axial peeling of deep side plates is a ductile phenomenon unlike shear peeling that is sudden and occurs in a narrow range of strain. The maximum moment that can be sustained by such side plated beams can be estimated from the numerical analysis by setting the strain in the internal tension reinforcement to be at its yield strain.

References

Ahmed ,M .(1996). Strengthening of reinforced concrete beams by bolting side plates to their sides, Master of Engg.Sc. thesis, The University of Adelaide, Adelaide, October 1996. 390 pages.

AS3600 (1994). Australian Standard- Concrete Structures, Standards Australia, 1994.

Burnet,M.J. (1998). Partial interaction design of composite steel and concrete flexural members. Ph.D. Thesis. The University of Adelaide, Adelaide,1998.

Warner,R.F.(1969). Biaxial moment thrust curvature relations. Journal of Structural Engg.,ASCE,Vol.95,No.ST5, May1969, pp.923-940.

CHAPTER-17: AXIAL PEELING WITHIN PLATE ENDS OF BEAMS BONDED WITH FULLY ANCHORED TENSION FACE PLATE OR SIDE PLATES

CONTENTS

17.1 Introduction

This chapter deals with the investigation carried on the axial peeling behaviour of the simply supported reinforced concrete beams bonded with full length steel side plates or tension face plates folded round the beam edges to avoid any premature peeling. The side plates used in this study are shallow so as to place them completely under the bending tension region, unlike the side plates of the beams tested in Chapter-16. The debonding phenomenon is evaluated for differing shear span to depth ratio. Finally, the test results are analysed using the procedures developed in Chapters 11 and 16.

17.2 Specimens

The objective of the present investigation is to study the axial peeling that occurs within the plate ends. Six tests were carried out by using two beams. The reinforcement details of the basic unplated beam are shown in Fig.17.1. One beam (Beam 2E) was bonded with full length side plates of 100 mm depth and 6 mm thickness as in Fig.17.2. The second beam (Beam 2F in Fig.17.6) was bonded with a full length tension face plate of 200 mm width and 6 mm thickness. The total area of cross section of the plate provided for beams 2E and 2F is kept the same (1200 mm^2). The plates were totally under bending tension, unlike the side plates in beams 2B, 2C and 2D (Chapter-16), and they were folded round the beam edges to avoid any premature peeling.

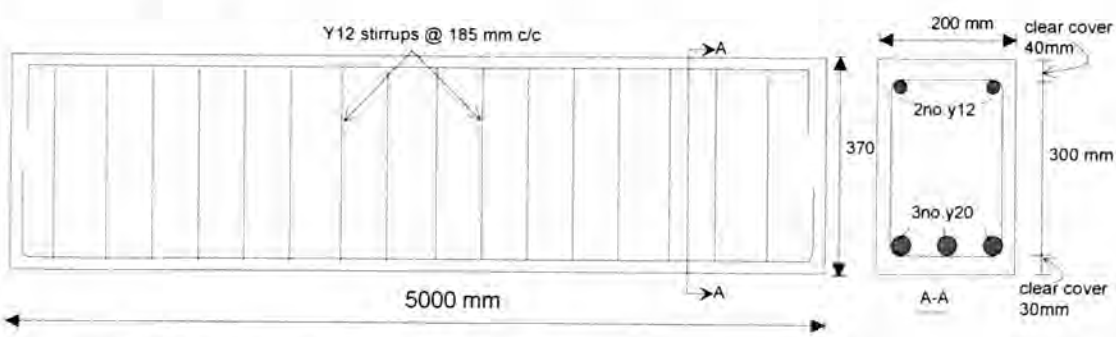

Fig.17.1 Reinforcement details of basic reinforced concrete beam

17.2.1 Tests on side plated beams

Three tests were conducted on the side plated beam. Firstly, it was tested by four-point loading and this test was designated as test-2E as shown in Fig.17.2. After, the completion of test-2E, the beam was repaired as shown in Fig.17.3 and new plates were bonded to the sides. Then, two identical but individual tests (Tests-2ES1 and 2ES2-(Refer Fig.17.4) were conducted on the two shear spans of the Beam-2E which was bonded with full length side plates (100mm deep and 6 mm thick) that were folded around the corners of the beam. The load was applied 1200 mm away from the nearest support; the failure in the longer shear span was prevented by clamping it as shown in Fig.17.5.

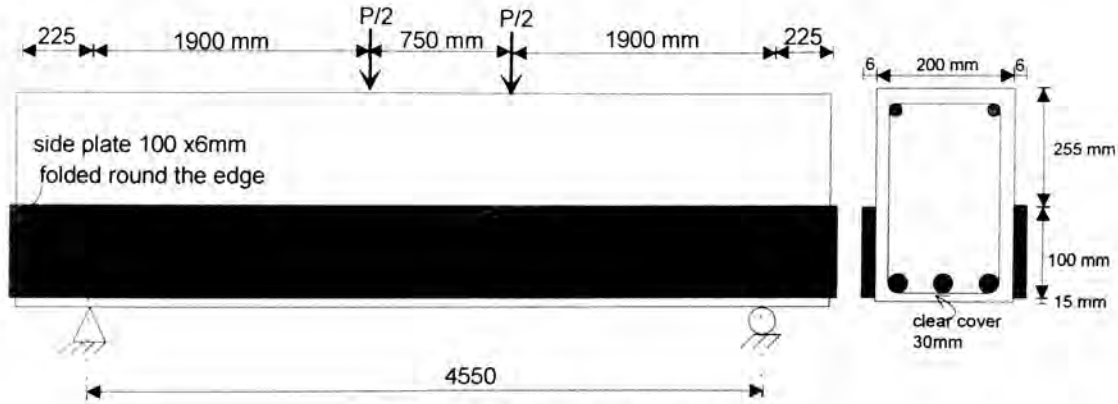

Fig.17.2. Details of Test-2E

Fig.17.3. Repairing of Beam-2E

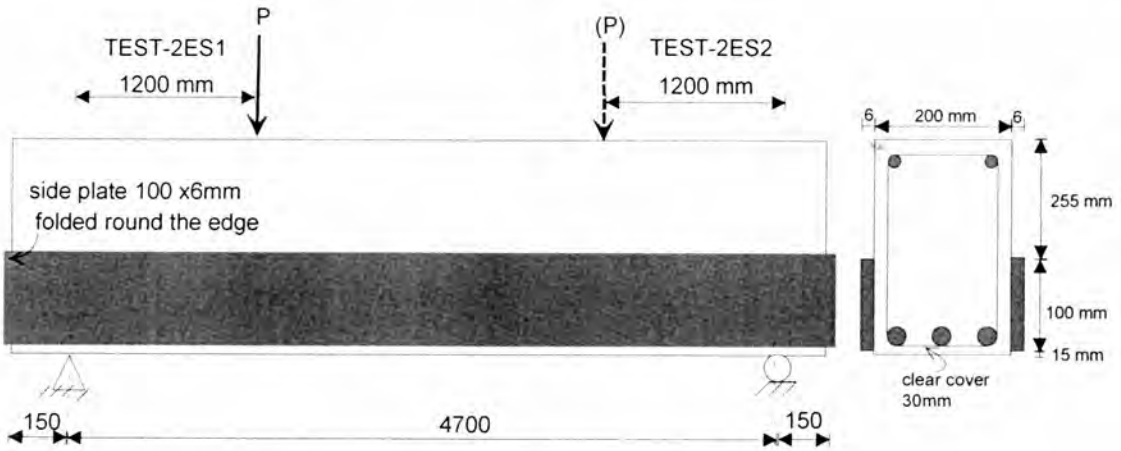

Fig.17.4. Details of Test-2ES1 and Test-2ES2

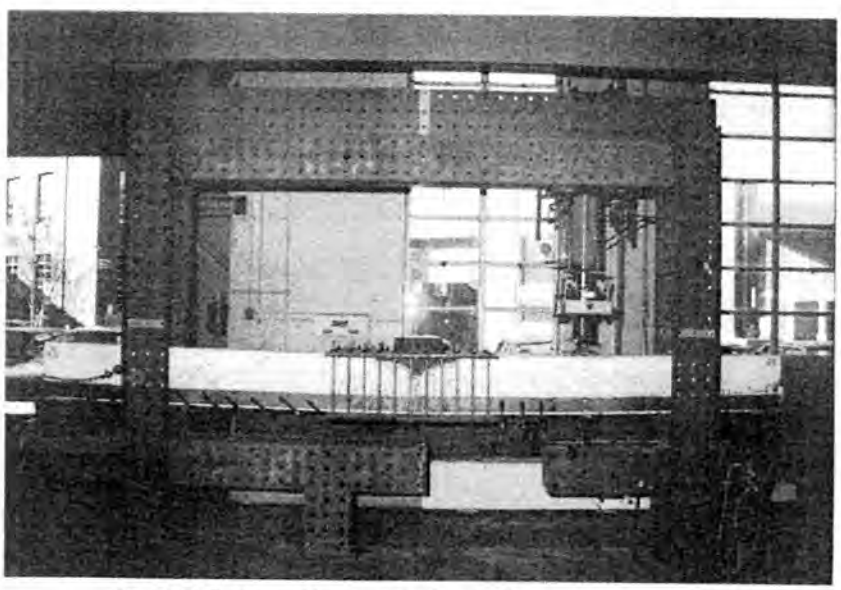

Fig.17.5. Loading and clamping arrangement

17.2.2 Tests on tension face plated beams

A total of three tests were conducted. Firstly, the beam was tested under four point loading and was designated as test-2F, as shown in Fig.17.6. Then, the same beam was tested under a single concentrated load after carrying out proper repair; this test was denoted as test-2FS1 and the details are shown in Fig.17.7. After the completion of test-2FS1, the damaged portion of the concrete was repaired as shown in Figs.17.8. Then test-2FS2 was carried out on the other shear span by applying the load at a distance 900 mm from the nearest support (Fig.17.9). The failure in longer shear span was prevented by clamping it.

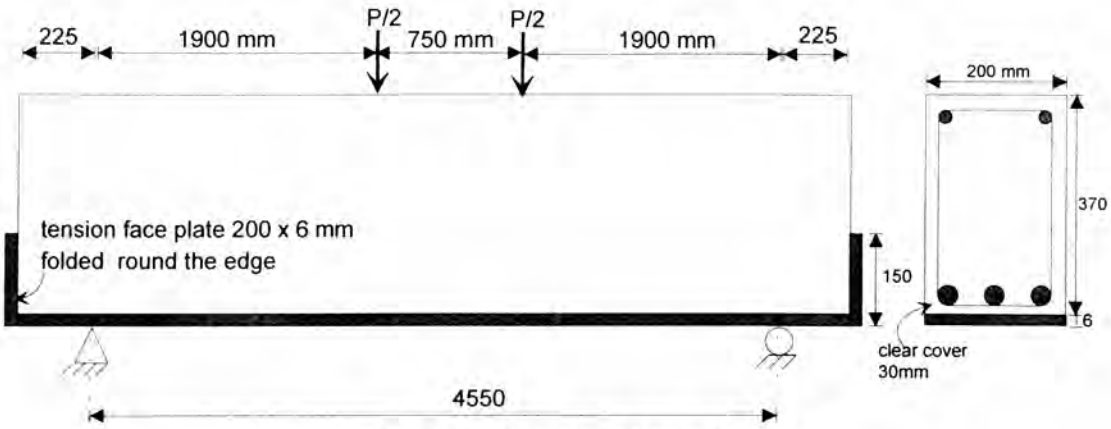

Fig.17.6. Details of Test-2F

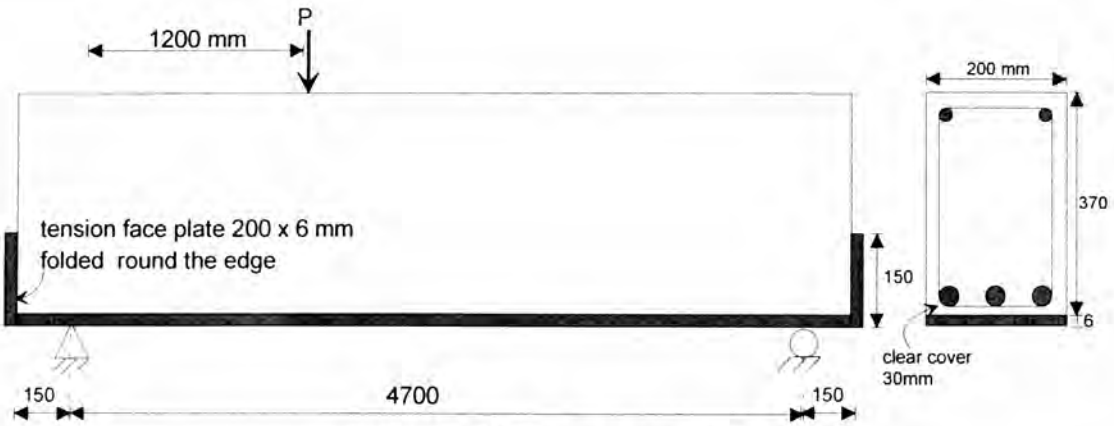

Fig.17.7.Details of Test-2FS1

Fig.17.8 Restoration of Beam 2F after damage

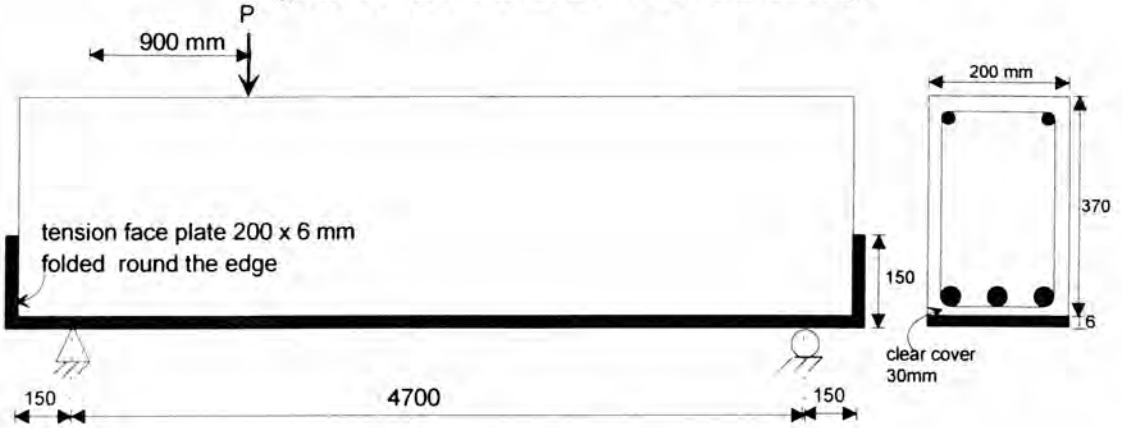

Fig.17.9.Details of Test-2FS2

17.3 Instrumentation

Strain gauges were bonded to the plates in order to detect the debonding at various sites of the plates and also to study the behaviour under flexure. The arrangements of the strain gauges and their numbering are shown in Figs. 17.10a-c for all the three tests conducted on the side plated beam and in Figs.17.11a-c for the tension face plated beam. The deflection at mid-span in the case of beams 2E and 2F and at load point in the case of beam 2FS1 were monitored by dial gauges as well as transducers.

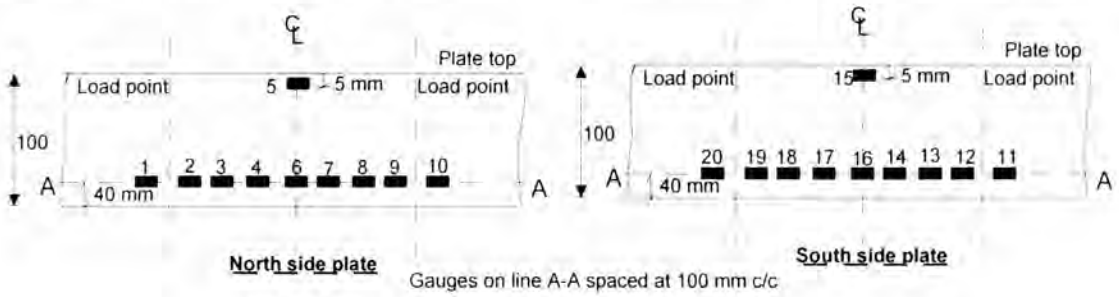

(a)Test-2E

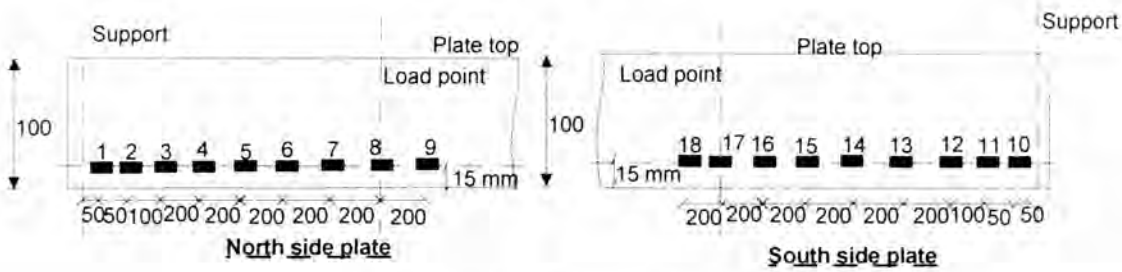

(b)Test-2ES1(Front elevation)

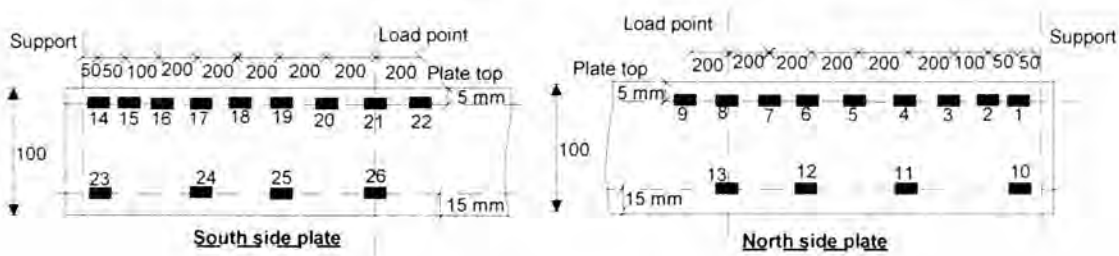

(c)Test-2ES2 (Front elevation)

Fig.17.10.Strain gauge arrangement for side plated beam

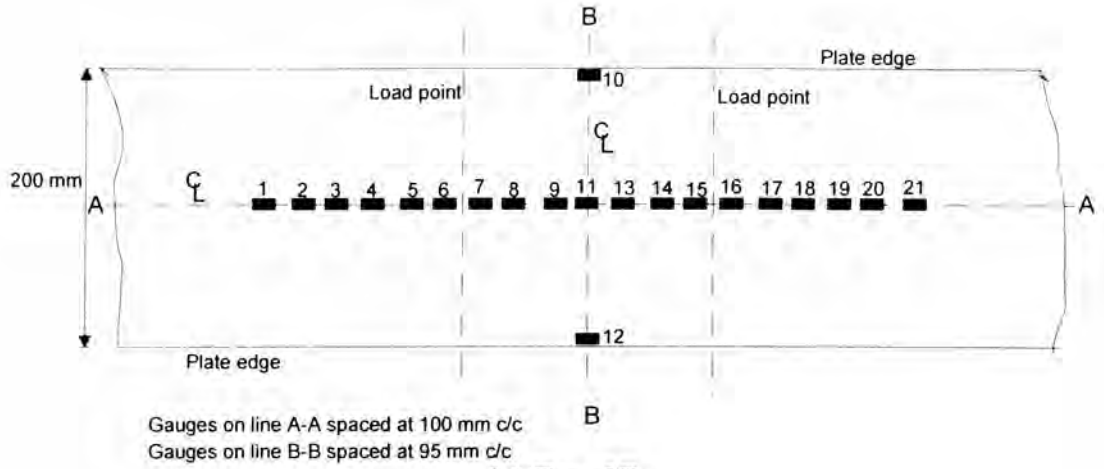

(a) Test-2F

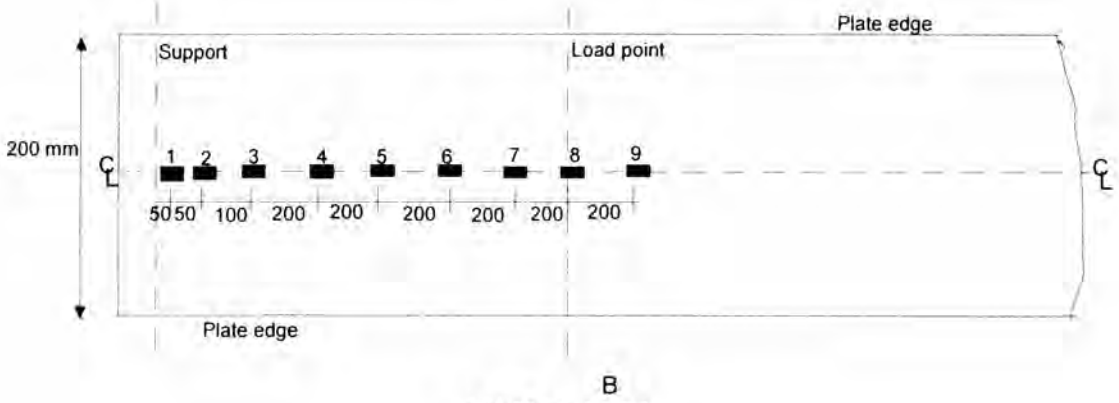

(b) Test-2FS1

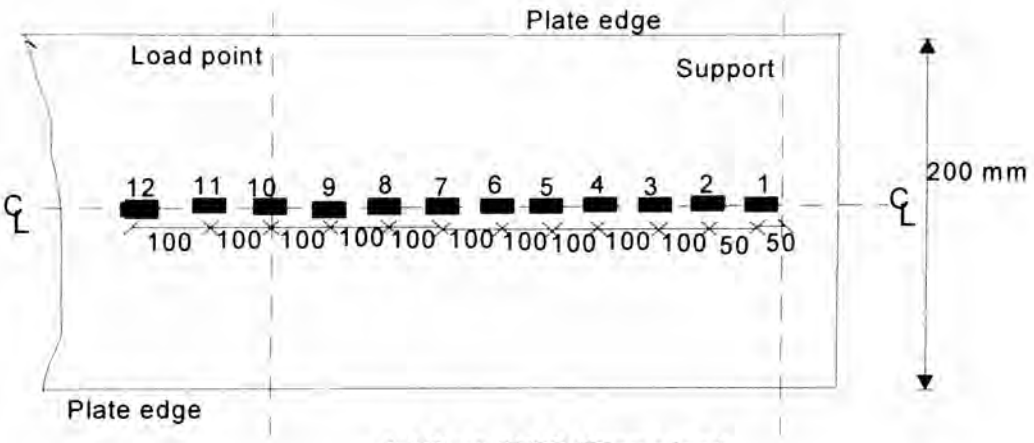

(c) Test-2FS2 (Plan view)

Fig.17.11. Strain gauge arrangement for the tension face plated beam

The strain profile across the beam depth were also monitored by means of demec discs bonded to the concrete surface on both sides in the constant moment regions in tests 2E and 2F; their arrangement and numbering are shown in Figs.17.12a and 17.12b. A few demec discs were also used in test 2FS2 as shown in Fig.17.12c.

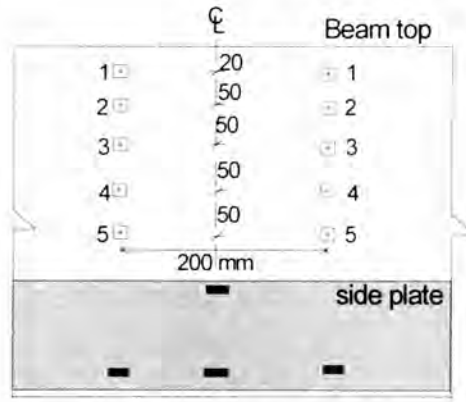

(a) Test-2E

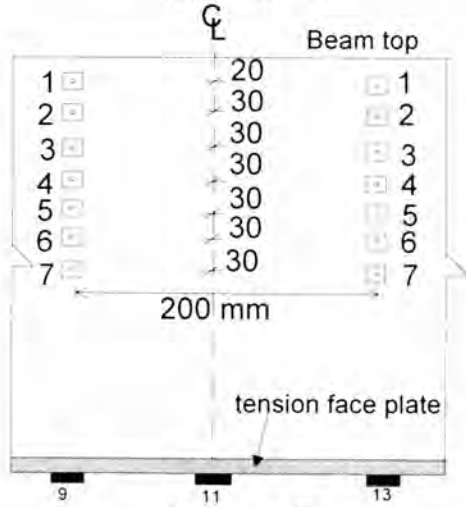

(b)Test-2F

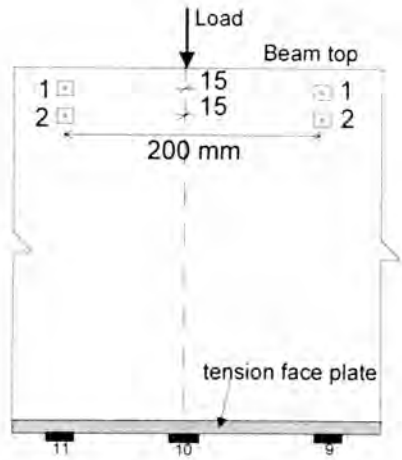

(c)Test-2FS2

Fig.17.12. Demec gauge arrangement

17.4 Material Properties

All the beams were cast in a single pour using ready mixed concrete supplied by a local manufacturer. Material properties of the concrete are shown in Table-17.1. In

this table, the individual values are of each test are given under the "i" column and their mean value under "m" column.

Table-17.1. Material properties of the concrete

Age	E_c (MPa)		f_b (MPa)		f_c (MPa)		f_{cu} (MPa)	
(days)	i	m	i	m	i	m	i	m
779	34572	35433	3.92	4.05	52.6	51.5	59.5	58.0
	3661		4.06		51.2		52.5	
	36117		4.27		51.0		61.9	
	34381		3.94		51.3			

where E_c= Elastic modulus of the concrete, f_c= Cylinder compressive strength of the concrete, f_{cu}= Cube compressive strength of the concrete and f_b= Brazilian tensile strength of the concrete.

Material properties of the steel plates, reinforcing bars and shear stirrups are shown in Table-17.2. The manufacturer's specifications of the material properties of the epoxy glue used for bonding the steel plates are indicated in Table-17.3.

Table-17.2. Material properties of the steel

Item	f_y (MPa)				f_u (MPa)			
Sample No.	1	2	3	Mean	1	2	3	Mean
Rebar Y20	438.9	440.5	449.7	443.0	528.0	527.4	529.6	528.3
Rebar Y12	454.5	458.0	455.3	456.0	552.6	550.8	552.6	552.0
Plate 6mm	360.7	365.7	368.1	364.8	493.6	487.8	490.9	490.7

where f_y = Yield strength of the steel and f_u = Ultimate strength of the steel.

Table-17.3. Material properties of the glue Hilti CA 273 after 2 days (as tested by the manufacturer)

Compressive strength (ISO 604)	Tensile strength (ISO 527)	Flexural strength (ISO 178)	Elastic modulus in compression (ASTM D 695)	Tensile bond strength (ISO 527)	Maximum operating temperature
110-120 MPa	30-40 MPa	20-30 MPa	5000-6000 MPa	10-15 MPa	80° C

17.5 Test results from side plated beam

17.5.1 Test-2E

Beam-2E was bonded with 100 mm deep and 6 mm thick steel plates to its sides and was fully anchored to avoid any premature failure (Fig.17.2). It was tested to fail in flexure by applying two equal, concentrated loads as shown in Fig.17.13. In the following discussion, the applied load P is indicated within brackets.

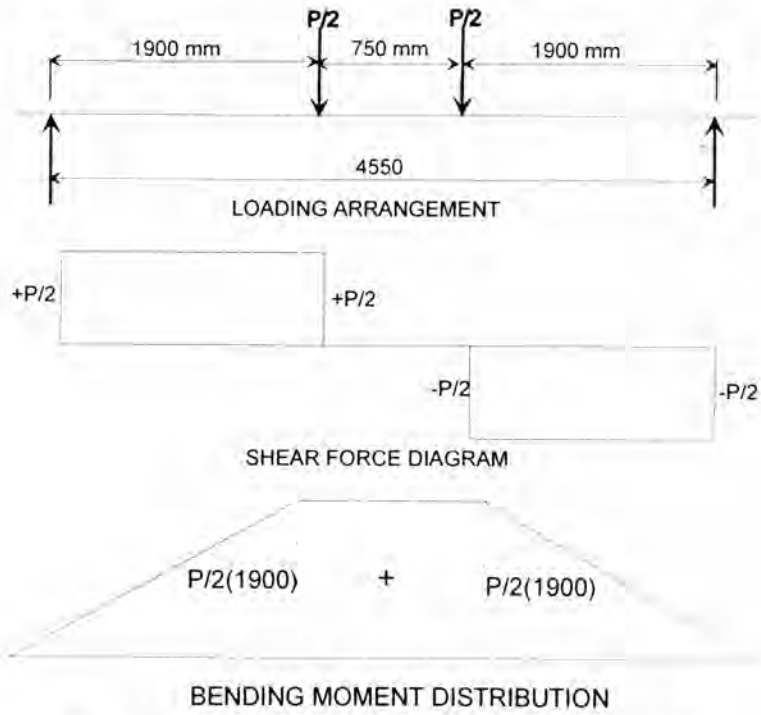

Fig.17.13. Loading arrangement for 2E and 2F

17.5.1.1 Crack propagation and failure mode

Crack growth could not be observed until the maximum bending moment M was 95.0 kNm (P=100 kN) due to the presence of side plates; at this moment a flexural crack was seen above the side plate in the constant moment region as shown in Fig.17.14a. This figure also shows the test rig, demec discs and strain gauges bonded to the side plates. As the applied load was increased, new flexural cracks appeared in the constant moment region and they extended vertically; flexural shear cracks and diagonal cracks formed in the shear spans as shown in Fig.17.14b.

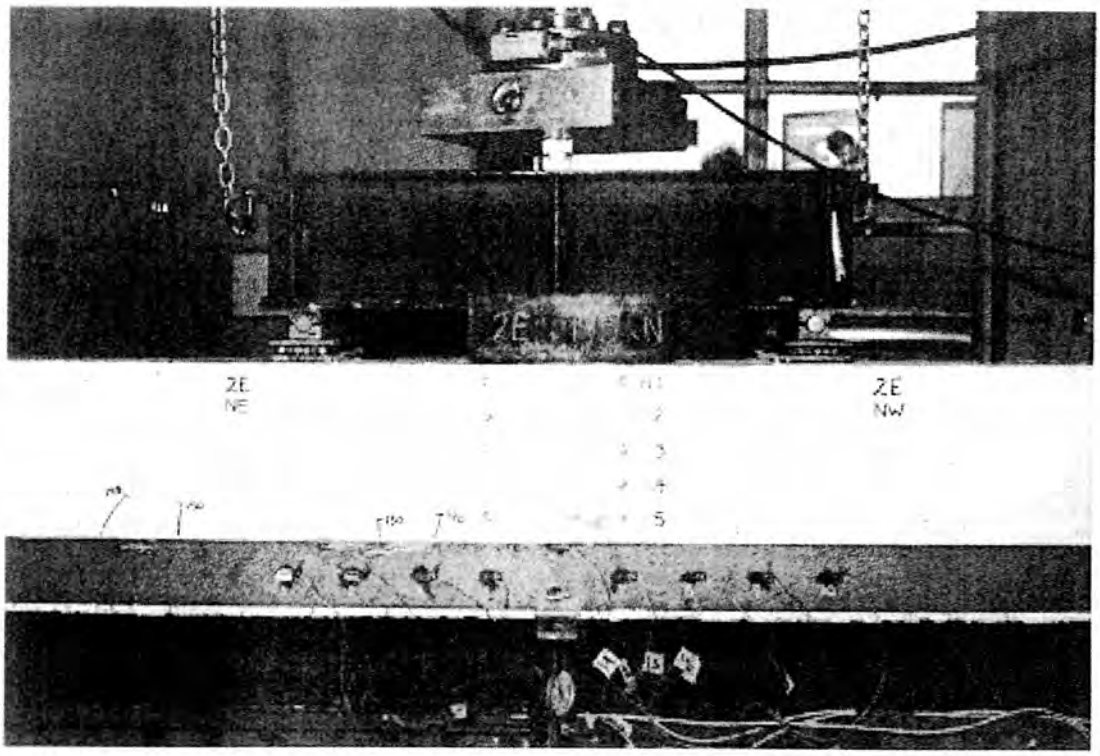

Fig.17.14(a). Crack pattern at P=195 kN

Fig.17.14(b). Overall crack pattern at closure of test

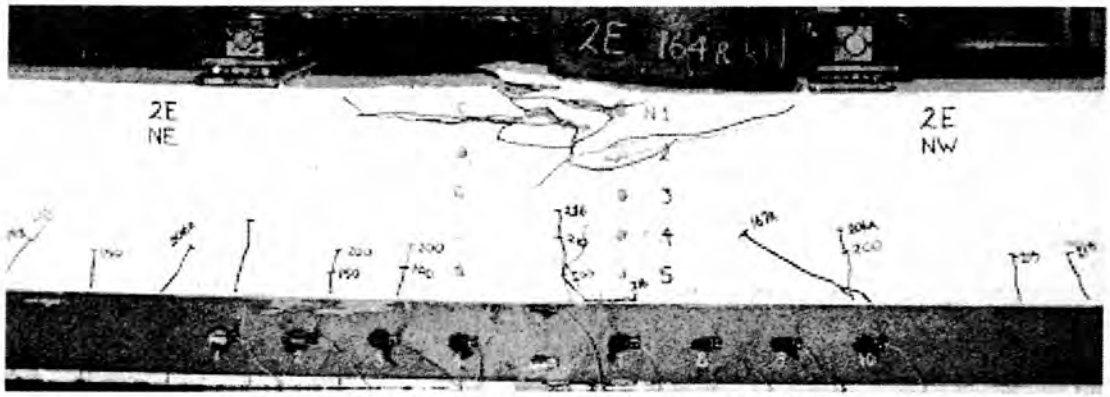

Fig.17.14(c). Concrete crushing in north side

Fig.17.14(d). Concrete crushing in south side

Fig.17.14(e). Close view of debonding crack beneath plate in constant moment region

Fig.17.14. Crack pattern and failure mode in Test-2E

The cracks in the shear span stabilised when the applied maximum moment was 199.5 kNm, corresponding to a shear force of 100 kN and applied load of 200 kN. On increasing the applied load by another 5 kN, local horizontal debonding cracks appeared on the top edge of the plates, from some of the existing flexural shear cracks. When the applied load was increased to 216 kN, corresponding to a maximum moment of 205.2 kNm, a horizontal debonding crack appeared both along the top and bottom edges of the side plates as shown in figures 17.14c and 17.14d. A close view of the debonding crack along the bottom edge of the side plate is shown in Fig.17.14e. It can be seen that the debonding crack was of limited length and it did not propagate along the plate length. At this stage, the load started to drop down and it was applied by incrementing the deflection by 2 mm.

When the applied moment was 203.4 kNm (P=214.1 kN), the top concrete fibres started crushing and the crushing zone increased on reapplication of load accompanied with large deflection and rapid drop in load. Thus, a crushed zone that had a length of about 500 mm and depth of about 110 mm was formed in the constant bending moment region of the plate, as shown in Figs.17.14c and 17.14d. As the beam was unable to sustain any further load, the test was terminated when the moment was 155.8 kNm (P=164 kN). It was observed that the debonding crack in the constant moment region did not propagate any further and the length was about 200 mm. Therefore, the axial peeling of these side plates which were totally under flexural tension was stable and the debonding crack did not shoot towards the plate ends.

17.5.1.2 Strain variation in side plates

Figures 17.15a-h show the variation of strains recorded at different gauge sites that are shown in Fig.17.10a with the maximum applied moment. Figures 17.15a-c show the strain distribution in both side plates at the gauge sites in which the maximum recorded strains were in the order of yield strain of the plate material (1800 microstrain). It can also be seen that the strain magnitudes at the gauge locations indicated in Figs.17.5a-c increased linearly with the increased applied moment until the maximum moment was about 160 kNm. From 160 kNm onwards, there was virtually no change in the strain magnitudes in Figs.17.5a-c till 205 kNm after which the strain readings started to decrease smoothly due to the crushing of concrete.

Figures 17.15e, 17.15f and 17.15g are of interest to the present study as they show the strain variation at the sites at which debonding in the constant moment region occurred. Figs 17.15e and 17.15f show the strains recorded at the gauge locations corresponding to the bottom level of the side plates in the mid-span. These

figures show that the strain magnitudes recorded at mid-span at the instance of debonding ranged between 10000 and 20000 microstrains; this is about 5 to 10 times more than the yield strain of the plate, indicating the plates were subject to strain hardening. Figure 17.15g shows that the top level plate strain is also greater than the yield strain. The long plateaus after the maximum moment level indicates the stable nature of debonding at all these sites in Fig.17.5e-g. Fig.17.15h shows the strain variation pertaining to gauges #10 and #11 in Fig.17.10a and the maximum strain ranged from 4200-9500 microstrains.

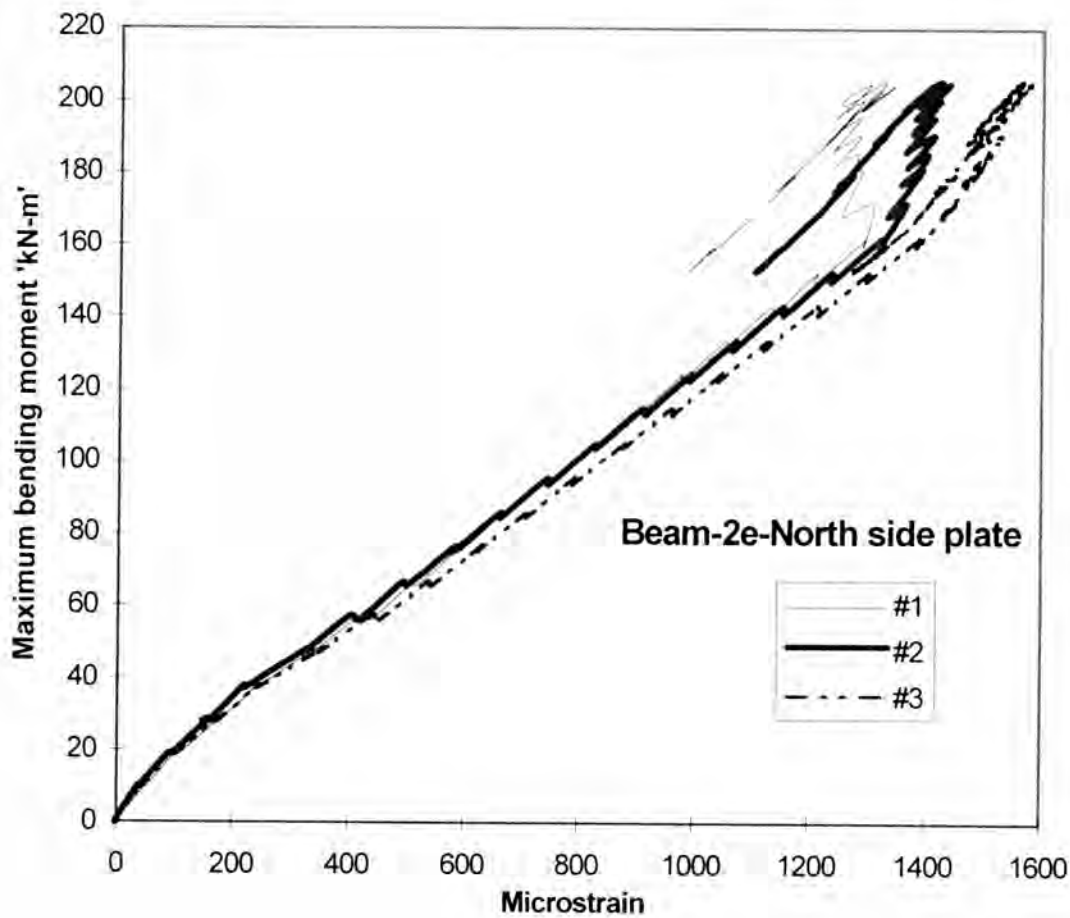

Fig.17.15(a)

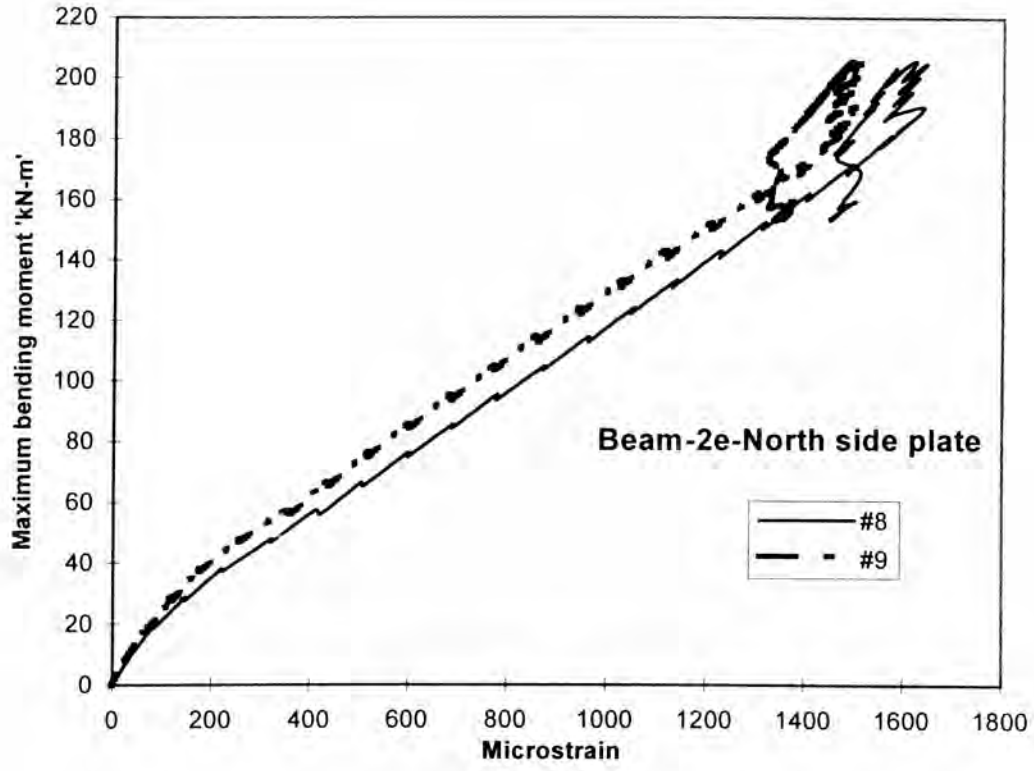

Fig.17.15 (b)

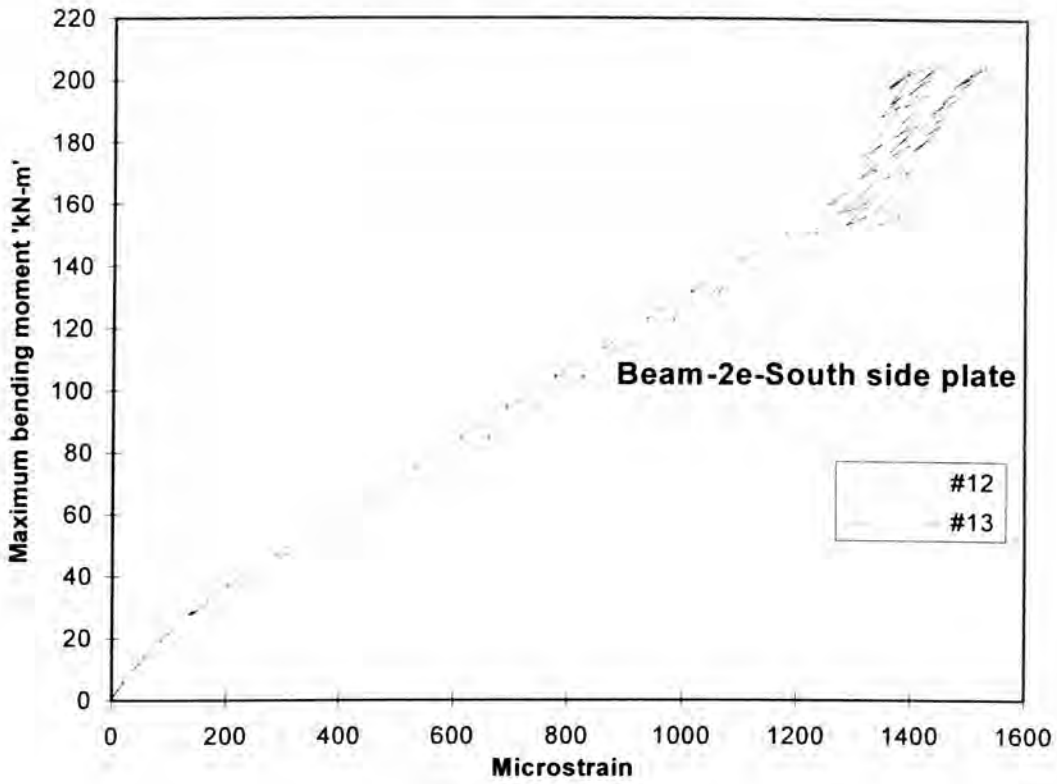

Fig.17.15(c)

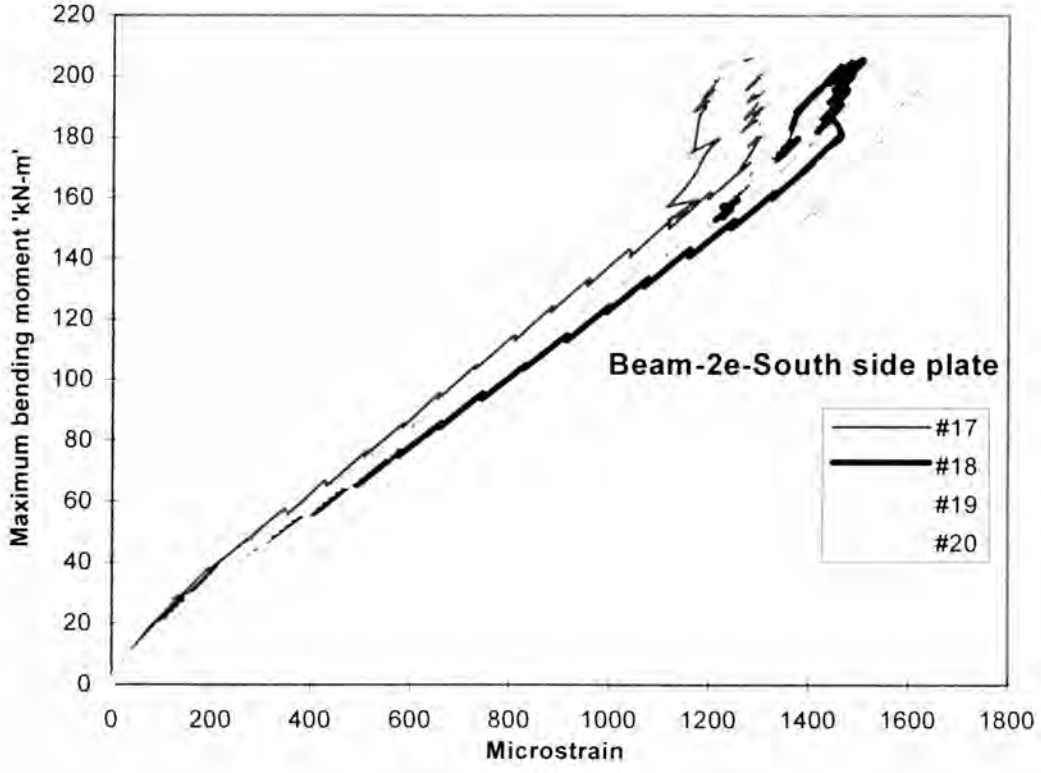

Fig.17.15 (d)

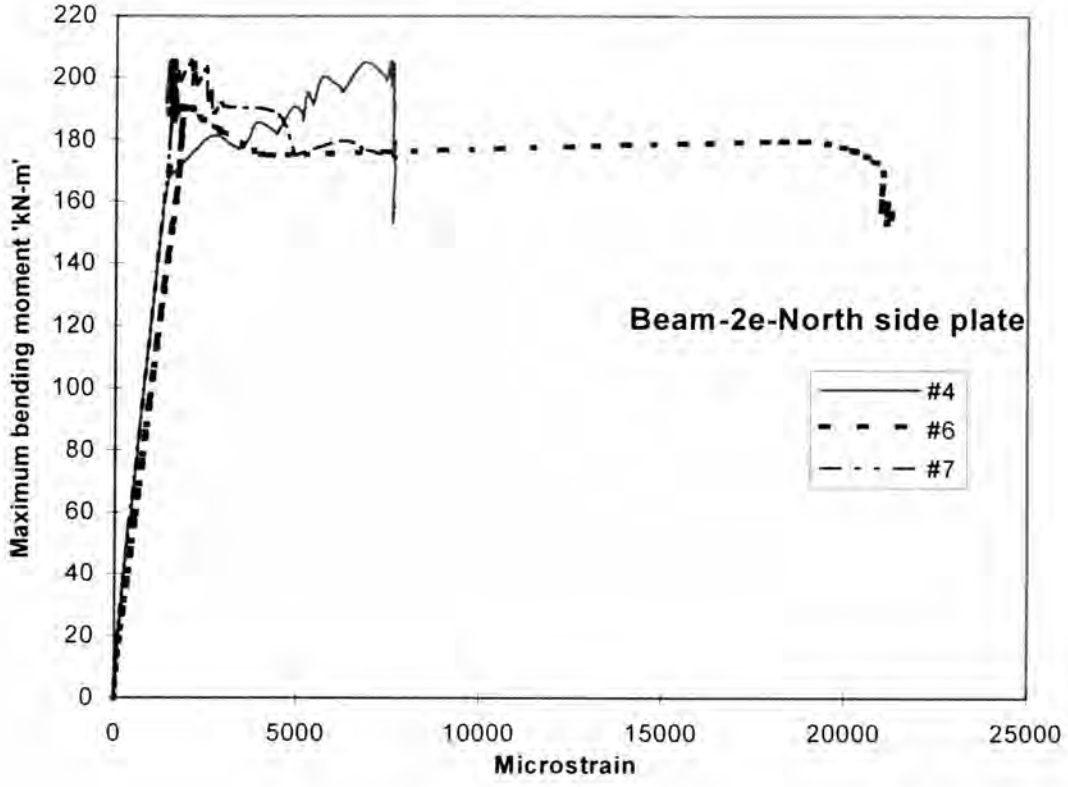

Fig.17.15(e)

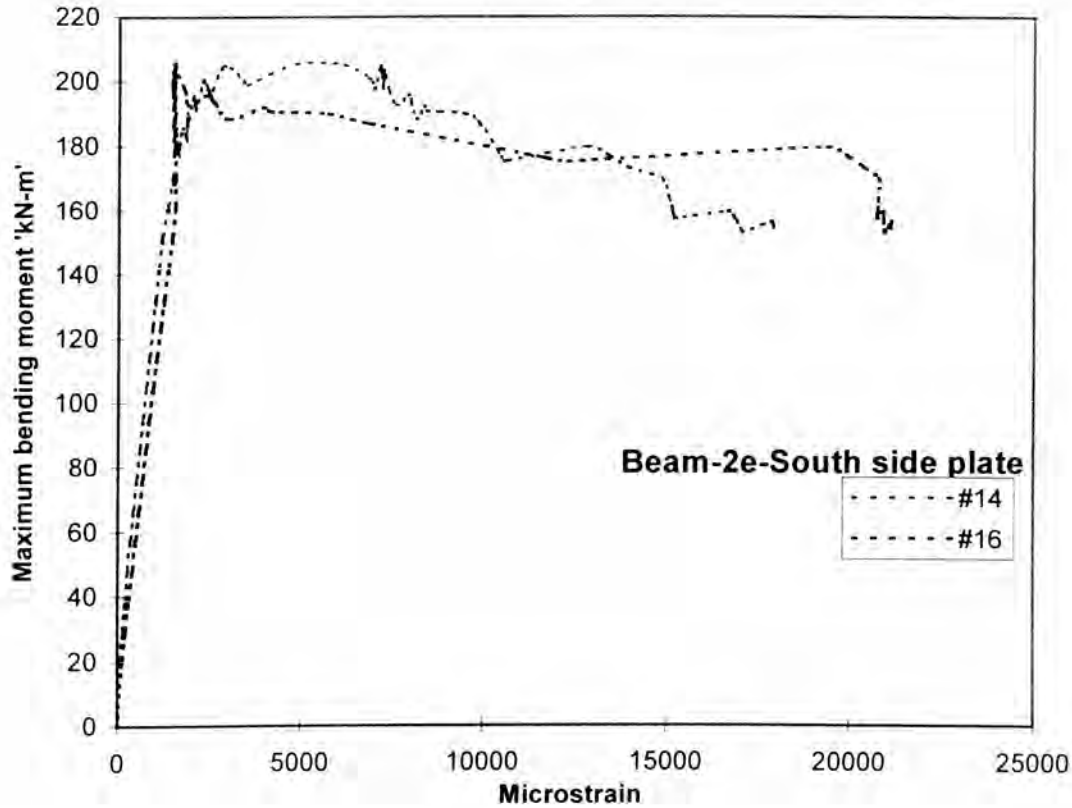

Fig.17.15 (f)

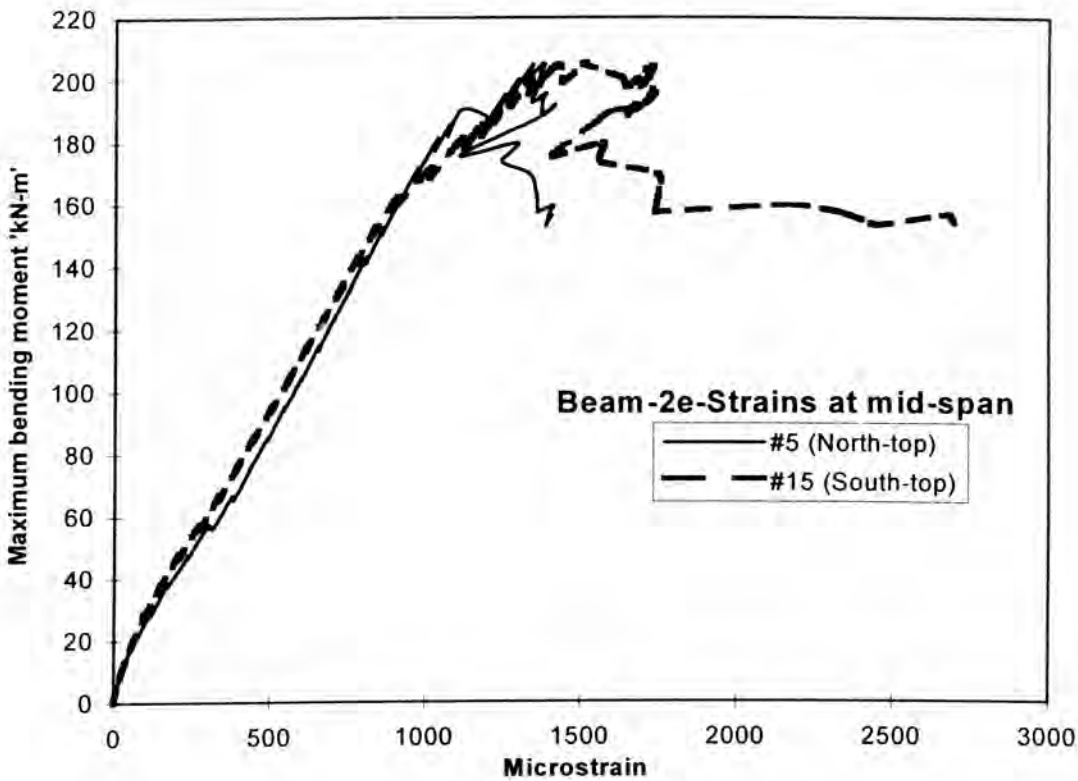

Fig.17.15 (g)

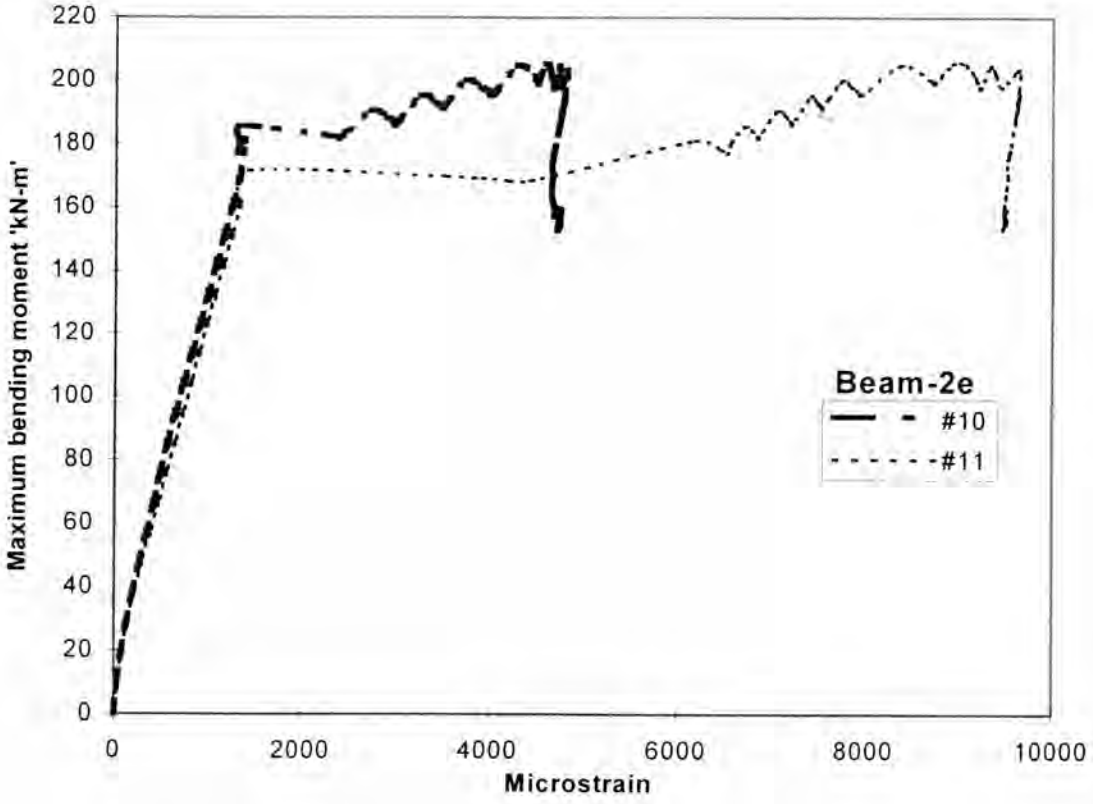

Fig.17.15(h)
Fig.17.15. Test-2E: Strain distribution in side plates

17.5.1.3 Strain profile across the depth of the beam

Figures 17.16a and 17.16b show plots of strain measurements made through the depth of the beam using demec gauges that were bonded to the concrete surface at the mid-span as shown in Fig.17.12a; the corresponding strains measured on the side plates are also indicated. The mean value of strains obtained from both sides was used for plotting.

It can be seen from Figs.17.16a and 17.16b that the neutral axis depth changed gradually from 180 mm to 170 mm as the applied moment was varied from 30 to 185 kNm. During this stage, the maximum compressive strain in the topmost concrete fibre was about 2000 microstrains. Thereafter, the neutral axis shifted swiftly due to extensive crack propagation and the neutral axis depth was only 140 mm at an applied moment 205 kNm (Fig.17.16b). This indicates the ductile nature of the beam as the plates were undergoing large amount of strains.

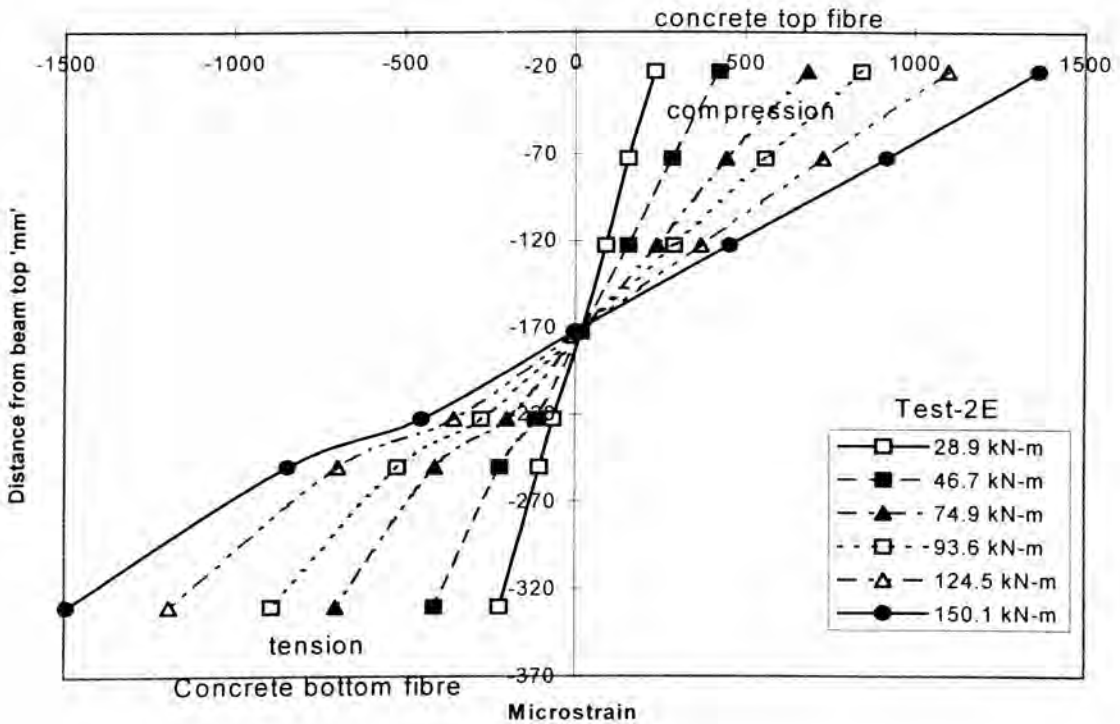

Fig.17.16(a)

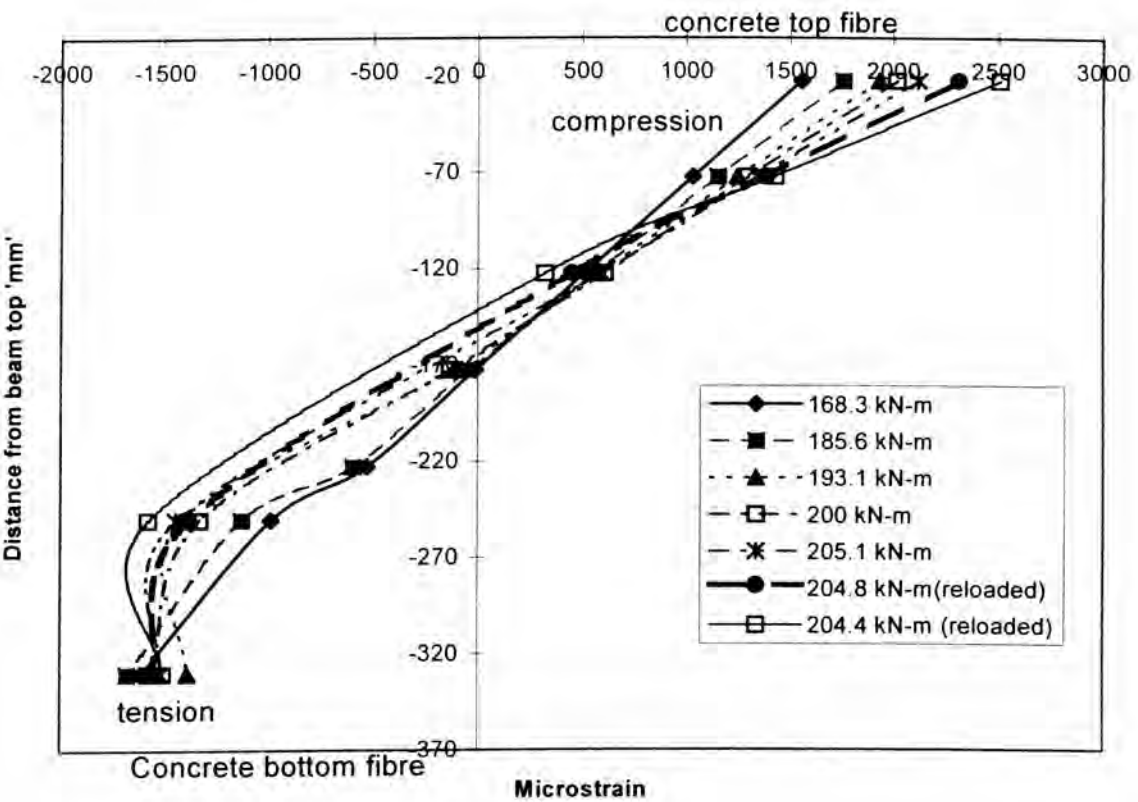

Fig.17.16(b)

Fig.17.16. Test-2E: Strain profile across the depth of the beam

17.5.1.4 Deflection

The variation of deflection measured at the centre of the beam with the moment at the centre is shown in Fig.17.17. The deflection was about 31.5 mm at the maximum bending moment 205 kNm and the final deflection value was about 50 mm when the test was terminated about 160 kNm. This indicates the ductile and stable nature of debonding process at the constant moment region.

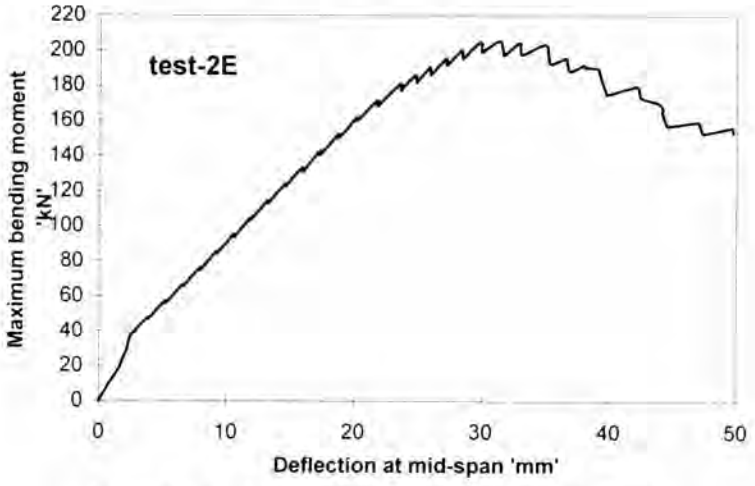

Fig.17.17. Test-2E: Moment Vs deflection

17.5.2 Test-2ES1

Test-2ES1 was carried out on the beam glued with 6 mm thick and 100 mm deep side plates by applying a single concentrated load at 1200 mm from the support (Fig.17.4). The shear force in the span (V) was 74.5 % of the applied load (P).

17.5.2.1 Crack propagation

The observation of crack propagation was hindered by the presence of side plates and the first cracks were observed in the vicinity of the load point at an applied load of 140 kN (Shear force V=104.3 kN). As the load was increased to 150 kN (V=111.8 kN), two inclined cracks formed at a distance 450 mm and 750 mm from the supports. At P=155 kN (V=115.4 kN), two more inclined cracks appeared one close to the support at a distance of 350 mm and another at 825 mm from the support as shown in

Fig.17.18a. Figure17.18a also shows the formation of a horizontal debonding crack (125 mm long) along the top edge of the plate orienting back towards the support that originated from the diagonal crack closer to the support.

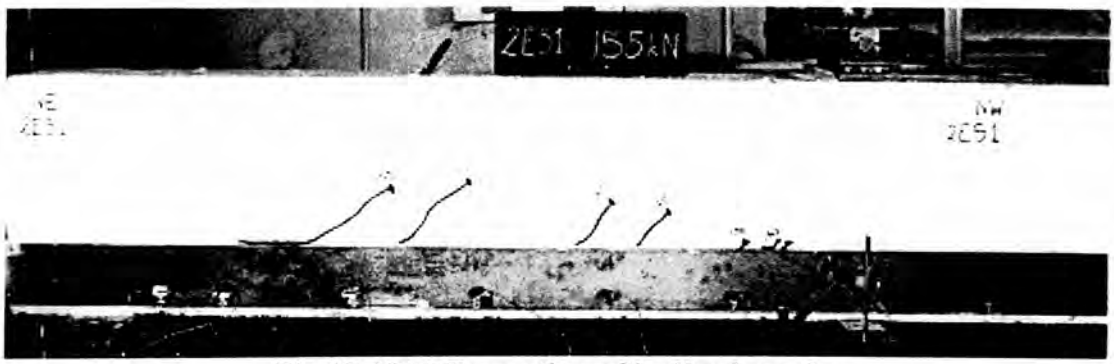

Fig.17.18(a).Formation of inclined cracks

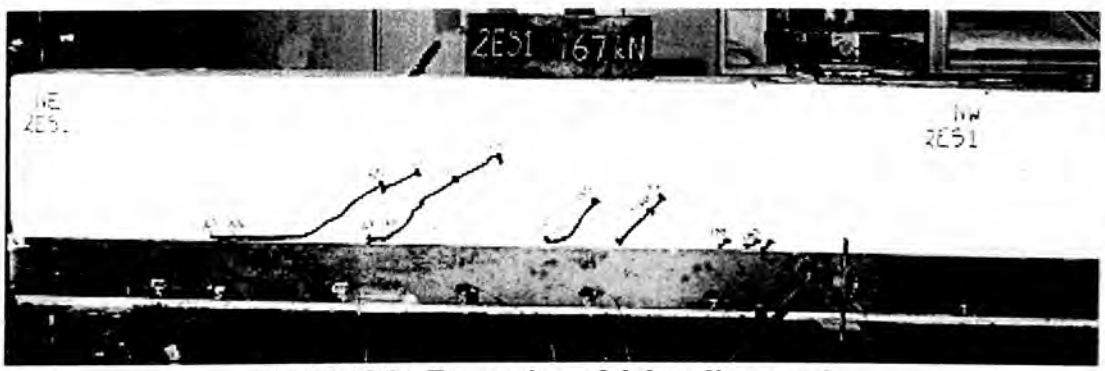

Fig.17.18(b).Formation of debonding cracks

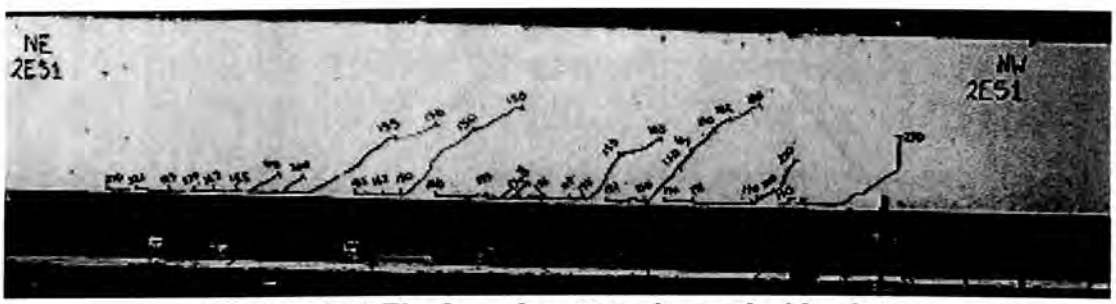

Fig.17.18(c).Final crack pattern in north side plate

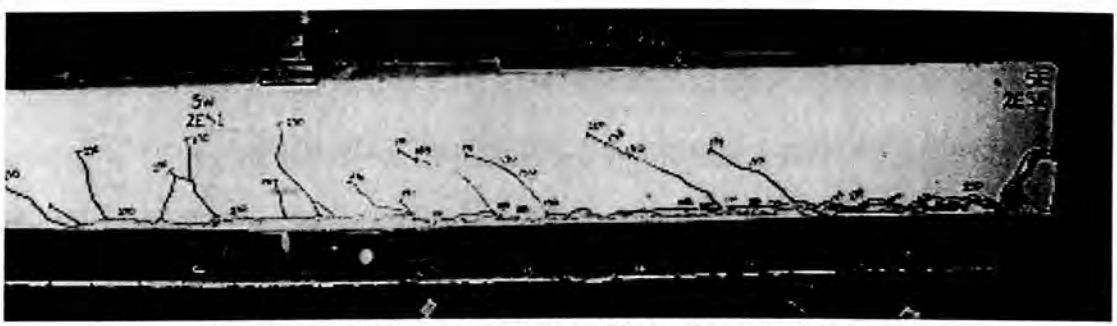

Fig.17.18 (d).Complete debonding of south side plate

Fig.17.18. Test-2ES1: Crack patterns

As the load was increased further in 3 kN increments, two more similar debonding cracks formed from the roots of two other inclined cracks. The three horizontal cracks propagated steadily backwards and they stabilised at an applied load of 185 to 188 kN (V=137.8 to 140 kN), as shown in Fig.17.18b. Debonding cracks also formed from the two inclined cracks close to the load point when the applied load was in the range of 191-194 kN (V=142.3-144.5 kN). Moreover, the debonding crack close to the support extended further when the applied load was 221 kN (V=164.6 kN), as can be seen from Fig.17.18c.

As the load was increased to 230 kN (V=171.3 kN), the south side plate debonded completely due to the formation of long horizontal debonding crack caused by the joining of all the individual debonding crack as shown in Fig. 17.18d. The anchorage at the beam corner separated from the concrete and new diagonal cracks also formed on either side of the load point. In the north side, the debonding crack close to the support extended over the support and new debonding cracks occurred around the load point, as shown in Fig. 17.18c. The load test was terminated at this stage, as the applied load abruptly dropped to 177 kN (V=131.9 kN).

17.5.2.2 Longitudinal strains in the side plates

Figures 17.19a and 17.19b show the variation of longitudinal strains recorded at various strain gauge sites (refer Fig.17.10b) along the bottom edge of the north and south side plates respectively. It shows that the strains increased linearly till the shear force in the shear span was 111.7 kN-115.5 kN at which the horizontal debonding crack was initiated. This is marked by the plateau in curves for gauges #1, #2,#3 and #4 in the north side and #10,#11,#12 and #13, which were the nearest gauges to the support. The kinks in the curves for other locations show the steady propagation of debonding cracks.

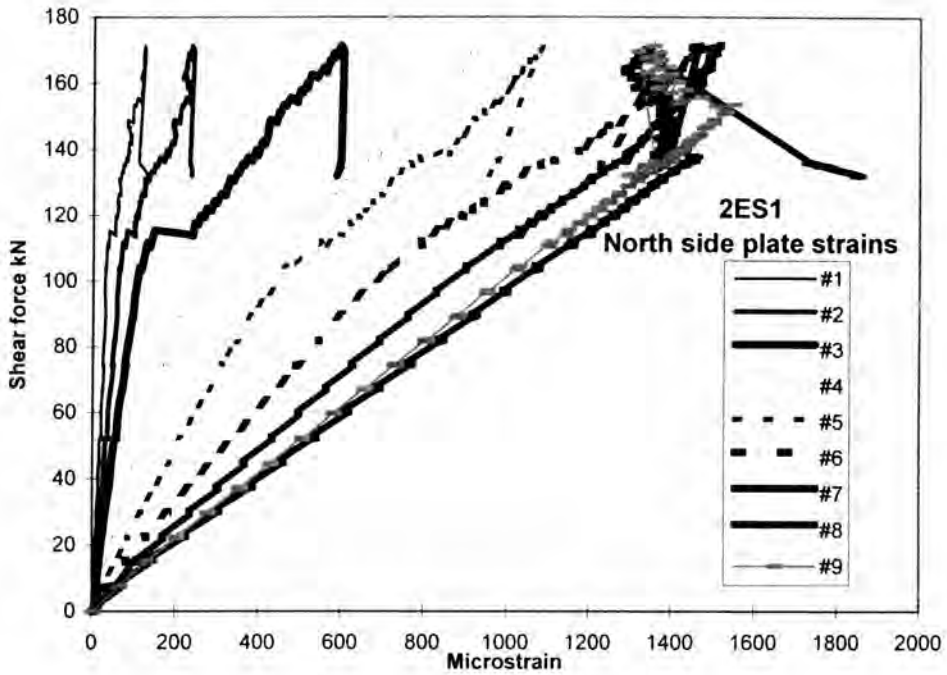

(a)

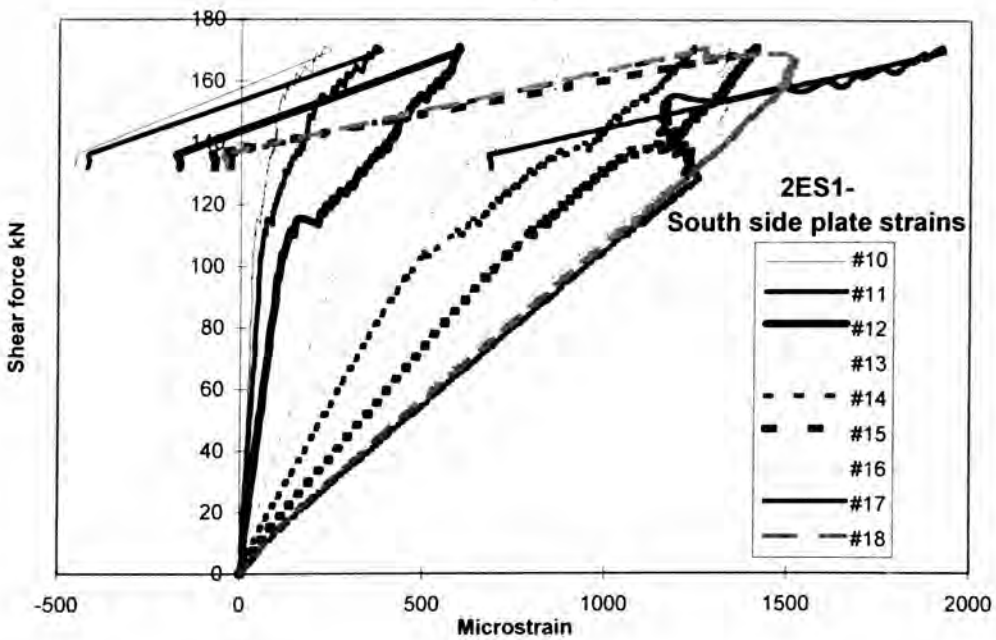

(b)

Fig.17.19. Test 2ES1: Longitudinal strains in side plates

The convergence of strain readings at the gauges close to the load point (i.e. #6, #7, #8 and #9 on the north side and at #13, #14, #15, and #16 on the south side) at V= 137.8 kN denotes the complete development of individual horizontal debonding cracks. Finally, the complete debonding of the south side plate is revealed by the

steep fall in both strain and shear force readings at all locations. However on the northern side locations, the drop in strain readings are comparatively small as this plate did not debond thoroughly at the termination of the test. The maximum strain recorded at the north side and south side plates were 1720 microstrains and 1925 microstrains, which compares well with the yield strain of the plate (1840 microstrains).

17.5.2.3 Deflection

Figure 17.20 shows the variation of deflection recorded at the load point of Test-2ES1 where the bending moment was maximum with the shear force in the shear span tested.. It also shows the occurrence of debonding at V=171.4 kN by the sudden drop in the load. The maximum deflection recorded was 20.6 mm.

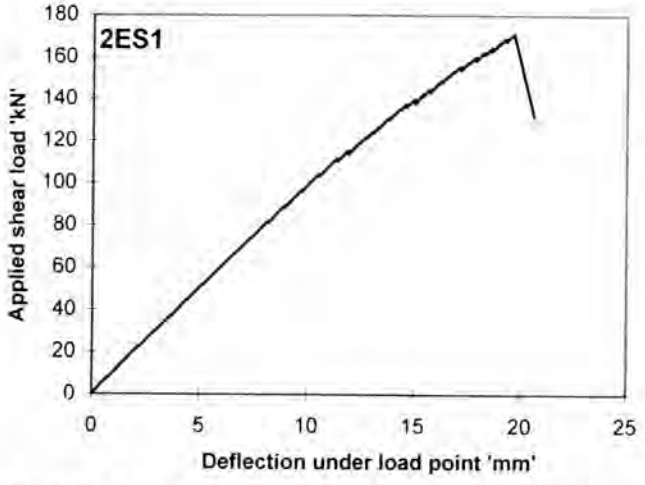

Fig.17.20. Test-2ES1: Deflection Vs Shear force in the span tested

17.5.3 Test-2ES2

Test-2ES2 is the same as test-2ES1 and it was conducted on the another span of the beam-2E, as shown in Fig.17.4.

17.5.3.1 Crack propagation and failure mode

Two inclined cracks could be seen above the side plate in Fig.17.21a, one at 250 mm and another at 400 mm from the load point when the applied load was 130 kN

(V=96.9 kN). A third inclined crack appeared in between these two cracks and also a debonding crack originated from the second crack along the top edge of the side plate when the applied load was 158 kN (V=117.7 kN), as shown in Fig.17.21b. As the load was increased to 161 kN (V=119.9 kN), horizontal debonding cracks originated from all the diagonal cracks and they set to extend backwards along the top edge of the side plate; the diagonal crack also extended upwards, as shown Fig.17.21c. This process stabilised when the applied load was 182 kN and no major crack growth were observed for the next 30 kN.

As the applied load was increased to 215 kN (V=160.2 kN), the south side plate debonded completely by the formation of long, horizontal crack along the plate top and new diagonal cracks, as shown in Fig.17.21d. The debonding crack close to the support on the northern side plate also extended to the support. At this stage, the load dropped to 180 kN (V=134.1 kN). On reapplication of the load to a value of 187 kN (V=139.3 kN), the north plate also debonded completely due to the formation of a long debonding crack and new inclined cracks, as depicted in Fig.17.21e. Finally, the load dropped to 134.3 kN (V=100 kN) at which the load test was terminated.

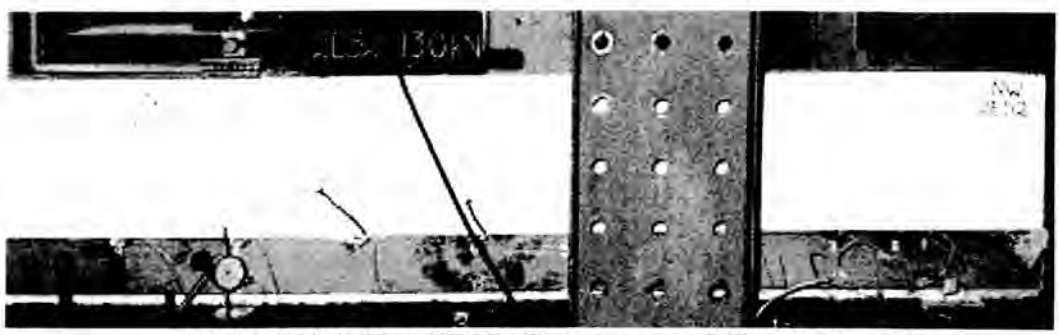

Fig.17.21(a). Test-2ES2: Occurrence of diagonal cracks

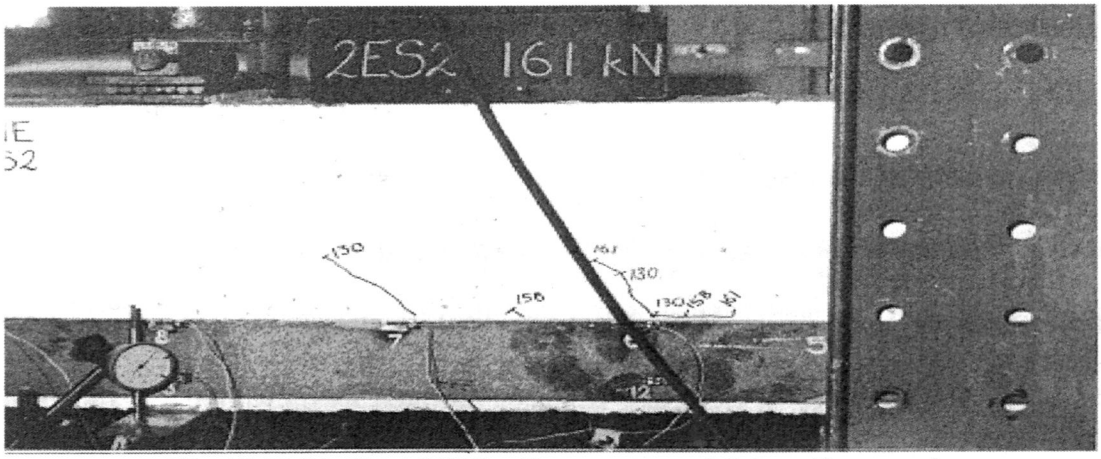

Fig.17.21(b). Test-2ES2: Occurrence of debonding crack

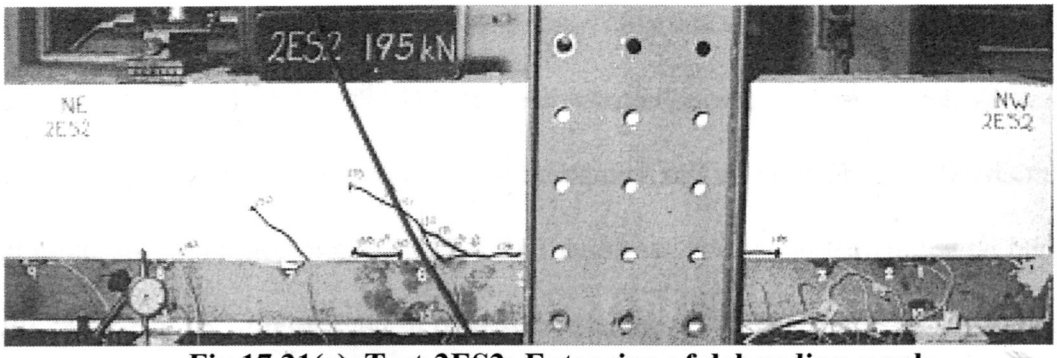

Fig.17.21(c). Test-2ES2: Extension of debonding crack

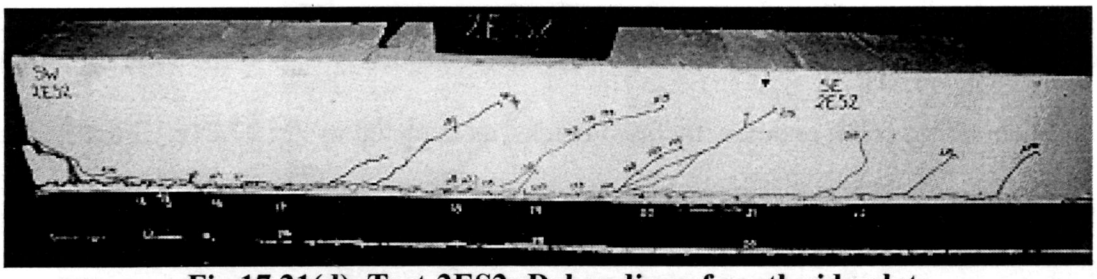

Fig.17.21(d). Test-2ES2: Debonding of south side plate

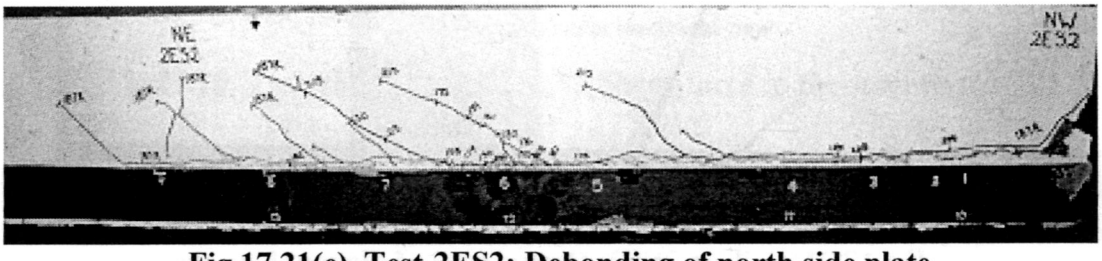

Fig.17.21(e). Test-2ES2: Debonding of north side plate

17.5.3.2 Longitudinal strains in side plates

Figures 17.22a-d illustrate the variation of strains recorded in all the sites (refer Fig.17.10c) with the shear force in the shear span tested. Initially, the strains increased as the applied load was increased but once the diagonal cracks started forming at a particular load, the gauges surrounding a particular crack show the

convergence of strains. The debonding of south side plate at a shear force of 160.2 kN is marked by the convergence and subsequent drop of all the location both on the top and bottom fibres of side plate as can be seen from Figs.17.22c and 17.22d. At this stage, the charts for strains on the north side (Figs.17.22a and 17.22b) show the drop in load. The subsequent debonding of north side plate is shown by steep drop both in load and strain readings at an applied shear load of 139.3 kN (reapplied) in Figs.17.22a and 17.22b. The peak strain magnitudes recorded on the north side plate were 1113 and 1270 microstrains on the top and bottom positions of the north side plate; the corresponding magnitudes for the south side plate were 1068 and 1319 microstrains. This suggests the plate did not yield as the yield strain for the plate is 1840 microstrains.

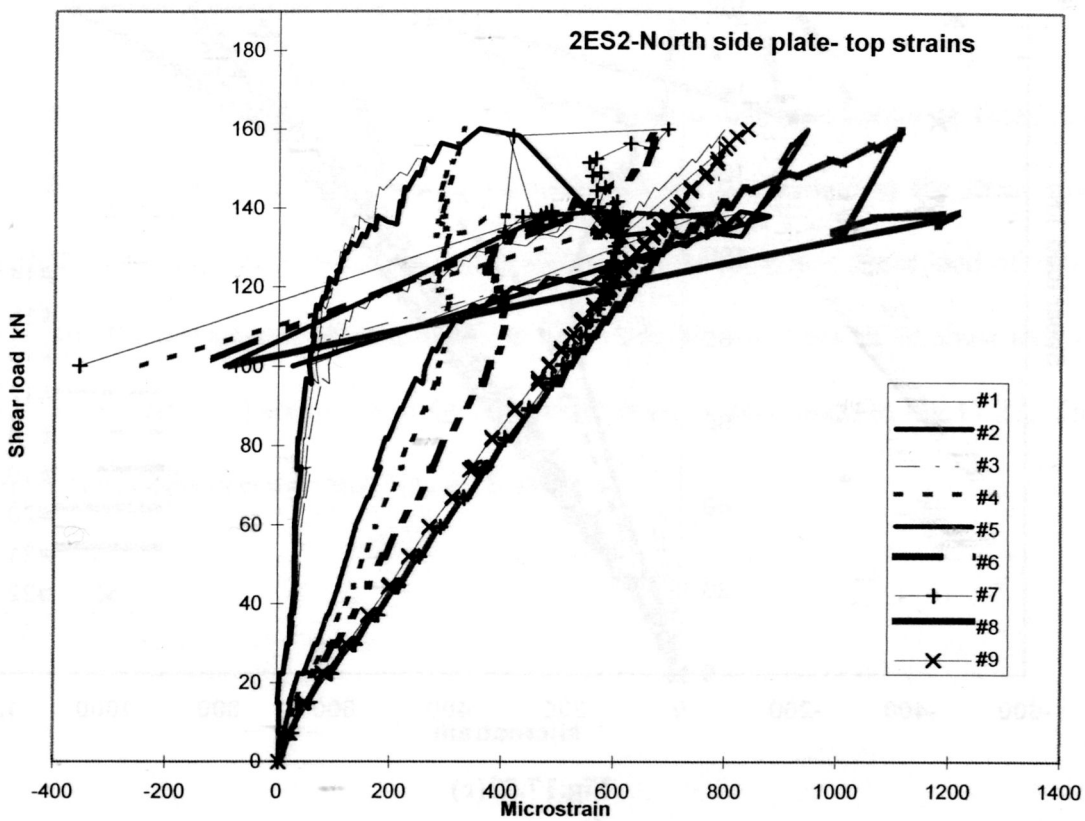

Fig.17.22(a)

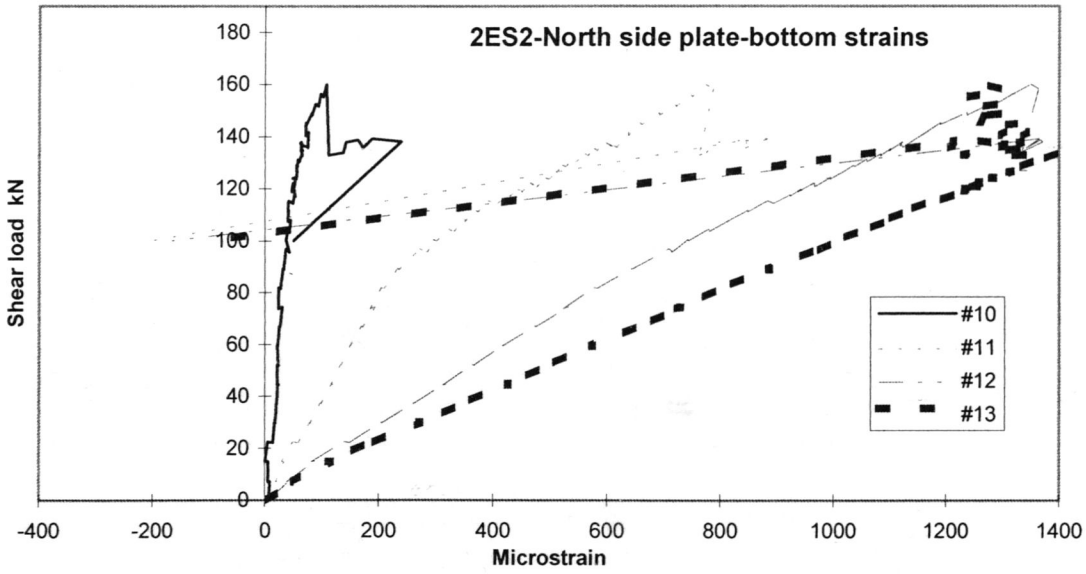

Fig.17.22(b)

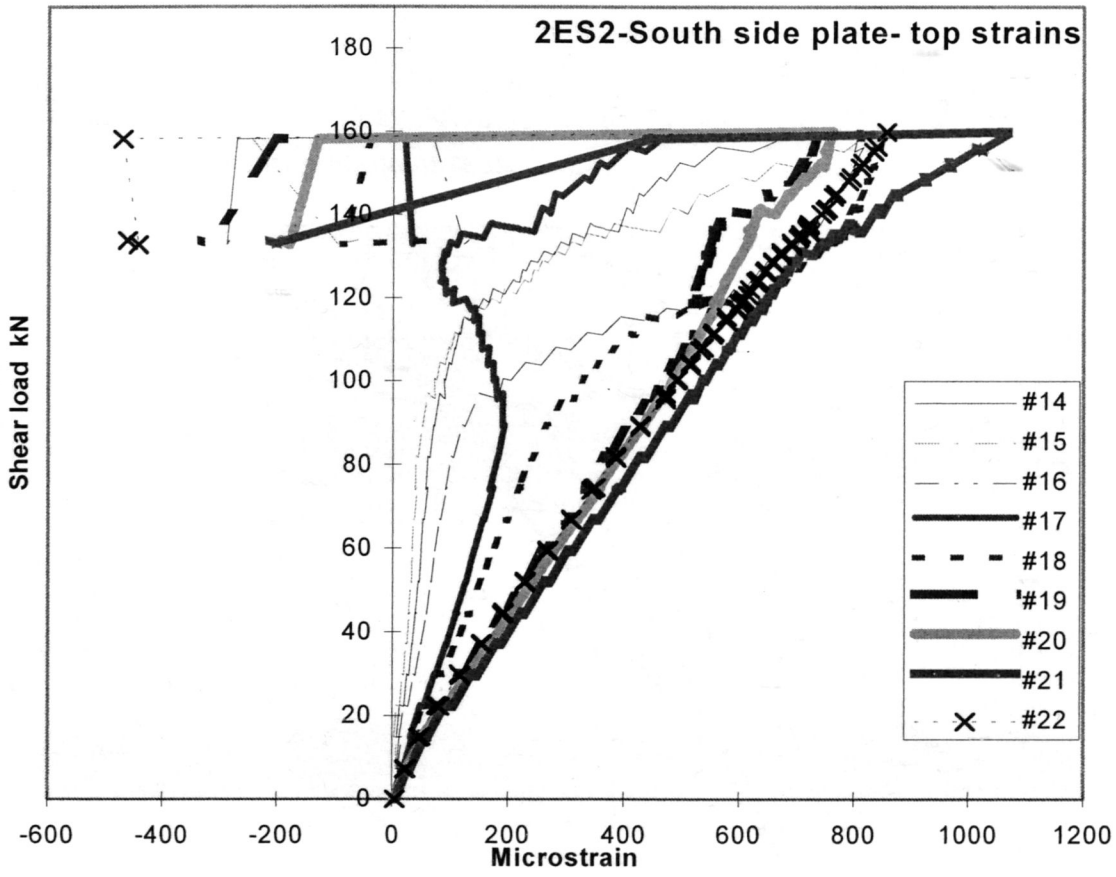

Fig.17.22(c)

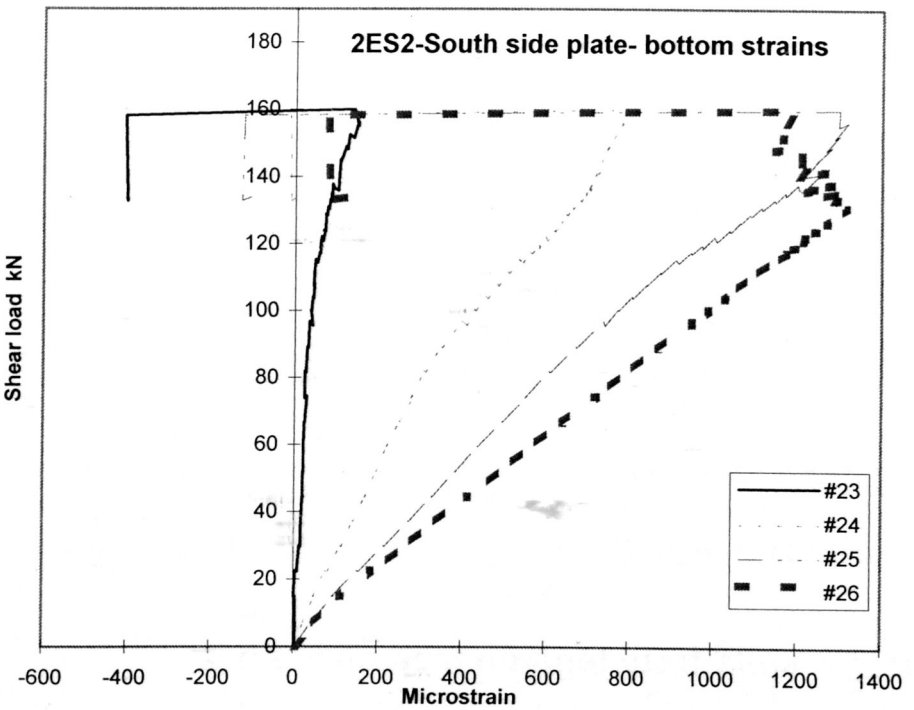

Fig.17.22(d)

Fig.17.22. Test-2ES2: Longitudinal strains in side plates

17.5.3 Deflection

Figure 17.23 shows the variation of deflection recorded at the load point of Test-2ES2 (where the bending moment was maximum) with the shear force in the shear span tested. The occurrence of debonding of the south side plate at a shear load of *1*60.2 kN and the subsequent debonding of the north side plate at a reapplied shear load of 139.3 kN (reloaded) are indicated by the sudden drop in shear loads in Fig.17.23. The maximum deflection recorded was 23.8 mm.

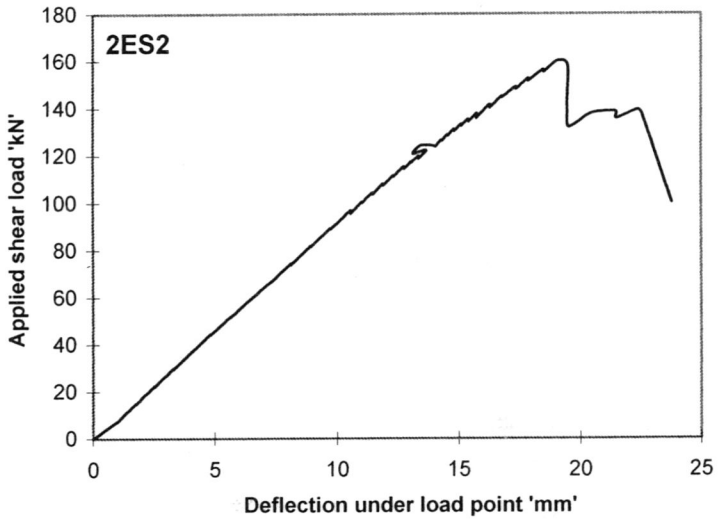

Fig.17.23. Test-2ES2: Deflection Vs Shear force in the span tested

17.6 Test results from tension face plated beam

17.6.1 Test-2F

Beam-2F was bonded with a 200 mm wide and 6 mm thick, fully anchored tension face plate, as shown in Fig.17.6 and it was tested to fail in flexure. The loading arrangement is same as Test-2E, which is shown in Fig.17.13.

17.6.1.1 Crack propagation and failure mode

The first flexural cracks occurred in the constant moment region and also below the load points and the region adjacent to the load points when the maximum moment was 47.5 kNm (P=50 kN). More flexural cracks appeared between the existing cracks as the moment was increased from 47.5 to 104.5 kNm (P=110 kN), as shown in Fig.17.24a. The existing flexural cracks grew vertically and no new cracks could be observed till the moment was 176 kNm (P=185 kN); at this stage a flexural shear crack appeared in the moment-shear region as shown in Figs. 17.24b and17.24c. Fig. 17.24b shows the crack pattern in the south-east shear span when the maximum moment was 235.6 kNm (P=248 kN). It can be seen that many diagonal cracks appeared in the shear span at regular intervals. Minor debonding cracks from the

roots of the flexural shear crack occurred in the range of 218.5 kNm to 235.6 kNm (P=230 kN to 248 kN).

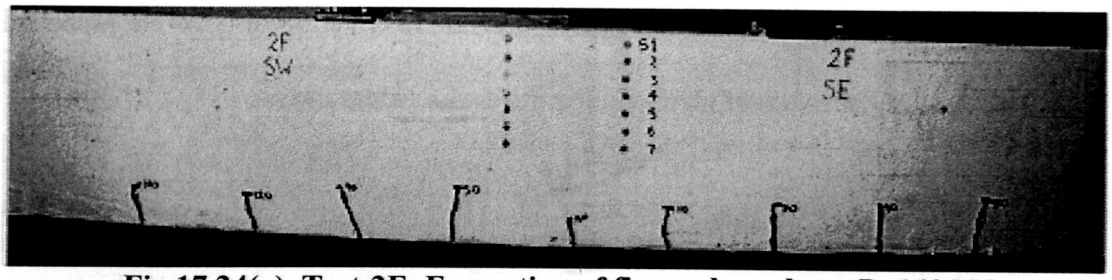

Fig.17.24(a). Test-2F: Formation of flexural cracks at P=140 kN

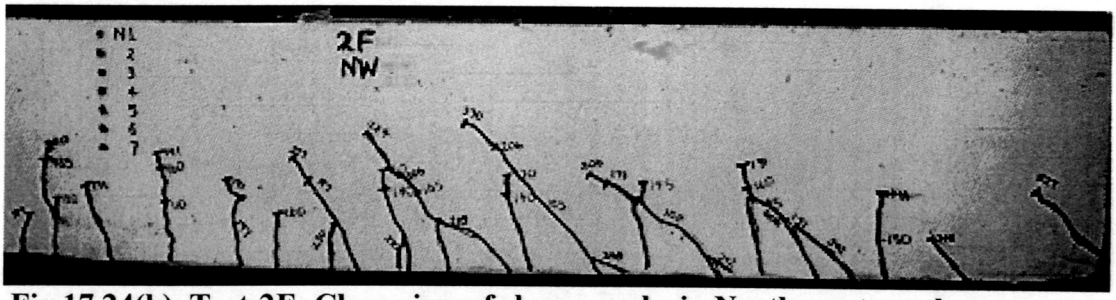

Fig.17.24(b). Test-2F: Close view of shear cracks in North-western shear span at P=248 kN

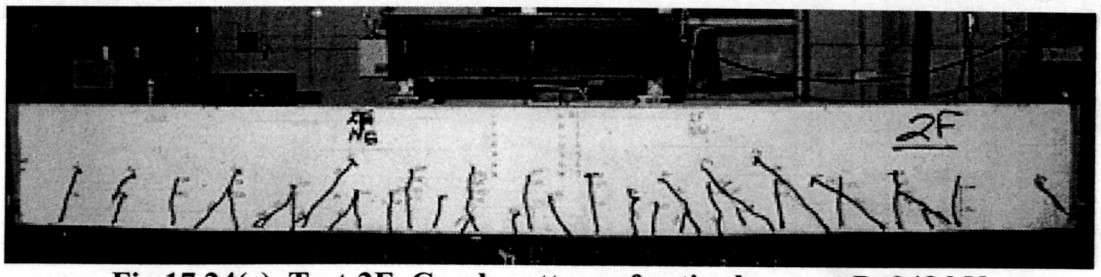

Fig.17.24(c). Test-2F: Crack pattern of entire beam at P=248 kN

When the moment was increased to 246 kNm (P=259 kN), a horizontal debonding crack appeared in between the two existing flexural cracks in the mid-span of the beam as shown in Fig. 17.25. As the maximum moment was increased to 249 kNm (P=262 kN), the horizontal debonding crack extended further towards the other flexural cracks in the constant moment region. At this stage, the beam was unable to maintain the applied load and it dropped to 260 kN as concrete crushing started in the extreme top fibres as shown in Figs. 17.26 and 17.27. The horizontal crack extended further and a fully fledged flexural hinge mechanism was formed as the load dropped further 230 kN (M=218.5 kNm) at which the load test was terminated. It can be seen

from Figs. 17.25-27 that the horizontal debonding crack did not extend beyond the middle two-third of the constant moment region. Furthermore, the peeling process was local and stable and the ultimate failure was due to crushing of concrete preceded by the yielding of the external plate and the internal reinforcement.

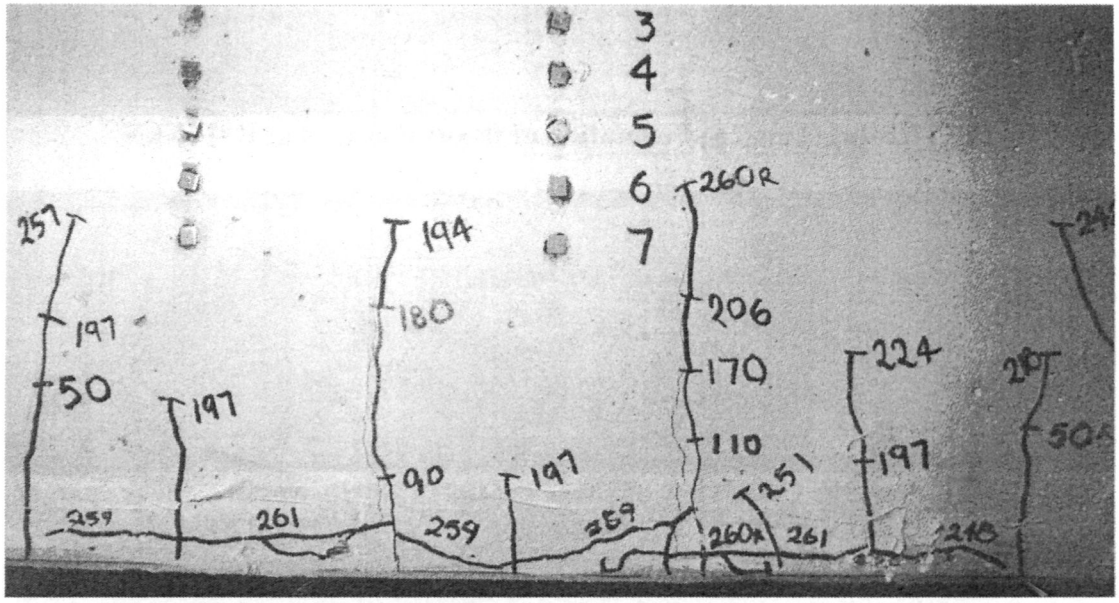

Fig.17.25. Test-2F: Debonding crack in the constant moment region

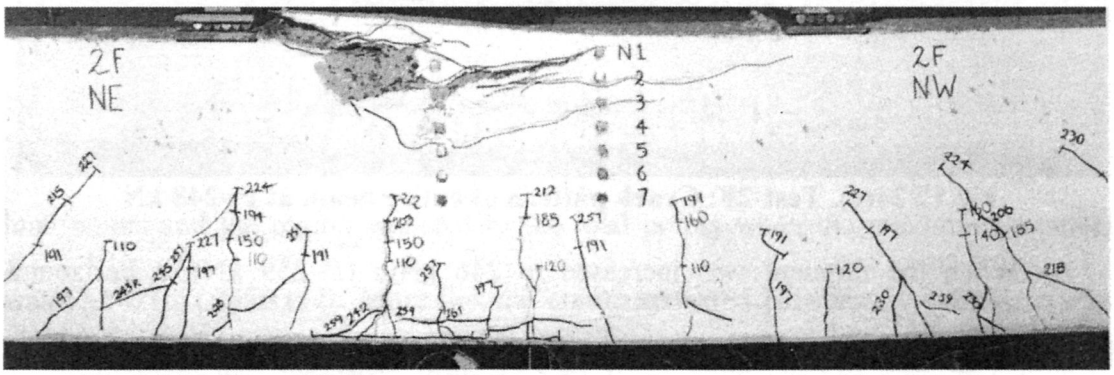

Fig.17.26. Test-2F: Flexural hinge formation on north side of the beam

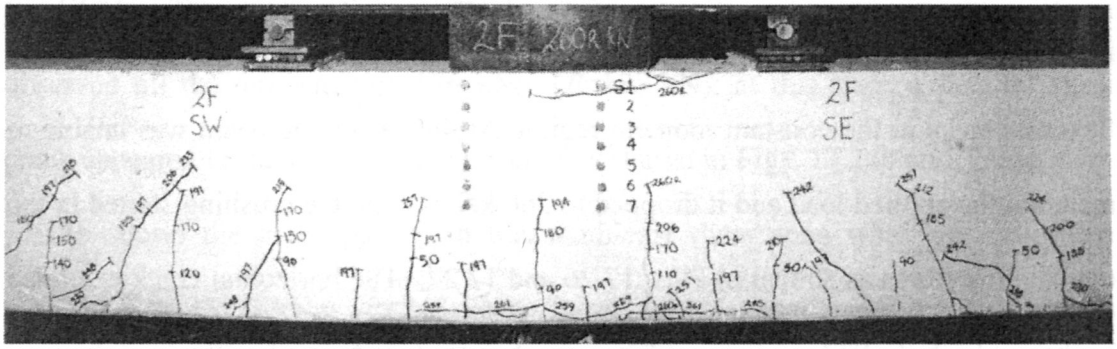

Fig.17.27. Test-2F: Flexural hinge formation on South side of the beam

17.6.1.2 Strains in the tension face plate

The variations in the strains in the plates are shown in Figs.17.28a-e; these charts should be read in conjunction with Fig.17.11a that shows the location of the strain gauges. The recorded strains are more than the yield strain of the plate material at all the locations of the gauges before local debonding occurred. Figs.17.28b-d are of interest as they show the strains recorded at the locations where the horizontal debonding crack occurred. It can be seen that the strains in the debonding locations tend to converge on debonding.

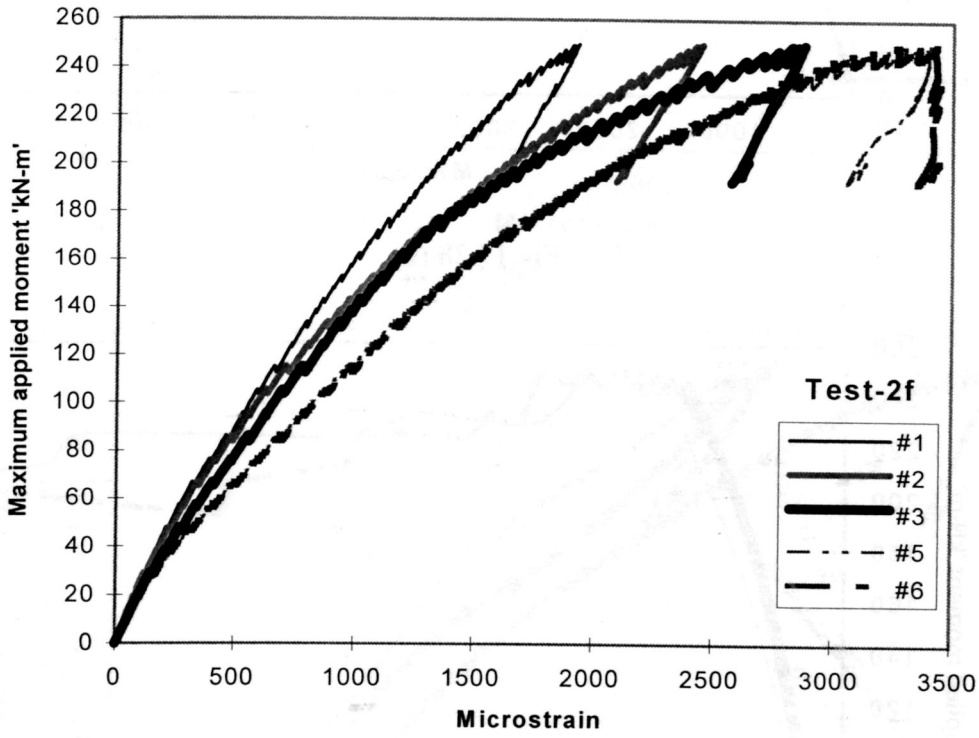

Fig.17.28(a)

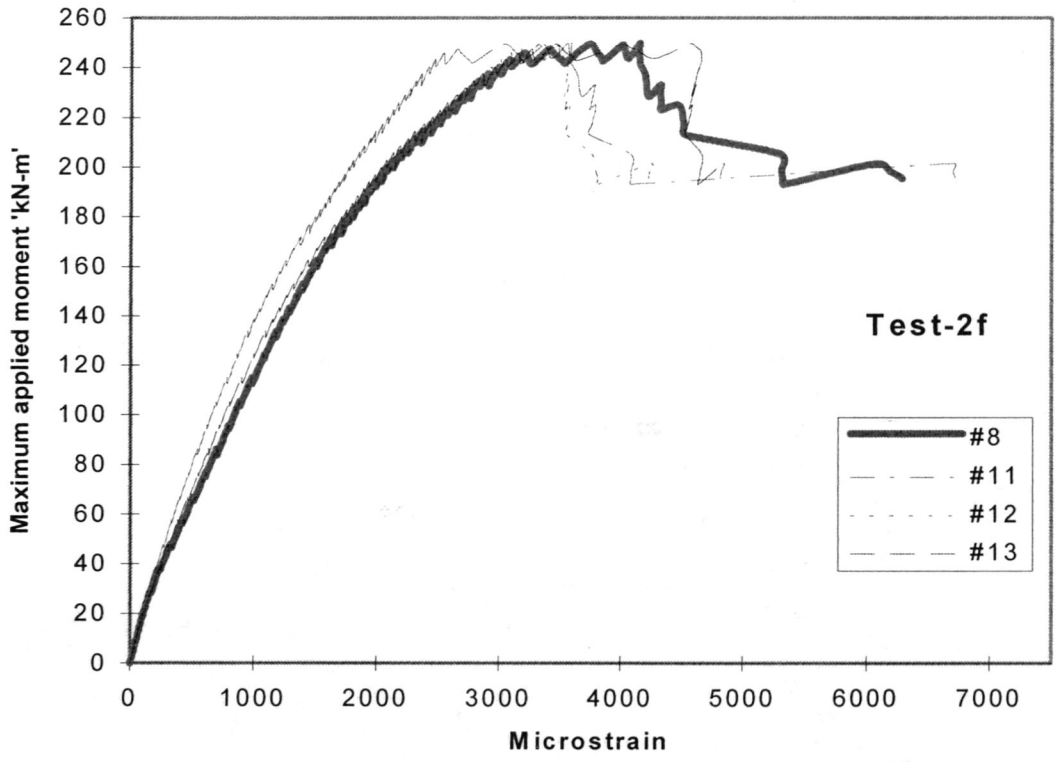

Fig.17.28 (b)

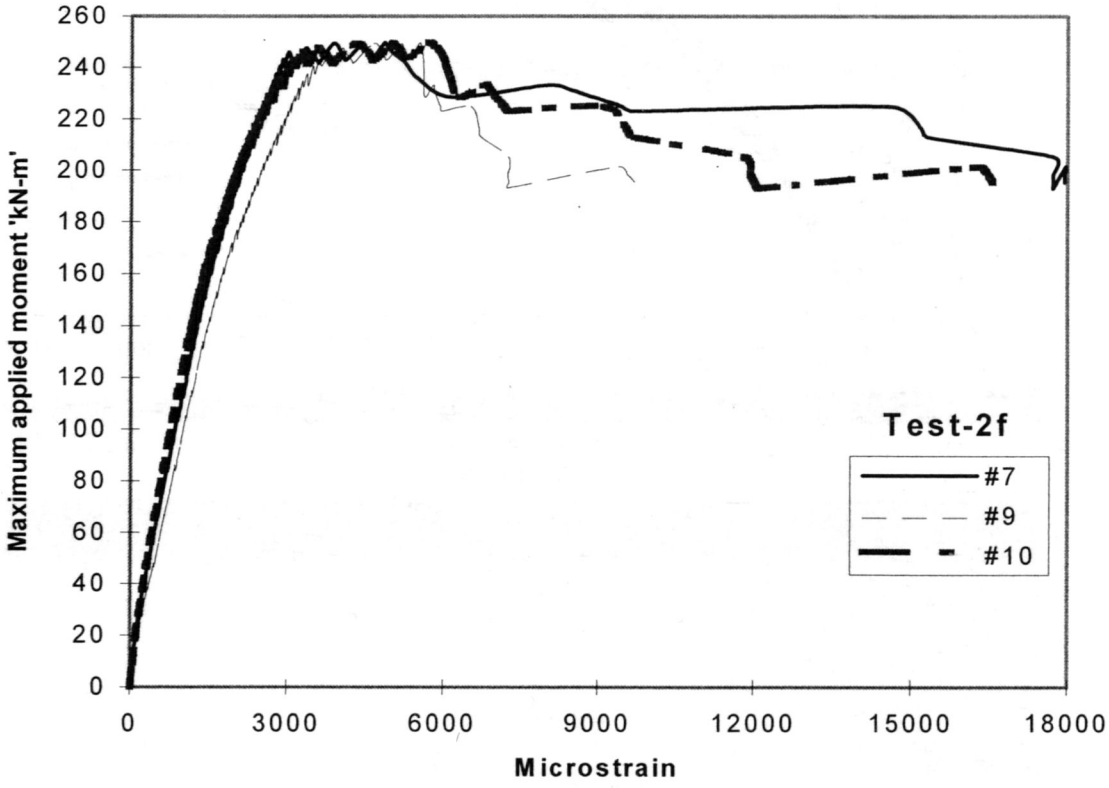

Fig.17.28 (c)

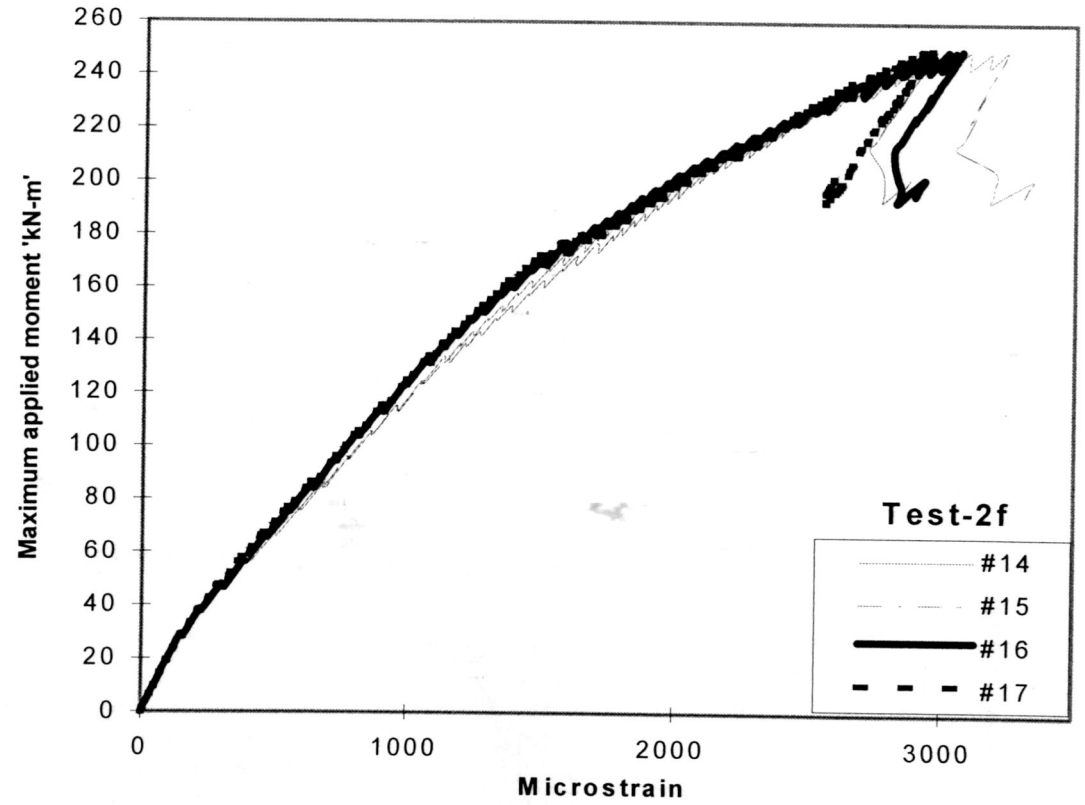

Fig.17.28(d)

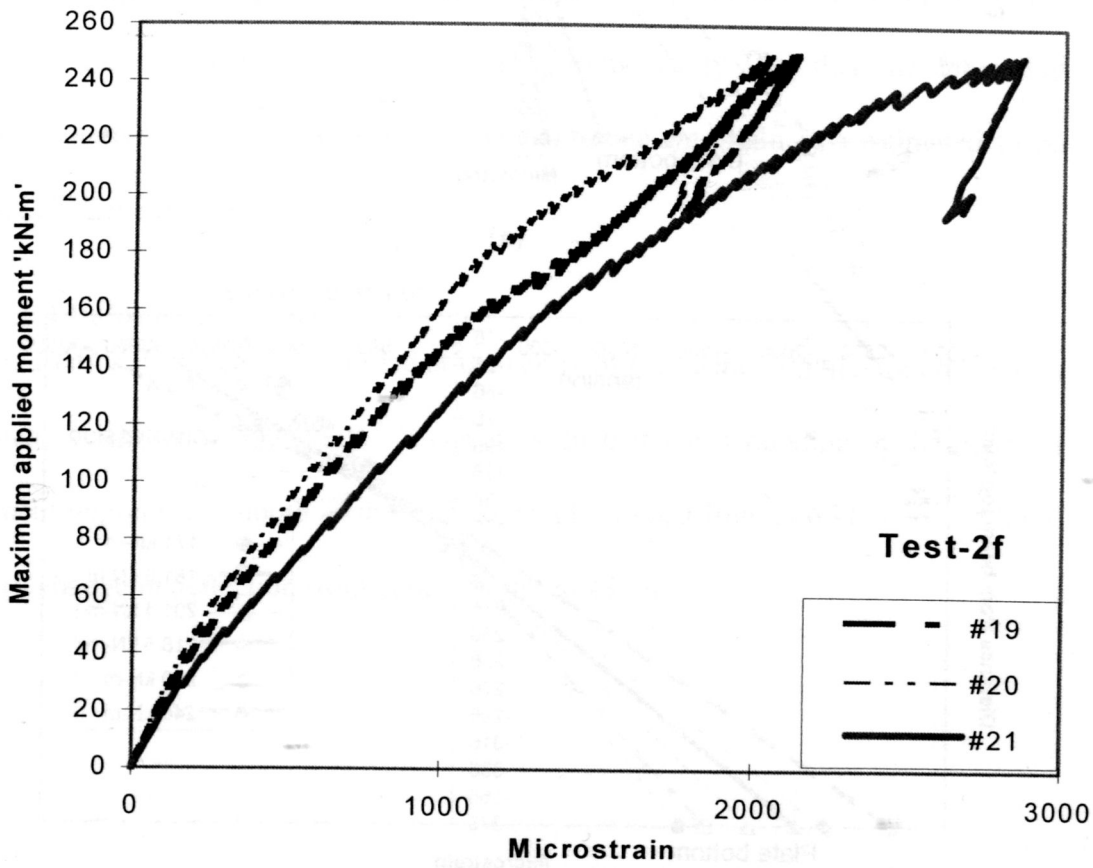

Fig.17.28 (e)

Fig.17.28 Test-2F: Strain variation in tension face plate

17.6.1.3 Strain profile across the depth of the beam

Figures 17.29a and 17.29b show plots of strain measurements made through the depth of the beam using demec gauges that were bonded to the concrete surface at the mid-span as shown in Fig.17.12b; the corresponding strains measured on the tension face plate by gauge strain gauge No.11 are also included. The mean value of strains obtained from both sides of the beam was used for plotting.

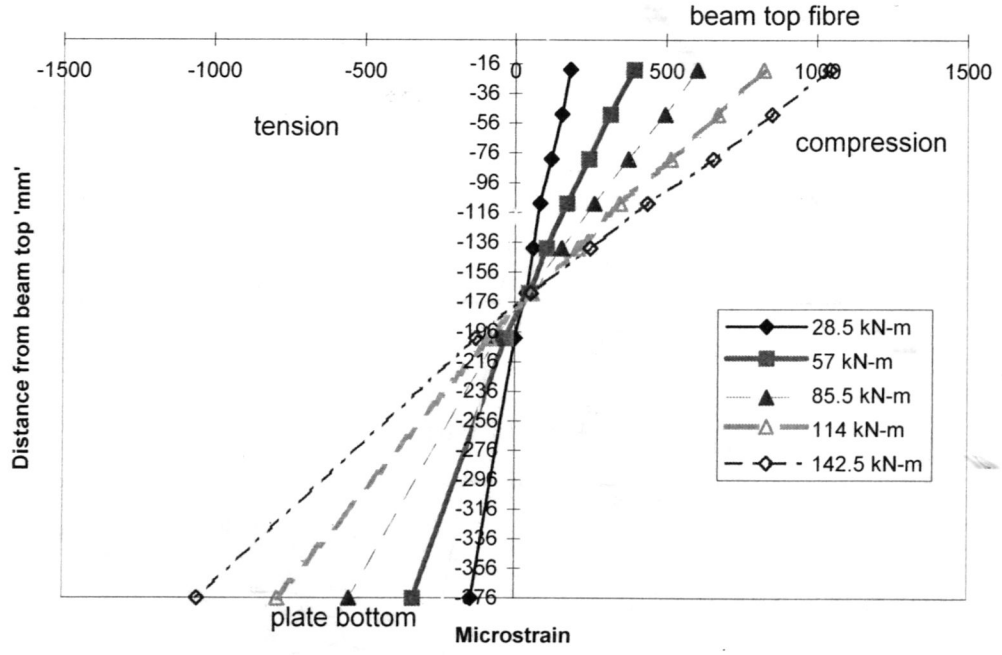

(a)

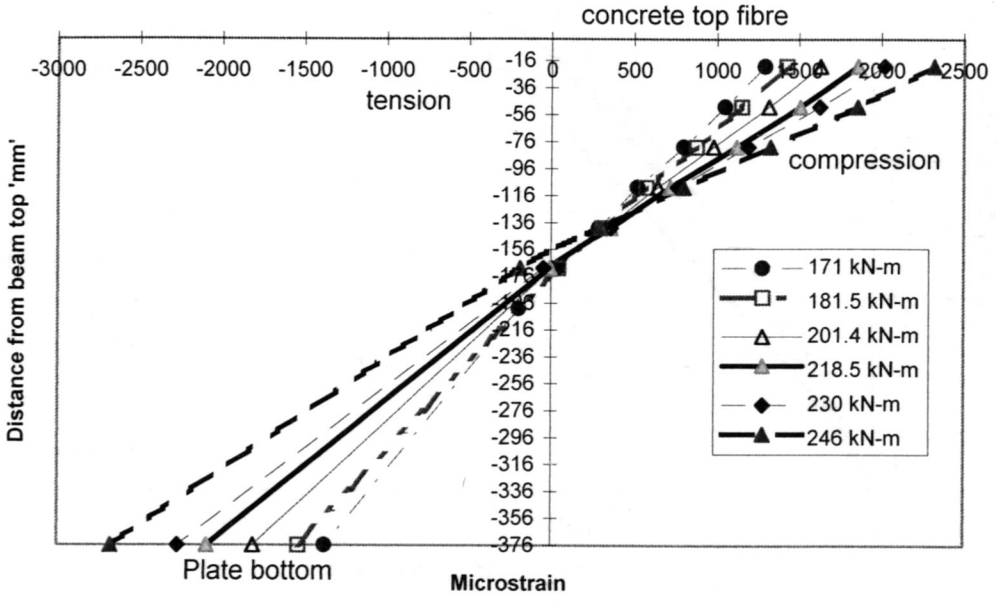

(b)

Fig.17.29. Test-2F:Strain profile across the depth of the beam

Figure 17.29a shows that the strain profiles were linear as there is no kink between the line connecting strain recorded by the lowermost demec gauge and the strain in the plate. The neutral axis position started moving up towards the concrete top as the neutral axis depth was about 200 mm when the moment at the centre was 28.5 kNm and it was about 180 mm as the moment was increased to 142.5 kNm.

Figure 17.29b shows as the concrete started to crush due to increased applied load, the lines connecting the concrete strains and plate strains show a kink. It also shows the neutral axis depth of the concrete strain profile reduced abruptly to 158 mm at 246 kNm at which the debonding crack occurred. By extrapolating the strain profile of the concrete alone, it was found that when the moment was 235.6 kNm, the strain at the internal tensile reinforcement was 2104 microstrain and at 241.3 kNm, it was 2334 microstrains. This shows that yielding of reinforcement (2250 microstrains) occurred between these two moment levels. Immediately after this, the debonding process started at 246 kNm at which the reinforcement strain was estimated to be about 2700 microstrains.

17.6.1.4 Deflection

The variation of deflection recorded at the centre of the beam with maximum bending moment is shown in Fig.17.30. It can be seen that the debonding in the constant moment region was smooth as the peak moment dropped from 246 kNm to 195 kNm with a change in deflection from about 35 mm to 48 mm.

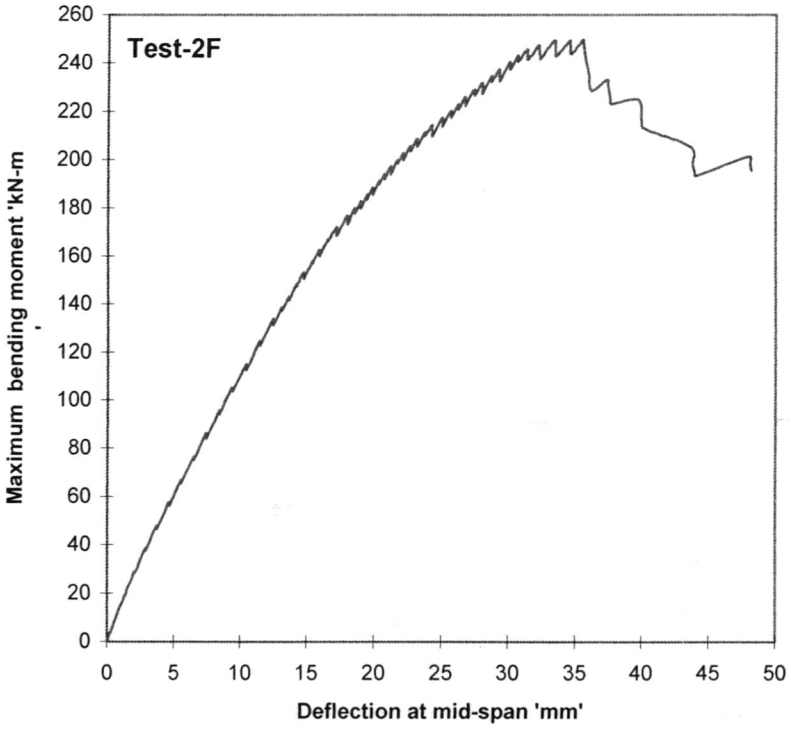

Fig.17.30. Test-2F: Maximum moment Vs deflection at centre

17.6.2 Test-2FS1

Test-2FS1 in Fig.17.7 was conducted on the same beam on which test-2F was conducted after repairing the portion of the concrete that was damaged, as shown in Fig.17.31. Positions of maximum moment and maximum shear force are coincidental for this case as shown in Fig.17.32. This is unlike test-2F where debonding under the constant moment region was studied.

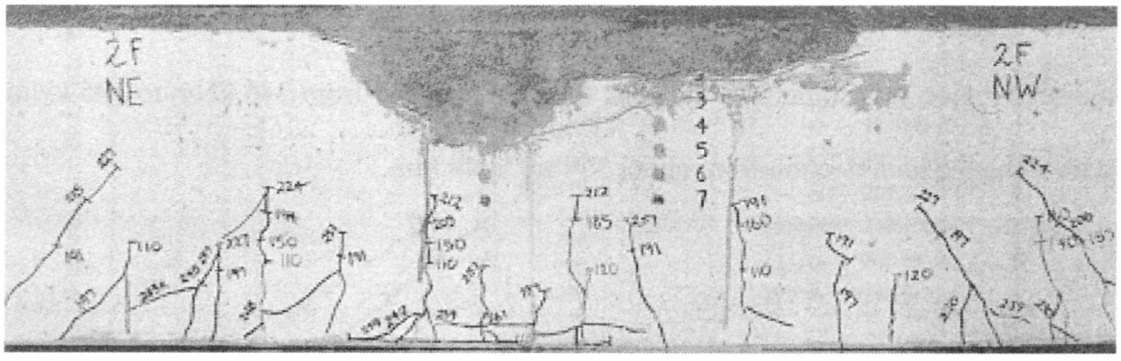

Fig.17.31. Beam-2F after carrying out repair for damaged concrete

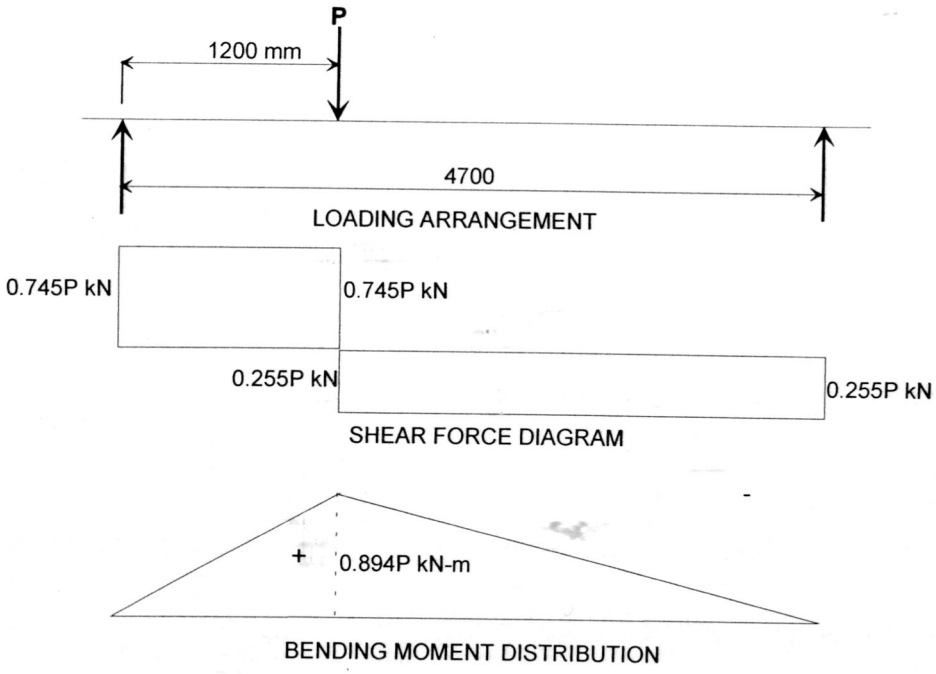

Fig.17.32. Loading arrangement for Test-2FS1

17.6.2.1 Crack propagation and failure mode

When the maximum moment in the shear span tested was 62.5 kNm (the applied load P= 70 kN and the shear force in the shear span V=52.1 kN), the existing inclined cracks from Test-2F opened up slightly. These cracks did not propagate further till the applied load was increased substantially to about 200 kN as shown in Fig.17.33. When the maximum moment was 89.4 kNm (P=100 kN, V=74.5 kN), a flexural crack occurred below the load point. As the moment was increased to 116.1 kNm (P=130 kN, V=96.8 kN), an inclined crack appeared at mid-way between the SE-SW shear span as shown in Fig. 17.33. At an applied moment of 147.4 kNm (P=165 kN, V=122.8 kN), another inclined crack appeared next to the 165 kN crack.

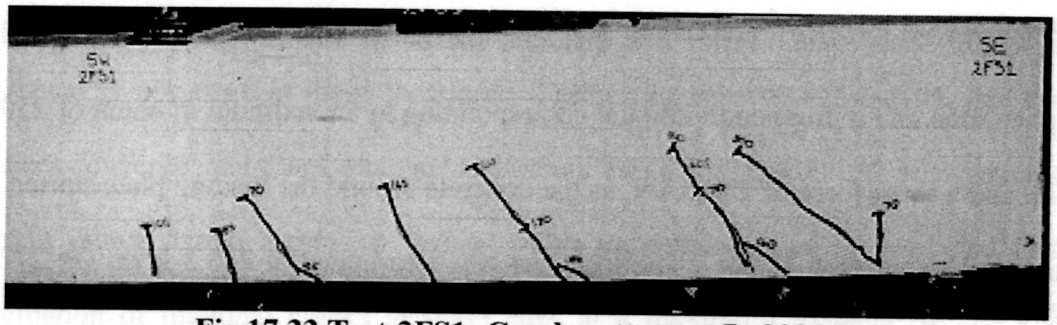

Fig.17.33.Test-2FS1: Crack pattern at P=200 kN

When the moment was 165.3 kNm (P=185 kN, V=137.7 kN), a flexural shear crack formed adjacent to the load point. When the moment was 178.7 kNm (P=200 kN, V=148.9 kN), an inclined crack extending to the mid-depth of the beam formed adjacent to the support and two other existing nearby inclined cracks also propagated further. As the load was increased, all the existing cracks grew in size and at 216.25 kNm (P=242 kN, V=180.2 kN), a horizontal debonding crack of about 4 cm length occurred from the root of the third inclined crack from the support as shown in Fig.17.34. Similar horizontal cracks also formed from the roots of all other cracks in the shear span at a moment of 232.3 kNm (P=260 kN, V=193.6 kN).

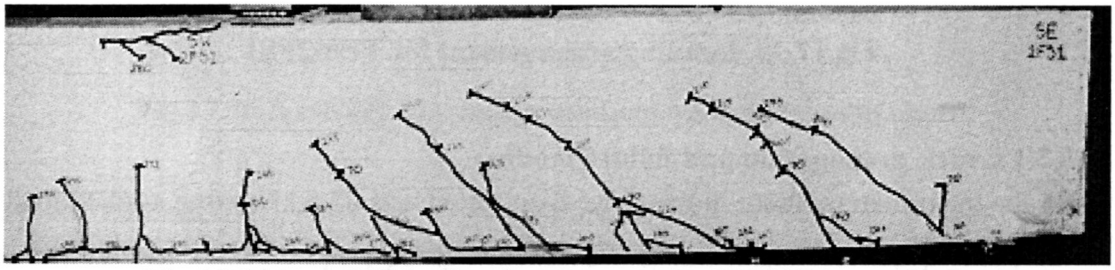

Fig.17.34.Test-2FS1: Crack pattern at P=280 kN (reapplied)

A new vertical crack formed adjacent to the load point in the longer shear span of the south side of the beam as shown in Fig.17.35, when the maximum moment was 243 kNm (P=272 kN, V=202.5 kN). When the moment was 259.1 kNm (P=290 kN, V=216 kN), two more new cracks formed in the longer shear span. Thereafter, all the flexural shear cracks in the vicinity of the load points were joined together at their roots by the formation of long horizontal debonding cracks simultaneously as shown in Fig. 17.35. It may be noted that this crack did not propagate beyond one-third of the shorter shear span. After this incident, the beam was not able to sustain the applied load and it dropped to 280 kN corresponding to a maximum moment of 250.2 kNm and a shear force of 208.5 kN, as the concrete around the loading plate started to crush as shown inFig.17.36. The load test was terminated at 243.5 kNm (P=272.5

kN, V=202.9 kN) to avoid further damage to the beam so as to be able to perform another test on it.

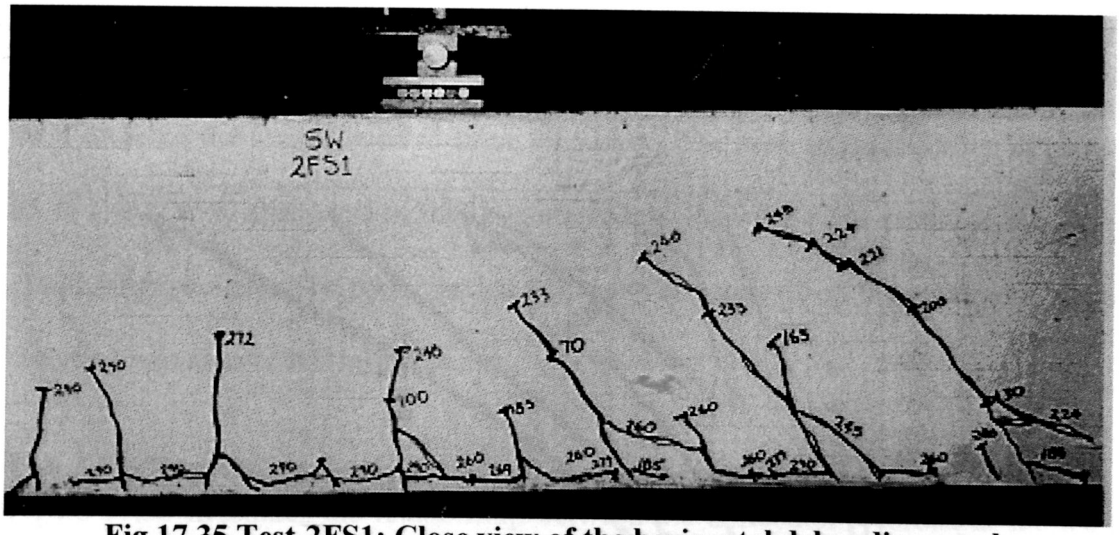

Fig.17.35.Test-2FS1: Close view of the horizontal debonding crack

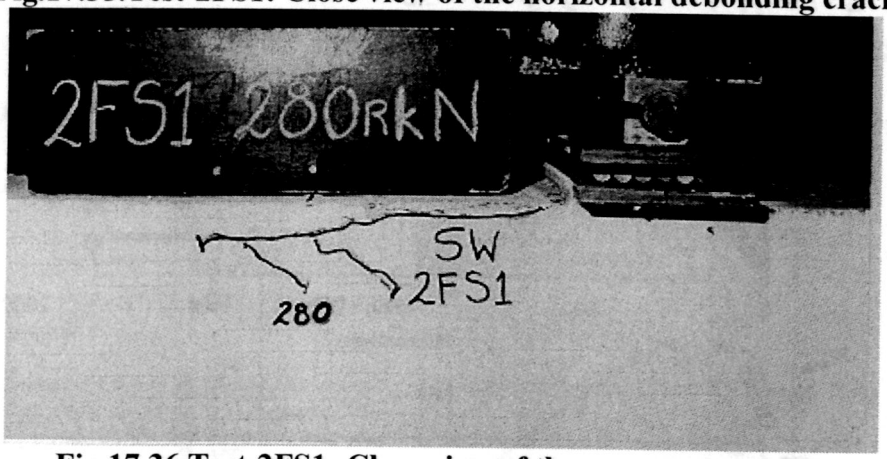

Fig.17.36.Test-2FS1: Close view of the concrete crushing

17.6.2.2 Strains in the tension face plate

Figures 17.37a and 17.37b show the variation of strain at all gauge locations that were shown in Fig.17.11b with the applied moment. It can be seen form Fig. 17.37a that at the plate sites at #1, #2, #3, and #4 that were bonded close to the supports, the peak strain before concrete crushing is less than the yield strain of the plate material as the moment is not large at these locations. Further, at sites #1,#2, and #3, the strain values converge, and there is a plateau at about 180 kNm (P=200 kN) after which the strain values started increasing further. This phenomenon can be attributed to the formation of diagonal cracks at these sites at a maximum moment of 180 kNm.

Furthermore, the strain readings at #4 between 200 kNm and 220 kNm show a reduction in magnitude and it intersects #3 at a maximum moment of 230 kNm. This is due to the rapid propagation of inclined crack above gauge #4 and the formation of minor debonding crack from the root of these cracks at this stage.

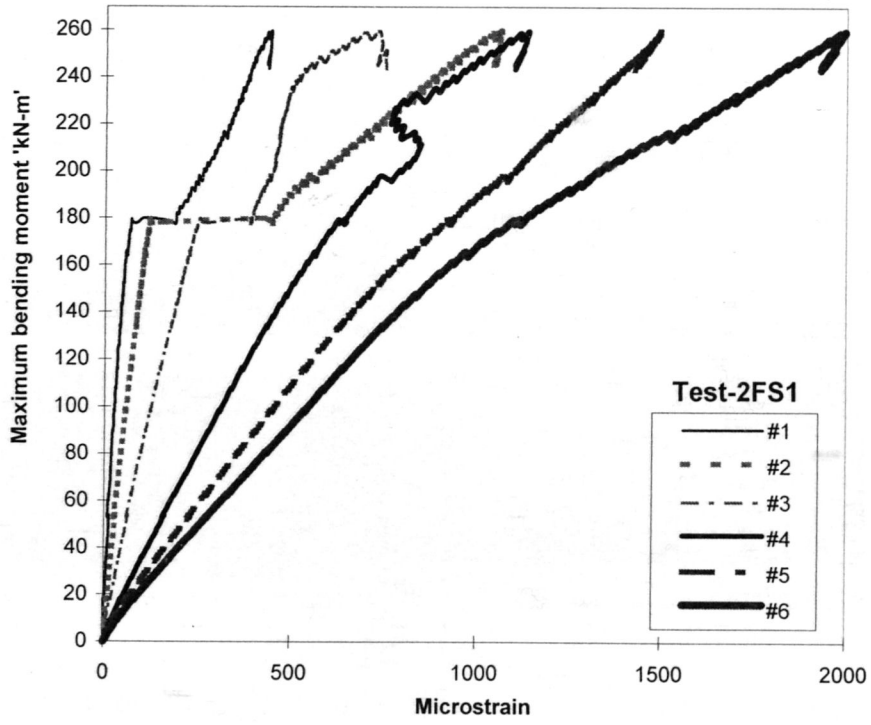

(a)

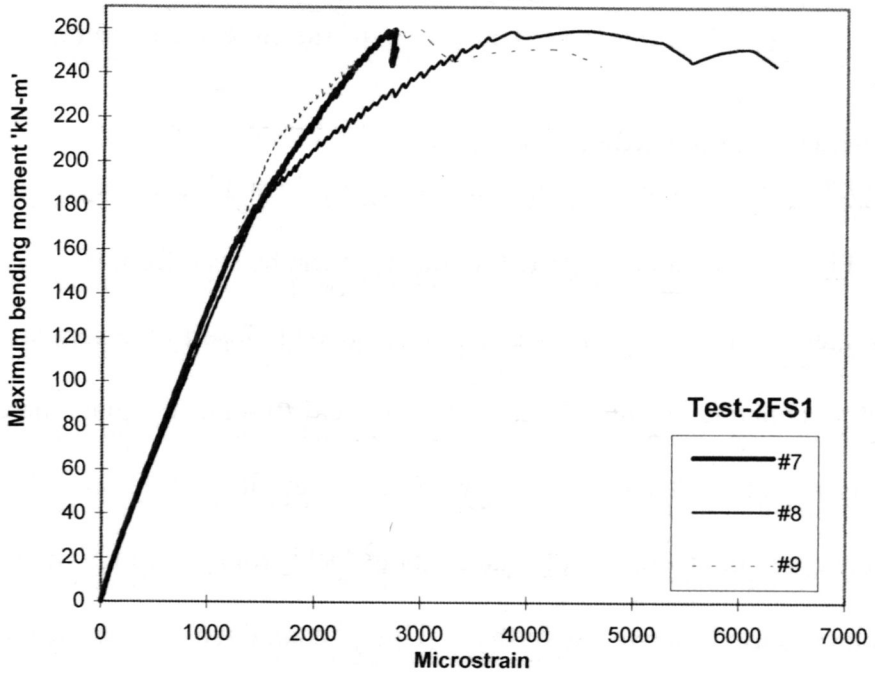

(b)

Fig.17.37. Test-2FS1: Strain variation in tension face plate

Figure 17.37b shows that the strain values at the maximum moment at gauges #7, #8 and #9 that were bonded at high moment and high shear regions were well above the yield strain of the plate. They intersect each other before the load started to drop showing the loss of bond at these locations. The peak strain recorded at gauge #5 is about 1500 microstrains that is slightly less than the yield strain of the plate (1800 microstrains). The plate yielded at the site at gauge #6 as the maximum strain recorded was about 2000 microstrain.s

17.6.2.3Deflection

Figure 17.38 illustrates the relationship between the deflection recorded at the load point and the shear force in the shear span tested. The maximum recorded deflection was 24.9 mm and the falling branch of the curve could not be obtained for this test as the test was terminated immediately after a slight drop in load.

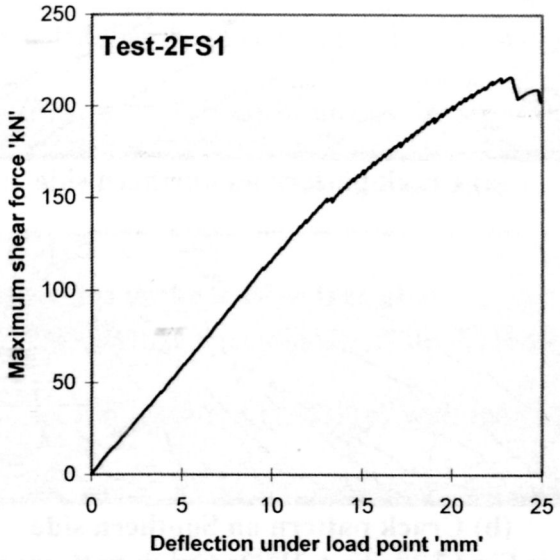

Fig.17.38. Test-2FS1: Shear force Vs deflection at load point

17.6.3 Test-2FS2

Test-2FS2 in Fig.17.9 was performed on the beam glued with a 6 mm thick steel plate to its tension face. The point load (P) was applied at a distance 900 mm from the support such that the shear force in the shear span tested was $0.8085P$.

17.6.3.1 Crack propagation and failure mode

Figures 17.39a and 17.39b show the complete crack pattern until failure of this span on both sides of the beam. It can be seen that two diagonal cracks formed at a distance of 200 mm and 650 mm from support, when the applied load (P) was 180 kN (V=145.5 kN). Another diagonal crack formed from the inside edge of the support plate when the applied load was 200 kN (V=161.7 kN) and a flexural shear crack formed beneath the load point at P=215 kN (V=173.8 kN). The two diagonal cracks adjacent to the support also extended upwards considerably and when the applied load was 225 kN, the tip of the second crack was just 70 mm below the top of the beam. One more shear crack formed at a distance of 500 mm from the support when the load was 240 kN (V=194 kN).

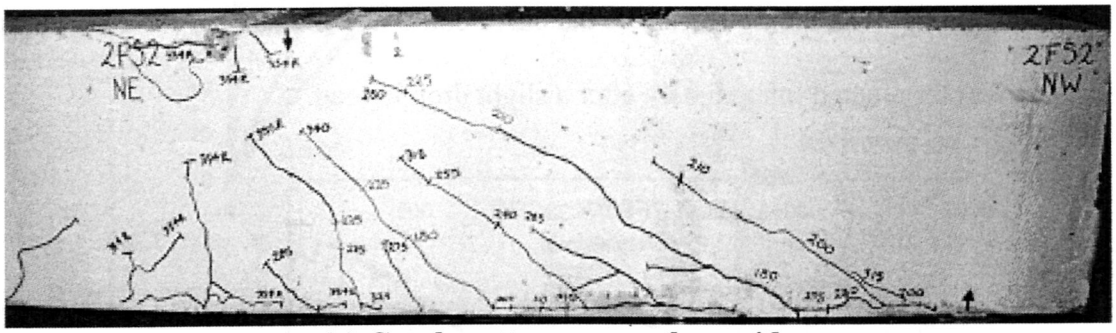

(a) Crack pattern on northern side

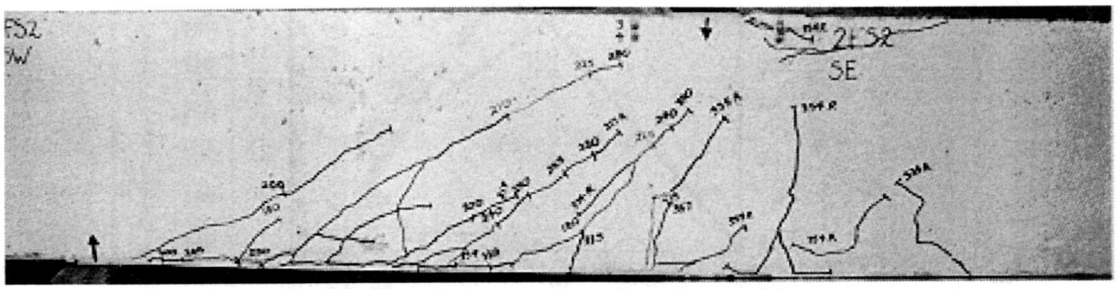

(b) Crack pattern on Southern side

Fig.17.39. Test-2FS2: Crack pattern

The second diagonal crack from the support extended horizontally backwards about 50 mm towards the support when the load was increased to 255 kN (V=206.2 kN), as shown in Fig.17.39a. This marked the gradual loss of bond between the concrete beam and steel plate. Similar horizontal debonding cracks originated from

the diagonal crack close to the load point at P=265 kN (V=214.2 kN). As the load was increased to 280 kN (V=226.4 kN), the debonding crack close to the support extended to the support plate, thus joining the two diagonal cracks close to the support. When the applied load was increased further, the second debonding crack started to move further and at 350 kN (V=283 kN) it joined with the first debonding crack to form a single crack of 500-600 mm length. Thus, all the four diagonal cracks close to the support were combined together at their base by the debonding crack and hence the bond between the concrete and plate interface was weakened considerably.

As the load was increased to 354 kN (V=286.2 kN), more flexural shear cracks formed on either side of the load point. Moreover, the top fibres of concrete adjacent to the load plate in the long shear span also started to crush. This caused the load to drop and the beam was unable to sustain further application of load, as concrete crushing became severe. The load also dropped to 330 kN (V=266.8 kN) and the test was ended. It may be noted that the tension face plate was not completely pulled off from the concrete cover as in side plated beams as the shear debonding crack could not progress beyond the support due to the onset of the concrete crushing.

17.6.3.2 Longitudinal strains in the tension face plate

Figures 17.40a and 17.40b illustrate the variation of strains recorded along the tension face plate at all gauge locations (refer Fig.17.11c) with the shear force in the shear span tested. Recall that gauge #1 is the closest to the support and gauge #10 corresponds to the load point, where the maximum shear and maximum moment occur. Gauges #11 and #12 were affixed in the longer shear span. The curves show linear trend till there was a change due to the formation of diagonal or debonding cracks. For example, the intersection of curves for gauges #1, #2, and #3 at V=162 kN denotes the formation of a diagonal shear crack encompassing these locations.

The convergence of curves #2, #3, #4 and #5 at V=226 kN marks the formation of a long horizontal debonding crack. The completion of shear debonding crack and the failure of the span is denoted by the intersection of the curve for every gauge with its neighbouring gauges at V=267 kN. The curves also show that the tension face plate yielded considerably in most of the gauge locations as the recorded peak strains were in the order of 4000 microstrains compared to the yield strain of the plate (1840 microstrains).

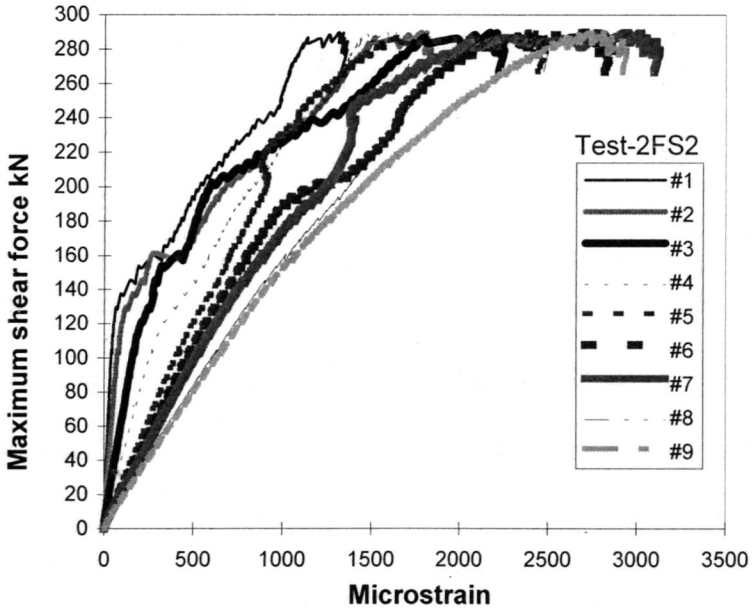

(a)

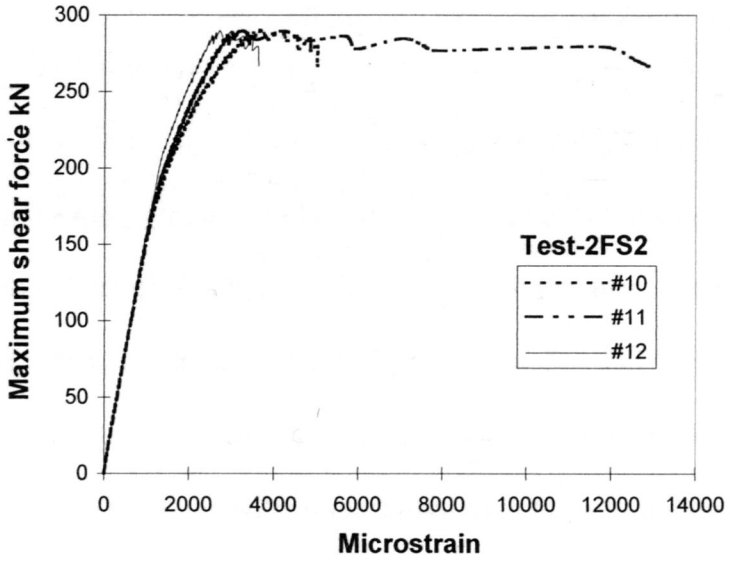

(b)

Fig.17.40. Test 2FS2: Longitudinal strains in the tension face plate

17.6.3.3 Deflection

Figure 17.41 shows the variation of deflection recorded at the load point of Test-2FS2 (where the maximum bending moment occurs) with the shear force in the shear span tested. It also shows the occurrence of debonding cracks by the plateau in the curve and the subsequent failure by crushing of concrete by the drop in shear force. The maximum deflection recorded was 25 mm.

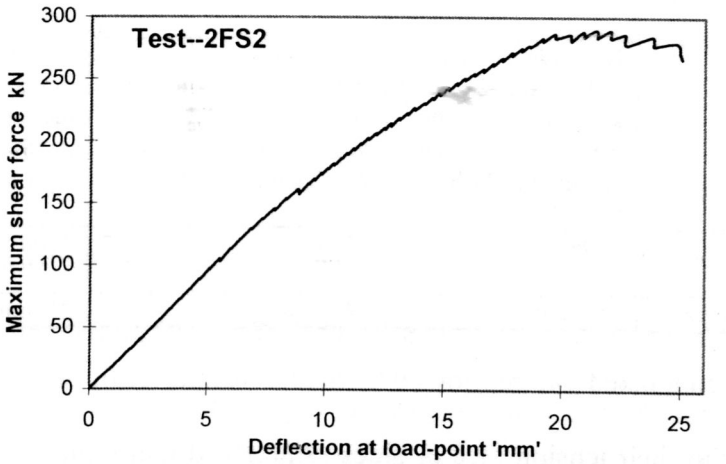

Fig.17.41. Test-2FS2: Deflection Vs Shear force in the span tested

17.7 Discussion of test results

Table-17.4 and Table-17.5 summarise the results obtained from all the tests.

TABLE-17.4: Test results-side plated beam

	Test-2E	Test-2ES1	Test-2ES2
shear span to depth ratio	5.14	3.24	3.24
Shear load and moment at first debonding crack	102.5 kN 204.3 kNm	115.4 kN 138.5 kNm	119.9 kN 143.88
Shear load and moment at full growth of all debonding crack	108.0 kN 205.2 kNm	140 kN 168 kNm	135.5 kN 162.6 kNm
Shear load and moment at complete peeling	After the formation of debonding cracks at 205.2 kNm (102.5 kN), the load started dropping and the concrete crushed at 203.4 kNm (107 kN) and the test was terminated at 155.8 kNm (82 kN) as the debonding crack stabilised and no further propagation occurred.	South side plate peeled at 171.3 kN (205.6 kNm)	South side plate peeled at 160.2 kN (192.2 kNm) and on reloading peeling of north side plate at 139.3 kN (167.2 kNm)
Maximum strain recorded (μstrain)	9594 (North) 21118(South)	1720 (North) 1925 (South)	1270 (North) 1319 (South)
Maximum deflection	31.5 mm	20.6 mm	23.8 mm

TABLE-17.5: Test results-tension face plated beam

	Test-2F	Test-2FS1	Test-2FS2
shear span to depth ratio	5.14	3.24	2.43
Shear load and moment at first debonding crack	129.5 kN 246.0 kNm	180.2 kN 216.3 kNm	206.2 kN 185.6 kNm
Shear load and moment at full growth of all debonding crack	131 kN 249.0 kNm	216 kN 259.1 kNm	283 kN (254.7 kNm) (all debonding crack joined together to form a single debonding crack)
Shear load and moment at failure	Debonding crack stabilised at 249 kNm and the failure was due to concrete crushing at 247 kNm(130 kN)	Debonding crack stabilised at 259.1 kNm and the failure was due to concrete crushing at 250.2 kNm (208.5 kN)	Complete peeling of plate did not occur as the concrete beneath load point crushed at 286.2 kN (257.6 kNm)
Maximum strain recorded (μstrain)	5699	6328	4000
Maximum deflection	48.0 mm	24.9 mm	25 mm

Tests conducted on reinforced concrete beams with fully anchored plates bonded either to their tension face or sides established that their behaviour is similar to that of normal reinforced concrete beams. In all the tests, the beams developed a large number of cracks before failure. Both plates and internal reinforcement yielded before failure that was caused by crushing of concrete, excepting tests 2ES1 and 2ES2 where the failure occurred by the peeling of the side plates

In the case of tests 2E and 2F, the debonding of plates was caused by horizontal debonding cracks that originated from the flexural cracks in the constant moment region and the debonding crack did not propagate beyond the constant moment region. Another noteworthy feature is that the tension face plated beam in test-2F carried a higher ultimate moment (249.5 kNm) than the side plated beam in test-2E (201.4 kNm), even though the area of cross section of the plate in both the cases was the same. This is due to the fact that the whole of the tension face plate is farther away from the neutral axis, thereby providing a higher lever arm and hence a higher moment capacity.

In the case of test-2FS1, the debonding area was under a high moment-high shear area. The plate length adjacent to load point yielded and the debonding was due to the horizontal debonding crack joining the roots of flexural shear cracks on either side of the load point. The failure was due to the crushing of concrete and the debonding of plate did not propagate all along the plate, although minor local debonding cracks originated from the inclined cracks near the support. In this test, the plated beam carried slightly higher moment (259.5 kNm) than in the case of Test-2F (249.5 kNm).

Figure 17.42 shows the experimental ultimate value of all the tests. It also includes the ultimate moment of the basic, non-plated beam (120 kNm) which was tested to fail under flexure by Ahamed (1996). It can be seen that the tension face plated beam was able to carry about 110 % more moment than the non-plated beam; the improvement in case of side plated beam was 70%.

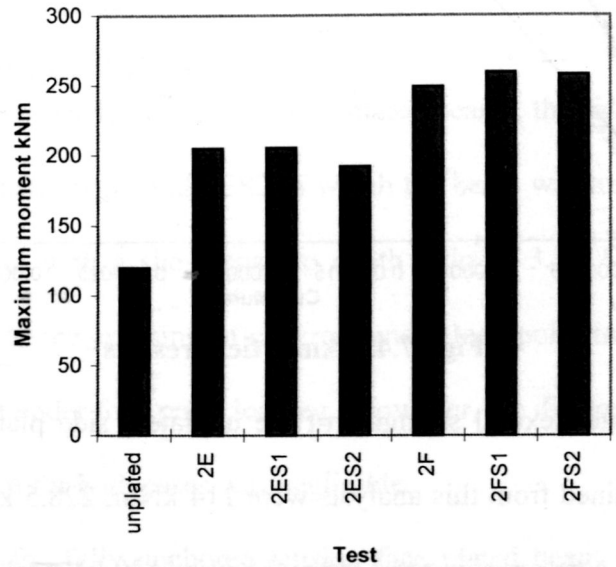

Fig.17.42. Comparing ultimate moments from tests

Tables 17.4 and 17.5 also indicate the maximum plate strains. It can be seen that for tests 2E and 2F, the magnitudes recorded in the constant bending moment region were several times larger than that of the yield strain of the plate material. In

case of tests 2ES1 and 2ES2 that were subject to a single concentrated load, the plates yielded just before failure.

17.8 Analysis of test results

17.8.1 Flexural strength

Figure 17.43 shows the complete moment-curvature relationships obtained from the numerical analysis as described in section 16.9.2. It compares the results of side plated and tension face plated beams with that the basic, unplated beam.

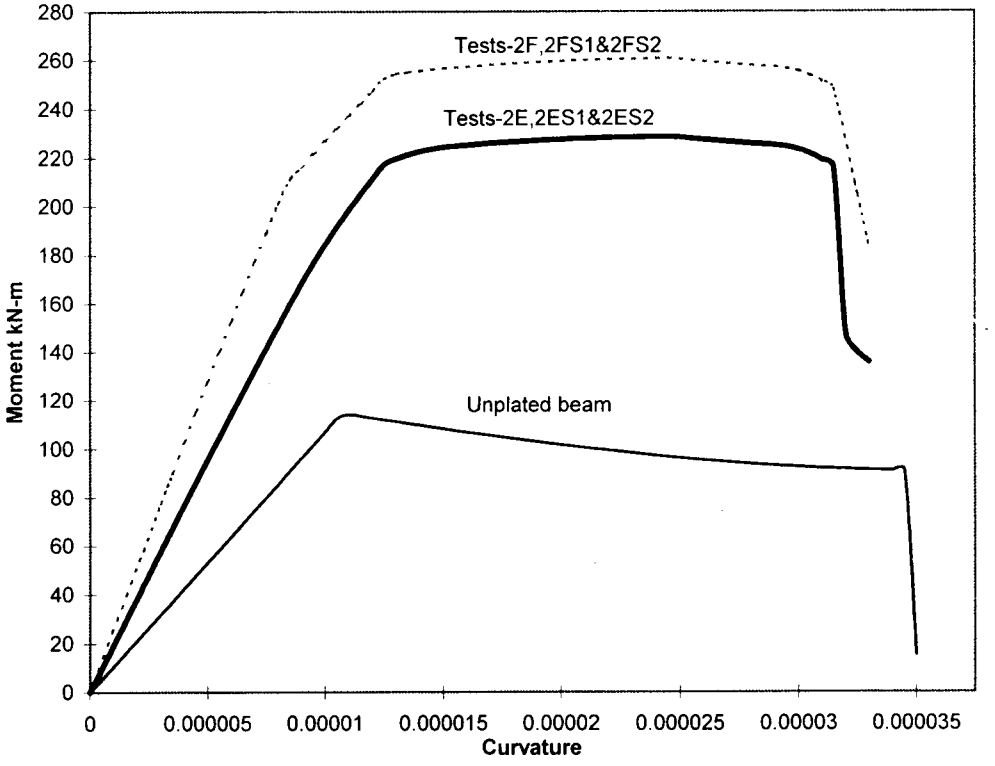

Fig.17.43. Analytical results

The ultimate flexural strengths of the unplated, side plated and tension face plated beams obtained from this analysis were 114 kNm, 228.5 kNm and 260.7 kNm respectively. The corresponding test strengths were 120 kNm, 205.6 kNm and 259.1 kNm. Therefore, it can be inferred that the numerical analysis could predict the strengths of the unplated and tension face plated beams and it overestimates the side plated beams strength by about 10%.

17.8.2 Shear peeling strength

The shear peeling strength of all the shear spans tested were determined by using the procedures outlined in Chapter-11. The theoretical shear peeling strength of the beams in the tests with the large shear span to depth ratio, i.e. tests 2E and 2F are 103 kN and 106 kN respectively. The corresponding maximum shear loads sustained by the beams were 108 kN and 131 kN. The theoretical shear peeling strength of the identical shear spans 2ES1 and 2ES2 is 120 kN. This compares with the experimental ultimate shear loads of 171.3 kN for 2ES1 and 160.2 kN for 2ES2. In the case of the tension face plated beam, the theoretical shear peeling strength for shear spans 2FS1 and 2FS2 are 123 kN and 136 kN. The corresponding test shear loads were 250.2 kN and 286.2 kN. The large discrepancy between the theoretical shear peeling strengths and the shear capacity of the beams is due to the fact that the actual failure did not occur by shear peeling as the external plates were fully anchored.

17.9 Concluding remarks

1. In case of the tests carried out on the side plated beams, the side plates peeled off in the identical tests 2ES1 and 2ES2 in which the beam was tested under a single concentrated load with a shear span to depth ratio of 3.2. On the other hand, failure was due to the crushing of concrete under load point in test 2E where the beam was tested under four point loading. However, the difference in the ultimate moment at failure for both cases was negligible.
2. The beam with the fully anchored tension face plated beam failed in the same fashion irrespective of the loading arrangement in the three different tests. The debonding cracks were formed well before the failure due to the crushing of concrete. The debonding cracks were localised and they did not propagate

towards the support. As in the tests on the side plated beam, the difference in ultimate moments at failure was negligible.

3. The procedure developed for calculating the flexural capacity of the plated in beams in Chapter-16 can be used to compute the flexural strength of the fully anchored plated beams. However, the procedure overestimates the strength by 10% in case of the side plated beam.

References

Ahmed,M .(1996). Strengthening of reinforced concrete beams by bolting side plates to their sides, Master of Engg.Sc. thesis, The University of Adelaide, Adelaide, October 1996. 390 pages.

PART-VII: CONCLUSIONS

CHAPTER-18: CONCLUSIONS

CONTENTS

18.1 Introduction

The findings contained within this thesis are explained in this chapter. In this study, the aspects pertaining to debonding of adhesively bonded steel plates and FRP plates were critically investigated. The following four major debonding modes were studied.

- The first major area of research was shear peeling in external plates of various configurations and the development of comprehensive analytical procedures to quantify the pure shear peeling strength of plated beams.
- The second area of study was flexural peeling of compression face plated beams and a comparison of flexural peeling between steel and FRP plated beams.
- The third major area was the interaction between the flexural and shear peeling modes in both compression face plated beams and side plated beams.
- Lastly, the fourth major area of study was axial peeling in deep side plated beams and beams bonded with anchored shallow side plates or anchored tension face plates.

The conclusions and findings from each of these major areas of study are summarised in the subsequent sections.

18.2 Studies on shear peeling mechanisms

18.2.1 Shear peeling in side steel plated beams

In this investigation, shear peeling of side plated beams were compared with that of tension face plated beams. The main parameters varied were the position of the side plates and the effect of shear stirrups on shear peeling. The following four major conclusions were arrived at from these tests conducted on the shear peeling in beams bonded with steel plates to their sides:

- firstly, the shear peeling in both side plated beams and tension face plated beams was always caused by the formation of a critical diagonal shear crack.
- secondly, the shear peeling strength of tension face plated beams was about 63% greater than the shear strength of the unplated reinforced concrete beam without shear stirrups, and placing the plates on the sides of the beams further improved the shear peeling strength by about 12% .
- thirdly, it was shown that the presence of stirrups has virtually no effect on shear peeling in side plates when the mean strains in the plate are tensile. However, the stirrups enhance the shear peeling strength when the strain is compressive.
- finally, the shear peeling resistance was shown to depend on the vertical position of the plate.

18.2.2 Shear peeling in side FRP plated beams

Under this investigation, the shear peeling mechanism in reinforced concrete beams bonded with shallow FRP plates to the sides was compared with that of steel plated beams. The major parameter varied was the elastic modulus of the external plates. These tests have shown that the shear peeling failure mechanism is qualitatively the same both for steel plates and FRP plated beams. However, the shear peeling strength increases with the decrease in the longitudinal elastic modulus of the plate material for the same area of cross section of the side plates. This is revealed by the fact that in plated beams with a very low plate modulus, the shear peeling strength is nearly the same as the ultimate shear strength of the unplated concrete beam with stirrups. In contrast, the steel plated beams debonded at a shear load only 25% higher than the shear strength of the unplated concrete beam without stirrups (V_{uc}).

18.2.3 Shear peeling in beams bonded with steel angles to their sides and tension faces

Tests on reinforced concrete beams bonded with steel angles have shown that the shear peeling mechanism is similar to that observed in side plated beams. That is to say, debonding is always caused by the formation of a critical diagonal crack and shear peeling occurs well before the internal shear stirrups are fully mobilised. However, the shear peeling strengths were 200 to 230 % higher than the shear strength of unplated concrete beam without stirrups (V_{uc}). Furthermore, the beam with a deeper angle carried about 20% more shear load, even though the total area of the angles was about 40% more than that of the shallow angles.

18.2.4 Shear peeling of compression face plated beams

Under this study, tests were carried out to compare the shear peeling mechanism of compression face plated beams with that of tension face plated beams. The main parameter varied was the thickness of the external plates used. Shear peeling of tension face plated beams occur by the formation of critical diagonal cracks in the vicinity of the plate end and their instantaneous propagation towards the load point. On the other hand, the complete shear peeling of compression face plated beams occurred in the following stages:

- the formation of the critical diagonal crack
- the extension of the critical diagonal crack along the bottom edge of the plate towards the load point.
- finally, complete shear peeling occurred due to the formation of a secondary debonding crack which propagated from the load point to the plate end for

comparatively thin plated beams or a secondary diagonal crack that propagated towards the support for the thick plated beams.

The other major conclusion from this study is that in both tension as well as compression face plated beams, shear peeling occurred at a shear load that was less than the ultimate shear strength of the reinforced concrete beam with shear stirrups. However, these shear peeling strengths were 50-100% more than the shear strength of the unplated concrete beam without shear stirrups (V_{uc}). Moreover, the shear peeling strengths of the compression face plated beams were about 30% more than that of the tension face plated beams, for the tests conducted under this study. The effect of plate thickness on the shear peeling strength of compression face plated beams was also found to be negligible.

18.3 Analytical procedures for computing shear peeling strength

The major outcome of this thesis is the development of a series of mathematical models using the shear friction and crack sliding failure concepts, to analyse the shear peeling phenomenon in steel plated beams of any configurations. All the models were validated using the test results from this thesis and other results from the literature. The procedures were generally developed for simply supported beams subject to a single concentrated point load. Nonetheless, it is shown in the thesis how these procedures can easily be modified to cater for uniformly distributed loads and different support conditions. As a first step, a procedure was developed to quantify the bond strength or axial peeling resistance of the plates due to the critical dependence of the shear peeling resistance in plated beams on the bond strength. This bond strength procedure in conjunction with the crack sliding model, for the shear strength of non-shear reinforced concrete beams, was used to develop a series of shear peeling mathematical models for a variety of steel plated

beams. This hybrid procedure recognizes the significance of the formation of a critical diagonal shear crack that can occur anywhere in the beam and the subsequent failure by sliding along the plane of the critical crack. It also incorporates the resistance provided by the external plates both to the crack formation and to the shear failure and the resulting debonding along the crack plane. The following are the major outcomes from this aspect of the study.

1. The shear peeling model for beams bonded with steel side plates is capable of accurate prediction of the shear peeling strength irrespective of the location of the plate along the depth of the beam. The only restriction placed is that the plate should be either within a predominantly tensile region or else a nominal amount of internal shear stirrups should be present which is the normal case.
2. Two procedures were developed to quantify the shear peeling strength of tension face plated beams. The first one is a general procedure, similar to the one developed for side plated beams as described in the part 1 above, as it can be used for any location of the plate end. The other procedure is a simple approximation which recognizes the fact that when tension face plate ends are terminated very close to the support, the shear load to cause peeling is closely approximated by the shear load to cause a diagonal crack at the plate end. The constraints in the test data used for calibrating the second procedure were also stated.
3. The procedure developed for angle plated beams represents an angle as a combination of a side plate and a soffit plate. Therefore, the equations developed for side and tension face plated beams were used to develop a shear peeling model for angle plated beams. The method shows a good correlation with the test results.

4. As tests showed that the shear peeling of compression face plated beams involves the following three stages, a procedure was developed to predict the shear load to cause these three milestones:
   - firstly, the shear load to cause the formation of a main diagonal crack away from the support was modelled as the shear strength of the unplated beam.
   - secondly, the shear load at the propagation of the main diagonal crack along the bottom edge of the plate to the load point can be obtained by adopting a similar procedure developed for tension face plated beams.
   - finally, the shear load at the completion of debonding was found to be the shear load to cause a diagonal crack from the support to the load point.
5. The improvement in the shear peeling strength of tension face plated beams due to bonding additional side plates were quantified by two empirical procedures, namely, the element strength approach and the shear strength approach. Based on a comprehensive series of tests, the improvement in shear peeling strength was found to lie between 6% of the bond strength and 15% of the yield strength of the two side plates, when the bond length lies within 80-200% of the depth of the side plates. However, the shear strength approach that tries to modify the equation for V_{uc} in most codes of practice was found to be unsuitable. To overcome these limits of the empirical methods, the sliding crack model approach was used to develop a general analytical procedure. In this method, the improvement in the shear peeling strength due to side plates was quantified as the resistance by the side plates to the propagation of a diagonal crack that originates at the tension face plate end that is predominantly

under shear. The theoretical formulation was found to have excellent correlation with test results.

6. The effect of additional side plates on the peeling strength when the tension face plates are terminated in shear/flexure regions was studied by computing both the pure flexural peeling capacity and the pure shear peeling resistance. These were used to develop interaction diagram that can be used in design.
7. A research of the literature showed that no generic model exists for axial peeling of FRP plates, as the models that are available are material dependent. This is an impediment in extending the existing models for steel plates to cover FRP plated beams.
8. Finally, it was shown that the procedures developed for beams under concentrated loads can be modified for beams subject to uniformly distributed loads. This was demonstrated for the case of side plated beams and tension face plated beams.

18.4 Flexural peeling mechanisms

18.4.1 Flexural peeling of steel plates bonded to the compression face of reinforced concrete beams

In this study, tests were carried out to compare the flexural peeling mechanism of compression face plated beams with that of tension face plated beams. The major parameter varied in this study was the thickness of the external steel plates. The pure flexural peeling moments of compression face plated beams have been quantified, and the compression face plated beams have been found to be 2.3 times stronger in pure flexural peeling than their corresponding tension face plated beams. This was established from test results that covered a wide range of parameters such as the thickness of the plates that

varied from 10 mm to 25 mm and the moment of inertia of the cracked plated section that ranged between 2.2 x 10^7 mm^4 and 159 x 10^7 mm^4.

18.4.2 Flexural peeling of FRP plates bonded to the tension face or sides of RC beams

In this study, the flexural peeling behaviour of RC beams bonded with FRP plates to the tension faces or sides were compared with that of steel plated beams. The major parameters varied in the study were the thickness and elastic modulus of the plates and hence, the plate stiffness. The tests have shown that the peeling mechanism is the same both for steel plated beams and FRP plated beams.

In the case of the side plated beams, the flexural peeling mechanism can be considered to be smooth and gradual as the fall in the strain readings occurred over a wide range of applied moment. Furthermore, the plate end cracks that impair the bond between the plate and the concrete propagated steadily and stabilised for a long period before the end of the tests. Two tentative relationships were also suggested for computing the pure flexural peeling strength of tension face plated beams and side plated beams. These relationships show that FRP plates are less likely to debond than steel plates.

18.5 Interaction between shear and flexural peeling modes

18.5.1 Interaction between flexural and shear peeling in compression face plated beams

In this study, the peeling behaviour of beams bonded with steel plates to the compression face when the plate ends are terminated in a region where both shear forces and bending moments are present was investigated. The study was conducted in two groups. Group I in which the plate ends are subjected to a smaller bending moment than in the other

regions of the plate which represents a plate on the compression face of a sagging moment region. In GroupII, the plate ends were at a higher moment than in the other locations of the plates which represents a tension face plate in the hogging moment region in continuous beams that is extended to the sagging moment region. The test results showed that there is no detrimental interaction between flexural peeling and shear peeling. In fact in Group II beams, the formation of a critical diagonal crack in the unplated region was beneficial as it relieved the curvatures at the plate end and hence enhanced the flexural peeling strength.

18.5.2 Interaction between flexural and shear peeling in side plated beams

In this study, the interaction between the shear and flexural peeling failure modes for beams bonded with steel plates to the sides was investigated and the interaction was shown to be negligible, unlike the interaction originally proposed by Oehlers, Nguyen and Bradford (Section 2.8.1.2).

18.6 Axial peeling

18.6.1 Beams bonded with deep side plates

The only parameter varied in this experimental study was the depth of the side plates, which were bonded from support to support of the simply supported beams. This study on reinforced concrete beams bonded with full length deep side plates has shown that axial peeling is a gradual process and hence the plated beams behaved in a ductile fashion. Adequate warning of impending debonding was available as the strains recorded at the instance of debonding were in the order of 8000-15000 microstrains. The maximum moment that can be sustained by these deep side plated beams is governed by the tension reinforcing bars just reaching their yield strain. Beyond these strains, the

tensile forces in the beams are shed rapidly to the plates inducing axial peeling of the plates.

18.7 Summary

The major contribution of this thesis is towards the development of design rules for shear peeling, axial peeling and interaction between shear and flexural peeling in steel plated beams. These design rules can be used with existing procedures for flexural peeling to produce a comprehensive design package for adhesively bonded steel plating that can now be used in practice. The research also showed that steel and fibre reinforced plastic (FRP) plated beams exhibit the same peeling mechanisms and tentative design rules have been developed for peeling of FRP plated beams.